Sapienza Università degli Studi di Roma

Doctoral School "Vito Volterra"
PhD Thesis in Earth Sciences

A Dissertation in Igneous Petrology
GEO/07 – XXXIII cycle

PETROGENESIS OF THE CENOZOIC MAGMATISM IN NORTH-WESTERN IRAN

Giulia Salari

Supervisor
Prof. Michele Lustrino
Sapienza Università di Roma

Co-Supervisor
Dr. Samuele Agostini
IGG-CNR Pisa

15th March 2021

Revised by:

Prof. Andrea Marzoli
Dipartimento di Geoscienze
Università degli Studi di Padova
Via G. Gradenigo 6 - 35131 Padova, Italia

Dr. Michele Mattioli
Dipartimento di Scienze Pure e Applicate (DiSPeA)
Università degli Studi di Urbino "Carlo Bo"
Via Ca' Le Suore 2-4 - 61029 Urbino (PU), Italia

Petrogenesis of the Cenozoic magmatism in the north-western Iran
PhD thesis. Sapienza University of Rome

Author's mail: giulia.salari@uniroma1.it

"For what it's worth…
It's never too late to be whoever you want to be.
There's no time limit, start whenever you want.
You can change or stay the same,
There are no rules to this thing.
We can make the best or the worst of it.
I hope you make the best of it.
And I hope you see things that startle you.
I hope you feel things you never felt before.
I hope you meet people with a different point of view.
I hope you live a life you're proud of.
If you find that you're not,
I hope you have the courage to start all over again."

Eric Roth

TABLE OF CONTENTS

List of Acronyms iii

Abstract 1

Aim of the PhD project and structure of the thesis 3

Introduction and state of the art 5

- Alkaline ultrabasic magmatism 6
- Investigating adakitic signatures 9

Geological setting 11

Analytical techniques 18

CHAPTER 1 – TAFRESH.....20

1.1 Sampling area 20

1.2 Results 22

1.2.1 Petrography 22

1.2.2 Whole rock geochemistry 25

1.3 Discussion 37

1.3.1 Magmatic lineages and differentiation processes in the Tafresh area.....38

1.3.2 Genesis of the strongly evolved rocks from the Tafresh area 40

1.3.3 Genesis of the Tafresh evolved rocks with adakitic geochemical fingerprint 41

1.3.4 Geodynamic implications 44

1.4 Conclusions 45

CHAPTER 2 – NOWBARAN 47

2.1 Sampling area 47

2.2 Petrography 50

2.3 Mineral chemistry 52

2.4 Major oxide content and variation 56

2.5 Mineralogical-geochemical classification 57

2.6 Trace element content and normalized diagram 59
2.7 Sr-Nd-Pb isotope ratios 63
2.8 Discussion 64
2.8.1 Fractional crystallization and crustal contamination 64
2.8.1.1 Interaction with sedimentary carbonates 67
2.8.2 The Nowbaran rocks in the context of the Bitlis-Zagros Orogen.....69
2.8.3 Carbonated-peridotite origin 69
2.8.4 Hornblendite-derived origin 70
2.8.5 Metasomatic phase (amphibole, phlogopite, apatite) constraints 72
2.8.6 P-T conditions of formation 74
2.8.7 Geodynamic setting derived from petrological considerations 77
2.9 Conclusions 81
CHAPTER 3 – BIJAR-QORVEH 83
3.1 Sampling area 83
3.2 Results 85
3.2.1 Petrography.....85
3.2.2 Mineral chemistry 94
3.2.3 Whole-rock chemistry 100
3.2.4 Sr-Nd-Pb isotopes 110
3.3 Discussion 112
3.4 Conclusions 120
Concluding remarks 121
References 124
Appendix Tables.....150
Supplementary Material S1 181
Supplementary Material S2 189

LIST OF ACRONYMS

UDMA	Urumieh-Dokthar Magmatic Arc
SSZ	Sanandaj-Sirjan Zone
ZFTB	Zagros fold-and-thrust Belt
ISA	Iran and SE Anatolia Cenozoic Igneous Rocks
ICP-AES	Inductively-Coupled Plasma Atomic Emission Spectrometry
ICP-MS	Inductively-Coupled Plasma Mass Spectrometry
EMPA	Electron Microprobe Analyses
IEC	Ion Exchange Chromatography
TIMS	Thermal Ionization Mass Spectrometer
MC-ICP-MS	Multi-collector Inductively-Coupled Plasma Mass Spectrometer
LILE	Large Ion Lithophile Elements
HFSE	High Field Strength Elements
LREE	Light Rare Earth Elements
MREE	Medium Rare Earth Elements
HREE	Heavy Rare Earth Elements
GLOSS	Global Subducting Sediments
HiMU-OIB	High-Mu Ocean Island Basalts
DMM	Depleted Morb Mantle
EM-I	Enriched Mantle I
EM-II	Enriched Mantle II
MORB	Middle Ocean Ridge Basalts
BSE	Bulk Silicate Earth
ChUR	Chondritic Uniform Reservoir
NHRL	Northern Hemisphere Reference Line

ABSTRACT

A petrological study has been conducted on three volcanic districts (Tafresh, Nowbaran and Bijar-Qorveh) of NW Iran with the purpose to give a contribution to the scientific community about the tectono-magmatic framework of the Arabia-Eurasia collision zone. These volcanoes belong to the so-called Urumieh-Dokthar Magmatic Arc (UDMA) running from NW to SE along the western margin of Iran, whose volcanism is related to the NE-ward Neotethys Ocean subduction beneath the Iranian plate since Early Cretaceous time, evolved into Arabia-Iran continental collision during early Cenozoic.

Tafresh investigated rocks mainly range from basaltic andesites to rhyolites and are probably linked to closed-system magma evolutionary processes. Such processes involved fractionation of i) mainly ferromagnesian minerals and plagioclase, followed by ii) removal of plagioclase and lesser amphibole (with minor clinopyroxene) and finally iii) lesser alkali feldspar and minor amphibole in the most evolved terms. LILE-enriched and HFSE-depleted geochemical signature (likely originated from a hydrous primitive melt equilibrated with a spinel-bearing peridotite source) inferred the typical subduction-related trend emplaced in a subduction-related setting. Strongly evolved rocks are supposed to be derived from crustal anatexis of a mixed meta-sedimentary source. One sample shows distinctive adakitic signature (high La/Yb and Sr/Y ratios, low Yb and HFSE contents) which are interpreted as the product of the melting of a meta-mafic source rock (i.e., subducted oceanic slabs) with residual garnet and amphibole.

Differently, Nowbaran Quaternary melanephelinites result by far the most peculiar igneous rocks of the entire Bitlis-Zagros Orogen. The absence of feldspars and melilite is coupled with extremely low SiO_2 content and very high CaO and Al_2O_3 abundances, leading to ultracalcic compositions. Moreover, these rocks show high Mg# and very high Ni and Cr values, which likely suggest a primitive character of these melts. Isotopic ratios and primitive-mantle normalized pattern indicate hybrid sources, as their trend exhibits subduction-related imprinting mixed with HiMU-OIB features. Such uncommon compositions are thought to be unlikely derived from a classic four-phase (i.e. C-H-free) peridotitic mantle or from digestion of carbonatic compositions. More likely, they are generated from carbonated apatite-hornblendite-rich metasomes which are

considered as the products of interaction between peridotitic matrix and partial melts derived from arc cumulates (formed by crystallization of hydrous and CO_2-bearing magmas generated during previous subduction-related arc).

On the other hand, two main volcanic cycles have been recognized in Bijar-Qorveh area. Upper Miocene (~9.2-8.3 Ma) compositions mostly range from trachy-andesites to trachytes (with minor rhyolitic terms) whereas Pleistocene (~1.3-0.5 Ma) samples are mostly represented by trachybasalts and tephrites, with lesser alkali basalts. Major and trace elements of Miocene rocks (i.e., Dehgolan and Qorveh) likely suggest fractional crystallization of ferromagnesian minerals then followed by removal of plagioclase and amphibole. These rocks exhibit high-K calcalkaline affinity, as also shown by primitive mantle-normalized patterns characterized by strong LILE and LREE enrichments, typical of subduction-related magmas. Only three Dehgolan samples show by far higher K_2O-TiO_2-P_2O_5 and Rb contents, which are thought to be related to a Ti-phlogopite-rich source rock. Quaternary samples (i.e., Qezelke Kand, Bijar and Takab) consist of alkaline series showing mainly sodic to strictly potassic (i.e. Takab) affinity. They show high Mg#, Ni and Cr content which probably is indicative that primary magma was not affected by extensive fractionation. Moreover, isotopic ratios and incompatible multielemental patterns show mixed features of both intraplate-like and subduction-related end members. Takab rocks always cluster distinctly, showing higher K_2O and Rb abundances which could be linked to a phlogopite-rich mantle source. Noteworthy, Qezelke Kand outcrops are characterized by the association of basic products with four high silica rocks which have been referred to as adakites, likely deriving from the melting of subducted basalts in eclogite facies. Bijar-Qorveh Miocene high-K volcanic products represent the final magmatic phase of the calcalkaline volcanism occurring in Central Iran during Tertiary period, whereas Quaternary basic magmatism is to be considered as the expression of regional tensional tectonics or related to variations in the source mineralogy during melting processes.

AIM OF THE PhD AND STRUCTURE OF THE THESIS

Aim of the PhD project is the investigation of three volcanic districts in NW Iran (Nowbaran, Tafresh and Bijar-Qorveh areas; Fig. 1) in terms of petrographic characterization, major and trace elements and isotopic compositions, with the purpose to better understand the mechanisms governing the petrological evolution of the Cenozoic magmatic system in western Iran.

The PhD thesis is divided in three main chapters:

- **Chapter 1** is a paper in press in "Periodico di Mineralogia" (2021) about Tafresh volcanic area. The paper has been written by Giulia Salari (Dipartimento di Scienze della Terra, Sapienza Università di Roma) in collaboration with Michele Lustrino (Dipartimento di Scienze della Terra, Sapienza Università di Roma), Mohammad Reza Ghorbani (Department of Geology, Tarbiat Modares University, Tehran), Samuele Agostini (CNR – Istituto di Geoscienze e Georisorse, Pisa) and Lorenzo Fedele (Dipartimento di Scienze della Terra, dell'Ambiente e delle Risorse, Università degli Studi di Napoli Federico II).

- **Chapter 2** is a paper submitted at "Journal of Petrology" about Nowbaran volcanic zone. This paper has been written by Michele Lustrino (Dipartimento di Scienze della Terra, Sapienza Università di Roma), Giulia Salari (Dipartimento di Scienze della Terra, Sapienza Università di Roma), Bahman Rahimzadeh (Department of Geology, Shahid Beheshti University, Tehran), Samuele Agostini (CNR – Istituto di Geoscienze e Georisorse, Pisa), Lorenzo Fedele (Dipartimento di Scienze della Terra, dell'Ambiente e delle Risorse, Università degli Studi di Napoli Federico II) and Fariborz Masoudi (Department of Geology, Shahid Beheshti University, Tehran).

- **Chapter 3** is a manuscript in preparation about Bijar-Qorveh volcanic field.

Concluding remarks resume the three chapters, exposing the main findings and the final discussions of the thesis.

Following Appendix Tables include whole-rock compositions, Sr-Nd-Pb isotopic ratios and Electron Microprobe Analyses of Chapters 1-3.

Supplementary Material S1 contains Chapter 2 (Nowbaran) experimental procedures of high-pressure forced multiple saturations which have been performed at the Institute of Geochemistry and Petrology (D-ERDW) at ETH Zürich, in collaboration with Prof. Max W. Schmidt.

Supplementary Material S2 is the paper "Leucitites within and around the Mediterranean area" written by Lustrino M., Fedele L., Agostini S., Prelević D. and Salari G. and published in *Lithos*, 2018, Vol. 324-325, pp. 216-233.

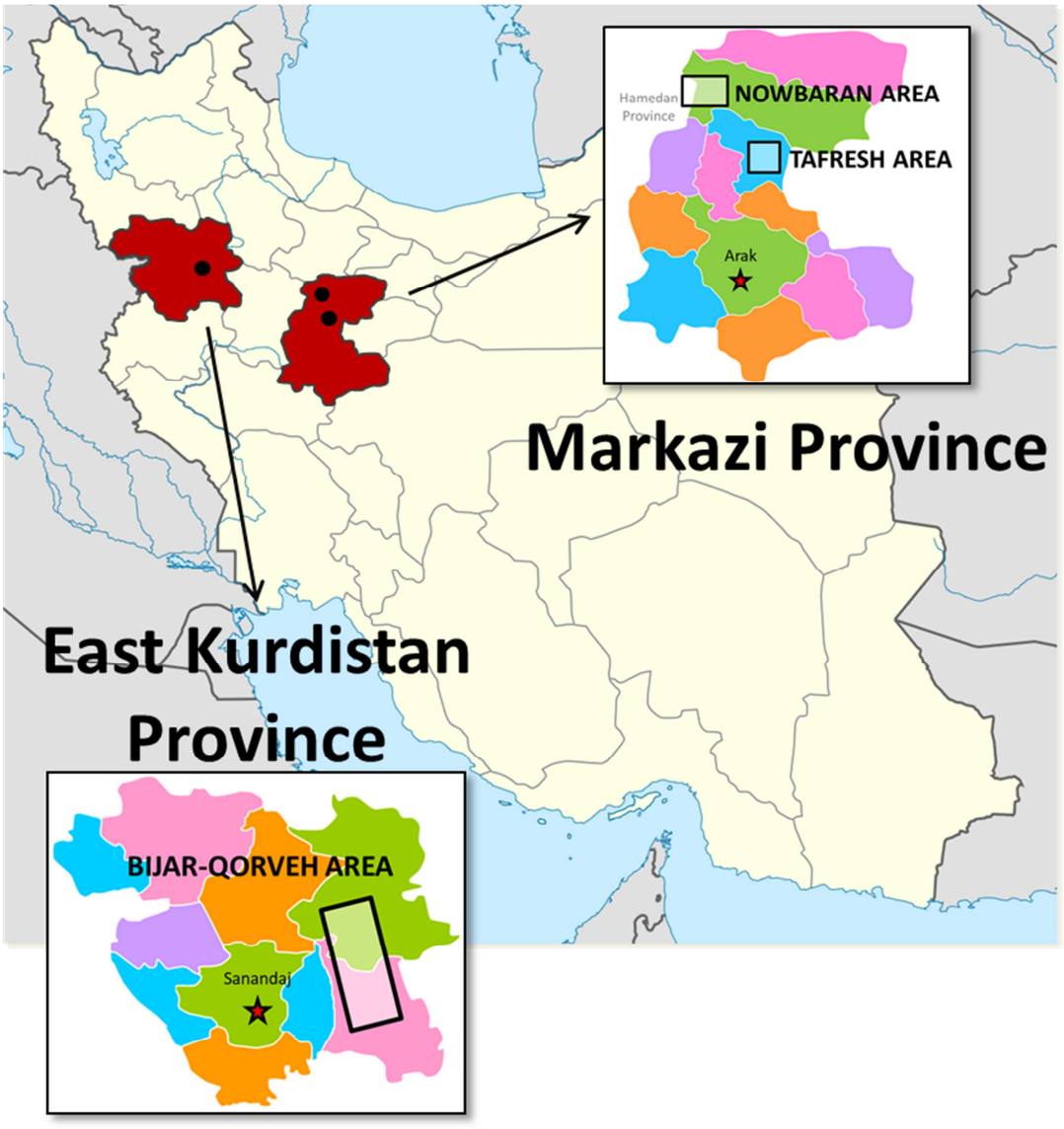

Fig. 1: *Geographic map of the studied regions (East Kurdistan and Markazi Provinces) in NW Iran. Black rectangles indicate the location of sampling sites.*

INTRODUCTION AND STATE OF THE ART

The Mediterranean Region is one of the world's most studied area and probably represents the most complex geodynamic settings on Earth. Its present-day geological configuration is the result of the creation and ensuing consumption of two major oceanic basins (i.e. Paleotethys and Neotethys) within an overall regime of prolonged interaction between the Eurasian and the African-Arabian plates (Cavazza and Wezek, 2003). The closure of these oceanic domains produced a system of orogenic belts which vary in terms of timing and tectonic setting (Cavazza and Wezek, 2003) and are interpreted as the end product of the Alpine-Himalayan orogenic cycle.

This complex scenario has been largely governed by several subduction zones and rifting environments (Carminati et al., 2012) where then magmatism and tectonics result strictly related.

As part of the Alpine-Himalayan Belt, the Zagros Orogen in western Iran has experienced an extremely complex geodynamic evolution, which stimulated a number of geological investigations on several interconnected topics dealing with geophysics, active tectonics, igneous and metamorphic response, as well as sedimentary evolution (Agard et al., 2005; Molinaro et al., 2005; Mouthereau et al., 2006, 2012; McQuarrie and van Hinsbergen, 2013; Koshnaw et al., 2018; Karasözen et al., 2019; Rabiee et al., 2020). Mesozoic-Cenozoic magmatism in Iran developed as a consequence of the NE-directed subduction of the Neotethyan oceanic lithosphere beneath the Eurasian plate which led to widespread volcanic products widely ranging for compositions, age and geographical distribution.

However, compared with its western (i.e. Alps) and eastern (i.e. Himalaya) counterparts, the Zagros Orogen remains less documented and numerous are the topics that still need to be solved (e.g. the timing of collision, the position of suture zone and the geochronological, chemical and spatial evolution of the igneous activity). In such a framework, multidisciplinary geological studies are extremely useful to unravel the uncertainties that still characterize the geodynamic reconstruction of the area, similarly to what has been instead proposed in the western Alpine-Himalayan Belt (e.g. Carminati et al., 2012; Faccenna et al., 2014; van Hinsbergen et al., 2020). A useful tool is represented by the petrological features inferred from petrography and whole-

rock geochemistry of the igneous rocks emplaced during the geological evolution of the orogenic belt. In the Zagros Orogen case, informations regarding the associated long-lasting magmatism occurring in the two subparallel NW-SE-oriented magmatic belts of the Sanandaj-Sirjan Zone and the Urumieh-Dokthar Magmatic Arc (covering more than 150 Myr; e.g. Omrani et al., 2008; Chiu et al., 2013), are however relatively limited.

Alkaline ultrabasic magmatism

The issue of alkaline ultrabasic rocks deserves some emphasis as these were found in one of the study area, i.e. Nowbaran (Chapter 2).

These very particular compositions did not found counterparts anywhere else in the entire Iranian plate and result completely different from the bulk of the Cenozoic andesitic-to-rhyolitic rocks cropping out in the Urumieh-Dokthar Magmatic Arc (hereafter UDMA, a >2000 long Cenozoic tectono-magmatic belt running NW-SE along the western margin of Iran (e.g., Rabiee et al., 2020; Chaharlang et al., 2020; Salari et al., 2020). UDMA compositions result embedded within an overall subduction-related framework and upper mantle partial melts generated in subduction systems are characterized by variable compositions, showing intermediate to acid SiO_2-oversaturated compositions with alkali content ranging from low (e.g. andesite to rhyolite association, Straub and Zellmer, 2012; Howe et al., 2015; Erràzuriz-Henao et al., 2019; Zheng, 2019), to high (with potassic to ultrapotassic affinities; e.g., Avanzinelli et al., 2009; Soder and Romer, 2018; Forster et al., 2019). UDMA rocks mostly have intermediate to acid compositions with subalkaline to mildly alkaline affinity, commonly with CIPW quartz- and hypersthene-normative mineralogy, whereas ultrabasic (i.e., <45 wt% SiO_2) and strongly SiO_2 undersaturated (i.e., CIPW larnite-normative) compositions are extremely rare if not completely absent.

Alkaline basic-ultrabasic compositions always drew the attention of researchers in igneous petrology field as their origin cannot be related to normal H- and C-free upper mantle paragenesis (e.g. Pilet, 2015; Tucker et al., 2019). Sodic and potassic variants of this volumetrically restricted field occur in different tectonic environments, such as continental and oceanic mid-plate settings, continental rifts as well as supra-subduction mantle wedges (e.g., Pilet, 2015; Lustrino et al., 2019a). These rocks are

mainly characterized by an enrichment of incompatible elements with respect to the primitive mantle, explained invoking tapping of sources at different depths, several styles of partial melting as well as variable volatile and lithology mixes in upper mantle regions.

Around the end of '60s and the beginning of '70s new experimental studies started to propose for strongly ultrabasic compositions partial melting conditions of ~3 GPa, T <1200 °C and *f* <5%, provided both H_2O and CO_2 are present (X_{CO2} <0.5; e.g., Green, 1969 CaO-rich compositions) do require the presence of carbonates in their mantle sources or at least interaction with carbonates at shallow depths (e.g., Lustrino et al., 2019b). This is reflected by the common association of these lithologies with plutonic and volcanic carbonatites (e.g., Mitchell, 2005; Woolley and Kjarsgaard, 2008; Tappe et al., 2020). The origin and the tectonic meaning of carbonatites have been debated for over 50 years (e.g., Mitchell, 2005; Yaxley et al., 2019). Essentially all the models require the obvious presence of mantle carbonates. Low degrees partial melting would generate dolomitic to magnesitic melts which are strongly reactive with the peridotitic matrix, making their reaching to the surface very hard (e.g., Hammouda and Keshav, 2015). Alternative (but overall similar) views include separation by immiscibility of CO_2-bearing SiO_2-poor/free liquids from CO_2-poor/free SiO_2-richer melts (e.g., Freestone and Hamilton, 1980, Amundsen 1987; Wallace and Green, 1988; Kjarsgaard and Hamilton, 1989; Baker and Wyllie, 1990; Lee and Wyllie 1994, 1997; Brooker, 1998; Harmer and Gittins, 1998; Dasgupta et al., 2006; Thomsen and Schmidt, 2008).

According to experimental petrology (Wyllie and Huang, 1975; Eggler, 1976; Eggler and Mysen, 1976; Wyllie, 1980; Falloon and Green 1989; Dalton and Presnall 1998; Presnall et al. 2002; Gudfinnsson and Presnall, 2005; Dasgupta and Hirschmann, 2006; Keshav and Gudfinnsson, 2013; Novella et al., 2014; Hammouda and Keshav, 2015) they can be produced by a carbonated peridotite through different partial melting degrees and different depth of source.

The *carbonate ledge* is a key feature of the CO_2-bearing peridotite solidus determined experimentally more than 50 years ago, marked by an abrupt decrease of solidus temperature at pressures ranging from ~2 to ~3 GPa (e.g., Wyllie, 1989). The sudden decrease of solidus temperature is determined by the appearance of dolomite in equilibrium with CO_2 vapor phase, forsterite, diopside and enstatite in an invariant

point whose exact position in T-P space is function of the overall chemical composition of the investigated ultramafic system, as well as the possible presence of other volatiles (e.g., Wyllie, 1989). In its most general view, volumes of upper mantle departing from the invariant point towards lower temperatures are characterized by the presence of dolomite + enstatite as the reacting products between CO_2 + olivine + diopside along the univariant line. At higher pressure (>3 GPa) a second carbonation reaction occurs, forming Mg-carbonate instead of Ca-Mg-carbonates according to the reaction: dolomite + enstatite = magnesite + olivine + diopside (e.g., Wyllie and Huang, 1976; Gudfinnsson and Presnall, 2005). Near-solidus partial melts at depths higher than the invariant point have carbonatitic compositions (e.g., Gudfinnsson and Presnall, 2005; Hammouda and Keshav, 2015). At pressures <2 GPa, these carbonatitic melts usually react with peridotitic matrix, exsolving CO_2 and consuming enstatite. The production of wehrlitic (i.e., enstatite-free) peridotitic fronts or channels allows stability of further carbonatitic melts at depths shallower than 2 GPa, eventually leading to the possibility of carbonatitic magma survive up to the surface.

Near-solidus partial melts of a carbonated peridotite at ~2-8 GPa (at corresponding T ~1000-1400 °C; Gudfinnsson and Presnall, 2005; Green, 2015) are carbonatitic (~40 wt% CaO and <10 wt% SiO_2) in compositions. These melts become richer in SiO_2 and poorer in CO_2 and CaO with increasing temperature as a consequence of the exhaustion of the carbonate component and the increased involvement of the main silicate and spinel phases in the melting process (e.g., Wyllie and Huang, 1975; Eggler, 1978; Falloon and Green, 1989; Gudfinnsson and Presnall, 2005; Dasgupta and Hirschmann, 2007; Foley et al., 2009; Hammouda and Keshav, 2015). A compositional transition, with a continuum from primary carbonatitic to melilititic (CaO ~25 wt% and SiO_2 ~25) and kimberlitic (CaO <20 wt% and SiO_2 ~30) melts with increasing temperature is experimentally demonstrated (e.g., Gudfinnsson and Presnall, 2005). Going farther from the solidus, the increasing melting temperature produces melts approaching nephelinitic and basanitic compositions (CaO ~10% wt% and SiO_2 ~40-45 wt%) and eventually alkali basalts at the highest degrees of partial melting (Hirose, 1997; Gudfinnsson and Presnall, 2005; Hammouda and Keshav, 2015). According to this view, the role of CO_2 in the genesis of “normal” alkaline basaltic magmas is minor, being this component strongly “diluted” in a volumetrically dominant peridotite-

derived melt flux. Thus increasing melting of carbonated peridotites is considered a relevant process to explain the genesis of SiO_2-undersaturated ultrabasic melts.

Investigating adakitic signature

Anomalous compositions referred to as adakites have been found both in Tafresh and Bijar-Qorveh studied areas. Adakitic compositions have been found throughout the Iranian magmatic arc: from northwest UDMA (Jahangiri, 2007; Azizi et al., 2014: Torkian et al., 2019) to the central part (Ghorbani and Bezenjani, 2011; Omrani et al., 2008) to southeast UDMA (Khodami et al., 2009; Omrani et al., 2008), thus it is worth investigating such unusual and particular compositions.

The term *adakite* was used for the first time by Defant and Drummond (1990) which refer to particular geochemical characteristics such as $SiO_2 \geq 56$ wt%, $Al_2O_3 \geq 15$ wt% (rarely lower), usually MgO < 3 wt% and low concentration of Y (≤ 18 ppm) and HREE (≤ 1.9 ppm). Other characteristics are also low HFSE and $^{87}Sr/^{86}Sr$ usually < 0.7040, suggesting an origin by melting of subducted basalts in eclogite facies. Martin (1986) introduced La/Yb and Sr/Y ratios as discriminating features of adakitic magmas, confirming a mafic source in which garnet and/or amphibole are residual phases (Rapp et al., 1991). The term adakite and the origin of such unusual compositions are still controversial as it is used in a variety of contexts. Moreover, they encompass compositions sometimes showing an extremely wide range of values, without any specific mineralogical or petrographic evidences that could allow their identification in regardless of the geochemical signature. Thus the genetic interpretation of these rocks is not yet well defined. In any case, two main hypotheses have been proposed for adakites petrogenesis, namely the melting of subducted oceanic slab (Defant and Drummond, 1990; Martin et al., 2005; Castillo, 2012), which remains the most accredited theory, and the melting of the lower crust by underplating or delamination (Petford and Atherton, 1996; Chung et al., 2003; Ma et al., 2012; Ribeiro et al., 2016). Thus definition of adakite actually encompasses both notions of pristine subducted slab melts and crustal melts which interacted with mantle peridotite (Castillo, 2006). Indeed some adakites show high-MgO values (and high Ni-Cr contents) which are may linked

to re-equilibration with peridotitic matrix during slab melts ascent (Rapp et al., 1999; Martin et al., 2005).

The UDMA likely experienced a transition from calcalkaline to adakitic magmatism during the final stages of subduction with a southeastward migration of adakitic activity (Oligo-Miocene in the NW UDMA, Early Miocene in the central part and Middle to Late Miocene in the SE UDMA; Chiu et al., 2013; Kouhestani et al., 2017) which is commonly interpreted to be a consequence of the crustal thickening due to the diachronous continental collision (Chiu et al., 2013). Moreover, these rocks usually result associated with high-Nb basalts (HNB) which whose formation is thought to be linked to similar metasomatic processes originated from slab melts (Sajona et al., 1994; Wang et al., 2006), namely melting of mantle wedge peridotite extensively metasomatized by slab-derived melts (and after the releasing of HFSE due to amphibole breakdown).

However the current literature on adakite becomes confusing because of the wide range of compositions and tectonic environments which do not allow direct identification in the processes involved in the genesis of these rocks. The origin of this term has been extensively debated over the past decades (Martin, 1986; Defant and Drummond 1990; Schiano et al., 1995; Castillo et al., 2007; Ribeiro et al., 2016) but nevertheless, their investigations have certainly enriched our understanding of material recycling at subduction zones and crustal evolutionary processes (Castillo, 2006).

GEOLOGICAL SETTING

The present-day geological framework of Iran belongs to the complex tectonic setting seeing the formation and evolution of the Mediterranean region, the eastward escape of the Anatolian plate directions (e.g. Bitlis-Zagros fold-and-thrust belts), overall grouped in the Alpine-Himalaya Orogenesis (Fig. 2).

Fig. 2: *Tectonic setting of the Arabia-Eurasia collision zone in the Eastern Mediterranean region. Velocities of Arabia with respect to Eurasia are also shown after ArRajehi et al., (2010). From Zhang et al., (2018).*

Turkey, Iran, Afghanistan and the terranes of Tibet were once the main components of the Cimmerian continent postulated by Sengör et al., (1984). These continental fragments peeled off the northern margin of Gondwana in Late Permian time and accreted to the southern margin of Eurasia by the end of Triassic (Dewey et al., 1973; Alavi, 1994; Ramezani and Tucker, 2003; Pang et al., 2004) during the so-called Cimmerian Orogeny (Fig. 3).

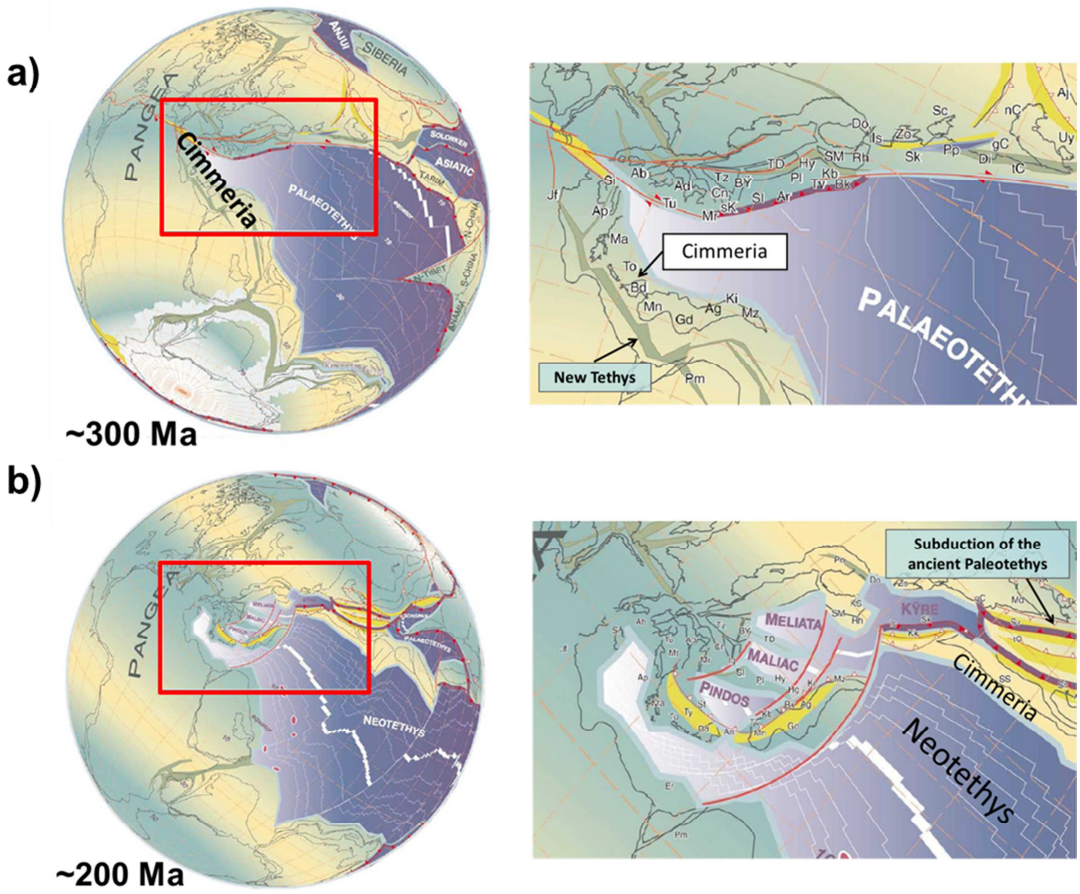

Fig. 3: *a) Cimmeria continent as Gondwana Superterrane during Early Permian time (~300 Ma). b) Cimmeria continent separated from northern Gondwana and collided with southern margin of Eurasia around Late Triassic time (~200 Ma) as Neotethyan Ocean opened and Paleotethys nearly completely subducted. Ab, Alboran; Ad, Adria; Ag, Aladag; Aj, Ajat; Ap, Apulia; Ar, Arna accretionary complex; Bd, Beydaghlari; Bk, Bolkardag; By, Beyshehir; Cn, Carnic-Julian; Do, Dobrogea; gC, great Caucasus; Gd, Geydag; Hy, Hydra; Is, Istanbul; ; Jf, Jeffara rift; Kb, Karaburun; Ki, Kirshehir; Ma, Mani; Mn, Menderes; Mr, Mrzlevodice fore-arc; Mz, Munzur dag; nC, north Caspian; Pl, Pelagonian ; Pm, Palmyra rift; Rh, Rhodope; Si, Sicanian; Sk, Sakarya; sK, south-Karawanken fore arc; Sl, Slavonia; SM, Serbo-Macedonian; tC, Transcaucasus; TD, Trans-Danubian; To,Talea Ori; Tu, Tuscan ; Tv, Tavas+Tavas seamount;Tz, Tizia. After Stampfli and Borel (2002).*

The NE-directed continental drift of Cimmeria is coupled with the opening of the Neotethyan Ocean during the Late Permian time and the consequent closure of the ancient Paleotethys Ocean during Late Triassic (Davoudzadeh and Schmidt, 1984; Stampfli and Pillevuit, 1993; Stampfli and Borel, 2002; Hassanzadeh et al., 2008; Wilmsen et al., 2009; Verdel et al., 2011; Stampfli et al., 2013) along the border of the Central-East-Iranian Microcontinent (CEIM). The closure of the Paleotethys Ocean is

identifiable in a discontinuous suture zone now cropping out along northern and eastern Iran from Alborz Mountains (south of Caspian sea) to Binalud Mountains (close to the boundary with Afghanistan and Turkmenistan; Fig. 4).

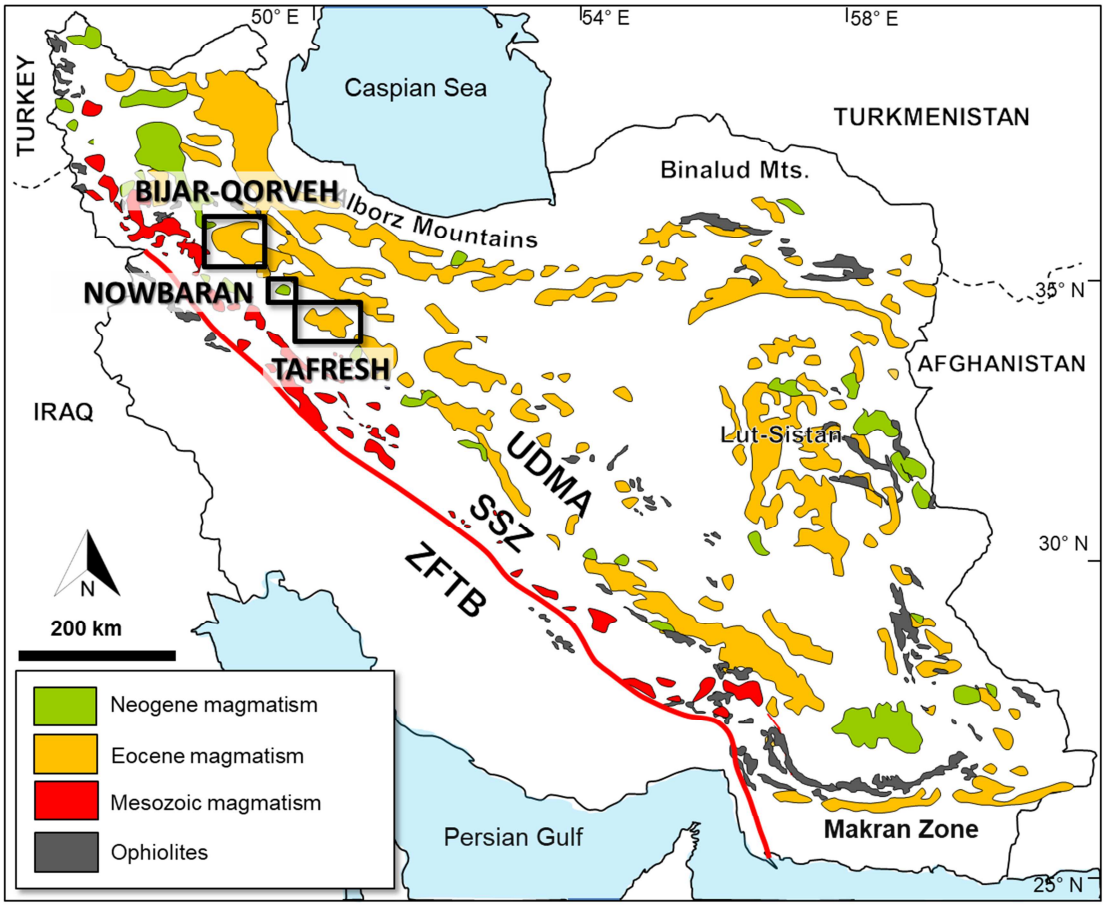

Fig. 4: *Simplified geological sketch map of Iran (after Shafaii Moghadam et al., 2016) with black rectangles indicating the location of the study areas (Tafresh, Nowbaran and Bijar-Qorveh).*

As consequence of the Late Jurassic-Early Cretaceous South Atlantic Ocean opening and the following counter-clockwise rotation of Africa-Arabia, Neotethys oceanic domain evolved to a diachronous collision of the Arabian plate along the southern Eurasian plate represented by the Gondwana-derived Iranian micro-continents (Dewey et al., 1973; Alavi, 1980, 1994: Berberian and King, 1981; Sengör, 1984, 1988; Pang et al., 2004; Agard et al., 2005).

From Cretaceous to the present, the continuous convergence between Arabian and Iranian plates has been accommodated by progressive continental crust thickening and

shortening (Berberian and King, 1981; Hassanzadeh and Wernicke, 2016). The continent-continent collision led to the formation of the E-W trending Bitlis Orogen in northernmost Arabia-Anatolia and of the NW-SE trending Zagros Orogen along the NE Arabia-SW Iran zones (Dewey et al., 1973; Sengör and Yilmaz, 1981 Yilmaz et al., 1993; Alavi, 1994; Parlak, 2006; Agard et al., 2011; Robertson et al., 2013). The exact timing of such collisional event is still debated, as several different lines of evidence provide estimates spanning a ~175 Myr time interval [i.e. from Late Triassic to Miocene; Agard et al., (2011); Verdel et al., (2011); Koshnaw et al., (2018)]. But detailed zircon U-Pb age data on the igneous products associated with this phase argue for an oblique convergence, which thus resulted in a progressively younger onset of the continental collision from NW to central up to SE Iran (from ~22 to ~10-6 Ma; Chiu et al., 2013). This is also in line with present-day kinematic data indicating Arabia-Eurasia convergence of ~20-30° oblique to the Zagros Orogen (Masson et al., 2007) and with the oceanic subduction being still active in the Makran zone at the south-easternmost tip of Iran (Burg, 2018).

Such a complex geodynamic evolution led to diffuse calcalkaline magmatism throughout time, developed along the western margin of Iran during latest Triassic-Early Jurassic time, culminating at ~170 Ma (Hassanzadeh and Wernicke, 2016). Other igneous districts related to the Arabia collision crop out in eastern Anatolia (e.g. Di Giuseppe et al., 2017; Karaoglu et al., 2020), the Lesser Caucasus/Alborz belt (northern Iran, where it merges with north-western UDMA; e.g. Asiabanha and Foden, 2012), Central Iran and the Lut-Sistan region (easternmost Iran; e.g. Pang et al., 2013).

The Zagros Orogen represents a NW-SE trending fold-and-thrust belt which extends from the Anatolian-Iranian border to the Makran area (Ellouz-Zimmermann et al., 2007; Smith et al., 2010b), with an overall SW-directed tectonic transport associated to the NE-directed oceanic subduction prior to the continental collision. The Zagros Orogenic Belt in western Iran is classically divided into three main NE-SE-directed tectono-magmatic units running parallel to each other (Fig. 4): 1) the Zagros fold-and-thrust belt (hereafter ZFTB), 2) the Sanandaj-Sirjan Zone (SSZ) and 3) the Urumieh-Dokthar Magmatic Arc (UDMA; Alavi, 1994; Mohajjel and Fergusson, 2000; Azizi and Jahangiri, 2009). The SSZ and UDMA zones belong to the hanging-wall plate (i.e. Eurasia) whereas the ZFTB represents the deformed Phanerozoic cover belonging to

the foot-wall plate (i.e. Arabian foreland; Agard et al., 2011). The Main Zagros Thrust is considered as the main suture zone defining the boundary between the Arabian and the Iranian plates (Stöcklin, 1968; Agard et al., 2005, 2006, 2011).

The ZFTB forms the most external part of the orogen and mainly consists of faulted and folded Paleozoic and Mesozoic successions (~4-7 km thick) overlain by Cenozoic silicoclastic and carbonate rocks (~3-5 km thick; Mehdipour Ghazi and Moazzen, 2015). The SSZ contains the most extensive and best preserved record of key events in the formation and evolution of the Neotethyan Ocean (Hassanzadeh and Wernicke, 2016). Its basement is formed by Late Proterozoic-Mesozoic metamorphic rocks such as gneiss and amphibolites (Horton et al., 2008; Mehdipour Ghazi and Moazzen, 2015; Hassanzadeh and Wernicke, 2016) overlaid by Mesozoic shallow-water sediments of the formerly passive continental margin, later intruded by large gabbroic and granitoid plutons (Leterrier, 1985; Rachidnejad-Omran et al., 2002; Mazhari et al., 2009; Dilek et al., 2010; Chiu et al., 2013; Mohajjel et al., 2013; Mehdipour Ghazi and Moazzen, 2015; Hassanzadeh and Wernicke, 2016). Magmatism in the SSZ comprises also scattered Paleocene to Late Eocene occurrences (~60-35 Ma; Mazhari et al., 2009; Azizi et al., 2011; Mahmoudi et al., 2011). SSZ igneous products thus comprise both volcanic and plutonic rocks, mostly with calcalkaline serial affinity classically interpreted to reflect an Andean-type arc system (Berberian and King, 1981; Agard et al., 2005, 2011; Shahbazi et al., 2010; Hassanzadeh and Wernicke, 2016; Deevsalar et al., 2017).

The igneous activity ceased in SSZ and shifted progressively northeastward to form the subparallel UDMA during Late Cretaceous-Paleogene time (Hassanzadeh and Wernicke, 2016). This NE migration occurred diachronously along strike and is considered to be interpreted as the flattening of the Neotethyan subduction angle (Agard et al., (2011; Berberian and King, 1981; Shahbpour, 2007; Verdel et al., 2011; Chiu et al., 2013). The UDMA reaches a maximum width of ~250 km and a total length of ~1800 km and comprises various plutonic and volcanic rocks with associated pyroclastic and volcanoclastic successions (Berberian and King, 1981; Alavi, 2004; Agard et al., 2011; Ghazi and Moazzen, 2015). As a whole, the igneous rocks range from basic to acid, with ultrabasic compositions not yet reported. A detailed geochronological scheme for UDMA magmatism is reported in Chiu et al., (2013) on the basis of an extensive set of zircon U-Pb absolute age data. According to these authors, the earliest

(~81-72 Ma) magmatic manifestations crop out in SE UDMA followed by a prolonged quiescent period. Magmatism peaked during Eocene (~55-45 Ma), emplacing products with calcalkaline (plus rarer transitional shoshonitic) affinity with the typical geochemical signature of subduction-related magmas (Farhoudi, 1978; Berberian and King, 1981; Emami, 1993, 2000; Shahabpour, 2005; Omrani et al., 2008; Verdel et al., 2011; Chiu et al., 2013). During Late Eocene the igneous activity in UDMA decreased in intensity (Emami et al., 1993) ceasing in the northwestern sector in Late Oligocene (~23 Ma) but continuing in the Central sector up to Early Miocene (~17 Ma) and in the southeastern portion of UDMA up to Late Miocene (~9-6 Ma; Chiu et al., 2013). Omrani et al., (2008) argued this magmatic quiescence in the UDMA during Oligocene-Miocene time and linked it to the Arabia-Eurasia continental collision (Chiu et al., 2013). Starting from Late Miocene, magmatic activity appeared to be less extensive across the Arabia-Eurasia suture zone and mostly concentrated towards the Anatolian border during Pliocene-Quaternary time (Davidson et al., 2004; Walker et al., 2009; Allen et al., 2013). Such magmatic activity was quite variable in terms of compositions (from basic to evolved, including adakitic types), serial affinity (from calcalkaline to alkaline, plus lesser shoshonitic and ultrapotassic) and even geochemical signature (varying from subduction-related to within-plate; Sengör and Kidd, 1978; Alberti, 1990; Pearce et al., 1990; Davidson et al., 2004; Jahangiri, 2007; Omrani et al., 2008; Kheirkhah et al., 2009, 2013; Walker et al., 2009; Ahmadzadeh et al., 2010; Lustrino et al., 2010, 2019; Verdel et al., 2011; Allen et al., 2013; Chiu et al., 2013; Pang et al., 2013; Neill et al., 2015; Fazlnia, 2019). The youngest rocks in UDMA consist of Pliocene to Quaternary lava flows and pyroclastics with calcalkaline affinity in Makran subduction system (~6-0.8 Ma) and intraplate basalts (~14-1.6 Ma) in southeast UDMA (Berberian and King 1981; Chiu et al., 2013).

Verdel et al. (2011) group the evolution of the Mesozoic-Cenozoic magmatism of Iran into three distinctive stages. The first began in Cretaceous with the flattening of the NE-directed subducting slab (which was steeper during the relatively low-volume SSMA magmatism), and was accompanied by the emplacement of arc-type magmas in the Alborz Mountains and Central Iran. This stage was probably crucial for the successive ones, as the long-lasting period (~50 Myr) of relatively slow (~3 cm/yr) flat slab subduction resulted in an extensive “preconditioning” of the mantle wedge via slab

fluids release. The successive stage is marked by Eocene extension and crustal thinning accompanying slab roll-back, which triggered mantle melting. This caused the emplacement of large volumes of igneous rocks with subduction-related geochemical fingerprint in continental and shallow submarine extensional basins. Finally, during the Oligocene, upwelling asthenosphere became the main source of magmas as lithosphere had significantly thinned. Decompression melting of such mantle sources produced mostly weakly evolved magmas with "within-plate-like" geochemical signature.

An alternative model for the switch in the geochemical signature of Cenozoic magmas of Iran is that of Allen et al. (2013), which assumes no asthenospheric upwelling because of the absence of regional scale extensions in the area, where lithosphere is ~150-200 km thick. The same author rather proposed a change in the mineralogy of the metasomatized lithospheric mantle. More in detail, Allen et al. (2013) propose that during this latest magmatic phase melting occurred in the garnet stability field during tectonic compression which forced peridotitic mantle out of pargasite stability field (i.e., to depths >3 GPa). The disappearance of amphibole caused a sharp decrease in the peridotite water storage capacity, leading to H_2O saturation, and, consequentially, to an abrupt decrease of solidus temperature. This generated both magmas with high La/Nb (similar to the subduction-related ones) at lower melting degrees, when amphibole and accessory rutile were residual phases, and magmas with lower La/Nb (more akin to within-plate ones), when amphibole and rutile were exhausted.

ANALYTICAL TECHNIQUES

A detailed petrographic investigation has been carried out on twenty-six samples from Tafresh volcanic district, twenty-one samples from Nowbaran and fifty-nine from Bijar-Qorveh area. Whole-rock chemical analyses and weight loss on ignition (LOI) for studied rocks were determined by ICP-AES (Inductively-Coupled Plasma Atomic Emission Spectrometry) and ICP-MS (Inductively-Coupled Plasma Mass Spectrometry), respectively, at Activation Laboratories (Ancaster, Ontario, Canada). Average detection limits range from 0.001 to 0.01 wt% from major elements, 0.1 to 30 ppm for trace elements and from 0.004 to 0.1 ppm for REE (www.actlabs.com for full details).

As deep weathering involves Tafresh samples (LOI up to ~9.5 wt%), neither mineral characterization by electron microprobe (EMP) analyses nor isotopic study have been performed on these rocks. On the other hand, nine representative samples from Nowbaran and nineteen from Bijar-Qorveh areas were instead selected for determining the main mineral compositions by EMP analyses at the laboratory of the Istituto di Geologia Ambientale e Geoingegneria (CNR, Rome) using a Cameca SX50 electron microprobe equipped with five wavelength-dispersive spectrometers (WDS). Minerals were analysed operating at 15 kV accelerating voltage and 15 nA beam current using 1 µm beam diameter for olivine, pyroxene and opaque minerals and 10 µm for foids in order to minimize the alkali loss. Counting times for all elements were 20 s for the peak position and 10 s for the background on each side of the peak. Standards used for calibration are: Na_2O = jadeite; MgO= periclase; TiO_2 = rutile; FeO = magnetite, SiO_2 and CaO = wollastonite; Al_2O_3 = corundum; MnO = rhodonite; K_2O = orthoclase; BaO = barite; SrO = celestine; NiO = pure nickel; FeO and MgO = olivine.

Two samples from Nowbaran have been also selected for X-ray powder diffraction (XRD) analysis carried out at Dipartimento di Scienze della Terra of Sapienza University of Rome. The powders were loaded into 0.7 mm diameter borosilicate capillary and the data were collected in transmission mode (5°-90°) using a parallel-beam Bruker AXS D8 Advance diffractometer operating in θ-θ geometry. The diffractometer was equipped with Göbel mirrors on the incident beam, Soller slits on both incident and (radial) diffracted beams, and a PSD VÅNTEC-1 detector.

A Sr-Nd-Pb isotopes study was carried out at the Istituto di Geoscienze e Georisorse – CNR of Pisa (Italy). Seven representative samples from Nowbaran and eighteen samples from Bijar-Qorveh areas have been selected for whole-rock isotopic ratios. Rock powders were dissolved in HF and HNO_3 and, after through drying, Sr and REE were purified in HCl solution through Ion Exchange Chromatography (IEC). Nd is separated from other REE using diluited HCl solution passing through an Eichrom® Ln Resin. Lead is extracted from the matrix after eluting with HBr and HCl. Strontium separates were loaded on Re filaments and analyzed using a Finnigan MAT 262 Thermal Ionization Mass Spectrometer (TIMS) running in dynamic mode, whereas Nd and Pb were performed with a ThermoFisher™ Neptune Plus MC-ICP-MS equipped with a combined cyclonic and Scott-type quartz spray chamber, Ni-cones, a MicroFlow PFA 100 µl/min self-aspiring nebuliser and a Teledyne Cetac ASX-560 Autosampler. Sr isotopic compositions were corrected for mass fractionation using $^{86}Sr/^{88}Sr=0.1194$. During the analytical period, the Sr standard NIST SRM 987 yielded average values of $^{87}Sr/^{86}Sr=0.710239\pm 0.000017$ (2SD; n=43) and measured values were adjusted at 0.710250 for $^{87}Sr/^{86}Sr$. Instrumental mass fractionation during Nd analyses was corrected using the $^{146}Nd/^{144}Nd$ ratio (= 0.7219). Mass interference correction was done using the ratios $^{147}Sm/^{144}Sm$ (= 4.838710), and $^{147}Sm/^{148}Sm$ (= 1.327400). The analytical accuracy and long-term external reproducibility for $^{143}Nd/^{144}Nd$ of reference material J-Ndi-1 was 0.512098 ± 5 (average of 17 replicates). For Pb correction, samples were spiked with an in-house Tl standard ($^{203}Tl/^{205}Tl$ = 0.4188924) to correct for mass bias fractionation. Measurements were carried out with Faraday cups set as follows: L3 ^{202}Hg, L2 ^{203}Tl, L1 ^{204}Pb, C ^{205}Tl, H1 ^{206}Pb, H2 ^{207}Pb, H3 ^{208}Pb. Cups L3 and L1 were coupled to 10^{12} Ohm amplifiers, whereas 10^{11} Ohm amplifiers were coupled with remaining cups. ^{202}Hg is measured to correct isobaric interferences of ^{204}Hg on ^{204}Pb, using the ratio $^{202}Hg/^{204}Hg$ (= 4.350370). However, ^{202}Hg values were always below detection limit. Analytical and instrumental blanks were measured for each mass and subtracted from sample signal. Sample/blank ratio is typically above 10^4. Accuracy and reproducibility are tested over each analytical session by replicates of international standards SRM 981. 28 replicates of SRM 981 standard gave results of 16.9355±0.0057, 15.4876±0.0040 and 36.6873±0.0130 (2σ errors) for the $^{206}Pb/^{204}Pb$, $^{207}Pb/^{204}Pb$ and $^{208}Pb/^{204}Pb$ ratios, respectively.

CHAPTER 1 – TAFRESH

1.1 Sampling area

The investigated rocks were collected in the Tafresh area, at the northwestern tip of the central UDMA (Fig. 5). According to the 1:100.000 Geological Maps of Tafresh (Hajian, 1977) and Farmahin (Hajian, 1970), the igneous rocks are mainly massive lavas and pyroclastic deposits with amphibole-rich andesitic composition, intruded by dykes and dioritic/granitoid bodies and associated sedimentary strata. A stratigraphic type-sequence for the central/north-western UDMA is exposed in the Tafresh area (Verdel et al., 2011), beginning with Mesozoic carbonatic and silicoclastic deposit, covered by Paleocene-Eocene volcanic and sedimentary deposits, and by the Upper Eocene to Lower Oligocene sedimentary and subordinate volcanic deposits of the Lower Red Formation. The sequence continues with the Oligocene to Lower Miocene Qom Formation, made of shallow marine carbonates and mafic volcanic rocks, then by Miocene gypsum deposits of the Upper Red Formation, and is closed by Pliocene-Quaternary continental deposits.

Regionally, the study area was affected by reverse and dextral faulting associated with thrusting of the Eocene volcano-sedimentary series over the Qom Formation and Pliocene conglomerates (Hajian, 1977; Raeisi et al., 2019). The dominant NW-SE striking of the thrusts is parallel to the regional tectonic fabric of the UDMA, with minimum perpendicular stresses allowing the emplacement of near E-W granitoid magmas (Raeisi et al., 2019).

The earliest geochronological estimates for the Tafresh area igneous rocks were mainly based on the fossiliferous record of the interbedded sedimentary deposits, suggesting an Eocene age (Hajian, 2001). Whole-rock K-Ar absolute age data for two adakitic rocks and one basaltic lava sample range from Upper Oligocene (~27 Ma) to Middle Miocene (~15 Ma; Ghorbani et al., 2014). A Lower Miocene zircon U-Pb age of 17.4 Ma has been provided for a granodioritic body from the nearby Qom locality (Chiu et al., 2013). Significantly older U-Pb and $^{40}Ar/^{39}Ar$ ages have been also reported by

Verdel et al. (2011), covering approximately the 57 to 44 Ma time interval (i.e., Upper Paleocene to Middle Eocene).

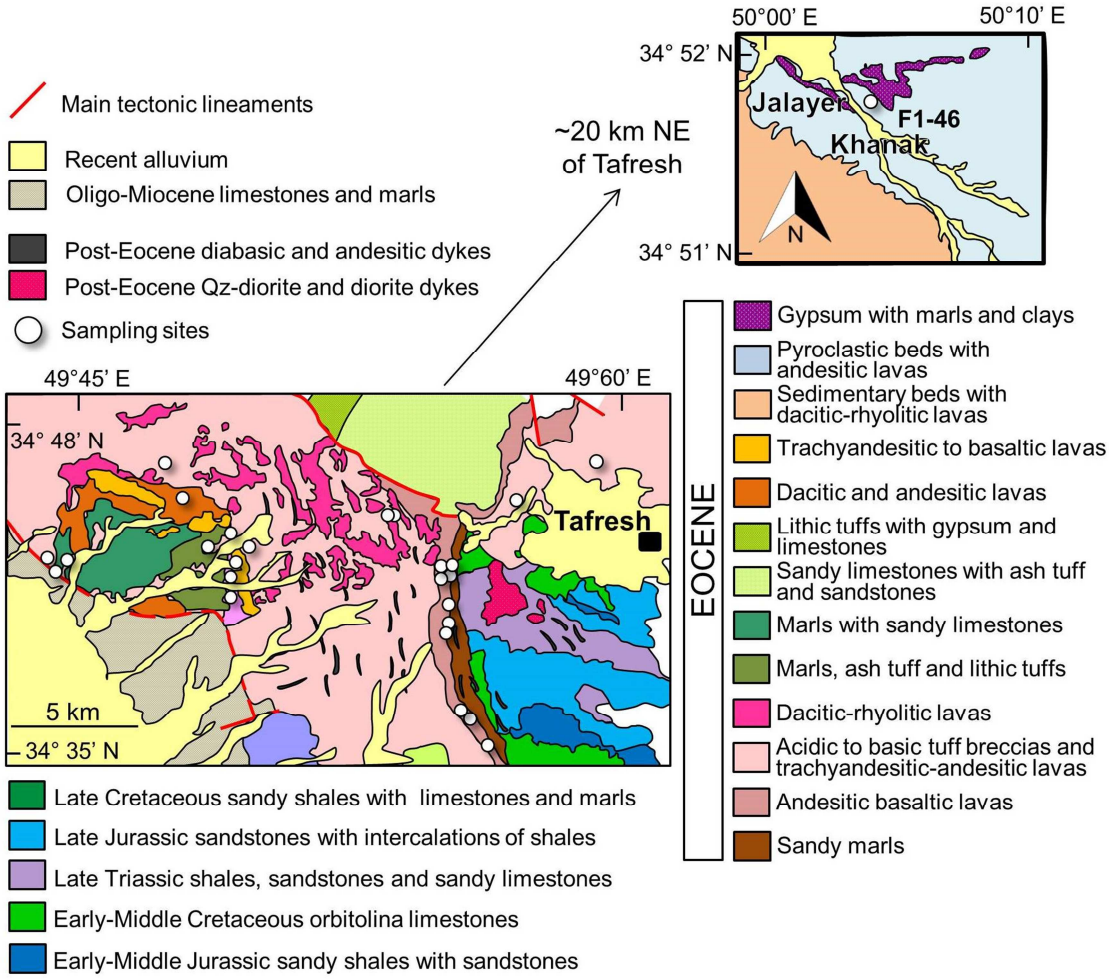

Fig. 5: *Simplified geological sketch map of the Tafresh area (after Hajan, 1970, 1977) with red white dots indicating sample locations.*

1.2 Results

1.2.1 Petrography

Tafresh igneous rocks are generally not well preserved, with abundant secondary phases partially to totally replacing primary minerals, and some calcite veins in the deeply altered samples (related to interaction with hydrothermal fluids and/or superficial weathering). A rough first-level distinction can be made between four groups of rock samples with different degrees of evolution, as inferred from mineral paragenesis and phase abundances (Fig. 6).

Weakly evolved rocks (samples F1-22, F1-33, F1-36, F2-12, F2-34, F3-24, F4-49, F4-58) generally show a fine/moderate-grained holocrystalline intergranular doleritic texture, almost entirely made by plagioclase and ferromagnesian minerals (plus accessory opaques) in approximately similar proportions (Fig. 6a). Plagioclase laths are generally better preserved (in some samples occurring also as few larger phenocrysts) with respect to mafic phases, with the latter being generally not easily distinguishable as they are totally replaced mainly by serpentine minerals or serpentine and calcite, more rarely by chlorite. Relatively fresh (or only partially replaced) crystals of clinopyroxene, fewer olivine and rare amphibole can be occasionally observed. Large plagioclase crystals (up to 1.2 cm in length and sometimes with “clast-like” appearance, possibly xenocrystic in origin) have been also recognized in samples F3-24 and F4-58.

Intermediate rocks (F1-9, F1-11A, F1-11B, F1-13, F3-6, F3-13, F3-23, F4-1, F4-10, F4-11, F4-15) display both moderately to strongly porphyritic (with both microcrystalline and devitrified groundmass; Fig. 6b,c) and holocrystalline fine- to moderate-grained hypidiomorphic textures (plus fewer finer-grained intergranular; Fig. 6d) dominated by plagioclase and amphibole. Plagioclase is the most abundant phase, occasionally present also as larger phenocrysts or grains up to 6 mm in length (Fig. 6b) and in monomineralic glomerules. Amphibole is the main mafic mineral (Fig. 6b,c,d), occurring both as fresh crystals and partially replaced by chlorite and calcite aggregates, sometimes forming larger phenocrysts/grains up to 5 mm in length. In samples F1-11A and F4-1, large anhedral amphibole (~3-4 mm in length, likely xenocrystic), in some instances poikilitically enclosing plagioclase laths (up to 8 mm in diameter, likely

representing cumulitic intergrowths), are also observed. Rarer clinopyroxene crystals, mostly replaced by serpentine and calcite aggregates, and accessory opaques are also present.

Evolved rocks (F1-8, F1-29, F1-46) show moderately porphyritic (with devitrified groundmass) to holocrystalline fine/moderate-grained intergranular textures dominated by feldspar crystals plus fewer ferromagnesian minerals (Fig. 6e). Plagioclase is still the main phase, forming large crystals up to 6 mm in length. Some alkali feldspar is also present, sometimes as large phenocrysts (~4 mm in length) or making monzonitic glomerules with plagioclase. The main mafic mineral is amphibole, commonly found as phenocrysts/grains (~3-4 mm) partially or totally replaced by chlorite or aggregates of chlorite and calcite/clay minerals. A few large biotite phenocrysts (~2 mm in length) have been found in sample F1-46. Opaque minerals are diffusely present as an accessory phase, occasionally as larger microphenocrysts/grains (up to 1 mm in diameter).

Strongly evolved rocks (F1-17, F1-18, F2-21, F3-3) have weakly- to moderately-porphyritic textures, generally with devitrified groundmass, and a remarkably leucocratic paragenesis dominated by plagioclase, alkali feldspar and quartz (Fig. 6f). Ferromagnesian minerals are extremely rare, typically represented by sparse amphibole microcrysts, commonly altered to chlorite and/or calcite. A few accessory opaques are also present as small groundmass phases. Sialic mineral clasts (mainly quartz, up to 1 mm) and holocrystalline fine-grained xenoliths made of feldspar and lesser amphibole, have been also observed in samples F1-17 and F1-18.

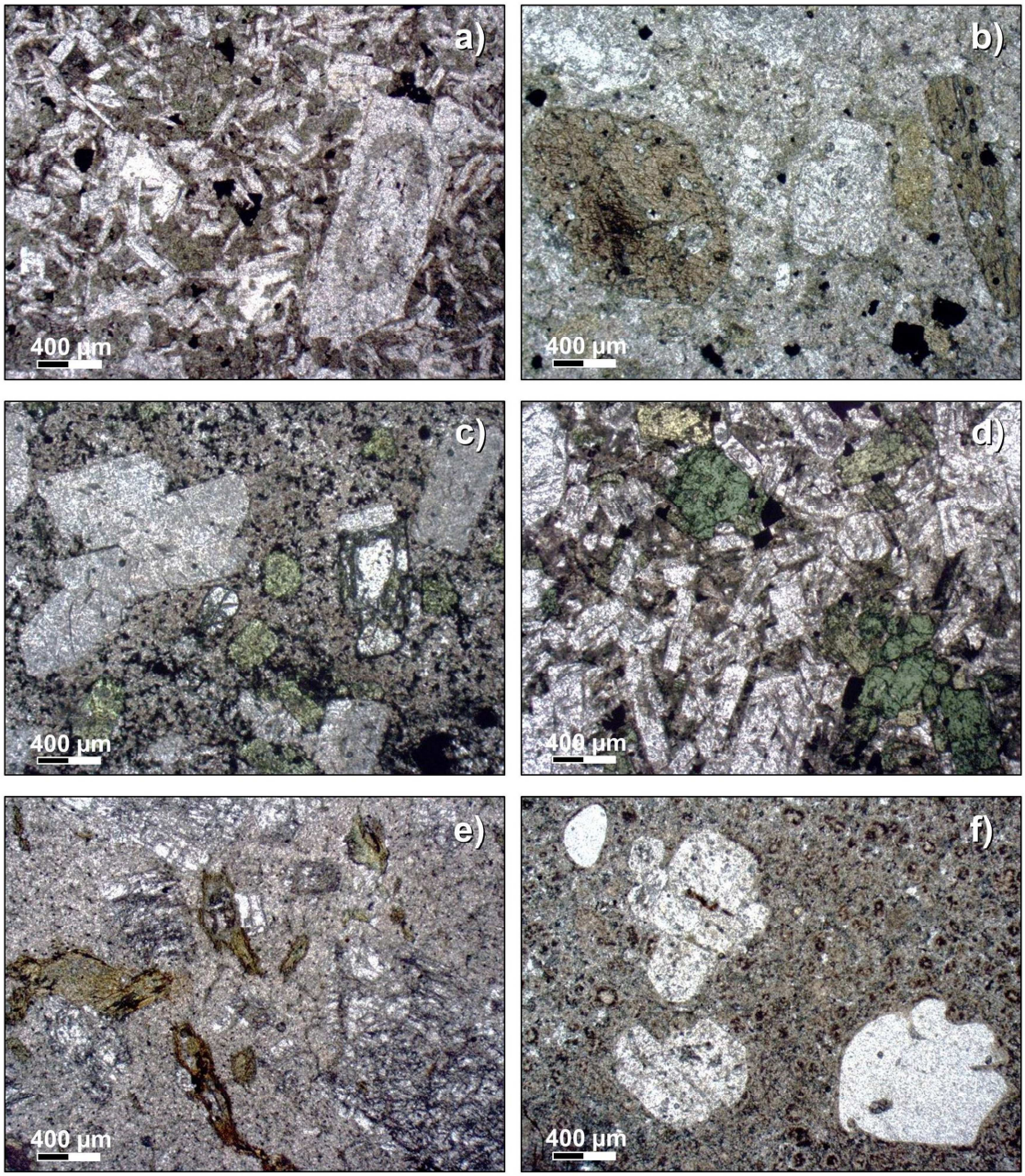

Fig. 6: *Representative plane-polarized light view photomicrographs for the investigated rock samples from the Tafresh area. a) Weakly evolved rock sample F3-24 showing a holocrystalline intergranular texture consisting of plagioclase (colourless, note the larger crystal on the right) and weathered altered ferromagnesian minerals (brownish green); b) intermediate rock sample F3-6 displaying a moderately porphyritic texture with phenocrysts of amphibole (yellow-green) and plagioclase set into a weathered altered (possibly devitrified?) groundmass; c) intermediate rock sample F4-11 showing a moderately porphyritic texture with phenocrysts of weathered altered plagioclase (dusty-looking), amphibole (light green) and clinopyroxene (colourless, e.g., right of the centre) set into a weathered Altered microcrystalline groundmass; d) intermediate rock sample F4-15 with a holocrystalline hypidiomorphic texture essentially made of plagioclase and amphibole crystals; e) evolved rock sample F1-8 showing a weakly porphyritic texture with phenocrysts of feldspars and amphibole set into a weathered altered (devitrified?) groundmass; f) strongly evolved rock sample F3-3 displaying a moderately porphyritic texture with phenocrysts of feldspars and quartz (e.g., embayed crystal at the lower right) set into a devitrified groundmass.*

1.2.2 Whole rock geochemistry

As previously observed, the investigated Tafresh rock samples generally show the evidence for variable alteration processes, which surely modified the original concentrations of major oxides and trace elements. In order to have a rough idea of the general preservation state, LOI values and CIPW-normative mineralogy have been taken into account, which allowed to make a distinction between (relatively) "fresh" (reported as green symbols in the petrochemical diagrams), "spoiled" (yellow) and "altered" (red) samples.

"Fresh" samples (n = 14) have LOI <4.0 wt.% (1.80-3.95 wt.%), and a SiO_2-oversaturated normative mineralogy that is overall in line with rock petrography (Appendix – Table 1). Decreasing mafic minerals (mainly *hypersthene*, from 20.7-21.0 to 13.9-17.9, down to 10.3 vol.%) and increasing *quartz* (from 2.53 to 7.60-16.7, up to 19.1 vol. %) and sum of sialic minerals (approximately from 73 to 74-81, up to 86 vol.%), are indeed observed moving from weakly evolved to intermediate, up to evolved rocks. The strongly evolved rocks have the lowest *hypersthene* (5.63-7.21 vol.%) and the highest *quartz* (27.6-35.3 vol.%) and sum of sialic minerals (88.5-90.2 vol.%), as well as also some CIPW-normative *corundum* (2.09-2.81 vol.%), indicative of their peraluminous character.

"Spoiled" samples (n = 10) have LOI between 4.0 and 6.5 wt.% (4.24-6.21 wt.%) and still show some rough consistency between their SiO_2-oversaturated normative mineralogy and observed petrography. Moving from weakly evolved to intermediate and more strongly evolved samples, an increase of *quartz* (from 4.30-8.81 to 5.35-13.4, up to 12.1-13.9 vol.%), and of the sum of sialic minerals (from 69.9-75.3 to 71.3-77.9, up to 79.0-84.5 vol.%), can be still envisaged. Some major inconsistencies are however evident, e.g.: 1) high *diopside* and *anorthite* of some weakly evolved (summing to >55 vol.%) and intermediate rocks (~45-50 vol.%), likely caused by relatively CaO-rich compositions associated to calcite plagues and veins, coupled with very low hypersthene (<1.16 vol.%); 2) intermediate sample F1-9 having *corundum* (1.63 vol.%), low *quartz* (5.35 vol.%) and very high *albite* (50.6 vol.%) and *hypersthene* (20.0 vol.%); 3) evolved sample F1-29 displaying some *corundum* (0.92 vol.%) and very high *albite* (47.3 vol.%) and *hypersthene* (15.9 vol.%). The relatively high CIPW-normative albite

could be related to selective removal of CaO from the original plagioclase during very low grade metamorphism or normal weathering.

"Altered" samples are represented by two weakly evolved rocks with LOI >9.0 wt.% (9.09-9.48 wt.%) and some unusual normative mineralogy. Sample F1-33 has relatively high *quartz* and *hypersthene* (respectively 3.57 and 26.9 vol.%) and low *orthoclase* (3.04 vol.%) and *anorthite* (21.1 vol.%), especially if compared to weakly-evolved fresh samples. On the other hand, F1-36 is SiO_2-undersaturated, with *olivine* (2.10 vol.%) and some *nepheline* (0.67 vol.%), and with *anorthite* and *diopside* summing to ~69 vol.%, likely due to the presence of secondary calcite veins, lowering the absolute SiO_2 whole-rock content. The high CIPW-normative hypersthene could be related to the common presence of serpentine-group minerals.

Well bearing in mind the above observations, the alteration effects on changing the composition of the investigated samples are evaluated through a comparison with literature data from the same area and from the entire UDMA. The latter group of data was restricted to rocks with "orogenic" affinity and filtered by removing analyses likely suffering from intense alteration, i.e., those with LOI >4.0 wt.% and with sum of major element oxides <98.0 wt.% or >102.0 wt.%. Data for which LOI values are not reported were cautiously discarded as well.

Classification and serial affinity

The investigated Tafresh rocks have been categorized using different classification schemes. Based on the TAS classification, Tafresh samples plot in the subalkaline field, with rock compositions being largely consistent with petrography, regardless of the degree of alteration (Fig. 7a). The weakly evolved rocks are mainly basaltic andesites (SiO_2 = 53.7-55.6 wt.%; Na_2O+K_2O = 3.24-5.67 wt.%), with one altered sample plotting in the basalt field with the lowest SiO_2 (49.0 wt.%) and sum of alkalis (3.03 wt.%). Intermediate rock samples are mostly andesites with 57.8-61.3 wt.% SiO_2 and 4.48-6.43 wt.% Na_2O+K_2O, except for two spoiled samples and one fresh sample falling in the field of basaltic andesites (the latter almost at the boundary with the andesite field) and one spoiled sample falling just above the andesite-trachyandesite divide. Evolved

rocks are quite homogeneous in terms of SiO_2 (62.8-63.5 wt.%), but display some larger variability in the sum of alkalis (4.59-7.32 wt.%), with two samples straddling the boundary between andesite and dacite and the alkali-richest spoiled sample falling in the latite field. Finally, the fresh strongly evolved rocks are all classified as rhyolites, with SiO_2 ranging from 71.6 and 74.0 wt.% and sum of alkalis in the range of 6.74-8.10 wt.%.

In order to compare the investigated Tafresh samples with those from the existing literature, the latter have been distinguished based on their main parageneses into: 1) "basaltic" (pl + cpx ± ol), 2) "andesitic" (pl + amph ± cpx), 3) "dacitic" (feld + amph ± bt) and 4) rhyolitic (feld + qtz). Although there is an overall consistency between literature and present samples in terms of general degree of rock evolution and SiO_2 content, literature samples display some major variation for the sum of alkalis, which spans a very wide compositional spectrum for all the lithotypes, except the rhyolitic ones. Notably, an overall good consistency is also evidenced with literature "orogenic" rocks from the UDMA. Worth noting, UDMA rocks also include dacitic compositions in the SiO_2 range of 64.0-70.0 wt.% (not represented in Tafresh rocks), as well as a few samples with high sum of alkalis, possibly belonging to a shoshonitic rock series.

Similar observations arise from the K_2O vs. SiO_2 diagram of Fig. 7b, where the investigated Tafresh rocks define mostly a medium-K to high-K calcalkaline series, with only a few K_2O-poor rock samples (0.29-0.51 wt.%) falling in the field for low-K tholeiitic rock series. Literature Tafresh samples are still very scattered due to their extremely variable K_2O contents, but they mainly lie in the fields for medium-K and high-K rock series. Finally, also literature UDMA rocks with "orogenic" affinity belong mainly to the medium- and high-K series, although there are also some samples with shoshonitic serial affinity and a few K_2O-poor outliers.

Additional classification plots, specifically thought for altered samples using immobile elements, are also taken into account in Fig. 8. The Zr/TiO_2 vs. Nb/Y plot again confirms the subalkaline serial affinity and the overall consistency between petrographic types and chemical compositions for the Tafresh samples from both this work and the existing literature, being classifiable mostly as andesite and dacite/rhyodacite. Similar considerations can be made for in the Th vs. Co diagram, where the investigated Tafresh samples mostly plot in the calcalkaline series field. Literature UDMA samples

are again largely consistent with Tafresh samples, defining a full calcalkaline rock series and including the most evolved compositions with shoshonitic affinity.

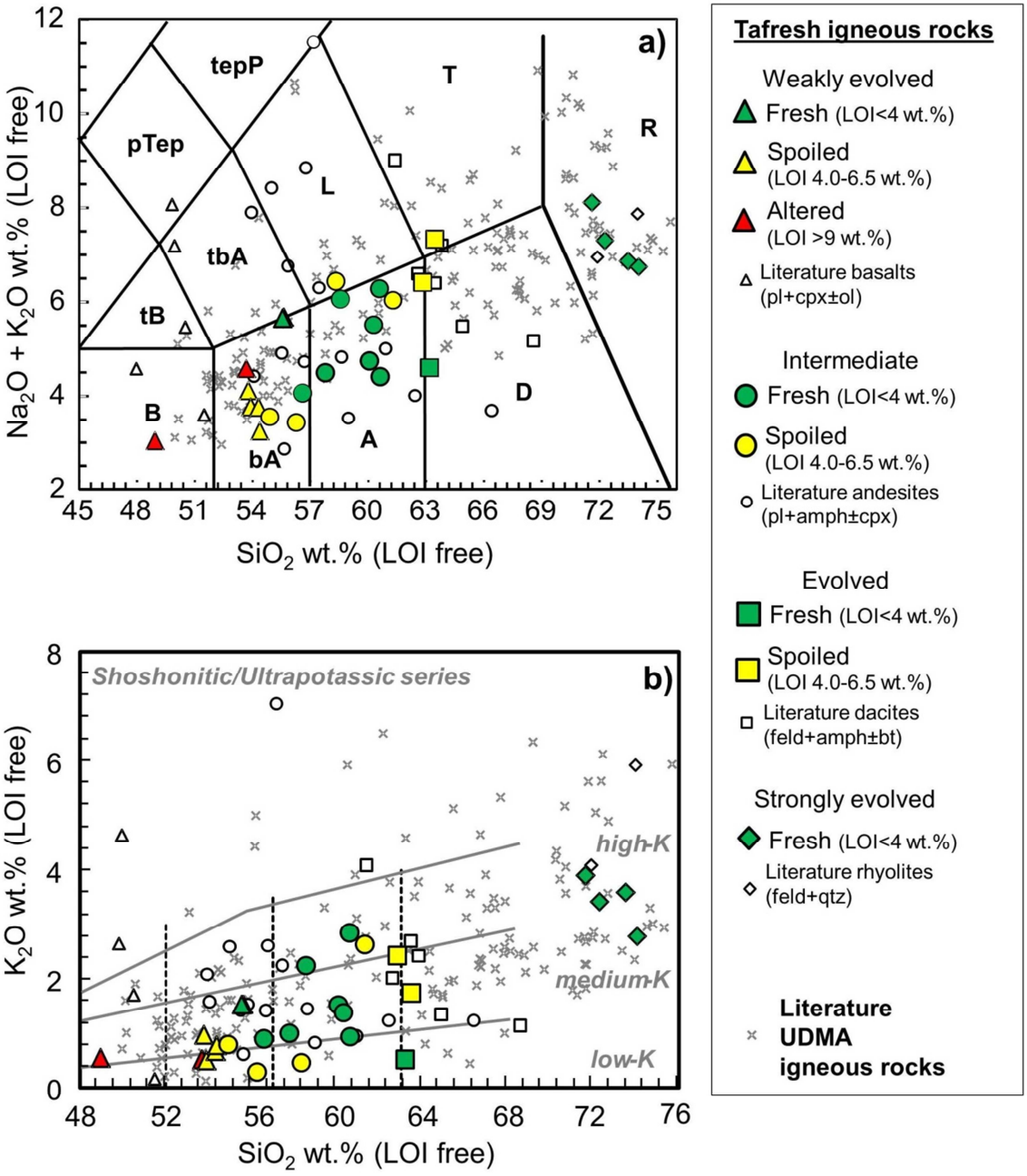

Fig. 7: *a) TAS (Total Alkali vs. Silica) and b) K_2O vs. SiO_2 (Le Maitre, 2002) classification diagrams for the Tafresh area rock samples from this work (of different degree of evolution and preservation; see text) and from the available literature (Ghorbani and Bezenjani, 2011; Khademi et al., 2019). Selected literature data for the UDMA rocks with "orogenic" affinity (Boccaletti et al., 1977; Riou et al., 1981; Jahangiri, 2007; Omrani et al., 2008; Sherafat et al., 2012; Maanijou et al., 2013; Yeganehfar et al., 2013; Azizi et al., 2014; Honarmand et al., 2014) are also reported for comparison (see text for further details). Abbreviations for rock names (in black): A = andesite; B = basalt; bA = basaltic andesite; D = dacite; L = latite; P = phonolite; pTep = phonotephrite; R = rhyolite; T = trachyte; tB = trachybasalt; tbA = trachybasaltic andesite; tepP = tephriphonolite.*

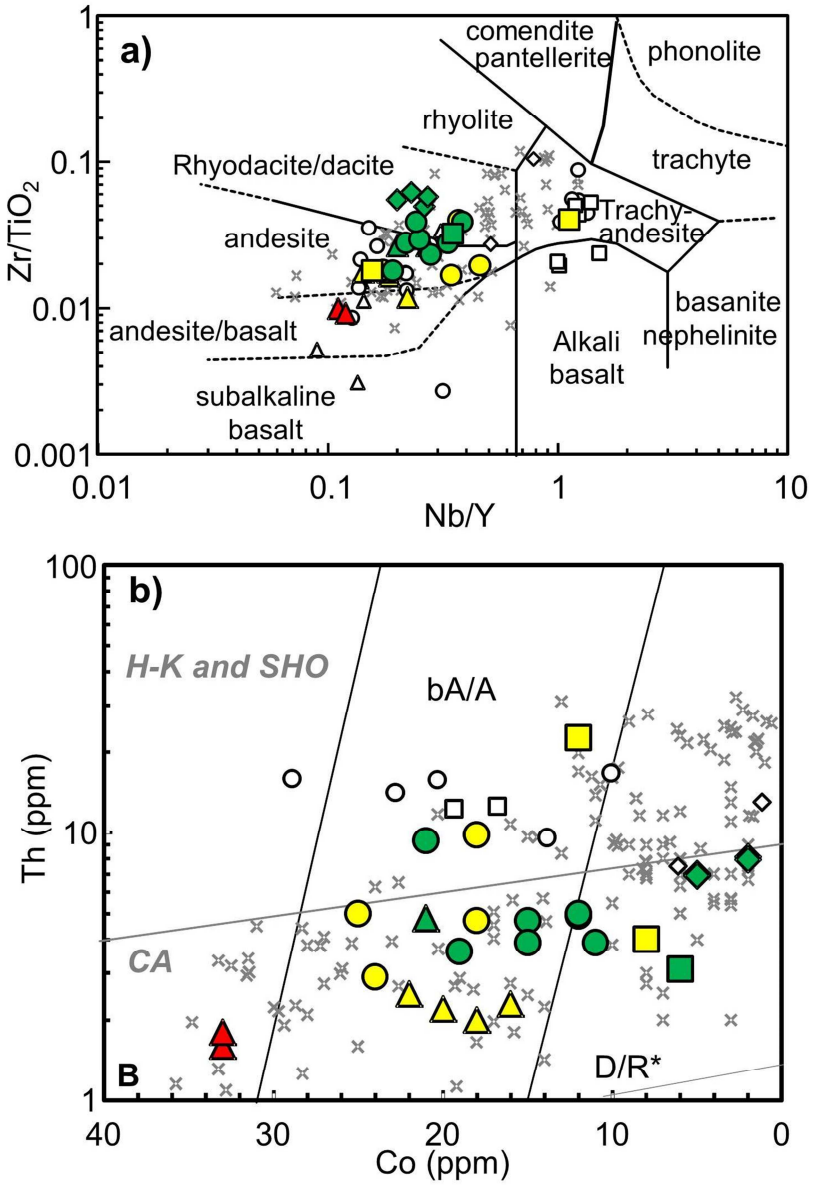

Fig. 8: *a) Zr/TiO_2 vs. Nb/Y (Winchester and Floyd, 1977) and b) Th vs. Co (Hastie et al., 2007) classification diagrams for the Tafresh area rock samples (this work and available literature) and for selected literature data for the UDMA rocks with "orogenic" affinity. Symbols and sources of bibliographic data as in Fig. 7. Abbreviations for rock names (in black): B = basalt; bA = basaltic andesite; D/R = dacite/rhyolite (* indicates that latites and trachytes also fall in these fields). Abbreviations for rock series (in grey): CA = calcalkaline; H-K = high-K calcalkaline; SHO = shoshonitic.*

Major and trace elements variations

The investigated Tafresh samples define some overall coherent differentiation trends in major element binary variation plots (Fig. 9), which are especially evident if only relatively fresh samples are taken into account. With increasing silica contents, a quite regular decrease is observed for TiO_2, Al_2O_3, Fe_2O_{3tot}, MgO and CaO, whereas K_2O increase, and Na_2O and P_2O_5 faintly increase up to the evolved rock samples and then decrease in the strongly evolved ones. Some major scattering is observed for spoiled and altered samples, mostly in some weakly evolved rocks with unusually high (19.7-20.4 wt.%) or low (15.0 wt.%) Al_2O_3, high Fe_2O_{3tot} (14.8 wt.%), low MgO (1.23-2.54 wt.%) and high CaO (11.2-15.2 wt.%, likely due to secondary calcite). Tafresh literature samples, although roughly in line with the above differentiation trends, display some more evident data scattering for most of the major elements. The observed trends are on the whole in line with those depicted by UDMA “orogenic” rocks.

Binary variation diagrams for trace elements (Fig. 10) are remarkably more scattered. A general decreasing trend can be envisaged for Sc and V only, well consistent with the trend defined by the UDMA “orogenic” rocks. On the other hand, Rb, Sr (very scattered), Ba, Zr and Nb define a trend of broad increase with increasing differentiation, while Y is mostly constant except from a few outliers. Among the evolved rocks, sample F1-46 generally plots close to a group of literature dacitic samples due to its relatively high Sr (506 ppm), Ba (866 ppm), Th (23 ppm), Cr and Ni (respectively 40 and 20 ppm), and low Y (8 ppm). It is interesting to note that many incompatible trace elements remain roughly constant or even record some slight decrease in the transition from the evolved to the strongly evolved samples (e.g., Sr, Ba, Y, Zr and Nb).

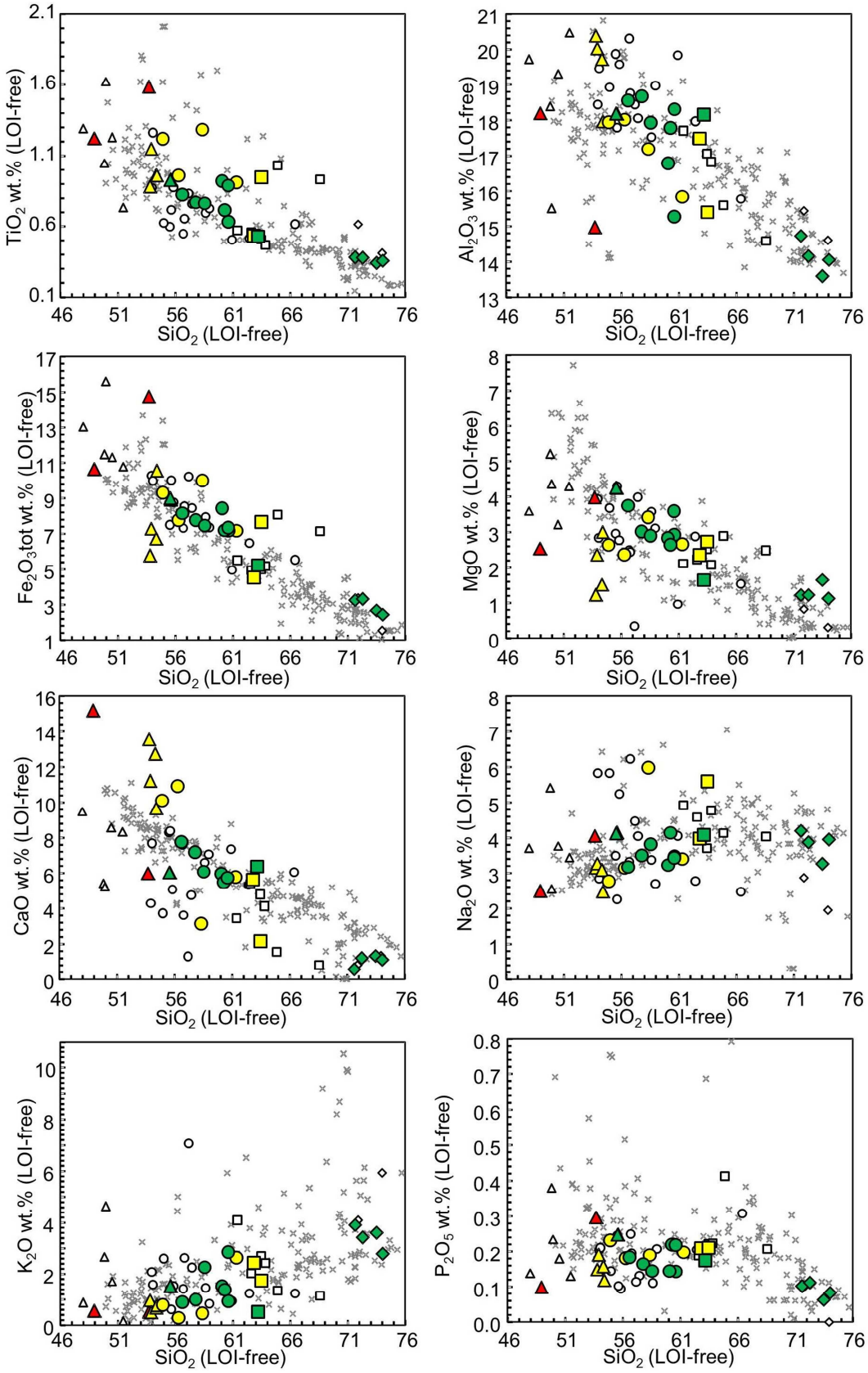

Fig. 9: *Major elements vs. SiO_2 binary variation diagrams for the Tafresh area rock samples (this work and available literature) and for selected literature data for the UDMA rocks with "orogenic" affinity. Symbols and sources of bibliographic data as in Fig.7.*

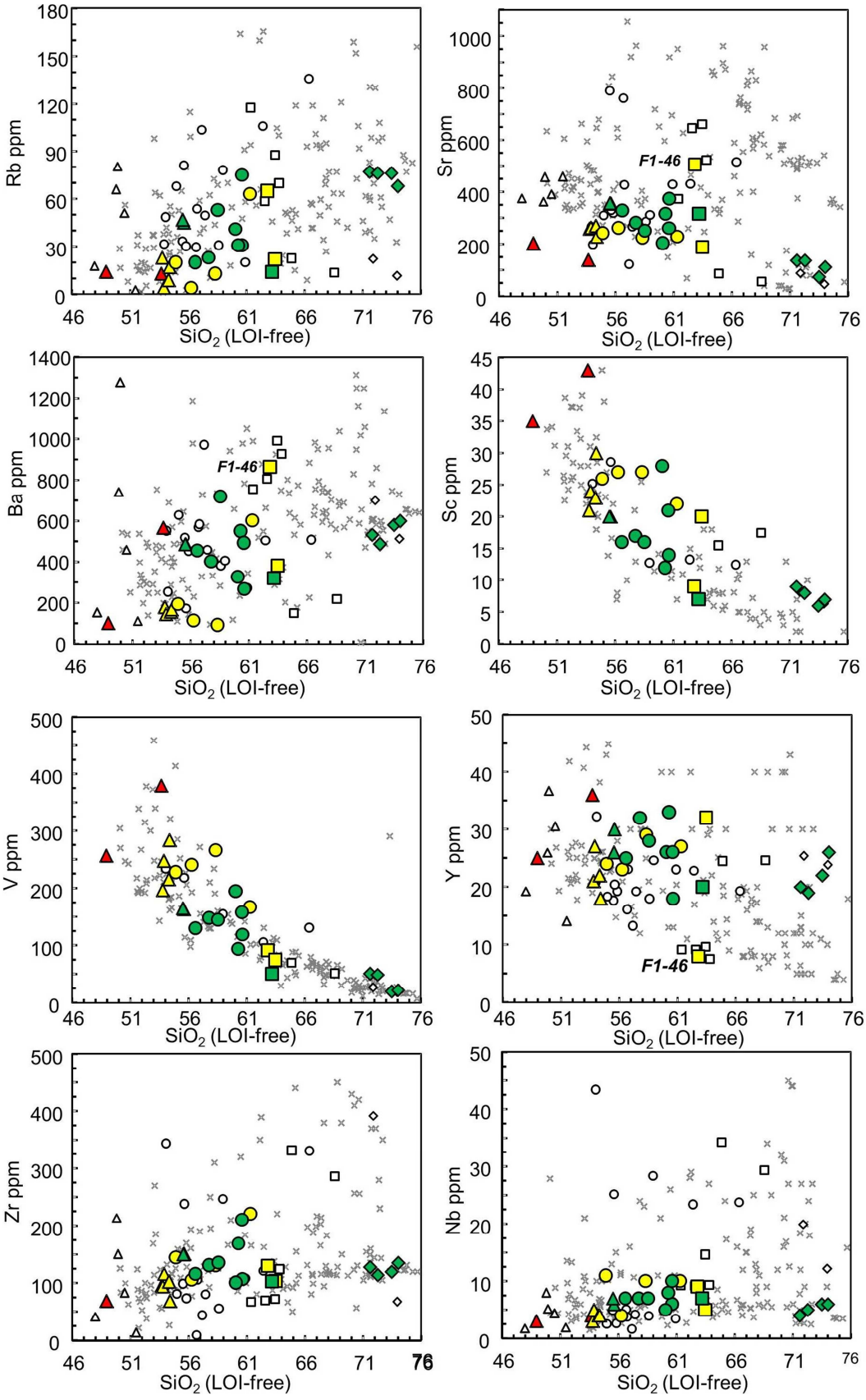

Fig. 10: *Selected trace elements vs. SiO_2 binary variation diagrams for the Tafresh area rock samples (this work and available literature) and for selected literature data for the UDMA rocks with "orogenic" affinity.*

Chondrite-normalized Rare Earth Elements patterns

The Rare Earth Elements (REE) concentrations of the investigated Tafresh rocks have been normalized to CI chondrite average estimate in Fig. 11. The patterns for the least evolved samples are slightly enriched in Light REE (LREE; La_N/Lu_N 1.91-5.12, N for normalized abundances) and nearly flat in Middle and Heavy REE (MREE and HREE; Dy_N/Lu_N 1.07-1.13), with normalized abundances for the most enriched REE at 28-83 times chondrite abundances (xCI; Fig. 11a). Some small troughs at Eu are also observed, with Eu/Eu* [$Eu_N/(Sm_N*Gd_N)^{0.5}$] in the range of 0.83-0.93. No substantial differences can be observed in rocks with different degree of preservation, with the slightly more enriched patterns of the relatively fresh samples possibly only reflecting their slightly more evolved character. Literature data for the Tafresh area and UDMA "orogenic" rocks with similar degrees of differentiation are in line with the present data, although three "anomalous" basaltic samples from Tafresh are also evidenced (samples T7, T19 and T2; Fig 8a).

Intermediate samples display very homogeneous patterns that are on the whole similar to the weakly evolved ones, reaching also slightly more enriched compositions with the highest normalized abundances in the range of 46-103 xCI, La_N/Lu_N 3.31-6.53, Dy_N/Lu_N 0.95-1.14 and Eu/Eu* = 0.70-0.90 (Fig. 11b). Tafresh andesitic rocks from the literature are mostly overlapping, although some slightly less enriched samples are also present. As for the evolved samples, two rocks display nearly identical patterns that are very similar to those for the intermediate rocks, (Fig. 11c). On the other hand, the spoiled sample F1-46 has not only the highest LREE (up to ~175 xCI), but also strong LREE/HREE (La_N/Lu_N 49.4), LREE/MREE (La_N/Sm_N 6.53) and even MREE/HREE (Dy_N/Lu_N 1.78), coupled with Eu/Eu* = 0.95. The pattern of this sample matches perfectly with the available literature data for Tafresh dacitic rocks.

Finally, the strongly evolved rocks have very homogeneous and peculiar REE patterns with no counterparts in the Tafresh literature. Indeed, these display slight LREE/HREE enrichment (La_N/Lu_N 5.27-5.99), MREE/HREE depletion (Dy_N/Lu_N 0.84-0.92, except for one sample with 1.00), strong Eu troughs (Eu/Eu* = 0.59-0.82), and normalized abundances up to 76-89 xCI (Fig. 11c).

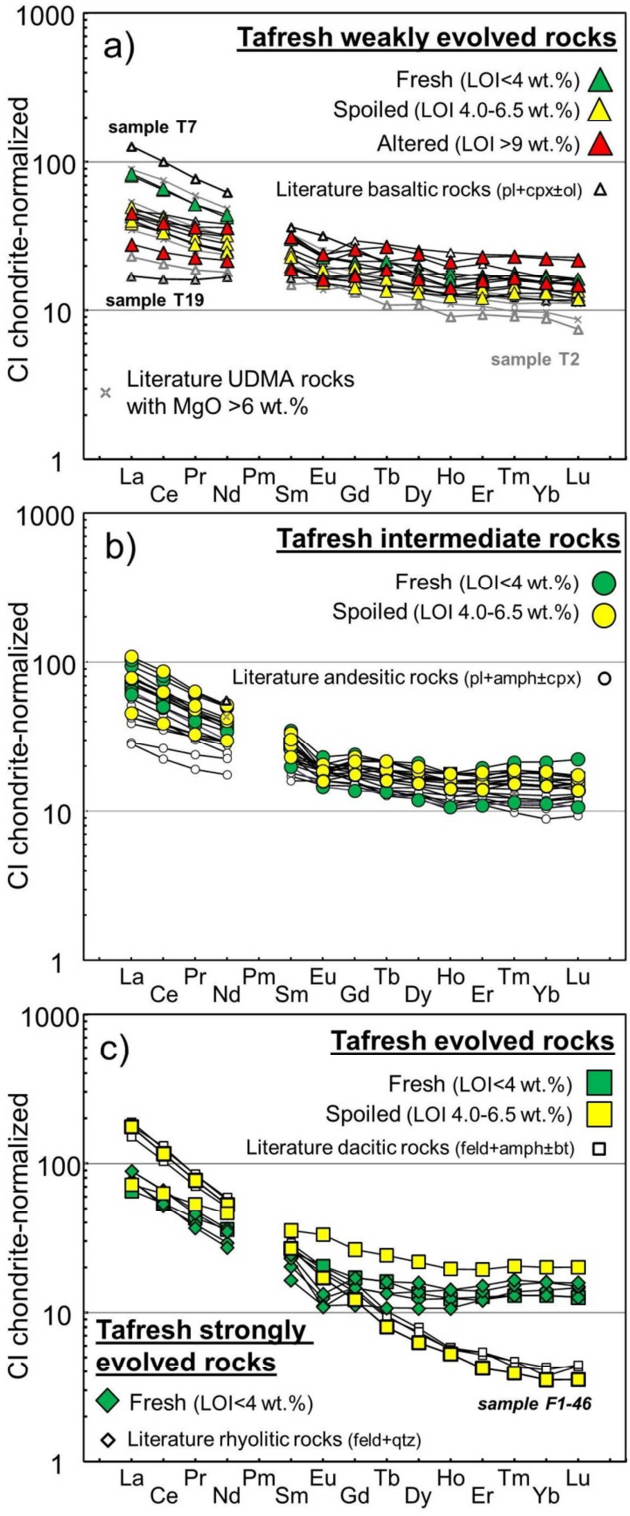

Fig. 11: *Chondrite-normalized (King et al., 2020) kingREE plots for the Tafresh area rock samples of a) weakly evolved (plus literature "basaltic", with a highlight on the "anomalous" samples T2, T7 and T19; see text for further details), b) intermediate (plus literature "andesitic") and c) evolved (plus literature "dacitic"; a highlight on sample F1-46 is also provided) and strongly evolved compositions. In a) literature data for weakly evolved (MgO >6 wt.%) UDMA rocks with "orogenic" affinity are also reported. Sources of bibliographic data as in Fig. 7.*

Primitive mantle-normalized multielemental patterns

In primitive mantle-normalized (hereafter PM-normalized)multielemental diagrams, the Tafresh least evolved rocks display some spiky patterns with major scattering for the most incompatible elements. This is likely due to their mobility in aqueous fluids, as observable from the differences of the patterns for spoiled and altered samples (Fig. 12a). The remaining least incompatible elements show significantly lower scattering, with marked enrichment in LILE (Large Ion Lithophile Elements) with respect to the HFSE (High Field Strength Elements), peaks at K and Pb, as well as troughs at Nb, Ta and Ti. These strongly resemble the patterns for average upper crustal rocks (e.g., Rudnick and Gao, 2014), the average composition of the Global Subducting Sediments (GloSS; Plank, 2014), and the typical subduction-related magmas (e.g., Zheng, 2019). Literature rocks from the Tafresh area and the UDMA with similar degree of differentiation show similar patterns, again excluding the three outliers, previously defined as “anomalous” basaltic samples (see previous section).

As observed for CI-normalized patterns, PM-normalized patterns for the intermediate rocks are extremely homogeneous (except for some scattering in the most incompatible fluid-mobile elements; Fig. 12b). Overall, a strong similarity can be envisaged with patterns for the weakly evolved rocks, although some general displacement to slightly higher abundances and a faint to moderate peak at Zr-Hf are also observed. Tafresh andesitic rocks from the literature are perfectly in line with these patterns, with some few exceptions (e.g., higher K, Pb peak and Zr-Hf depletion). Evolved Tafresh rocks define two distinctive groups of rocks with peculiar PM-normalized patterns, both characterized by the overall LILE-HFSE enrichment observed for the weakly evolved and intermediate samples (Fig. 12c). Sample F1-46 and dacitic rocks from the literature have the strongest LILE enrichment of the entire dataset, coupled with a marked depletion for MREE, Y and HREE and a small but evident peak at Sr. On the other hand, the remaining two evolved samples display a pattern virtually identical to that of the most enriched intermediate rocks. The patterns for the strongly evolved Tafresh rocks is also very similar, except for having smaller Pb peaks and a marked depletion at Sr and P.

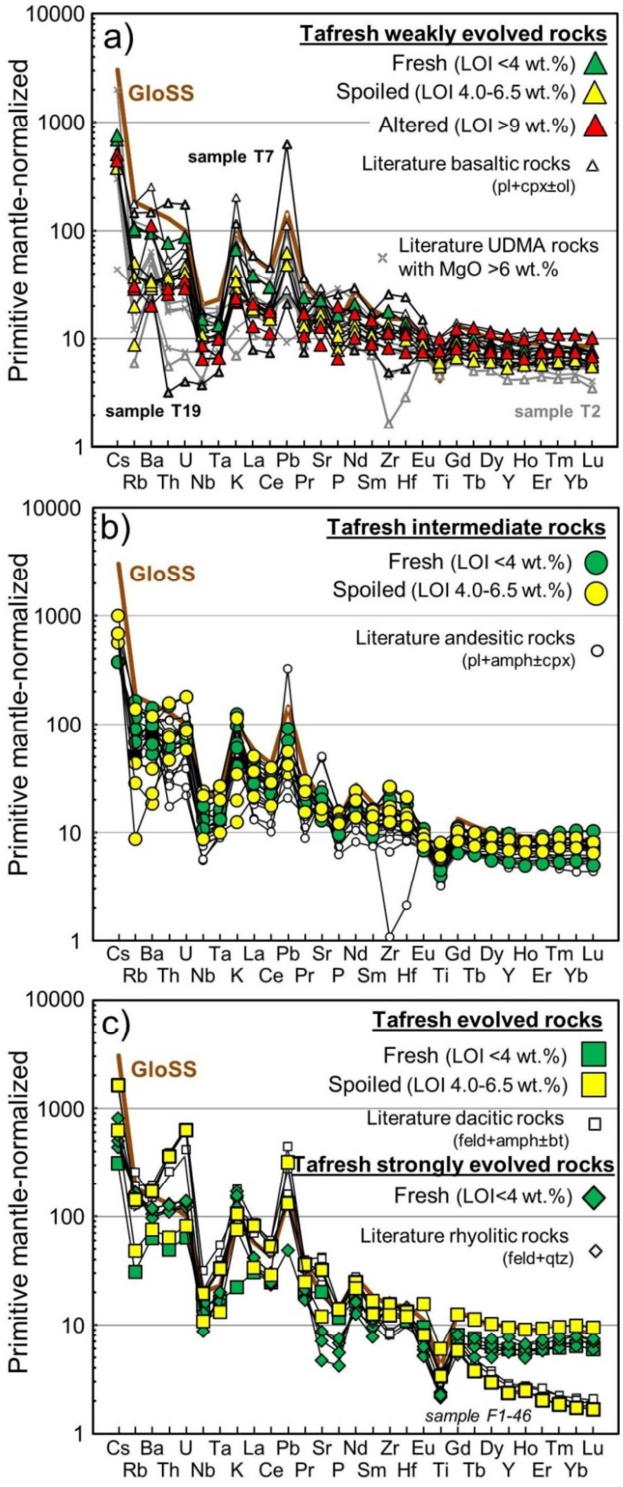

Fig. 12: *Primitive mantle-normalized (Lyubetskaya and Korenaga, 2007) multielemental plots for the Tafresh area rock samples of a) weakly evolved (plus literature "basaltic", with a highlight on the "anomalous" samples T2, T7 and T19; see text for further details), b) intermediate (plus literature "andesitic") and c) evolved (plus literature "dacitic"; a highlight on sample F1-46 is also provided) and strongly evolved compositions. The pattern for the estimated composition of Global Subducting Sediments (GloSS-2; Plank, 2014) is included for comparison. In a) literature data for weakly evolved (MgO >6 wt.%) UDMA rocks with "orogenic" affinity are also reported. Sources of bibliographic data as in Fig. 7.*

1.3 Discussion

The investigated rocks from the Tafresh area include a relatively large variety of lithotypes, covering the entire compositional spectrum for a typical subduction-related "orogenic" subalkaline to mildly alkaline series. Intermediate compositions are by far the most represented, with much rarer weakly evolved and evolved lithotypes and some strongly evolved leucocratic compositions. Field and petrographic evidence suggest that the outcropping rocks were emplaced not only in a "volcanic" environment, but also at various depths within the crust (e.g., textures including both porphyritic, possibly with glassy groundmass, as well as holocrystalline medium- to coarse-grained hypidiomorphic and fine- to medium-grained intergranular "dolerite-like" types). Notwithstanding the overall poor preservation due the alteration processes, geochemical data define on the whole some generally coherent trends that, at least at a first level of investigation, support the existence of some genetic relation linking them. However, several observations suggest that additional processes other than simple closed-system fractional crystallization were also active: 1) presence of possibly xenocrystic large crystals in textural disequilibrium; 2) presence of large amphibole oikocrysts (with plagioclase inclusions), likely cumulitic in origin; 3) presence of xenoliths in the strongly evolved rocks; 4) observation of some sparse "anomalous" geochemical features (e.g., sample F1-46, incompatible element contents not linearly increasing with the degree of differentiation) that do not seem to be related to alteration processes only.

It is therefore evident that reconstructing the petrogenetic processes operating together in the Tafresh area could be a particularly hard task, with numerous processes possibly acting together and thus overlapping their effects. In the following sections, a qualitative/semi-quantitative treatment of such processes in tentatively undertaken, with the aim of shedding some light on the petrogenesis of the outcropping rocks and making some inferences in the larger framework of the geodynamic evolution of the UDMA.

1.3.1 Magmatic lineages and differentiation processes in the Tafresh area

Assessing whether the investigated Tafresh rocks represent a single liquid line of descent or rather include two or more independent magmatic lineages is greatly complicated by the aforementioned bad preservation state that generally characterizes them. Alteration processes not only variably (and rather unpredictably) modified original rock compositions, but also significantly obscured the primary paragenesis, thus making also the proposed lithological distinction not completely reliable. Consequently, the recognized rock types should not be considered as coherent, homogeneous groupings, and some overlap between rocks with similar degrees of evolution should be expected.

Bearing this in mind, a quite regular evolutionary trend seems to be recognizable from the weakly evolved to the intermediate rocks based on both variation and CI- and PM-normalized diagrams. The main fractionating phases are likely represented by ferromagnesian minerals (mostly clinopyroxene and olivine) and plagioclase, then followed by an assemblage made up of plagioclase, amphibole and minor clinopyroxene (e.g., CaO being roughly constant up to ~53 wt.% SiO_2, then firmly decreasing), in broad good accordance with petrography. This trend possibly extends also to the evolved rock samples (with a decrease in fractionating amphibole and the onset of alkali feldspar fractionation), with the only exception of sample F1-46, which has been observed to display some rather “anomalous” features. This sample, collected in a different location, ~20 km N from the main sampling area, is characterized by high Sr, low Y, coupled with high LREE/HREE, LREE/MREE and MREE/HREE ratios, typical of adakitic magmas (as well as for tonalite-trondhjemite-granodiorite “TTG” suites, widespread during the Archean; e.g., Martin et al. 2005; Palin et al., 2016). The occurrence of such compositions is widely recognized in the literature for both the Tafresh area (“dacitic” rocks; Ghorbani and Bezenjani, 2011; Ghorbani et al., 2014) and the entire UDMA (Jahangiri, 2007; Khodami et al., 2009; Omrani et al., 2008; Sherafat et al., 2012; Yeganehfar et al., 2013; Azizi et al., 2014, 2019; Ghorbani et al., 2014; Pang et al., 2016; Alirezaei et al., 2017; Torkian et al., 2019; Kheirkhah et al., 2020). The genesis of these peculiar rock compositions will be considered in a following section.

Numerous lines of evidence suggest that Tafresh strongly evolved rocks are not genetically linked with the main products cropping out in the area. The large compositional gap of ~5 wt.% SiO_2 separating them from the evolved rocks (not taking into account the rocks with adakitic signature) suggests the absence of a continuous spectrum of magma compositions. In addition, the transition from the two lithotypes is not characterized by a clear decrease in elements that are strongly partitioned in feldspars such as Na_2O, K_2O and Ba (although there is a decrease in Eu and, less evident, in Sr). For this reason, a focus on this group of rocks is provided in a further following section.

We therefore conclude that most of the Tafresh rocks likely represent the products of a single liquid line of descent with the typical features of a magma series generated from subduction-modified mantle sources. These include: 1) Al-rich, Fe-poor whole rock compositions, likely reflecting water-rich and oxidized source regions; 2) plagioclase-phyric, olivine-poor hydrous mineral-bearing paragenesis; 3) LILE-enriched and HFSE-depleted PM-normalized patterns; 4) predominance of intermediate "andesitic" lithotypes; 5) scarcity (or even complete lack) of primitive lithotypes. Based on the latter, it is clear that no specific inferences can be made on the nature of the mantle source(s), which can be only approximately assumed to be represented by a metasomatized peridotite in the spinel stability field (as indicated by the flat HREE PM-normalized pattern of the least evolved Tafresh rocks). Primitive melts were likely hydrous, as also confirmed by presence of abundant amphibole in the intermediate rocks, which also suggests that differentiation processes occurred at shallow to moderate depths. Following experimental results for "orogenic" magmas, the observed crystallisation sequence with plagioclase appearing on the liquidus before amphibole requires that primitive melts were not particularly rich in H_2O [<4.5 wt.%, based on the phase diagrams of Melekhova et al. (2015) for a high-MgO basalt] and that these evolved at ~4 kbar [see the phase diagram of Pichavant et al. (2002) for a basaltic andesite with ~6 wt.% H_2O].

1.3.2 Genesis of the strongly evolved rocks from the Tafresh area

The genesis of strongly evolved rocks is likely unrelated to that of the main magmatic suite emplaced in the Tafresh area. The frankly peraluminous nature of such rocks [A/CNK = Al/(Ca+Na+K) = 1.16-1.22, compared to the 1.22-1.45 range in literature samples] makes them more akin to melts generated from crustal anatexis of metaigneous or metasedimentary protoliths (e.g., I- and S-type granites; e.g., Clemens et al., 2011; Chappell et al., 2012), rather than to typically highly fractionated melts from metaluminous parental magma (e.g., M-type granites). The latter could be also weakly peraluminous, if substantial fractionation of metaluminous phases such amphibole occurs (Chappell et al., 2012), but this does not seem the case of Tafresh strongly evolved rocks, in which amphibole remains as a subordinate phase. This is also supported by the lack of a marked MREE depletion that would be expected if significant amphibole fractionation had occurred, given the high $^{amphibole/melt}D_{MREE}$ (e.g., Nandedkar et al., 2016). Therefore, the Tafresh strongly evolved rocks can be related either to partial melting of Al-rich (meta-) igneous or sedimentary rocks from the local crust, (e.g., the Neoproterozoic and Paleozoic and Mesozoic basement rocks; Bagheri and Stampfli, 2008; Horton et al., 2008) or to interaction of metaluminous evolved magmas with Al-rich crustal rocks.

The first hypothesis (crustal anatexis) is somewhat more in line with the leucocratic nature of such rocks, indicating a composition that is possibly close to that of the granite minimum in the petrogeny's residua system. However, a discrimination between a meta-igneous or meta-sedimentary source seems not so straightforward, as high-SiO_2 melts from these two sources share many similarities (e.g., Chappell, 1999; Chappell and White, 2001; Clemens and Stevens, 2012; Jagoutz and Klein, 2018). The very low CaO/FeO (0.61-0.86, plus one literature sample with 1.18) and low Sr (47-137 ppm) of Tafresh strongly evolved rocks is more consistent with a sedimentary source. On the other hand, the quite regular major and trace element variation trends and the linear decline of P_2O_5 at increasing SiO_2 would rather suggest a metaigneous source rock. In addition, other geochemical parameters reveal some evident differences between strongly evolved samples from this study and the two literature samples from Khademi et al. (2019). The latter have low Na_2O (1.94-2.86 wt.%) and Al_2O_3/TiO_2 (25.2-

35.8), very low Rb/Sr (0.25) and Rb/Ba (0.02-0.03) and relatively high CaO/Na_2O (0.29-0.68), suggestive of a (relatively) plagioclase-rich, clay-poor source (e.g., Sylvester, 1998). On the other hand, the strongly evolved Tafresh rocks reported here have relatively high Na_2O (3.26-4.20 wt.%), Rb/Sr (0.55-1.03) and Rb/Ba (0.11-0.16), plus slightly higher Al_2O_3/TiO_2 and generally lower CaO/Na_2O (0.14-0.41), more in line with a meta-pelitic source rock. On such basis, it could be tentatively proposed that Tafresh strongly evolved rocks originated from the melting of a heterogeneous metasedimentary source consisting of both meta-pelitic and (relatively) plagioclase-rich meta-greywacke components.

As an alternative, a process of interaction between a metaluminous melt with upper crustal Si-Al-rich lithologies is also viable, provided that some phase in which MREE are preferentially partitioned is simultaneously fractionating, in order to produce the observed slight MREE depletion. This could be obtained through both some limited amphibole fractionation (see above), or fractionation of accessory phases such as apatite and titanite, which also preferentially host MREE with respect to LREE and HREE (e.g., Prowatke and Klemme, 2006a,b).

1.3.3 Genesis of the Tafresh area evolved rocks with adakitic geochemical fingerprint

As highlighted in a previous section, Tafresh evolved rocks include products resembling adakitic compositions that deserve additional considerations. The supposed adakitic signature can reflect primary features or rather it could be acquired due to alteration processes. For this reason, we decided to compare their overall geochemistry with those of adakitic/TTG magmas as reported by Martin et al. (2005). With respect to the latter, Tafresh rocks have: 1) slightly lower SiO_2 (61.4-63.8 wt.%, vs. mostly >64 wt.%); 2) relatively low Na_2O (i.e., 3.7-4.9 wt.% vs. 3.0-7.0 wt.%); 3) higher K_2O/Na_2O (0.4-0.8 vs. <0.5); 4) higher sum of ferromagnesian elements (Fe_2O_{3tot} + MgO + MnO + TiO_2 = 7.5-8.3 wt.% vs. <5.0 wt.%); 5) La_N/Yb_N only moderately high (34-49 vs. up to 150). Finally, when plotted in the classical adakite discrimination diagrams (Fig. 13) these rocks plot well within the field for adakitic melts (along with numerous other

UDMA occurrences from the existing literature). It is therefore concluded that such evolved rocks should be actually considered as adakites, and some of the above small deviations from the typical adakite geochemical fingerprint might be due to secondary mobilization of some major elements during alteration.

Adakitic melts are classically interpreted to represent the product of slab melting in active and hot subduction zones, with variable extents of interaction with the peridotitic matrix (e.g., Defant and Drummond, 1990; Drummond and Defant, 1990; Martin et al., 2005; Moyen, 2009; Castillo, 2012; Ma et al., 2012; Breitfeld et al., 2019; Liu et al., 2019).

Adakite occurrences have also been reported for subduction-unrelated geological settings, supporting alternative models involving, e.g., melting of the lower crust (e.g., Chung et al., 2003; Wang et al., 2006; Ma et al., 2012). Finally, more recent models proposed to produce the high Sr/Y and La/Yb "adakitic" signature (e.g., Macpherson et al., 2006; Rodríguez et al., 2007; Kamei et al., 2009; Moyen, 2009; Castillo, 2012; Ribeiro et al., 2016; Bellver-Baca et al., 2020), point to different mechanisms, including melting of a high Sr/Y crustal source at 5-10 kbar, fractionation of Sr-rich and Y-poor amphibole (± apatite) at shallow depths, or fractionation of garnet and Mg-rich amphibole at high pressure.

In the genesis of Tafresh adakites, garnet and amphibole seem to have both played some role. As for the first, the crucial observation is the depletion in HREE with respect to both LREE and MREE, given the well known preferential partitioning of HREE within garnet lattice (i.e., $^{garnet/melt}D_{HREE}$ >60; e.g., Taylor et al., 2015). On the other hand, the depletion of MREE, which are preferentially partitioned in amphibole (see previous section), with respect to LREE, is the best evidence for the latter. Although the common presence of amphibole in the intermediate Tafresh rocks renders fractionation of this phase a likely process, no evidence has ever been reported for garnet fractionation. This suggests that Tafresh adakites originated from the melting of a mafic source rock with residual garnet and amphibole, possibly represented by the metamorphosed subducted slab or by the lower continental crust. Since there is no geochemical parameter that could help to unequivocally assess which of the above two sources could be the most likely, some clues in this sense could be tentatively retrieved

by taking into account the overall geodynamic setting in which Tafresh rocks have been emplaced. This is discussed more in detail in the following section.

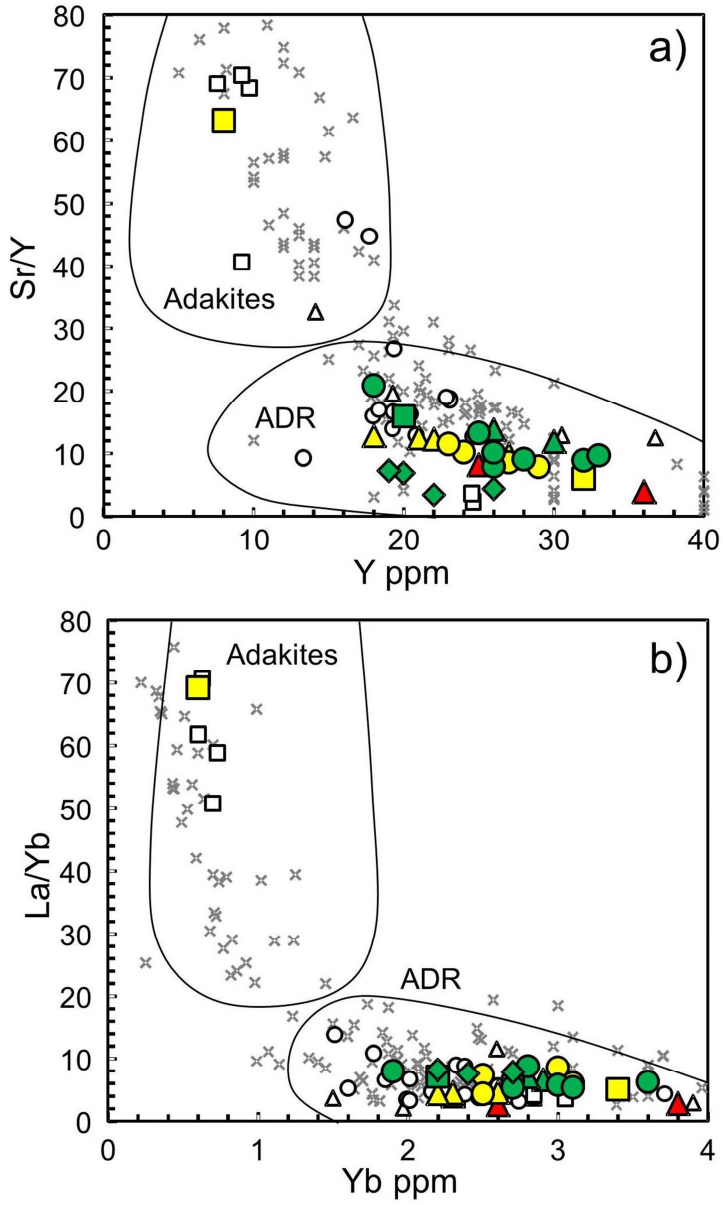

Fig. 13: *a) Sr/Y vs. Y and b) La/Yb vs. Yb diagrams [Drummond and Defant (1990), modified after Richards and Kerrich (2007)], used to distinguish adakites from "normal" arc andesite, dacite and rhyolite (ADR), for the Tafresh area rock samples (this work and available literature) and for selected literature data for the UDMA rocks with "orogenic" affinity. Symbols and sources of bibliographic data as in Fig. 7.*

1.3.4 Geodynamic implications

The investigated rocks from the Tafresh area display a large variety of petrographic and geochemical features attesting for numerous magmatic processes, including genesis and differentiation of "normal" subduction-related subalkaline series (from a variably metasomatized peridotite mantle source), genesis of subordinate magmas with adakitic signature and of crustal anatectic strongly evolved magmas. Such large variability is common in post-collisional geodynamic settings (e.g., Prelević and Seghedi 2013; Couzinié et al., 2016; Fedele et al. 2016), which is thus the most likely scenario for the emplacement of the studied rocks. This is also in line with geochronological data for the onset of continent collision in NW/central UDMA around 22-16 Ma, although the range of ages obtained for the rocks from the Tafresh area (~57-15 Ma) suggests that magmatism developed also during pre-collisional stages.

Within this framework, of particularly interest is the occurrence of rocks with adakitic signature throughout the UDMA. The genesis of such magmas is classically retained to mark the final stages of the subduction process or even the stages immediately following the onset of continental collision, being thus ascribed to melting of the subducted oceanic lithosphere during a post-collisional phase (adakites from Tabriz, Marand and Jolfa, NW UDMA, Isfahan, central UDMA, Dehaj, SE UDMA; Jahangiri, 2007; Khodami et al., 2009; Shaker Ardakani, 2016), a slab break-off (Anar, central/SW UDMA; Omrani et al., 2008) or a slab roll-back event (Tafresh and Nain, central/NW UDMA; Ghorbani and Bezenjani, 2011; Yeganehfar et al., 2013; Ghorbani et al., 2014). A few reports of rocks with adakitic signatures related to deep-level fractionation have been also documented for NW (Sanandaj, Upper Miocene; Azizi et al., 2014), central (Yazd Province, Pliocene-Quaternary; Sherafat et al., 2012) and SE UDMA (Kerman, Middle Miocene; Alirezaei et al., 2017).

More recently, Pang et al. (2016) questioned the slab melting models, proposing that Pleistocene Anar adakites are the product of the melting of lower crustal cumulates (metamorphosed to eclogite-facies rocks). These mafic lithologies were possibly induced to partially melt by the thermal perturbations associated with the post-collisional magmatism of Iran. The increase of the geothermal gradient was ascribed either to asthenospheric upwelling associated to the formation of a slab window or to

lithospheric thickening during collision. Such alternative model, which was also proposed by Torkian et al. (2019) and by Kheirkhah (2020) for the genesis of the Miocene adakites from NW UDMA (Sheyda volcano) and of the adakites from Dehaj (SE UDMA), respectively, seems consistent with the collisional setting in which the studied Tafresh adakites were likely emplaced.

Nevertheless, since post-Eocene igneous rocks from the Tafresh area have been emplaced during a time lapse from pre- to post-collisional stages, the slab break-off and slab roll-back hypotheses could not be definitively rejected. This is even more evident in the light of the very recent recognition of pre-collisional (Paleocene, ~58-56 Ma) granitoids with adakitic signature in NW UDMA (Saqqez-Takab), which Azizi et al. (2019) ascribed to the partial melting of lower crustal rocks due to the asthenospheric upwelling related with slab roll-back (or even to deep-level amphibole fractionation of "normal" calcalkaline magmas). In the light of the previously recalled progressive inception of the continental collision moving from NW to SE, it could be also reasonable to hypothesize that more than just a single kind of process could have been active to produce the UDMA adakites. Further studies on these rocks are thus needed, including detailed petrochemical characterization and accurate absolute age data.

1.4 Conclusions

Igneous rocks from the Tafresh area of the UDMA testify for widespread Cenozoic magmatism resulting in a large spectrum of rock types, variably affected by secondary processes. Most of the investigated igneous products, ranging in composition from weakly evolved to evolved lithotypes (with intermediate andesitic rock types being the most common) likely belong to a calcalkaline suite with orogenic affinity.

Primitive magmas (not represented in the geological record) likely originated from a peridotite mantle source, previously metasomatized by addition of subduction-related fluids (as indicated by the typical LILE-enriched and HFSE-depleted geochemical signature), which melted in the spinel stability field. Differentiation processes were mainly driven by fractional crystallization of 1) ferromagnesian minerals (mostly clinopyroxene and olivine) and plagioclase, 2) plagioclase and amphibole, and finally 3)

plagioclase and alkali feldspars, in good accordance with both petrographic and whole-rock geochemical evidence.

Additional rock types include rarer evolved rocks with adakitic geochemical fingerprint (Sr-enriched and Y- and HREE-depleted) and leucocratic peraluminous strongly evolved rocks. The first are ascribed to melting of a meta-mafic source rock (either the subducting oceanic slab or the lower continental crust) leaving a garnet and amphibole-bearing residue, while the second are likely the product of the anatexis of a mixed meta-sedimentary (i.e., including both pelitic and greywacke lithologies) crustal source.

The association of such a large variety of magma types in a relatively narrow area is consistent with a post-collisional geodynamic setting, although additional more detailed petrological investigations, are still considered necessary in order to unequivocally elucidate the complex geodynamic scenario of the investigated area.

CHAPTER 2 – NOWBARAN

2.1 Sampling area

The investigated area is ~200 km SW of Tehran, in the Markazi Province, at an average elevation of ~1600-1800 m a.s.l. The volcanic rocks crop out west of the town of Nowbaran, between the Saveh and Hamadan cities (Fig. 14), covering a surface of less than 50 km^2 over an area of ~1200 km^2. The volcanic cones, with basal dimensions ranging from ~150x280 m^2 to 2500x2400 m^2, form small lava flows with minor pyroclastic deposits (Fig. 15), distributed in an eastern and a western district. The eastern volcanic outcrops are represented by the three rural areas of Dakhan, Fastaq and Chalfakhreh (Khalatbari Jafari and Alaie Mahabadi, 1998). The main volcanic cones of this district are located at Dakhan and consists of 9 coalescent N-S trending small volcanoes, aligned for a total length of ~7 km, ~20 km west of Nowbaran. Two small volcanic vents erupted ~7 km north of the Dakhan line, north of Chalfakhreh village, and another one crops out ~9 km east of Dakhan line, close to the village of Fastaq. Twenty-seven samples were collected and seventeen of them were analysed from the eastern district. Six additional samples were collected near the Qezel Hesar area from two main emission centres, in the western district, ~60 km southwest of Nowbaran and ~17 km southeast of Famenin city. Four of them have been chosen for whole-rock chemical investigations.

Lava flows are usually short (<3 km) and thin (<30 m thick). The emission centres reach a height lesser than 100 m. No literature data is available for these volcanic rocks, with the exception of small notes written in Farsi (the official language of Iran). According to the geological map of Geological Survey of Iran (1:100,000 scale, Noubaran sheet), Quaternary basanitic-nephelinitic lava flows and scoria deposits cover Oligo-Miocene marls and massive biomicritic limestones of the Qom Formation. No radiometric ages are available for the investigated samples, albeit the morphological features and the freshness of the samples are indicative of their young age.

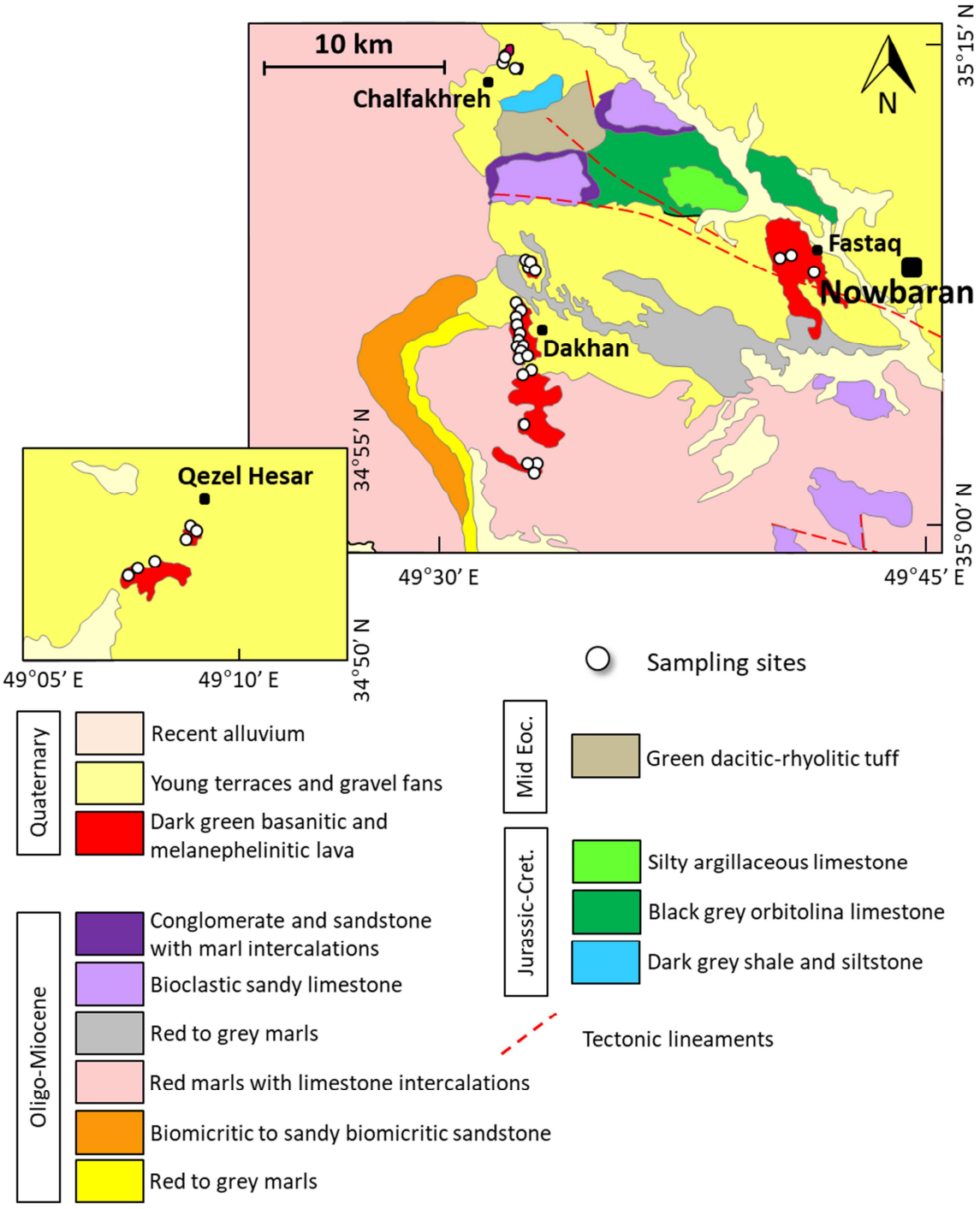

Fig. 14: *Geological sketch map of the Nowbaran area [modified from Khalatbari et al., (1998) and Alaie Mahabadi and Fodazi (2002)] with sampling locations.*

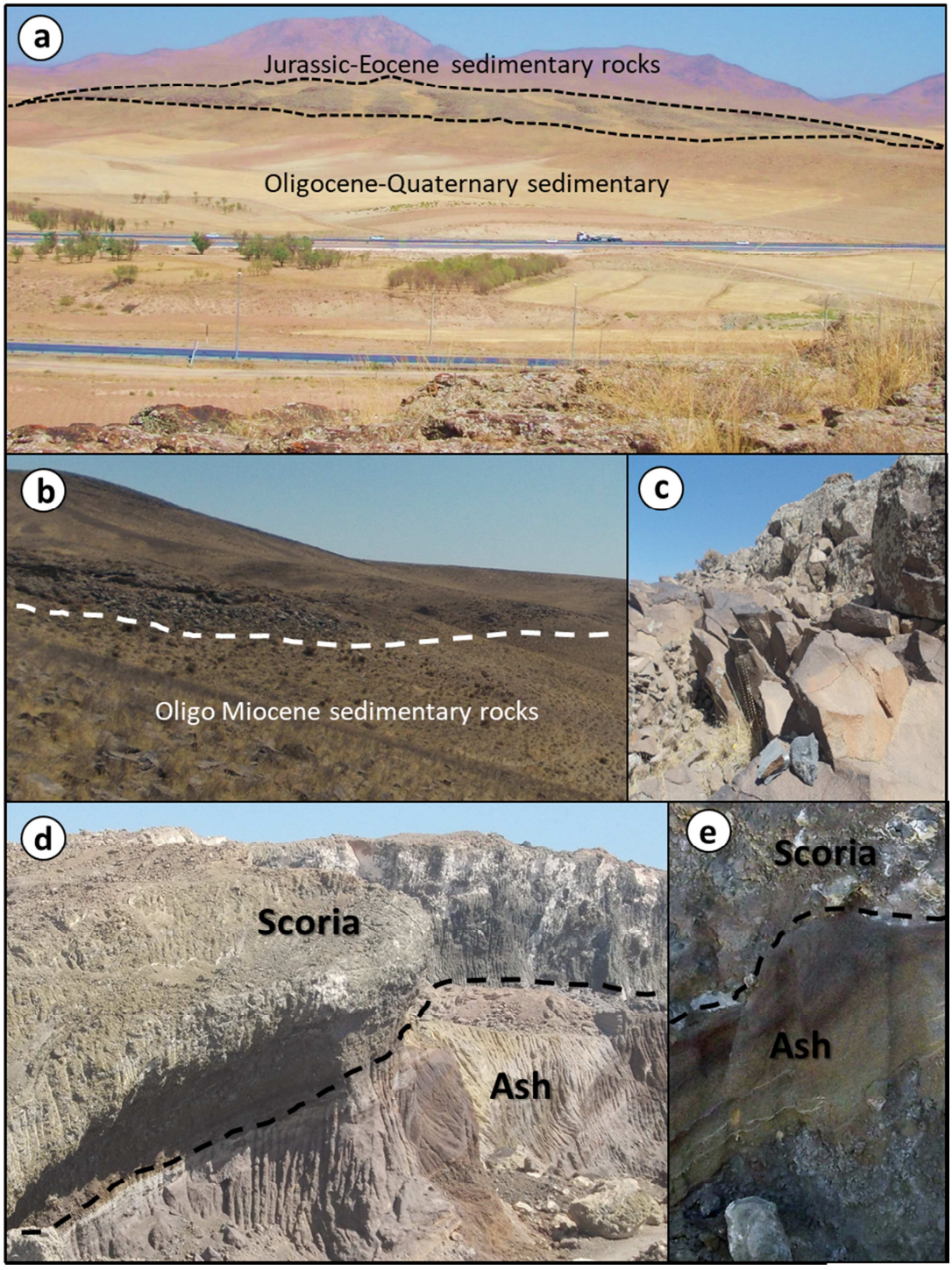

Fig. 15: *Representative field photographs for the Nowbaran area. a) View of a small shield volcano in the Dokhan area (~800x800 m and a maximum thickness of ~37 m), viewed to north cropping out Oligocene-Quaternary sedimentary rocks, with Jurassic-Eocene sedimentary rocks in the background; b) Emission centre with the highest eruptive thickness (~70 m) of all the volcanoes west of the Nowbaran, viewed to south; c) Contact between two lava units, viewed to north; d) Scoria-ash contact in Dokhan area with ~50 m thick scoria level in a cave front viewed to south-east; e) Close-up image of alternating ash and scoria units.*

2.2 Petrography

The investigated rocks are blackish, with a dark green colour in hand specimen. They are fine- to very fine-grained massive to vesicular porphyritic volcanic rocks, with a phenocryst load, essentially clinopyroxene ± olivine, ranging from ~5 to ~20% (Fig. 16a,b). Nearly half of the samples are massive rocks showing hypocrystalline texture, whereas the remaining half is vesicular and shows mostly hypohyaline textures. In this second group, vesicles, often filled by calcite, reach up to 60% of the thin section surface. They range from <0.2 mm up to ~5 mm in size, with rounded to irregular shapes. The mineralogical assemblage is similar in both groups and mainly consists of abundant clinopyroxene and olivine, followed by widespread calcite, nepheline, phlogopite and accessory apatite, perovskite and opaques as groundmass phases.

Euhedral tabular clinopyroxene (Fig. 16c) is the most abundant phase, occurring as the only microphenocrysts in about one third of the samples, whereas it is confined to the groundmass in two olivine-dominated samples. Clinopyroxene shows an average size of ~0.5 mm but it reaches up 1.5 mm in the most massive samples. It appears zoned and often clusters into aggregates or is included in larger calcite plagues (Fig. 16d). Subhedral to euhedral olivine is missing in about one third of the samples. Olivine microphenocrysts (~0.2-0.5 mm in size, rarely up to 1 mm) are more abundant than clinopyroxene in vesicular samples. Olivine often shows iddingsitic rims (Fig.16e) and it is sometimes found as aggregated crystals together with clinopyroxene. Calcite occurs as widespread large plagues (Fig. 16d,f), up to 3 mm in size, and often includes smaller clinopyroxene, apatite or opaque crystals. Calcite is also locally observed as partially filling vesicles and fractures. Euhedral to subhedral tabular phlogopite commonly occurs in about half of the samples (both in massive and vesicular samples), with a common opacitic aspect due to diffuse replacement by opaque oxides (Fig. 16g). Average length is ~3 mm, reaching up 5 mm. Tabular apatite is disseminated in a few samples only from the Dakhan district, reaching up to 0.2 mm in size (Fig. 16h).

Groundmass is composed by brownish glass plus variable amounts of small (<0.1 mm) clinopyroxene, widespread anhedral nepheline (Fig. 16i) and scarce iddingsitized olivine. In one Fastaq sample, rare perovskite crystals have been observed. Nepheline,

perovskite and other phases were identified by SEM-EMP analysis due to their very small grain sizes (Fig. 16j).

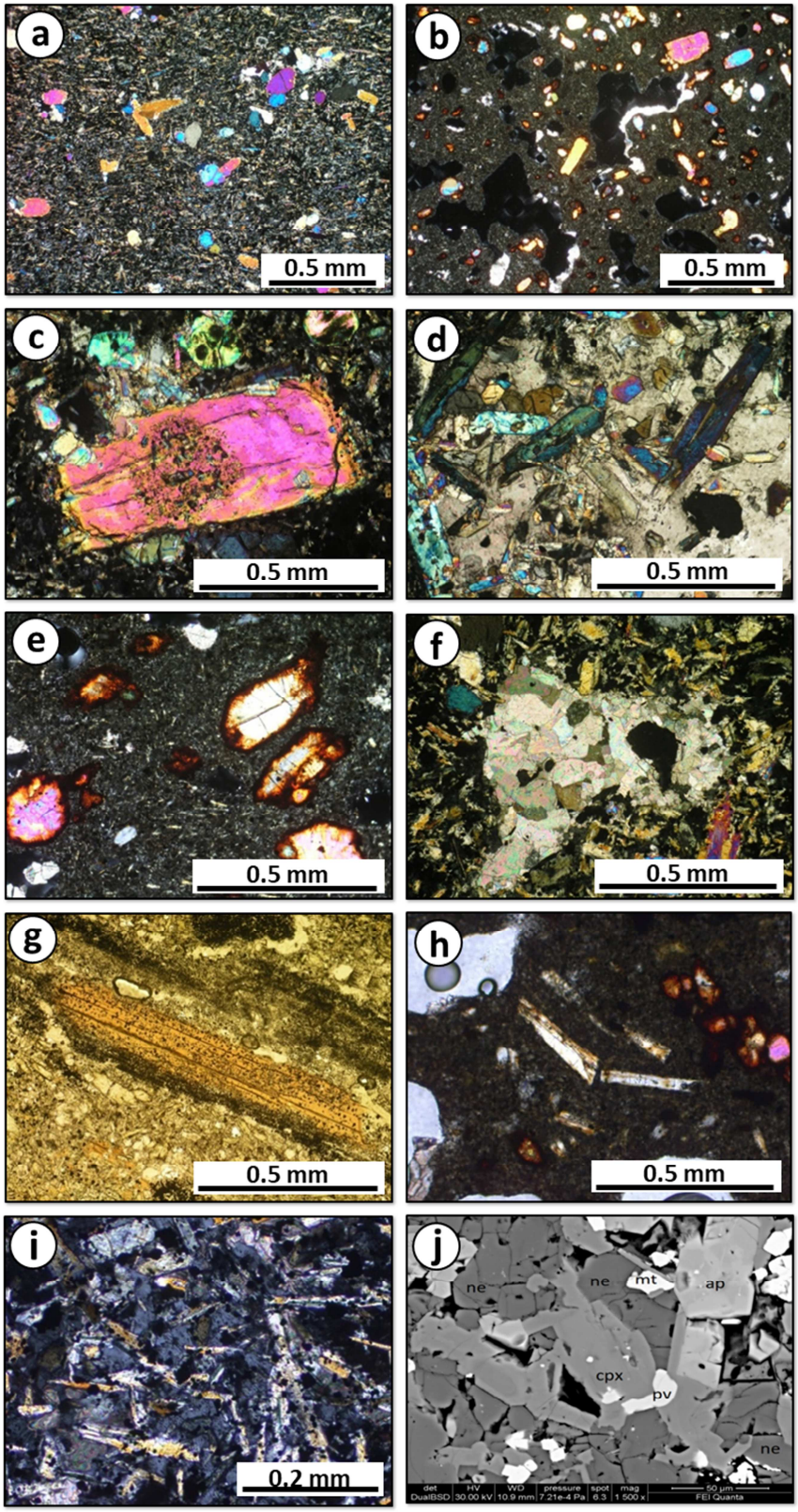

Fig. 16: *(caption on the next page)*

Fig. 16: *Representative photomicrographs (a-l, crossed polarizers view, except g, plane-polarized light view) and SEM-back scattered electron image (j) for the investigated Nowbaran rocks. a) massive and b) vesicular porphyritic texture; c) zoned euhedral clinopyroxene set into a holocrystalline groundmass made of clinopyroxene, nepheline and opaque phases; d) large calcite plague including clinopyroxene crystals; e) subhedral olivine crystals with iddingsitic rims set into a holocrystalline groundmass; f) large calcite plague; g) euhedral phlogopite crystal partially replaced by opaque oxides; h) tabular apatite microcryst; i) anhedral groundmass nepheline microcysts; j) holocrystalline groundmass with clinopyroxene (cpx), nepheline (ne), magnetite (mt), apatite (ap) and perovskite (pv).*

2.3 Mineral Chemistry

Nine representative samples were analysed for mineral chemistry. We report compositions of olivines, clinopyroxenes, carbonates, micas, foids, apatites, perovskites and opaque minerals for 313 analyses, fully reported in Appendix (Table 2 – Table 9).

Olivine is Mg-rich (Table 2), with microphenocrysts (Fo_{85-90}) largely overlapping in composition groundmass crystals (Fo_{85-91}; Fig. 17a). CaO content is quite variable, ranging from ~0.03 to ~0.91 wt%. NiO ranges between 0.03 and 0.55 wt%, without any clear correlation with MgO.

Clinopyroxenes fall exclusively in the diopside field ($Wo_{46-50}En_{40-48}Fs_{6-10}$; Table 3), with ~38% of the analyses showing a slight Ca-excess ($Wo_{50-53}En_{34-44}Fs_{6-13}$; Fig. 17b). Diopside shows Mg# [i.e., $Mg/(Mg+Fe^{2+})$] ranging from 0.80 to 0.89 and FeO in the ~3.6-6.3 wt% range. Several oxides show a good negative correlation with SiO_2 (TiO_2 = 0.2-4.2, R^2 = 0.88; Al_2O_3 = 0.1-8.1 wt%, R^2 = 0.91; FeO = 3.6-7.9 wt%, R^2 = 0.91; MgO 11.3-16.9 wt%, R^2 = 0.89), while the remaining are cloudy distributed with respect to silica. Diopside compositions with stoichiometric Ca-excess (i.e., Wo >50% mol) do not show substantial differences with “normal” diopside, albeit they tend to show lower Mg# = ~0.72-0.88 vs. 0.80-0.89), slight higher FeO (~3.9-7.9 wt% vs. 3.6-6.3 wt%) and Al_2O_3 (0.7-8.1 wt% vs. 0.1-5.0 wt%). About half of the clinopyroxenes has a slight deficiency of $Si+Al^{IV}$ to fill the tetrahedral site, and up to 0.06 apfu of Fe^{3+} is required to reach charge balance. Clinopyroxenes included in calcite plagues tend to have high MgO (av. ~16.0 wt%) and CaO (av. ~24.6 wt%), but are not well distinguished from groundmass or phenocryst compositions.

Brown mica was found in Dakhan and Qezel Hesar samples only. It occurs as a diffuse groundmass phase, mostly characterized by high MgO (~16.6-21.0 wt%; Table 4) and Mg# (~83.1-91.3), falling in the phlogopite composition. Only one sample from Dakhan shows lower Mg# (~0.70) because of its much higher FeO (~13.6 wt% vs. 3.5-6.2 wt% of the other Nowbaran micas). Nowbaran mica shows variable Al_2O_3 (9.3-22.3 wt%), indicating abundant eastonite content (Fig. 17c) and remarkably high TiO_2 (3.4-8.3 wt%) and F (3.4-7.0 wt%).

Carbonate minerals are CaO-rich (~52.2-57.7 wt%; Table 5) and generally have <1 wt% MgO, leading to almost pure calcite composition [Ca# = Ca/(Ca+Mg) = 0.98-1.00], except for Qezel Hesar calcites (MgO = 2.2-3.2 wt%, Ca# = 0.92-0.95). Nowbaran calcite is iron-poor (FeO <0.23 wt%, except one Dakhan sample with FeO ~1.5 wt%) and Sr-poor (SrO <0.1 wt%, with the exception of one Dakhan sample with SrO = 0.32 wt%).

Opaque minerals are represented by Ti-magnetite s.s. only (Usp_{35-54}; Table 6), with FeO_{tot} ~69.0-81.3 wt% and TiO_2 varying between ~8.0 and ~18.6 wt% (Fig. 17d). Al_2O_3 is always low (<1.5 wt%, with the exception of two outliers from Qezel Hesar with Al_2O_3 = 2.5-2.7 wt%), similarly to Cr_2O_3 (<0.8 wt%, with the exception of two analyses from Qezel Hesar and one from Dakhan with Cr_2O_3 1.6-2.3 and 1.1 wt%, respectively). MgO varies in a larger range (1.9-5.7 wt%).

Fluorapatite is a common groundmass phase, with CaO ranging from 51.1 to 55.3 wt%, P_2O_5 from 35.3 to 39.9 wt%, and F from 0.8 to 5.2 wt% (Table 7). The britholite component is always low, with SiO_2 <1.8 wt%. The SO_3 content remains low (<1.5 wt%).

Nepheline is a widespread groundmass phase with variable compositions: $Ne_{69-84}Ks_{8-32}Sil_{0-18}$ (Fig. 17e; Table 8). The parameter Na# [=Na/(Na+K)] clusters in two ranges, from 0.88 to 0.90 in the Qezel Hesar samples, and from 0.69 to 0.74 in the remaining. Qezel Hesar samples are also characterized by lower ferric iron (expressed as FeO = 1.0-1.9 wt%) compared to the rest of the samples (FeO = 1.8-2.1 wt%). CaO is always low (<0.6 wt%), with only three Qezel Hesar samples in the 1.0-1.6 wt% range.

Sodalite-group minerals are S-dominated and are roughly subdivided into two main types (Table 8). Qezel Hesar samples show relatively low SO_3 and Al_2O_3 content (~5.0-6.0 wt% and ~21.7-29.7 wt%, respectively) with relatively high silica (~34.6-39.9 wt%) and Cl (~1.0-1.9 wt%). The remaining sodalite crystals are characterized by higher SO_3 (~8.1-10.5 wt%), basically higher Al_2O_3 (~26.6-30.1 wt%) and slightly lower silica and Cl

(~32.6-34.8 wt% and ~0.4-1.0 wt%, respectively). Na_2O, K_2O and CaO vary in the same range in both sodalite types (~12.4-18.9 wt%, ~0.3-2.1 wt% and ~2.8-12.1 wt%, respectively). Based on these compositions, they correspond to the hauyne-lazurite solid solution series (though with lower CaO; Fig. 17f).

Perovskite is present as tiny accessory phase and only in one sample from Fastaq (NB24) it was possible to obtain three quantitative analyses (Table 9). One analysis approaches the perovskite *sensu stricto* end-member ($CaTiO_3$), while the other two show a Ti-Si substitution to form a still unnamed $CaSiO_3$ end-member (Mitchell et al., 2017). One of the two Si-bearing perovskites is also alkali-rich (Na_2O = 5.0 wt%; K_2O = 2.0 wt%).

Whole rock X-ray powder diffraction analyses (XRPD) clearly revealed the presence of hydrous alumosilicates referred to as zeolites. More specifically, analcime was identified in almost all the SiO_2-richest samples (whole-rock SiO_2 >39.8 wt%, from Dakhan and Qezel Hesar), showing very high silica content (~50.0-57.0 wt%) and Al_2O_3 between ~22.0 and 23.8 wt%. Na_2O is highly variable (~4.4-10.0 wt%), K_2O is low (~0.2-0.8 wt%) and CaO is <1.9 wt%. Only four Qezel Hesar analyses show high CaO (~8.6-10.7 wt%) compared to the average Nowbaran zeolites (~0.3-2.8 wt%), thus approaching the laumontite composition.

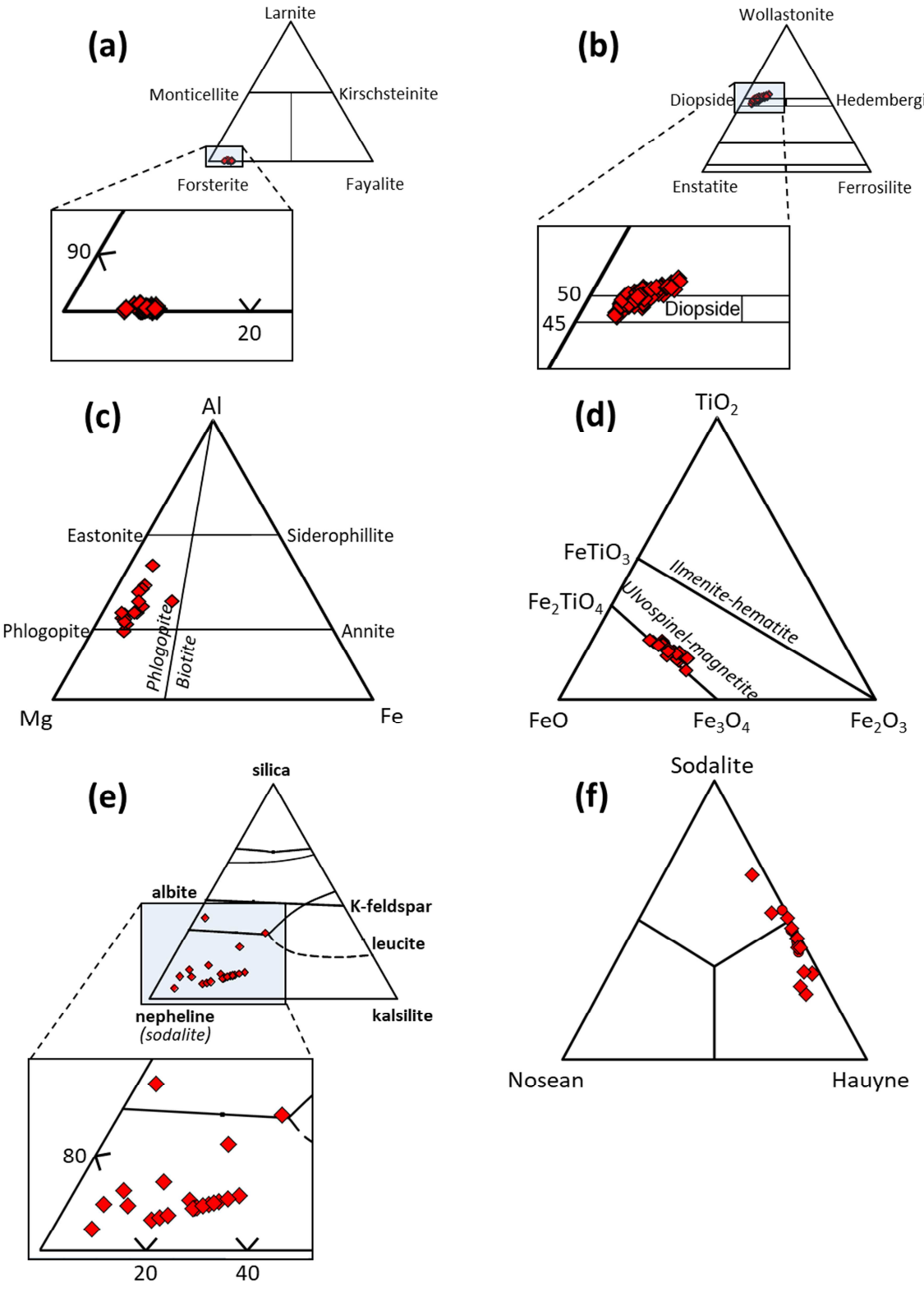

Fig. 17: *Composition of a) olivine, b) clinopyroxene, c) brown mica, d) opaque minerals, e) nepheline and f) sodalite from the investigated Nowbaran rocks.*

2.4 Major oxide content and variation

Twenty-one Nowbaran rocks collected in four main districts (Dakhan, Fastaq, Chalfakhreh and Qezel Hesar) have been analysed for major oxide and trace element composition. The results are reported in Table 10.

The studied rocks are ultrabasic, with SiO_2 ranging from ~35.4 to ~41.4 wt% and a modest though variable alkali content (Na_2O = 1.8-5.4 wt%, K_2O = 0.2-2.3 wt%, Na_2O+K_2O = 2.2-6.2 wt%; Fig. 18a). The MgO (8.7-13.3 wt%) and Mg# (0.69-0.74) are particularly high. Another fundamental peculiarity of these rocks is their ultracalcic nature, i.e., CaO/Al_2O_3 >1 (1.1-1.9).

With the exception of Al_2O_3, (R^2 = 0.75), none of the major oxides is correlated in any way with SiO_2. CO_2 shows an interesting negative correlation with SiO_2 (R^2 = 0.82), but no correlation with CaO (R^2 = 0.17). The mass loss on ignition (LOI) is high (average 4.4 wt%) and without any correlation with SiO_2. It mostly varies between 2.6 and 5.1 wt% (with three samples in the 6.0-10.4 wt% range) and shows no correlation with SiO_2. No systematic difference can be found between the rocks from the four districts, except for Qezel Hesar rocks showing the highest SiO_2, Al_2O_3 and Fe_2O_{3tot}, and the lowest CaO, K_2O and CO_2. If these latter are not taken into account, Nowbaran rocks display a good Fe_2O_{3tot} vs. MgO correlation (R^2 = 0.87).

As already outlined, the peculiarity of Nowbaran rocks lies in their extremely low SiO_2 content, particularly evident when compared to Iran and SE Anatolia Cenozoic igneous rocks (i.e., those related to the Bitlis-Zagros suture zone; Fig. 19). Nowbaran rocks cluster towards the Si-poor end of major oxide trends, which in some cases are relatively well defined, while in other instances the relationships are cloudier. Nowbaran rocks have also the highest MgO (up to 13.3 wt%), CaO (up to 18.3 wt%) and P_2O_5 (up to 3.4 wt%), as well as the lowest Al_2O_3 (down to 9.4 wt%), as well as very high TiO_2 (2.0-2.6 wt%) and Fe_2O_{3tot} (8.6-11.3 wt%), among the highest values recorded in the area. On the other hand, large spreads characterize Na_2O and K_2O (1.8-5.4 wt% and 0.2-2.3 wt%, respectively), spanning the entire literature range for these oxides (Fig. 19).

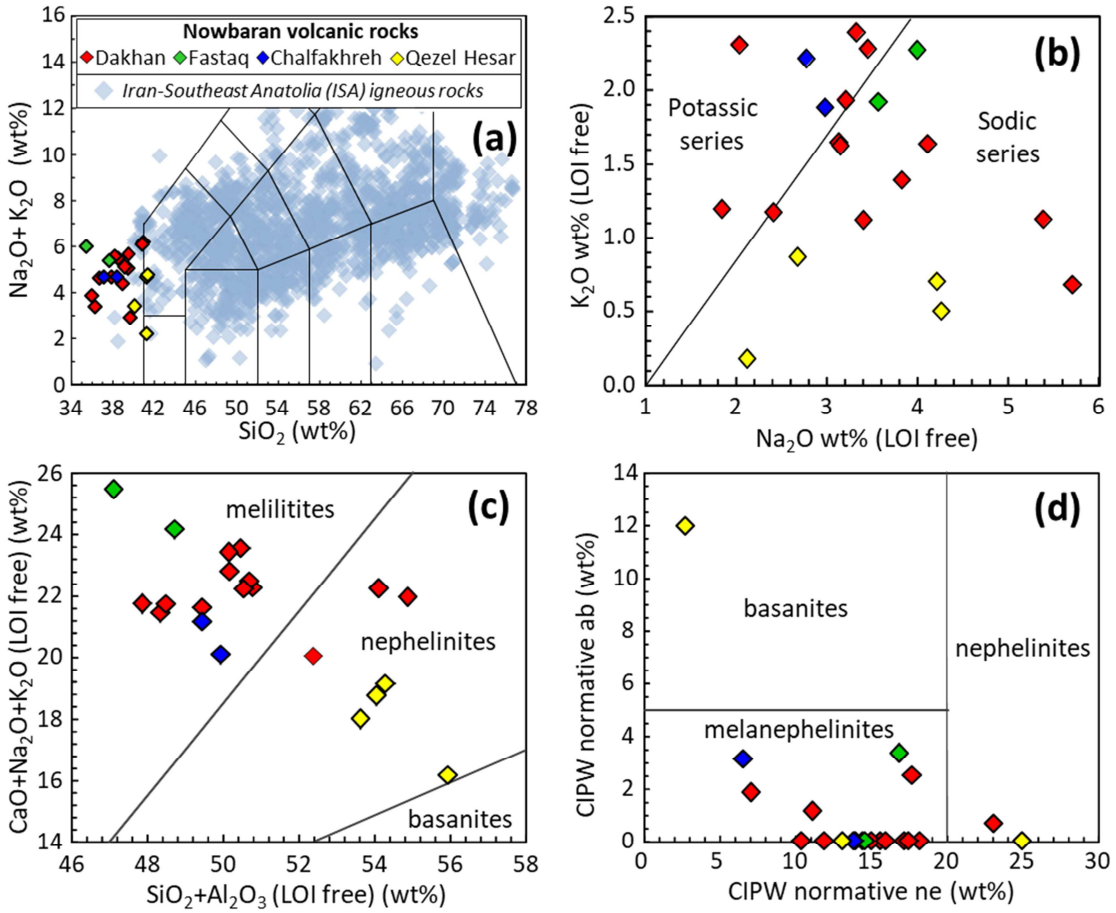

Fig. 18: *a) Total Alkali vs. Silica (TAS; Le Maitre, 2002), b) K_2O vs. Na_2O (Middlemost, 1975), c) $CaO+Na_2O+K_2O$ vs. $SiO_2+Al_2O_3$ and d) CIPW normative albite vs. CIPW normative nepheline (Le Bas, 1989) classification diagrams for the investigated Nowbaran rocks from the various sampled locations. In a) literature data for Iran and SE Anatolia Cenozoic rocks (ISA) are also reported for comparison.*

2.5 Mineralogical-geochemical classification

The extremely low SiO_2 of Nowbaran volcanic rocks is definitely atypical and uncommon when compared with the other Cenozoic UDMA igneous rocks. This peculiarity is clearly noticeable in the TAS diagram (Fig. 18a), where most of the Nowbaran samples fall into the foidite-melilitite field, with a few Qezel Hesar samples straddling the basanite-tephrite and the picro-basalt fields (Le Bas, 2000). About 60% of the analysed Nowbaran rocks plot in the sodic field in the K_2O vs. Na_2O diagram of Middlemost (1975; Fig. 18b), with only a few samples (from Dakhan and Chalfakhreh) falling in the potassic field.

If recalculated on a LOI-free basis (not shown), a few of the Nowbaran rocks plot in the basanite-tephrite and picrobasalt fields in the TAS diagram. The lack of feldspars in all the Nowbaran rocks makes both the basanite and tephrite definitions as inappropriate. According to IUGS (Le Maitre, 2002) a picrobasalt is defined on chemical grounds only, i.e., a volcanic rock with SiO_2 41-45 wt%, Na_2O+K_2O <3 wt% and MgO <12 wt%. However, for the sake of clarity and considering only the measured major oxide content (i.e., not recalculated to LOI-free basis) we would refer to the Nowbaran rocks as strongly ultrabasic foidites, with details provided below.

Given their peculiar mineralogical and whole-rock chemical composition of the investigated rocks, the appropriate classification scheme is that of Le Bas (1989) for nephelinitic and basanitic rocks. Following this diagram, Nowbaran rocks fall in the melilitite and nephelinite fields (Fig. 18c). However, the relatively low CIPW normative larnite content (<7%), and, above all, the absence of modal melilite do not allow us to classify Nowbaran rocks as melilitites (by definition volcanic rocks with >10% modal melilite and >10% CIPW normative larnite; Le Maitre, 2002). Taking into consideration the CIPW normative nepheline vs. CIPW normative albite diagram (Fig. 18d; Le Bas, 1989), Nowbaran rocks fall mostly in the melanephelinite field, showing <20 wt% normative nepheline and <5 wt% normative albite. Two samples from Dakhan and Qezel Hesar having higher CIPW normative nepheline fall in the nephelinite field. Finally, the Qezel Hesar sample previously referred to as picrobasalt shows ~12 wt% CIPW normative albite, falling in the basanite field of Fig. 18d, a term that we will not use, though.

The term melanephelinite originally indicated a special group of nephelinites with 1) abundant clinopyroxene and little or no olivine among the modal mafic phases, 2) little, if any, nepheline confined in the groundmass, and 3) CIPW normative nepheline (Le Bas, 1989). Being Nowbaran rocks clinopyroxene- and olivine-phyric, and having <20% CIPW normative nepheline (with two exceptions) and <5% CIPW normative albite (with only one exception), the omni-comprehensive melanephelinite term will be used in this work.

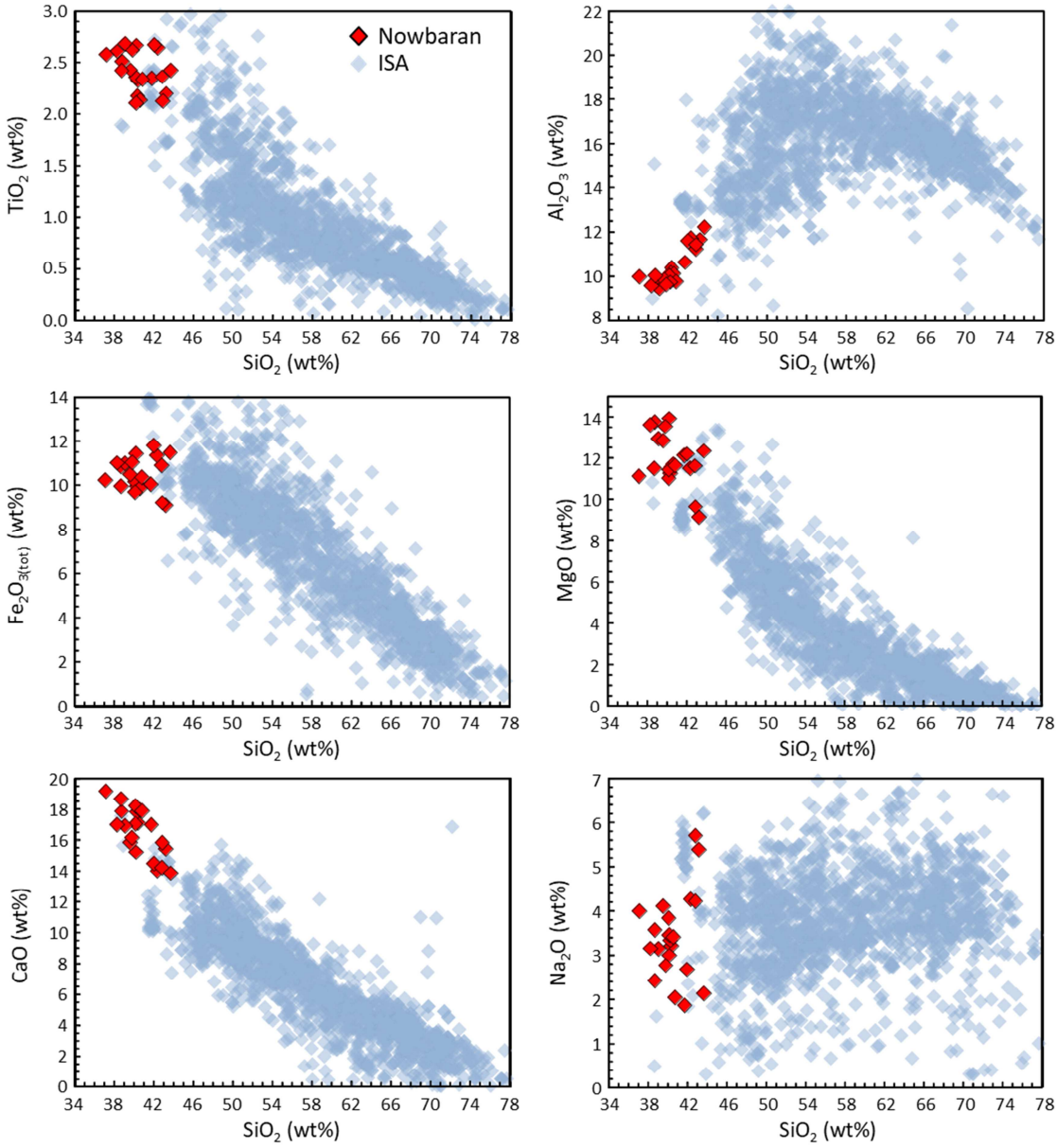

Fig. 19: *Selected major- elements vs. Silica variation diagrams for the investigated Nowbaran rocks. Literature data for Iran and SE Anatolia Cenozoic rocks (ISA) are also reported for comparison.*

2.6 Trace element content and normalized diagrams

The variation of the trace elements in Nowbaran rocks is noteworthy, because no trend can be defined when compared to SiO_2, MgO or CaO. The investigated four districts fully overlap as concerns both the incompatible and compatible element contents. The only comments can be made comparing the Nowbaran rocks to the Iran

and SE Anatolia Cenozoic igneous rocks (hereafter referred to "ISA" rocks). Nowbaran rocks show a general enrichment in Sr (~1900-3900 ppm; Table 10), which is striking, considering that >99% of ISA rocks have Sr <2000 ppm). Albeit not as extreme, Nowbaran rocks are also particularly enriched in Ba (~1300-2500 ppm) compared to >90% of neighbouring rocks, whereas Rb (~14-61 ppm) and Cs (mostly <2 ppm) are fully within the literature range of ISA rocks. Among transition metals, Sc (~14-19 ppm), V (~130-260 ppm) and Cu (~50-100 ppm) are well within the ISA rock range, while Cr (~260-480 ppm), Co (~43-54 ppm), Ni (~230-360 ppm) and Zn (~120-180 ppm) cluster close to the rare highest concentrations recorded in ISA rocks. High Field Strength Elements (HFSE) and Y are relatively enriched in Nowbaran rocks (Zr ~280-420 ppm; Nb ~53-81 ppm; Hf ~6.0-8.5 ppm; Ta ~3.0-4.5 ppm), clustering together with the basic-ultrabasic ISA rocks.

Concerning the Rare Earth Element (REE), the lightest REE (LREE, from La to Eu) are particularly more abundant in Nowbaran rocks (e.g., La ~120-290 ppm; Eu ~4-7 ppm) than in the ISA rocks (>99% of the samples having La <150 ppm and Eu <4 ppm). On the other hand, the heavier REE (HREEE, from Gd to Lu) of Nowbaran rocks fully overlap the bulk of ISA rocks. Pb (~11-40 ppm), Th (~15-42 ppm) and U (~2-6 ppm) are moderately enriched in Nowbaran rocks, whose compositions are matched by a minority of ISA magmas.

CI-chondrite-normalized patterns (normalization after King et al., 2020) for Nowbaran rocks are mildly to strongly fractionated, as typically observed for ultrabasic, CaO-rich lithologies (Fig. 20a). The $(La/Lu)_N$ ratios (where the "N" subscript means CI-chondrite-normalized values) range from ~60 to ~150, with La_N ~380-950 and Lu_N ~5-7, without any substantial difference among the four investigated districts. Nowbaran rocks are also characterized by a moderate/high MREE/HREE fractionation [e.g., $(Sm/Yb)_N$ ~11-23; average = 15 ± 3]. The correlation of La with the other REE decreases with increasing atomic mass, from R^2 = 1.00 for Ce to R^2 = 0.05 for Lu. No Eu anomaly (Eu/Eu* = 0.99-1.07) and no correlation between REE fractionation with SiO_2, MgO or CaO has been observed.

Primitive mantle-normalized incompatible multielemental patterns (normalization after Lyubetskaya and Korenaga, 2007) for Nowbaran rocks are reported in Fig. 20b. Patterns are quite fractionated, with deep troughs at Rb and K, minor troughs at Pb

and Ti and peaks at Cs, Th-U and La-Ce. Most of the incompatible elements are clustered between 10 and 1000 times the primitive mantle estimate, with HREE showing the lowest degree of enrichment. The composition of the rocks from the four districts is overlapping in terms of interelemental fractionation, but Qezel Hesar samples (those with the highest SiO_2 and the lowest CaO) show the lowest enrichment in the most incompatible elements (left portion of the diagram), except for Ce, and the highest enrichment for the least incompatible elements (i.e., HREE; Fig. 20b). Fastaq rocks have commonly the highest incompatible element contents, and the two other districts of Dakhan and Chalfakhreh plot in between these two extremes.

When compared to the classical HiMU-OIB (High-Mu Ocean Island Basalts, where Mu = $\mu = {}^{238}U/{}^{204}Pb$) of St. Helena Island (Kawabata et al., 2011), Nowbaran rocks do not show peaks at Nb-Ta and Ti, but share the troughs at K and Pb (albeit less pronounced) and have much lower HREE (Fig. 20b). Nowbaran rocks often plot in intermediate position between HiMU-OIB and the average composition of global subducting sediments (GloSS, considered as a reference of the enrichment factor registered in subduction zones; Plank, 2014), especially for the Nb-Ta pair. Despite Nowbaran rocks do not show any peak at Pb, typical of GloSS and other magmas emplaced in subduction-related settings, their Pb content is higher than the GloSS average (11-41 ppm, average 23.5 ppm, compared to 21.2 ppm for GloSS). Similarly to what observed for GloSS, Nowbaran rocks are also characterized by evident Ti troughs.

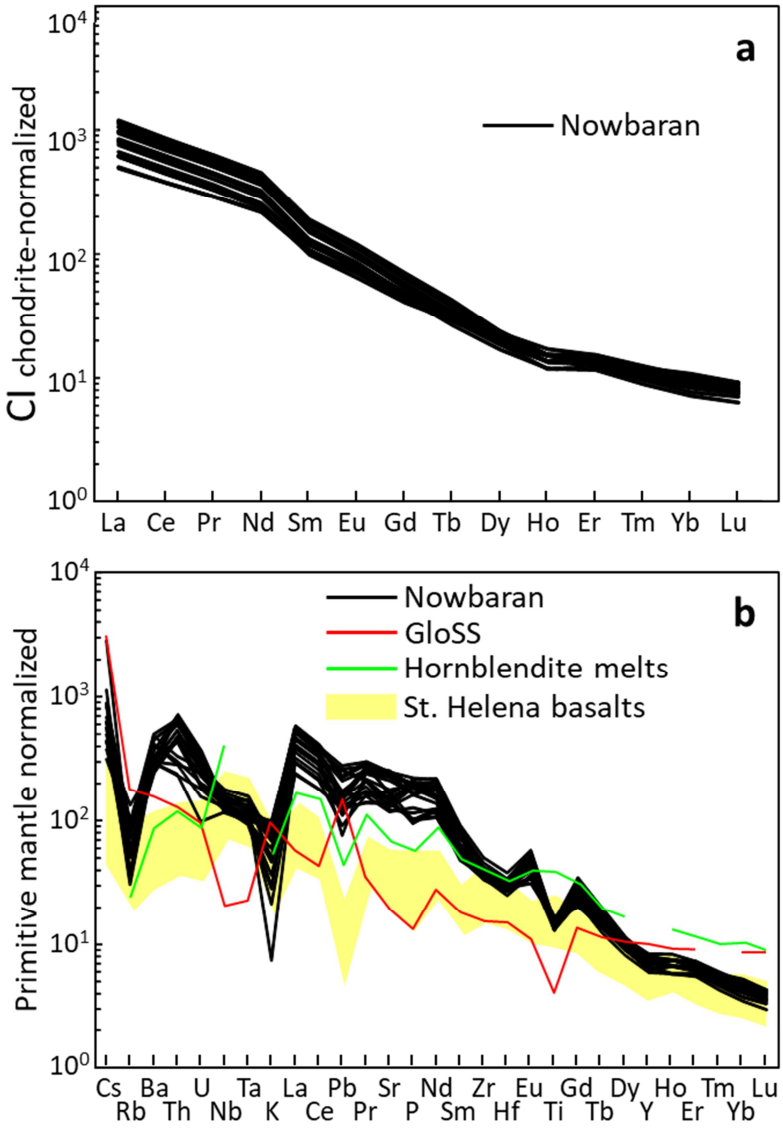

Fig. 20: *a) Cl-chondrite-normalized (after King et al., 2020) REE patterns and b) primitive mantle-normalized (after Lyubetskaya and Korenaga, 2007) incompatible multielemental patterns for the investigated Nowbaran rocks. In b) the field for HiMU-OIB basalts from St. Helena Island (from Kawabata et al., 2011) and the average composition of the global subducting sediments (GloSS; Plank, 2014) are also reported for comparison.*

2.7 Sr-Nd-Pb isotope ratios

Seven representative samples were selected for Sr-Nd-Pb isotopic ratio measurements, namely four samples are from Dakhan and one for each from the Fastaq, Chalfakhreh and Qezel Hesar districts. The measured isotopic ratios are reported in Table 10.

No recalculation to initial values has been performed due to the very young age, likely <1 Ma, low Rb/Sr (<0.02), Sm/Nd (<0.16), U/Pb (<0.3) and Th/Pb (<1.4). In the $^{143}Nd/^{144}Nd$ vs. $^{87}Sr/^{86}Sr$ diagram (Fig. 21a), Nowbaran rocks cluster in a relatively narrow field ($^{87}Sr/^{86}Sr$ = 0.70519-0.70564; $^{143}Nd/^{144}Nd$ = 0.51263-51269), straddling the ChUR (Chondritic Uniform Reservoir) estimate but displaced towards Sr isotopic compositions more radiogenic than BSE (Bulk Silicate Earth). Both $^{87}Sr/^{86}Sr$ and $^{143}Nd/^{144}Nd$ values do not show any correlation with SiO_2 (R^2 = 0.05 and 0.25, respectively; only $^{87}Sr/^{86}Sr$ reported in Fig. 21b) or vs. MgO (R^2 = 0.19 and 0.04, respectively). Nowbaran rocks also show narrow $^{206}Pb/^{204}Pb$ (18.54-18.66), $^{207}Pb/^{204}Pb$ (15.66-15.68) and $^{208}Pb/^{204}Pb$ ranges (38.66-38.79), clustering in a small area on the right of the 4.56 Ga Geochron and above the NHRL (Northern Hemisphere Reference Line; Fig. 21c, d).

Isotopic ratios of Nowbaran rocks fully plot within those of literature ISA rocks, in between the DMM (Depleted MORB Mantle) and EM-II (Enriched Mantle II) mantle end-members in the $^{143}Nd/^{144}Nd$ vs. $^{87}Sr/^{86}Sr$ diagram, and define almost the same isotopic field as that of the western Mediterranean arc magmas (e.g., Lustrino et al., 2011). The same can be held also for Pb isotopes, albeit Nowbaran and ISA rocks are displaced towards slightly lower $^{206}Pb/^{204}Pb$. In $^{208}Pb/^{204}Pb$ and $^{207}Pb/^{204}Pb$ vs. $^{206}Pb/^{204}Pb$ diagrams, Nowbaran rocks mostly overlap the EM-II mantle end-member. As observed for Sr and Nd isotopes, no substantial correlation among Pb isotopic ratios and SiO_2 is observed, and only a crude negative correlation with MgO is found for $^{206}Pb/^{204}Pb$ (R^2 = 0.52) and $^{208}Pb/^{204}Pb$ (R^2 = 0.60).

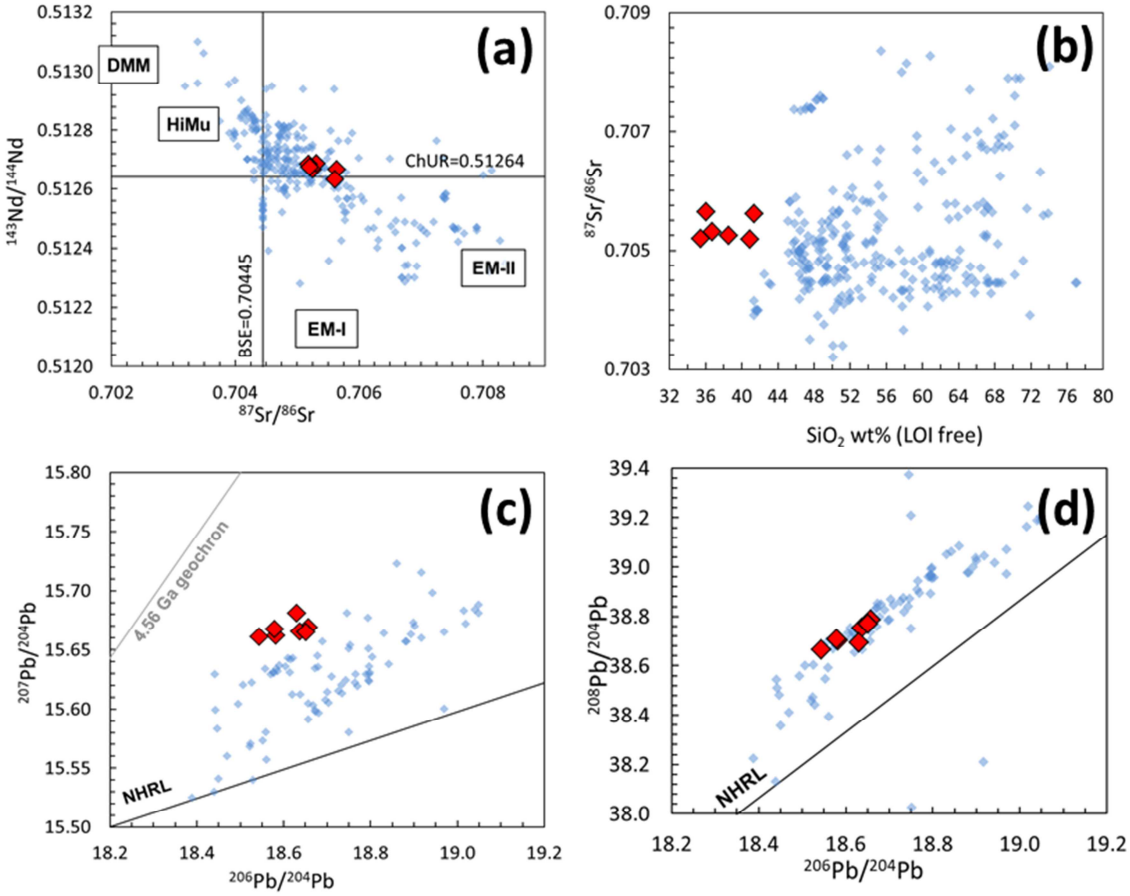

Fig. 21: *a) $^{143}Nd/^{144}Nd$ vs. $^{87}Sr/^{86}Sr$, b) $^{87}Sr/^{86}Sr$ vs. SiO_2, c) $^{207}Pb/^{204}Pb$ vs. $^{206}Pb/^{204}Pb$ and d) $^{208}Pb/^{204}Pb$ vs. $^{206}Pb/^{204}Pb$ for the investigated Nowbaran rocks. Literature data for Iran and SE Anatolia Cenozoic rocks (ISA) are reported for comparison. Also shown are the isotopic compositions for BSE (Bulk Silicate Earth) and ChUR (Chondritic Uniform Reservoir), the DMM (Depleted MORB Mantle), HiMu (high-μ) and EM-I and EM-II (Enriched Mantle I and II) end-members (Lustrino and Anderson, 2015), the 4.56 Ga Geochron and the Northern Hemisphere Reference Line (NHRL; Hart, 1984).*

2.8 Discussion

2.8.1 Fractional crystallization and crustal contamination

The general lack of correlation between major oxides for the Nowbaran melanephelinites prevents a clear identification of the minerals potentially involved during fractional crystallization processes and points to the existence of slightly different magma batches in each of the four investigated districts. The high MgO, Mg#, Cr and Ni match the compositions of melts in equilibrium with mantle paragenesis (Righter and Rosas-Elguera, 2001; Downes et al., 2004; Azizi et al., 2014; Witte et al.,

2017), despite Nowbaran magmas are very different from the typical basaltic compositions generated by volatile-free four-phase peridotitic rocks.

Any process involving contamination with typical felsic upper crustal lithologies is untenable for Nowbaran rocks, not only for their ultrabasic composition, but also for their abundances of the most incompatible elements, as well as other features (e.g., Ti troughs, relatively high Nb-Ta contents and extremely high Sr values), by far higher than the typical continental crust values (e.g., Rudnick and Gao, 2014, and references therein). Above all, the absence of major oxide and trace element correlation with any other parameter can be hardly explained in terms of crustal digestion by mantle-derived melts. As an example, Nowbaran trace elements ratios (e.g., Zr/Nb = 4.2-6.5, Ba/Nb = 17-42, Ba/La = 5-15) are much different from typical continental crust values (Zr/Nb = ~14; Ba/Nb = ~84; Ba/La = ~27; Rudnick and Gao, 2014), as also supported by the lack of correlation between $^{87}Sr/^{86}Sr$ and SiO_2 (Fig. 21b) or MgO. Crustal contamination involving CaO-rich lithologies is considered in the following section.

2.8.1.1 Interaction with sedimentary carbonates

Calcium-rich lithologies belonging to the Oligo-Miocene Qom Formation occur in the substratum of the Nowbaran area. These carbonate-rich rocks rarely crop out, being mostly covered by Miocene and Plio-Quaternary volcanic deposits. Near the Qom Basin, the Qom Formation reaches a maximum thickness of ~1 km (Reuter et al., 2009), which may be relevant when considering the ascent of small volumes of magma. Experimental petrology studies indicate the possibility for silicatic magma to digest high amounts of sedimentary carbonatic rocks, resulting in hybrid SiO_2-poor, CaO-rich compositions (e.g., Lustrino et al., 2019b, 2020). In some cases, the production of exsolved carbonatitic melts (e.g., Di Rocco et al., 2012; Shaw, 2018) or magmatic calcite crystallized from CaO-doped magma (e.g., Gozzi et al., 2014) is reported.

Carbonatites *sensu stricto* (i.e., mantle-derived) are considered as the solidification products of melts strongly enriched in incompatible elements, in particular LREE, Sr, Ba and P (Jones et al., 2013; Song et al., 2016). On the other hand, sedimentary rocks like limestones and marls are sterile rocks, showing low incompatible element contents

(e.g., La ~2-40 ppm; Di Battistini et al., 2001; Lustrino et al., 2020). In the La vs. CaO diagram (Fig. 22), average compositions of worldwide volcanic carbonatites and plutonic Ca-carbonatites are reported together with the typical compositions of CaO-rich sedimentary rocks (marls and limestones) from central Italy (Lustrino et al., 2020). Nowbaran rocks are far away from the typical composition of volcanic carbonatites and plutonic Ca-carbonatites, having much lower CaO (<19 wt%) and La (<280 ppm). Interestingly, Vosighi Abedini (1981), quoting unpublished radiogenic $^{87}Sr/^{86}Sr$ isotopic ratios, assumes that the carbonate fraction in Nowbaran rocks is of secondary origin. The impossibility to check any data renders this statement at least dubious.

No Ca-rich rims nor any reaction rims around olivine, or limestone xenoliths have been observed in Nowbaran thin sections. Also, the absence of significant trends in major oxides and incompatible elements, as well as Sr-Nd-Pb isotopic ratios, are inconsistent with a process of crustal assimilation involving sedimentary carbonates. Consequently, the possibility that the original magma was significantly modified after digestion of limestones and/or dolostones is considered negligible.

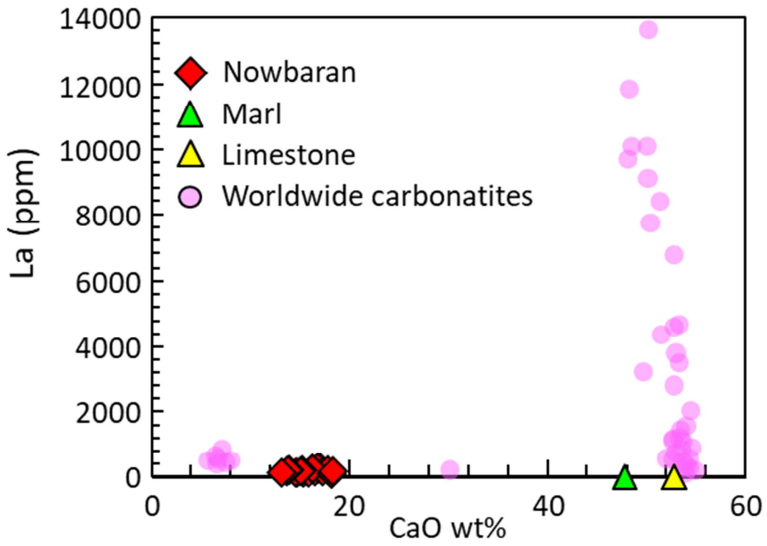

Fig. 22*: La vs. CaO diagram for the investigated Nowbaran rocks from the various sampled locations. The Ca-carbonatites from GEOROC site (pink circles), together with marls, marly limestones and limestones from central Italy (Di Battistini et al., 2001; Lustrino et al., 2020) are shown for comparison.*

2.8.2 The Nowbaran rocks in the context of the Bitlis-Zagros Orogen

Despite the extremely widespread area of comparison and the variable age of emplacement (>65 Myr), the bulk of ISA rocks define roughly coherent trends of evolution (Fig. 19). Assuming SiO_2 as indicative of the degree of evolution of a magma, ISA rocks show negative correlation for TiO_2, Fe_2O_{3tot}, MgO and CaO, classically associated to fractionation of ferromagnesian minerals (mostly olivine, clinopyroxene and Ti-magnetite). Alumina shows the typical bell-shaped trend, peaking at ~55 wt% SiO_2, indicating the strong involvement of feldspars in the cumulating assemblages of mildly to strongly evolved melts. In this framework, the position of Nowbaran rocks is outstanding. The rocks from this small and up to now unknown volcanic district cannot be explained with a model involving the generation of partial melts from a classical four-phase H-C-free peridotite. The absence of feldspars, the low SiO_2 and high CaO require the presence of additional lithologies in the mantle sources.

The strong REE fractionation of Nowbaran magmas, as testified by $(La/Lu)_N$ up to ~150 (Fig. 20a), may be indicative of residual garnet, albeit the overall source mineralogy is not consistent with a classical garnet lherzolite. Indeed, partial melts of such kind of source (e.g., Grove et al., 2013) are significantly different from Nowbaran rocks in terms of major oxide contents and mineral parageneses (e.g., much higher SiO_2 and Al_2O_3, coupled with lower CaO and TiO_2, as well as plagioclase-rich assemblage).

Some petrographic and geochemical characteristics of Nowbaran rocks have been found also in Quaternary nephelinites from Mahabad lavas (Iran Azerbaijan, ~500 km northwest of Nowbaran; Kheirkhah et al., 2013) and Çatak (SE Anatolia, Bitlis Massif, Turkey; Özdemir et al., 2019).

Mahabad small-volume mafic lavas result comparable to Nowbaran rocks from a petrographic point of view. Indeed, despite being classified mostly as basanites with minor nephelinites and alkali basalts, these rocks are plagioclase-free clinopyroxene- and olivine-phyric lavas with a nepheline-bearing fine-grained groundmass. Excluding the few compositions with the highest SiO_2 (46.6-47.0 wt%), the Mahabad rocks show lower TiO_2 (<1.7 wt%) and higher Al_2O_3 (>12.4 wt%) with respect to Nowbaran melanephelinites (>2 wt% and <11.4 wt% for TiO_2 and Al_2O_3, respectively). Moreover,

Mahabad rocks show generally lower CaO (13.5-14.9 wt% vs. 13.1-18.3 wt%) and lower P_2O_5 (1.5-1.7 wt% vs. 1.4-3.3 wt%), and higher SiO_2 (40.6-42.3 wt% vs. 35.4-41.4 wt%). The high Mg# (0.6-0.7), Ni (~250-300 ppm) and Cr (~300-400 ppm) of the ultrabasic Mahabad rocks are close to Nowbaran compositions and likely indicate equilibrium with peridotitic mantle. These features, coupled with homogeneous low $^{87}Sr/^{86}Sr$ (0.70441-0.70445) and high $^{143}Nd/^{144}Nd$ (0.51269-0.51270) of Mahabad ultrabasic rocks excludes significant crustal contamination. Worth nothing, also Mahabad lavas pierced limestone successions (of Jurassic-Cretaceous and Miocene age).

The comparison of Nowbaran rocks with Mahabad lavas is particularly relevant also because both districts cover a very restricted area and are relatively young manifestations (late Quaternary, although no absolute age determination is available). The primitive mantle-normalized incompatible element patterns of the two districts share remarkable similarities and nearly complete overlap. Mahabad rocks are only displaced toward slightly less enriched compositions, but with intra-elemental fractionation similar to what recorded at Nowbaran. Kheirkhah et al. (2013) proposed that Mahabad magmas derive from amphibole-rich metasomatic veins or eclogite from the lithospheric mantle, but provided no quantitative constrains.

Also the Quaternary (~0.6 Ma) rocks from Çatak are petrographically comparable with Nowbaran melanephelinites, being characterized by clinopyroxene, olivine, Ti-magnetite and nepheline, and lacking feldspar. Regarding major oxides, a partial overlap with Nowbaran rocks can be observed only for TiO_2 (2.05-2.39 wt%), K_2O (0.94-1.99 wt%) and P_2O_5 (1.56-1.84 wt%). The remaining oxides are either higher (Al_2O_3 = 12.9-13.3 wt%, Fe_2O_{3tot} = 13.3-14.3 wt%, MnO = 0.18-0.19 wt%, Na_2O = 4.65-5.92 wt%) or lower (MgO = 8.44-9.68 wt%, CaO = 9.90-11.6 wt%) in Çatak rocks. On the other hand, the primitive mantle-normalized multielemental patterns share several similarities, among which the deep troughs at Rb-K and Ti are the most striking (Fig. 20b). A complex and poorly constrained petrogenetic model involving extreme melt extraction (23%) from a phlogopite and apatite-bearing garnet peridotite, followed by ~2% metasomatic enrichment by a “MORB type melt”, and eventually 4% of further melt extraction has been proposed by Özdemir et al. (2019) to explain the genesis of Çatak volcanic rocks. The same authors also proposed a blended origin for Çatak magmas as generated by two melts mixing in a ratio ranging from ~30:70 to ~95:5.

These two melts should derive from 0.5-0.75% melting of a phlogopite garnet peridotite and from 20-30% melting of hornblendite veins.

2.8.3 Carbonated-peridotite origin

Several lines of evidence (i.e., diamond inclusions, high CO_2 output from arc volcanoes, carbonatitic magmas) indicate significant carbon storage in Earth mantle (e.g., Yaxley et al., 2019). Partial melting of subducted carbonated rocks, dissolution of carbonate minerals (e.g., dolomite breakdown) or serpentinite dehydration in subduction zones are able to release carbon dioxide from slab into fluids percolating mantle wedges. Thus, the release of COH fluids deriving from carbonates and hydrous minerals influences both the carbon recycling and magmatism at subduction zones (e.g., Scambelluri et al., 2016; Sun and Dasgupta, 2020).

As already mentioned above, low-degree partial melting of a carbonate-bearing peridotite would generate dolomitic to magnesitic melts characterized by strong mobility due to the high density and viscosity contrast with the upper mantle matrix. The arrival of these carbonatitic melts at the surface is controlled by the carbonate ledge, an invariant point which governs the melting processes in the upper mantle (i.e. P ~ 2-8 GPa; Gudfinnsson and Presnall, 2005) in function of the overall compositions and of the temperature. Thus ultrabasic compositions such as those observed at Nowbaran, strongly depends on the presence of carbonates in their mantle sources (Wyllie and Huang, 1976; Brey and Green, 1977; Eggler, 1978; Wendlandt and Mysen, 1980; Wallace and Green, 1988; Falloon and Green, 1989; Hirose, 1997), as a link between ultrabasic magmas and carbonatitic liquids is reflected by the common association of nephelinites, melilitites with plutonic and volcanic carbonatites.

Alternatively, the linkage of carbonatitic melts with silicatic melts with increasing SiO_2 could be interpreted as the effect of strongly ultrabasic melts dissolving mantle enstatite during their upwelling, crystallizing olivine and increasing the SiO_2 content of the reacted magma. According to this view, the sequence of carbonatitic to melilititic to kimberlitic and eventually nephelinitic, basanitic and alkali basaltic compositions is not related to increasing temperature (and consequent increase of melting degree),

but it is simply the effect of the reaction between carbonatitic-silicatic strongly ultrabasic melts with normal peridotite matrix (e.g., Gervasoni et al., 2017).

2.8.4 Hornblendite-derived origin

Low-degree melts of amphibole-rich (hornblendite) metasomatic veins in the lithosphere is another hypothesis to explain the origin of SiO_2-undersaturated alkaline melts in oceanic islands and in intracontinental settings. Low-degree melts of H_2O- or CO_2-bearing garnet peridotitic mantle could infiltrate within the lithospheric mantle producing anhydrous and hydrous metasomatic fronts (Pilet et al., 2008, 2011; Pilet, 2015). These lithologies are characterized by lower solidus temperature compared to average volatile-free peridotite, making them prone to melting at normal upper mantle conditions and producing basic-ultrabasic alkaline magmas (Pilet et al., 2008, 2011; Pilet, 2015). Melting experiments carried out at 1.5 GPa and 1150 °C on natural hornblendite and clinopyroxene-hornblendite produced liquids with nephelinitic to basanitic compositions, as a consequence of the dominant incongruent melting of amphibole (Pilet et al., 2008). With increasing temperature (~1275 °C), the role of clinopyroxene melting becomes predominant, producing compositions progressively richer in silica and alkali poorer (Pilet et al., 2008, 2011; Pilet, 2015). Consequently, ultrabasic magmas can be, at least in line of principle, generated within the lithospheric mantle by melting of amphibole-rich cumulates, which are actually expected to form also beneath arc volcanoes (e.g., Medard et al., 2006; Tiepolo et al., 2014; Wang et al., 2019).

Medard et al. (2006) investigated the melting behaviour of amphibole wehrlites, in an attempt to reproduce the rare ultra-calcic nepheline-normative melt inclusions found in arc magmas by carrying out melting experiments at 1.0 GPa at various temperatures. Initial melts (~1175 °C), generated at ~20% partial melting of an amphibole wehrlite (more properly an amphibole olivine websterite), are strongly nepheline-normative and highly enriched in Na_2O, K_2O and Al_2O_3 (>19 wt%), but relatively depleted in CaO (<11 wt%) and MgO. With increasing temperature (~1350 °C) and at very high melt fraction (*f* ~80%), ultra-calcic melts (CaO up to ~18 wt%) with low Al_2O_3 (<10 wt%) and

high MgO (~14 wt%) are produced. These compositions mimic in some instances the composition of Nowbaran rocks, but they have lower TiO_2 (~1.5 wt%), and Na_2O (~1.5 wt%), and, more strikingly, much higher SiO_2 (~46 wt%). Slightly silica-poorer ultrabasic compositions (SiO_2 ~44 wt%) can be produced from an amphibole wehrlite only for lower degrees of melting (*f* ~35-40%), but in this case CaO and MgO are lower than in Nowbaran rocks (~15 wt% and ~10 wt%, respectively).

Hornblendite experimental melts obtained by Pilet et al. (2008) match closer the Nowbaran melanephelinite compositions, with SiO_2 ~36.8-39.2 wt%, K_2O ~1.2-2.0 wt% and Na_2O ~2.6-3.9 wt%. However, the similarities between the hornblendite-derived experimental melts and the natural compositions found at Nowbaran stop here, as the first are significantly more enriched in TiO_2 (~3.6-6.9 wt%) and Al_2O_3 (~11.4-14.2 wt%; Fig. 23) and more depleted in P_2O_5 (0.1-1.7 wt%). As concerns the remaining major oxides, hornblendite-derived melts produced with different starting compositions and at different temperatures are roughly overlapping with Nowbaran rocks, but define completely different evolutionary trends with SiO_2.

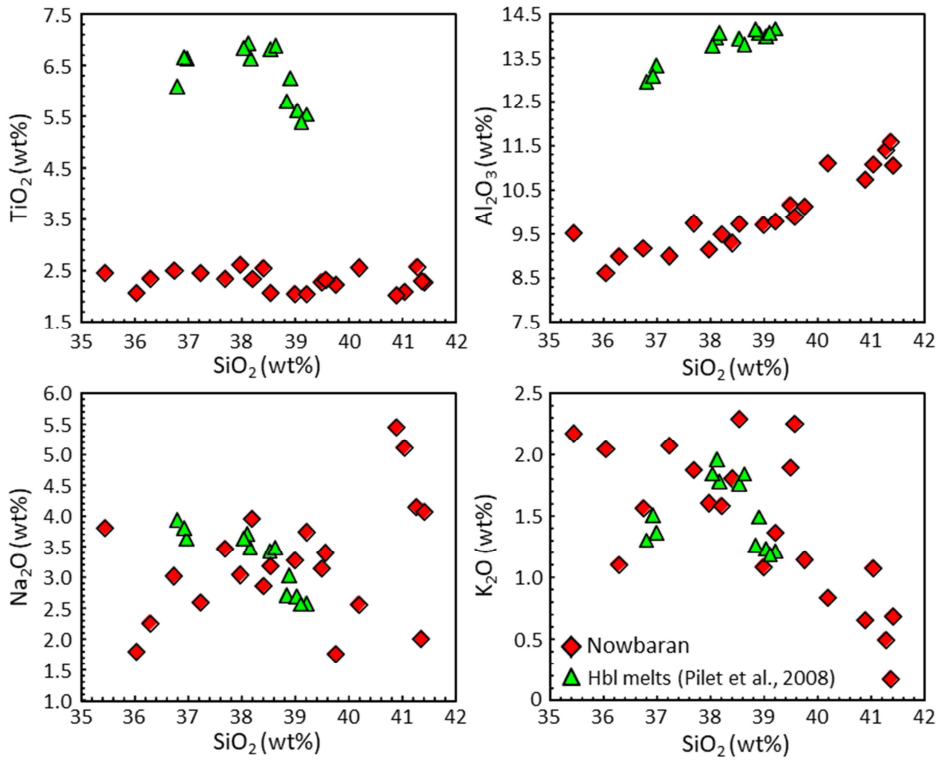

Fig. 23: *Selected major- elements vs. SiO_2 variation diagrams comparing the composition of the investigated Nowbaran rocks with that of hornblendite experimental melts (Pilet et al., 2008).*

2.8.5 Metasomatic phase (amphibole, phlogopite, apatite) constraints

Nowbaran melanephelinites show marked troughs in K and Rb in primitive mantle-normalized diagrams, which possibly suggest the presence of a residual K-bearing phase in the mantle source (e.g., phlogopite or K-richterite). Amphibole, mica and apatite are the major hosts for lithophile elements in the upper mantle (Adam et al., 1993; LaTourette et al., 1995; Ionov et al., 1997). Amphibole and mica commonly occur in metasomatic veins (produced by fluid percolation and metasomatic reactions with the originally dry peridotite matrix; Ionov et al., 1997; Pilet, 2015) and/or cumulates in the lithospheric mantle, and thus always play an important role for trace elements distributions in magmatic processes.

Phlogopite in basaltic melts shows high KD_{Rb} (1.9-5.8; Green et al., 1993; LaTourette et al. 1995; Adam and Green, 2006) and KD_{Ba} (3.7-10; Villemant et al., 1981; LaTourette et al. 1995), whereas amphibole behaves as an incompatible host both for Rb (KD_{Rb} = 0.14-0.58; Adam et al. 1993; Green et al., 1993; Brenan et al., 1995; LaTourette et al. 1995; Adam and Green, 2006) and Ba (KD_{Ba} = 0.12-0.60; Matsui et al. 1977; Adam et al. 1993; Green et al., 1993; Brenan et al., 1995; LaTourette et al. 1995). Given the marked K and Rb troughs observed in Nowbaran rocks, the presence of residual phlogopite in the mantle sources of the area could be taken into account. Several observations, however, seem to be odd with this.

First, no correlation can be observed between K and Rb in Nowbaran rocks. Furthermore, Ba is quite enriched in Nowbaran lavas, decoupled from Rb. Consequentially, phlogopite is probably not (the only) responsible for the Rb-Ba-K content of Nowbaran melanephelinites. It is rather possible to ascribe such enrichments to the melting of another volatile-bearing mineral, e.g., amphibole. Indeed, as evidenced in the previous paragraph, amphibole-bearing metasomatic veins may have been involved in the genesis of ultrabasic magmas. This is also consistent with the Rb/Sr vs. Ba/Rb and Rb/Ba vs. Ba/Sr diagrams of Fig. 24, where the major involvement of amphibole over phlogopite is clearly evidenced. Amphibole occurrence in the source is also consistent with the generally high Na_2O and Na_2O/K_2O of Nowbaran rocks (mostly >3.0 and 1.5, respectively). However, the strong enrichment in

U-Th-LREE-Sr of Nowbaran rocks cannot be simply related to the presence of amphibole in the source, but rather also the requires presence of some apatite, being this phase a major host for U, Th, LREE and Sr (Ionov et al., 1997). This could also explain the high P_2O_5 (1.4-3.3 wt%) of the investigated rocks and the relatively good positive correlation observed between P_2O_5 and CaO (R^2 = 0.77).

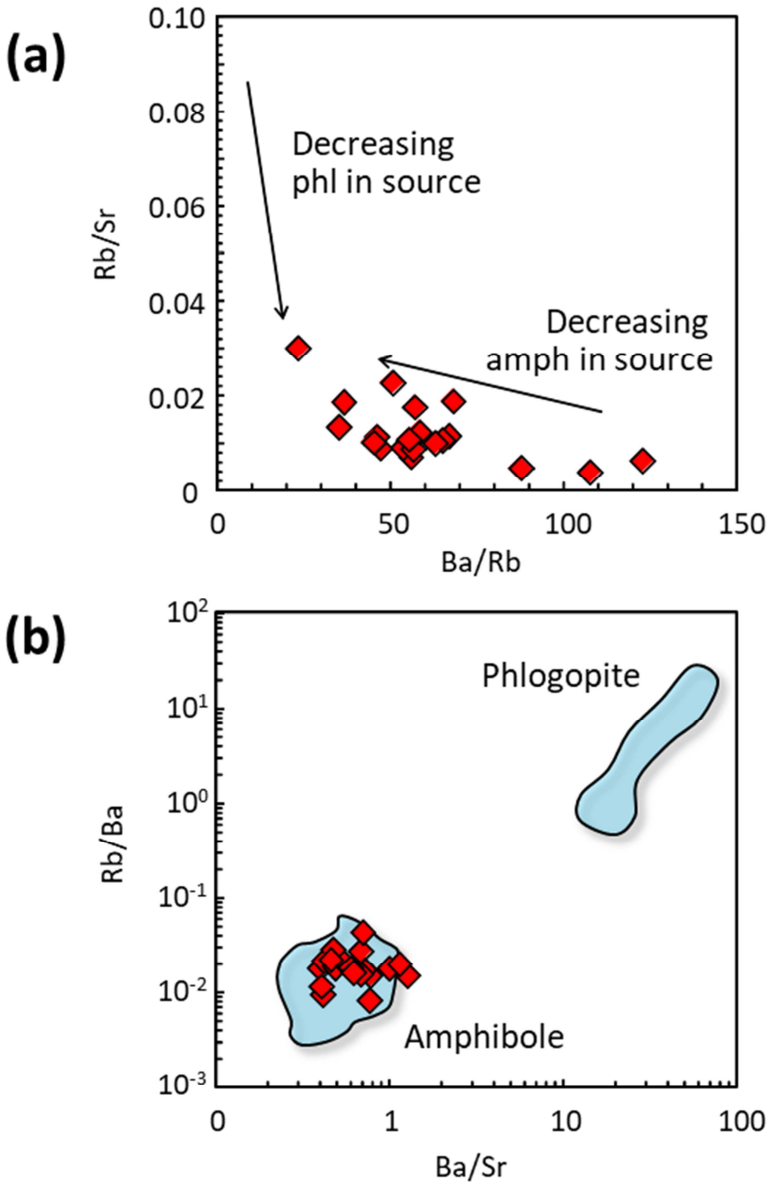

Fig. 24: *a) Rb/Sr vs. Ba/Rb and b) Rb/Ba vs. Ba/Sr diagrams for the investigated Nowbaran rocks, showing the effects of amphibole and phlogopite in the source. In b) the fields for amphibole and phlogopite (from Hawkesworth et al., 1987) are also reported.*

2.8.6 P-T conditions of formation

Estimating geothermobarometric conditions of formation for igneous rocks is a hard task because of the presence of several problems and hardly quantifiable parameters. First of all, the concept itself of equilibrium melts is valid essentially in laboratories only. Mantle partial melts are typically generated in variable temperature and pressure ranges. Even the single chemical composition of igneous rock represents the sum of fractionated liquids produced during increasing degrees of melting and accumulated during polybaric magma extraction (e.g., Lee et al., 2009; Hole and Natland, 2020). In addition, primitive melts (e.g., Foley and Pintér, 2018) reach the surface only rarely, because magmas usually experience variable amounts of fractional crystallization (e.g., O'Hara, 1968). Several models have been proposed to back-calculate the composition of primitive compositions from the parental melts in a rock suite (e.g., Lee et al., 2009; Danyuschevsky and Plechov, 2011; Herzberg and Asimow, 2015), but a complete agreement on such procedures – mostly related to the fact that magmas can be saturated also in plagioclase and clinopyroxene in addition to olivine – has not been reached (e.g., see discussion in Hole and Natland, 2020). The presence of cognate phases (i.e., minerals or glomerules derived from more primitive melt compositions belonging to the same magmatic lineage, commonly referred also to as antecrysts) or xenocrysts/xenoliths (of upper crustal to upper mantle origin), as well as the presence of secondary minerals, have the potential to bias the original composition of the investigated melt. In addition, typical geothermobarometers represent best-fit equations of melts and melt-mineral pairs obtained in laboratory and only rarely are based on calorimetric and volumetric data (e.g., Putirka, 2008).

Many of the geothermobarometers used in igneous petrology are designed for basaltic compositions (e.g., Lee et al., 2009; Hora et al., 2013; Plank and Forsyth, 2016) in equilibrium with olivine + orthopyroxene (± clinopyroxene ± spinel/garnet) sources, and more rarely for differentiated compositions (e.g., Masotta et al., 2013). Virtually no specific efforts have been devoted to geothermobarometric calibrations on ultrabasic melts. Very recently, Sun and Dasgupta (2020) filled this gap, proposing a new geothermobarometric model based on 202 literature experiments carried out in a large range of T (900-1968 °C) and P (1.6-10 GPa), and with CO_2 ranging from 0 to 45 wt%

and H_2O from 0 to 57 wt%. The resulting experimental melts cover the entire range from nearly pure carbonatitic to nearly pure basaltic compositions (e.g., SiO_2 = 6.6-48.8 wt%; Al_2O_3 = 0.3-18.3 wt%; CaO = 3.9-45.0 wt%; MgO = 8.8-38.2 wt%). Although the proposed model is expressly designed for kimberlitic magmas, it can be used for a large spectrum of ultrabasic compositions including melilites, nephelinites and basanites.

The application of Sun and Dasgupta (2020) geothermobarometer gives equilibrium temperatures in the 1214-1347 °C range (average = 1282 °C, ± 31 °C) and P range of 2.2-2.9 GPa (average = 2.5 GPa, ± 0.2 GPa; Fig. 25). These are the estimates calculated if uncorrected measured whole-rock compositions are employed (option 0 of Sun and Dasgupta, 2020). The pressures would indicate derivation close to the spinel-garnet peridotite facies transition, calculated in literature at ~1.9-2.4 GPa range for average geotherms (Klemme and O'Neill, 2000; Ziberna and Klemme, 2016). This result agrees with the moderately fractionated MREE/HREE ratios of Nowbaran rocks [$(Sm/Yb)_N$ ~11-23], compatible with a mixed spinel-garnet mantle assemblage (but in this case amphibole-rich).

Fractionation of olivine and CO_2 degassing of Nowbaran primitive magma *en-route* to the surface could have modified the composition of the analysed rocks. The hypothetical amount of olivine lost can be calculated assuming step-by-step addition of small amounts of olivine until reaching a whole-rock composition in equilibrium with the hypothetical $K_D(Fe\text{-}Mg)^{olivine/melt}$. The results of the experimental studies reviewed by Sun and Dasgupta (2020) indicate $K_D(Fe\text{-}Mg)^{olivine/melt}$ in CO_2-bearing ultrabasic systems ranging from 0.28-0.66, higher than the value accepted in literature (i.e., 0.30 ± 0.03; Mollo and Hammer, 2017). The amount of CO_2 lost during magma degassing at shallow depths can be calculated using the CO_2-SiO_2 correlation proposed by Sun and Dasgupta (2020), i.e., $CO_2 = 43.77 - 0.90*SiO_2$. Back-adding given amounts of olivine to the analysed rocks and increasing the CO_2 amount until reaching the hypothetical value for a given SiO_2 content of the analysed rock, led to different geothermobarometic estimates (option 3 of Sun and Dasgupta, 2020). These values indicate much hotter (1410-1504 °C; average = 1455 °C, ± 27 °C) and deeper conditions (4.0-4.8 GPa; average = 4.4 GPa, ± 0.2 GPa; Fig. 25). These new geothermobarometric estimates are considered very unlike because Nowbaran magmas have the features of low-degree and low-volume melts and are certainly not entirely equilibrated in the garnet stability

field. Compared with the measured values, the increase of CO_2 only, to reach equilibrium with SiO_2 (option 2 of Sun and Dasgupta, 2020) would produce only slightly higher P (2.5-3.3 GPa; average = 2.8 GPa, ± 0.2 GPa) at slightly lower T estimates (1198-1309 °C; average = 1261 °C, ± 30 °C). In conclusion, the hypothetical equilibrium temperature and pressure equilibrium of Nowbaran magmas indicate the base of the lithosphere under normal thermal regimes.

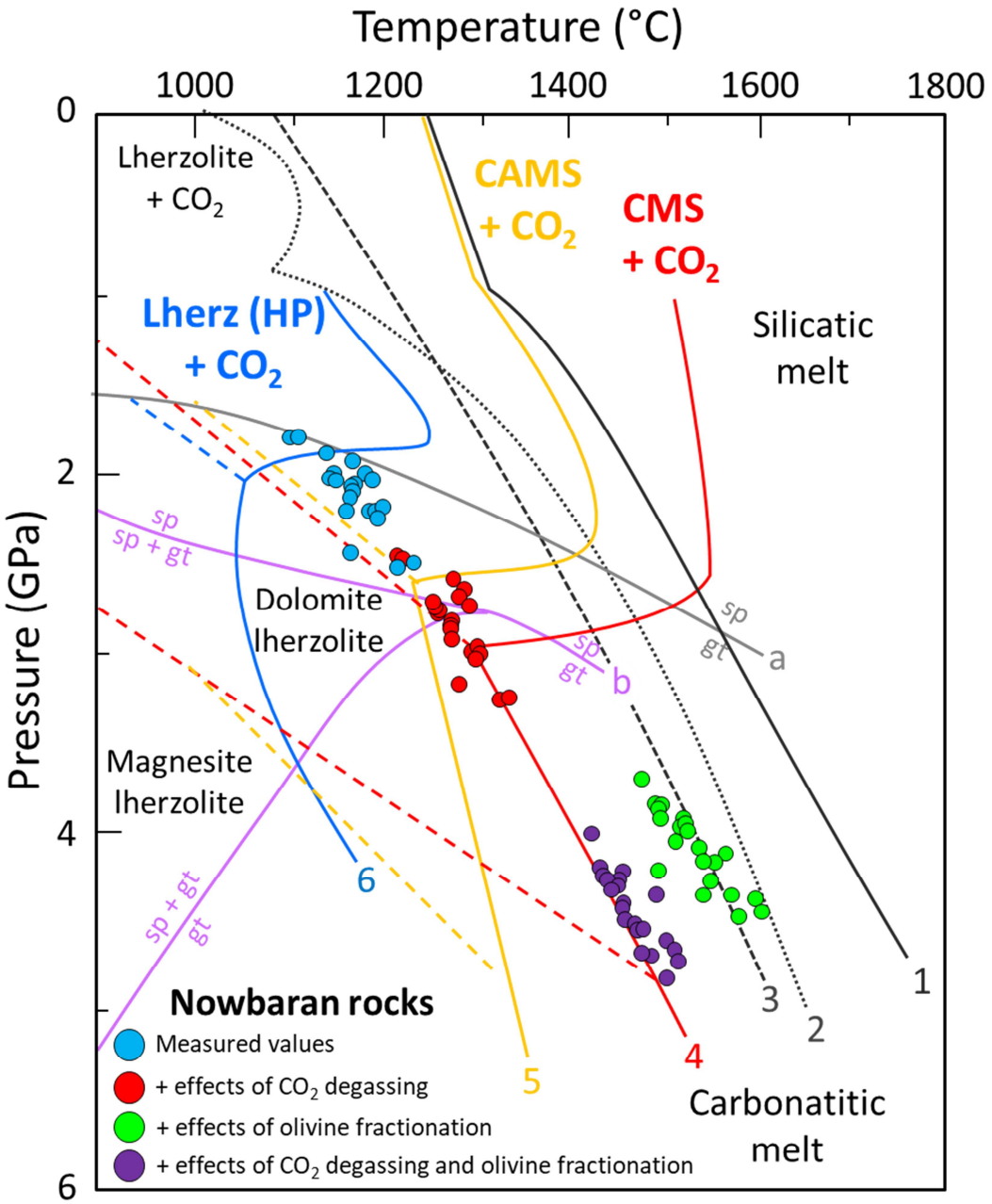

Fig. 25*: (caption on the next page)*

Fig. 25: *Temperature-Pressure diagram showing: (1) = simplified haplo-peridotitic system CAMS ($CaO-Al_2O_3-MgO-SiO_2$) solidus (Gudfinnsson and Presnall, 2005); (2) = fertile peridotite volatile-free solidus (Herzberg and Asimow, 2015); (3) = fertile peridotite volatile-free solidus (Hirschmann, 2000); (4) = simplified haplo-peridotitic system CMS ($CaO-MgO-SiO_2$) + CO_2 solidus (Eggler, 1978); (5) = simplified haplo-peridotitic system CAMS + CO_2 solidus (Gudfinnsson and Presnall, 2005); (6) = lherzolite (HP = Hawaiian Pyrolite) + CO_2 solidus (Falloon and Green, 1989). The three solidi with CO_2 (lines 4, 5 and 6) show an abrupt decrease of temperature at variable depths, known as the "carbonate ledge", caused by the appearance of dolomite after the reaction: CO_2 (vapour) + forsterite + diopside = dolomite + enstatite. With increasing complexity of the system (i.e. from CMS to lherzolitic compositions) the zerovariant point connecting CO_2 vapour + solid dolomite + dolomitic melt + olivine + diopside + enstatite + spinel/garnet moves towards lower temperature and lower pressure. In the diagram are also reported the spinel/garnet stability fields in CAMS systems (Klemme and O'Neill, 2000) and the spinel/spinel+garnet/garnet fields in a depleted mantle xenolith natural sample (Pali-Aike, Argentina; sample LS1) calculated by the thermodynamic model of Ziberna and Klemme (2016). The dashed lines departing from the three zerovariant points separate the stability of dolomite-bearing mantle and CO_2-bearing mantle. The other dashed lines indicate the stability limits of dolomite- and magnesite-bearing mantle. Four set of geothermobarometric estimates of Nowbaran rocks using the models of Sun and Dasgupta (2020) are reported. Details in the text.*

2.8.7 Geodynamic setting derived from petrological considerations

Oceanic and continental intraplate regions are the typical tectonic settings where to find ultrabasic melts (e.g., Lustrino and Wilson, 2007; Pfander et al., 2018; Mazzeo et al., 2020). No ultrabasic melts have ever been found along oceanic ridges and they rarely occur in intra-oceanic arcs or in continental supra-subduction/collisional regimes. Basic-ultrabasic compositions particularly rich in K_2O (e.g., leucitites) or CaO (e.g., kamafugites) occur in subduction settings too (e.g., Melluso et al., 2010; Lustrino et al., 2019a, 2020), and are to some degree associated to digestion of shallow carbonates in upper crustal magma chambers (see discussion in Lustrino et al., 2019b, 2020). Interestingly, the presence of CaO-rich melilitites and kamafugites in central Italy is also interpreted in a completely different way, i.e., not linked to any recent subduction activity (e.g., Di Battistini et al., 2001) or any subduction event at all (e.g., Stoppa et al., 2016). With some important exceptions, strongly alkaline potassic (leucitites) and sodic (nephelinites) ultrabasic melts define settings away from typical oceanic subduction, requiring either mid-plate conditions or subduction of marly components.

Plagioclase-free ultrabasic melts with nephelinitic to melilititic compositions are almost never found above active or fossil supra-subduction mantle wedges. To the best of the authors' knowledge, the only exceptions are represented by the nephelinitic-limburgitic occurrences in Japan and in Colombia. Yamaguchi (1964) report the presence of mantle xenolith-bearing limburgites (feldspar-free, olivine-clinopyroxene-phyric hyalo nepheline-basanites, according to Le Maitre, 2002) in SW Japan (Sukumozuka and Ogusoyama, northern Chugochu district) with ultrabasic composition (SiO_2 = 42.9-43.8 wt%), moderate content of alkalis (Na_2O+K_2O = 3.8-4.5 wt%), CaO (11.2-12.3 wt) and Al_2O_3 (10.7-13.4 wt%). These compositions are less extreme than those of Nowbaran rocks, with which they show limited compositional overlap. The presence of plagioclase in SW Japan limburgites is another fundamental difference with Nowbaran rocks. More recently, Tatsumi et al. (1999) reported the presence of melilite-olivine nephelinite at Hamada, very close to Ogusoyama locality reported by Yamaguchi (1964). Hamada nephelinites have SiO_2 (36.2-38.0 wt%) and MgO (8.3-9.8 wt%) clustering in the lower end of Nowbaran melanephelinites (35.4-41.3 wt% and 8.7-13.3 wt% for SiO_2 and MgO, respectively). On the other hand, TiO_2 (2.50-2.65 wt%) and Al_2O_3 (11.1-11.8 wt%) in Hamada nephelinites plot in the upper end of Nowbaran rocks (2.03-2.61 wt% and 8.61-11.4 wt%, respectively), while Fe_2O_{3tot} (14.0-15.0 wt%) is much higher in Hamada than Nowbaran rocks (8.6-11.3 wt%). The low Mg# (0.56-0.61; average = 0.58) and Ni (65-87 ppm) of Hamada nephelinites are very different from Nowbaran melanephelinites and indicate lack of equilibrium with typical peridotitic mantle rocks. Despite this, the abundant presence of lherzolite and wehrlite xenoliths in Hamada nephelinites led Tatsumi et al. (1999) to assume equilibrium with mantle lithologies, but leaving unexplained the origin of the low Mg# and Ni. Paradoxically, Nowbaran melanephelinites, which show much more primitive compositions, at least theoretically in equilibrium with typical peridotitic lithologies, are mantle xenolith-free, whereas melts with evolved compositions such as the Hamada nephelinites are characterized by the abundant presence of mantle xenolith cargo. In addition, Hamada nephelinites are surprisingly low in radiogenic ^{87}Sr ($^{87}Sr/^{86}Sr$ = 0.7038-0.7039) and strongly enriched in radiogenic ^{143}Nd ($^{143}Nd/^{144}Nd$ = 0.51280-0.51285), ratios extremely different from those recorded in Nowbaran melanephelinites ($^{87}Sr/^{86}Sr$ = 0.7052-0.7056; $^{143}Nd/^{144}Nd$ = 0.51263-0.51269).

Experimental results using one Hamada nephelinite doped only with water (0.57 wt% H_2O) and with mixed water-carbon dioxide (0.57 wt% H_2O + 5-8 wt% CO_2) at 1.05 to 1.8 GPa and 1200 to 1300 °C (Tatsumi et al., 1999) indicate saturation with olivine and clinopyroxene and the complete absence of orthopyroxene. These evidences led Tatsumi et al. (1999) to hypothesize for Hamada nephelinites a wehrlitic mantle source, formed after interaction of a carbonatitic melt with mantle enstatite to produce a forsterite-diopside-rich wehrlitic metasomatic fronts. No comment on the anomalous subduction setting is reported.

Mantle xenolith-bearing nephelinites emplaced above a subduction system are recorded also in SE Colombia (Acevedo area; Kroonenberg et al., 1987; Rodriguez Garcia and Gonzalez, 2004; Borrero and Castillo, 2006). The only three partially complete whole-rock analyses available for these rocks (Kroonenberg et al., 1982, 1987), plus three rock analyses for which only SiO_2, Al_2O_3 and Na_2O+K_2O are reported (Rodriguez Garcia and Gonzalez, 2004) indicate ultrabasic compositions falling in the nephelinite and basanite fields (SiO_2 = 40.2-43.4 wt%; Na_2O+K_2O = 2.8-5.3 wt%), rich in MgO (12.4-14.8 wt%). Also in this case, a detailed petrogenetic model has not yet been presented and at least three general processes have been proposed in literature. These are: 1) subduction of an oceanic spreading rift (Kroonenberg et al., 1987); 2) small degree partial melting caused by pull-apart basin opening above a subduction system (Rodriguez Garcia and Gonzalez, 2004) and 3) upwelling of the Galapagos mantle plume in a mantle window opened within the Nazca Plate as consequence of the arrival at the trench of the Carnegie Ridge and the Malpelo Rift (Borrero and Castillo, 2006). These models tend to explain the highly anomalous occurrence of very small volumes of very young sodic ultrabasic melts in a subduction setting, associated with magmas with clear and classical subduction-related geochemical signatures.

The ultimate origin of the igneous activity in Nowbaran area shares the same problems evidenced for Japanese and Colombian subduction-related nephelinitic melts. In addition, in the Iranian melanephelinite rocks no active subduction is present, being the geological setting rather classifiable to as post-collisional. Evaluating the behaviour of elements with different mobility in fluids (e.g., Th, Ta and Yb) can furnish useful constraints on the petrogenetic processes responsible for specific trace element enrichments. The Th/Yb vs. Ta/Yb diagram (Fig. 26a) proposed by Pearce (1983) can be

used to test the role of metasomatic changes related to subduction in the genesis of Nowbaran rocks. About half of the samples lie within the mantle array, the remaining plotting towards slightly higher Th/Ta, thus suggesting the involvement of a subduction component. Such component can be observed also in the La vs. Nb diagram (Fig. 26b), where the high La/Nb (>2) is consistent with melts generated within supra-subduction mantle wedges. Although Ta/Yb values and Nb concentrations seem to suggest that the degree of partial melting for these melts was roughly constant, the clear positive correlation between La/Lu and La (R^2 = 0.91) can be interpreted as the effect of variable degrees of partial melting from a common source. The absence of correlation between La/Lu and CaO (R^2 = 0.09) indicates that at the lowest degrees of melting carbonate minerals are not significantly contributing to melt production.

As a final observation regarding the general tectonic setting, it is to note that Pliocene active faults in the UDMA (Qom, Saveh and Indes), as well as older (late Cretaceous) fault systems (Tafresh, Kashan and Zefreh) are dominated by a prevailing right-lateral slip component (Babaahmadi et al., 2010). These fault systems accommodate the oblique motion of Arabia with respect to Eurasia (Tabaei et al., 2016). It is therefore possible that a fault transfer zone area accommodating the displacement of the main faulting structures allowed the passive sub-lithospheric mantle upwelling. The ultimate Quaternary volcanic activity in Nowbaran area would involve low-degree melt extraction from a subduction-modified fossil mantle wedge as consequence of a structural response to the extensional local tectonics, such as the N-S trending fissure zone of Nowbaran area seems to indicate.

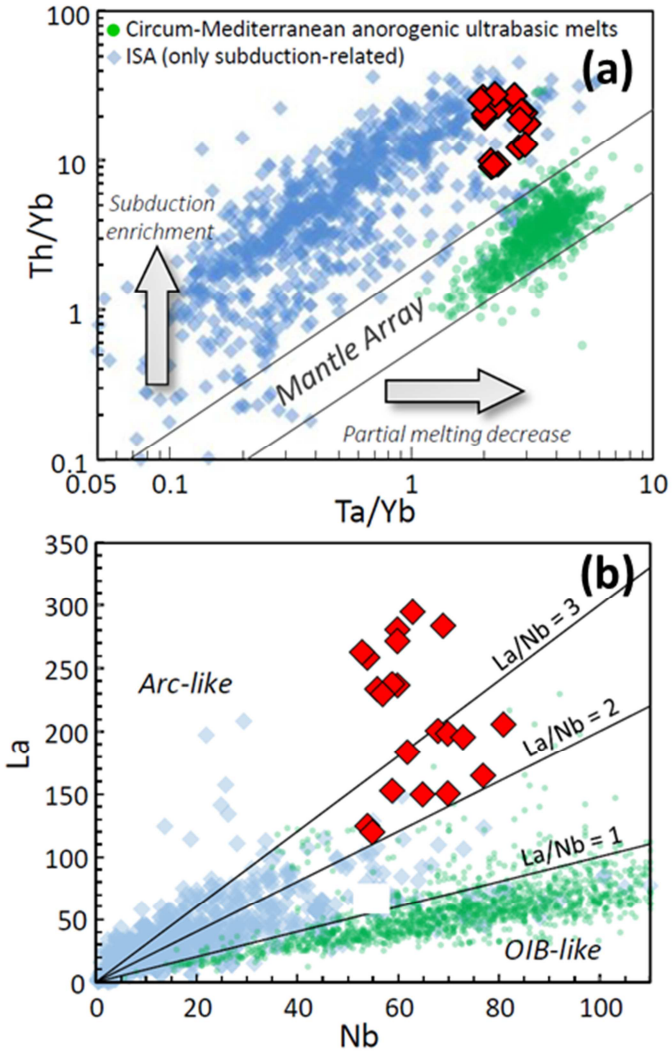

Fig. 26: *a) Th/Yb vs. Ta/Yb and b) La vs. Nb diagrams for the investigated Nowbaran rocks, with arrows indicating the effects of increasing degrees of partial melting and involvement of a subduction component. The field of Meso-Cenozoic ISA subduction-related igneous rocks and of circum-Mediterranean anorogenic ultrabasic igneous rocks(Lustrino and Wilson, 2007; Lustrino, 2011) are reported for comparison.*

2.9 Conclusions

Low-degree partial melts with exotic compositions have been emplaced during the Quaternary west of Nowbaran town (NW Iran). These magmas postdate the intermediate to acid volcanic rocks showing classical subduction-related geochemical characteristics of the post-collisional Urumieh-Dokhtar Magmatic Arc. The absence of plagioclase and melilite and the abundant presence of clinopyroxene phenocrysts plus

olivine, nepheline and other sodalite-hauyne-group feldspathoid confined in the groundmass allow classifying these rocks as melanephelinites.

Nowbaran melanephelinites are by far the most peculiar igneous rocks of the entire Bitlis-Zagros Orogen, showing ultrabasic (SiO_2 = 35.4-41.4 wt%) and ultracalcic (CaO/Al_2O_3 = 1.13-1.92) compositions. The high MgO (8.7-13.3 wt%) and Mg# (0.69-0.74), together with high Ni (230-360 ppm) and Cr (260-480 ppm) indicate the primitive character of these melts.

The Sr-Nd-Pb isotopic ratios of Nowbaran melanephelinites plot within the field of Urumieh-Dokhtar Magmatic Arc and SE Anatolia. Patterns in primitive mantle-normalized multielemental diagram are intermediate between the classical subduction-related magmas and mid-plate HiMU-OIB.

The mantle sources that generated the Nowbaran magmas cannot be identified in a C-H-free peridotite. A mixed source made up of carbonate-bearing apatite-hornblendite metasomatic layers is considered to have developed during the prolonged NE-directed subduction of Neotethys Ocean before Arabia-Iran collision. Amphibole-rich metasomatic volumes may have formed as consequence of partial melting of amphibole-rich cumulates formed during fractional crystallization of arc magmas close to Moho depths. Several large-scale faults (Saveh, Indes, Qom) accommodate the oblique motion of Arabia with respect to Eurasia from Pliocene. A passive mantle upwelling along these transfer zones may have favoured formation and upwelling of the small volume Quaternary volcanic activity at Nowbaran in response to the extensional local tectonics, compatible with the N-S trending fissure zone of the studied volcanoes in Nowbaran.

CHAPTER 3 – BIJAR-QORVEH

3.1 Sampling area

Petrographic and whole-rock chemical analyses were carried out on 59 rock samples from Bijar-Qorveh volcanic field. The investigated volcanic area is located ~50 km East of Sanandaj city, dispersed over a total area of ~3500 kmq between the cities of Bijar (North) and Qorveh (South) in the Iranian Kurdistan province (Fig.27).

Three samples were collected in a small area which is approximately 35 km N of Bijar and ~35 km S of Takab town. Ten samples were collected along four different volcanoes being collocated from 10 to 40 km S of Bijar. Seventeen samples are from a semi-circular area adjacent to Qezelke Kand town, nearly 25 km N of Qorveh, whereas twelve further samples were collected ~ 18 E of Qorveh cities. Seventeen additional samples were located ~20 km W the main volcanic field, about 15 km N Dehgolan town and ~40 km NE Sanandaj city.

The area is considered to belong to the SSZ (Boccaletti et al. 1977; Keshavarzi et al. 2011) or to the UDMA (Azizi and Jahangiri 2008; Azizi and Moinevaziri 2009). Azizi and Moinevaziri (2009) included the Bijar area in the Hamadan-Tabriz volcanic belt which is characterised by Miocene to Quaternary widespread volcanic activity. Indeed the magmatism in this area mainly developed in two phases: the first Upper Miocene phase (~9.2-8.3 Ma; Boccaletti et al., 1977), is represented by andesitic to rhyolitic domes and associated pyroclastic deposits (Boccaletti et al. 1977) with high-K calcalkaline affinity. The second Pleistocene phase (~1.3-0.5 Ma) is characterized by undersaturated alkaline products, generally as well preserved spatter and cinder cones often associated to thin and relatively large lava flows (Boccaletti et al. 1977). Note worthing that Boccaletti et al. (1977) reported the association of basic products with two rhyolitic domes in the south-easternmost outcrops (i.e. Qezelke kand area, near Sarajukh village).

The whole region is characterized by Cenozoic carbonatic and silicoclastic sediments covered by widespread Paleocene-Eocene volcanic deposits, mainly consisting of andesitic lavas and pyroclastic. Volcanics are followed by Oligocene red conglomerate

and sandstone (i.e. Lower Red Formation) covered by Oligo-Miocene marine Qom Formation, principally characterized by sandy marls with intercalations of thin bedded limestone. The sequence continues with Miocene red sandstone with intercalations of red sandy marls (Upper Red Formation) and Plio-Quaternary mafic volcanic rocks, up to recent alluviums and continental deposits.

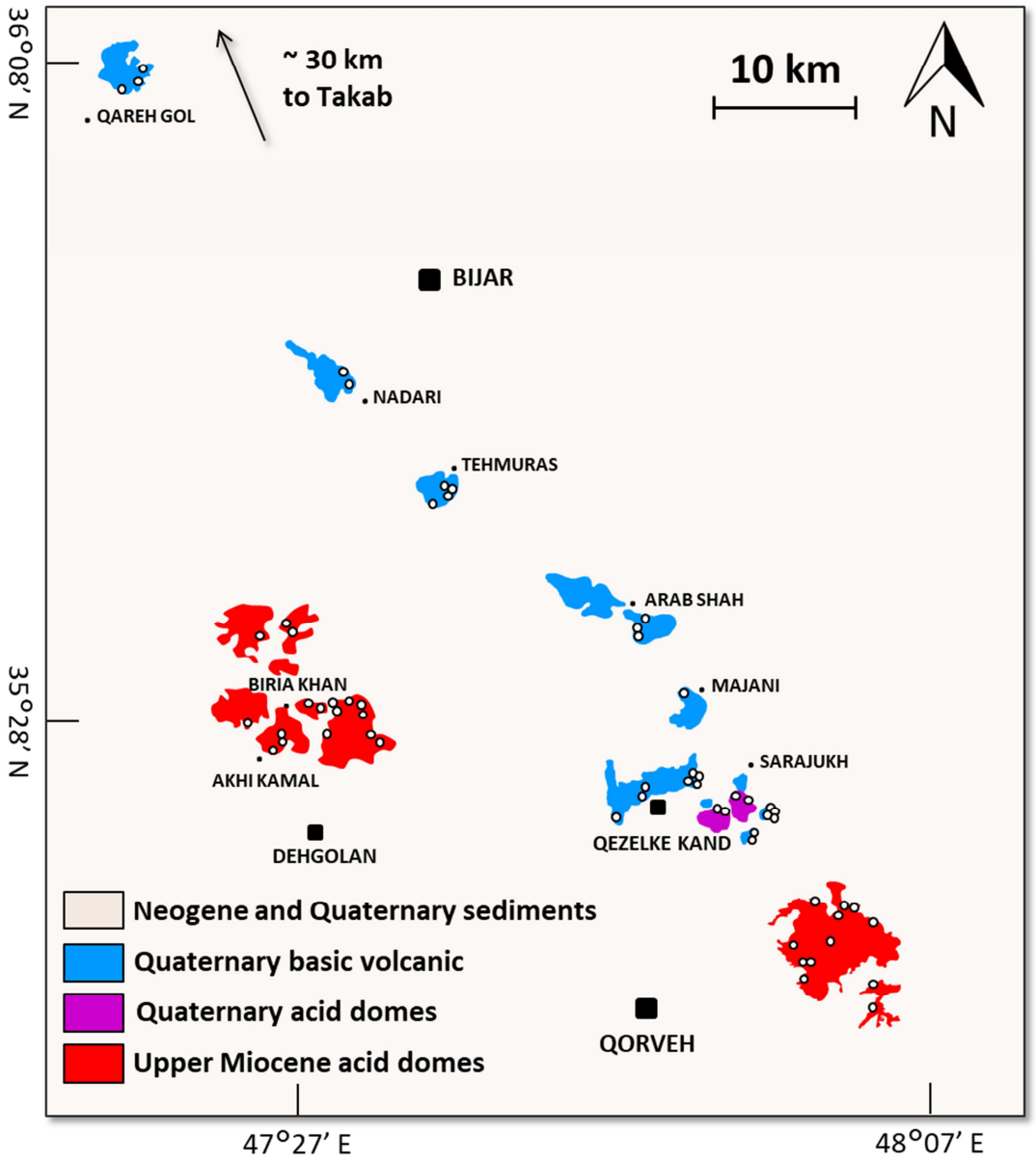

Fig. 27: *Sketch map of the investigated volcanic area, showing Takab-Bijar-Qezelke Kand-Dehgolan-Qorveh main districts. Modified after Boccaletti et al., (1977).*

3.2 Results

3.2.1 Petrography

Dehgolan

The rocks from Dehgolan area are fine-grained porphyritic massive rocks with isotropic to trachytic textures (Fig. 28a, b). Only one sample exhibits vesicles up to 3 mm in size. Porphyric index (P.I. = the area occupied by phenocrysts over the total area of the thin section) ranges from ~5 to ~30%. The most abundant phenocryst is euhedral to subhedral plagioclase, followed by widespread hornblende, biotite, clinopyroxene, orthopyroxene, scarce quartz, rare sanidine and opaque minerals (Fig. 28). Large zoned plagioclase is up 3 mm in size and often shows sieve texture (Fig. 28a) at the core with widespread glass inclusions. Euhedral brown hornblende occurs in almost half of the samples and is ~0.2-0.5 mm in size. It is strongly zoned and often shows opacitic rims (Fig. 28c, d). Euhedral biotite is up 2 mm in size and is frequently altered in chlorite or sericite or characterized by opacitic rims as well. Biotite phenocrysts sometimes appear locally iso-oriented. Clinopyroxene is pale green augite and is usually smaller than 0.5 mm. It occurs as anhedral to subhedral zoned crystals clustered in glomerules with orthopyroxene (Fig. 28e). Scarce quartz (~5%) appears as highly fractured phenocrysts reaching up 2-3 mm in size or with embayed texture (Fig. 28f), whereas rare sanidine (~2%) is 0.2-0.5 mm in size. Widespread secondary interstitial calcite and titanite are often observed in some of the samples. Holocrystalline to hypohyaline groundmass is mostly made up of plagioclase, hornblende, opaques and occasionally biotite and rare apatite (only in few samples). Note worthing that three samples show quarz rounded xenocrysts reaching up ~1 mm in size.

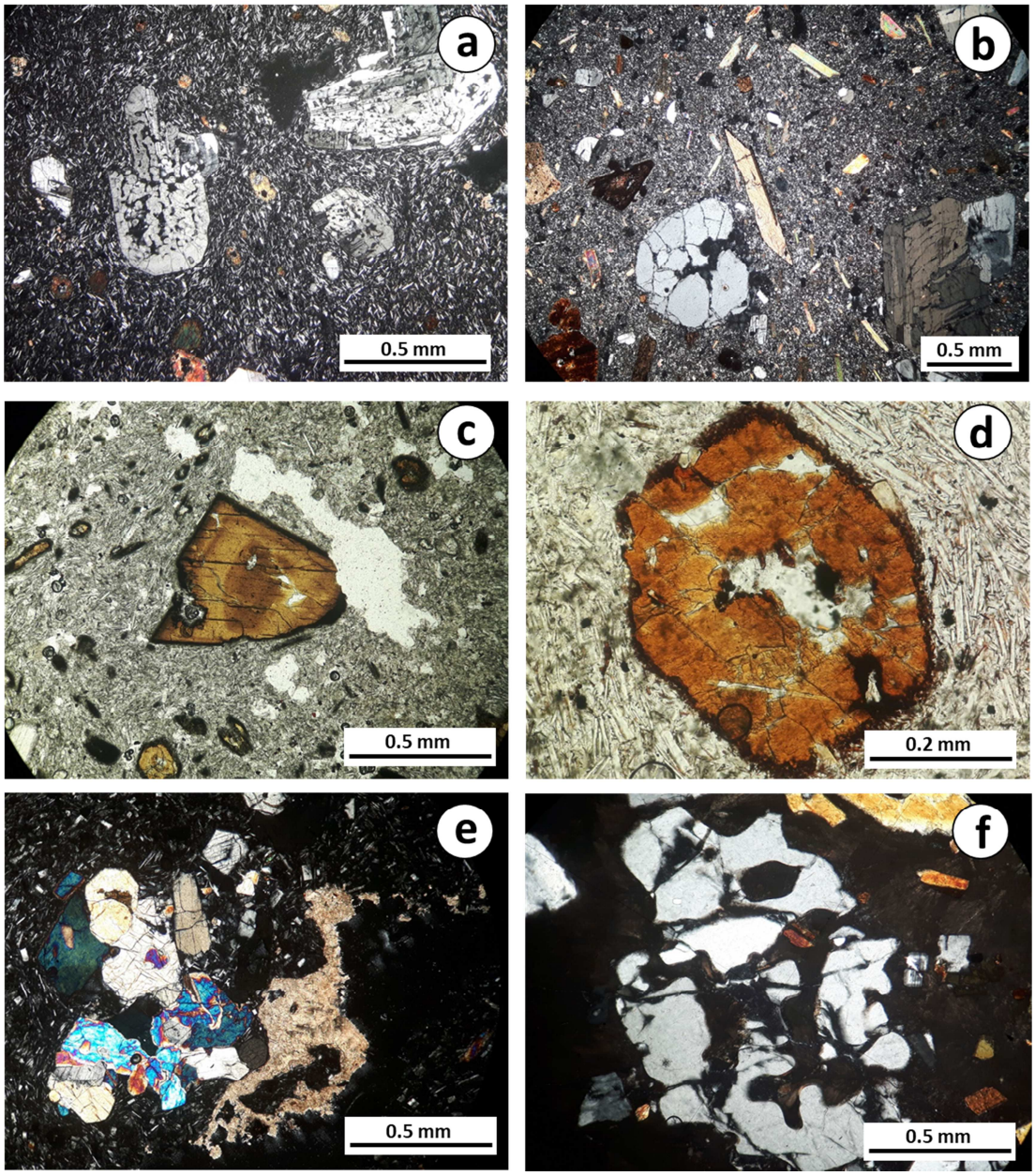

Fig. 28: *Representative photomicrographs of Dehgolan thin sections: a) and b) crossed polarizers view showing porphyritic massive with isotropic to trachytic texture. Plagioclase phenocrysts often exhibit sieve texture; c) and d) plane-polarized light view of subhedral to euhedral amphibole phenocrysts often showing zonation and opacitic rims; e) glomerules of anhedral to subhedral clinopyroxenes occurring along with orthopyroxene (crossed polarizers view) ; f) quarz xenocryst showing embayed texture at crossed polarizers view.*

Qorveh

Samples from East of Qorveh are fine-grained massive exhibiting porphyritic hypohyaline to holocrystalline isotropic hiatal texture with P.I. ~20-30% (Fig. 29a, b). Only one sample shows P.I. <5%. The most abundant phenocrysts consist mainly of plagioclase, hornblende, clinopyroxene, orthopyroxene and opaques. Only in two samples plagioclase is joined by biotite, scarce sanidine and rare quartz (Fig. 29b). Euhedral to subhedral tabular plagioclase occurs as single crystal or as glomerophyric texture, with size ranging from less than 0.2 mm up to 5 mm. It often shows widespread alteration, strong zoning and sieve texture (Fig. 29c, d). Highly zoned brown hornblende is present in all but two samples with euhedral shape and size ranging from ~0.2 mm up to 3 mm (in one sample it reaches ~1 cm in size; Fig. 29e, f). Hornblende appears generally replaced by opaque minerals and rarely occurs as clustered into aggregates. Rare subhedral to anhedral clinopyroxene is diopside (size ~0.5 mm) and in one sample occurs as locally altered glomerocrystals. Small (size ~0.5 mm) and scarce orthopyroxene occurs only in two samples. In two rocks, mafic phase is mainly represented by euhedral biotite crystals, occurring along with scarce small sanidine and quartz. Biotite microphenocrysts are generally up ~1.0 mm in size, except when included in plagioclase (smaller than 0.2 mm). Nearly half of the samples show a hypocrystalline groundmass made up of feldspars (mostly plagioclase) and hornblende, whereas the remaining rocks exhibit a hypohyaline groundmass showing brownish glass associated to the same paragenesis.

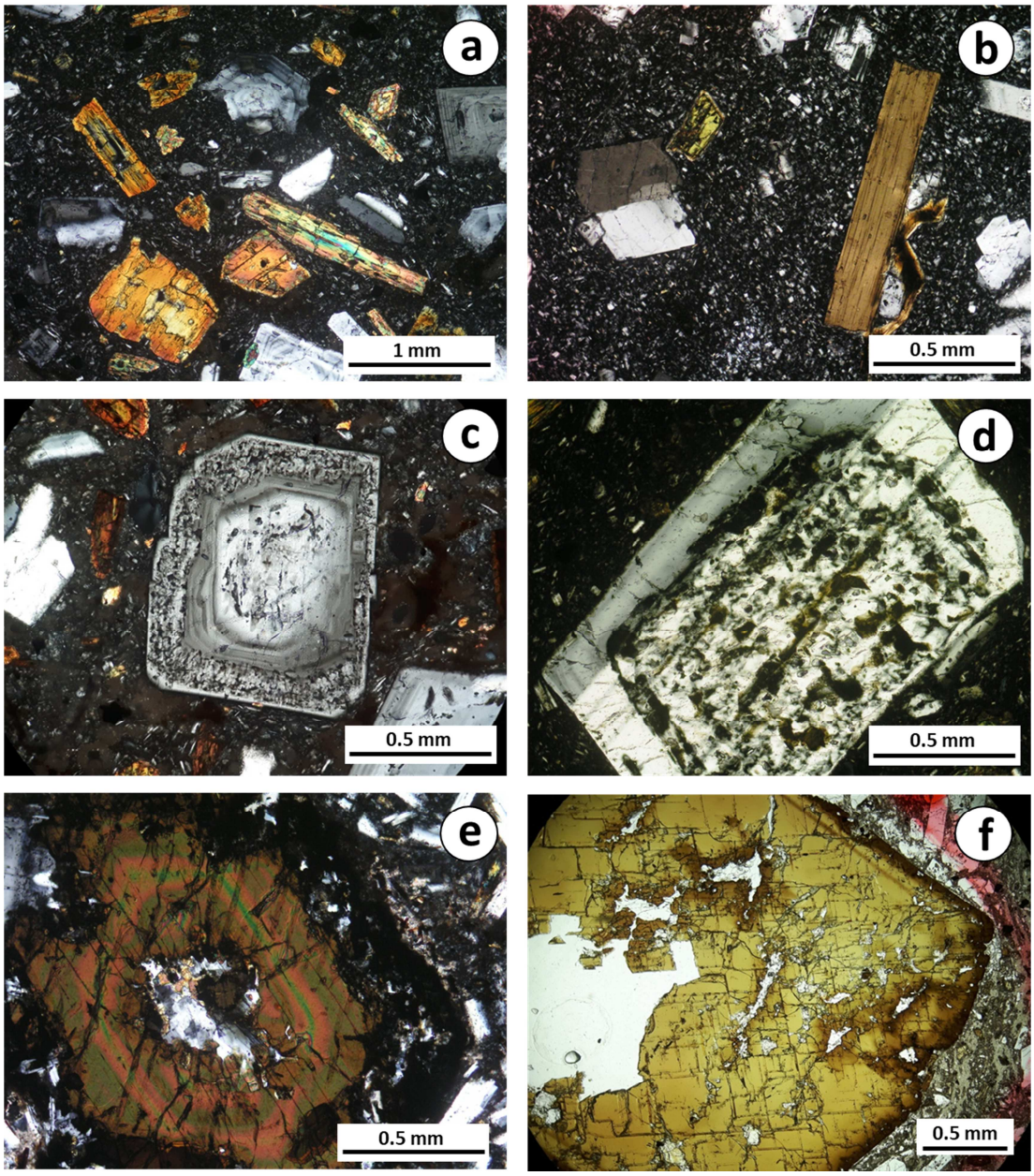

Fig. 29: *Representative photomicrographs of Qorveh thin sections at crossed polarizers view (except "f", at plane-polarized view): a) and b) fine-grained massive porphyritic rocks showing hypohyaline to holocrystalline isotropic texture. c) and d) euhedral phenocrysts of plagioclase with evident zonation and sieve texture. e) subhedral amphibole phenocryst showing strongly opacized rims. f) amphibole euhedral megacryst.*

Qezelke Kand

The volcanic district of Qezelke Kand includes a wider range of lithotypes, grouped in two main types: thirteen vesicular clinopyroxene-olivine phyric (P.I. ~5-15%) basalts (Fig. 30a, b) and four massive andesitic rocks. With the exception of these four massive samples, all the phyric basalts show rounded to elongated vesicles, sometimes interconnected, ranging from ~1 to ~80% (Fig. 30c). Fractured olivine consists of large crystals (up to 5 mm in size) varying from totally fresh to commonly altered to hiddingsite, whereas zoned pale green augite is smaller (maximum 0.5 mm in size) and is sometimes clustered in aggregates. Holocrystalline to hypohyaline groundmass mainly consists of plagioclase and mafic phases (clinopyroxene and olivine).

The four massive andesites show porphyric isotropic to trachytoid holocrystalline textures. Phenocrysts are hornblende, plagioclase, biotite and scarce sanidine. Euhedral to subhedral plagioclase ranges from ~0.2 to ~3 mm (one phenocryst even reaches 5 mm) and rarely appears as clustered aggregates. Plagioclase is zoned and always shows sieve textures. Brown hornblende is maximum 1 mm in length and is zoned and well preserved. It does not exhibit opacitic rim and sometimes appears as partially included in plagioclase. Widespread tabular biotite ~2 mm in size (Fig. 30d), sometimes altered in chlorite or replaced by opaque minerals. Rare tabular sanidine (<5%) occurs as small crystals reaching maximum 0.2 mm in size. It is worth noting that two samples exhibit rare large quartz xenocrysts often showing coronitic texture (overgrowth of clinopyroxene microcrysts). Groundmass mainly consists of plagioclase and hornblende.

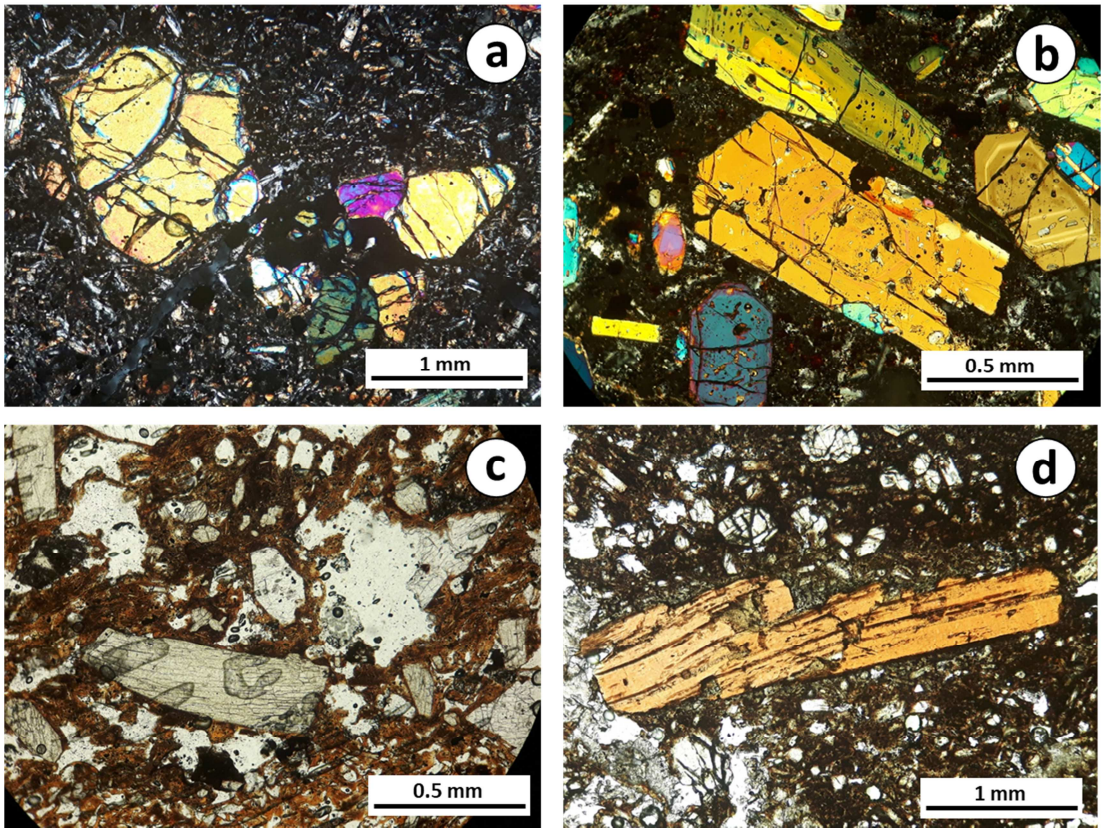

Fig. 30: *Representative photomicrographs of Qezelke Kand thin sections at crossed polarizers view (a-b) and plane-polarized view (c-d): a) and b) clinopyroxene-olivine phyric rocks showing holocrystalline to hypohyaline groundmass mainly consisting of feldspars along with rarer mafic phases. c) vesicular hypohyaline texture with olivine and clinopyroxene phenocrysts. d) biotite anhedral tabular phenocryst occurring in high silica sample.*

Bijar

Rocks from Bijar area are fine-grained massive to vesicular porphyric basaltic rocks. Samples can be divided in two main groups: most of the samples are from barely to moderately vesicular with isotropic microcrystalline texture ranging from holocrystalline to hypohyaline groundmass (Fig. 31a, b), whereas three samples are massive and exhibit trachytic hypocrystalline texture. Vesicles are from ~5 to ~40% (only in one sample vesicles are up to 80%; Fig. 31c) and show circular or irregular shape. They are up to 6 mm in size and are empty to totally filled by calcite.

Paragenesis of vescicular samples consists of euhedral to subhedral clinopyroxene and olivine. Abundant clinopyroxene is pale green augite, strongly zoned, commonly fractured and locally clustered in aggregates (Fig. 31d). Augite reaches 1.5 mm in size whereas euhedral olivine reaches a maximum size of 0.5 mm and is often rimmed by hiddingsite. One vescicular sample is also characterized by euhedral phenocrysts of biotite up to 1.5 mm in size which are frequently altered in chlorite. Note that biotite crystals often grow along the edges of the vesicles stretched along a preferred direction. In this sample also rare quartz xenocrysts are observed. Groundmass phases are feldspars, clinopyroxene, olivine and opaques.

The massive samples instead exhibit abundant large olivine followed by clinopyroxene and feldspars. Subhedral to euhedral olivine shows alteration rim and common fractures are filled by pale green serpentine (Fig. 31e). Clinopyroxene (pale green augite) is often arranged in aggregates and also scarce euhedral sanidine occurs and it is from ~0.2 to ~1 mm in size (Fig. 31f). Groundmass exhibits the same mineralogical phases of vescicular rocks, with the addition of widespread interstitial serpentine. Interstitial calcite is also commonly observed.

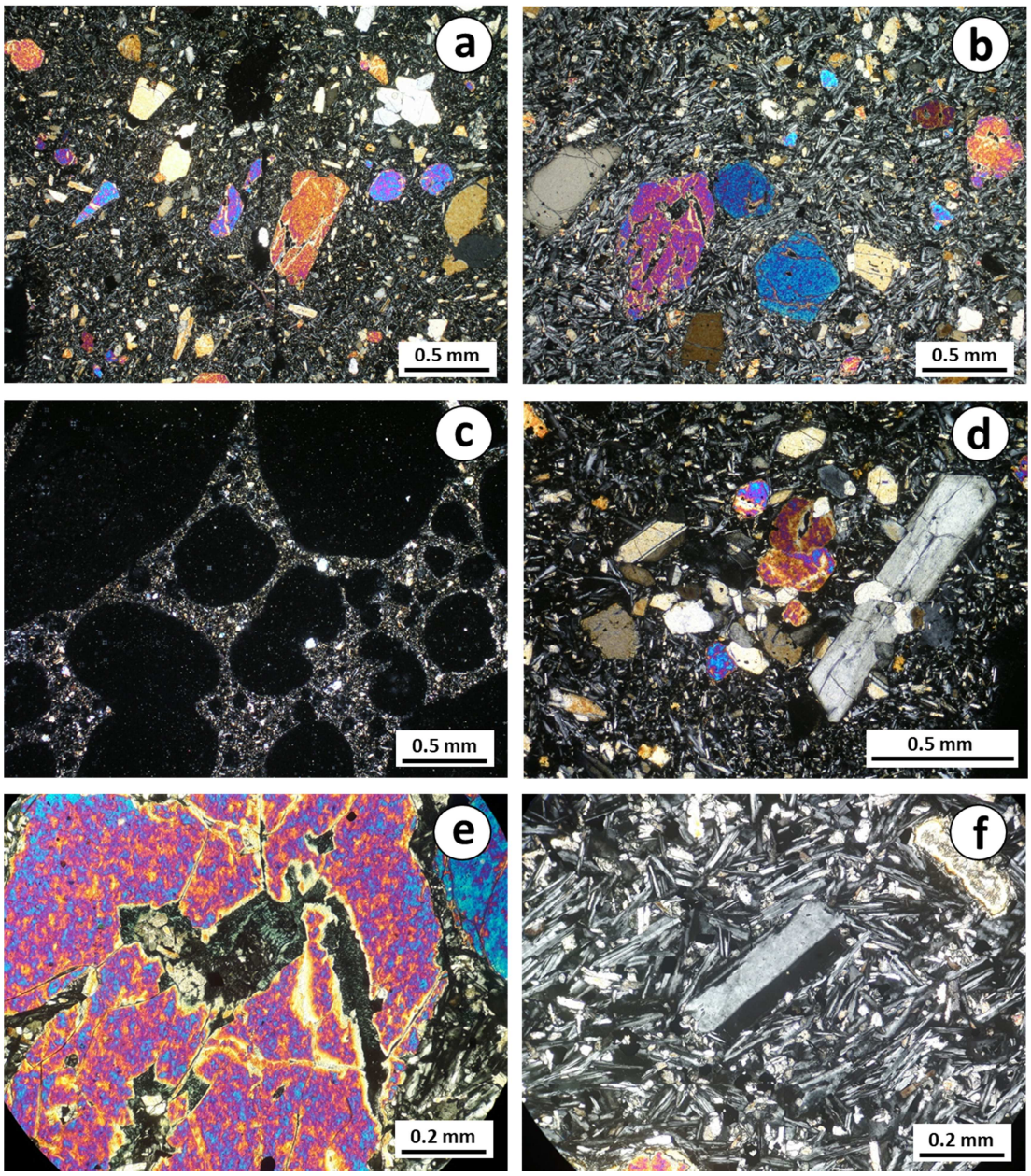

Fig. 31: *Representative photomicrographs of Bijar thin sections at crossed polarizers view: a) and b) fine-grained massive porphyric rocks showing phenocrysts of subhedral olivine and clinopyroxene with holocrystalline groundmass; c) highly vesiculated sample showing hypocrystalline groundmass; d) clinopyroxene micro and phenocrysts often occurring as locally clustered in aggregates; e) olivine phenocryst showing widespread fractures filled by serpentine; f) rare microphenocryst of sanidine.*

Takab

Three samples from Takab area are defined as fine-grained basalts with porphyric texture (Fig. 32a, b). The rocks display isotropic to trachytoid texture with holocrystalline to hypocrystalline groundmass. P.I. is around 10-15 % and the samples are massive except one which exhibits ~5% of vesicles 1 to 3 mm in size. Phenocrysts are represented by euhedral to subhedral olivine and clinopyroxene (Fig. 32). In some samples widespread biotite and zeolites occur as well. Abundant fractured olivine always shows hiddingsite rims (Fig. 32) and strong alteration in serpentine, reaching up 5 mm in size. Clinopyroxene is diopside showing size smaller than 0.5 mm. It is moderately zoned and often appears in monocrystalline aggregates. More rarely clinopyroxene is in glomerocrystals with olivine. Biotite mostly appears as anhedral small crystal or more rarely as euhedral crystal (reaching up 0.5 mm in size) and is included in larger irregular zeolitic plagues. Groundmass consists of feldspars, hiddingsitized olivine, clinopyroxene and opaques.

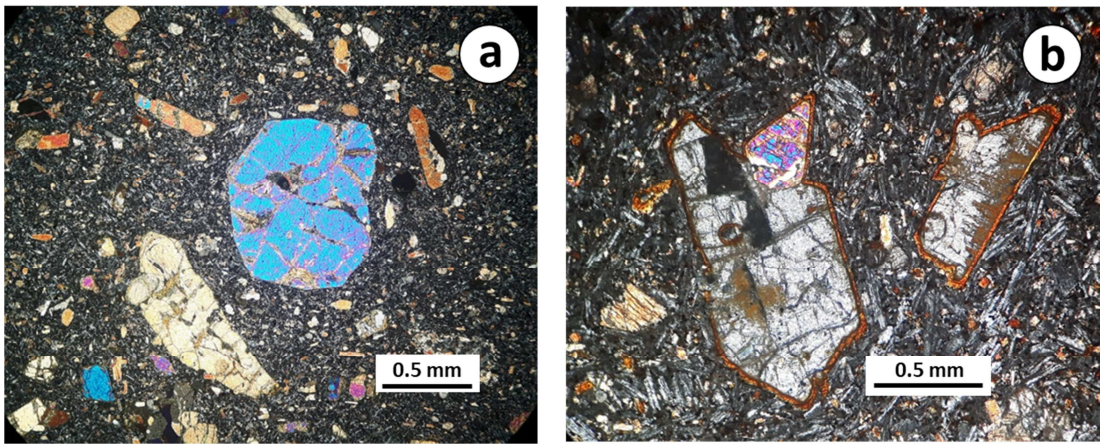

Fig. 32: *Representative photomicrographs of Takab thin sections at crossed polarizers view: a) and b) porphyritic massive rock with isotropic to trachytoid texture and holocrystalline to hypocrystalline groundmass. Clinopyroxene microphenocrysts occur along with fractured anhedral olivine always showing hiddingsite rims and strong alteration in serpentine.*

3.2.2 Mineral chemistry

Electron microprobe analyses are reported in Appendix (Table 11-Table 16) and have been performed on 19 representative polished thin sections (3 from Bijar, 4 from Qezelke Kand, 2 from Takab, 4 from Dehgolan and 6 from Qorveh). A total of 418 points were examined, specifically 31 olivines, 87 pyroxenes, 188 feldspars, 44 amphiboles, 42 micas and 26 opaques.

Olivine

Olivine phenocrysts occur in the samples previously referred as alkaline compositions (i.e. Qezelke Kand, Bijar and Takab). The olivines of these groups do not show any particular differences except for Mg content from Qezelke Kand rocks (Fo_{83-87}; Table 11), which results slightly higher respect with Bijar and Takab (Fo_{69-87} and Fo_{75-85},respectively; Fig. 33). Ni content is relatively high in Qezelke Kand and Bijar olivines (0.12-0.43 wt% and 0.06-0.38 wt%) and moderately low in Takab rocks (0.04-0.22 wt%), resulting roughly correlated with MgO values. CaO is similar in both Qezelke Kand and Bijar analyses (~0.14-0.37 wt%) whereas shows a narrower range (~0.20-0.27 wt%) in Takab olivines.

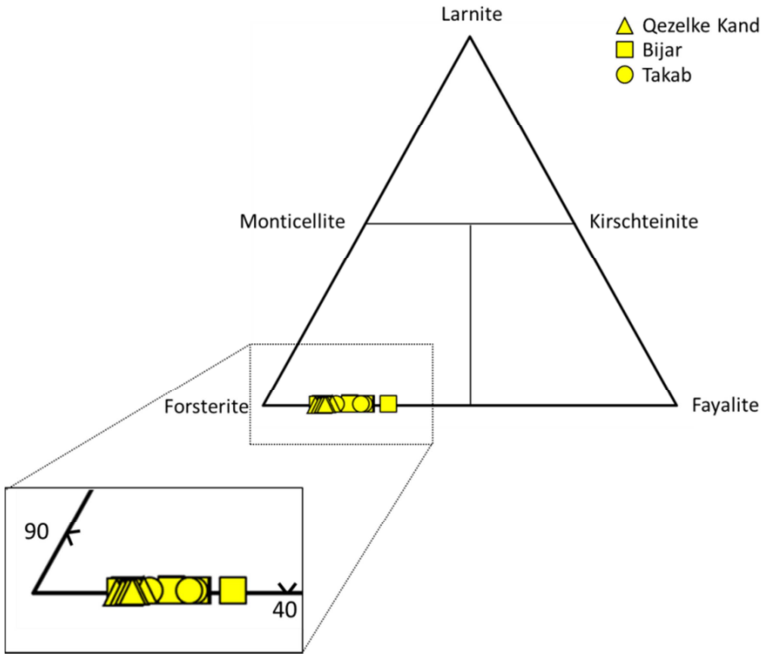

Fig. 33: *Forsterite-Fayalite-Larnite ternary diagram for classification of olivines.*

Pyroxenes

EMP analyses of Nowbaran clinopyroxenes are reported in Table 12. Clinopyroxenes commonly occur in all the samples whereas orthopyroxene has been found only in Dehgolan and Qorveh rocks. Clinopyroxenes from alkaline samples show quite similar compositions, falling mostly in diopside field ($Wo_{45-49}En_{36-48}Fs_{7-15}$; Fig. 34) with lesser terms (~15% of the analyses) falling in augite field ($Wo_{42-45}En_{44-49}Fs_{9-11}$). Diopside shows Mg# [i.e., $Mg/(Mg+Fe^{2+})$] ranging between 0.81 and 0.99 with FeO=3.9-8.9 wt%, whereas augite shows Mg# between 0.81 and 0.91 and FeO content between 4.7 and 7.4 wt%. Some of major oxide abundances are fairly similar in all of the alkaline groups, showing a good negative correlation if plotted against silica (i.e. TiO_2=0.5-3.3 wt% with R^2=0.87; Al_2O_3=1.9-7.8 wt% with $R^2$0.79). FeO show a roughly negative correlation (R^2=0.62) while on the other hand CaO (~2.0-23.4 wt%) distribution is rather cloudy if plotted vs. SiO_2. Clinopyroxenes from Qorveh fall into diopside ($Wo_{45-48}En_{40-48}Fs_{7-12}$) and augite ($Wo_{43-45}En_{43-50}Fs_{7-12}$) field. Mg# values are 0.83-0.99 and 0.87-0.96 (respectively for diopside and augite) while major oxides show similar abundances (i.e. total range TiO_2=0.3-0.6 wt%, Al_2O_3=0.8-4.0 wt%, FeO=3.7-8.5 and CaO=21.4-23.4) without any particular correlation with silica. Noteworthy that Qorveh FeO content show a compositional gap between 4.1 and 6.1 wt%. On the other hands, Dehgolan clinopyroxenes are characterized only by augitic compositions ($Wo_{42-44}En_{48-52}Fs_{6-8}$) with Mg# ranging between 0.87 and 0.92. No correlations between major oxides (e.g. TiO_2=0.2-0.4 wt%, FeO=4.0-5.4 wt% and CaO=20.5-22.6) are visible if compared to silica content, except for Al_2O_3 (~0.4-2.7 wt%) which show a clear negative correlation with R^2=0.83.

Compositions indicated as calcalkaline in literature, namely Qorveh and Dehgolan, are both characterized by orthopyroxene occurrence, specifically clinoenstatite compositions (respectively $Wo_{2-3}En_{68-74}Fs_{24-29}$ and $Wo_2En_{85-88}Fs_{10-13}$). Worth mentioning Dehgolan high Mg# (0.75-0.91) and relatively low FeO content (~6.2-8.6 wt%) respect with Qorveh (Mg#=0.63-0.79 and FeO~14.8-18.5 wt%).

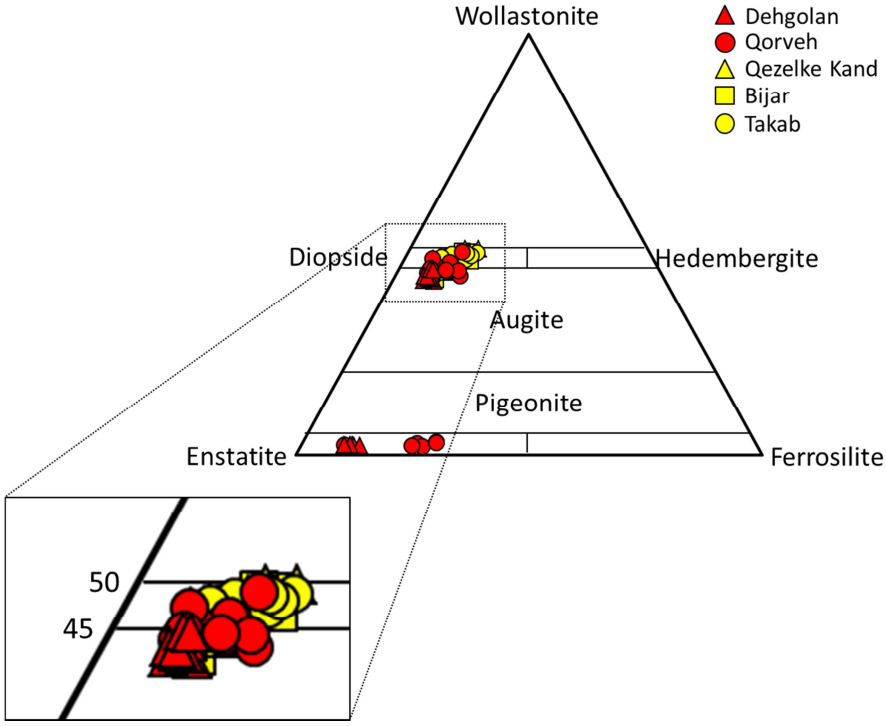

Fig. 34: *Classification diagrams of pyroxenes, after Morimoto et al., (1988).*

Feldspars

Feldspars phenocrysts commonly occur in Dehgolan and Qorveh rocks, whereas are restricted as widespread groundmass phase in alkaline samples (i.e. Bijar, Qezelke Kand and Takab). Dehgolan phenocrysts fall into oligoclase-andesine composition with $An_{20-39}Ab_{54-77}Or_{2-8}$ (Fig. 35; Table 13) while plagioclase groundmass microliths mostly show andesine terms ($An_{27-46}Ab_{52-68}Or_{2-6}$). Qorveh phenocrysts exhibit similar composition ranging from oligoclase to andesine ($An_{24-51}Ab_{47-71}Or_{2-6}$) and an overlapping of values is visible for groundmass plagioclase as well ($An_{22-51}Ab_{47-72}Or_{2-7}$). In two samples of Qorveh district, sanidine occurs as common phenocryst and as groundmass, showing $An_{1-2}Ab_{22-35}Or_{63-77}$ without any particular compositional variation. Qezelke Kand more differentiated rocks show plagioclase both as groundmass ($An_{21-52}Ab_{46-74}Or_{2-7}$) and as phenocrysts ($An_{28-40}Ab_{58-70}Or_{2-3}$) in four more differentiated samples. Feldspars is by far the most abundant phase in groundmass of alkaline rocks. Plagioclase occurs in Bijar rocks only as groundmass crystals with compositions ranging from andesine to labradorite ($An_{30-67}Ab_{32-61}Or_{1-10}$), whereas Takab feldspars are present in the

groundmass mostly as Na-rich sanidine ($An_{6-8}Ab_{41-52}Or_{40-52}$) or as labradorite ($An_{54-60}Ab_{39-43}Or_{2-5}$).

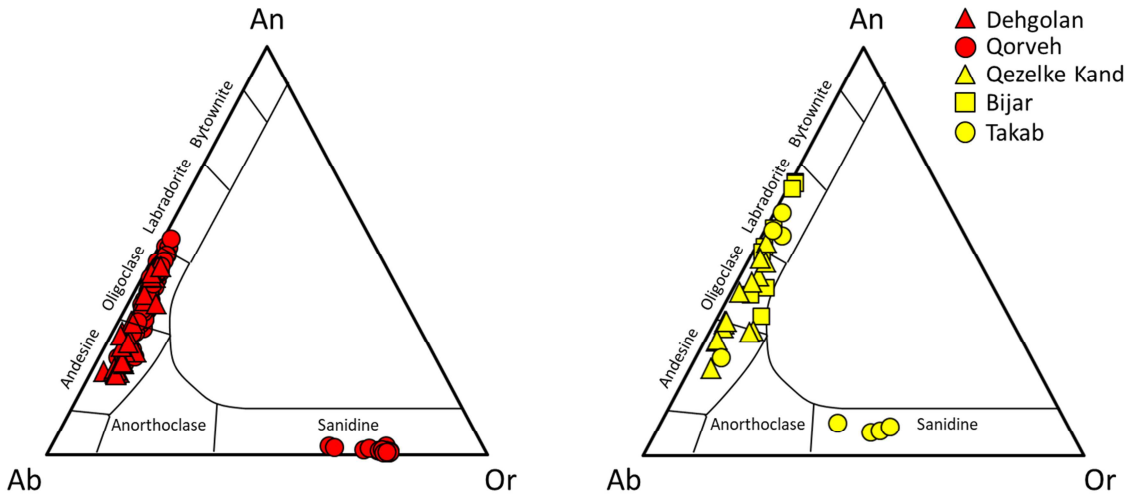

Fig. 35: *An-Ab-Or feldspar ternary diagram after Deer et al. (1992). Abbreviations: Ab = albite; Or = orthoclase; An = anorthite.*

Mica

Brown mica was found as phenocryst in almost all the investigated rocks except for Bijar samples. Qorveh micas show Mg# 0.44-0.66 falling mostly into biotite field, with FeO ~14.0-21.5 wt% and Al_2O_3 ranging between 13.6 and 18.7 wt% (Fig. 36; Table 14). Dehgolan micas exhibit higher Mg# (0.52-0.76) approaching phlogopite compositions. Only three analyses show extremely high Mg# (0.91-0.93) as FeO abundances results clearly lower (~3.2-4.4 wt%) respect to the average district values (~11.1-19.8 wt%). Moreover, noteworthy F high content of Dehgolan (~0.3-3.9 wt%) respect with Qorveh micas (0.2-1.3 wt%). TiO_2 abundances are high in both district (~1.5-5.1 wt%) and K_2O is quite homogeneous as well (~7.2-9.8 wt%.). In alkaline rocks, brown mica crystals are restricted to the groundmass or as microphenocrysts, occurring in Qezelke Kand and Takab samples with slightly different compositions. Takab phlogopite (Mg# 0.75-0.80) results TiO_2 rich (7.0-7.4 wt%), with FeO ranging between 8.5 and 8.8 wt% and Al_2O_3 values between 11.6 and 12.5 wt%. Qezelke Kand micas are phlogopite as well (Mg#

0.82-0.87), showing lower TiO_2 and FeO abundances (~3.1-3.8 wt% and ~5.3-7.6 wt%) but higher Al_2O_3 (~15.3-15.8 wt%). K_2O is similar is both the districts, namely ~8.7-9.7 wt%.

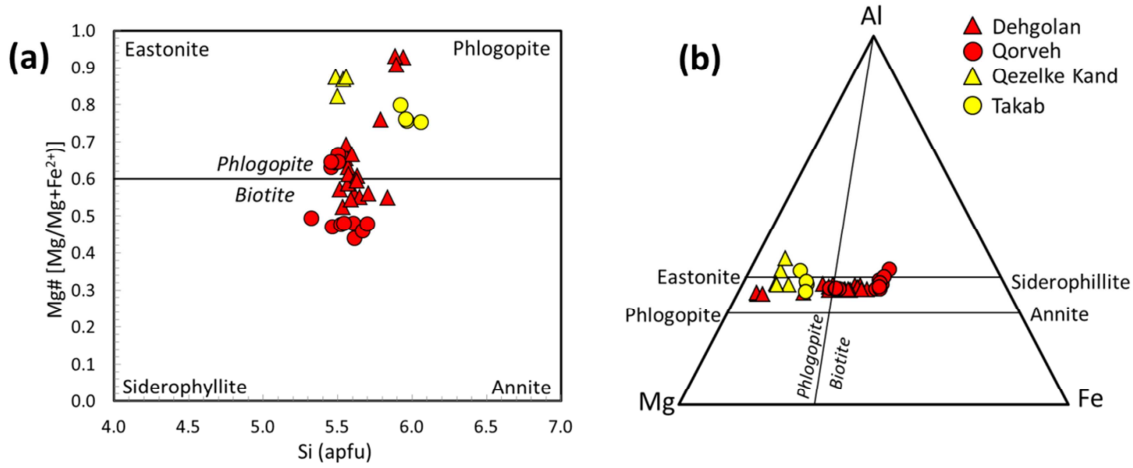

Fig. 36*: a) Classification diagram of brown mica after Rieder et al. (1998) and b) Al-Mg-Fe mica classification diagram*

Amphibole

Amphibole represents the most abundant mafic mineral in Dehgolan and Qorveh samples. According to Leake et al. (1997) classification (Fig.37a), Qorveh and Dehgolan amphiboles are classified as *calcic* amphibole, since Ca in the B site is ≥ 1.5 (specifically ~1.6-1.9; Table 15). The sum of Na and K in the A site is in general ≥ 0.5 (i.e. ~0.4-1.0), indeed nearly half of Dehgolan amphiboles (Fig. 37b) shows $(Na+K)_A < 0.5$, but they are classified as calcic as well. Qorveh amphiboles show high Mg# (~0.59-0.84) and Si ~5.7-6.6 apfu, falling mostly in Mg-Hastingsite field with lesser terms falling in edenitic composition (^{VI}Al ranges from 0.03 to 0.67 apfu whereas Fe^{3+} is 0.0-1.2 apfu). F content is extremely high (0.1-1.9 apfu). Dehgolan calcic amphiboles exhibit similar values, with showing a narrower range for Mg# (0.52-0.79) and Si content (6.3-6.9 apfu), falling similarly in Mg-Hastingsite-Edenite field (^{VI}Al=0.00-0.49 with Fe^{3+}=0.43-1.1 apfu). Nearly half of the analyzed amphiboles show $(Na+K)_A \leq 0.49$ (respect with the others showing $(Na+K)_A$ between 0.51 and 0.89) and have been classified as Mg-Hornblendite. F content is lower respect to Qorveh samples, with only 0.3 apfu maximum.

Amphiboles from one sample from Qezelke Kand were also analyzed and then classified as Mg-Hastingsite, with Si ranging in a very narrow range (6.0-6.3 apfu) and Mg# showing values 0.58-0.73. ^{VI}Al is 0.14-0.28 and Fe^{3+} is 0.58-0.87 apfu. F content is ~ 0.0-0.2 apfu.

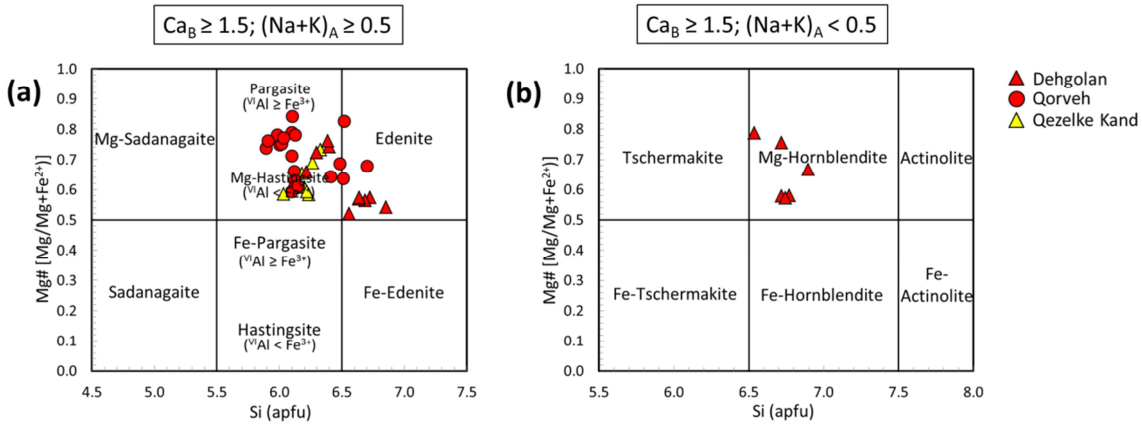

Fig. 37: *Classification of calcic (i.e. $Ca_B \geq 1.5$ apfu) amphiboles, after Leake et al., (1997). a) Calcic amphiboles with $(Na+K)_A \geq 0.5$ and b) calcic amphiboles with $(Na+K)_A < 0.5$.*

Opaques

Opaque oxides of Qorveh rocks belong to the ilmenite-hematite solid solution (Fig. 38), with Ilm_{58-78} (Table 16). TiO_2 content is ~28.5-38.8 wt% and FeO is ~50.3-61.6 wt%. MgO values range between ~1.2 and ~3.3 wt% where Al_2O_3 is extremely low (< 0.2 wt%). Otherwise, the alkaline compositions opaques belong to the ulvospinel-magnetite solid solution (Usp_{53-70}). Overall compositions are quite homogeneous except for one Takab sample (Usp_{20-24}) which exhibits lower TiO_2 (1.4-2.1 wt%) and FeO (25.2-33.3 wt%) but higher MgO (9.9-11.9 wt%), Cr_2O_3 (35.3-38.0) and Al_2O_3 (14.8-16.7) respect to the overall alkaline compositions (TiO_2=15.7-23.5 wt%, FeO=64.2-72.6 wt%, MgO=1.6-4.8 wt%, Cr_2O_3=0.0-5.0 and Al_2O_3=0.7-5.0 wt%). This opaque phase has been referred to as chromite.

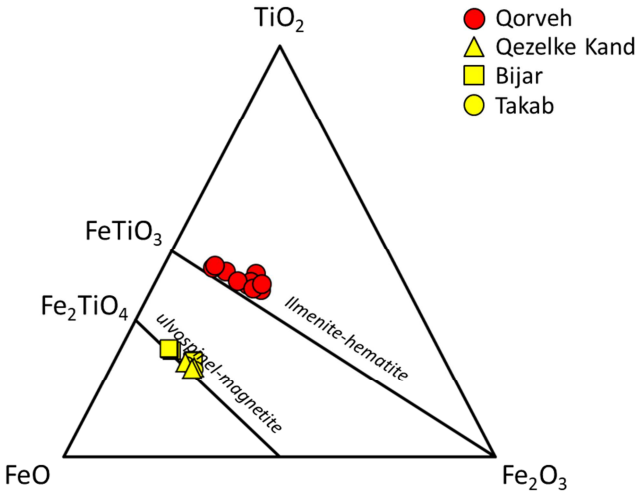

Fig. 38: *Compositional diagrams for Fe–Ti opaque minerals showing the major solid solution series of magnetite-ulvospinel and hematite-ilmenite, after Bacon and Hirschmann (1988).*

3.2.3 Whole-rock chemistry

Major elements

Whole-rock compositions are reported in Table 17. On the basis of the total alkali vs. silica diagram (Le Maitre, 2002; Fig. 39), the investigated samples can be divided into two main groups. Dehgolan and Qorveh rocks are the most silica-rich samples falling close to the alkaline-subalkaline dividing line (Irvine and Baragar, 1971) showing andesite-trachyandesitic and dacite-trachytic compositions, with minor rhyolitic terms (SiO_2 ~59.4-74.8 wt% and alkali ~6.6-8.6 wt%). Only three samples from Dehgolan exhibit trachytic compositions with significantly higher alkali content (~9.3-10.0 wt%, with SiO_2 ~65.3-67.2) respect with the overall values. On the other hand, Qezelke Kand, Bijar and Takab rocks show a rather restricted spread in the TAS diagram, with SiO_2 ranging from ~45.6-51.6 wt% and total alkalis from ~4.1-8.4 wt%, with most of the compositions ranging from trachybasalts to tephrites with lesser alkali basalts, trachybasaltic andesites and phonotephrites (Fig. 39). Noteworthy that four samples from Qezelke Kand totally deviate from the average compositions of the district showing SiO_2-richer compositions (~61.9-67.4 wt%) overlapping the Qorveh and Dehgolan samples.

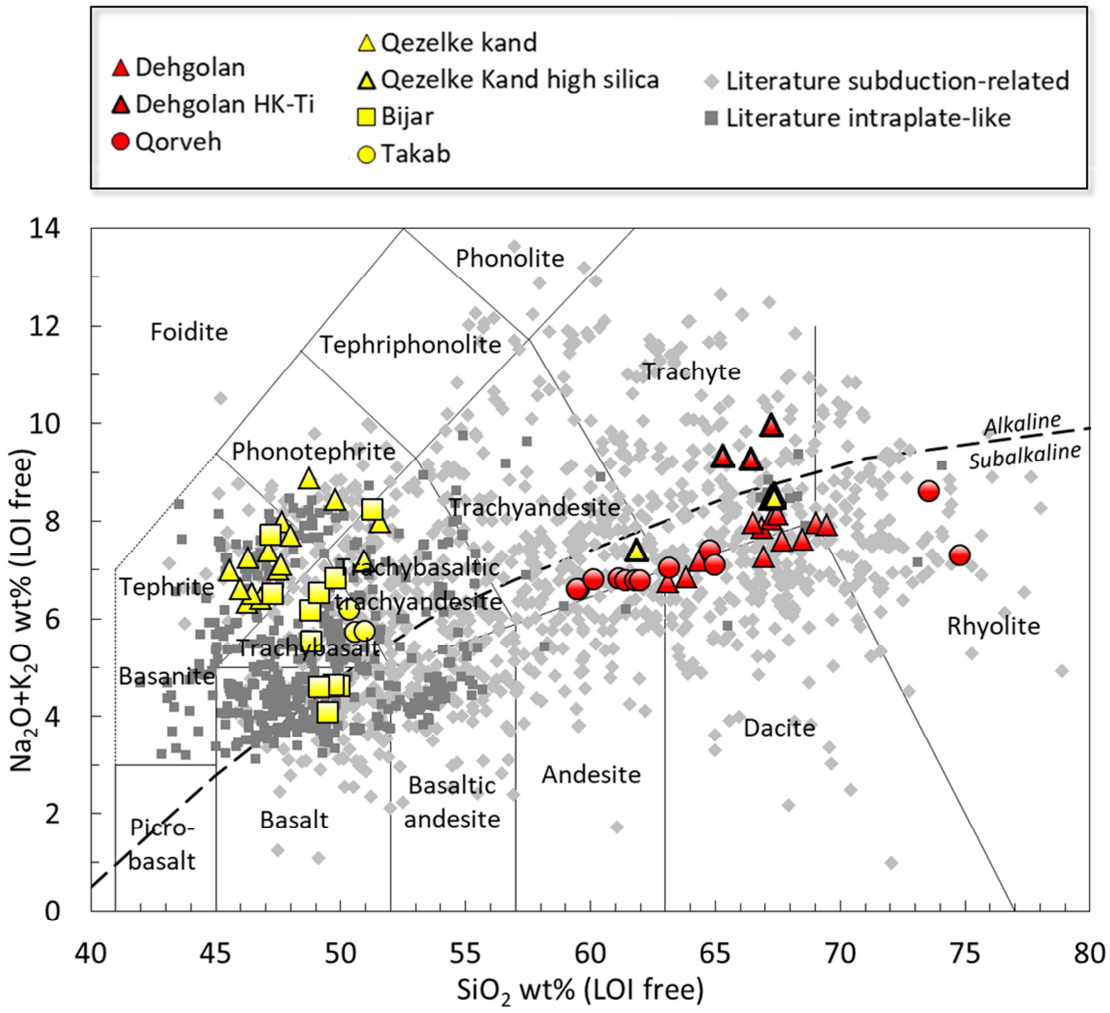

Fig. 39: *Total Alkali vs. Silica (TAS; Le Maitre, 2002), After Le Maitre (2002). Literature subduction-related and intraplate-like compositions are plotted for comparison. All the data are recalculated on a LOI-free basis. Dashed line indicates the limit between alkaline-subalkaline field after Irvine and Baragar (1971).*

According to Peccerillo and Taylor (1976) classification scheme (Fig. 40a), the Miocene investigated rocks (i.e. Dehgolan and Qorveh) belong to the high-K series (showing respectively K_2O=2.6-4.6 wt% and K_2O=2.3-5.0 wt%) with only three alkali-rich samples from Dehgolan falling in the trachytic field (K_2O=5.2-6.2 wt%). Most of them can be defined as calcalkaline compositions with lesser terms showing tholeiitic affinity (Miyashiro 1974; Fig. 40b). Moreover, Dehgolan rocks result grouped in low-Fe and high-Fe suites (i.e. FeO*/MgO; Arculus, 2003; Fig. 40b) with FeO=2.7-4.1 wt% and MgO=0.3-4.1 wt%. Qorveh samples can be instead classified as mostly low- to medium-Fe suites as FeO is ~0.9-6.4 wt% and MgO is relatively low (i.e. ~0.1-3.3 wt%). The four

high-silica samples from Qezelke Kand fall into low-Fe classification with only one sample showing high-Fe content (specifically FeO=2.5-5.5 wt% and MgO=0.7-1.0 wt%).

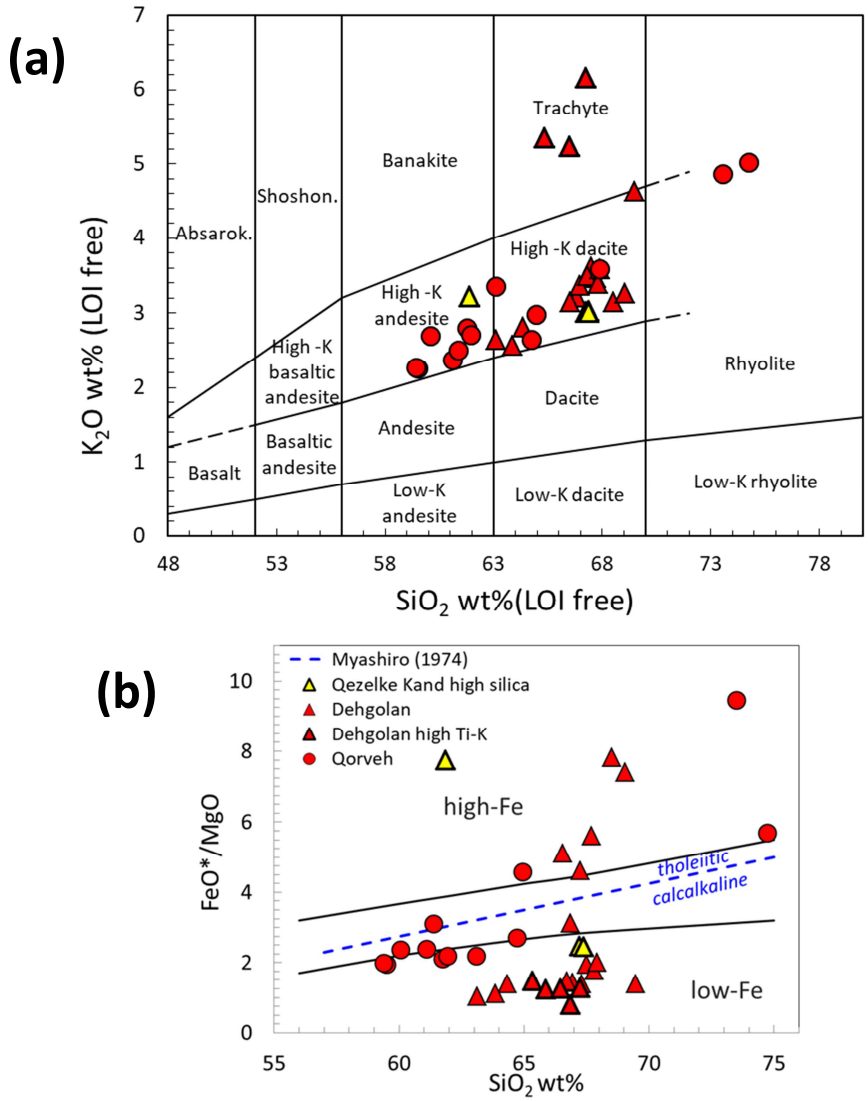

Fig. 40*: a) K_2O vs. SiO_2 diagram (after Peccerillo and Taylor (1976) and b) FeO*/MgO vs. SiO_2 discrimination diagram after Arculus (2003). Dashed blue line is from Miyashiro (1974).*

All the high-K calcalkaline samples show quite homogeneous Al_2O_3 and CaO abundances (total range ~13.5-17.9 wt% and ~1.1-6.4 wt%, respectively) with negative correlations with silica content. But interestingly three samples from Dehgolan show distinctly higher K_2O (~5.4-6.2 wt%), TiO_2 (~0.7-0.9 wt%) and P_2O_5 (~0.6-0.9 wt%) respect with the overall calcalkaline series (K_2O=2.3-5.0; TiO_2=0.1-0.8 wt% and wt% and

P_2O_5=0.0-0.3 wt%). Moreover, it is worth noting to remark the high Mg# of some of Dehgolan and Qorveh intermediate and evolved rocks, with values ~Mg#=0.61-0.69 (showing the highest MgO content, i.e. ~2.3-4.0 wt%) and ~Mg#=0.51-0.65 (with high MgO ~2.4-3.3 wt%), respectively.

Concerning the Quaternary alkaline rocks, Middlemost (1975) classification diagram (Fig. 41) can be useful to define a mainly sodic character for Qezelke Kand and Bijar districts (Na_2O ~3.7-5.8 wt% and ~2.6-6.2 wt%, respectively), with lesser terms towards potassic compositions (K_2O ~1.6-3.7 and ~1.4-3.3 wt%). Otherwise rocks from Takab are clearly characterized by a more potassic affinity (Na_2O=2.8-3.0 wt% and K_2O=2.9-3.2 wt%; Fig. 42). These alkaline samples show similar ranges for major oxides, e.g. Al_2O_3 ~14.3-17.9 wt%, MgO ~0.1-4.0, FeO ~7.5-10.5 wt% and CaO ~1.1-6.4 wt%, with the four Qezelke Kand high silica samples chemically overlapping the Miocene rocks, showing only slightly higher Na_2O (~4.2-5.5 wt%) respect with the overall calcalkaline compositions (~2.3-4.8 wt%). Mg# of these rocks is absolutely unvaried (i.e. Mg#=0.48) with constant MgO=1.00 wt% and FeO=0.38 wt%.

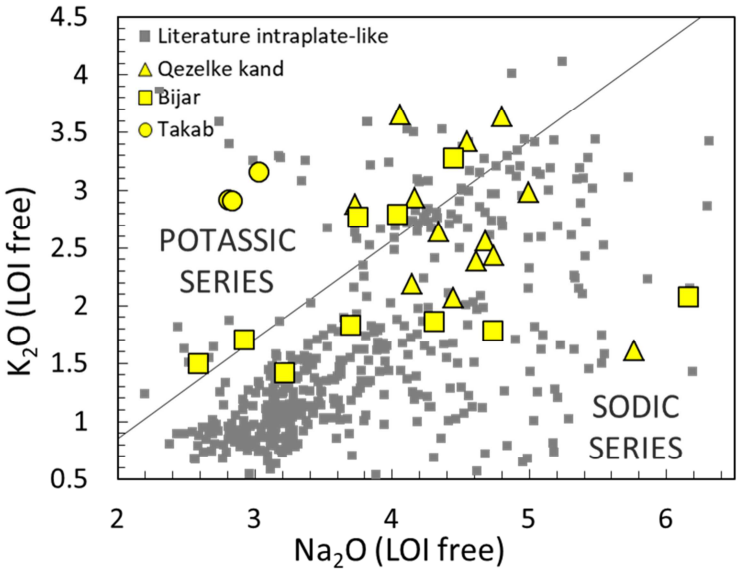

Fig. 41: *Classification diagram for alkaline series after Middlemost (1975).*

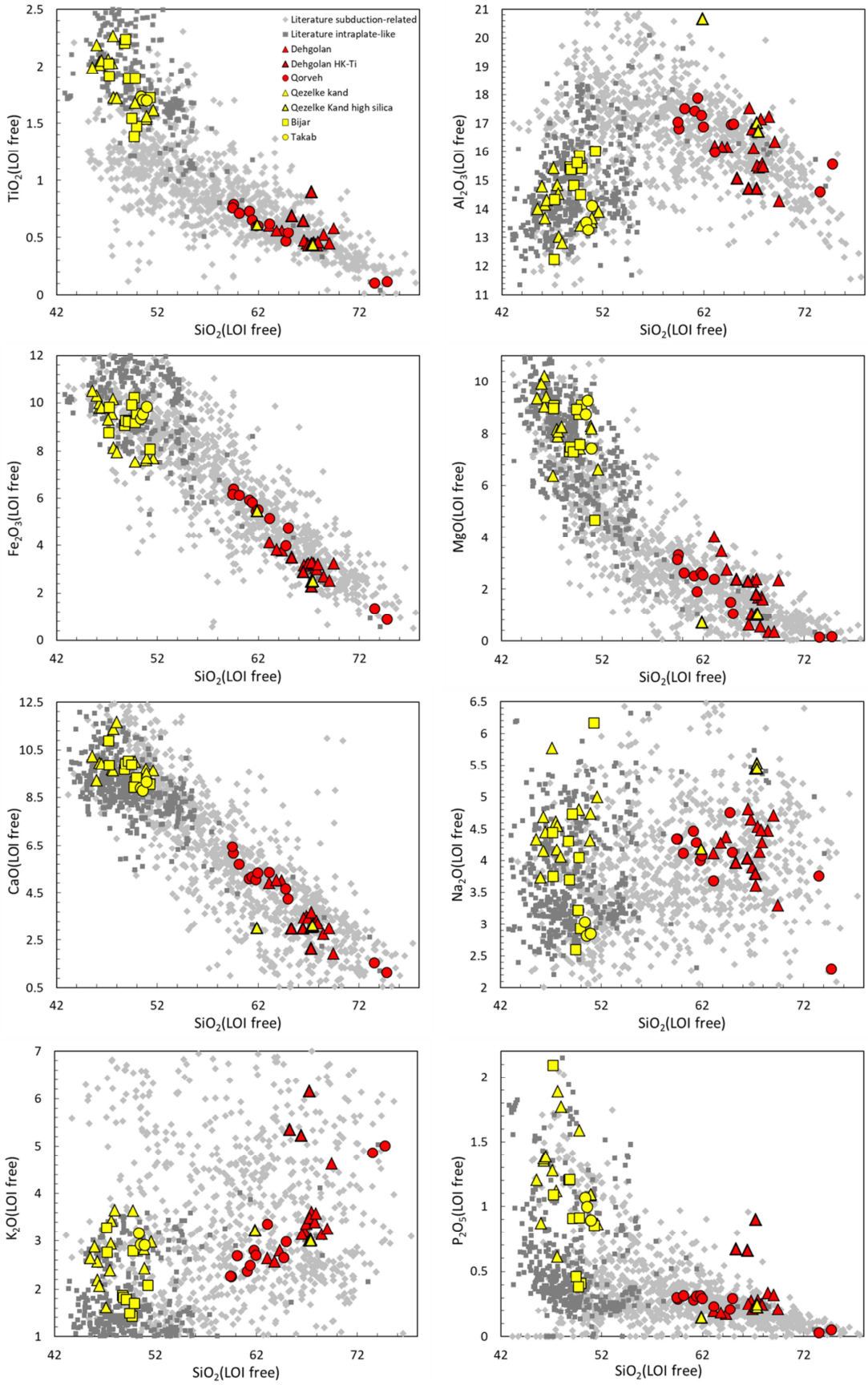

Fig. 42: *Harker diagrams for studied samples (recalculated on a LOI-free basis).*

Trace elements and primitive mantle-normalized diagram

Abundances of trace elements of Dehgolan and Qorveh districts retrace literature subduction-related compositions (Fig. 43).They do not show any particular correlation with silica content except for Rb (~72-173 ppm; Table 17) which evidently increases towards more differentiated compositions. On the other hand, Sr (~470-1364 ppm), Sc (~1-13 ppm), V (~14-130 ppm) and REE exhibit a clear negative correlation if plotted vs. SiO_2. Pb is relatively high, respectively with ~26-48 ppm in Dehgolan and ~31-69 ppm in Qorveh rocks. Only one andesitic rock from Qorveh exhibit Pb~91 ppm. Dehgolan high Ti-K-P samples always distinguish from the overall compositions due to extremely high U (~14-17 ppm), Th (~46-52 ppm) and REE abundances, as well as high Cr (~110-320 ppm) and Ni (~40-70) content.

Alkaline rocks trace elements compositions appear as distributed in scattered patterns vs. SiO_2 and MgO. Qezelke Kand and Bijar rocks exhibit similar trace elements concentrations and totally overlap with intraplate-like trends, showing general low LILE abundances (i.e. Rb ~22-109 and Cs~0.9-2.1). Ba is extremely variable with values ranging from 492 to 2075, whereas Sr varies between 504 and 3293. Interestingly to note that Takab rocks always cluster distinctly as they are characterized by far higher Rb (~63-172 ppm) and Cs (~4.1-24.3), but lower Sr (~504-760 ppm) and REE concentrations compared to Qezelke Kand and Bijar rocks. Finally, Qezelke Kand high silica rocks trace elements concentrations totally fall within with more differentiated rocks except for extremely low Rb values (~64-88 ppm).

Primitive mantle-normalized diagrams (after Lyubetskaya and Korenaga, 2007) for investigated districts are reported in Fig. 44. Dehgolan and Qorveh samples show quite homogeneous patterns, characterized by marked troughs in Nb, Ta and Ti which resemble typical subduction-related magmas compositions. Indeed the average composition of the Global Subducting Sediments (GloSS; Plank, 2014) is reported for comparison, showing identical trend as the above mentioned districts except for an anomalous enrichment for Dehgolan and Qorveh rocks in Ba (up to ~597 xPM; times primitive mantle abundances), U (up to ~873 xPM) and Th (up to ~532 xPM). Sr in these rocks is particularly enriched as well, with values up to ~86 times PM abundances. They are also characterized by a strong LREE enrichment and a slight depletion in HREE

(maximum ~12 times xCI) showing $(La/Lu)_N$ values ranging from ~8 to ~37. Three Dehgolan high Ti-K-P samples follow identical overall pattern but absolutely showing the highest enriched compositions for incompatible elements (i.e. Th up to ~837 xPM and U up to ~965 xPM) and strong REE fractionation pattern as testified by $(La/Lu)_N$ = 41-48. Four high silica samples from Qezelke Kand district is characterized by similar pattern but interestingly is marked by far higher LREE and MREE abundances (La_N/Lu_N=39-41 and Dy_N/Lu_N=1.2-1.6) respect with the other silica-rich compositions (La_N/Lu_N=8.2-36.6 and Dy_N/Lu_N=0.9-1.5).

Differently, the alkaline rocks display much more variable patterns, resembling some mixed features of both HiMU-OIB and subduction-related end members. In Fig. 44, the classical HiMU-OIB (Kawabata et al., 2011) of St. Helena Island pattern is shown. If compared to St. Helena compositions, the analyzed rocks do not show the evident Nb-Ta enrichment but rather share a slight trough in Pb and K, showing lesser HREE content (being below 5 xCI) as well. On the other hand, alkaline rocks exhibit extremely high U and Th contents (~69-277 and ~136-427 xPM) which even reach up values of ~607 xPM and ~600 xPM, respectively, in Takab samples. Bijar and Qezelke Kand compositions are also characterized by a marked trough in Ti, partially revoking a subduction imprinting. Moreover, a strong fractionation pattern is testified by high LREE/HREE and LREE/MREE ratios (respectively La_N/Lu_N=13.7-75.4 and La_N/Sm_N=4.2-6.3). Takab district, as already noted in trace elements diagrams (Fig. 41), represents a distinct group showing slight different patterns and less enriched abundances, i.e. La_N/Lu_N=13.8-18.3 and La_N/Sm_N=2.5-2.6.

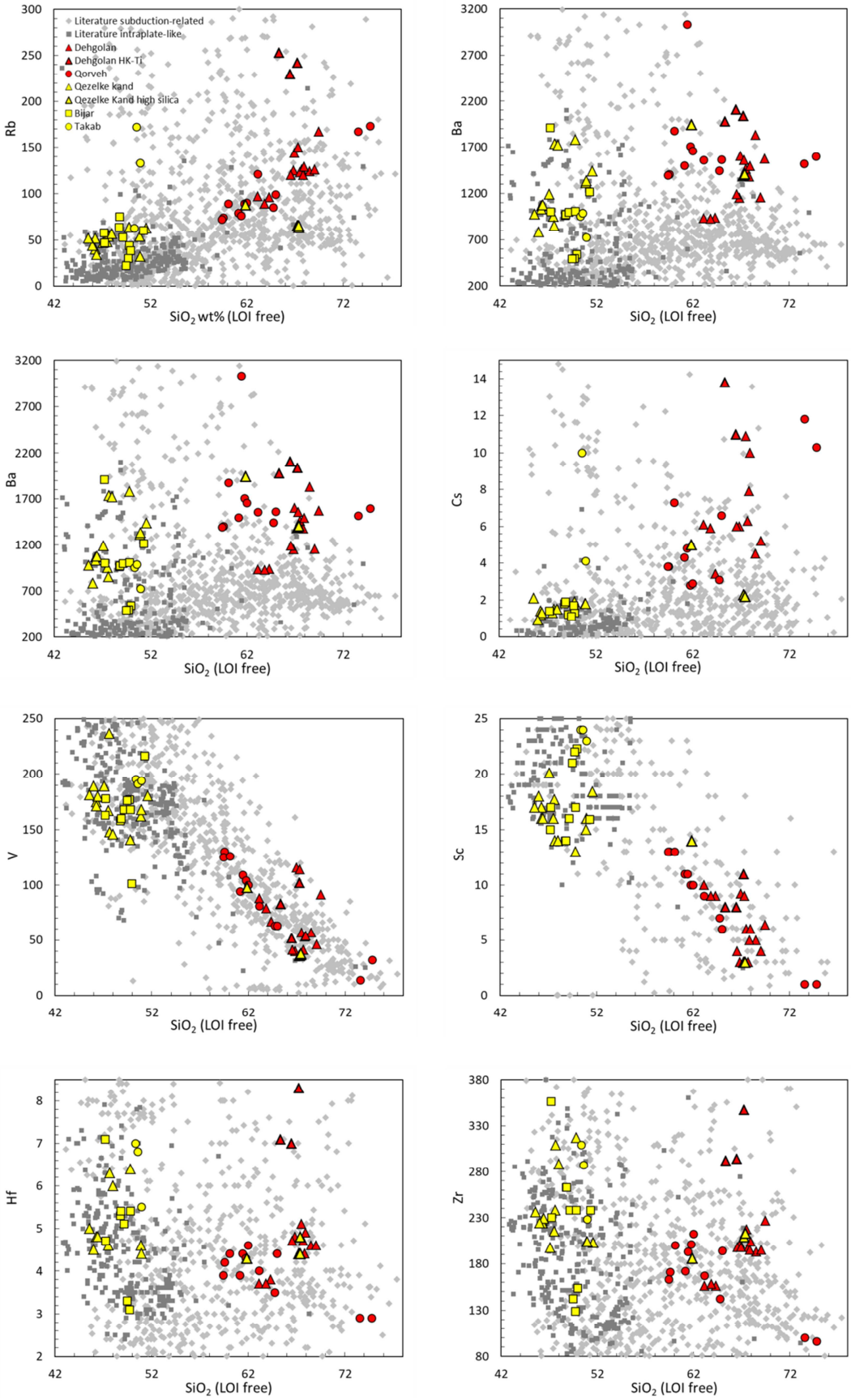

Fig. 43: *Selected trace elements vs. SiO_2 diagrams for Bijar-Qorveh rocks (recalculated on a LOI-free basis).*

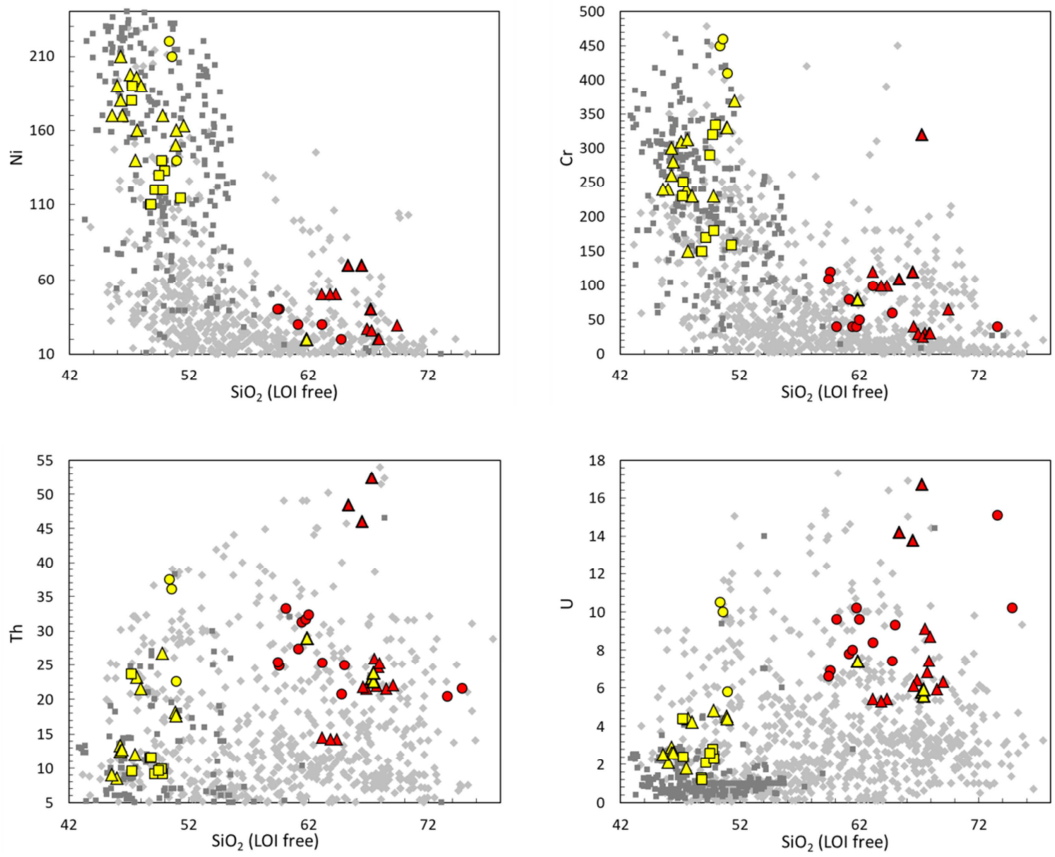

Fig. 43: *(continued)*

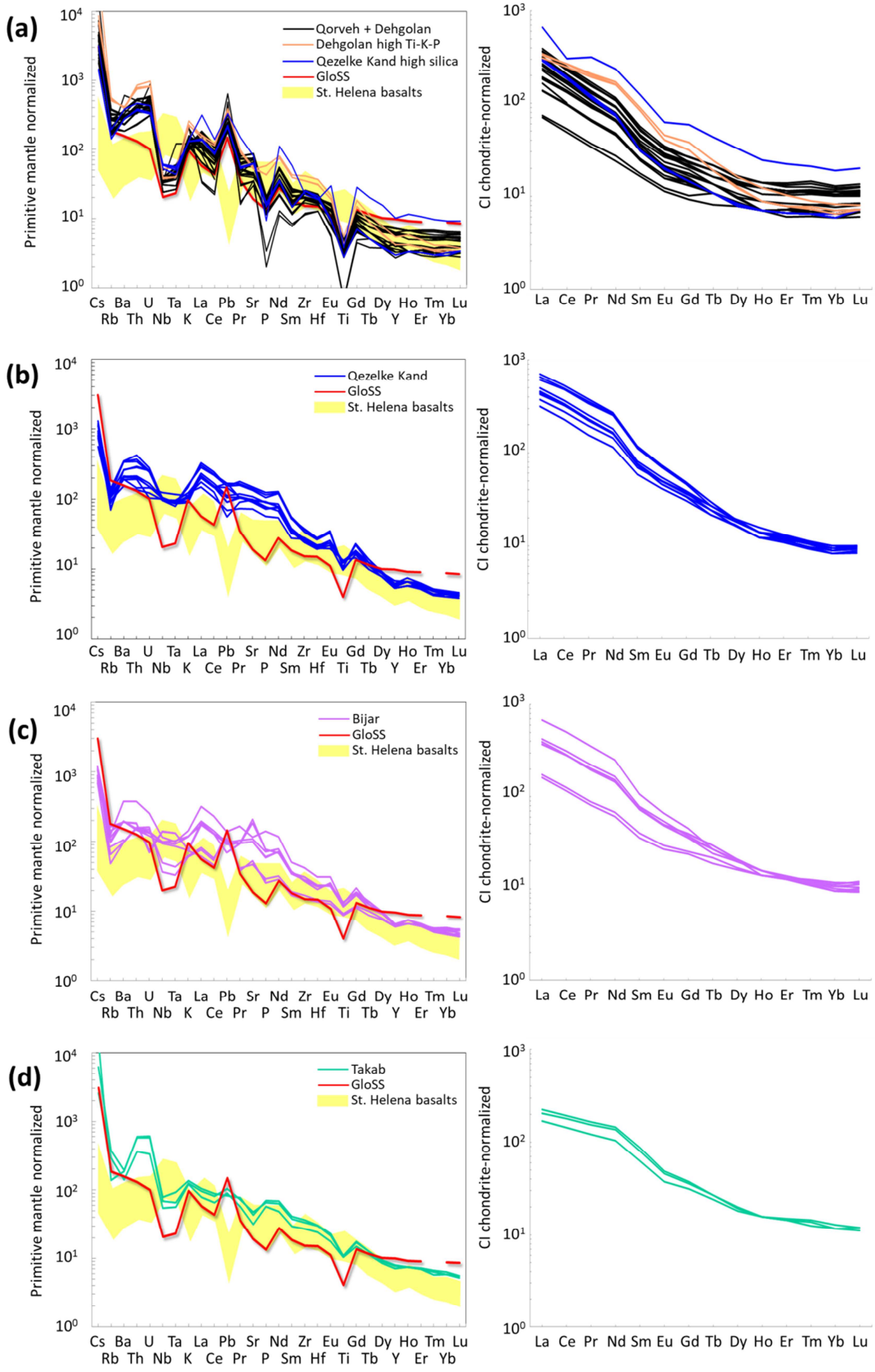

Fig. 44: *Primitive mantle-normalized (after Lyubetskaya and Korenaga, 2007) incompatible elements diagrams and CI-chondrite-normalized (after King et al., 2020) REE patterns for a) silica-rich samples, b) Qezelke Kand, c) Bijar and d) Takab alkaline rocks.*

3.2.4 Sr-Nd-Pb isotopes

Sr-Nd-Pb isotopic ratios of Dehgolan and Qorveh were age-corrected to ~9 Ma (Table 17), whereas no recalculation to alkaline samples initial values has been performed as they are likely only ~1 Ma.

In the $^{143}Nd/^{144}Nd$ vs. $^{87}Sr/^{86}Sr$ diagram (Fig. 45), Dehgolan and Qorveh rocks are distinctly plotted towards Sr isotopic compositions more radiogenic than BSE (Bulk Silicate Earth), showing $^{87}Sr/^{86}Sr$=0.706163-0.707726 and $^{143}Nd/^{144}Nd$=0.512417-0.512551. Dehgolan high Ti-K-P sample shows by far more enriched radiogenic values (i.e. $^{87}Sr/^{86}Sr$=0.71111; $^{143}Nd/^{144}Nd$=0.512229), totally deviating from the average values of the district. Alkaline compositions show a relatively narrow range with $^{87}Sr/^{86}Sr$=0.704773-0.705709 and $^{143}Nd/^{144}Nd$=0.512525-0.512711, not considering Takab rocks as they exhibit extremely wide and variable values ($^{87}Sr/^{86}Sr$=0.704768-0.707585; $^{143}Nd/^{144}Nd$=0.512277-0.512723). Qezelke Kand high silica samples partially overlap with the richer silica compositions, clearly falling into the enriched mantle quadrant. Both $^{87}Sr/^{86}Sr$ and $^{143}Nd/^{144}Nd$ values do not show any correlation with SiO_2 or vs. MgO, apart from a rough/weak negative correlation for Dehgolan rocks with silica (R^2 = 0.53). Silica-rich samples also show a narrow range for $^{206}Pb/^{204}Pb$ (18.88-19.00), $^{207}Pb/^{204}Pb$ (15.69-15.74) and $^{208}Pb/^{204}Pb$ ranges (39.00-39.14), falling on the right of the 4.56 Ga geochron, falling above the NHRL (Northern Hemisphere Reference Line; Fig. 45), whereas alkaline compositions are clustered with slightly lower radiogenic $^{206}Pb/^{204}Pb$ (18.48-18.98), $^{207}Pb/^{204}Pb$ (15.64-15.69) and $^{208}Pb/^{204}Pb$ ranges (38.54-39.09), without any particular distinctions within the different districts. Noteworthy Qezelke Kand high silica samples cover the entire range of values ($^{206}Pb/^{204}Pb$=18.71-18.97, $^{207}Pb/^{204}Pb$=15.66-15.71 and $^{208}Pb/^{204}Pb$=38.76-39.11). As observed for Sr and Nd isotopes, no substantial correlations are observed for Pb isotopic ratios with SiO_2 or MgO content.

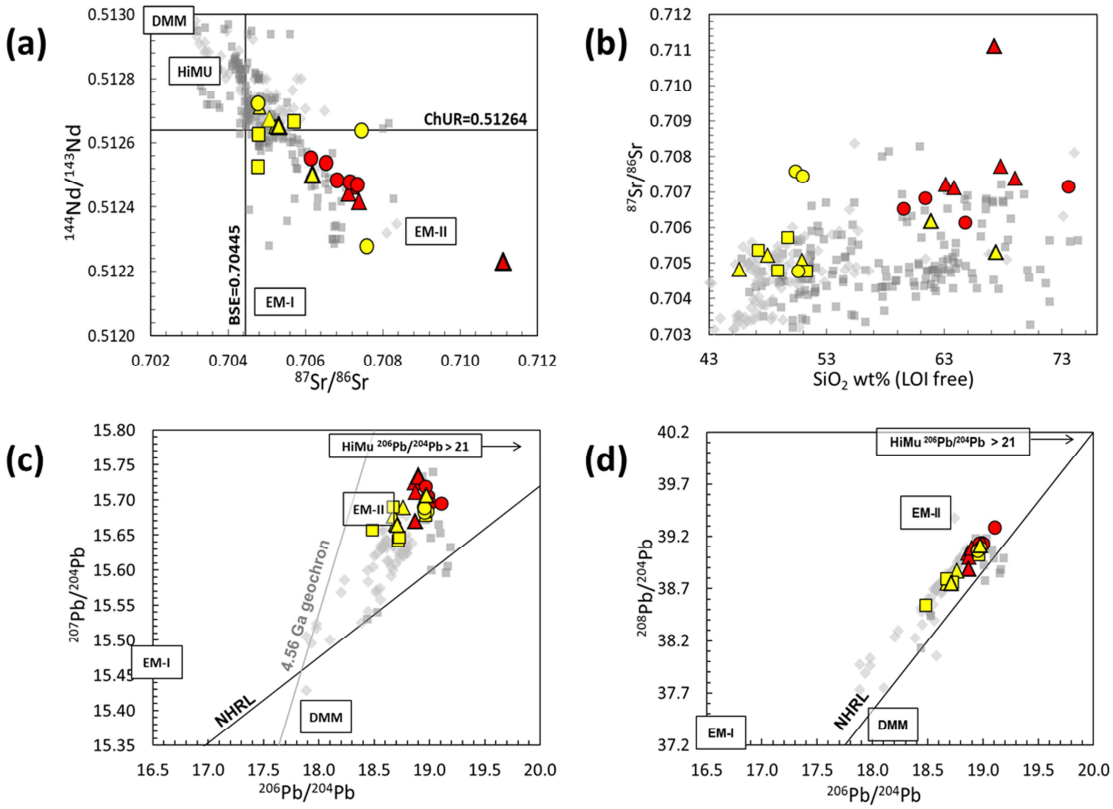

Fig. 45: *a) $^{143}Nd/^{144}Nd$ vs. $^{87}Sr/^{86}Sr$ isotopic ratios and b) $^{87}Sr/^{86}Sr$ vs. SiO_2 diagram for investigated samples. c) $^{207}Pb/^{204}Pb$ vs. $^{206}Pb/^{204}Pb$ and d) $^{208}Pb/^{204}Pb$ vs. $^{206}Pb/^{204}Pb$ diagrams. NHRL is the Northern Hemisphere Reference Line from Hart (1984). ChUR = Chondritic Uniform Reservoir; BSE = Bulk Silicate Earth; DMM = Depleted MORB Mantle; HiMU = high μ (where $\mu=^{238}U/^{204}Pb$); EM-I = Enriched Mantle I; EM-II = Enriched Mantle II.*

3.3 Discussion

Investigated samples from Bijar-Qorveh area include several rock series varying from Miocene trachy-andesitic to rhyolitic compositions to Quaternary trachybasaltic-tephritic-phonotephritic terms. Miocene rocks belong to high-K calcalkaline series whereas Quaternary samples consist of alkaline series showing mainly sodic to strictly potassic (i.e. Takab) affinity. Studied rocks of Bijar-Qorveh volcanic districts are comparable with identical compositions examined in Boccaletti et al., (1977) who identified two main magmatic events occurring in this region during Tertiary period. The authors indeed interpreted high-K calcalkaline volcanic rocks as the final products of the calcalkaline Tertiary phase of central Iran (Boccaletti et al., 1977) whereas they interpreted the second volcanic cycle as basic magmatism related to regional tensional tectonics.

Concerning calcalkaline compositions, a quite regular evolutionary trend is observed for Qorveh and Dehgolan rocks (not considering the three Dehgolan high K-Ti-P samples, which will be discussed in a separated section). Some of major elements, i.e. MgO, Fe_2O_{3tot} and CaO, decrease as silica increases (Fig. 42) along with Ni, Cr, Sc and V (Fig. 43). Moreover Ni, Cr, Sc and V correlate positively with MgO. This is indicative that the liquid line of descent was deeply controlled by crystallization of some ferromagnesian elements such as olivine and pyroxene. The further negative correlation of TiO_2 and Al_2O_3 vs. silica is likely suggestive for magnetite, plagioclase and amphibole fractionation during magma ascent and this statement also results in accordance with petrographic observations. Primitive mantle-normalized multi-elemental patterns of Dehgolan and Qorveh (Fig. 44a) samples show a marked Ti trough associated with Pb positive peak, Nb-Ta negative anomalies and LILE and LREE enrichments. These peculiar characteristics totally resemble GloSS (composition of the global subducting sediments; Plank, 2014) pattern and can be easily attributed to subduction-related signatures. The subduction imprinting is also confirmed by the Sr-Nd isotopic ratios as the compositions clearly fall in the mantle enriched quadrant (Fig. 45a). Moreover, the slight positive correlation of $^{87}Sr/^{86}Sr$ vs. silica content reveals that crustal contamination played a rather substantial role in the genesis of these magmas and that their ascent was likely associated with open-system processes. Additionally,

the high enrichment in Sr-U-Th, along with LREE, could be possibly linked to apatite occurrence in the melting source as this mineralogical phase represents the major host for these elements (Ionov et al., 1997).

On the contrary, three high K-Ti-P samples from Dehgolan always distinguish within this district even though they do not show any petrographic difference or evidence respect with the main group. They entirely overlap Dehgolan primitive mantle-normalized patterns (Fig. 44a) but showing much higher U-Th-Sr-LREE and Rb abundances (as well as a considerable HFSE enrichment). A hypothesis for this discrepancy could be attributed to the different degree of partial melting of the apatite-rich source. Indeed very low degree of partial melting will led to extremely high content of highly incompatible elements in the mantle melt and they appear to be as weaker concentrations progressively with the proceeding of the partial melting. A single liquid line of descent is then observed for Dehgolan and Qorveh intermediate to more evolved rocks, with Dehgolan high K-Ti-P samples showing the more enriched compositions to Qorveh rhyolites representing the most differentiated volcanic products. Nevertheless, apatite occurrence in mantle source is not able to account for the high concentration of TiO_2, K_2O, Rb and HFSE of these rocks, thus an additional mineralogical phase is probably required. Pargasitic amphibole and phlogopite commonly occur as veins, pockets or cumulates within lithospheric mantle, produced by metasomatic reactions between percolating fluids and the original dry peridotitic matrix. These mineralogical phases are hosts for large-ion lithophile elements (e.g. Rb, Ba and LILE; Ionov et al., 1997; Mayer et al., 2014) and major-trace elements abundances of high K-Ti-P samples suggest that amphibole or phlogopite probably played an important role in the genesis of these geochemical features. Nevertheless, phlogopite is the most likely candidate as exhibits by far higher Kd_{Rb} (~1.9-5.8; Green et al., 1993; LaTourette et al. 1995; Adam and Green, 2006) respect with amphibole (Kd_{Rb}=0.14-0.58; Adam et al. 1993; Green et al., 1993; Brenan et al., 1995; LaTourette et al. 1995; Adam and Green, 2006). Moreover, TiO_2 content can reach concentrations up to ~6.5 wt% in phlogopite (Arai et al., 1986), whereas is only ~0.9 wt% in pargasitic amphibole (Niida, 1977), varying with increasing temperature (0.5-1.2 wt%; Niida and Green, 1999). Phlogopite-derived origin is also supported by the highest Rb/Sr ratios (0.26-0.31) observed for the high K-Ti-P samples (Fig. 46), which are coupled with the

lowest Ba/Rb values (7.8-9.2). All these aspects suggest that the genesis of these three samples could be likely attributed to Ti-phlogopite occurrence in the mantle source which gradually decreases as partial melting proceeds (Allen et al., 2013). On the other hand, it is worth noting that amphibole seems to play a key role in the genesis of Qorveh compositions, as Ba/Rb ratios are rather higher (9.1-21.1) although PM-mantle normalized do not exhibit any particular amphibole-derived geochemical imprinting. However only one Qorveh sample (i.e. trachyandesite IR4) shows an uncommonly high Ba/Rb ratio (~39.9) due to extremely high Ba content (~3031 ppm).

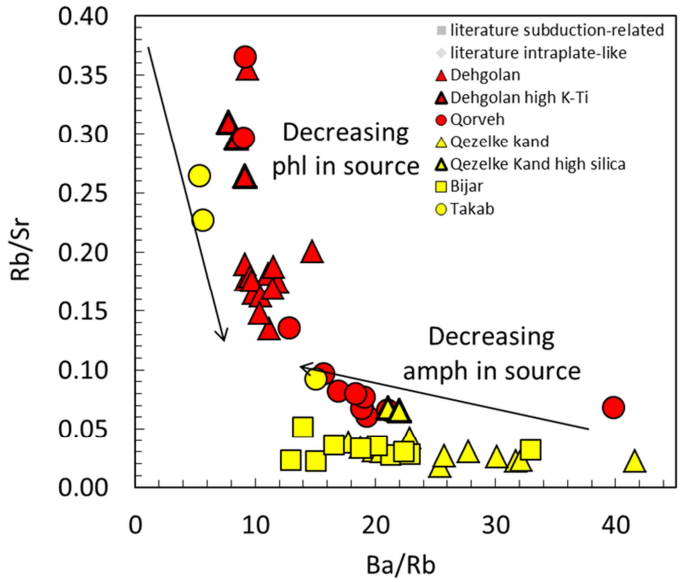

Fig. 46: *Rb/Sr vs. Ba/Rb diagram after Allen et al., (2013).*

Qezelke Kand basic products result associated with four high silica samples in the south-easternmost outcrops, which certainly deserve some more emphasis as they show some anomalous geochemical features. Specifically, these rocks exhibit extremely low Yb content (only ~1 ppm) and generally low HFSE abundances (in particular Y ~10 ppm), as well as high La/Yb and Sr/Y ratios (~64-68 and ~98-100, respectively; Fig. 47) and high Sr content (~817-872 ppm). All these geochemical features are consistent with adakitic characteristics (SiO_2 ~67.3 wt%, Al_2O_3 ~16.9 wt% and MgO ~1.0 wt%).

As above mentioned (*paragraph "Introduction – Investigating adakitic signature"*), this term is still controversial as the genesis for these geochemical features are not well defined. It likely refers to a magmatic origin linked to melting of lower crust (by delamination or underplating) or, more likely, to melting of basaltic compositions in eclogite facies (namely subducted oceanic slabs). Thus, according to this latter hypothesis, high values of La/Yb and Sr/Y as well as low abundances of Y and Yb are ascribed to residual garnet and/or amphibole in the mantle source.

Adakitic magmas are reported throughout UDMA (e.g. Jahangiri, 2007; Omrani et al., 2008; Azizi et al., 2014) and occurrence of slab melting in this area is revealed by these unusual geochemical compositions, whose slab-melts fingerprint is likely to be a consequence of the particular conditions in the study area. Qezelke Kand high silica rocks of the studied area definitely resemble adakites literature data (e.g. Jahangiri, 2007; Omrani et al., 2008; Azizi et al., 2014; Fig. 48) because trace elements ratios of these four samples totally retrace the entire adakitic field (Fig. 47).

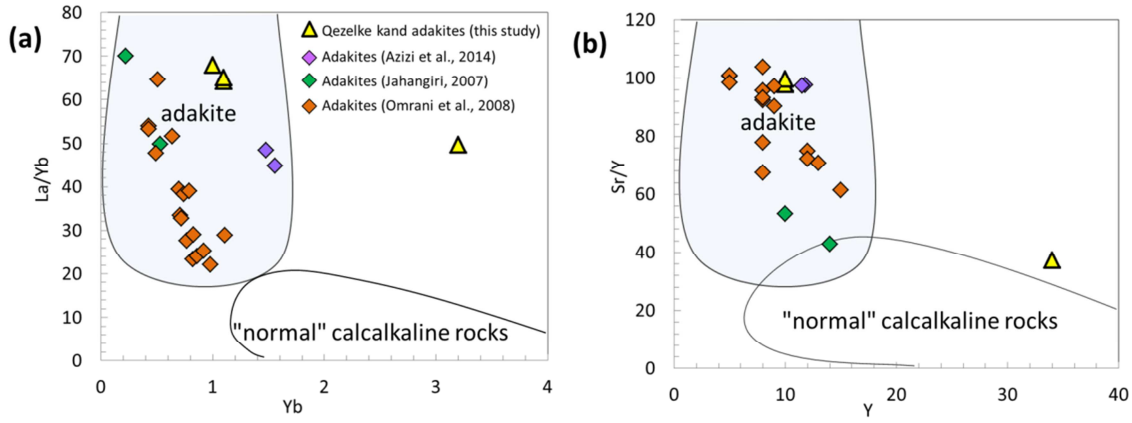

Fig. 47: *a) La/Yb vs. Yb and b) Sr/Y vs. Y discrimination diagrams showing adakite and "normal" calcalkaline compositions domains, after Drummond and Defant (1990) and after Martin (1999), respectively. Adakitic compositions of the studied area are compared with literature data (Qezelke Kand area from Azizi et al., 2014; East Azerbaijan Nahand and Jolfa areas from Jahangiri, 2007; Central Iran Anar and Baft areas from Omrani et al., 2008).*

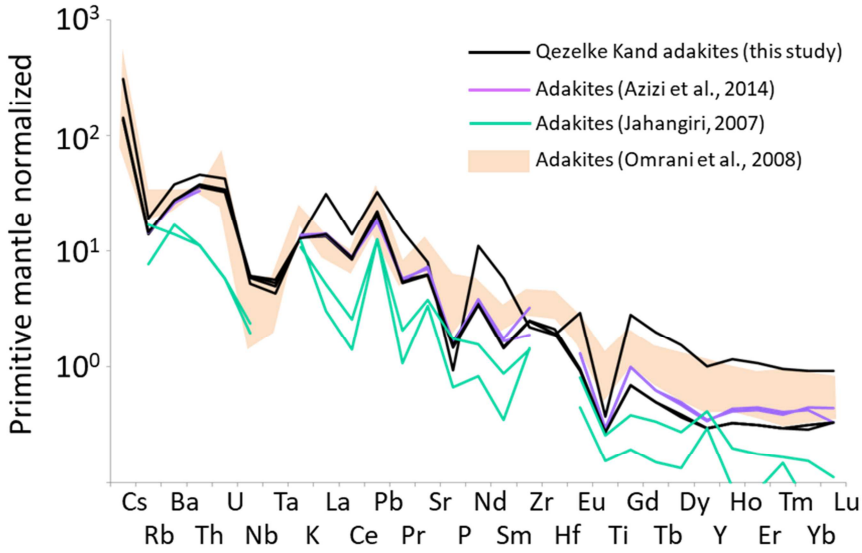

Fig 48: *Primitive mantle-normalized (after Lyubetskaya and Korenaga, 2007) incompatible multielemental patterns for the investigated Qezelke Kand high silica rocks. Adakitic compositions of the studied area are compared with literature data (Qezelke Kand area from Azizi et al., 2014; East Azerbaijan Nahand and Jolfa areas from Jahangiri, 2007; Central Iran Anar and Baft areas from Omrani et al., 2008).*

With regard to alkaline volcanic products (with the exception of Takab compositions which will be discussed shortly), Bijar and Qezelke Kand samples are characterized by various geochemical characteristics. Relatively high Mg# of these rocks (=0.57-0.71) undoubtedly is indicative that primary magma was not affected by extensive fractionation and, furthermore, silica negative correlation with MgO, Fe_2O_{3tot} and CaO clearly demonstrate olivine and clinopyroxene crystallization, being also consistent also with Boccaletti et al., (1977). Primitive mantle-normalized incompatible elements diagrams (Fig. 44b, c) follow a spiky and highly variable patterns, which certainly reflects heterogenous mantle sources. These patterns share both some subduction-related features (e.g. Ti trough, LILE and LREE enrichment) and some HiMU-OIB characteristics (e.g. slight Nb-Ta negative anomaly). Boccaletti et al. (1977) argued that heterogeneous Pleistocene volcanism in Bijar area is to consider as the expression of local disjointing processes which affected the Iranian plate chiefly in proximity of the main NW-SE transcurrent lineaments. On the other hand, Allen et al., (2013) supported a simpler hypothesis involving a variation in the source mineralogy during melting processes, with the first phase of magmatism dominated by amphibole and rutile in the

melting source whereas the second phase is controlled by their exhaustion in the mantle source. This latter theory would be able to account the potassic magmatism of Takab which thus could indicate the participation in the partial melting of hydrated minerals such a phlogopite and apatite as well.

Felsic xenocrysts in both silica-rich and silica-poor (i.e. alkaline) samples are rather common (i.e. Asiabanha et al., 2017; Salehi et al., 2018), and testify the crustal interaction of the ascent magma. Moreover, quartz xenocrysts appear as embayed, indicating disequilibrium with the host rocks (Salehi et al., 2018) and are considered as scavenged from the metamorphic basement during the eruptions (Asiabanha et al., 2017).

Thermobarometric estimates. Thermobarometric formulations could represent useful tools to constrain magmatic conditions and crystallization parameters. The geothermobarometer of Ridolfi et al. (2010) was applied to the Bijar-Qorveh calcalkaline rocks in which amphiboles are the main mafic phenocrysts. Oxygen fugacity and hygrometric equations of Ridolfi et al., (2010) were also used to constrain the P-T-fO2-H2O path of the system during the emplacement of Bijar-Qorveh magmas.

Five amphiboles analysis (specifically two from Dehgolan and three from Qorveh area) were considered as unsuitable for thermobarometric estimates due to their high Al# (e.g. VIAl/AlT = 0.40), as Al# > 0.21 likely indicates xenocrysts of crustal or mantle materials (Ridolfi et al., 2010), or due to not charge balanced compositions (e.g. total of siteA apfu > 1.000).

Results of calculations for amphibole parameters are shown in Fig. 49: crystallization temperatures of Qezelke Kand high silica amphiboles vary in a relatively narrow range (T ~942-984°C) whereas pressure range is ~3.2-5.3 kbar, corresponding to a depth of ~10.7-17.7 km (calculated using an average crust density ρ=2.7 gr/cm^3). The accuracy (σ_{est}) for temperature estimates is ±22°C and the uncertainty for pressure range is ±0.3-0.6 kbar. Oxygen fugacity and hygrometric equations of Ridolfi et al., (2010) were also used to constrain the P-T-fO2-H2O path of the system during the emplacement of Bijar-Qorveh magmas. The deviation (ΔNNO) from NNO buffer is 0.1-1.2 (error of ± 0.4 log

unit) for Qezelke Kand melts, indicating highly oxidized environments. On the other hands, Dehgolan amphiboles show different physical-chemical conditions, as crystallization temperature indicates a wide range interval (~832-967°C) in an extremely various depth region (~1.4-4.5 kbar, i.e. 4.7-14.9 km). The temperature σ_{est} is always ±22°C, and maximum error for pressure values is 0.2-0.5 kbar. In $\log f_{O2}$ vs. T diagram (Fig. 49b), Dehgolan amphiboles likely cluster in two different groups showing ΔNNO=0.6-0.8 and ΔNNO=1.2-1.9 values (with error of ± 0.4 log unit), likely reflecting two different stages for crystallization processes. Qorveh amphiboles record the highest temperature crystallization values (860-1012°C) with pressures varying over a wide interval (~1.5-5.1 kbar; max error ~0.2-0.6 kbar). The redox condition is given by fO2 showing a deviation from the NNO buffer of ~0.1-1.7.

High $H2O_{melt}$ compositions (overall content ~4.0-6.6 wt%; Fig. 49c) result in equilibrium with Qezelke Kand and Dehgolan amphiboles, whereas Qorveh amphiboles record the lower $H2O_{melt}$ concentrations (~1.9-6.1 wt%).

All these investigated parameters describe physical-chemical conditions related to a subduction framework, such as overall high temperatures and low pressures along with high water content melts and the oxygen fugacity of the system constrained between NNO and NNO+2.

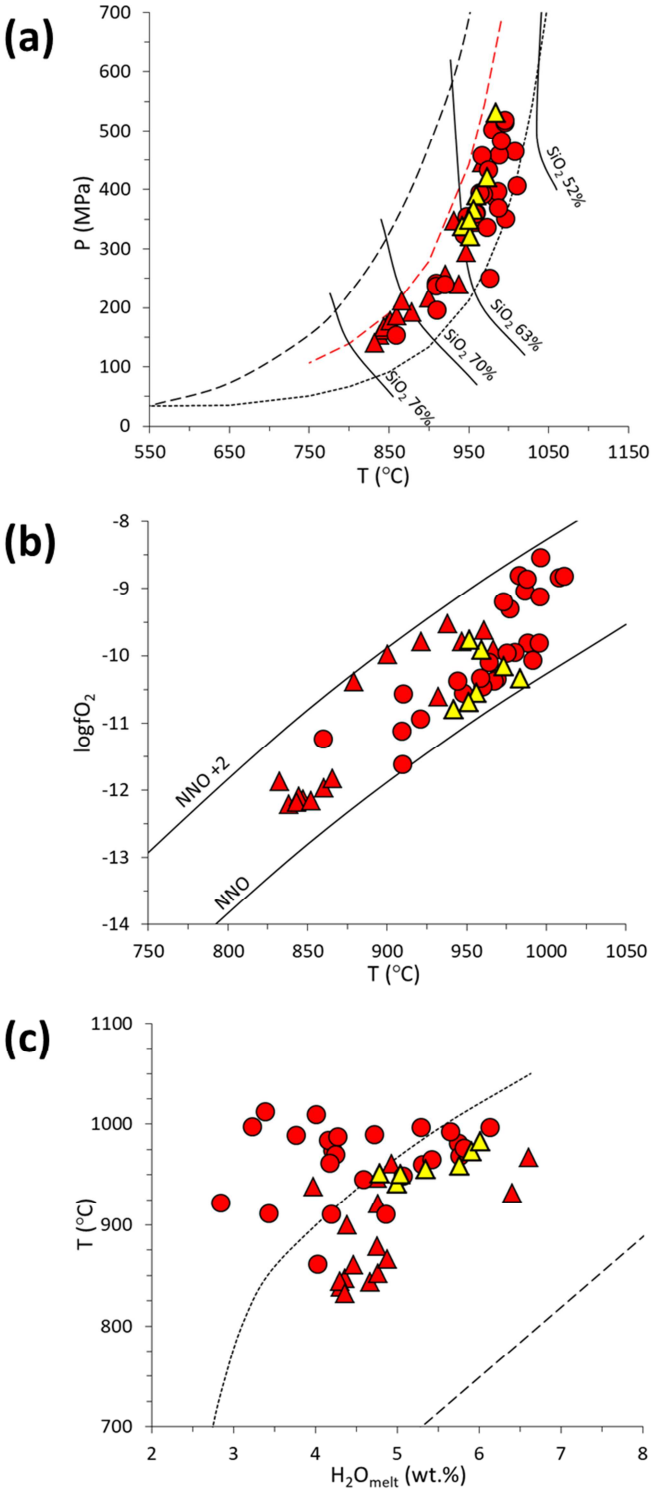

Fig. 49: Crystallization conditions for analyzed amphiboles of Bijar calcalkaline rocks, calculated after Ridolfi et al., (2010): (a) P vs. T diagram. Black dotted line indicates the maximum thermal stability curve, black dashed line is the upper limit of consistent amphibole whereas the red dotted line divides consistent experimental products with different crystallinity (i.e. 35–50% and 12–35%; Ridolfi et al., 2010). The isopleths show the anhydrous SiO_2 content (wt%) of the melt which decreases with the P-T stability curve. (b) Oxygen fugacity vs. temperature diagram showing the nickel-nickel oxide (NNO) buffers. (c) T vs. H_2O_{melt} diagrams with the maximum thermal stability (black dotted line) and the (lower) limit (black dashed line) of consistent amphiboles.

3.4 Conclusions

Bijar-Qorveh volcanic field includes a large variety of volcanic products ranging from trachyandesitic-trachytic compositions (with lesser rhyolitic terms) for Miocene rocks, to trachybasalts and tephrites (with lesser alkali basalts) for Quaternary samples. Miocene volcanic rocks (i.e. Dehgolan and Qorveh) fall close to the alkaline-subalkaline dividing line and exhibit high-K calcalkaline character with typical subduction-related affinity, as also shown by the LILE-LREE enrichments and by Nb-Ta negative anomalies. A single liquid line of descent is observed for Dehgolan and Qorveh rock series, with major and trace elements trends suggesting a crystallization of ferromagnesian minerals followed by removal of plagioclase and amphibole. Only three samples from Dehgolan totally deviate the overall chemical compositions showing high enrichment in K_2O, TiO_2 and P_2O_5, as well as high Rb abundances, likely attributed to a Ti-phlogopite-rich source rock. Noteworthy that high abundances of U-Th-Sr-LREE are thought to be related to apatite occurrence in the melting source of Dehgolan rocks.

Quaternary alkaline samples show more heterogeneous compositions, ranging from sodic to strictly potassic (i.e. Takab) terms. Bijar and Qezelke Kand alkaline samples are olivine-clinopyroxene phyric rocks and show high Mg#, indicating that primary magma was not affected by extensive fractionation. They chemically resemble mixed features of subduction-related magmas and HiMU-OIB characteristics, reflecting hybrid sources. Takab rocks always cluster distinctly, being characterized by higher K_2O and Rb contents which probably indicate phlogopite occurrence in mantle source. Finally, four Qezelke Kand high silica samples totally overlap Miocene chemical compositions and exhibit some geochemical uncommon features, i.e. low Yb and HFSE content with high La/Yb and Sr/Y ratios. All these characteristics are referred to as adakitic compositions whose genesis is likely related to melting of lower continental crust or, more likely, of subducted oceanic slabs with amphibole and/or garnet as residual phase. The investigated rocks belong to the two main magmatic events occurred during Tertiary period in Central Iran. More specifically, Miocene high-K rocks might represent the final phase of the calcalkaline volcanism whereas the Quaternary basic magmatism seem to be related to variations in the source mineralogy or to regional tensional tectonics.

CONCLUDING REMARKS

The investigated areas span a wide range of volcanic products in terms of age and chemical compositions, developed as a consequence of the NE-directed subduction of the Neotethyan oceanic lithosphere beneath the Eurasian plate during Early Cenozoic times.

The investigated rocks of Tafresh area include a wide compositional range, showing mainly basalt-andesitic to rhyolitic terms and are considered to be genetically linked to a three-step closed-system evolutionary process. It involves first the fractionation of ferromagnesian minerals (mostly clinopyroxene and olivine) and plagioclase, followed by a second removal of plagioclase and lesser amphibole (plus minor clinopyroxene) and eventually, in the most evolved phases, the crystallization of plagioclase with lesser alkali feldspar and minor amphibole. Tafresh rocks define a typical calcalkaline series generated from a subduction-modified mantle wedge, characterized by the classical LILE-enriched and HFSE-depleted compositions. The basaltic andesite magmas do not represent primitive compositions, but are likely derived from an unsampled hydrous primitive melt equilibrated in a spinel-bearing metasomatized peridotite source, evolving at shallow to moderate crustal depths. Additional lithotypes cropping out in the Tafresh area include much rarer strongly evolved leucocratic rocks and evolved rocks with adakitic signature. The first are thought to derive from crustal anatexis of a meta-sedimentary source, whereas the latter are interpreted as the product of the melting of a meta-mafic source rock with residual garnet and amphibole. The association of magmatic rocks pointing to all such different petrogenetic processes in a relatively limited area is strongly suggestive of emplacement in a post-collisional stage.

Differently, Nowbaran Quaternary volcanic district revealed peculiar compositions as feldspars and melilite are totally absent whereas clinopyroxene and olivine, plus nepheline and sodalite-hauyne-group feldspathoid confined in the groundmass are quite abundant and allowed the classification of these rocks as melanephelinites. Extremely low SiO_2 (~35.4-41.4 wt%) is coupled with very high CaO (~13.1-18.3 wt%) and low Al_2O_3 (~8.6-11.6 wt%), leading to ultracalcic compositions (i.e., CaO/Al_2O_3 >1). Other less peculiar, but still noteworthy, characteristics of Nowbaran magmas are the high MgO (8.7-13.3 wt%) and Mg# (0.69-0.74), coupled with a variable alkali content

(Na_2O = 1.8-5.4 wt%; K_2O = 0.2-2.3 wt%) and variably high LOI (1.9-10.4 wt%). Isotopic ratios ($^{87}Sr/^{86}Sr$ = 0.7052-0.7056; $^{143}Nd/^{144}Nd$ = 0.51263-0.51266; $^{206}Pb/^{204}Pb$ = 15.54-18.66; $^{207}Pb/^{204}Pb$ = 15.66-15.68; $^{208}Pb/^{204}Pb$ = 38.66-38.79) show small variations and plot within the literature field for the Cenozoic volcanic rocks of western Iran. Primitive mantle-normalized patterns are intermediate between typical subduction-related melts and HIMU-OIB magmas, emphasizing a hybrid source. The origin of the peculiar composition of Nowbaran magmas cannot be related to partial melting of C-H-free peridotitic mantle, nor to digestion of limestones and marls by "normal" basaltic melts. Rather, we favour the hypothesis of an origin from carbonated hornblendite-rich metasomes. These mantle volumes are considered as the products of interaction between peridotitic matrix and partial melts derived from arc cumulates. These cumulates would originate as consequence of fractional crystallization of hydrous and CO_2-bearing magmas generated during previous subduction-related arc magmatism, before continent-continent collision. Mixing of melts derived from such subduction-modified mantle sources with liquids devoid of any subduction imprint, passively upwelling from slab break-off tears would generate the peculiar compositions recorded in Nowbaran volcanic district.

Volcanism in Bijar-Qorveh area occurred through two main events during Tertiary period, i.e. Miocene calcalkaline magmatism followed by Quaternary alkaline products. Miocene volcanic manifestations are here represented by Dehgolan and Qorveh districts, with high-K andesites and trachytes and minor rhyolitic terms, whereas trachybasalts and tephrites (with lesser alkali basalts) outcropping in Qezelke Kand, Bijar and Takab sites belong to the Quaternary alkaline magmatic event. Dehgolan and Qorveh rocks are characterized by high-K compositions and likely represent the post-collisional magmatic events of Central Iran. Major and trace elements entirely fall within the literature data and suggest a single liquid line of descent characterized first by fractionation of olivine and clinopyroxene, followed by removal of plagioclase and amphibole. Primitive-mantle normalized diagrams totally resemble subduction-related features, showing LILE-LREE enrichments and Nb-Ta negative anomalies. Only three samples from Dehgolan exhibit unusual K_2O-TiO_2-P_2O_5 enrichments, along with high Rb concentrations, likely being indicative of a Ti-phlogopite-rich melting source. With regards to alkaline compositions, they show high Mg# values, certainly suggesting that

primary magma was not affected by extensive fractionation. Moreover, in terms of major and trace elements, alkaline rocks exhibit mixed features of subduction-related magmas and HiMU-OIB characteristics which probably are indicative of hybrid sources. Takab samples always cluster distinctly, showing high K_2O and Rb contents which could be related to phlogopite-rich source rock. Noteworthy, in Qezelke Kand district, silica-poor rocks occur along with silica-rich compositions. More specifically, anomalous chemical compositions have been here referred to as adakites as they show high La/Yb and Sr/Y ratios, with low Yb and HFSE contents. Adakites still remains a controversial term, but these rocks are thought to be probably originated by melting of subducting oceanic slabs or lower continental crust, with amphibole and/or garnet as residual phases, making all such different petrogenetic processes in a relatively limited area strongly suggestive of emplacement in a post-collisional stage.

REFERENCES

Adam, J., 1993. Proton microprobe determined partitioning of Rb, Sr, Ba, Y, Zr, Nb and Ta between experimentally produced amphiboles and silicate melts with variable F content. Chem. Geol. 109, 29-49.

Adam, J., Green, T., 2006. Trace element partitioning between mica- and amphibole-bearing garnet lherzolite and hydrous basanitic melt: 1. Experimental results and the investigation of controls on partitioning behaviour. Contrib. Mineral. Petrol. 152, 1-17.

Agard, P., Monié, P., Gerber, W., Omrani, J., Molinaro, M., Meyer, B., Labrousse, L., Vrielynck, B., Jolivet, L., Yamato, P., 2006. Transient, synobduction exhumation of Zagros blueschists inferred from P-T, deformation, time, and kinematic constraints: Implications for Neotethyan wedge dynamics. J. Geophys. Res. 111, B11401, doi:10.1029/2005JB004103.

Agard, P., Omrani, J., Jolivet, L., Mouthereau, F., 2005. Convergence history across Zagros (Iran): constraints from collisional and earlier deformation. Int. J. Earth Sci. 94, 401-419.

Agard, P., Omrani, J., Jolivet, L., Whitechurch, H., Vrielynck, B., Spakman, W., Monié, P., Meyer, B., Wortel, R., 2011. Zagros orogeny: a subduction-dominated process. Geol. Mag. 148, 692-725.

Ahmadzadeh, G., Jahangiri, A., Lentz, D., Mojtahedi, M., 2010. Petrogenesis of Plio-Quaternary post-collisional ultrapotassic volcanism in NW of Marand, NW Iran. J. Asian Earth Sci. 39, 37-50.

Alaie Mahabadi, S. Fodazi, M., 2002. Geological map of the Razan, Scale 1/100,000. Geol. Surv. Iran.

Alavi, M., 1980. Tectonostratigraphic evolution of the Zagrosides of Iran. Geology 8, 144-149.

Alavi, M., 1994. Tectonics of the Zagros orogenic belt of Iran: new data and interpretations. Tectonophysics 229, 211-238.

Alberti, A.A., Comin-Chiaramonti, P., Sinigoi, S., 1980. Neogene and Quaternary volcanism in Eastern Azerbaijan (Iran): some K-Ar age determinarions and geodynamic implications. Int. J. Earth Sci. 69, 1, 216-225.

Alirezaei, A., Arvin, M., Dargahi, S., 2017. Adakite-like signature of porphyry granitoid stocks in the Meiduk and Parkam porphyry copper deposits, NE of Shahr-e-Babak, Kerman, Iran: constrains on geochemistry. Ore Geol. Rev. 88, 370-83.

Allen, M.B., Kheirkhah, M., Neill, I., Emami, M.H., Mcleod, C.L., 2013. Generation of arc and within-plate chemical signatures in collision zone magmatism: Quaternary lavas from Kurdistan Province, Iran. J. Petrol. 54, 887-911.

Amundsen, H.E.F., 1987. Evidence for liquid immiscibility in the upper mantle. Nature 327, 692-695.

Arculus, R. J., 2003. Use and abuse of the terms calcalkaline and calcalkalic. J. Petrol. 44, 929-935.

Arvin, M., Pan, Y., Dargahi, S., Malekizadeh, A., Babaei, A., 2007. Petrochemistry of the Siah-Kuh granitoid stock southwest of Kerman, Iran: Implications for initiation of Neotethys subduction, J. Asian Earth Sci. 30, 474-489.

Asiabanha, A., Foden, J., 2012. Post-collisional transition from an extensional volcano-sedimentary basin to a continental arc in the Alborz Ranges, N-Iran. Lithos 148, 98-111.

Avanzinelli, R., Lustrino, M., Mattei, M., Melluso, L., Conticelli, S., 2009. Potassic and ultrapotassic magmatism in the circum-Tyrrhenian region: Significance of carbonated pelitic vs. pelitic sediment recycling at destructive plate margins. Lithos 113, 213–227.

Azizi, H., Asahara, Y., Tsuboi, M., Takemura, K., Razyani, S., 2014. The role of heterogenetic mantle in the genesis of adakites northeast of Sanandaj, northwestern Iran. Chem. Erde 74, 87-97.

Azizi, H., Jahangiri, A., 2008. Cretaceous subduction-related volcanism in the northern Sanandaj-Sirjan Zone, Iran. J. Geodyn. 45, 178-190.

Azizi, H., Stern, R.J., Topuz, G., Asahara, Y., Shafaii Moghadam, H., 2019. Late Paleocene adakitic granitoid from NW Iran and comparison with adakites in the NE Turkey: adakitic melt generation in normal continental crust. Lithos 346-347, 105-151.

Azizi H., Tanaka, T., Asahara, Y., Chung, S.L., Zarrinkoub, M.H., 2011. Discrimination of the age and tectonic setting for magmatic rocks along the Zagros thrust zone, northwest Iran, using the zircon U-Pb age and Sr-Nd isotopes. J. Geodyn. 52, 304-320.1

Babaahmadi, A., Safaei, H., Yassaghi, A., Vafa, H., Naeimi, A., Madanipour, S., Ahmadi, M., 2010. A study of Quaternary structures in the Qom region, West Central Iran. J. Geodyn. 50, 355-367.

Bagheri, S., Stampfli, G.M., 2008. The Anarak, Jandaq and Posht-e-Badam metamorphic complexes in central Iran: new geological data, relationships and tectonic implications. Tectonophysics 451, 123-155.

Baker, M.B., Wyllie, P.L., 1990. Liquid immiscibility in a nepheline-carbonate system at 25 kbar and implications for carbonatite origin. Nature 346, 168-170.

Bellver-Baca, M.T., Chiaradia, M., Beate, B., Beguelin, P., Deriaz, B., Mendez-Chazarra, N., Villagómez, D., 2020. Geochemical evolution of the Quaternary Chachimbiro Volcanic Complex (frontal volcanic arc of Ecuador). Lithos 356-357, 105237.

Berberian, M., King, G.C.P., 1981. Towards a paleogeography and tectonic evolution of Iran. Can. J. Earth Sci. 18, 210-265.

Boccaletti, M., Innocenti, F., Manetti, P., Mazzuoli, R., Motamed, A., Pasquare, G., Radicati di Brozolo, F., Sobhani, E.A., 1977. Neogene and quaternary volcanism of the Bijar Area (Western Iran). Bull. Volcanol. 40, 121-132.

Borrero, C.A., Castillo, H., 2006. Vulcanitas del S-SE de Colombia: retro-arco alcalino y su posible relacion con una ventana astenosferico. Bol. Geol. 28, 23-34.

Brenan, J.M., Shaw, H.F., Ryerson, F.J., Phinney, D.L., 1995. Experimental-Determination Trace-Element Partitioning between Pargasite and a Synthetic Hydrous Andesitic Melt. Earth Planet. Sci. Lett. 135, 1-11.

Breitfeld, H.T., Macpherson, C., Hall R., Thirlwall, M., Ottley, C.J., Hennig-Breitfeld, J., 2019. Adakites without a slab: remelting of hydrous basalt in the crust and shallow mantle of Borneo to produce the Miocene Sintang Suite and Bau Suite magmatism of West Sarawak. Lithos 344-345, 100-121.

Brey, G., Green, D.H., 1977. Systematic study of liquidus phase relations in olivine melilitite + H_2O + CO_2 at high pressures and petrogenesis of an olivine melilitite magma. Contrib. Mineral. Petrol. 61, 141-162.

Brooker, R.A., 1998. The effect of CO_2 saturation on immiscibility between silicate and carbonate liquids: an experimental study. J. Petrol. 39, 1905-1915.

Bultitude, R.J., Green, D.H., 1968. Experimental study at high pressures on the origin of olivine nephelinite and olivine melilite nephelinite magmas. Earth Planet. Sci. Lett. 3, 325-337.

Bultitude, R.J., Green, D.H., 1971. Experimental study of crystal-liquid relationships at high pressures in olivine nephelinite and basanite compositions. J. Petrol. 12, 121-147.

Burg, J.P., 2018. Geology of the onshore Makran accretionary wedge: synthesis and tectonic interpretation. Earth-Sci. Rev. 185, 1210-1231.

Carminati, E., Lustrino, M., Doglioni, C., 2012. Geodynamic evolution of the central and western Mediterranean: Tectonics vs. igneous petrology constraints. Tectonophysics 579, 173-192.

Castillo, P.R., 2012. Adakite petrogenesis. Lithos 134-135, 304-316.

Cavazza, W., Wezek, F.C., 2003. The Mediterranean region – a geological primer: Episodes, 26, 160-168.

Chaharlang, R., Ducea, M.N., Ghalamghash, J., 2020. Geochemical evidences for quantifying crustal thickness over time in the Urumieh-Dokhtar magmatic arc (Iran). Lithos 374-375, 105723.

Chappell, B.W., 1999. Aluminium saturation in I- and S-type granites and the characterization of fractionated haplogranites. Lithos 46, 535-551.

Chappell, B.W., Bryant, C.J., Wyborn, D., 2012. Peraluminous I-type granites. Lithos 153, 142-153.

Chappell, B.W., White, J.R., 2001. Two contrasting granite types: 25 years later. Aust. J. Earth Sci. 48, 489-499.

Chebotarev, D.A., Veksler, I.V., Wohlgemuth-Ueberwasser, C., Doroshkevich, A.G., Koch-Müller, M., 2019. Experimental study of trace element distribution between calcite, fluorite and carbonatitic melt in the system CaCO3 + CaF2 + Na2CO3 ± Ca3(PO4)2 at 100 MPa. Contrib. Mineral Petrol 174, 4.

Chiu, H.Y., Chung, S.L., Zarrinkoub, M.H., Mohammadi, S.S., Khatib, M.M., Iizuka, Y., 2013. Zircon U-Pb age constraints from Iran on the magmatic evolution related to Neotethyan subduction and Zagros orogeny. Lithos 162-163, 70-87.

Clague, D.A., Frey, F.A., Garcia, M.O., Huang, S., McWilliams, M., Beeson, M.H., 2016. Compositional heterogeneity of the Sugarloaf melilite nephelinite flow, Honolulu volcanics, Hawai'i. Geochim. Cosmochim. Acta 185, 251-277.

Chung, S.L., Liu, D., Ji, J., Chu, M.F., Lee, H.Y., Wen, D.J., Lo, C.H., Lee T.Y., Qian, Q., Zhang, Q., 2003. Adakites from continental collision zones: Melting of thickened lower crust beneath southern Tibet. Geology 31, 1021-1024.

Clemens, J.D., Stevens, G., 2012. What controls chemical variation in granitic magmas? Lithos 134-135, 317-329.

Clemens, J.D., Stevens, G., Farina, F., 2011. The enigmatic source of I-type granites: the peritectic connection. Lithos 126, 174-181.

Couzinié, S., Laurent, O., Moyen, J.F., Zeh, A., Bouilhol, P., Villaros, A., 2016. Post-collisional magmatism: crustal growth not identified by zircon Hf-O isotopes. Earth Planet. Sci. Lett. 456, 182-195.

Dalton, J.A., Presnall, D.C., 1998b. The continuum of primary carbonatitic-kimberlitic melt compositions in equilibrium with lherzolite: Data from the system CaO-MgO-Al_2O_3-SiO_2-CO_2 at 6 GPa. J. Petrol. 39, 1953-1964.

Dalton, J.A., Wood, B.J., 1993. The partitioning of Fe and Mg between olivine and carbonate and the stability of carbonate under mantle conditions. Contrib. Mineral. Petrol. 114, 501-509.

Danyuschevsky, L.V., Plechov, P., 2011. Petrolog3: integrated software for modeling crystallization processes. Geochem. Geophys. Geosyst. 12, https://doi.org/10.1029/2011GC003516.

Dasgupta, R., Hirschmann, M.M., Smith, N.D., 2007. Partial melting experiments on peridotite + CO2 at 3 GPa and genesis of alkalic ocean island basalts. J. Petrol. 48, 2093-2124.

Dasgupta, R., Hirschmann, M.M., Stalker, K., 2006. Immiscible transition from carbonate-rich to silicate-rich melts in the 3 GPa melting interval of eclogite plus CO_2 and genesis of silica-undersaturated ocean island lavas. J. Petrol. 47, 647-671.

Davidson, J., Hassanzadeh, J., Berzins, R., Stockli, D.F., Bashukooh, B., Turrin, B., Pandamouz, A., 2004. The geology of Damavand volcano, Alborz Mountains, northern Iran. Geol. Soc. Am. Bull. 116, 16-29.

Davoudzadeh, M., Schmidt, K., 1984. A review of the Mesozoic paleogeography and paleotectonic evolution of Iran. Neues Jb. Geol. Paläont. Abh. 168, 182-207.

Deevsalar, R., Shinjo, R., Ghaderi, M., Murata, M., Hoskin, P.W.O., Oshiro, S., Neill, I., 2017. Mesozoic-Cenozoic mafic magmatism in Sanandaj-Sirjan Zone, Zagros Orogen (Western Iran): geochemical and isotopic inferences from Middle Jurassic and Late Eocene gabbros. Lithos 284-285, 588-607.

Defant, M.J., Drummond, M.S., 1990. Derivation of some modern arc magmas by melting of young subducted lithosphere. Nature 347, 662-665.

Dewey, J.F., Pitman, W.C., Ryan, W.B.F., Bonnin, J., 1973. Plate tectonic and the evolution of the Alpine system. Geol. Soc. Am. Bull. 84, 3137-80.

Di Battistini, G., Montanini, A., Vernia, L., Venturelli, G., Tonarini, S., 2001. Petrology of melilite-bearing rocks from the Montefiascone Volcanic Complex (Roman Magmatic Province): new insights into the ultrapotassic volcanism of Central Italy. Lithos 59, 1-24.

Di Giuseppe, P., Agostini, S., Lustrino, M., Karaoğlu, O., Savaşçin, M.Y., Manetti, P., Ersoy, Y., 2017. Transition from compression to strike-slip tectonics revealed by Miocene-Pleistocene volcanism west of the Karliova Triple Junction (East Anatolia). J. Petrol. 58, 2055-2087.

Di Rocco, T., Freda, C., Gaeta, M., Mollo, S., Dallai, L., 2012. Magma Chambers Emplaced in Carbonate Substrate: Petrogenesis of Skarn and Cumulate Rocks and Implications for CO_2 Degassing in Volcanic Areas. J. Petrol. 53, 2307-2332.

Dilek, Y., Imamverdiyev, N., Altunkaynak, S., 2010. Geochemistry and tectonics of Cenozoic volcanism in the Lesser Caucasus (Azerbaijan) and the peri-Arabian region: collision-induced mantle dynamics and its magmatic fingerprint. Int. Geol. Rev. 52, 4-6, 536-578.

Downes, H., Balaganskaya, E., Beard, A., Liferovich, R., Demaiffe, D., 2005. Petrogenetic processes in the ultramafic, alkaline and carbonatitic magmatism in the Kola Alkaline Province: A review. Lithos 85, 48-75.

Drummond, M.S., Defant, M.J., 1990. A model for trondhjemite–tonalite–dacite genesis and crustal growth via slab melting: Archaean to modern comparisons. J. Geophys. Res. 95, 21503-21521.

Eggler, D.H., 1978. The effect of CO_2 upon partial melting of peridotite in the system Na_2O-CaO-Al_2O_3-MgO-SiO_2-CO_2 to 35 kb, with an analysis of melting in a peridotite-H_2O-CO_2 system. Am. J. Sci. 278, 305-343

Eggler, D.H., Holloway, J.R., 1977. Partial melting of peridotite in the presence of H_2O and CO_2: Principles and review. In: Dick, H.J.B (ed.), Magma Genesis: Oregon Dep. Geol. Mineral Ind. Bulletin, 96, 15.36.

Ellouz-Zimmermann, N., Lallemant, S.J., Castilla, R., Mouchot, N., Leturmy, P., Battani, A., Buret, C., Cherel, L., Desaubliaux, G., Deville, E., Ferrand, J., Lügcke, A., Mahieux, G., Mascle, G., Mühr, P., Pierson-Wickmann, A.C., Robion, P., Schmitz, J., Danish, M., Hasany, S., Shahzad, A., Tabreez, A., 2007. Offshore Frontal Part of the Makran Accretionary Prism: The Chamak Survey (Pakistan). In: Lacombe, O., Roure, F., Lavé, J., Vergés, J. (eds.) Thrust Belts and Foreland Basins. Front. Earth Sci.. doi.org/10.1007/978-3-540-69426-7_18.

Emami, M.H., 2000. Magmatism in Iran. Geological Survey of Iran, Tehran.

Emami, M.H., Sadeghi, M.M.M., Omrani, S.J., 1993. Magmatic map of Iran. Tehran: Geological Survey of Iran.

Erràzuriz-Henao, C., Gòmez-Tuena, A., Duque-Trujillo, J., Weber, M., 2019. The role of subducted sediments in the formation of intermediate mantle-derived magmas from the northern Colombian Andes. Lithos 336-337, 151-168.

Faccenna, C., Becker, T.W., Auer, L., Billi, A., Boschi, L., Brun, J.P., Capitanio, F.A., Funiciello, F., Horvath, F., Jolivet, L., 2014. Mantle dynamics in the Mediterranean. Rev. Geophys. 52, 283-332.

Falloon, T.J., Green, D.H., 1989. The solidus of carbonated, fertile peridotite. Earth Planet. Sc. Lett. 94, 364-370.

Farhoudi, G., 1978. A comparision of Zagros geology to island arcs. J. Geol. 86, 323-334.

Fazlnia, A., 2019. Origin and magmatic evolution of the Quaternary syn-collision alkali basalts and related rocks from Salmas, northwestern Iran. Lithos 344-345, 297-310.

Fedele, L., Seghedi, I., Chung, S.-L., Laiena, F., Lin, T.-H., Morra, V., Lustrino, M., 2016. Post-collisional magmatism in the Late Miocene Rodna-Bârgău district (East Carpathians, Romania): Geochemical constraints and petrogenetic models. Lithos 266-267, 367-382.

Foley, S.F., Pintér Z., 2018. Primary melt compositions in the Earth's mantle. In: Kono, Y. & Sanloup, C. (eds.) Magmas under pressure Elsevier, Amsterdam, 3-42.

Foley, S.F., Yaxley, G.M., Rosenthal, A., Buhre, S., Kiseeva, E.S., Rapp, R.P., Jacob, D.E., 2009. The composition of near-solidus melts of peridotite in the presence of CO_2 and H_2O between 40 and 60 kbar. Lithos 112, 274-283.

Forster, M.W., Prelevic, D., Buhre, S., Mertz-Kraus, R., Foley, S.F., 2019. An experimental study of the role of partial melts of sediments versus mantle melts in the sources of potassic magmatism. J. Asian Earth Sci. 177, 76-88.

Freestone, I.C., Hamilton, D.L., 1980. The role of liquid immiscibility in the genesis of carbonatites - An experimental study. Contrib. Mineral. Petrol. 73, 105-117.

Furman, T., Graham, D., 1999. Erosion of lithospheric mantle beneath the East African Rift system: geochemical evidence from the Kivu volcanic province. Lithos 48, 237-262.

Gervasoni, F., Klemme, S., Rohrbach, A., Grutzner, T., Berndt, J., 2017. Experimental constraints on mantle metasomatism caused by silicate and carbonate melts. Lithos 282-283, 173-186.

Ghorbani, M.R., Bezenjani, R.N., 2011. Slab partial melts from the metasomatizing agent to adakite, Tafresh Eocene volcanic rocks, Iran. Island Arc 20, 188-202.

Ghorbani, M.R., Graham, I.T., Ghaderi, M., 2014. Oligocene-Miocene godynamic evolution of the central part of the Urumieh-Dokhtar Arc of Iran. Int. Geol. Rev. 56, 8, 1039-1050.

Gozzi, F., Gaeta, M., Freda, C., Mollo, S., Di Rocco, T., Marra, F., Dallai, L., Pack, A., 2014. Primary magmatic calcite reveals origin from crustal carbonate. Lithos 190, 191-203.

Green, D.H., 1969. The origin of basaltic and nephelinitic magmas in the Earth's interior. Tectonophysics 7, 409-422.

Green, T.H., Adam, J., Site, S.H., 1993. Proton microprobe determinated trace element partition coefficients between pargasite, augite and silicate or carbonatitite melts. EOS, Trans. Am. Geophys. Un. 74, 340.

Green, D.H., Ringwood, A.E., 1967. The genesis of basaltic magmas. Contrib. Mineral. Petrol. 15, 103-190.

Grove, T.L., Holbin, E.S., Barr, J.A., Till, C.B., Krawczynski, J., 2013. Melts of garnet lherzolite: experiments, models and comparison to melts of pyroxenite and carbonated lherzolite. Contrib. Mineral. Petrol. 166, 887-910.

Guarino, V., Wu, F., Lustrino, M., Melluso, L., Brotzu, P., Gomes, C.B., Ruberti, E., Tassinari, C.C.G., Svisero, D.P., 2013. U-Pb ages, Sr-Nd- isotope geochemistry and petrogenesis of kimberlites, kamafugites and phlogopite-picrites of the Alto Paranaiba Igneous Province, Brazil. Chem. Geol. 353, 65-82.

Gudfinnsson, G.H., Presnall, D.C., 1996. Melting relations of model lherzolite in the system CaO-MgO-Al_2O_3-SiO_2 at 2.4-3.4 GPa and the generation of komatiites, J. Geophys. Res. 101, 701-27.

Gudfinnsson, G.H., Presnall, D.C., 2005. Continuous gradations among primary carbonatitic, kimberlitic, melilititic, basaltic, picritic, and komatiitic melts in equilibrium with garnet lherzolite at 3-8 GPa. J. Petrol. 46, 1645-1659.

Haase, K.M., Beier, C., Regelous, M., Rapprich, V., Renno, A., 2017. Spatial variability of source composition and petrogenesis in rift and rift flank alkaline lavas from the Eger Rift, Central Europe. Chem. Geol. 455, 304-314.

Hajian, J., 1970. Geological Map of the Farmahin. Geological Survey of Iran, Scale 1:100,000.

Hajian, J., 1977. Geological Map of the Tafresh Area: Tehran. Geological Survey of Iran, Scale 1:100,000.

Hajian, J., 2001. Geology of Tafresh: Tehran. Geological and Mineralogical Exploration Survey of Iran, report 82.

Hammouda, T., Keshav, S., 2015. Melting in the mantle in the presence of carbon: review of experiments and discussion on the origin of carbonatites. Chem. Geol. 418, 171-188.

Harmer, R.E., Gittins, J., 1998. The case for primary, mantle-derived carbonatite magma. J. Petrol. 39, 1895-1903.

Hart, S.R., 1984. A large-scale isotope anomaly in the southern hemisphere mantle. Nature 309, 753-757.

Hassanzadeh, J., Stockli, D.F., Horton, B.K., Axen, G.J., Stockli, L.D., Grove, M., Schmitt, A.K., Walker, J.D., 2008. U-Pb zircon geochronology of late Neoproterozoic-Early Cambrian granitoids in Iran: Implications for paleogeography, magmatism, and exhumation history of Iranian basement. Tectonophysics 451, 71-96.

Hassanzadeh, J., Wernicke, B.P., 2016. The Neotethyan Sanandaj-Sirjan zone of Iran as an archetype for passive margin-arc transitions. Tectonics 35, 586-621.

Hastie, A.R., Kerr, A.C., Pearce, J.A., Mitchell, S.F., 2007. Classification of altered volcanic island arc rocks using immobile trace elements: development of theTh-Co discrimination diagram. J. Petrol. 48, 2341-2357.

Hawkesworth, C.J., van Calsteren, P., Rogers, N.W., Menzies, M.A., 1987. Isotope variations in recent volcanics: a trace-element perspective. In: Menzies, M.H., Hawkesworth, C.J. (eds.) Mantle Metasomatism. NewYork Academic Press, 365-388.

Herzberg, C., Asimow, P.D., 2015. PRIMELT MEGA.XLSM software for primary magma calculation: peridotite primary magma MgO contents from the liquidus to the solidus. Geochem. Geophys. Geosyst. 16, 563-578.

Haghipour, A., Aghanabati, A. 1989. Geological map of Iran. Ministry of mine and metals- geological survey of Iran, second edition.

Hirose, K., 1997. Partial melt compositions of carbonated peridotite at 3 GPa and role of CO_2 in alkali-basalt magma generation. Geophys. Res. Lett. 24, 2837-2840.

Hirschmann, M. M. (2000). Mantle solidus: Experimental constraints and the effects of peridotite composition. Geochem. Geophys. Geosyst. 1, 2000GC000070, doi:10.1029/2000GC000070.

Hole, M.J., Natland, J.H., 2020. Magmatism in the North Atlantic Igneous Province; mantle temperatures, rifting and geodynamics. Earth-Sci. Rev. 206, 102794.

Honarmand, M., Omran, N.R., Neubauer, F., Emami, M.H., Nabatian, G., Liu, X., Dong, Y., von Quadt, A., Chen, B., 2014. Laser-ICP-MS U-Pb zircon ages and geochemical and Sr-Nd-Pb isotopic compositions of the Niyasar plutonic complex, Iran: constraints on petrogenesis and tectonic evolution. Int. Geol. Rev. 56, 1, 104-132.

Hora, J.M., Kronz, A., Moller-McNett, S., Worner, G., 2013. An Excel-based tool for evaluating and visualizing geothermobarometry data. Comp. Geosci. 56, 178-185.

Horton, B.K., Hassanzadeh, J., Stockli, D.F., Axen, G.J., Gillis, R.J., Guest, B., Amini, A., Fakhari, M.D., Zamanzadeh, S.M., Grove, M., 2008. Detrital zircon provenance of Neoproterozoic to Cenozoic deposits in Iran: implications for chronostratigraphy and collisional tectonics. Tectonophysics 451, 97-122.

Howe, T.M., Lindsay, J.M., Shane, P., -2015. Evolution of young andesitic-dacitic systems beneath Dominica, Lesser Antilles. J. Volcanol. Geotherm. Res. 297, 69-88.

Ionov, D.A., Griffin, W.L., O'Reilly, S.Y.O., 1997. Volatile-bearing minerals and lithosphere trace elements upper mantle. Chem. Geol. 141, 153-184.

Irvine, T.N. and Baragar, W.R.A., 1971. A guide to the chemical classification of the common volcanic rocks. Can. J. Earth Sci., 8,523.

Jagoutz, O., Klein, B., 2018. On the importance of crystallization-differentiation for the generation of SiO_2-rich melts and the compositional build-up of arc (and continental) crust. Am. J. Sci. 318, 29-63.

Jahangiri, A., 2007. Post-collisional Miocene adakitic volcanism in NW Iran: Geochemical and geodynamic implications. J. Asian Earth Sci. 30, 433-447.

Jones, A.P., Genge, M., Carmody, L., 2013. Carbonate melts and carbonatites. Rev. Mineral. Geochem. 75, 289-322.

Kamei, A., Miyake, Y., Owada, M., Kimura, J., 2009. A pseudo adakite derived from partial melting of tonalitic to granodioritic crust, Kyushu, southwest Japan arc. Lithos 112, 615-625.

Karaoğlu, O., Gulmez, F., Goçmengil, G., Lustrino, M., Di Giuseppe, P., Manetti, P., Savasçin, M.Y., Agostini, S., 2020. Petrological evolution of Karliova-Varto volcanism (Eastern Turkey): magma genesis in a transtensional triple-junction tectonic setting. Lithos, 364-365, 105524.

Karasözen, E., Nissen, E., Bergman, E.A., Ghods, A., 2019. Seismotectonics of the Zagros (Iran) from orogen-wide, calibrated earthquake relocations. J. Geophys. Res. Solid Earth 124, 9109-9129.

Kawabata, H., Hanyu, T., Chang, Q., Kimura, J.-I., Nichols, A.R.L., Tatsumi, Y., 2011. The petrology and geochemistry of St. Helena alkali basalts: evaluation of the oceanic crust-recycling model for HIMU OIB. J. Petrol. 52, 791-838.

Keshav, K., Gudfinnsson, G.H., 2010, Experimentally dictated stability of carbonated oceanic crust to moderately great depths in the Earth: Results from the solidus determination in the system CaO-MgO-Al_2O_3-SiO_2-CO_2. J. Geophys. Rev. 115, B05205, doi:10.1029/2009JB006457.

Keshav, S., Gudfinnsson, G.H., 2013. Silicate liquid-carbonatitic liquid transition along the melting curve of model, vapor-saturated peridotite in the system CaO-MgO-Al_2O_3-SiO_2-CO_2 from 1.1 to 2 GPa. J. Geophys. Res. 118, 3341-3353.

Khademi, F., Asiabanha, A., Foden, J., Davoodi, Z., 2019. Extensional magmatism in a continental collision zone, Tafresh area, western central Iran: structural, geochemical and mineralogical considerations. Period. Di Mineral. 88, 1-18.

Khalatbari Jafari, M., Alaie Mahabadi, S., 1998. Geological map of the Nobaran Quadrangle, Scale 1/100,000. Geol. Surv. Iran.

Kheirkhah, M., Allen, M.B., Emami, M., 2009. Quaternary syn-collision magmatism from the Iran/Turkey borderlands. J. Volcanol. Geotherm. Res. 182, 1-12.

Kheirkhah, M., Neill, I., Allen, M.B., Ajdari, K., 2013. Small-volume melts of lithospheric mantle during continental collision: late Cenozoic lavas of Mahabad, NW Iran. J. Asian Earth Sci. 74, 37-49.

Kheirkhah, M., Neill, I., Allen, M.B., Emami, M.H., Shahraki Ghadimi A., 2020. Distinct sources for high-K and adakitic magmatism in SE Iran. J. Asian Earth Sci. 196, 104355.

Khodami, M., Noghreyan, M., Davoudian, A.R., 2009. Pliocene-Quaternary adakite volcanism in the Isfahan area, Central Iranian magmatic belt. Neues Jahrb. für Mineral. Abhandlungen 186, 235-248.

King, A.J., Philips, K.J.H., Vita-Finzi, C., Russell, S.S., 2020. Terrestrial modification of the Ivuna meteorite and a reassessment of the chemical composition of the CI type specimen. Geochim. Cosmochim. Acta 268, 73-89.

Kjarsgaard, B.A., Hamilton, D.L., 1989. The genesis of carbonatites by liquid immiscibility. In: Bell, K. (ed.) Carbonatites: Genesis and Evolution Unwin Hyman, London, 388-404.

Klemme, S., O'Neill, H.S., 2000. The near-solidus transition from garnet lherzolite to spinel lherzolite. Contrib. Mineral. Petrol. 138, 237-248.

Kogarko, L.N., Veselovskiy, R.V., 2019. Geodynamic origin of carbonatites from the absolute paleotectonic reconstructions. J. Geodyn. 125, 13-21.

Koshnaw, R.I., Stockli, D.F., Schlunegger, F., 2018. Timing of the Arabia-Eurasia continental collision - evidence from detrital zircon U-Pb geochronology of the Red Bed Series strata of the northwest Zagros hinterland, Kurdistan region of Iraq. Geology 47, 47-50.

Kouhestani, H., Ghaderi, M., Emami, M.H., Meffre, S., Kamenetsky, V., McPhie, J., Zaw, K., Bezenjani, R.N.,2017. Compositional characteristics and geodynamic significance of late Miocene volcanic rocks associated with the Chah Zard epithermal gold–silver deposit, southwest Yazd, Iran. Island Arc, 27, Issue 1.

Kroonenberg, S.B., Pichler, H., Diederix, H., 1982. Cenozoic alkalibasaltic to ultrabasic volcanism in the uppermost Magdalena Valley, Southern Huila Department, Colombia. Geol. Norand., 5, 19-26.

Kroonenberg, S.B., Pichler, H., Schmitt-Riegraf, C., 1987. Young alkalibasaltic to nephenlinitic volcanism in the Southern Colombian Andes – origin by subduction of a spreading rift? Zbl. Geol. Palaont. Teil. 7/8, 919-936.

Kushiro, I., 1969. Discussion of the paper "The origin of basaltic and nephelinitic magmas in the Earth's interior" by D.H. Green. Tectonophysics 7, 427-436.

LaTourette, T., Hervig, R.L., Holloway, J.R., 1995. trace element partitioning between amphibole, phlogopite, and basanite melt. Earth Planet. Sci. Lett. 135, 13-30.

Le Bas, M.J., 1989. Nephelinitic and basanitic rocks. J. Petrol. 30, 1299-1312.

Le Bas, M.J., 2000. IUGS reclassification of the high-Mg and picritic volcanic rocks. J. Petrol. 41, 1467-1470.

Le Maitre, R.W. (Ed.), 2002. Igneous Rocks: A Classification and Glossary of Terms. Recommendations of the International Union of Geological Sciences Subcommission on the Systematics of Igneous Rocks. Cambridge University Press, Cambridge, UK, pp. 256.

Lee, C.T.A., Luffi, P., Plank, T., Dalton, H., Leeman, W.P., 2009. Constraints on the depths and temperatures of basaltic magma generation on Earth and other terrestrial

planets using new thermobarometers for mafic magmas. Earth Planet. Sci. Lett.279, 20-33.

Lee, W.J., Wyllie, P.J., 1994. Experimental data bearing on liquid immiscibility, crystal fractionation, and the origin of calciocarbonatites and natrocarbonatites. Int. Geol. Rev. 36, 797-819.

Lee, W., Wyllie, P.J., 1997. Liquid immiscibility between nephelinite and carbonatite from 1.0 to 2.5 GPa compared with mantle melt compositions. Contrib. Mineral. Petrol. 127, 1-16.

Leterrier, J., 1985. Mineralogical, geochemical and isotopic evolution of two Miocene mafic intrusions from the Zagros (Iran). Lithos 18, 311-329.

Liu, H., Leng, W., 2020. Plume-Tree Structure Induced by Low-Viscosity Layers in the Upper Mantle. Geophys. Res. Lett 47, e2019GL086508, doi.org/ 10.1029/2019GL086508.

Liu, J., Xie, C., Li, C., Fan, J., Wang, M., Wang, W., Yu, Y., Dong, Y., Hao, Y., 2019. Origins and tectonic implications of Late Cretaceous adakite and primitive high-Mg andesite in the Songdo area, southern Lhasa subterrane, Tibet. Gondwana Res. 76,185-203.

Lyubetskaya, T., Korenaga, J., 2007. Chemical composition of Earth's primitive mantle and its variance: 1. Methods and results. J. Geophys. Res. 112, B03211, doi:10.1029/2005JB004223.

Lobach-Zhuchenko, S.B., Rollinson, H., Chekulaev, V.P., Savatenkov, V.M., Kovalenko, A.V., Martin, H., Guseva, N.S., Arestova, N.A., 2008. Petrology of a Late Archaean, Highly Potassic, Sanukitoid Pluton from the Baltic Shield: Insights into Late Archaean Mantle Metasomatism. J. Petrol. 49, 393-420.

Lustrino, M., Anderson, D.L., 2015. The mantle isotopic printer: Basic mantle plume geochemistry for seismologists and geodynamicists. In Foulger, G.R., Lustrino, M., King, S.D. (eds.): The Interdisciplinary Earth: A Volume in Honor of Don L. Anderson, Geol. Soc. Am. Spec. Paper 514 and Am. Geophys. Un. Spec. Publ. 71, 257–279, doi:10.1130/2015.2514(16).

Lustrino, M., Agostini, S., Chalal, Y., Fedele, L., Stagno, V., Colombi, F., Bouguerra, A., 2016. Exotic lamproites or natural ultrapotassic rocks? The late Miocene volcanic rocks from Kef Hahouner, NE Algeria, in the frame of the circum-Mediterranean lamproites. J. Volcanol. Geotherm. Res. 327, 539-553.

Lustrino, M., Keskin, M., Mattioli, M., Lebedev, V.A., Chugaev, A., Sharkov, E., Kavak, O., 2010. Early activity of the largest Cenozoic shield volcano in the circum-Mediterranean area: Mt. Karacadağ, SE Turkey. Eur. J. Mineral. 22, 343-362.

Lustrino, M., Fedele, L., Agostini, S., Prelević, D., Salari, G., 2019a. Leucitites within and around the Mediterranean area. Lithos 324-325, 216-233. doi:10.1016/j.lithos.2018.11.007

Lustrino, M., Luciani, N., Stagno, V., 2019b. Fuzzy petrology in the origin of carbonatitic/pseudocarbonatitic Ca-rich ultrabasic magma at Polino (central Italy). Sci. Rep. 9, 9212. doi:10.1038/s41598-019-45471-x.

Lustrino, M., Ronca, S., Caracausi, A., Ventura Bordenca, C., Agostini, S., Faraone, D.B., 2020. Strongly SiO_2-undersaturated, CaO-rich kamafugitic Pleistocene magmatism in central Italy (San Venanzo volcanic complex) and the role of shallow depth limestone assimilation. Earth-Sci. Rev. 208, 103256.

Lustrino, M., Wilson, M., 2007. The Circum-Mediterranean anorogenic Cenozoic igneous province. Earth Sci. Rev. 81, 1-65.

Ma, Q., Zheng, J., Griffin, W.L., Zhang, M., Tang, H., Su, Y., Ping, X., 2012. Triassic “adakitic” rocks in an extensional setting (North China): Melts from the cratonic lower crust. Lithos 149, 159-173.

Maanijou, M., Aliani, F., Miri, M., Lentz, D.R., 2013. Geochemistry and petrology of igneous assemblage in the south of Qorveh area, west Iran. Chem. Erde 73, 181-196.

Macpherson, C.G., Dreher, S.T., Thirlwall, M.F., 2006. Adakites without slab melting: High pressure differentiation of island arc magma, Mindanao, the Philippines. Earth Planet. Sci. Lett. 243, 581-593.

Mahmoudi, S., Corfu, F., Masoudi, F., Mehrabi, B., Mohajjel, M., 2011. U-Pb dating and emplacement history of granitoid plutons in the northern Sanandaj-Sirjan Zone, Iran. J. Asian Earth Sci. 41, 238-249.

Martin, H., 1986. Effect of steeper Archean geothermal gradient on geochemistry of subduction zone magmas. Geology 14,753-756.

Martin, L.H.J., Schmidt, M.W., Mattsson, H.B., Guenther, D., 2013. Element partitioning between immiscible carbonatite and silicate melts for dry and H_2O-bearing systems at 1-3 GPa. J. Petrol. 54, 2301-2338.

Martin, H., Smithies, R.H., Rapp, R., Moyen, J.-F., Champion, D., 2005. An overview of adakite, tonalite-trondhjemite-granodiorite (TTG), and sanukitoid: relationships and some implications for crustal evolution. Lithos 79, 1-24.

Masotta, M., Mollo, S., Freda, C., Gaeta, M., Moore, G., 2013. Clinopyroxene-liquid thermometers and barometers specific to alkaline differentiated magmas. Contrib. Mineral. Petrol. 166, 1545-1561.

Masson, F.D.R., Anvari, M., Djamour, Y., Walpersdorf, A., Tavakoli, F., Daignières, M., Nankali, H., Van Gorp, S.B., 2007. Large-scale velocity field and strain tensor in Iran inferred from GPS measurements: new insight for the present-day deformation pattern within NE Iran. Geophys. J. Int. 170, 436-40.

Mazhari, S.A., Bea, F., Amini, S., Ghalamghash, J., Molina, J.F., Montero, P., Scarrow, J.H., Williams, I.S., 2009. The Eocene bimodal Piranshahr massif of the Sanandaj-Sirjan Zone, NW Iran: A marker of the end of the collision in the Zagros orogen. J. Geol. Soc. Lond. 166, 53-69.

Mazzeo, F.C., Rocco, I., Tucker, R.D., Morra, V., D'Antonio, M., Melluso, L., 2020. Olivine melilitites, mantle xenoliths, and xenocrysts of the Takarindiona District: petrogenesis, magmatic evolution, and the sub-continental lithospheric mantle of East-Central Madagascar. J. Afr. Earth Sci. 174, 104059.

Matsui, Y., Onuma, N., Nagasawa, H., Higuchi, H., Banno, S., 1977. Crystal structure control in trace element partitioning between crystal and magma. Bull. Soc. Fr. Minéral. Crist. 100, 315-324.

McQuarrie, N., van Hinsbergen, D.J., 2013. Retrodeforming the Arabia-Eurasia collision zone: age of collision versus magnitude of continental subduction. J. Geol. 41, 315-318.

Medard, E., Schmidt, M.W., Schiano, P., Ottolini, L., 2006. Melting of Amphibole-bearing Wehrlites: an experimental study on the origin of ultra-calcic nepheline-normative melts. J. Petrol. 47, 481-504.

Mehdipour Ghazi, J., Moazzen, M., 2015. Geodynamic evolution of the Sanandaj-Sirjan Zone, Zagros Orogen, Iran. Turk. J. Earth Sci. 24, 513-528.

Melekhova, E., Blundy, J., Robertson, R., Humphreys, M.C.S., 2015. Experimental evidence for polybaric differentiation of primitive arc basalt beneath St. Vincent, Lesser Antilles. J. Petrol. 56, 161-192.

Melluso, L., Conticelli, S., de' Gennaro, R., 2010. Kirschsteinite in the Capo di Bove melilite leucitite lava (cecilite), Alban Hills, Italy. Mineral. Mag., 74, 887-902.

Middlemost, E.A.K., 1975. The Basalt Clan. Earth Sci. Rev. 11, 337-564.

Milholland, C.S., Presnall, D.C., 1998. Liquidus phase relations in the system CaO-MgO-Al_2O_3-SiO_2 at 3.0 GPa: The aluminous pyroxene thermal divide and high-pressure fractionation of picritic and komatiitic magmas. J. Petrol. 39, 3-27.

Mitchell, R.H., 2005. Carbonatites and carbonatites and carbonatites. Can. Mineral. 43, 2049-2068.

Mitchell, R.H., Welch, M.D., Chakhmouradian, A.R., 2017. Nomenclature of the perovskite supergroup: a hierarchical system of classification based on crystal structure and composition. Mineral. Mag. 81, 411-461.

Miyashiro, A., 1974. Volcanic rock series in island arcs and active continental margins. Am. J. Sci. 274, 321-355.

Mohajjel, M., Fergusson, C.L., Sahandi, M.R., 2003. Cretaceous–Tertiary convergence and continental collision, Sanandaj–Sirjan Zone, western Iran. J. Asian Earth Sci. 21, 397-412.

Mohajjel, M., Fergusson, C.L., 2000. Dextral transpression in Late Cretaceous continental collision, Sanandaj–Sirjan Zone, western Iran. J. Struct. Geol. 22, 1125-1139.

Molinaro, M., Leturmy, P., Guezou, J.C., Frizon de Lamotte, D., Eshraghi, S.A., 2005. The structure and kinematics of the southeastern Zagros fold–thrust belt, Iran: from thin-skinned to thick-skinned tectonics. Tectonics 24, doi:10.1029/2004TC001633.

Mollo, S., Hammer, J.E., 2017. Dynamic crystallization in magmas. EMU Notes Mineral. 16, 373-418.

Mouthereau, F., Lacombe, O., Meyer, B., 2006. The Zagros folded belt (Fars, Iran): constraints from topography and critical wedge modelling. Geophys. J. Int. 165, 336-356.

Mouthereau, F., Lacombe, O., Vergés, J., 2012. Building the Zagros collisional orogen: Timing, strain distribution and the dynamics of Arabia/Eurasia plate convergence. Tectonophysics 532-535, 27-60.

Moyen, J.F., 2009. High Sr/Y and La/Yb ratios: the meaning of the “adakitic signature”. Lithos 112, 556-574.

Nabyl, Z., Massuyeau, M., Gaillard, F., Tuduri, J., Iacono-Marziano, G., Rogerie, G., Le Trong, E., Di Carlo, I., Melleton, J., Bailly, L., 2020. A window in the course of alkaline

magma differentiation conductive to immiscible REE-rich carbonatites. Geochim. Cosmochim. Acta 282, 297-323.

Nandedkar, R.H., Hürlimann, N., Ulmer, P., Müntener, O., 2016. Amphibole-melt trace element partitioning of fractionating calcalkaline magmas in the lower crust: an experimental study. Contrib. to Mineral. Petrol. 171, 71,

Neill, I., Meliksetian, K., Allen, M.B., Navasardyan, G., Kuiper, K., 2015. Petrogenesis of mafic collision zone magmatism: the Armenian sector of the Turkish-Iranian Plateau. Chem. Geol. 403, 24-41.

Novella, D., Keshav, S., Gudfinnsson, G.H., Ghosh, S., 2014. Melting phase relations of model carbonated peridotite from 2 to 3 GPa in the system CaO-MgO-Al_2O_3-SiO_2-CO_2 and further indication of possible unmixing between carbonatite and silicate liquids. J. Geophys. Res. 119, 2780-2800.

O'Hara, M.J., 1968. Are ocean floor basalts primary magmas? Nature 220, 683-686.

Omrani, J., Agard, P., Whitechurch, H., Benoit. M., Prouteau, G., Jolivet, L., 2008. Arc-magmatism and subduction history beneath the Zagros Mountains, Iran: a new report of adakites and geodynamic consequences. Lithos 106, 380-398.

Özdemir, Y., Mercan, C, Oyan, V., Özdemir, A.A., 2019. Composition, pressure, and temperature of the mantle source region of quaternary nepheline-basanitic lavas in Bitlis Massif, Eastern Anatolia. Lithos 328-329, 115-129.

Palin, R.M., White, R.W., Green, E.C.R., 2016. Partial melting of metabasic rocks and the generation of tonalitic-trondhjemitic-granodioritic (TTG) crust in the Archaean: Constraints from phase equilibrium modelling. Precambrian Res. 287, 73-90.

Pang, K.N., Chung, S.L., Zarrinkoub, M.H., Chiu, H.X., Li, X.H., 2014. On the magmatic record of the Makran arc, southeastern Iran: Insights from zircon U-Pb geochronology and bulk-rock geochemistry. Geochem. Geophys. Geosyst. 15, 2151-2169.

Pang, K.N., Chung, S.L., Zarrinkoub, M.H., Khatib, M.M., Mohammadi, S.S., Chiu, H.Y., Chu, C.H., Lee, H.Y., Lo, C.H., 2013. Eocene-Oligocene post-collisional magmatism in the Lut-Sistan region, eastern Iran: magma genesis and tectonic implications. Lithos 180-181, 234-251.

Pang, K.N., Chung, S.L., Zarrinkoub, M.H., Li, X.H., Lee, H.Y., Lin, T.H., Chiu, H.Y., 2016. New age and geochemical constraints on the origin of Quaternary adakite-like lavas in the Arabia-Eurasia collision zone. Lithos 264, 348-359.

Pearce, J.A., 1983. Role of the sub-continental lithosphere in magma genesis at active continental margins. In: Hawkesworth, C.J., Norry, M.J. (eds.) Continental Basalts and Mantle Xenoliths. Shiva, Cheshire, U.K., 230-249.

Pearce, J.A., Bender, J.F., Delong, S.E., Kidd, W.S.F., Low, P.J., Guner, Y., Sargolu, F., Yilmaz, Y., Moorbath, S., Mitchell, J.G., 1990. Genesis of collision volcanism in eastern Anatolia, Turkey. J. Volcanol. Geotherm. Res. 44, 189-229.

Peccerillo, A., 2017. Cenozoic volcanism in the Tyrrhenian Sea region. Springer Int. Publ. 399 pp.

Peccerillo, A., Taylor, S.R., 1976. Geochemistry of Eocene calc-alkaline volcanic rocks from the Kastamonu Area, northern Turkey. Contrib. Mineral. Petrol. 58, 63-81.

Petford, N., Atherton, M., 1996. Na-rich partial melts from newly underplated basaltic crust: the Cordillera Blanca batholith, Perù. J. Petrol. 37, 1491-1521.

Pichavant, M., Martel, C., Bourdier, J.L., Scaillet, B., 2002. Physical conditions, structure and dynamics of a zoned magma chamber: Mount Pelée (Martinique, Lesser Antilles Arc). J. Geophys. Res. 107, B5, 2093, doi:10.1029/2001JB000315.

Pilet, S., Baker, M.B., Stolper, E.M., 2008. Metasomatized lithosphere and the origin of alkaline lavas. Science 320, 916-919.

Pilet, S., Baker, M.B., Müntener, O., Stolper, E.M., 2011. Monte Carlo Simulations of metasomatic enrichment in the lithosphere and implications for the source of alkaline basalts. J. Petrol. 52, 1415-1442.

Pilet, S., 2015. Generation of low-silica alkaline lavas: petrological constraints, models, and thermal implications. In Foulger, G.R., Lustrino, M. & King, S.D. (eds.): The Interdisciplinary Earth: A Volume in Honor of Don L. Anderson, Geol. Soc. Am. Spec.Paper 514 and Am. Geophys. Un. Spec. Publ. 71, 281–304.

Plank, T., 2014. The Chemical Composition of Subducting Sediments. In: Keeling R.F. (ed.) Treatise on Geochemistry, Elsevier, Amsterdam, 607-629, 2nd ed., doi: 10.1016/B978-0-08-095975-7.00319-3.

Plank, T., Forsyth D.W., 2016. Thermal structure and melting conditions in the mantle beneath the Basin and Range province from seismology and petrology. Geochem. Geophys. Geosyst. 17, 1312-1338.

Prelević, D., Seghedi, I., 2013. Magmatic response to the post-accretionary orogenesis within Alpine-Himalayan belt - preface. Lithos 180-181, 1-4.

Presnall, D.C., Dixon, J.R., O'Donnell, T.H., Dixon, S.A., 1979. Generation of mid-ocean ridge tholeiites, J. Petrol. 20, 3-35.

Prowatke, S., Klemme, S., 2006a. Trace element partitioning between apatite and silicate melts. Geochim. Cosmochim. Acta 70, 4513-4527.

Prowatke, S., Klemme, S., 2006b. Rare Earth element partitioning between titanite and silicate melts: Henry's Law revisited. Geochim. Cosmochim. Acta 70, 4997-5012.

Rabiee, A., Rossetti, F., Asahara, Y., Azizi, H., Lucci, F., Lustrino, M., Nozaem, R., 2020. Long-lived, Eocene-Miocene stationary magmatism in NW Iran along a transform plate boundary. Gondw. Res. 85, 237-262.

Raeisi, D., Mirnejad, H., Sheibi, M., 2019. Emplacement mechanism of the Tafresh granitoids, central part of the Urumieh-Dokhtar Magmatic Arc, Iran: evidence from magnetic fabrics. Geol. Mag. 156, 1510-1526.

Rachidnejad-Omran, N., Hachem Emami, M., Sabzehei, M., Rastad, E., Bellon, H., Piquè, A., 2002. Lithostratigraphy and Palaeozoic to Palaeocene history of some metamorphic complexes from Muteh area, Sanandaj-Sirjan zone (southern Iran). Compt. Rend. Geosci. 334, 1185-1191.

Ramezani, J., Tucker, R., 2003. The Saghand Region, Central Iran: U-Pb geochronology, petrogenesis and implications for Gondwana tectonics. Am. J. Sci. 303, 622-665.

Rapp, R.P., Watson, E.B., Miller, C.F., 1991. Partial melting of amphibolite/eclogite and the origin of Archean trondhemites and tonalities. Precambrian Res. 51, 1-25.

Rapp, R.P., Shimizu N., Norman, M.D., Applegate, G.S., 1999. Reaction between slab-derived melts and peridotite in the mantle wedge: experimental constraints at 3.8 GPa. Chem. Geol. 160, 335-356.

Reuter, M., Piller, W.E., Harzhauser, M., Mandic, O., Berning, B., Rögl, F., Kroh, A., Aubry, M.P., Wielandt-Schuster, U., Hamedani, A., 2009. The Oligo-/Miocene Qom Formation (Iran): evidence for an early Burdigalian restriction of the Tethyan Seaway and closure of its Iranian gateways. Int. J. Earth Sci. 98, 627-650. https://doi.org/10.1007/s00531-007-0269-9.

Ribeiro, J.M., Maury, R.C., Grégoire, M., 2016. Are adakites slab melts or high-pressure fractionated mantle melts? J. Petrol. 57, 839-862.

Richards, J., Kerrich, R., 2007. Special paper: Adakite-like rocks: their diverse origins and questionable role in metallogenesis. Econ. Geol. 102, 537-576.

Ridolfi, F., Renzulli, A., Puerini, M., 2010. Stability and chemical equilibrium of amphibole in calc-alkaline magmas: an overview, new thermobarometric formulations and application to subduction-related volcanoes. Contrib. Mineral. Petrol. 160, 45-66

Righter, K., Rosas-Elguera, J., 2001. Alkaline lavas in the volcanic front of the western mexican volcanic belt: geology and petrology of the Ayutla and Tapalpa volcanic fields. J. Petrol. 42, 2333.-2361.

Riou, R., Dupuy, C., Dostal, J., 1981. Geochemistry of coexisting alkaline and calc-alkaline volcanic rocks from northern Azerbaijan (N.W. Iran). J. Volcanol. Geotherm. Res. 11, 253-275.

Rodriguez Garcia, G., Gonzalez, I.H., 2004. Caracteristicas geoquimicas y marco tectonico de los basaltos alcalinos del sur de Colombia. Bol. Ciencias Tierra 16, 9-22.

Rodríguez, C., Sellés, D., Dungan, M., Langmuir, C., Leeman, W., 2007. Adakitic dacites formed by intracrustal crystal fractionation of water-rich parent magmas at Nevado de Longav Volcano (36.28°S; Andean Southern Volcanic Zone, Central Chile). J. Petrol. 11, 2033-2061.

Rudnick, R.L., Gao, S., 2014. Composition of the continental crust. In: Holland, H.D., Turekian, K.K. (eds.), Treatise on Geochemistry, 2nd ed. 4, The Crust. Elsevier, Amsterdam, 1-51.

Salehi N., Torkian A., Furman T., 2018. Olivine-hosted melt inclusions in Pliocene–Quaternary lavas from the Qorveh-Bijar volcanic belt, western Iran: implications for source lithology and cooling history. Int. Geol. Rev. 62,1828-1844.

Sajona, F.G., Bello, H., Maury, R.C., Pubellier, M., Cotten, J., Rangin, C., 1994. Magmatic response to abrupt changes in geodynamic settings: Pliocene-Quaternary calc-alkaline and Nb-enriched lavas from Mindanao (Philippines). Tectonophysics, 237, 47-72.

Salari, G., Lustrino, M., Ghorbani, M.R., Agostini, S., Fedele, L., 2021. Petrological characterization of the Cenozoic igneous rocks of the Tafresh district, central Urumieh-Dokhtar Magmatic Arc (Iran). Per. Mineral. 90, 59-83.

Scambelluri, M., Bebout, G.E., Belmonte, D., Gilio, M., Campomenosi, N., Collins, N., Crispini, L., 2016. Carbonation of subduction-zone serpentinite (high-pressure ophicarbonate; Ligurian Western Alps) and implications for the deep carbon cycling. Earth Planet. Sci. Lett. 441, 155-166.

Schiano, P., Clocchiatti, R., Shimizu, N., Maury, R.C., Jochum, K.P., Hofmann, A.W., 1995. Hydrous, silica-rich melts in the sub-arc mantle and their relationship with erupted arc lavas. Nature 377, 595-600.

Schmidt, M.W., Dardon, A., Chazot, G., Vannucci, R., 2004. The dependence of Nb and Ta rutile-melt partitioning on melt composition and Nb/Ta fractionation during subduction processes. Earth Planet. Sci. Lett. 226, 415-432.

Sengör, A.M.C., Altiner, D., Cin, A., Ustaömer, T., Hsü, K.J., 1988. Origin and assembly of the Tethysides orogenic collage at the expense of Gondwana Land. In: Audley-Charles, M.G., Hallam, A. (eds.) Gondwana and Tethys. Geol. Soc. Spec. Publ. 37, 119-181.

Sengör, A.M.C., Yilmaz, Y., Sungurlu, O., 1984. Tectonics of the Mediterranean Cimmerides: nature and evolution of the western termination of Palaeo-Tethys. Geol. Soc. Spec. Publ. 17, 77-112.

Sengör, A.M.C., Kidd, W.S.F., 1979. Post-collisional tectonics of the Turkish-Iranian plateau and a comparison with Tibet. Tectonophysics 55, 361-376.

Shahbazi, H., Siebel W., Pourmoafee, M., Ghorbani, M., Sepahi, A.A., Shang, C.K., Abedini, M.V. 2010. Geochemistry and U-Pb zircon geochronology of the Alvand plutonic complex in Sanandaj-Sirjan Zone (Iran): new evidence for Jurassic magmatism. J. Asian Earth Sci. 39, 668-683.

Shafaii, M., Griffin, W.L., Kirchenbaur, M., Garbe-Schonberg, D., Khedr, M.Z., Kimura, J.-I., Stern, R.J., Ghorbani, G., Murphy, R., O'Reilly, S.Y., Arai, S., Maghdour-Mashhour, R., 2018. Roll-back, extension and mantle upwelling triggered Eocene potassic magmatism in NW Iran. J. Petrol. 59, 1417-1465.

Shahabpour, J., 2005. Tectonic evolution of the orogenic belt in the region located between Kerman and Neyriz. J. Asian Earth Sci. 24, 405-417.

Shahabpour, J., 2007. Island-arc affinity of the Central Iranian Volcanic Belt. J. Asian Earth Sci. 30, 652-665.

Shaker, Ardakani A., 2016. Post-collisional Plio-Pleistocene Anar-Dehaj adakitic subvolcanic domes in the central volcanic belt of Iran: geochemical characteristics and tectonic implications. Period. Mineral. 85, 185-200.

Shaw, C.S.J., 2018. Evidence for the presence of carbonate melt during the formation of cumulates in the Colli Albani Volcanic District, Italy. Lithos 310-311, 105-119.

Sherafat, S., Yavuz F., Noorbehesht, I., Yıldırım, D.K., 2012. Mineral chemistry of Plio-Quaternary subvolcanic rocks, southwest Yazd Province, Iran. Int Geol Rev 54, 1497-1531.

Skala, R., Ulrych, J., Ackerman, L., Krmiceck, L., Fediuk, F., Balogh, K., Hegner, E., 2015. Upper Cretaceous to Pleistocene melilitic volcanic rocks of the Bohemian Massif: petrology and mineral chemistry. Geol. Carpath. 66, 197-216.

Smit, J., Burg, J.P., Dolati, A., Sokoutis, D., 2010. Effects of mass waste events on thrust wedges: Analogue experiments and application to the Makran accretionary wedge. Tectonics 29, TC3003, doi:10.1029/2009TC002526.

Soder, C.G., Romer, R.L., 2018. Post-collisional potassic-ultrapotassic magmatism of the Variscan Orogen: implications for mantle metasomatism during continental subduction. J. Petrol. 59, 1007-1034.

Song, W., Xu, C., Smith, M.P., Kynicky, J., Huang, K., Wei, C., Zhou, L., Shu, Q., 2016. Origin of unusual HREE-Mo-rich carbonatites in the Qinling orogen, China. Sci. Rep., 6, Article number 37377.

Stampfli, G.M., Borel, G.D., 2002. A plate tectonic model for the Paleozoic and Mesozoic constrained by dynamic plate boundaries and restored synthetic oceanic isochrones: Earth Planet. Sci. Lett. 196, 17-33.

Stampfli, G.M., Hochard, C., Vérard, C., Wilhem, C., vonRaumer, J., 2013. The formation of Pangea. Tectonophysics 593, 1-19.

Stampli, G.M., Pillevuit, A., 1993. An alternative Permo-Triassic reconstruction of the kinematics of the Tethyan realm. In: Dercourt J, Ricou L-E,Vrielinck B (eds) Atlas Tethys Palaeoenvironmental Maps. Explanatory Notes. Gauthier-Villars, Paris, 55-62.

Stocklin, J., 1968. Structural history and tectonics of Iran: A review. Am. Ass. Petrol. Geol. Bull. 52, 1229-1258.

Stoppa, F., Pirajno, F., Schiazza, M., Vladykin, N.V., 2016. State of the art: Italian carbonatites and their potential for critical-metal deposits. Gondwana Res. 37, 152-171.

Stoppa, F., Rosatelli, G., Wall, F., Jeffriest, T., 2005. Geochemistry of carbonatite-silicate pairs in nature: a case history from Central Italy. Lithos 85,26-47.

Stoppa F., Woolley, A.R., Cundari, A., 2002. Extension of the melilite-carbonatite province in the Apennines of Italy: the kamafugite of Grotta del Cervo, Abruzzo. Mineral Mag. 66, 555-574.

Straub, S.M., Zellmer, G.F., 2012. Volcanic arcs as archives of plate tectonic change. Gondw. Res. 21, 495-516.

Sun, C., Dasgupta, R., 2020. Thermobarometry of CO_2-rich, silica-undersaturated melts constraints lithosphere thinning through time in areas of kimberlitic magmatism. Earth Planet. Sci. Lett. 550, 116549.

Sylvester, P.J., 1998. Strongly peraluminous granites. Lithos 45, 29-44.

Tabaei, M., Mehdizadeh, R., Esmaeili, M., 2016. Stratigraphical evidences of the Qom-Zefreh Fault system activity, Central Iran. J. Tethys 4, 18-26.

Tappe, S., Stracke, A., van Acken, D., Strauss, H., Luguet, A., 2020. Origins of kimberlites and carbonatites during continental collision – insights beyond decoupled Nd-Hf isotopes. Earth-Sci. Rev., 208, 103287.

Tatsumi, Y., Arai, R., Ishizaka, K., 1999. The petrology of a melilite-olivine nephelinite from Hamada, SW Japan. J. Petrol. 40, 497-509.

Taylor, R.J.M., Harley, S.L., Hinton, R.W., Elphick, S., Clark, C., Kelly, N.M., 2015. Experimental determination of REE partition coefficients between zircon, garnet and melt: a key to understanding high-T crustal processes. J. Metamorph. Geol. 33, 231-248.

Tiepolo, M., Tribuzio, R., Ji, W.Q., Wu, F.Y., Lustrino, M., 2014. Alpine Tethys closure as revealed by amphibole-rich mafic and ultramafic rocks from the Adamello and the Bergell intrusions (Central Alps). J. Geol. Soc. Lond. 171, 793-799.

Thomsen, T.B., Schmidt, M.W., 2008. Melting of carbonated pelites at 2.5-5.0 GPa, silicate-carbonatite liquid immiscibility, and potassium-–carbon metasomatism of the mantle. Earth Planet. Sci. Lett. 267, 17-31.

Torkian, A., Furman, T., Salehi, N., Veloski, K., 2019. Petrogenesis of adakites from the Sheyda volcano, NW Iran. J. African Earth Sci. 150, 194-204.

Tucker, J.M., Hauri, E.H., Pietruszka, A.J., Garcia, M.A., Marske, J.P., Trusdell, F.A., 2019. A high carbon content of the Hawaiian mantle from olivine-hosted inclusions. Geochim. Cosmochim. Acta 254, 156-172.

van Hinsbergen, D.J.J., Lippert, P.C., Li S., Huang, W., Advokaat, E.L., Spakman, W., 2019. Reconstructing Greater India: paleogeographic, kinematic, and geodynamic perspectives. Tectonophysics 760, 69-94.

van Hinsbergen, D.J.J., Torsvik, T.H., Schmid, S.M., Matenco, L.C., Maffione, M., Vissers, R.L.M., Gurer, D., Spakman, W., 2020. Orogenic architecture of the Mediterranean region and kinematic reconstructions of its tectonic evolution since the Triassic. Gondw. Res. 81, 79-229.

Verdel, C., Wernicke, B.P., Hassanzadeh, J., Guest, B., 2011. A Paleogene extensional arc flare-up in Iran. Tectonics 30, TC3008, doi:10.1029/2010TC002809.

Veksler, I.V., Dorfman, A.M., Dulski, P., Kamentetsky, V.S., Danyushevsky, L.V., Jeffries, T., Dingwell, D.B., 2012. Partitioning of elements between silicate melt and immiscible fluoride, chloride, carbonate, phosphate and sulfate melts, with implications to the origin of natrocarbonatite. Geochim. Cosmochim. Acta 79, 20-40.

Vernant, P., Nilforoushan, F., Hatzfeld, D., Abbassi, M.R., Vigny, C., Masson, F., Nankali, H., Martinod, A., Ashtiani, A., Bayer, R., Tavakoli, F., Chery, J., 2004. Present-day crustal deformation and plate kinematics in the Middle East constrained by GPS measurements in Iran and northern Oman. Geophys. Int. J. 157, 381-398.

Verplanck, P.L., Mariano, A.N., Mariano, A., 2016. Rare earth element ore geology of carbonatites. In: P. Verplanck, M. Hitzman (eds.), Rare Earth and critical elements in ore deposits. Reviews in Economic Geology 18, 5-32).

Villemant, B., Jaffrezic, H., Joron, J.L., Treuil, M., 1981. Distribution coefficients of major and trace elements; fractional crystallization in the alkali basalt series of Chaine des Puys (Massic Central, France). Geochim. Cosmochim. Acta 45, 1997-2016.

Vosoghi, Abedini, M., 1981. An introduction to the Fourth Era melilite basalts in the Dokhan area. Geological Survey and Mineral Explorations of Iran (GSI) (in farsi). Report 1361-15, 7 pp.

Walker, R.T., Gans, P., Allen, M.B., Jackson, J., Khatib, M., Marsh, N., Zarrinkoub, M., 2009. Late Cenozoic volcanism and rates of active faulting in eastern Iran. Geophys. J. Int. 177, 783-805.

Wallace, M.E., Green, D.H., 1988. An experimental determination of primary carbonatite magma composition. Nature 335, 343-346.

Wang, J., Wang, Q., Dan, W., Yang, J.H., Yang, Z.Y., Sun, P., Qi, Y., Hu, W.L., 2019. The role of clinopyroxene in amphibole fractionation of arc magmas: evidence from mafic intrusive rocks within the Gangdese arc, southern Tibet. Lithos 338-339, 174-188.

Wang, Q., Xu, J.F., Jian, P., Bao, Z.W., Zhao, Z.H., Li, C.F., Xiong, X.L., Ma, J.L., 2006. Petrogenesis of adakitic porphyries in an extensional tectonic setting, Dexing, South China: implications for the genesis of porphyry copper mineralization. J. Petrol. 47, 119-144.

Watson, E.B., 1976. Two-liquid partition coefficients: experimental data and geochemical implications. Contrib. Mineral. Petrol. 56, 119-134.

Wendlandt, R.F., Mysen, B.O., 1980. melting phase relations of natural peridotite + CO_2 as a function of degree of partial melting at 15 and 30 kbar. Am. Mineral. 65, 37-44.

Wilmsen, M., Fürsich, F.T., Seyed-Emami, K., Majidifard, M.R., Taheri, J., 2009. The Cimmerian Orogeny in northern Iran: Tectonostratigraphic evidence from the foreland. Terra Nova 21, 211-218.

Winchell, H., 1947. The Honolulu series, Oahu, Hawaii. Bull. Geol. Soc. Am. 58, 1-48.

Winchester, J.A., Floyd, P.A., 1977. Geochemical discrimination of different magma series and their differentiation products using immobile elements. Chem. Geol. 20, 325-343.

Witte, M., Jung, S., Pfänder, J.A., Romer, R.L., Mayer, B. Garbe-Schönberg, G., 2017. OIB signatures in basin-related lithosphere-derived alkaline basalts from the Batain basin (Oman) – constraints from 40Ar/39Ar ages and Nd-Sr-Pb-Hf isotopes. Lithos 286-287, 109-124.

Woolley, A.R., Kempe, D.R.C., 1989. Carbonatites: Nomenclature, average chemical compositions, and element distribution. In: Bell, K. (ed.) Carbonatites: Genesis and Evolution, Unwin Hyman, London, 1-14.

Woolley, A.R., Kjarsgaard, B.A., 2008. Paragenetic types of carbonatite as indicated by the diversity and relative abundances of associated silicate rocks: evidence from a global database. Can. Mineral. 46, 741-752.

Wyllie, P.J., 1989. Origin of carbonatites: evidence from phase equilibrium studies. In: Bell, K. (ed.) Carbonatites: Genesis and evolution, Unwin Hyman, London, 500-545.

Wyllie, P.J., Huang, W.L., 1975. Peridotite, kimberlite, and carbonatite explained in the system CaO-MgO-SiO_2-CO_2. Geology 3, 621-624.

Wyllie, P.J., Huang, W.L., 1976. Carbonation and melting reactions in the system CaO-MgO-SiO_2-CO_2 at mantle pressures with geophysical and petrological applications. Contrib. Mineral. Petrol. 54, 79-107.

Yamaguchi, M., 1964. Petrogenic significance of ultrabasic inclusions in basaltic rocks from Southwest Japan. Mem. Fac. Sci. Kyushu Univ. 15, 163-219.

Yaxley, G.M., Ghosh, S., Kiseeva, E.S., Mallik, A., Spandler, C., Thomson, A.R., Walter, M.J., 2019. CO_2-rich melts in Earth. In: Orcutt, B.N., Daniel I., Dasgupta R. (eds.) Deep carbon – past to present. Cambridge Univ. Press. 129-162.

Yeganehfar, H., Ghorbani, M.R., Shinjo, R., Ghaderi, M., 2013. Magmatic and geodynamic evolution of Urumieh–Dokhtar basic volcanism, Central Iran: major, trace element, isotopic, and geochronologic implications. Int. Geol. Rev. 55, 767-786.

Zheng, Y.F., 2019. Subduction zone geochemistry. Geosci. Front. 10, 1223-1254.

Ziberna, L., Klemme, S., 2016. Application of thermodynamic modelling to natural mantle xenoliths: examples of density variations and pressure-temperature evolution of the lithospheric mantle. Contrib. Mineral. Petrol. 171:16, DOI 10.1007/s00410-016-1229-9.

Appendix Tables

Table 1. Major (wt%) and trace (ppm) elements concentrations, LOI (wt%) and CIPW-normative mineralogy (in vol.%, calculated assuming Fe2O3/FeO = 0.15) for the investigated rock samples from Tafresh area.
(Normative minerals: qtz=quartz; cor=corundum; or=orthoclase; ab=albite; an=anorthite; ne=nepheline; di=diopside; hy=hypersthene; ol=olivine; mt=magnetite; il=ilmenite; ap=apatite). Bdl=below detection limits

sample	F2-12	F2-34	F1-22	F3-24	F4-49	F4-58	F1-33	F1-36	F1-11A	F1-11B	F3-6	F3-13	F4-1	F4-10	F4-11	F1-9	F1-13	F4-15	F3-23	F1-8	F1-29	F1-46	F1-17	F1-18	F2-21	F3-3
lithotype	weakly evolved								intermediate											evolved			strongly evolved			
preservation	fresh			spoiled			weathered		fresh				spoiled							fresh	spoiled		fresh			
SiO_2	53.81	53.89	50.89	51.67	50.46	50.68	48.98	44.69	56.31	56.86	59.23	58.23	55.28	57.53	58.26	55.56	58.90	52.17	52.89	61.56	60.44	60.27	70.45	70.95	70.11	71.23
TiO_2	0.90	0.90	1.09	0.92	0.89	0.83	1.45	1.12	0.75	0.74	0.62	0.89	0.81	0.68	0.85	1.22	0.87	1.16	0.90	0.51	0.90	0.51	0.38	0.37	0.33	0.34
Al_2O_3	17.59	17.64	18.90	18.76	16.66	19.21	13.66	16.61	18.19	17.41	17.88	16.27	18.12	16.96	14.68	16.37	15.21	17.04	16.93	17.68	14.66	16.77	14.49	13.90	12.97	13.52
Fe_2O_3tot	8.63	8.74	6.87	6.39	9.80	5.45	13.48	9.71	7.57	7.24	7.00	8.17	7.95	6.86	7.04	9.51	6.89	8.83	7.29	5.10	7.29	4.33	3.19	3.25	2.54	2.33
MnO	0.17	0.17	0.11	0.12	0.11	0.14	0.17	0.14	0.17	0.14	0.11	0.15	0.16	0.18	0.12	0.05	0.13	0.12	0.11	0.14	0.11	0.07	0.05	0.05	0.03	0.07
MgO	4.10	4.12	2.23	1.44	2.78	1.16	3.62	2.32	2.94	2.81	2.85	2.74	3.65	2.52	3.45	3.25	2.55	2.50	2.22	1.59	2.60	2.25	1.20	1.20	1.57	1.08
CaO	5.84	5.85	10.60	12.11	8.96	12.76	5.45	13.86	7.00	5.89	5.57	5.76	7.57	5.22	5.50	2.98	5.54	9.60	10.25	6.20	2.05	5.38	0.56	1.18	1.26	1.08
Na_2O	4.01	4.00	3.08	2.93	2.29	2.96	3.70	2.27	3.40	3.70	3.39	3.12	3.09	3.94	3.29	5.69	3.26	2.62	2.95	3.97	5.32	3.81	4.13	3.80	3.11	3.80
K_2O	1.48	1.48	0.47	0.64	0.72	0.91	0.47	0.50	0.97	2.18	0.91	1.47	0.87	1.31	2.74	0.43	2.53	0.75	0.27	0.50	1.65	2.33	3.84	3.36	3.43	2.68
P_2O_5	0.24	0.24	0.18	0.15	0.11	0.14	0.27	0.09	0.16	0.14	0.14	0.14	0.18	0.21	0.21	0.18	0.19	0.22	0.17	0.17	0.20	0.20	0.10	0.11	0.06	0.08
LOI	3.68	3.62	5.61	5.34	6.12	4.84	9.09	9.48	2.85	2.98	3.28	3.95	2.76	3.57	3.65	5.41	4.83	5.91	6.21	3.24	4.24	4.95	1.80	2.30	3.11	2.83
Total	100.50	100.60	100.00	100.50	98.90	99.07	100.30	100.80	100.30	100.10	101.00	100.90	100.50	98.98	99.79	100.60	100.90	100.90	100.20	100.70	99.46	100.90	100.20	100.50	98.51	99.03
Rb	45	47	4	9	17	23	13	14	23	53	31	41	20	31	75	13	63	20	4	14	22	65	77	76	76	68
Sr	355	357	264	270	229	260	139	203	282	252	374	204	330	317	262	226	229	243	263	317	189	506	137	137	74	112
Ba	488	488	147	158	170	181	568	102	405	721	268	329	457	553	496	94	604	196	116	321	383	866	534	489	583	602
Cs	1.10	1.20	bdl	bdl	0.60	0.60	0.80	0.70	bdl	0.60	0.60	0.60	bdl	bdl	1.10	0.90	1.60	1.10	1.10	0.50	1.00	2.60	0.70	0.80	0.90	1.30
Sc	20	20	24	23	30	21	43	35	17	16	14	28	16	12	21	27	22	26	27	7	20	9	9	8	6	7
V	163	165	248	216	284	197	380	257	148	145	119	195	130	94	158	266	167	228	241	51	75	92	51	49	20	22
Cr	30	30	50	60	60	60	30	50	bdl	bdl	30	bdl	40	40	80	bdl	70	50	60	bdl	bdl	40	bdl	bdl	bdl	bdl
Co	21	21	22	20	16	18	33	33	15	12	11	15	19	12	21	18	18	25	24	6	8	12	5	5	2	2
Ni	bdl	bdl	30	20	bdl	30	bdl	30	bdl	bdl	bdl	bdl	bdl	bdl	30	bdl	30	20	30	bdl	bdl	20	bdl	bdl	bdl	bdl
Cu	20	20	10	30	20	20	220	110	10	100	10	20	10	bdl	30	10	20	40	40	bdl	20	20	bdl	bdl	bdl	bdl
Zn	90	90	200	60	80	40	110	80	90	130	80	80	80	100	70	480	80	60	160	60	210	50	50	40	40	50
Y	30	26	27	22	18	21	36	25	32	28	18	26	25	33	26	29	27	24	23	20	32	8	20	19	22	26
Zr	151	150	116	103	69	94	96	69	131	136	107	101	116	169	211	131	221	145	106	103	104	130	128	114	120	135
Nb	6	7	5	4	4	3	4	3	7	7	6	5	7	8	10	10	10	11	4	7	5	9	4	5	6	6
Hf	3.2	3.2	2.8	2.6	1.7	2.2	2.5	1.7	3.0	3.1	2.4	2.5	2.7	4.1	4.7	3.1	4.8	3.4	2.6	2.5	2.7	3.0	3.3	2.7	3.0	3.1
Ta	0.4	0.4	0.3	0.3	0.2	0.2	0.3	0.2	0.4	0.5	0.4	0.4	0.4	0.6	0.8	0.6	0.8	0.7	0.3	0.5	0.4	1.0	0.6	0.5	0.6	0.6
La	19.0	19.6	11.7	10.2	9.5	9.1	10.7	6.6	17.3	16.6	15.1	14.4	17.4	22.2	24.4	18.6	25.6	18.3	10.8	15.5	17.1	41.5	18.2	17.9	21.1	21.1
Ce	39.4	40.3	25.2	22.1	20.4	20.5	23.8	15.0	35.9	34.9	30.2	30.6	34.7	46.2	49.8	38.5	52.9	37.8	23.7	32.9	38.5	71.0	31.6	32.9	40.4	40.1
Pr	4.88	4.88	3.30	2.95	2.64	2.67	3.45	2.16	4.47	4.31	3.63	3.82	4.21	5.68	5.89	4.84	6.05	4.58	3.12	4.04	5.08	7.33	3.68	3.48	4.57	4.35
Nd	19.6	20.5	15.0	13.1	11.5	11.8	16.8	10.1	18.1	18.0	13.9	16.0	17.1	23.3	23.7	19.6	24.0	18.9	13.8	16.7	21.6	24.7	13.6	12.6	16.9	16.2
Sm	4.70	4.60	3.70	3.50	3.00	3.00	4.80	2.90	4.30	4.20	3.00	3.90	4.00	5.30	5.10	4.60	5.10	4.20	3.50	3.90	5.40	4.10	3.10	2.50	3.50	3.70
Eu	1.33	1.32	1.10	0.96	0.88	0.94	1.38	0.93	1.11	1.03	0.84	1.02	1.13	1.33	1.09	1.07	1.18	1.07	0.92	1.18	1.92	0.99	0.72	0.64	0.63	0.77
Gd	4.4	4.3	4.0	3.6	2.9	3.2	5.3	3.5	4.2	4.2	2.8	3.7	3.7	4.9	4.5	4.4	4.7	4.0	3.6	3.5	5.4	2.5	3.0	2.3	3.0	3.5
Tb	0.8	0.7	0.7	0.6	0.5	0.6	1.0	0.7	0.7	0.7	0.5	0.7	0.6	0.8	0.8	0.8	0.8	0.7	0.6	0.6	0.9	0.3	0.5	0.4	0.5	0.6
Dy	4.4	4.5	4.3	3.7	3.3	3.6	6.1	4.1	4.6	4.3	3.0	4.1	4.2	5.3	4.6	5.0	4.7	4.4	3.9	3.4	5.5	1.6	3.1	2.7	3.5	4.0
Ho	1.0	0.9	0.8	0.8	0.7	0.7	1.2	0.8	1.0	0.9	0.6	0.9	0.9	1.0	0.9	1.0	1.0	0.9	0.8	0.7	1.1	0.3	0.7	0.6	0.8	0.8
Er	2.8	2.7	2.5	2.3	2.0	2.2	3.8	2.6	2.8	2.7	1.8	2.6	2.5	3.2	2.7	3.0	2.9	2.5	2.3	2.1	3.2	0.7	2.0	2.0	2.3	2.5
Tm	0.43	0.44	0.41	0.37	0.33	0.36	0.59	0.42	0.48	0.45	0.29	0.41	0.41	0.54	0.44	0.48	0.46	0.39	0.39	0.33	0.52	0.10	0.35	0.33	0.39	0.42
Yb	2.9	2.8	2.6	2.3	2.2	2.3	3.8	2.6	3.0	3.1	1.9	2.7	2.7	3.6	2.8	3.1	3.0	2.5	2.5	2.2	3.4	0.6	2.4	2.2	2.7	2.7
Lu	0.41	0.41	0.38	0.34	0.30	0.32	0.55	0.37	0.42	0.43	0.27	0.38	0.41	0.56	0.41	0.44	0.42	0.39	0.35	0.32	0.51	0.09	0.37	0.32	0.38	0.40
Pb	bdl	bdl	9.0	7.0	bdl	7.0	bdl	bdl	bdl	13.0	bdl	bdl	bdl	6.0	10.0	5.0	8.0	6.0	6.0	bdl	46.0	19.0	bdl	7.0	bdl	bdl
Th	4.8	4.8	2.5	2.2	2.3	2.0	1.6	1.8	4.7	4.9	3.9	3.9	3.6	5.0	9.3	4.7	9.8	5.0	2.9	3.1	4.0	22.6	7.0	6.9	8.1	7.9
U	1.5	1.5	0.8	0.7	0.7	0.7	0.6	0.5	1.5	1.5	1.3	1.2	1.1	1.6	3.1	1.5	3.1	1.4	1.0	1.1	1.4	10.9	2.1	2.3	2.4	2.4
Ga	18.0	19.0	18.0	17.0	18.0	18.0	16.0	15.0	18.0	18.0	17.0	17.0	18.0	19.0	15.0	18.0	16.0	17.0	16.0	17.0	17.0	18.0	14.0	13.0	13.0	13.0
qz	2.54	2.53	5.70	6.41	8.81	4.30	3.57	0.00	10.36	7.60	16.67	14.72	9.33	11.92	10.79	5.35	13.41	9.10	10.41	19.14	12.14	13.87	27.75	30.77	34.25	35.27
cor	0.00	0.00	0.00	0.00	0.00	0.00	0.00	0.00	0.00	0.00	1.56	0.00	0.00	0.08	0.00	1.63	0.00	0.00	0.00	0.00	0.92	0.00	2.81	2.17	2.09	2.70
or	9.04	9.01	2.94	3.98	4.59	5.71	3.04	3.24	5.88	13.27	5.50	8.96	5.26	8.11	16.84	2.67	15.56	4.66	1.70	3.03	10.24	14.35	23.06	20.22	21.24	16.46

Table 1. (continued)

sample	F2-12	F2-34	F1-22	F3-24	F4-49	F4-58	F1-33	F1-36	F1-11A	F1-11B	F3-6	F3-13	F4-1	F4-10	F4-11	F1-9	F1-13	F4-15	F3-23	F1-8	F1-29	F1-46	F1-17	F1-18	F2-21	F3-3
lithotype	weakly evolved								intermediate											evolved			strongly evolved			
preservation	fresh			spoiled			weathered		fresh				spoiled							fresh	spoiled		fresh			
ab	35.06	34.88	27.60	26.06	20.88	26.58	34.31	19.81	29.52	32.24	29.36	27.23	26.77	34.94	28.95	50.55	28.71	23.33	26.56	34.48	47.27	33.61	35.52	32.75	27.58	33.42
an	26.48	26.60	38.51	38.00	35.62	38.67	21.13	36.86	32.33	25.19	27.35	26.87	33.79	25.70	17.89	14.29	20.19	34.23	34.22	29.71	9.31	22.70	2.16	5.23	6.14	5.03
ne	0.00	0.00	0.00	0.00	0.00	0.00	0.00	0.67	0.00	0.00	0.00	0.00	0.00	0.00	0.00	0.00	0.00	0.00	0.00	0.00	0.00	0.00	0.00	0.00	0.00	0.00
lc	0.00	0.00	0.00	0.00	0.00	0.00	0.00	0.00	0.00	0.00	0.00	0.00	0.00	0.00	0.00	0.00	0.00	0.00	0.00	0.00	0.00	0.00	0.00	0.00	0.00	0.00
di	1.52	1.41	13.34	20.45	9.70	19.14	5.55	32.01	1.86	3.30	0.00	1.39	2.87	0.00	7.50	0.00	5.95	12.11	15.71	0.61	0.00	3.10	0.00	0.00	0.00	0.00
wo	0.00	0.00	0.00	0.00	0.00	2.08	0.00	0.00	0.00	0.00	0.00	0.00	0.00	0.00	0.00	0.00	0.00	0.00	0.00	0.00	0.00	0.00	0.00	0.00	0.00	0.00
hy	20.69	20.90	7.39	1.16	15.55	0.00	24.86	0.00	16.19	14.69	16.16	16.55	17.88	15.52	13.93	20.03	12.13	11.30	7.14	10.27	15.85	9.70	6.90	7.01	7.21	5.63
ol	0.00	0.00	0.00	0.00	0.00	0.00	0.00	2.10	0.00	0.00	0.00	0.00	0.00	0.00	0.00	0.00	0.00	0.00	0.00	0.00	0.00	0.00	0.00	0.00	0.00	0.00
cs	0.00	0.00	0.00	0.00	0.00	0.00	0.00	0.00	0.00	0.00	0.00	0.00	0.00	0.00	0.00	0.00	0.00	0.00	0.00	0.00	0.00	0.00	0.00	0.00	0.00	0.00
mt	1.54	1.55	1.25	1.16	1.82	1.00	2.55	1.83	1.34	1.29	1.24	1.45	1.40	1.24	1.26	1.72	1.24	1.60	1.34	0.90	1.32	0.78	0.56	0.57	0.46	0.42
il	1.77	1.76	2.18	1.83	1.82	1.68	3.01	2.32	1.46	1.45	1.20	1.75	1.57	1.35	1.69	2.44	1.73	2.31	1.82	1.00	1.80	1.01	0.72	0.72	0.65	0.68
ap	0.59	0.59	0.45	0.37	0.28	0.35	0.70	0.23	0.39	0.34	0.34	0.34	0.44	0.52	0.52	0.45	0.47	0.55	0.43	0.41	0.50	0.49	0.24	0.27	0.15	0.20
Tot	99.23	99.22	99.37	99.42	99.08	99.50	98.72	99.07	99.33	99.35	99.38	99.27	99.29	99.38	99.37	99.13	99.38	99.20	99.33	99.55	99.34	99.61	99.72	99.71	99.77	99.79

Table 2: EMP analysis for Nowbaran olivine compositions

Sample	Point	SiO_2	FeO	MnO	MgO	CaO	NiO	Total	Si	Ti	Fe''	Mn	Mg	Ca	Ni	Cr	Total	Fo	Fa	Total	Fo	Fa	La	Total
NB13	1-6 ol gm	38.76	13.77	0.33	46.27	0.03	0.17	99.33	0.97	0.00	0.29	0.01	1.72	0.01	0.00	0.00	3.00	85.70	14.30	100.00	85.33	14.24	0.43	100.00
NB13	1-10 ol gm	38.83	12.96	0.28	47.10	0.03	0.19	99.39	0.97	0.00	0.27	0.01	1.75	0.01	0.00	0.00	3.00	86.63	13.37	100.00	86.28	13.32	0.40	100.00
NB13	2-6 ol gm	38.12	13.73	0.31	45.80	0.06	0.11	98.13	0.96	0.00	0.29	0.01	1.73	0.01	0.00	0.00	3.00	85.60	14.40	100.00	85.06	14.31	0.64	100.00
NB13	2-7 ol gm	38.71	13.03	0.28	46.17	0.06	0.22	98.48	0.97	0.00	0.27	0.01	1.73	0.01	0.00	0.00	3.00	86.33	13.67	100.00	86.02	13.62	0.37	100.00
NB13	2-8 ol gm	38.34	13.34	0.23	47.08	0.07	0.31	99.38	0.96	0.00	0.28	0.00	1.75	0.01	0.01	0.00	3.00	86.29	13.71	100.00	85.99	13.67	0.34	100.00
NB13	7-4 ol gm	38.69	13.66	0.26	45.78	0.13	0.20	98.71	0.97	0.00	0.29	0.01	1.72	0.01	0.00	0.00	3.00	85.66	14.34	100.00	85.24	14.27	0.49	100.00
NB25	1-11 large euhedral ol rim	39.90	13.00	0.28	45.73	0.14	0.03	99.08	1.00	0.00	0.27	0.01	1.71	0.02	0.00	0.00	3.00	86.25	13.75	100.00	85.47	13.63	0.90	100.00
NB25	1-12 same euhedral ol core	40.17	11.84	0.16	47.14	0.14	0.01	99.45	1.00	0.00	0.25	0.00	1.75	0.00	0.00	0.00	3.00	87.65	12.35	100.00	87.45	12.32	0.23	100.00
NB24	1-6 ol pheno rim	39.58	11.90	0.28	47.31	0.16	0.20	99.42	0.98	0.00	0.25	0.01	1.75	0.01	0.00	0.00	3.00	87.64	12.36	100.00	87.10	12.28	0.61	100.00
NB24	1-7 ol pheno core	40.48	11.59	0.22	47.53	0.17	0.36	100.35	1.00	0.00	0.24	0.00	1.74	0.01	0.01	0.00	3.00	87.97	12.03	100.00	87.61	11.98	0.41	100.00
NB24	5-1 ol pheno rim	39.55	12.25	0.31	47.28	0.18	0.19	99.76	0.98	0.00	0.25	0.01	1.74	0.01	0.00	0.00	3.00	87.31	12.69	100.00	86.78	12.61	0.61	100.00
NB24	5-2 same ol pheno core	40.25	11.66	0.19	47.87	0.18	0.43	100.58	0.99	0.00	0.24	0.00	1.75	0.01	0.01	0.00	3.00	87.98	12.02	100.00	87.73	11.99	0.28	100.00
NB24	2-17 ol in cpx core	41.27	9.85	0.28	47.72	0.18		99.29	1.02	0.00	0.20	0.01	1.75	0.02	0.00	0.00	3.00	89.62	10.38	100.00	88.57	10.26	1.17	100.00
NB24	2-18 ol in cpx core	41.34	10.44	0.19	46.53	0.19		98.70	1.03	0.00	0.22	0.00	1.73	0.02	0.00	0.00	3.00	88.82	11.18	100.00	87.75	11.04	1.21	100.00
NB24	3-3 ol in cpx core	41.47	10.81	0.22	47.64	0.19		100.33	1.01	0.00	0.22	0.00	1.74	0.02	0.00	0.00	3.00	88.71	11.29	100.00	87.64	11.16	1.20	100.00
NB15	1-13 ol in pheno cpx	39.70	12.62	0.23	46.61	0.20	0.30	99.65	0.99	0.00	0.26	0.00	1.73	0.01	0.01	0.00	3.00	86.82	13.18	100.00	86.52	13.14	0.34	100.00
NB15	1-5 ol gm	39.36	13.15	0.23	45.87	0.20	0.21	99.02	0.99	0.00	0.28	0.00	1.72	0.01	0.00	0.00	3.00	86.15	13.85	100.00	85.78	13.79	0.43	100.00
NB15	1-7 ol gm	39.86	13.04	0.26	46.46	0.20	0.25	100.07	0.99	0.00	0.27	0.01	1.72	0.01	0.00	0.00	3.00	86.39	13.61	100.00	86.12	13.56	0.32	100.00
NB15	1-16 ol gm	39.36	12.74	0.22	46.13	0.21	0.21	98.87	0.99	0.00	0.27	0.00	1.73	0.01	0.00	0.00	3.00	86.58	13.42	100.00	86.26	13.37	0.38	100.00
NB2	1-3 gm ol	41.28	10.99	0.44	47.99	0.21	0.17	101.08	1.01	0.00	0.22	0.01	1.74	0.02	0.00	0.00	3.00	88.61	11.39	100.00	87.93	11.30	0.77	100.00
NB2	1-14 gm ol	41.04	10.97	0.44	47.26	0.22	0.23	100.16	1.01	0.00	0.23	0.01	1.73	0.02	0.00	0.00	3.00	88.48	11.52	100.00	87.71	11.42	0.87	100.00
NB2	1-17 gm ol	40.76	10.62	0.47	46.97	0.24	0.17	99.22	1.01	0.00	0.22	0.01	1.74	0.02	0.00	0.00	3.00	88.75	11.25	100.00	87.90	11.14	0.96	100.00
NB2	2-7 gm ol	41.48	11.47	0.44	47.56	0.24	0.26	101.44	1.01	0.00	0.23	0.01	1.73	0.02	0.00	0.00	3.00	88.09	11.91	100.00	87.39	11.82	0.79	100.00
NB2	2-7 gm ol bis	41.26	11.39	0.43	47.59	0.25	0.14	101.05	1.01	0.00	0.23	0.01	1.73	0.01	0.00	0.00	3.00	88.17	11.83	100.00	87.51	11.74	0.75	100.00
NB8	1-1 pheno ol core	40.90	11.00	0.15	47.66	0.25	0.51	100.48	1.01	0.00	0.23	0.00	1.75	0.00	0.01	0.00	3.00	88.54	11.46	100.00	88.38	11.44	0.18	100.00
NB8	1-2 pheno ol core	40.80	11.47	0.18	47.26	0.26	0.55	100.51	1.01	0.00	0.24	0.00	1.74	0.00	0.01	0.00	3.00	88.02	11.98	100.00	87.86	11.96	0.18	100.00
NB8	1-11 ol gm	40.35	10.87	0.21	47.29	0.27	0.27	99.24	1.00	0.00	0.23	0.00	1.75	0.01	0.01	0.00	3.00	88.58	11.42	100.00	88.30	11.38	0.32	100.00
NB8	1-12 ol gm	40.35	11.55	0.20	47.49	0.27	0.32	100.18	1.00	0.00	0.24	0.00	1.75	0.00	0.01	0.00	3.00	88.00	12.00	100.00	87.82	11.98	0.21	100.00
NB8	2-14 gm ol core	39.73	11.14	0.16	45.88	0.12	0.39	100.37	1.02	0.00	0.24	0.00	1.73	0.01	0.00	0.00	3.00	87.71	12.29	100.00	87.39	12.24	0.37	100.00
NB8	2-14 gm ol rim	39.62	11.31	0.14	45.52	0.15	0.32	99.07	1.01	0.00	0.32	0.01	1.64	0.01	0.00	0.00	3.00	83.56	16.44	100.00	83.11	16.35	0.54	100.00
NB8	2-9 gm ol	40.24	11.69	0.19	44.10	0.45	0.07	100.73	1.00	0.00	0.28	0.01	1.70	0.01	0.01	0.00	3.00	85.66	14.34	100.00	85.32	14.28	0.39	100.00
NB8	3-1 ol gm	41.21	11.70	0.20	46.82	0.27	0.18	99.51	0.99	0.00	0.28	0.01	1.71	0.01	0.00	0.00	3.00	85.99	14.01	100.00	85.65	13.96	0.40	100.00
NB8	random gm ol core	39.76	11.10	0.14	45.90	0.19	0.42	101.07	1.01	0.00	0.18	0.00	1.79	0.00	0.01	0.00	3.00	90.73	9.27	100.00	90.69	9.27	0.04	100.00
NB8	random gm ol rim	40.05	10.17	0.19	46.55	0.52	0.10	101.32	1.01	0.00	0.26	0.00	1.72	0.00	0.01	0.00	3.00	87.09	12.91	100.00	86.88	12.88	0.24	100.00
NB8	random gm ol core	39.85	11.96	0.20	44.51	0.33	0.12	100.41	1.00	0.00	0.26	0.00	1.72	0.01	0.01	0.00	3.00	86.82	13.18	100.00	86.59	13.15	0.27	100.00
NB8	random gm ol rim	39.51	12.42	0.25	43.39	0.67	0.13	101.35	1.00	0.00	0.26	0.00	1.72	0.00	0.01	0.00	3.00	86.76	13.24	100.00	86.62	13.21	0.17	100.00
NB28	3-17 gm ol	39.71	15.18	0.41	43.27	0.28	0.22	100.66	0.98	0.00	0.27	0.00	1.73	0.00	0.01	0.00	3.00	86.50	13.50	100.00	86.41	13.49	0.10	100.00
NB28	3-23 gm ol	40.15	13.74	0.27	46.04	0.28	0.25	99.42	0.99	0.00	0.27	0.00	1.73	0.00	0.01	0.00	3.00	86.47	13.53	100.00	86.43	13.52	0.04	100.00
NB28	3-25 ol	39.58	13.33	0.24	45.87	0.28	0.20	99.57	0.98	0.00	0.28	0.01	1.73	0.01	0.01	0.00	3.00	86.25	13.75	100.00	85.94	13.70	0.36	100.00
NB28	3-27 big ol pheno core	41.65	9.03	0.15	49.53	0.28	0.43	99.78	0.98	0.00	0.28	0.00	1.73	0.01	0.00	0.00	3.00	86.01	13.99	100.00	85.72	13.95	0.33	100.00

Table 2: (continued)

Sample	Point	SiO_2	FeO	MnO	MgO	CaO	NiO	Total	Si	Ti	Fe''	Mn	Mg	Ca	Ni	Cr	Total	Fo	Fa	Total	Fo	Fa	La	Total
NB28	3-28 big ol pheno rim	40.99	12.42	0.18	47.01	0.29	0.43	101.47	1.01	0.00	0.18	0.00	1.79	0.00	0.01	0.00	3.00	90.84	9.16	100.00	90.77	9.15	0.07	100.00
NB28	3-30 gm ol	40.22	12.64	0.23	46.70	0.30	0.34	100.81	1.01	0.00	0.18	0.00	1.79	0.00	0.01	0.00	3.00	90.68	9.32	100.00	90.61	9.32	0.08	100.00
NB28	1-1 pheno ol core	40.62	12.80	0.17	47.07	0.30	0.38	99.62	1.01	0.00	0.28	0.00	1.70	0.01	0.00	0.00	3.00	85.97	14.03	100.00	85.65	13.98	0.37	100.00
NB28	1-1 pheno ol core bis	39.77	13.08	0.23	46.99	0.30	0.29	101.36	1.01	0.00	0.26	0.00	1.71	0.01	0.01	0.00	3.00	86.92	13.08	100.00	86.68	13.05	0.27	100.00
NB28	1-4 same pheno ol rim	39.33	12.93	0.20	46.35	0.31	0.30	101.77	1.00	0.00	0.27	0.01	1.71	0.00	0.01	0.00	3.00	86.54	13.46	100.00	86.33	13.43	0.24	100.00
NB28	1-6 micro ol core	39.09	13.19	0.24	46.43	0.32	0.30	101.01	0.99	0.00	0.27	0.00	1.73	0.01	0.01	0.00	3.00	86.63	13.37	100.00	86.40	13.33	0.26	100.00
NB28	1-11 micro ol rim	39.12	13.48	0.23	46.45	0.32	0.18	99.47	0.99	0.00	0.26	0.00	1.73	0.00	0.01	0.00	3.00	86.73	13.27	100.00	86.52	13.24	0.24	100.00
NB28	3-1 same big pheno ol core	41.88	8.94	0.14	49.71	0.36	0.45	99.36	0.97	0.00	0.26	0.00	1.75	0.01	0.01	0.00	3.00	86.97	13.03	100.00	86.75	12.99	0.26	100.00
NB28	3-2 big pheno ol rim	41.54	9.03	0.13	49.28	0.38	0.45	101.27	1.01	0.00	0.27	0.00	1.71	0.01	0.00	0.00	3.00	86.22	13.78	100.00	85.98	13.74	0.28	100.00
NB28	3-23 gm ol	40.31	13.23	0.23	45.46	0.39		99.62	1.00	0.00	0.27	0.00	1.72	0.01	0.00	0.00	3.00	86.47	13.53	100.00	86.14	13.48	0.38	100.00
NB28	4-6 micro ol core	41.04	12.54	0.22	46.71	0.46	0.40	101.21	1.01	0.00	0.26	0.00	1.71	0.01	0.01	0.00	3.00	86.66	13.34	100.00	86.38	13.29	0.33	100.00
NB28	4-5 micro ol rim	40.93	12.98	0.25	46.77	0.46	0.38	100.50	0.99	0.00	0.27	0.00	1.72	0.01	0.00	0.00	3.00	86.25	13.75	100.00	85.92	13.69	0.39	100.00
NB28	5-1 micro ol	40.17	12.91	0.22	46.90	0.48	0.34	100.60	0.99	0.00	0.27	0.01	1.71	0.01	0.00	0.00	3.00	86.18	13.82	100.00	85.75	13.75	0.51	100.00
NB28	5-2 micro ol core	39.57	12.61	0.22	46.20	0.49	0.39	101.28	0.99	0.00	0.26	0.01	1.73	0.01	0.01	0.00	3.00	87.01	12.99	100.00	86.75	12.95	0.30	100.00
NB28	5-4 micro ol rim	38.80	12.52	0.21	46.87	0.57	0.40	100.52	1.00	0.00	0.27	0.00	1.72	0.01	0.00	0.00	3.00	86.61	13.39	100.00	86.39	13.35	0.26	100.00
NB28	5-4 same micro ol rim	40.79	13.19	0.17	46.30	0.59	0.24	99.54	0.99	0.00	0.27	0.01	1.73	0.01	0.00	0.00	3.00	86.42	13.58	100.00	86.09	13.53	0.38	100.00
NB33	2-2 ol rim	40.76	12.77	0.22	46.54	0.65	0.26	101.21	1.00	0.00	0.26	0.00	1.71	0.02	0.01	0.00	3.00	86.66	13.34	100.00	85.91	13.22	0.86	100.00
NB33	3-2 ol core	39.97	13.15	0.23	46.29	0.67	0.18	100.50	0.99	0.00	0.27	0.00	1.71	0.02	0.00	0.00	3.00	86.25	13.75	100.00	85.49	13.62	0.89	100.00
NB33	3-2bis ol rim	39.88	13.23	0.29	46.29	0.71	0.20	100.60	0.99	0.00	0.27	0.01	1.71	0.02	0.00	0.00	3.00	86.18	13.82	100.00	85.37	13.69	0.94	100.00
NB33	3-3 micro ol	40.18	12.53	0.28	47.06	0.88	0.35	101.28	0.99	0.00	0.26	0.01	1.72	0.02	0.01	0.00	3.00	87.01	12.99	100.00	86.00	12.84	1.15	100.00
NB33	3-4 micro ol	39.96	12.80	0.21	46.44	0.89	0.23	100.52	0.99	0.00	0.26	0.00	1.71	0.02	0.00	0.00	3.00	86.61	13.39	100.00	85.59	13.23	1.18	100.00
NB33	3-5 micro ol	39.21	12.92	0.24	46.09	0.91	0.17	99.54	0.98	0.00	0.27	0.01	1.72	0.02	0.00	0.00	3.00	86.42	13.58	100.00	85.37	13.42	1.21	100.00

Table 3: EMP analysis for Nowbaran clinopyroxene compositions

Sample	Point	SiO_2	CaO	FeO	MgO	MnO	TiO_2	Al_2O_3	Cr_2O_3	Na_2O	Total	Si	Ti	Al (T)	Al (M1)	Al (tot)	Fe^{3+} (T)	Fe^{3+} (M1)	Fe^{3+}(tot)	Fe^{2+}	Fe(tot)	Mn	Mg	Ca	Na	Cr	Total	Mg#	Wo	En	Fs	Total
NB13	1-1 cpx pheno rim	49.70	24.58	4.96	14.81	0.07	1.87	2.70	0.07	0.42	99.16	1.84	0.05	0.12	0.00	0.12	0.04	0.08	0.12	0.04	0.15	0.00	0.82	0.98	0.03	0.00	4.00	0.84	50.05	41.96	7.99	100.00
NB13	1-2 same cpx pheno mantle	47.81	24.74	6.18	13.91	0.04	1.71	4.10	0.07	0.38	98.94	1.78	0.05	0.18	0.00	0.18	0.04	0.15	0.18	0.01	0.19	0.00	0.77	0.99	0.03	0.00	4.00	0.80	50.55	39.54	9.92	100.00
NB13	1-3 same cpx pheno core	53.83	22.39	3.96	16.80	0.05	0.38	1.92	0.20	0.67	100.19	1.95	0.01	0.05	0.04	0.08	0.00	0.03	0.03	0.09	0.12	0.00	0.91	0.87	0.05	0.01	4.00	0.88	45.80	47.80	6.40	100.00
NB13	1-4 same cpx pheno cribrose core	52.82	22.52	3.87	16.23	0.05	0.58	2.48	0.21	0.77	99.52	1.93	0.02	0.07	0.04	0.11	0.00	0.05	0.05	0.07	0.12	0.00	0.88	0.88	0.05	0.01	4.00	0.88	46.77	46.88	6.35	100.00
NB13	1-5 cpx gm	53.18	24.22	4.37	16.07	0.12	0.71	1.83	0.01	0.40	100.90	1.93	0.02	0.07	0.01	0.08	0.00	0.05	0.05	0.08	0.13	0.00	0.87	0.94	0.03	0.00	4.00	0.87	48.36	44.64	7.00	100.00
NB13	2-1 cpx ph	50.35	24.06	5.47	14.57	0.08	1.52	3.47	0.11	0.34	99.97	1.86	0.04	0.14	0.01	0.15	0.00	0.07	0.07	0.10	0.17	0.00	0.80	0.95	0.02	0.00	4.00	0.83	49.44	41.66	8.90	100.00
NB13	2-2 cpx ph mantle	53.35	24.15	4.20	16.43	0.10	0.71	1.87	0.02	0.33	101.14	1.93	0.02	0.07	0.01	0.08	0.00	0.05	0.05	0.08	0.13	0.00	0.89	0.93	0.02	0.00	4.00	0.87	47.94	45.40	6.66	100.00
NB13	2-3 cpx ph rim	52.99	21.92	3.63	16.82	0.09	0.60	1.57	0.12	0.52	98.26	1.96	0.02	0.04	0.03	0.07	0.00	0.01	0.01	0.10	0.11	0.00	0.93	0.87	0.04	0.00	4.00	0.89	45.45	48.53	6.03	100.00
NB13	2-4 cpx ph cribcore	52.65	24.46	3.65	15.82	0.05	0.44	1.05	0.08	0.48	98.66	1.95	0.01	0.05	0.00	0.05	0.01	0.06	0.06	0.05	0.11	0.00	0.87	0.97	0.03	0.00	4.00	0.89	49.56	44.60	5.84	100.00
NB13	4-1 cpx gm	52.28	23.87	4.25	15.62	0.05	0.82	2.54	0.04	0.50	99.96	1.91	0.02	0.09	0.02	0.11	0.00	0.05	0.05	0.08	0.13	0.00	0.85	0.94	0.04	0.00	4.00	0.87	48.76	44.38	6.86	100.00
NB13	5-10 cpx microph	53.60	23.70	3.61	16.25	0.04	0.64	1.88	0.03	0.39	100.15	1.95	0.02	0.05	0.03	0.08	0.00	0.00	0.00	0.11	0.11	0.00	0.88	0.93	0.03	0.00	4.00	0.89	48.21	45.99	5.80	100.00
NB13	6-1 cpx in cc	55.93	24.65	3.78	15.96	0.08	0.20	0.14	0.00	0.65	101.38	2.02	0.01	0.00	0.01	0.01	0.00	0.00	0.00	0.11	0.11	0.00	0.86	0.95	0.05	0.00	4.00	0.88	49.42	44.53	6.05	100.00
NB13	6-2 cpx in cc	53.53	25.21	4.54	15.90	0.15	0.46	0.27	0.04	0.55	100.66	1.95	0.01	0.01	0.00	0.01	0.04	0.06	0.11	0.03	0.14	0.00	0.86	0.98	0.04	0.00	4.00	0.86	49.43	43.39	7.19	100.00
NB13	6-3 cpx in cc	52.09	24.89	4.63	15.63	0.10	0.90	0.78	0.02	0.55	99.60	1.92	0.02	0.03	0.00	0.03	0.05	0.07	0.12	0.02	0.14	0.00	0.86	0.98	0.04	0.00	4.00	0.86	49.45	43.21	7.34	100.00
NB13	6-5 cpx ph	49.60	24.74	4.37	15.02	0.05	1.81	2.23	0.01	0.45	98.29	1.85	0.05	0.10	0.00	0.10	0.05	0.08	0.13	0.01	0.14	0.00	0.84	0.99	0.03	0.00	4.00	0.86	50.40	42.57	7.03	100.00
NB13	6-6 cpx ph mantle	52.57	24.51	3.74	16.10	0.07	0.62	1.74	0.05	0.43	99.82	1.92	0.02	0.07	0.00	0.07	0.00	0.07	0.08	0.04	0.11	0.00	0.88	0.96	0.03	0.00	4.00	0.88	49.14	44.90	5.96	100.00
NB13	6-7 cpx ph	53.07	22.68	3.74	16.93	0.06	0.38	1.63	0.17	0.60	99.27	1.94	0.01	0.06	0.01	0.07	0.00	0.06	0.06	0.05	0.11	0.00	0.92	0.89	0.04	0.00	4.00	0.89	46.09	47.87	6.03	100.00
NB13	6-8 cpx ph	50.80	22.64	6.26	14.30	0.09	0.64	3.46	0.04	1.08	99.31	1.88	0.02	0.12	0.03	0.15	0.00	0.14	0.14	0.05	0.19	0.00	0.79	0.90	0.08	0.00	4.00	0.80	47.66	41.90	10.44	100.00
NB25	1-13 cpx gm	51.41	24.52	4.81	15.44	0.08	1.92	1.66		0.51	100.34	1.88	0.05	0.07	0.00	0.07	0.04	0.05	0.09	0.06	0.15	0.00	0.84	0.96	0.04	0.00	4.00	0.85	49.22	43.12	7.66	100.00
NB25	2-1 cpx gm	50.86	24.92	5.22	14.31	0.08	2.19	2.19	0.05	0.60	100.43	1.87	0.06	0.10	0.00	0.10	0.03	0.05	0.08	0.08	0.16	0.00	0.78	0.98	0.04	0.00	4.00	0.83	50.90	40.65	8.46	100.00
NB25	2-2 cpx gm	52.42	24.57	4.56	14.88	0.09	1.47	0.74	0.05	0.74	99.52	1.94	0.04	0.03	0.00	0.03	0.03	0.03	0.06	0.08	0.14	0.00	0.82	0.97	0.05	0.00	4.00	0.85	50.24	42.33	7.43	100.00
NB25	2-3 cpx gm	51.86	24.47	4.82	14.39	0.12	2.01	1.56	0.05	0.72	100.00	1.91	0.06	0.07	0.00	0.07	0.02	0.03	0.04	0.10	0.15	0.00	0.79	0.97	0.05	0.00	4.00	0.84	50.61	41.42	7.97	100.00
NB25	2-4 cpx gm	49.30	24.98	4.96	14.43	0.05	2.01	1.72	0.00	0.80	98.24	1.85	0.06	0.08	0.00	0.08	0.08	0.08	0.16	0.00	0.16	0.00	0.81	1.00	0.06	0.00	4.00	0.84	50.96	40.96	8.08	100.00
NB25	3-2 cpx gm	46.64	21.29	7.88	11.56	0.11	2.63	5.00	0.01	0.92	96.05	1.81	0.08	0.19	0.04	0.23	0.00	0.07	0.07	0.19	0.26	0.00	0.67	0.89	0.07	0.00	4.00	0.72	48.82	36.88	14.30	100.00
NB25	3-2 bis cpx gm	44.95	21.04	14.75	13.51	0.16	2.06	2.51		0.70	99.67	1.70	0.06	0.11	0.00	0.11	0.19	0.24	0.43	0.04	0.47	0.00	0.76	0.85	0.05	0.00	4.00	0.62	40.87	36.52	22.61	100.00
NB24	1-4 cpx gm	43.54	24.61	7.66	11.33	0.03	4.00	7.62	0.06	0.43	99.27	1.64	0.11	0.34	0.00	0.34	0.02	0.16	0.18	0.06	0.24	0.00	0.64	0.99	0.03	0.00	4.00	0.72	53.06	33.99	12.95	100.00
NB24	1-9 cpx gm	47.29	24.96	6.60	12.96	0.14	2.86	4.60	0.03	0.48	99.90	1.76	0.08	0.20	0.00	0.20	0.04	0.11	0.15	0.05	0.21	0.00	0.72	1.00	0.03	0.00	4.00	0.78	51.73	37.36	10.91	100.00
NB24	1-13 cpx gm	49.76	24.94	4.95	14.22	0.03	1.45	4.41	0.66	0.38	100.79	1.82	0.04	0.18	0.01	0.19	0.00	0.10	0.10	0.05	0.15	0.00	0.78	0.98	0.03	0.02	4.00	0.84	51.31	40.70	8.00	100.00
NB24	2-14 cpx micropheno core	48.72	21.31	6.32	19.16	0.21	1.90	1.89	0.08	0.61	100.19	1.76	0.05	0.08	0.00	0.08	0.15	0.04	0.20	0.00	0.20	0.01	1.03	0.83	0.04	0.00	4.01	0.84	40.06	50.10	9.84	100.00
NB24	2-15 same cpx micropheno mantle	54.27	23.45	4.55	15.63	0.02	0.62	1.29	0.54	0.61	100.98	1.97	0.02	0.03	0.03	0.06	0.00	0.00	0.00	0.14	0.14	0.00	0.85	0.91	0.04	0.02	4.00	0.86	48.09	44.60	7.31	100.00
NB24	2-16 same cpx micropheno rim	43.63	24.43	7.95	11.44	0.04	4.17	8.10	0.04	0.55	100.34	1.63	0.12	0.36	0.00	0.36	0.02	0.18	0.20	0.05	0.25	0.00	0.64	0.98	0.04	0.00	4.00	0.72	52.43	34.18	13.39	100.00
NB24	2-19 cpx micropheno mantle	53.55	24.88	3.69	16.09	0.08	0.73	1.79	0.01	0.33	101.14	1.94	0.02	0.06	0.01	0.08	0.00	0.04	0.04	0.08	0.11	0.00	0.87	0.96	0.02	0.00	4.00	0.89	49.56	44.58	5.86	100.00
NB24	2-20 same cpx micropheno rim	46.99	24.63	6.62	12.99	0.15	3.41	5.14	0.04	0.53	100.50	1.74	0.09	0.22	0.00	0.22	0.04	0.11	0.14	0.06	0.20	0.00	0.72	0.98	0.04	0.00	4.00	0.78	51.32	37.66	11.02	100.00
NB24	3-1 cpx mantle micropheno	53.78	25.09	3.66	16.29	0.03	0.79	1.83	0.03	0.30	101.80	1.93	0.02	0.07	0.01	0.08	0.00	0.04	0.04	0.07	0.11	0.00	0.87	0.97	0.02	0.00	4.00	0.89	49.55	44.75	5.69	100.00
NB24	3-1bis cpx mantle micropheno	52.58	25.08	3.92	15.71	0.07	0.94	2.73	0.01	0.37	101.42	1.90	0.03	0.10	0.01	0.12	0.00	0.06	0.06	0.05	0.12	0.00	0.84	0.97	0.03	0.00	4.00	0.88	50.11	43.67	6.22	100.00
NB24	3-2 same cpx rim micropheno	49.78	25.08	5.22	14.51	0.08	2.14	3.48	0.02	0.46	100.76	1.82	0.06	0.15	0.00	0.15	0.03	0.09	0.12	0.04	0.16	0.00	0.79	0.98	0.03	0.00	4.00	0.83	50.77	40.86	8.37	100.00
NB15	1-1 phen cpx core	53.87	23.30	3.82	16.26	0.09	0.51	2.09	0.19	0.59	100.71	1.95	0.01	0.05	0.04	0.09	0.00	0.02	0.02	0.10	0.12	0.00	0.88	0.90	0.04	0.01	4.00	0.88	47.58	46.19	6.23	100.00
NB15	1-14 same ph cpx rim	47.88	24.68	6.23	13.41	0.10	2.70	4.16	0.03	0.48	99.67	1.78	0.08	0.18	0.00	0.18	0.04	0.10	0.14	0.06	0.19	0.00	0.74	0.98	0.03	0.00	4.00	0.79	51.13	38.63	10.24	100.00
NB15	1-4 cpx gm	53.19	23.85	3.83	15.71	0.05	0.56	2.18	0.47	0.55	100.38	1.94	0.02	0.06	0.03	0.09	0.00	0.03	0.03	0.09	0.12	0.00	0.85	0.93	0.04	0.01	4.00	0.88	48.95	44.84	6.21	100.00
NB15	1-3 cpx gm	53.87	24.19	3.65	16.33	0.08	0.54	1.72	0.02	0.44	100.85	1.95	0.01	0.05	0.02	0.07	0.00	0.03	0.03	0.08	0.11	0.00	0.88	0.94	0.03	0.00	4.00	0.89	48.55	45.60	5.85	100.00
NB15	1-12 cpx gm	49.04	24.60	5.69	13.96	0.08	2.40	3.70	0.09	0.45	100.02	1.81	0.07	0.16	0.00	0.16	0.02	0.08	0.11	0.07	0.18	0.00	0.77	0.97	0.03	0.00	4.00	0.81	50.70	40.02	9.29	100.00
NB15	2-5 big ph cpx rim	45.38	24.29	7.25	11.95	0.05	3.01	6.92	0.09	0.46	99.41	1.70	0.08	0.30	0.01	0.31	0.00	0.15	0.15	0.07	0.23	0.00	0.67	0.98	0.03	0.00	4.00	0.75	52.12	35.66	12.22	100.00
NB15	2-14 same ph cpx core	52.91	23.91	3.89	15.97	0.11	0.72	2.17	0.07	0.40	100.15	1.93	0.02	0.07	0.02	0.09	0.00	0.03	0.03	0.09	0.12	0.00	0.87	0.93	0.03	0.00	4.00	0.88	48.54	45.12	6.34	100.00
NB15	2-9 cpx gm	52.87	24.08	5.04	14.39	0.25	1.18	0.66	0.02	0.89	99.36	1.96	0.03	0.03	0.00	0.03	0.01	0.04	0.05	0.10	0.16	0.01	0.80	0.96	0.06	0.00	4.00	0.84	49.92	41.52	8.57	100.00
NB15	2-17 cpx pheno rim	50.32	24.28	5.37	14.15	0.09	2.16	3.09	0.00	0.44	99.90	1.86	0.06	0.13	0.00	0.13	0.00	0.05	0.05	0.11	0.17	0.00	0.78	0.96	0.03	0.00	4.00	0.82	50.35	40.82	8.83	100.00
NB15	2-18 same cpx ph core	50.65	24.34	5.34	13.91	0.06	1.21	3.71	0.00	0.42	99.64	1.87	0.03	0.13	0.04	0.16	0.00	0.05	0.05	0.11	0.17	0.00	0.77	0.97	0.03	0.00	4.00	0.82	50.81	40.38	8.81	100.00
NB2	1-2 cpx	53.28	24.47	4.88	15.90	0.12	0.77	1.52	0.01	0.41	101.36	1.93	0.02	0.06	0.00	0.06	0.01	0.06	0.07	0.08	0.15	0.00	0.86	0.95	0.03	0.00	4.00	0.85	48.46	43.81	7.73	100.00
NB2	1-4 gm cpx	52.87	25.00	4.38	15.61	0.03	0.97	1.78	0.06	0.30	101.00	1.92	0.03	0.08	0.00	0.08	0.00	0.05	0.05	0.08	0.13	0.00	0.85	0.97	0.02	0.00	4.00	0.86	49.83	43.30	6.87	100.00
NB2	1-12 gm cpx	53.45	24.19	4.19	15.74	0.16	1.52	0.86	0.00	0.74	100.84	1.94	0.04	0.04	0.00	0.04	0.02	0.03	0.05	0.08	0.13	0.00	0.85	0.94	0.05	0.00	4.00	0.87	48.88	44.26	6.86	100.00
NB2	1-16 gm	48.83	22.30	5.76	14.38	0.08	2.59	3.43	0.06	0.67	98.11	1.84	0.07	0.15	0.00	0.15	0.01	0.06	0.08	0.10	0.18	0.00	0.81	0.90	0.05	0.00	4.00	0.82	47.58	42.69	9.73	100.00
NB2	2-1 cpx pheno core	52.82	24.65	3.85	16.73	0.10	0.49	1.26	0.00	0.34	100.24	1.92	0.01	0.05	0.00	0.05	0.03	0.08	0.10	0.02	0.12	0.00	0.91	0.96	0.02	0.00	4.00	0.89	48.32	45.64	6.04	100.00
NB2	2-1 cpx pheno rim	51.94	24.24	4.12	16.39	0.06	0.74	2.08	0.05	0.50	100.12	1.89	0.02	0.09	0.00	0.09	0.02	0.10	0.12	0.00	0.13	0.00	0.89	0.95	0.04	0.00	4.00	0.88	48.19	45.32	6.49	100.00
NB2	2-2 gm cpx	51.51	24.60	4.22	15.92	0.06	0.73	2.00	0.00	0.44	99.48	1.89	0.02	0.09	0.00	0.09	0.02	0.10	0.12	0.01	0.13	0.00	0.87	0.97	0.03	0.00	4.00	0.87	49.10	44.23	6.67	100.00
NB2	2-5 gm cpx	53.04	24.71	3.86	16.56	0.14	0.56	1.38	0.00	0.34	100.58	1.92	0.02	0.06	0.00	0.06	0.02	0.07	0.09	0.03	0.12	0.00	0.90	0.96	0.02	0.00	4.00	0.88	48.58	45.29	6.14	100.00
NB2	2-6 gm cpx	50.30	25.11	4.45	15.27	0.05	1.94	1.99	0.04	0.59	99.74	1.85	0.05	0.09	0.00	0.09	0.06	0.08	0.14	0.00	0.14	0.00	0.84	0.99	0.04	0.00	4.00	0.86	50.31	42.57	7.12	100.00
NB2	2-12 gm	50.96	24.22	4.28	15.94	0.04	0.76	1.98	0.06	0.71	98.95	1.88	0.02	0.09	0.00	0.09	0.04	0.10	0.13	0.00	0.13	0.00	0.88	0.96	0.05	0.00	4.00	0.87	48.61	44.52	6.87	100.00
NB20	1-3 gm cpx	53.15	24.14	3.82	15.68	0.07	0.84	1.68	0.01	0.41	99.79	1.86	0.05	0.14	0.02	0.16	0.00	0.06	0.06	0.11	0.17	0.00	0.78	0.94	0.04	0.00	4.00	0.82	49.28	44.53	6.19	100.00
NB20	1-4 gm cpx	52.59	23.56	4.00	15.44	0.05	0.75	2.20	0.04	0.48	99.09	1.86	0.05	0.14	0.02	0.16	0.00	0.06	0.06	0.11	0.17	0.00	0.78	0.94	0.04	0.00	4.00	0.82	48.87	44.57	6.56	100.00

Table 3: (continued)

Sample	Point	SiO_2	CaO	FeO	MgO	MnO	TiO_2	Al_2O_3	Cr_2O_3	Na_2O	Total	Si	Ti	Al (T)	Al (M1)	Al (tot)	Fe^{3+} (T)	Fe^{3+} (M1)	Fe^{3+}(tot)	Fe^{2+}	Fe(tot)	Mn	Mg	Ca	Na	Cr	Total	Mg#	Wo	En	Fs	Total
NB20	1-5 cpx gm	53.03	24.08	4.06	15.58	0.02	0.74	2.02	0.01	0.52	100.07	1.94	0.02	0.06	0.03	0.09	0.00	0.03	0.03	0.09	0.12	0.00	0.85	0.94	0.04	0.00	4.00	0.87	49.20	44.30	6.50	100.00
NB20	1-10 cpx gm	52.15	23.29	4.54	15.03	0.06	1.03	2.80	0.01	0.56	99.47	1.86	0.05	0.14	0.02	0.16	0.00	0.06	0.06	0.11	0.17	0.00	0.78	0.94	0.04	0.00	4.00	0.82	48.74	43.75	7.51	100.00
NB20	1-11 cpx gm	53.43	23.81	4.03	15.41	0.07	0.65	1.55	0.04	0.40	99.38	1.97	0.02	0.03	0.04	0.07	0.00	0.00	0.00	0.12	0.12	0.00	0.85	0.94	0.04	0.00	4.01	0.87	49.15	44.26	6.60	100.00
NB20	1-12 cpx gm	53.33	23.73	3.98	15.24	0.03	0.65	2.04	0.00	0.50	99.50	1.96	0.02	0.04	0.05	0.09	0.00	0.00	0.00	0.12	0.12	0.00	0.84	0.94	0.04	0.00	4.00	0.87	49.37	44.12	6.51	100.00
NB20	1-13 cpx gm	53.85	23.59	3.65	15.81	0.05	0.56	1.38	0.05	0.39	99.31	1.98	0.02	0.02	0.04	0.06	0.00	0.00	0.00	0.11	0.11	0.00	0.87	0.93	0.03	0.00	4.00	0.89	48.67	45.38	5.95	100.00
NB20	1-15 cpx gm	53.57	23.92	3.70	16.38	0.06	0.48	1.40	0.02	0.44	99.97	1.95	0.01	0.05	0.01	0.06	0.00	0.03	0.03	0.08	0.11	0.00	0.89	0.93	0.03	0.00	4.00	0.89	48.17	45.91	5.91	100.00
NB20	1-16 cpx gm	53.05	22.65	4.94	14.94	0.08	0.97	1.85	0.02	0.69	99.17	1.86	0.05	0.14	0.02	0.16	0.00	0.06	0.06	0.11	0.17	0.00	0.78	0.94	0.04	0.00	4.00	0.82	47.82	43.90	8.27	100.00
NB20	1-17 cpx gm	53.73	23.53	4.59	15.90	0.09	0.60	1.63	0.06	0.51	100.64	1.86	0.05	0.14	0.02	0.16	0.00	0.06	0.06	0.11	0.17	0.00	0.78	0.94	0.04	0.00	4.00	0.82	47.73	44.88	7.39	100.00
NB20	1-19 cpx gm	53.33	23.25	3.72	16.10	0.06	0.58	1.69	0.03	0.35	99.09	1.86	0.05	0.14	0.02	0.16	0.00	0.06	0.06	0.11	0.17	0.00	0.78	0.94	0.04	0.00	4.00	0.82	47.85	46.09	6.06	100.00
NB20	1-19 gm cpx	52.94	24.32	3.65	15.83	0.12	0.61	1.44	0.03	0.35	99.28	1.95	0.02	0.05	0.01	0.06	0.00	0.03	0.03	0.08	0.11	0.00	0.87	0.96	0.02	0.00	4.00	0.89	49.35	44.67	5.97	100.00
NB20	1-20a gm cpx	52.33	23.76	3.99	15.44	0.02	0.73	2.20	0.00	0.52	98.99	1.93	0.02	0.07	0.03	0.10	0.00	0.04	0.04	0.09	0.12	0.00	0.85	0.94	0.04	0.00	4.00	0.87	49.12	44.41	6.47	100.00
NB20	1-21a gm cpx	52.56	23.79	3.85	16.02	0.07	0.62	1.48	0.00	0.41	98.79	1.94	0.02	0.06	0.01	0.06	0.00	0.04	0.04	0.07	0.12	0.00	0.88	0.94	0.03	0.00	4.00	0.88	48.40	45.36	6.23	100.00
NB20	2-4 cpx gm	50.68	22.54	5.57	14.15	0.08	2.26	2.93	0.00	1.20	99.41	1.86	0.05	0.14	0.02	0.16	0.00	0.06	0.06	0.11	0.17	0.00	0.78	0.94	0.04	0.00	4.00	0.82	48.32	42.22	9.46	100.00
NB20	2-7 cpx gm	50.58	23.73	5.46	14.26	0.12	1.69	3.57	0.08	0.53	100.03	1.86	0.05	0.14	0.02	0.16	0.00	0.06	0.06	0.11	0.17	0.00	0.78	0.94	0.04	0.00	4.00	0.82	49.50	41.40	9.10	100.00
NB20	random cpx	50.78	15.88	6.48	15.82	0.17	0.80	8.39	0.15	1.27	99.73	1.85	0.02	0.15	0.21	0.36	0.00	0.00	0.00	0.20	0.20	0.01	0.86	0.62	0.09	0.00	4.00	0.81	36.86	51.09	12.05	100.00
NB8	1-14b gm cpx	44.30	23.53	7.30	11.68	0.07	4.22	6.24	0.09	0.56	98.00	1.69	0.12	0.28	0.00	0.28	0.03	0.11	0.13	0.10	0.23	0.00	0.66	0.96	0.04	0.00	4.00	0.74	51.68	35.68	12.65	100.00
NB28	1-7 gm cpx	48.83	24.27	5.40	14.44	0.03	1.69	3.82	0.14	0.39	99.02	1.82	0.05	0.17	0.00	0.17	0.02	0.11	0.13	0.04	0.17	0.00	0.80	0.97	0.03	0.00	4.00	0.83	49.93	41.34	8.73	100.00
NB28	1-11A gm cpx	46.11	24.00	6.70	13.34	0.16	2.55	5.15	0.00	0.50	98.50	1.73	0.07	0.23	0.00	0.23	0.04	0.16	0.20	0.01	0.21	0.01	0.75	0.97	0.04	0.00	4.00	0.78	50.09	38.74	11.17	100.00
NB28	1-12A cpx gm	48.15	24.07	5.67	14.55	0.14	1.81	3.92	0.23	0.32	98.86	1.80	0.05	0.17	0.00	0.17	0.03	0.12	0.15	0.03	0.18	0.00	0.81	0.96	0.02	0.01	4.00	0.82	49.27	41.44	9.28	100.00
NB28	2-1 micro cpx	50.82	24.35	5.02	14.96	0.11	1.37	3.54	0.21	0.39	100.76	1.85	0.04	0.15	0.01	0.15	0.00	0.09	0.09	0.07	0.15	0.00	0.81	0.95	0.03	0.01	4.00	0.84	49.53	42.33	8.14	100.00
NB28	2-2 micro cpx	50.18	23.97	5.08	14.99	0.04	1.41	3.64	0.29	0.44	100.04	1.84	0.04	0.16	0.00	0.16	0.00	0.10	0.10	0.05	0.16	0.00	0.82	0.94	0.03	0.01	4.00	0.84	49.10	42.71	8.19	100.00
NB28	2-1A gm cpx	48.58	23.55	5.70	13.94	0.10	2.01	4.98	0.32	0.50	99.69	1.80	0.06	0.20	0.02	0.22	0.00	0.10	0.10	0.08	0.18	0.00	0.77	0.93	0.04	0.01	4.00	0.81	49.61	40.86	9.54	100.00
NB28	2-13A gm cpx	48.53	24.07	5.76	14.26	0.08	1.83	4.25	0.19	0.34	99.31	1.80	0.05	0.19	0.00	0.19	0.01	0.11	0.12	0.05	0.18	0.00	0.79	0.96	0.02	0.01	4.00	0.82	49.65	40.94	9.41	100.00
NB28	3-12 gm cpx	47.64	23.72	6.23	13.58	0.16	2.04	4.84	0.04	0.36	98.60	1.79	0.06	0.21	0.00	0.21	0.00	0.12	0.12	0.08	0.20	0.00	0.76	0.95	0.03	0.00	4.00	0.80	49.84	39.68	10.48	100.00
NB28	3-14 gm cpx	48.91	23.98	6.29	14.13	0.07	1.87	4.03	0.00	0.41	99.69	1.81	0.05	0.18	0.00	0.18	0.01	0.11	0.12	0.07	0.19	0.00	0.78	0.95	0.03	0.00	4.00	0.80	49.34	40.45	10.22	100.00
NB28	3-16 gm cpx	50.61	23.94	5.65	14.58	0.12	1.77	2.79	0.00	0.76	100.22	1.86	0.05	0.12	0.00	0.12	0.02	0.10	0.12	0.06	0.17	0.00	0.80	0.94	0.05	0.00	4.00	0.82	49.12	41.63	9.25	100.00
NB28	3-19gm cpx	47.77	24.05	5.70	13.42	0.02	2.04	5.62	0.68	0.43	99.72	1.77	0.06	0.23	0.02	0.25	0.00	0.11	0.11	0.07	0.18	0.00	0.74	0.96	0.03	0.02	4.00	0.81	50.97	39.57	9.47	100.00
NB28	3-22 gm cpx	49.55	23.84	5.70	14.50	0.07	1.70	3.88	0.22	0.40	99.85	1.83	0.05	0.17	0.00	0.17	0.00	0.10	0.10	0.08	0.18	0.00	0.80	0.94	0.03	0.01	4.00	0.82	49.14	41.59	9.28	100.00
NB28	3-23 gm cpx	51.23	23.68	4.88	15.04	0.07	1.40	3.24	0.32	0.38	100.24	1.88	0.04	0.12	0.02	0.14	0.00	0.04	0.04	0.11	0.15	0.00	0.82	0.93	0.03	0.01	4.00	0.85	48.85	43.17	7.97	100.00
NB28	3-29 px microcryst	45.64	23.95	6.47	12.74	0.07	2.73	6.61	0.26	0.58	99.04	1.71	0.08	0.29	0.00	0.29	0.00	0.17	0.18	0.03	0.20	0.00	0.71	0.96	0.04	0.01	4.00	0.78	51.19	37.89	10.92	100.00
NB28	4-2 pheno cpx rim	50.51	24.17	5.13	14.70	0.03	1.51	3.59	0.28	0.34	100.27	1.86	0.04	0.14	0.01	0.16	0.00	0.07	0.07	0.09	0.16	0.00	0.81	0.95	0.02	0.01	4.00	0.84	49.68	42.03	8.29	100.00
NB28	4-3 pheno cpx core	50.97	24.22	4.98	14.95	0.07	1.32	3.34	0.33	0.40	100.57	1.86	0.04	0.14	0.01	0.14	0.00	0.07	0.07	0.08	0.15	0.00	0.81	0.95	0.03	0.01	4.00	0.84	49.48	42.48	8.05	100.00
NB28	4-4 gm cpx	47.51	24.28	6.09	13.09	0.09	2.30	5.84	0.36	0.52	100.07	1.76	0.06	0.24	0.01	0.25	0.00	0.13	0.13	0.06	0.19	0.00	0.72	0.96	0.04	0.01	4.00	0.79	51.31	38.50	10.19	100.00
NB28	5-3 micro cpx	51.62	24.69	4.81	15.23	0.08	1.29	3.10	0.33	0.37	101.51	1.87	0.04	0.13	0.00	0.13	0.00	0.08	0.08	0.07	0.15	0.00	0.82	0.96	0.03	0.01	4.00	0.85	49.68	42.63	7.69	100.00
NB33	1-3 gm cpx	45.03	23.40	9.18	12.68	0.23	2.69	4.73	0.04	0.60	98.56	1.70	0.08	0.21	0.00	0.21	0.08	0.18	0.27	0.02	0.29	0.01	0.72	0.95	0.04	0.00	4.00	0.71	48.37	36.45	15.18	100.00
NB33	2-1A gm cpx	45.39	23.59	6.94	12.21	0.05	3.17	6.67	0.33	0.69	99.04	1.70	0.09	0.30	0.00	0.30	0.00	0.16	0.16	0.06	0.22	0.00	0.68	0.95	0.05	0.01	4.00	0.76	51.24	36.90	11.85	100.00
NB33	2-3A gm cpx	47.42	22.61	7.63	12.57	0.19	2.59	4.53	0.01	1.21	98.75	1.78	0.07	0.20	0.00	0.20	0.02	0.16	0.18	0.06	0.24	0.01	0.70	0.91	0.09	0.00	4.00	0.75	48.94	37.85	13.21	100.00
NB33	2-18 gm cpx	45.44	23.82	7.35	12.01	0.07	3.18	6.78	0.05	0.60	99.30	1.70	0.09	0.30	0.00	0.30	0.00	0.15	0.15	0.08	0.23	0.00	0.67	0.96	0.04	0.00	4.00	0.74	51.43	36.07	12.50	100.00
NB33	3-4A gm cpx	44.38	23.66	7.85	11.98	0.09	3.44	7.24	0.04	0.57	99.25	1.67	0.10	0.32	0.00	0.32	0.01	0.18	0.19	0.05	0.25	0.00	0.67	0.95	0.04	0.00	4.00	0.73	50.86	35.82	13.32	100.00
NB33	3-10A gm cpx	45.04	21.42	8.23	10.89	0.10	3.16	8.52	0.08	1.82	99.25	1.68	0.09	0.32	0.06	0.37	0.00	0.22	0.22	0.04	0.26	0.00	0.61	0.86	0.13	0.00	4.00	0.70	49.73	35.17	15.10	100.00
NB33	random gm cpx	45.04	24.23	7.16	12.41	0.05	2.81	6.83	0.04	0.49	99.06	1.69	0.08	0.30	0.00	0.30	0.01	0.19	0.20	0.03	0.22	0.00	0.69	0.97	0.04	0.00	4.00	0.76	51.41	36.63	11.95	100.00
NB33	random gm	44.22	23.74	6.65	12.04	0.07	3.29	7.35		0.50	97.85	1.68	0.09	0.32	0.01	0.33	0.00	0.16	0.16	0.05	0.21	0.00	0.68	0.97	0.04	0.00	4.00	0.76	51.91	36.62	11.46	100.00
NB33	random gm bis	43.83	23.33	7.28	12.29	0.08	3.43	7.49		0.47	98.20	1.66	0.10	0.33	0.00	0.33	0.01	0.18	0.19	0.04	0.23	0.00	0.69	0.95	0.03	0.00	4.00	0.75	50.52	37.03	12.45	100.00

Table 4: EMP analysis for Nowbaran mica compositions

Sample	Point	SiO_2	TiO_2	Al_2O_3	FeO	MnO	MgO	CaO	Na_2O	K_2O	SO_3	F	Cl	P_2O_5	Total	Si	Ti	Al	Fe	Mn	Mg	Ca	Na	K	Ba	Cr	F	Cl	Total	Mg#	K#
NB13	3-2 bt gm	36.17	6.19	19.11	5.54	0.07	18.93	0.05	0.37	7.33	0.01	5.29	0.01		99.06	5.25	0.68	3.27	0.67	0.01	4.10	0.01	0.10	1.36	0.00	0.00	2.43	0.01	17.87	85.9	92.8
NB13	3-4 bt gm	34.68	4.68	22.30	4.88	0.06	16.63	0.51	3.03	6.64	0.71	4.33	0.26		98.69	4.98	0.50	3.77	0.59	0.01	3.56	0.08	0.84	1.21	0.00	0.06	1.96	0.06	17.63	85.9	59.0
NB13	4-3 bt gm	32.63	7.27	17.07	13.59	0.20	17.47	0.09	0.30	6.45	0.03	3.76	0.01		98.87	4.91	0.82	3.03	1.71	0.03	3.92	0.01	0.09	1.24	0.00	0.00	1.79	0.00	17.54	69.6	93.5
NB13	7-2 bt interst	37.11	6.04	18.52	5.41	0.10	19.46	0.05	0.32	7.94	0.00	5.21	0.02		100.15	5.32	0.65	3.13	0.65	0.01	4.16	0.01	0.09	1.45	0.00	0.00	2.36	0.00	17.83	86.5	94.3
NB13	7-3 bt interst	36.55	6.72	17.42	4.98	0.07	19.46	0.05	0.28	8.29	0.02	4.64	0.00		98.48	5.31	0.73	2.98	0.60	0.01	4.21	0.01	0.08	1.54	0.00	0.00	2.13	0.00	17.60	87.5	95.1
NB2	1-6 gm bt	40.06	6.49	10.49	5.29	0.00	19.73	0.07	0.55	9.03	0.01	4.85	0.02	0.04	96.65	5.95	0.72	1.84	0.66	0.00	4.37	0.01	0.16	1.71	0.00	0.00	2.28	0.01	17.69	86.9	91.6
NB2	1-7 gm	40.93	6.29	9.33	5.36	0.08	19.96	1.35	0.59	8.75	0.05	4.90	0.01	0.04	97.62	6.04	0.70	1.62	0.66	0.01	4.39	0.21	0.17	1.65	0.00	0.00	2.28	0.00	17.74	86.9	90.7
NB2	1-11 gm bt	43.73	5.80	6.53	5.52	0.06	17.91	8.49	0.67	7.06	0.00	3.58	0.00	0.04	99.37	6.35	0.63	1.12	0.67	0.01	3.87	1.32	0.19	1.31	0.00	0.00	1.64	0.00	17.10	85.3	87.4
NB2	1-23 bt pheno	37.60	5.40	12.04	4.11	0.05	20.99	0.02	0.37	8.38	0.05	5.77	0.00	0.00	94.78	5.73	0.62	2.16	0.52	0.01	4.77	0.00	0.11	1.63	0.00	0.00	2.78	0.00	18.35	90.1	93.7
NB2	1-23 bt pheno bis	36.66	5.83	12.29	4.19	0.03	20.07	0.01	0.37	7.85	0.03	5.67	0.01	0.00	93.00	5.70	0.68	2.25	0.54	0.00	4.65	0.00	0.11	1.56	0.00	0.00	2.78	0.00	18.28	89.5	93.4
NB2	random gm bt	38.36	5.82	11.05	4.71	0.01	20.09	0.06	0.36	8.43	0.02	5.10	0.01	0.01	94.02	5.87	0.67	1.99	0.60	0.00	4.58	0.01	0.11	1.64	0.00	0.00	2.47	0.00	17.94	88.4	93.2
NB20	1a random gm bt	35.36	8.01	12.12	5.93	0.13	17.98	0.05	0.43	7.77	0.01	4.15	0.01	0.00	91.95	5.54	0.94	2.24	0.78	0.02	4.20	0.01	0.13	1.55	0.00	0.00	2.06	0.00	17.46	84.4	93.2
NB20	3-16 gm bt	35.52	8.30	12.09	5.49	0.12	17.99	0.15	0.46	8.09	0.01	3.70	0.01	0.00	91.93	5.53	0.97	2.22	0.71	0.02	4.17	0.02	0.14	1.61	0.00	0.00	1.82	0.00	17.21	85.4	93.2
NB20	3-18 gm bt	37.29	7.99	12.01	5.47	0.07	18.28	0.09	0.49	8.22	0.01	3.66	0.02	0.00	93.61	5.67	0.91	2.15	0.70	0.01	4.14	0.01	0.15	1.59	0.00	0.00	1.76	0.00	17.10	85.6	93.2
NB28	1-1A gm	37.92	6.12	8.45	8.33	0.11	12.63	12.55	0.79	3.09	0.06	1.65	0.02	2.35	94.07	6.02	0.73	1.58	1.11	0.01	2.99	2.14	0.24	0.63	0.00	0.00	0.83	0.00	16.29	73.0	72.0
NB28	3-20 gm bt	38.43	4.48	21.43	5.68	0.01	6.15	1.03	8.54	3.74	0.99	1.07	0.41	0.06	92.01	5.60	0.49	3.68	0.69	0.00	1.34	0.16	2.41	0.69	0.00	0.00	0.49	0.10	15.66	65.9	22.4
NB28	4-12A gm bt	41.26	7.26	15.67	7.87	0.08	9.12	1.51	2.05	5.77	0.04	2.00	0.09	0.00	92.71	6.15	0.81	2.75	0.98	0.01	2.03	0.24	0.59	1.10	0.00	0.00	0.94	0.02	15.63	67.4	64.9

Table 5: EMP analysis for Nowbaran carbonate compositions

Sample	Point	CaO	MgO	MnO	FeO	SrO	BaO	Total	Fe''	Mn	Mg	Ca	Sr	Total	Ca#
NB13	1-11 cc gm	54.47	0.56	0.03	0.03	0.08	0.00	55.16	0.00	0.00	0.01	0.98	0.00	1.00	0.99
NB13	4-2 cc interst	54.60	0.39	0.01	0.02	0.04	0.05	55.10	0.00	0.00	0.01	0.99	0.00	1.00	0.99
NB13	5-1 cc interst	54.43	0.44	0.00	0.02	0.04	0.01	54.94	0.00	0.00	0.01	0.99	0.00	1.00	0.99
NB13	5-2 cc interst	54.09	0.80	0.00	0.06	0.04	0.00	54.99	0.00	0.00	0.02	0.98	0.00	1.00	0.98
NB13	5-3 cc interst	54.71	0.58	0.03	0.03	0.00	0.00	55.34	0.00	0.00	0.01	0.98	0.00	1.00	0.99
NB13	5-13 cc interst	53.11	0.73	0.04	0.00	0.09	0.00	53.97	0.00	0.00	0.02	0.98	0.00	1.00	0.98
NB13	6-11 cc plague	57.70	0.15	0.00	0.01	0.00	0.00	57.86	0.00	0.00	0.00	1.00	0.00	1.00	1.00
NB13	6-14 cc plague	54.52	0.72	0.00	0.09	0.08	0.05	55.46	0.00	0.00	0.02	0.98	0.00	1.00	0.98
NB13	7-1 cc interst	56.23	0.28	0.00	0.23			56.75	0.00	0.00	0.01	0.99	0.00	1.00	0.99
NB13	7-5 cc interst	55.19	0.07	0.03	0.10	0.01	0.00	55.39	0.00	0.00	0.00	1.00	0.00	1.00	1.00
NB2	2-3 cc	55.60	0.21	0.04	0.03	0.02		55.89	0.00	0.00	0.01	0.99	0.00	1.00	0.99
NB2	random cc	54.51	0.22	0.00	0.00	0.02		54.76	0.00	0.00	0.01	0.99	0.00	1.00	0.99
NB8	1-3a cc	54.34	0.19	0.00	0.15	0.32		55.00	0.00	0.00	0.00	0.99	0.00	1.00	1.00
NB8	1-4 cc	54.72	0.31	0.00	0.08	0.01		55.13	0.00	0.00	0.01	0.99	0.00	1.00	0.99
NB8	1-5 cc	54.55	0.26	0.03	0.00	0.00		54.84	0.00	0.00	0.01	0.99	0.00	1.00	0.99
NB8	1-6b cc	56.96	0.11	0.00	0.04	0.00		57.12	0.00	0.00	0.00	1.00	0.00	1.00	1.00
NB8	1-10 cc gm	52.57	0.36	0.09	1.54			54.56	0.02	0.00	0.01	0.97	0.00	1.00	0.99
NB8	1-13 cc gm	53.84	0.25	0.00	0.24			54.33	0.00	0.00	0.01	0.99	0.00	1.00	0.99
NB8	1-15a cc	56.61	0.16	0.02	0.10	0.03		56.92	0.00	0.00	0.00	0.99	0.00	1.00	1.00
NB8	2-8 cc	48.36	0.27	0.00	0.33	0.03		48.98	0.01	0.00	0.01	0.99	0.00	1.00	0.99
NB28	1-2 cc in ol vein	52.18	3.01	0.00	0.11	0.03		55.34	0.00	0.00	0.07	0.92	0.00	1.00	0.93
NB28	1-9 cc in ol vein	52.23	3.20	0.00	0.10	0.02		55.55	0.00	0.00	0.08	0.92	0.00	1.00	0.92
NB28	2-5 gm	53.69	2.21	0.05	0.05			55.99	0.00	0.00	0.05	0.94	0.00	1.00	0.95

Table 6: EMP analysis for Nowbaran opaque compositions

Sample	Point	TiO_2	Al_2O_3	FeO	MnO	MgO	Cr_2O_3	Total	Ti	Al	Fe'''	Fe''	Mn	Mg	Cr	Total	Usp	Mg#	Cr#
NB13	6-9 mt in cc	13.88	0.74	76.78	1.29	4.79	0.00	97.48	0.44	0.04	1.22	1.08	0.05	0.30	0.00	3.13	0.42	0.21	0.00
NB13	6-10 mt in cc	14.15	0.61	76.93	1.21	4.74	0.00	97.63	0.45	0.03	1.21	1.09	0.04	0.30	0.00	3.12	0.43	0.21	0.00
NB13	7-6 mt gm	10.98	0.36	76.84	1.01	5.42	0.42	95.03	0.36	0.02	1.37	0.98	0.04	0.36	0.01	3.14	0.35	0.26	0.44
NB13	7-7 mt gm	12.40	0.35	74.38	1.15	5.12	0.37	93.78	0.41	0.02	1.28	1.03	0.04	0.34	0.01	3.13	0.39	0.24	0.41
NB13	7-8 mt gm	12.55	0.31	74.33	1.29	5.22	0.31	94.01	0.42	0.02	1.28	1.02	0.05	0.34	0.01	3.13	0.39	0.24	0.40
NB15	1-10 mt gm	12.79	0.47	73.37	1.28	5.56	0.55	94.01	0.42	0.02	1.25	1.01	0.05	0.36	0.02	3.14	0.40	0.26	0.44
NB15	2-6 mt gm	12.68	0.41	74.25	1.21	5.29	0.29	94.12	0.42	0.02	1.27	1.02	0.04	0.35	0.01	3.13	0.40	0.24	0.32
NB15	2-15 mt gm	12.89	0.42	73.92	1.22	5.42	0.44	94.31	0.42	0.02	1.26	1.02	0.05	0.35	0.02	3.13	0.40	0.25	0.41
NB15	2-16 mt gm	12.78	0.48	73.89	1.23	5.52	0.52	94.42	0.42	0.02	1.26	1.01	0.05	0.36	0.02	3.14	0.40	0.25	0.42
NB15	2-19 mt gm	12.50	0.64	74.70	1.25	4.43	0.25	93.78	0.42	0.03	1.26	1.06	0.05	0.29	0.01	3.13	0.40	0.21	0.21
NB2	1-21 op	10.63	0.08	77.50	0.90	3.21	0.76	93.07	0.37	0.00	1.37	1.09	0.03	0.22	0.03	3.11	0.35	0.16	0.87
NB2	1-22 op	11.68	0.10	79.63	1.00	3.49	1.08	96.97	0.38	0.00	1.33	1.10	0.04	0.23	0.04	3.11	0.37	0.17	0.88
NB20	2-13 op	11.18	0.39	74.51	1.11	5.72	0.13	93.03	0.38	0.02	1.35	0.96	0.04	0.38	0.00	3.14	0.36	0.28	0.18
NB28	1-8A gm op	16.79	1.46	68.99	1.09	5.28	0.06	93.66	0.47	0.06	1.00	1.14	0.03	0.29	0.00	3.00	0.48	0.20	0.02
NB28	1-12 gm op	16.24	1.42	69.24	1.19	4.82	0.05	92.96	0.46	0.06	1.02	1.15	0.04	0.27	0.00	3.00	0.47	0.18	0.02
NB28	1-13 gm op	12.52	0.40	76.02	0.84	1.89	0.16	91.82	0.37	0.02	1.24	1.23	0.03	0.11	0.00	3.00	0.37	0.08	0.21
NB28	2-6A gm op	17.97	0.24	72.80	1.25	2.49	0.04	94.79	0.51	0.01	0.97	1.33	0.04	0.14	0.00	3.00	0.51	0.09	0.11
NB28	2-10A gm op	18.59	0.35	72.08	0.92	2.35	0.26	94.55	0.53	0.02	0.92	1.37	0.03	0.13	0.01	3.00	0.54	0.09	0.33
NB28	3-9 gm op	15.79	0.77	73.84	1.13	3.78	0.08	95.39	0.44	0.03	1.09	1.20	0.04	0.21	0.00	3.00	0.45	0.14	0.07
NB28	3-21 gm op	16.14	0.89	72.68	1.14	4.16	0.14	95.15	0.45	0.04	1.06	1.18	0.04	0.23	0.00	3.00	0.46	0.16	0.10
NB28	3-31 op	14.13	2.50	72.26	0.79	4.96	0.55	95.20	0.39	0.11	1.10	1.09	0.02	0.27	0.02	3.00	0.41	0.19	0.13
NB28	3-32 op	13.51	2.71	72.49	0.62	4.93	1.58	95.84	0.37	0.12	1.11	1.08	0.02	0.27	0.05	3.00	0.40	0.19	0.28
NB28	4-10 gm op	16.17	0.55	72.12	1.08	3.59	2.35	95.85	0.45	0.02	1.01	1.22	0.03	0.20	0.07	3.00	0.47	0.14	0.74
NB33	2-5A gm op	7.99	0.25	81.32	1.08	2.17	0.03	92.84	0.23	0.01	1.53	1.07	0.04	0.12	0.00	3.00	0.23	0.10	0.07

Table 7: EMP analysis for Nowbaran apatite compositions

Sample	Point	SO_3	P_2O_5	SiO_2	MgO	CaO	FeO	F	Cl	Total	Ca	Fe	Mg	P	Si	Cl	F	OH	Total
NB13	2-10 ap gm	1.16	37.77	1.01	0.08	55.03	0.18	5.17	0.02	100.41	9.87	0.02	0.02	5.35	0.17	0.01	2.73	-1.74	16.43
NB13	5-14 ap in cc	0.33	36.51	0.87	0.09	54.96	0.07	3.70	0.03	96.57	10.23	0.01	0.02	5.37	0.15	0.01	2.03	-1.04	16.78
NB13	6-12 ap in cc	0.53	38.93	1.08	0.10	55.17	0.04	4.47	0.07	100.39	9.79	0.01	0.02	5.46	0.18	0.02	2.34	-1.36	16.46
NB24	1-2 ap gm	0.83	39.57	0.90	0.05	54.12	0.20	4.85	0.02	100.55	9.57	0.03	0.01	5.53	0.15	0.01	2.53	-1.54	16.29
NB24	2-4 ap gm	1.05	38.68	1.17	0.15	55.06	1.61	3.26	0.05	101.03	9.83	0.22	0.04	5.46	0.20	0.01	1.72	-0.73	16.75
NB24	3-4 ap gm	1.00	38.56	1.30	0.11	55.53	0.27	3.30	0.05	100.12	9.96	0.04	0.03	5.46	0.22	0.01	1.75	-0.76	16.70
NB15	1-2 ap gm	0.82	35.35	0.94	0.53	51.08	5.29	3.46	0.03	97.49	9.63	0.78	0.14	5.26	0.17	0.01	1.92	-0.93	16.97
NB15	1-11 ap gm	0.69	36.95	1.01	0.07	53.02	0.37	3.58	0.03	95.71	9.92	0.05	0.02	5.46	0.18	0.01	1.98	-0.99	16.63
NB15	2-1 ap gm	1.24	37.24	1.09	0.14	55.13	0.23	3.87	0.06	98.99	10.07	0.03	0.04	5.38	0.18	0.02	2.09	-1.10	16.70
NB15	2-4 ap gm	1.02	36.88	1.12	0.15	55.49	0.20	4.13	0.08	99.07	10.13	0.03	0.04	5.32	0.19	0.02	2.22	-1.25	16.71
NB15	2-11 ap gm	1.49	36.24	1.20	0.10	55.14	0.31	2.99	0.06	97.54	10.30	0.05	0.03	5.35	0.21	0.02	1.65	-0.67	16.93
NB2	1-1 ap gm	1.06	35.55	1.09	0.42	48.27	8.38	3.47	0.00	98.23	9.09	1.23	0.11	5.29	0.19	0.00	1.93	-0.93	16.91
NB2	1-5 ap gm	0.48	39.60	1.73	0.35	52.81	0.21	3.87	0.01	99.06	9.39	0.03	0.09	5.56	0.29	0.00	2.03	-1.03	16.35
NB2	1-9 gm ap	0.98	37.52	2.20	0.15	49.97	0.75	3.84	0.02	95.43	9.28	0.11	0.04	5.50	0.38	0.01	2.10	-1.11	16.31
NB2	2-9 gm ap	0.95	39.14	0.91	0.14	52.75	2.37	4.29	0.01	100.56	9.41	0.33	0.03	5.52	0.15	0.00	2.26	-1.26	16.44
NB2	1-18 gm	0.75	39.89	1.22	0.09	51.84	0.45	3.32	0.00	97.57	9.37	0.06	0.02	5.70	0.21	0.00	1.77	-0.77	16.36
NB2	1-19 gm	1.17	39.03	1.53	0.07	51.43	0.41	3.73	0.03	97.39	9.36	0.06	0.02	5.61	0.26	0.01	2.00	-1.01	16.31
NB20	1-7a gm ap	1.02	38.22	1.65	0.13	51.58	0.24	3.82	0.01	96.67	9.47	0.03	0.03	5.54	0.28	0.00	2.07	-1.07	16.36
NB20	1-15a gm ap	1.30	28.45	12.09	2.13	39.62	1.67	3.26	0.10	88.60	7.77	0.26	0.58	4.41	2.21	0.03	1.89	-0.92	16.22
NB8	1-7 gm ap	1.04	39.03	1.14	0.24	53.77	0.31	1.72	0.08	97.32	9.87	0.04	0.06	5.66	0.20	0.02	0.93	0.05	16.83
NB8	1-8 ap gm	1.09	39.25	1.07	0.21	54.59	0.31	1.50	0.07	98.07	9.97	0.04	0.05	5.66	0.18	0.02	0.81	0.17	16.91
NB8	1-10 gm bis	1.06	38.76	0.99	0.26	53.61	0.90	1.51	0.07	97.15	9.90	0.13	0.07	5.66	0.17	0.02	0.82	0.16	16.92
NB8	gm random	1.13	37.95	1.02	0.29	53.75	0.70	1.57	0.08	96.49	10.03	0.10	0.07	5.60	0.18	0.02	0.87	0.11	16.98
NB8	1-2a gm ap	1.25	36.80	1.10	0.45	51.10	4.68	3.74	0.06	99.18	9.41	0.67	0.12	5.36	0.19	0.02	2.03	-1.05	16.75
NB8	1-5a gm ap	1.16	39.45	1.13	0.27	54.05	0.56	1.15	0.11	97.87	9.89	0.08	0.07	5.70	0.19	0.03	0.62	0.35	16.93
NB8	1-8a gm ap	1.17	38.57	1.17	0.33	53.53	1.02	2.22	0.06	98.06	9.81	0.15	0.08	5.58	0.20	0.02	1.20	-0.21	16.82
NB8	1-13 gm ap	1.26	39.22	1.09	0.28	53.01	1.02	1.34	0.08	97.29	9.76	0.15	0.07	5.71	0.19	0.02	0.73	0.25	16.87
NB8	1-18 gm ap	1.27	39.72	1.06	0.28	54.10	0.65	0.91	0.09	98.07	9.88	0.09	0.07	5.73	0.18	0.03	0.49	0.48	16.96

Table 7: (continued)

Sample	Point	SO_3	P_2O_5	SiO_2	MgO	CaO	FeO	F	Cl	Total	Ca	Fe	Mg	P	Si	Cl	F	OH	Total
NB8	1-3b gm bis	1.20	39.06	1.15	0.26	53.66	0.76	2.17	0.07	98.32	9.78	0.11	0.07	5.63	0.20	0.02	1.17	-0.19	16.77
NB8	1-15b gm ap	1.30	39.03	1.05	0.21	54.49	0.38	0.76	0.06	97.28	10.07	0.05	0.05	5.70	0.18	0.02	0.42	0.57	17.06
NB8	1-7b gm ap	1.16	39.26	1.11	0.21	54.44	0.44	2.78	0.06	99.46	9.80	0.06	0.05	5.59	0.19	0.02	1.48	-0.49	16.69
NB8	2-3 gm ap	1.15	39.58	1.05	0.25	53.88	0.16	0.86	0.07	96.99	9.92	0.02	0.06	5.76	0.18	0.02	0.47	0.51	16.94

Table 8: EMP analysis for Nowbaran foid compositions

Sample	Point	SiO_2	TiO_2	Al_2O_3	FeO	MnO	MgO	CaO	Na_2O	K_2O	P_2O_5	SO_3	SrO	BaO	F	Cl	Total	Si	Al	Fe^{2+}	Fe^{3+}	Mg	Ca	Na	K	Cl	S	Total	Na#	ne	ks	sil	Total
NB13	1-7 foid gm	32.58	0.00	28.60	0.31	0.00	0.04	5.72	13.59	2.11	0.11	10.24	1.23	0.08	0.00	0.48	95.07	5.70	5.90		0.04	0.01	1.07	4.61	0.47	0.14	3.36	21.32					
NB13	1-8 foid gm	33.90	0.03	29.62	0.66	0.01	0.10	4.52	13.47	1.69	0.10	9.32	1.22	0.33	0.00	0.59	95.54	5.80	5.97		0.09	0.02	0.83	4.47	0.37	0.17	2.99	20.71					
NB13	1-9 foid gm	32.96	0.12	29.50	0.65	0.03	0.04	5.05	14.22	1.72	0.14	9.89	1.16	0.17	0.00	0.70	96.34	5.67	5.98		0.09	0.01	0.93	4.74	0.38	0.20	3.18	21.19					
NB13	2-11 foid gm	33.14	0.05	29.34	0.51	0.06	0.04	4.93	13.87	1.74	0.06	10.35	1.24	0.10	0.00	0.56	96.00	5.72	5.97		0.07	0.01	0.91	4.65	0.38	0.17	3.35	21.24					
NB13	4-5 foid gm	34.61	0.00	30.36	0.57	0.00	0.07	4.28	12.81	1.81	0.13	8.74	1.10	0.10	0.00	1.02	95.58	5.83	6.03		0.08	0.02	0.77	4.18	0.39	0.29	2.76	20.35					
NB13	4-6 foid gm	34.76	0.02	30.35	0.50	0.00	0.08	4.40	12.67	1.80	0.07	8.80	1.30	0.06	0.00	0.88	95.69	5.85	6.02		0.07	0.02	0.79	4.14	0.39	0.25	2.78	20.30					
NB13	4-7 foid gm	34.81	0.02	30.13	0.52	0.04	0.06	4.52	12.39	1.74	0.15	8.62	1.66	0.40	0.00	0.81	95.87	5.88	6.00		0.07	0.02	0.82	4.06	0.37	0.23	2.73	20.18					
NB13	4-8 foid gm	33.81	0.07	30.16	0.55	0.01	0.09	4.63	12.64	1.57	0.12	9.29	1.40	0.55	0.05	0.68	95.63	5.78	6.08		0.08	0.02	0.85	4.19	0.34	0.20	2.98	20.52					
NB25	1-14 gm	41.12	0.11	31.54	1.86	0.03	0.32	0.41	14.39	9.61	0.17	0.03			0.04	0.02	99.63	8.22	7.43	0.31			0.09	5.58	2.45			24.08	0.69	69.3	30.5	0.2	100
NB25	3-1 ne gm	41.08	0.43	26.76	2.37	0.03	2.33	4.14	11.61	8.01	0.21	0.00			0.00	0.00	96.96	8.63	6.63	0.42			0.93	4.73	2.15			23.49	0.69	69.9	31.7	-1.6	100
NB24	1-3 ne gm	41.43	0.10	31.75	2.03	0.02	0.27	0.24	14.94	9.38	0.02	0.00			0.03	0.01	100.23	8.21	7.42	0.34			0.05	5.74	2.37			24.14	0.71	70.8	29.3	-0.1	100
NB24	1-5 ne gm	41.43	0.07	31.24	2.14	0.03	0.64	0.57	14.90	8.79	0.32	0.03			0.11	0.00	100.26	8.26	7.34	0.36			0.12	5.76	2.24			24.07	0.72	71.8	27.9	0.3	100
NB24	1-8 ne gm	42.20	0.09	31.62	2.11	0.02	0.25	0.19	14.84	9.11	0.02	0.02			0.00	0.00	100.46	8.31	7.34	0.35			0.04	5.67	2.29			24.00	0.71	68.8	27.8	3.3	100
NB24	2-2 ne gm	42.20	0.12	31.95	2.06	0.00	0.33	0.21	14.86	9.06	0.03	0.01			0.00	0.01	100.84	8.28	7.39	0.34			0.04	5.66	2.27			23.98	0.71	69.0	27.7	3.3	100
NB24	2-11 ne gm	42.17	0.03	31.66	2.13	0.00	0.38	0.13	15.19	8.58	0.00	0.02			0.10	0.00	100.39	8.31	7.35	0.35			0.03	5.80	2.16			24.00	0.73	70.3	26.1	3.6	100
NB15	1-6 foid gm	32.69	0.06	27.79	0.77	0.00	0.05	5.00	15.62	1.12	0.08	9.60			0.00	0.46	93.22	5.73	5.75		0.11	0.01	0.94	5.31	0.25	0.14	3.15	21.40					
NB15	1-15 foid gm	33.50	0.04	27.63	0.69	0.03	0.08	4.64	15.69	0.94	0.09	9.09			0.00	0.45	92.89	5.84	5.68		0.10	0.02	0.87	5.30	0.21	0.13	2.97	21.11					
NB15	1-8 ne gm	41.36	0.08	31.35	2.04	0.00	0.23	0.17	15.03	8.10	0.02	0.02			0.00	0.00	98.38	8.28	7.40	0.34			0.04	5.84	2.07			23.97	0.74	71.1	25.2	3.7	100
NB15	1-9 ne gm	41.14	0.09	30.88	1.85	0.01	0.22	0.21	14.75	7.53	0.00	0.00			0.00	0.00	96.68	8.35	7.38	0.31			0.05	5.80	1.95			23.84	0.75	70.3	23.6	6.1	100
NB15	2-2 foid gm	32.57	0.01	27.59	0.60	0.02	0.04	5.38	16.06	1.18	0.07	10.37			0.00	0.32	94.22	5.71	5.70		0.09	0.01	1.01	5.46	0.26	0.10	3.41	21.76					
NB15	2-10 ne gm	42.15	0.01	31.90	2.05	0.00	0.24	0.19	15.63	8.33	0.05	0.00			0.00	0.01	100.57	8.27	7.38	0.34			0.04	5.95	2.08			24.06	0.74	72.6	25.4	1.9	100
NB15	2-12 foid gm	32.83	0.02	27.88	0.98	0.00	0.06	4.62	15.92	0.98	0.11	10.50			0.00	0.46	94.34	15.96	5.75		0.14	0.01	0.86	5.40	0.22	0.14	3.44	31.76					
NB15	2-20 foid gm	33.58	0.09	27.69	0.91	0.07	0.16	4.31	15.90	1.26	0.12	8.65			0.05	0.89	93.66	5.81	5.65		0.13	0.04	0.80	5.33	0.28	0.26	2.81	20.94					
NB15	2-21 foid gm	32.78	0.06	27.91	0.88	0.06	0.08	4.26	16.03	1.14	0.08	10.07			0.00	0.65	93.99	5.74	5.76		0.13	0.02	0.80	5.44	0.25	0.19	3.30	21.48					
NB20	2-12 gm	32.61	0.86	26.63	4.66	0.00	0.20	3.26	15.18	1.48	0.08	8.13	0.65	0.06	0.08	0.65	94.53	5.75	5.53		0.69	0.05	0.62	5.19	0.33	0.20	2.68	20.29					
NB28	1-3A gm foid	34.63	0.49	24.51	1.89	0.00	1.26	5.67	15.72	0.62	1.13	6.03			0.25	1.54	93.74	5.98	4.99		0.27	0.32	1.05	5.26	0.14	0.45	1.95	19.81					
NB28	1-4A gm foid	41.64	0.13	29.46	1.16	0.00	0.14	1.56	17.21	3.54	1.12	0.03			0.14	0.01	96.13	8.49	7.08	0.20			0.34	6.80	0.92			23.83	0.88	87.14	11.80	1.06	100
NB28	1-5A gm foid	47.32	0.07	31.45	1.13	0.01	0.00	0.16	18.22	3.06	0.02	0.00			0.00	0.02	101.45	8.86	6.94	0.18			0.03	6.61	0.73			23.34	0.90	75.18	8.30	16.52	100
NB28	1-10A gm	37.68	0.14	29.72	0.57	0.00	0.04	2.77	18.86	1.26	0.10	5.77			0.08	1.52	98.50	5.96	5.54		0.08	0.01	0.47	5.78	0.25	0.41	1.71	20.20					
NB28	1-14 gm	39.95	0.51	22.00	1.99	0.07	3.69	7.75	15.18	0.26	0.08	5.44			0.01	1.87	98.78	6.36	4.13		0.27	0.88	1.32	4.69	0.05	0.50	1.62	19.82					
NB28	2-2A gm foid	45.13	0.05	32.42	1.16	0.00	0.03	0.35	18.20	3.67	0.00	0.00			0.02	0.01	101.03	8.55	7.24	0.18			0.07	6.68	0.89			23.62	0.88	79.51	10.56	9.93	100
NB28	2-5A gm foid	35.85	0.81	21.72	2.14	0.04	3.02	12.05	13.00	0.59	3.77	4.98			0.00	0.99	98.96	6.01	4.29		0.30	0.76	2.17	4.23	0.13	0.28	1.56	19.72					
NB28	2-11A gm foid	45.07	0.08	32.46	1.13	0.03	0.03	0.33	18.16	3.52	0.00	0.00			0.03	0.00	100.84	8.55	7.26	0.18			0.07	6.68	0.85			23.59	0.89	79.34	10.13	10.53	100
NB28	2-12A gm foid	43.18	0.06	30.96	1.05	0.00	0.03	1.08	17.74	3.10	0.04	1.28			0.00	0.21	98.73	8.51	7.20	0.17			0.23	6.78	0.78			23.67	0.90	84.19	9.68	6.13	
NB28	3-16 gm foid	38.95	1.31	18.31	3.18	0.05	4.66	16.28	10.35	1.76	1.47	0.00			0.21	0.00	96.53																
NB28	3-18 gm foid	37.89	0.08	27.29	0.56	0.02	0.08	3.55	15.89	1.55	0.06	5.73			0.00	0.97	93.66	6.24	5.30		0.08	0.02	0.63	5.08	0.33	0.27	1.77	19.71					
NB28	4-10 gm foid	35.62	1.25	26.05	1.57	0.06	1.33	2.89	16.41	1.39	0.21	5.90			0.31	1.73	94.72	6.02	5.19		0.22	0.34	0.52	5.38	0.30	0.49	1.87	20.34					0
NB28	4-12A gm foid	43.88	0.08	31.77	1.22	0.00	0.05	0.39	17.73	3.61	0.00	0.01			0.00	0.03	98.78	8.52	7.27	0.20			0.08	6.67	0.89			23.63	0.88	79.86	10.69	9.45	100
NB28	4-13A gm ap	37.77	1.10	16.17	2.96	0.08	4.89	14.03	8.70	1.74	4.11	0.01			0.70	0.12	92.39																
NB28	3-20 gm	45.35	0.21	29.87	1.29	0.00	0.29	1.03	15.99	3.36	0.44	0.04	0.07	0.38	0.00	0.02	98.33	8.88	6.90	0.21			0.22	6.07	0.84			23.12	0.88	71.85	9.94	18.21	100

Table 9: EMP analysis for Nowbaran perovskite compositions

Sample	Point	SiO_2	TiO_2	Al_2O_3	FeO	MnO	MgO	CaO	Na_2O	K_2O	P_2O_5	SO_3	F	Cl	Total	Si	Ti	Al	Fe	Mn	Mg	Ca	Na	Total
NB24	1-11 pv gm	10.77	42.25	0.71	2.52	0.00	3.87	33.80	0.82	0.04	0.04	0.00	0.13	0.03	94.97	0.25	0.73	0.02	0.05	0.00	0.13	0.83	0.04	2.04
NB24	2-21 pv gm	0.11	53.83	0.16	1.75	0.00	0.07	35.64	0.75	0.10	0.00	0.02	0.12	0.01	92.57	0.00	1.00	0.00	0.04	0.00	0.00	0.94	0.04	2.02
NB24	3-12 pv gm	9.83	39.84	6.55	1.81	0.00	0.69	28.43	5.00	2.00	0.04	0.00	0.12	0.00	94.31	0.23	0.70	0.18	0.04	0.00	0.02	0.71	0.23	2.10

Table 10. Whole-rock major (wt%), trace (ppm) and Sr-Nd-Pb isotopic ratios for Nowbaran samples.

Sample	NB1	NB2	NB3	NB7	NB8	NB10	NB13	NB15	NB16	NB17	NB19	NB20	NB21	NB22	NB23	NB25	NB26	NB28	NB30	NB31	NB33
Locality	Dakhan	Dakhan	Dakhan	Dakhan	Dakhan	Dakhan	Dakhan	Dakhan	Dakhan	Dakhan	Dakhan	Dakhan	Dakhan	Fastaq	Fastaq	Chalfakhreh	Chalfakhreh	Qezel Hesar	Qezel Hesar	Qezel Hesar	Qezel Hesar
SiO_2	39.49	39.76	38.54	39.57	36.29	37.97	38.99	39.21	38.20	36.04	36.74	41.04	40.89	37.69	35.45	38.40	37.23	41.27	40.19	41.41	41.36
TiO_2	2.28	2.23	2.08	2.33	2.35	2.61	2.05	2.06	2.34	2.06	2.51	2.09	2.03	2.36	2.46	2.55	2.45	2.58	2.56	2.28	2.30
Al_2O_3	10.16	10.12	9.72	9.88	8.99	9.13	9.70	9.78	9.48	8.61	9.17	11.07	10.73	9.74	9.52	9.29	9.00	11.40	11.10	11.05	11.58
Fe_2O_{3tot}	9.76	9.54	9.49	10.00	10.13	10.65	9.47	9.46	10.10	9.14	10.54	8.61	8.77	9.67	9.75	10.89	10.30	11.04	11.27	10.52	10.85
MnO	0.13	0.13	0.13	0.14	0.14	0.16	0.13	0.14	0.14	0.13	0.15	0.11	0.11	0.13	0.13	0.16	0.16	0.16	0.16	0.17	0.17
MgO	11.29	11.54	10.76	10.86	12.90	12.58	11.22	11.16	12.39	10.29	13.06	8.67	9.20	11.19	10.62	13.30	12.67	11.19	11.65	11.23	11.68
CaO	16.72	16.18	17.03	16.81	16.71	16.45	17.22	17.77	15.29	15.78	16.26	14.66	15.12	18.17	18.31	14.53	15.11	13.62	13.82	13.73	13.11
Na_2O	3.14	1.76	3.18	3.40	2.26	3.04	3.27	3.74	3.96	1.80	3.02	5.11	5.44	3.47	3.81	2.85	2.59	4.15	2.56	4.07	2.01
K_2O	1.89	1.14	2.29	2.25	1.10	1.60	1.08	1.36	1.58	2.04	1.56	1.07	0.65	1.87	2.17	1.80	2.07	0.49	0.83	0.68	0.17
P_2O_5	2.90	2.83	2.41	3.31	2.77	2.93	2.91	3.00	2.93	2.43	2.90	2.52	2.47	3.05	3.21	1.72	1.90	1.55	1.49	1.52	1.41
L.O.I.	2.62	5.13	4.90	1.86	7.04	3.11	3.58	2.96	3.68	10.44	4.30	3.78	3.26	3.13	4.01	4.30	6.80	3.13	4.81	3.89	6.04
Total	100.38	100.36	100.53	100.40	100.69	100.22	99.62	100.63	100.09	98.76	100.20	98.73	98.67	100.47	99.44	99.79	100.28	100.58	100.44	100.55	100.68
CO_2	0.52	0.69	1.68	0.21	2.64	1.21	0.87	1.06	1.42	3.76	1.69	0.16	0.05	1.75	2.68	1.20	2.69	0.22	0.28	0.67	0.20
Mg#	0.72	0.73	0.72	0.71	0.74	0.73	0.73	0.73	0.73	0.72	0.74	0.69	0.70	0.72	0.71	0.73	0.73	0.70	0.70	0.71	0.71
$^{87}Sr/^{86}Sr$			0.705251							0.705644	0.705314		0.705186		0.705202	0.705459					0.705613
ε_{Sr}			11.37							16.95	12.26		10.45		10.67	14.32					16.51
$^{143}Nd/^{144}Nd$			0.512665							0.512665	0.512686		0.512685		0.512673	0.512665					0.512631
ε_{Nd}			0.49							0.49	0.90		0.88		0.64	0.49					-0.18
$^{206}Pb/^{204}Pb$			18.657							18.637	18.583		18.651		18.579	18.544					18.631
$^{207}Pb/^{204}Pb$			15.669							15.665	15.662		15.665		15.667	15.661					15.681
$^{208}Pb/^{204}Pb$			38.787							38.753	38.700		38.769		38.707	38.665					38.693
Rb	26	41	44	34	35	24	24	14	36	42	33	23	17	40	27	17	61	24	45	36	24
Sr	3673	3928	2515	3850	3891	2076	2784	3656	1926	1858	2692	2186	3674	2157	2375	2695	2034	2237	3347	3564	2423
Ba	1462	2278	2518	1609	1888	1613	1363	1509	2462	2132	1937	1502	1493	1474	1252	2088	1434	1334	1594	1632	1513
Cs		1.3	0.5	1.0		0.9		0.9	0.6	0.7	0.8	1.4	0.7	1.4	1.0	1.8	0.7		1.0	1.1	4.5
Sc	15	15	15	15	16	16	19	15	20	18	16	19	16	19	16	19	14	17	14	14	20
V	167	193	170	187	180	191	198	189	207	70	194	260	193	257	149	244	129	183	182	182	233
Cr	360	480	320	290	270	380	360	320	450	270	340	370	300	380	280	350	280	450	260	270	320
Co	47	47	49	44	51	48	81	48	54	52	43	47	44	47	54	44	52	54	46	39	48
Ni	310	360	290	260	270	330	300	290	330	310	290	280	290	290	360	250	340	360	230	240	250
Cu	90	100	100	80	90	70	360	80	70	90	90	50	80	50	90	50	80	80	100	80	50
Zn	180	170	160	160	180	150	160	160	140	130	160	140	160	140	160	120	180	170	160	160	120
Y	26	25	25	24	26	21	25	24	23	21	27	24	24	23	22	27	20	21	24	24	28
Zr	333	317	423	287	342	323	354	311	327	304	388	284	315	281	328	332	292	323	349	341	348
Nb	60	54	69	53	63	68	81	60	77	70	60	54	59	55	70	59	62	73	56	57	65
Hf	6.7	6.2	8.6	6.8	7.3	6.9	7.3	6.2	6.8	6.5	7.8	6.1	6.4	6.1	6.8	7.0	5.7	6.6	7.4	7.3	7.0
Ta	3.1	2.9	3.6	3.0	3.4	4.4	4.7	3.1	4.3	4.0	3.3	3.3	2.9	3.1	3.7	3.5	3.3	3.8	3.1	2.8	3.8
La	280	258	283	262	294	200	205	236	164	150	271	124	237	119	198	152	183	195	233	229	149
Ce	526	485	534	484	550	383	394	454	316	287	503	243	458	239	386	294	348	376	444	438	283
Pr	57.4	53.8	60.5	54.3	60.8	43.2	43.6	50.9	35.3	31.9	56.4	28.4	51.4	27.9	43.1	33.9	38.6	42.5	48.9	49.4	32.1
Nd	202	185	217	191	213	150	157	182	123	113	204	107	180	104	151	123	137	150	176	175	119
Sm	25.8	23.9	29.7	24.9	27.6	20.1	20.7	23.9	17.0	15.5	27.9	16.6	24.0	16.0	20.1	18.4	18.6	19.8	23.6	23.9	18.5
Eu	6.10	5.72	7.09	5.91	6.54	4.93	5.10	5.55	4.23	3.83	6.99	4.38	5.83	4.16	4.95	4.87	4.49	4.85	5.68	5.58	4.78
Gd	12.6	11.7	15	11.9	13.4	10.4	10.4	12.1	9.4	8.7	14.1	9.8	11.6	9.2	10.2	10.4	9.5	10.1	11.4	12	10.5
Tb	1.3	1.3	1.6	1.2	1.4	1.2	1.2	1.3	1.1	1.1	1.5	1.1	1.3	1.1	1.1	1.3	1.0	1.1	1.2	1.2	1.3
Dy	5.5	5.2	6.2	5.4	5.9	5	5.1	5.5	5	4.8	6.2	5.3	5.4	5.1	4.9	5.6	4.4	4.9	5.1	5.4	6
Ho	0.9	0.8	0.9	0.8	0.9	0.8	0.9	0.9	0.9	0.8	0.9	0.9	0.9	0.8	0.7	0.9	0.7	0.8	0.8	0.8	1.0

Table 10. (continued)

Sample	NB1	NB2	NB3	NB7	NB8	NB10	NB13	NB15	NB16	NB17	NB19	NB20	NB21	NB22	NB23	NB25	NB26	NB28	NB30	NB31	NB33
Locality	Dakhan	Dakhan	Dakhan	Dakhan	Dakhan	Dakhan	Dakhan	Dakhan	Dakhan	Dakhan	Dakhan	Dakhan	Dakhan	Fastaq	Fastaq	Chalfakhreh	Chalfakhreh	Qezel Hesar	Qezel Hesar	Qezel Hesar	Qezel Hesar
Er	2.4	2.2	2.4	2.2	2.5	2.1	2.2	2.3	2.3	2.1	2.4	2.2	2.2	2.1	2.0	2.4	1.9	2.1	2.2	2.2	2.5
Tm	0.26	0.26	0.29	0.29	0.32	0.26	0.28	0.28	0.29	0.27	0.30	0.28	0.27	0.26	0.25	0.30	0.23	0.25	0.27	0.28	0.31
Yb	1.6	1.5	1.4	1.5	1.7	1.5	1.6	1.6	1.6	1.4	1.5	1.5	1.5	1.5	1.3	1.7	1.2	1.4	1.5	1.5	1.8
Lu	0.20	0.21	0.19	0.19	0.22	0.19	0.21	0.22	0.23	0.22	0.20	0.21	0.21	0.21	0.18	0.23	0.16	0.19	0.21	0.21	0.23
Pb	32	23	40	21	33	16	16	21	17	19	38	18	30	18	37	23	20	22	11	25	13
Th	42.1	38.9	40.8	39.2	44.6	27.4	30.1	33.4	20.8	19.0	37.1	15.0	32.9	14.4	29.0	17.9	27.4	27.8	41.2	40.8	17.7
U	6.2	5.1	6.1	5.8	6.3	4.0	4.6	4.6	4.6	3.5	5.5	1.7	4.6	3.1	3.3	2.7	3.3	4.5	4.4	5.0	4.2
Ga	22	22	22	22	22	21	20	21	19	17	21	20	21	20	22	20	17	21	23	23	20

Table 11: EMP analysis for Bijar-Qorveh olivine compositions

Sample	Location	Description	SiO_2	MgO	CaO	MnO	FeO	NiO	Total	Si	Fe''	Mn	Mg	Ca	Ni	Total	Mg#	Fo	Fa	La	Total
Q-T34	Bijar	Ol 1	40.68	45.93	0.20	0.24	13.28	0.32	100.66	1.01	0.28	0.01	1.70	0.01	0.01	3.00	0.86	85.81	13.92	0.27	100.00
Q-T34	Bijar	Ol 2	40.48	45.30	0.28	0.35	13.90	0.20	100.50	1.01	0.29	0.01	1.68	0.01	0.00	3.00	0.85	84.99	14.62	0.38	100.00
Q-T34	Bijar	Ol 3	40.86	45.65	0.18	0.23	13.01	0.34	100.27	1.02	0.27	0.00	1.69	0.00	0.01	3.00	0.86	86.01	13.74	0.25	100.00
Q-T34	Bijar	Ol 4	40.75	45.44	0.27	0.26	13.63	0.20	100.55	1.01	0.28	0.01	1.69	0.01	0.00	3.00	0.86	85.29	14.35	0.37	100.00
Q-T36	Bijar	ol micropheno 1-6	39.00	40.40	0.34	0.44	19.07	0.07	99.32	1.01	0.41	0.01	1.56	0.01	0.00	3.00	0.79	78.68	20.84	0.48	100.00
Q-T36	Bijar	same ol microphen core 1-7	40.18	45.40	0.21	0.27	13.36	0.38	99.80	1.01	0.28	0.01	1.70	0.01	0.01	3.00	0.86	85.59	14.13	0.28	100.00
Q-T36	Bijar	ol gm 2-1	38.60	40.20	0.25	0.54	19.40	0.22	99.21	1.00	0.42	0.01	1.55	0.01	0.00	3.00	0.79	78.43	21.22	0.34	100.00
Q-T36	Bijar	ol gm 2-2	38.68	39.43	0.29	0.66	21.51	0.08	100.65	1.00	0.46	0.01	1.52	0.01	0.00	3.00	0.77	76.26	23.34	0.41	100.00
Q-T39	Bijar	micropheno ol 1-2	38.85	37.71	0.20	0.45	22.31	0.06	99.58	1.02	0.49	0.01	1.47	0.01	0.00	3.00	0.75	74.86	24.85	0.29	100.00
Q-T39	Bijar	pheno ol 1-3	38.93	38.32	0.26	0.46	22.73	0.08	100.78	1.01	0.49	0.01	1.48	0.01	0.00	3.00	0.75	74.77	24.87	0.36	100.00
Q-T39	Bijar	pheno ol rim 2-3	39.06	41.13	0.20	0.33	19.54	0.17	100.42	1.00	0.42	0.01	1.57	0.01	0.00	3.00	0.79	78.74	20.99	0.27	100.00
Q-T39	Bijar	pheno ol core 2-4	40.32	46.47	0.16	0.21	12.65	0.33	100.12	1.00	0.26	0.00	1.72	0.00	0.01	3.00	0.87	86.58	13.22	0.21	100.00
Q-T39	Bijar	ol in glom with cpx 4-5	38.70	38.36	0.21	0.50	22.32	0.14	100.22	1.01	0.49	0.01	1.49	0.01	0.00	3.00	0.75	75.17	24.53	0.30	100.00
Q-T39	Bijar	pheno ol rim 4-6	37.71	34.51	0.28	0.60	26.91	0.10	100.10	1.01	0.60	0.01	1.37	0.01	0.00	3.00	0.70	69.29	30.31	0.40	100.00
Q-T39	Bijar	pheno ol core 4-7	40.25	46.57	0.14	0.18	12.80	0.32	100.26	1.00	0.27	0.00	1.72	0.00	0.01	3.00	0.87	86.48	13.34	0.18	100.00
Q-T5	Qezelke Kand	ol micropheno 2-4	40.64	45.43	0.23	0.15	13.49	0.19	100.12	1.01	0.28	0.00	1.69	0.01	0.00	3.00	0.86	85.46	14.24	0.30	100.00
Q-T5	Qezelke Kand	ol pheno rim 2-5	39.97	43.59	0.37	0.30	15.51	0.12	99.87	1.01	0.33	0.01	1.64	0.01	0.00	3.00	0.83	82.94	16.55	0.51	100.00
Q-T5	Qezelke Kand	same ol pheno core 2-6	40.67	45.51	0.20	0.23	13.84	0.20	100.65	1.01	0.29	0.00	1.69	0.01	0.00	3.00	0.85	85.20	14.53	0.27	100.00
Q-T6	Qezelke Kand	ol microphen 1-8	39.32	46.50	0.15	0.22	12.66	0.33	99.18	0.98	0.26	0.00	1.74	0.00	0.01	3.00	0.87	86.58	13.22	0.20	100.00
Q-T6	Qezelke Kand	ol micropheno 1-9	40.07	45.62	0.16	0.24	13.86	0.30	100.24	1.00	0.29	0.01	1.70	0.00	0.01	3.00	0.85	85.26	14.53	0.21	100.00
Q-T6	Qezelke Kand	ol microphen 2-1	40.16	46.84	0.17	0.20	12.06	0.43	99.84	1.00	0.25	0.00	1.73	0.00	0.01	3.00	0.87	87.19	12.59	0.22	100.00
Q-T6	Qezelke Kand	ol microphen 2-2	40.31	46.10	0.19	0.13	13.20	0.28	100.22	1.00	0.27	0.00	1.71	0.00	0.01	3.00	0.86	85.94	13.80	0.25	100.00
Q-T6	Qezelke Kand	ol microphen 2-3	39.95	45.97	0.19	0.28	13.37	0.29	100.05	1.00	0.28	0.01	1.71	0.01	0.01	3.00	0.86	85.75	13.99	0.26	100.00
Q-T6	Qezelke Kand	Ol microphen 3-3	39.44	45.92	0.17	0.22	12.92	0.38	99.04	0.99	0.27	0.00	1.72	0.00	0.01	3.00	0.86	86.17	13.60	0.23	100.00
Q-T16	Qezelke Kand	ol gm 1-3	39.67	45.11	0.29	0.26	13.48	0.25	99.05	1.00	0.28	0.01	1.70	0.01	0.01	3.00	0.86	85.31	14.30	0.39	100.00
Q-T16	Qezelke Kand	ol gm 4-3bis	40.63	44.47	0.26	0.30	14.56	0.20	100.41	1.02	0.30	0.01	1.66	0.01	0.00	3.00	0.84	84.19	15.46	0.36	100.00
Q-T16	Qezelke Kand	ol gm 4-4bis	40.09	44.79	0.29	0.25	14.12	0.21	99.75	1.01	0.30	0.01	1.68	0.01	0.00	3.00	0.85	84.64	14.96	0.40	100.00
T4	Takab	2-1 big ol pheno rim	36.88	39.20	0.27	0.65	22.59	0.04	99.62	0.96	0.49	0.01	1.52	0.01	0.00	3.00	0.76	75.29	24.34	0.37	100.00
T4	Takab	2-3 same big ol pheno core	38.33	43.35	0.21	0.38	16.58	0.22	99.06	0.98	0.35	0.01	1.65	0.01	0.00	3.00	0.82	82.10	17.61	0.28	100.00
T4	Takab	2-4 ol micropheno rim	37.69	39.56	0.24	0.62	21.84	0.13	100.07	0.98	0.47	0.01	1.53	0.01	0.00	3.00	0.76	76.10	23.56	0.34	100.00
T6	Takab	1-1tris big pheno ol core	38.26	45.09	0.20	0.26	14.41	0.20	98.42	0.97	0.31	0.01	1.71	0.01	0.00	3.00	0.85	84.57	15.16	0.26	100.00

Table 12: EMP analysis for Bijar-Qorveh pyroxene compositions

Sample	Location	Description	SiO_2	TiO_2	Al_2O_3	Cr_2O_3	MgO	CaO	MnO	FeO	Na_2O	Total	Si	Ti	$Al_{(tot)}$	$Al_{(T)}$	$Al_{(M1)}$	$Fe^{3+}{}_{(M1)}$	Fe^{2+}	Mn	Mg	Ca	Na	Total	Mg#	Wo	En	Fs	Total
Q-T34	Bijar	Cpx 1-1	46.86	2.13	5.72	0.22	13.52	22.80	0.12	7.19	0.51	99.06	1.75	0.06	0.25	0.25	0.00	0.16	0.07	0.00	0.75	0.91	0.04	4.00	0.92	48.19	39.75	12.06	100.00
Q-T34	Bijar	Cpx 1-2	46.08	2.31	6.58	0.09	12.90	22.70	0.10	8.02	0.57	99.35	1.72	0.06	0.29	0.28	0.01	0.18	0.07	0.00	0.72	0.91	0.04	4.00	0.91	48.31	38.20	13.49	100.00
Q-T34	Bijar	Cpx 1-3	49.07	1.59	4.52	0.19	14.63	22.67	0.18	6.84	0.47	100.16	1.81	0.04	0.20	0.19	0.00	0.13	0.08	0.01	0.80	0.89	0.03	4.00	0.91	46.74	41.96	11.30	100.00
Q-T34	Bijar	Cpx 1-4	49.94	0.98	4.65	0.17	15.37	21.56	0.06	6.23	0.32	99.28	1.85	0.03	0.20	0.15	0.05	0.07	0.12	0.00	0.85	0.85	0.02	4.00	0.87	45.06	44.69	10.26	100.00
Q-T34	Bijar	Cpx 1-5	50.03	1.19	3.22	0.18	15.59	23.06	0.10	6.29	0.41	100.06	1.84	0.03	0.14	0.14	0.00	0.12	0.05	0.00	0.85	0.91	0.03	4.00	0.95	46.36	43.61	10.03	100.00
Q-T34	Bijar	Cpx 1-6	46.68	2.17	6.51	0.74	13.47	22.74	0.00	6.88	0.47	99.65	1.73	0.06	0.28	0.27	0.02	0.14	0.08	0.00	0.75	0.91	0.03	4.00	0.91	48.54	40.00	11.46	100.00
Q-T36	Bijar	Cpx microphen 1-1	52.73	0.55	3.89	0.38	16.83	20.01	0.14	5.45	0.77	100.75	1.91	0.02	0.17	0.09	0.07	0.04	0.13	0.00	0.91	0.77	0.05	4.00	0.88	41.87	49.00	9.13	100.00
Q-T36	Bijar	Cpx microphenо 1-2	51.75	0.94	4.45	0.12	15.83	21.05	0.17	6.47	0.77	101.55	1.86	0.03	0.19	0.14	0.05	0.08	0.11	0.01	0.85	0.81	0.05	4.00	0.88	43.62	45.64	10.74	100.00
Q-T36	Bijar	Cpx microphenо 1-2bis	50.85	1.15	4.66	0.14	15.16	21.63	0.18	6.51	0.69	100.97	1.85	0.03	0.20	0.15	0.05	0.08	0.11	0.01	0.82	0.84	0.05	4.00	0.88	45.12	43.99	10.90	100.00
Q-T36	Bijar	cribrose Cpx pheno clear rim 2-3	50.88	1.18	3.22	0.07	15.53	22.60	0.17	6.57	0.41	100.63	1.86	0.03	0.14	0.14	0.00	0.10	0.10	0.01	0.85	0.89	0.03	4.00	0.90	45.69	43.68	10.64	100.00
Q-T36	Bijar	same cribrose Cpx pheno clear mantle 2-4	51.73	0.91	2.96	0.33	16.40	22.09	0.14	5.76	0.48	100.79	1.88	0.02	0.13	0.12	0.01	0.09	0.08	0.00	0.89	0.86	0.03	4.00	0.91	44.62	46.08	9.30	100.00
Q-T36	Bijar	same cribrose Cpx pheno spongy mantle 2-5	51.83	0.80	3.21	0.52	16.24	22.11	0.12	5.42	0.55	100.81	1.88	0.02	0.14	0.12	0.02	0.08	0.08	0.00	0.88	0.86	0.04	4.00	0.91	45.10	46.08	8.82	100.00
Q-T36	Bijar	same cribrose Cpx pheno spongy core 2-6	51.30	0.97	3.45	0.36	15.56	22.38	0.09	5.38	0.50	99.99	1.88	0.03	0.15	0.12	0.03	0.06	0.10	0.00	0.85	0.88	0.04	4.00	0.89	46.34	44.82	8.84	100.00
Q-T36	Bijar	cribrose Cpx clear rim 3-1	45.62	2.34	6.29	0.01	13.24	22.44	0.21	8.19	0.67	99.02	1.71	0.07	0.28	0.28	0.00	0.21	0.03	0.01	0.74	0.90	0.05	4.00	0.96	47.32	38.85	13.83	100.00
Q-T36	Bijar	same cribrose Cpx clear mantle 3-2	50.01	0.82	3.78	0.68	15.63	21.62	0.05	5.37	0.66	98.61	1.85	0.02	0.17	0.15	0.02	0.11	0.06	0.00	0.86	0.86	0.05	4.00	0.94	45.42	45.69	8.89	100.00
Q-T36	Bijar	same cribrose Cpx spongy core 3-3	49.76	0.91	3.94	0.67	15.48	22.31	0.17	5.52	0.56	99.31	1.84	0.03	0.17	0.16	0.01	0.13	0.04	0.01	0.85	0.88	0.04	4.00	0.95	46.20	44.60	9.20	100.00
Q-T39	Bijar	Cpx gm 1-4	51.90	0.75	3.14	0.41	15.95	22.01	0.17	6.16	0.35	100.83	1.89	0.02	0.13	0.11	0.03	0.06	0.13	0.01	0.87	0.86	0.02	4.00	0.87	44.79	45.15	10.06	100.00
Q-T39	Bijar	Cpx gm 2-2	50.07	0.95	4.99	0.57	14.78	22.55	0.10	6.05	0.38	100.43	1.83	0.03	0.22	0.17	0.05	0.07	0.11	0.00	0.81	0.88	0.03	4.00	0.88	47.06	42.92	10.02	100.00
Q-T39	Bijar	Cpx gm 4-1	48.88	1.77	5.19	0.10	13.54	21.99	0.18	8.58	0.45	100.67	1.80	0.05	0.23	0.20	0.03	0.10	0.17	0.01	0.75	0.87	0.03	4.00	0.82	46.13	39.52	14.35	100.00
Q-T39	Bijar	Cpx microphenо 4-4	49.29	1.00	5.36	0.56	14.49	22.74	0.15	6.57	0.37	100.53	1.81	0.03	0.23	0.19	0.04	0.11	0.09	0.00	0.79	0.89	0.03	4.00	0.90	47.23	41.87	10.90	100.00
Q-T39	Bijar	Cpx microphenо 4-8	49.59	0.96	5.25	0.73	14.79	22.60	0.13	5.95	0.47	100.46	1.81	0.03	0.23	0.19	0.04	0.11	0.08	0.00	0.81	0.89	0.03	4.00	0.91	47.16	42.94	9.91	100.00
Q-T5	Qezelke Kand	Cpx pheno rim 1-1	49.43	1.88	4.38	0.01	14.10	23.23	0.19	7.40	0.37	100.98	1.81	0.05	0.19	0.19	0.00	0.11	0.12	0.01	0.77	0.91	0.03	4.00	0.86	47.63	40.22	12.15	100.00
Q-T5	Qezelke Kand	Cpx pheno core 1-2	51.01	1.23	3.27	0.30	15.35	23.44	0.00	5.90	0.41	100.91	1.86	0.03	0.14	0.14	0.00	0.09	0.09	0.00	0.83	0.92	0.03	4.00	0.91	47.45	43.23	9.32	100.00
Q-T5	Qezelke Kand	Cpx gm 1-3	45.13	3.25	7.77	0.01	12.18	22.92	0.16	8.63	0.55	100.59	1.67	0.09	0.34	0.33	0.01	0.17	0.10	0.00	0.67	0.91	0.04	4.00	0.87	49.05	36.26	14.69	100.00
Q-T5	Qezelke Kand	Cpx gm 1-6	50.91	1.22	3.12	0.27	15.62	23.14	0.09	5.81	0.38	100.54	1.86	0.03	0.13	0.13	0.00	0.09	0.08	0.00	0.85	0.91	0.03	4.00	0.91	46.77	43.92	9.31	100.00
Q-T5	Qezelke Kand	Cpx microphen 2-9	48.53	1.94	5.25	0.22	14.18	23.31	0.11	6.99	0.53	101.06	1.77	0.05	0.23	0.23	0.00	0.15	0.06	0.00	0.77	0.91	0.04	4.00	0.92	47.98	40.61	11.41	100.00
Q-T6	Qezelke Kand	Cpx microphen 1-1	49.56	1.20	3.09	0.26	15.43	23.06	0.19	5.86	0.40	99.04	1.84	0.03	0.13	0.13	0.00	0.12	0.04	0.01	0.85	0.92	0.03	4.00	0.96	46.82	43.59	9.59	100.00
Q-T6	Qezelke Kand	Cpx microphen 1-2	52.25	1.01	2.88	0.39	16.13	22.84	0.11	5.11	0.45	101.16	1.89	0.03	0.12	0.11	0.02	0.06	0.10	0.00	0.87	0.89	0.03	4.00	0.90	46.28	45.47	8.26	100.00
Q-T6	Qezelke Kand	Cpx gm dirty 1-6	45.55	2.55	6.21	0.26	13.27	22.93	0.15	7.66	0.55	99.12	1.70	0.07	0.27	0.27	0.00	0.18	0.03	0.00	0.74	0.92	0.04	4.00	0.96	48.29	38.88	12.84	100.00
Q-T6	Qezelke Kand	Cpx microphen in glom 2-4	50.55	1.25	3.31	0.11	15.26	23.06	0.17	6.20	0.37	100.29	1.86	0.03	0.14	0.14	0.00	0.10	0.09	0.01	0.83	0.91	0.03	4.00	0.90	46.81	43.10	10.10	100.00
Q-T6	Qezelke Kand	Cpx microphen 2-5	48.72	1.93	5.43	0.34	14.22	23.02	0.09	6.51	0.52	100.78	1.78	0.05	0.23	0.22	0.02	0.12	0.08	0.00	0.78	0.90	0.04	4.00	0.91	48.00	41.25	10.74	100.00
Q-T6	Qezelke Kand	Cpx microphen 2-9	49.91	1.15	3.14	0.17	15.45	23.11	0.07	5.64	0.41	99.06	1.85	0.03	0.14	0.14	0.00	0.11	0.05	0.00	0.85	0.92	0.03	4.00	0.95	47.10	43.81	9.09	100.00
Q-T6	Qezelke Kand	Cpx microphen 3-4	45.79	2.62	6.31	0.16	13.22	23.02	0.13	6.97	0.59	98.82	1.72	0.07	0.28	0.28	0.00	0.18	0.04	0.00	0.74	0.92	0.04	4.00	0.95	49.03	39.17	11.81	100.00
Q-T6	Qezelke Kand	Cpx microphen 3-5	50.39	1.21	3.00	0.18	15.58	23.35	0.07	5.60	0.42	99.82	1.85	0.03	0.13	0.13	0.00	0.11	0.05	0.00	0.85	0.92	0.03	4.00	0.95	47.22	43.83	8.95	100.00
Q-T16	Qezelke Kand	Cpx pheno core 1-1	50.53	0.60	3.64	0.67	16.18	22.30	0.06	4.03	0.65	98.66	1.86	0.02	0.16	0.14	0.02	0.11	0.01	0.00	0.89	0.88	0.05	4.00	0.98	46.46	46.89	6.65	100.00
Q-T16	Qezelke Kand	same Cpx pheno core 1-1bis	52.00	0.61	3.58	0.73	16.46	22.09	0.04	4.22	0.75	100.48	1.88	0.02	0.15	0.12	0.04	0.08	0.05	0.00	0.89	0.86	0.05	4.00	0.95	45.72	47.40	6.88	100.00
Q-T16	Qezelke Kand	same Cpx pheno rim 1-2	51.07	0.98	3.90	0.13	15.81	23.08	0.04	4.77	0.62	100.38	1.86	0.03	0.17	0.14	0.02	0.11	0.04	0.00	0.86	0.90	0.04	4.00	0.96	47.27	45.05	7.69	100.00
Q-T16	Qezelke Kand	cribrose Cpx rim 2-1	52.38	0.59	2.59	0.27	16.65	22.98	0.05	3.90	0.48	99.89	1.91	0.02	0.11	0.09	0.02	0.07	0.05	0.00	0.90	0.90	0.03	4.00	0.94	46.68	47.06	6.26	100.00
Q-T16	Qezelke Kand	cribrose Cpx mantle 2-2	51.90	0.59	2.77	0.22	16.89	22.81	0.13	3.95	0.59	99.84	1.89	0.02	0.12	0.11	0.01	0.11	0.01	0.00	0.92	0.89	0.04	4.00	0.99	46.09	47.48	6.44	100.00
Q-T16	Qezelke Kand	cribrose Cpx core 2-3	52.98	0.59	3.54	0.16	16.39	21.74	0.11	4.55	0.75	100.81	1.91	0.02	0.15	0.09	0.06	0.04	0.10	0.00	0.88	0.84	0.05	4.00	0.90	45.12	47.33	7.55	100.00
Q-T16	Qezelke Kand	Cpx gm 2-6	51.23	0.84	3.41	0.04	15.10	21.11	0.18	7.41	0.71	100.02	1.88	0.02	0.15	0.12	0.03	0.09	0.14	0.01	0.83	0.83	0.05	4.00	0.85	43.94	43.73	12.34	100.00
Q-T16	Qezelke Kand	Cpx gm close to Bt 3-3	50.65	0.87	3.97	0.02	15.31	21.41	0.15	6.38	0.73	99.48	1.86	0.02	0.17	0.14	0.04	0.10	0.09	0.00	0.84	0.84	0.05	4.00	0.90	44.78	44.55	10.66	100.00
Q-T16	Qezelke Kand	Cpx gm 4-5	52.30	0.74	3.15	0.07	16.20	23.08	0.08	4.51	0.58	100.70	1.84	0.04	0.16	0.16	0.00	0.09	0.16	0.01	0.77	0.90	0.03	4.00	0.83	46.91	45.81	7.28	100.00
T4	Takab	1-5 gm cpx	49.28	1.57	3.72	0.04	13.87	22.38	0.20	7.99	0.36	99.41	1.92	0.02	0.08	0.08	0.00	0.06	0.11	0.00	0.88	0.90	0.02	4.00	0.89	46.60	40.18	13.22	100.00
T4	Takab	2-5 cpx pheno core	53.01	0.51	1.94	0.94	16.86	22.38	0.12	4.20	0.45	100.41	1.86	0.04	0.14	0.14	0.00	0.09	0.09	0.00	0.82	0.92	0.02	4.00	0.90	45.49	47.67	6.84	100.00
T4	Takab	2-6 cpx gm	50.31	1.30	3.26	0.31	14.97	23.34	0.13	5.91	0.33	99.85	1.90	0.02	0.09	0.09	0.00	0.07	0.07	0.00	0.88	0.91	0.03	4.00	0.92	47.79	42.62	9.59	100.00
T4	Takab	2-7 cpx gm	51.94	0.61	2.04	0.70	16.18	23.16	0.09	5.01	0.36	100.10	1.90	0.02	0.11	0.10	0.01	0.04	0.11	0.00	0.86	0.90	0.03	4.00	0.89	46.68	45.36	7.97	100.00
T4	Takab	4-1 cpx microphenо core	51.57	0.80	2.46	1.01	15.67	22.76	0.10	4.72	0.37	99.46	1.78	0.06	0.26	0.22	0.04	0.10	0.18	0.00	0.69	0.90	0.04	4.00	0.80	47.11	45.13	7.77	100.00
T4	Takab	4-1 same cpx microphenо rim	47.62	2.21	5.90	0.00	12.38	22.47	0.00	8.92	0.52	100.02	1.93	0.01	0.10	0.07	0.03	0.02	0.12	0.00	0.91	0.85	0.03	4.00	0.88	48.24	36.95	14.82	100.00
T6	Takab	2-1 cpx microphenо core	52.99	0.48	2.27	0.85	16.75	21.70	0.10	4.72	0.45	100.30	1.80	0.06	0.23	0.20	0.03	0.09	0.17	0.01	0.73	0.90	0.03	4.00	0.81	44.51	47.79	7.70	100.00
T6	Takab	2-2 same cpx microphenо rim	47.84	2.03	5.24	0.03	13.00	22.25	0.17	8.23	0.36	99.14	1.79	0.05	0.22	0.21	0.01	0.13	0.11	0.01	0.75	0.92	0.02	4.00	0.87	47.50	38.60	13.90	100.00
T6	Takab	2-3 cpx glom rim	47.67	1.78	4.98	0.02	13.43	22.90	0.16	7.67	0.34	98.94	1.89	0.02	0.14	0.11	0.02	0.06	0.10	0.00	0.88	0.86	0.03	4.00	0.90	48.07	39.22	12.71	100.00
T6	Takab	2-5 cpx gm	52.56	0.73	1.92		16.22	23.05	0.14	5.69	0.28	100.58	1.93	0.01	0.08	0.07	0.01	0.04	0.09	0.00	0.91	0.87	0.03	4.00	0.91	45.49	47.67	6.84	100.00

Table 12: (continued)

Sample	Location	Description	SiO_2	TiO_2	Al_2O_3	Cr_2O_3	MgO	CaO	MnO	FeO	Na_2O	Total	Si	Ti	$Al_{(tot)}$	$Al_{(T)}$	$Al_{(M1)}$	$Fe^{3+}{}_{(M1)}$	Fe^{2+}	Mn	Mg	Ca	Na	Total	Mg#	Wo	En	Fs	Total
T6	Takab	3-10 cpx pheno core	51.49	0.64	3.15	0.99	16.10	21.83	0.05	5.08	0.49	99.82	1.91	0.01	0.12	0.09	0.03	0.07	0.10	0.01	0.96	0.80	0.03	4.00	0.91	45.28	46.45	8.28	100.00
Q-T27	Dehgolan	cpx microphen 1-1	52.36	0.40	2.69	0.10	17.59	20.49	0.21	5.42	0.41	99.67	1.94	0.01	0.09	0.06	0.04	0.02	0.12	0.01	0.95	0.83	0.03	4.00	0.89	41.51	49.58	8.91	100.00
Q-T27	Dehgolan	cpx microphen 1-2	53.24	0.28	2.10	0.23	17.39	21.26	0.16	4.60	0.36	99.62	1.96	0.01	0.06	0.04	0.02	0.03	0.10	0.01	1.00	0.81	0.03	4.00	0.91	43.24	49.20	7.56	100.00
Q-T27	Dehgolan	cpx microphen 2-7	54.03	0.24	1.38	0.37	18.54	20.74	0.17	4.11	0.41	99.99	1.96	0.01	0.06	0.04	0.02	0.02	0.13	0.01	0.98	0.82	0.02	4.00	0.88	41.58	51.72	6.70	100.00
Q-T27	Dehgolan	cpx microphen rim 3-4	54.07	0.23	1.33	0.11	18.03	21.09	0.18	4.94	0.27	100.23	1.96	0.01	0.08	0.04	0.05	0.00	0.13	0.01	0.96	0.80	0.03	4.00	0.88	42.04	50.00	7.97	100.00
Q-T27	Dehgolan	same cpx microphen core 3-5	54.42	0.25	1.98	0.22	17.90	20.76	0.18	4.45	0.45	100.61	1.99	0.01	0.02	0.01	0.01	0.01	0.11	0.00	1.00	0.84	0.02	4.00	0.90	42.13	50.54	7.34	100.00
Q-T29	Dehgolan	cpx gm 2-4	54.97	0.27	0.47	0.10	18.64	21.71	0.16	3.98	0.23	100.53	1.98	0.01	0.03	0.02	0.00	0.02	0.12	0.01	0.99	0.84	0.02	4.00	0.90	42.67	50.97	6.36	100.00
Q-T29	Dehgolan	cpx gm 3-4	54.77	0.39	0.60	0.02	18.50	21.65	0.23	4.40	0.23	100.77	1.99	0.01	0.02	0.01	0.01	0.01	0.12	0.00	0.96	0.87	0.02	4.00	0.89	42.45	50.46	7.09	100.00
Q-T29	Dehgolan	cpx gm 3-5	54.74	0.32	0.42	0.00	17.80	22.34	0.11	4.27	0.28	100.29	2.00	0.01	0.02	0.00	0.02	0.00	0.13	0.00	0.97	0.87	0.00	4.00	0.88	44.22	49.01	6.77	100.00
Q-T29	Dehgolan	cpx gm 3-6	55.21	0.32	0.48	0.01	17.96	22.56	0.14	4.25	0.00	100.92	2.00	0.01	0.02	0.00	0.02	0.00	0.14	0.01	0.95	0.86	0.02	4.00	0.87	44.26	49.02	6.73	100.00
Q-T29	Dehgolan	cpx microphen 4-1	55.11	0.24	0.54	0.00	17.50	22.21	0.23	4.59	0.28	100.68	1.88	0.01	0.15	0.12	0.02	0.11	0.08	0.01	0.85	0.88	0.04	4.00	0.92	44.14	48.38	7.48	100.00
IR1	Qorveh	Cpx microphen 4-1	51.67	0.34	3.42	0.06	15.65	22.69	0.20	6.24	0.53	100.79	1.88	0.01	0.16	0.12	0.04	0.09	0.10	0.01	0.87	0.84	0.03	4.00	0.90	45.86	44.00	10.15	100.00
IR1	Qorveh	Cpx microphen rim 4-2	51.49	0.49	3.75	0.09	16.10	21.45	0.23	6.39	0.48	100.47	1.88	0.01	0.17	0.12	0.05	0.09	0.12	0.01	0.76	0.91	0.05	4.00	0.87	43.75	45.71	10.54	100.00
IR1	Qorveh	Cpx microphen 4-3	51.78	0.34	3.97	0.07	13.93	23.27	0.24	6.90	0.75	101.25	1.95	0.01	0.03	0.03	0.00	0.06	0.18	0.01	0.86	0.84	0.04	4.00	0.83	48.25	40.19	11.55	100.00
IR1	Qorveh	Cpx gm 4-6	53.36	0.40	0.78	0.00	15.70	21.40	0.44	8.49	0.53	101.10	1.89	0.01	0.15	0.11	0.03	0.07	0.06	0.00	0.91	0.86	0.03	4.00	0.94	42.61	43.49	13.90	100.00
IR1	Qorveh	Cpx glom core 3-1	52.53	0.40	3.47	0.97	16.93	22.26	0.13	4.29	0.50	101.48	1.90	0.01	0.09	0.09	0.00	0.10	0.13	0.01	0.84	0.85	0.04	4.00	0.87	45.18	47.81	7.00	100.00
IR1	Qorveh	Cpx glom 3-2	51.96	0.39	2.01	0.71	15.32	21.77	0.42	7.79	0.59	100.95	1.91	0.02	0.09	0.09	0.00	0.07	0.06	0.00	0.93	0.88	0.02	4.00	0.94	43.98	43.07	12.95	100.00
IR1	Qorveh	Cpx glom 3-3	52.90	0.57	2.03	0.50	17.22	22.84	0.14	4.63	0.36	101.18	1.93	0.01	0.09	0.07	0.02	0.04	0.08	0.00	0.96	0.84	0.03	4.00	0.92	45.21	47.43	7.37	100.00
IR1	Qorveh	Cpx glom 3-4	53.58	0.27	2.11	0.61	17.78	21.72	0.11	4.13	0.43	100.72	1.86	0.01	0.17	0.14	0.04	0.11	0.08	0.01	0.87	0.84	0.04	4.00	0.92	43.64	49.71	6.65	100.00
IR2	Qorveh	Cpx pheno rim 1-1	50.87	0.54	4.01	0.05	16.01	21.45	0.21	6.14	0.54	99.80	1.92	0.01	0.06	0.06	0.00	0.07	0.04	0.00	0.93	0.92	0.02	4.00	0.96	44.06	45.75	10.19	100.00
IR2	Qorveh	Same cpx pheno rim 1-2	52.70	0.32	1.47	0.58	17.02	23.44	0.13	3.73	0.35	99.73	1.89	0.01	0.10	0.10	0.00	0.11	0.01	0.00	0.98	0.84	0.03	4.00	0.99	46.75	47.23	6.01	100.00
IR2	Qorveh	Cpx pheno rim 2-1	52.11	0.27	2.32	0.58	18.02	21.69	0.07	4.12	0.47	99.63	1.91	0.01	0.11	0.09	0.02	0.07	0.05	0.00	0.94	0.86	0.03	4.00	0.95	43.35	50.11	6.54	100.00
IR2	Qorveh	Same cpx pheno core 2-2	52.36	0.34	2.57	0.56	17.29	21.92	0.05	4.12	0.49	99.71	1.95	0.00	0.05	0.05	0.01	0.03	0.19	0.01	1.71	0.05	0.00	4.00	0.90	44.52	48.87	6.62	100.00
Q-T27	Dehgolan	opx microphen 1-3	56.62	0.09	1.30	0.37	33.28	1.25	0.18	7.42	0.06	100.56	1.95	0.00	0.05	0.05	0.00	0.04	0.18	0.00	1.72	0.05	0.00	4.00	0.91	2.34	86.57	11.09	100.00
Q-T27	Dehgolan	opx microphen 1-4	56.24	0.12	1.17	0.22	33.37	1.21	0.13	7.72	0.01	100.18	1.96	0.00	0.04	0.04	0.00	0.03	0.21	0.00	1.70	0.04	0.00	4.00	0.89	2.25	86.35	11.40	100.00
Q-T27	Dehgolan	opx microphen 2-4	56.35	0.12	0.92	0.15	32.72	1.20	0.16	8.56	0.03	100.23	1.97	0.00	0.04	0.03	0.01	0.01	0.19	0.01	1.73	0.05	0.00	4.00	0.90	2.24	85.04	12.72	100.00
Q-T27	Dehgolan	opx microphen 2-5	57.57	0.09	1.00	0.31	33.87	1.24	0.20	7.09	0.02	101.38	1.93	0.00	0.07	0.07	0.00	0.04	0.14	0.00	1.74	0.04	0.00	4.00	0.93	2.29	87.18	10.53	100.00
Q-T27	Dehgolan	opx microphen 4-5	55.98	0.10	1.64	0.80	33.84	1.21	0.13	6.23	0.06	99.98	1.96	0.01	0.05	0.04	0.02	0.00	0.47	0.02	1.43	0.05	0.00	4.00	0.75	2.27	88.40	9.32	99.99
IR2	Qorveh	Opx in pheno amph rim 5-7	54.23	0.39	1.21	0.00	26.50	1.36	0.61	15.45	0.03	99.78	1.91	0.01	0.05	0.05	0.00	0.07	0.40	0.02	1.45	0.04	0.00	4.00	0.79	2.68	72.62	24.70	100.00
IR2	Qorveh	Opx in pheno amph rim 5-4	53.16	0.46	1.29	0.00	27.11	1.09	0.76	16.83	0.07	100.77	1.98	0.01	0.04	0.02	0.02	0.00	0.45	0.02	1.45	0.04	0.00	4.00	0.76	2.07	71.78	26.15	100.00
IR2	Qorveh	Opx in pheno amph rim 5-5	54.50	0.45	0.97	0.00	26.80	1.09	0.57	14.82	0.07	99.24	2.02	0.01	0.02	0.00	0.02	0.00	0.53	0.02	1.32	0.06	0.02	4.00	0.71	2.15	74.01	23.84	100.00
IR5	Qorveh	Opx in coarse inclusion 1-6	55.78	0.28	0.56	0.01	24.41	1.50	0.67	17.55	0.33	101.09	1.98	0.01	0.01	0.01	0.00	0.02	0.52	0.03	1.35	0.06	0.02	4.00	0.72	3.02	68.35	28.63	100.00
IR5	Qorveh	Opx in coarse inclusion 1-7	53.44	0.28	0.34	0.04	24.45	1.40	0.84	17.51	0.22	98.51	1.96	0.01	0.02	0.02	0.00	0.05	0.51	0.03	1.35	0.04	0.02	4.00	0.73	2.81	68.38	28.81	100.00
IR5	Qorveh	Opx in coarse inclusion 1-8	53.29	0.19	0.55	0.07	24.55	1.14	0.81	18.54	0.30	99.43	1.96	0.01	0.02	0.02	0.00	0.51	0.03	1.35	0.04	0.00	0.00	0.73	0.63	2.25	67.77	29.98	100.00

Table 13: EMP analysis for Bijar-Qorveh feldspar compositions

Sample	Location	Description	SiO_2	TiO_2	Al_2O_3	MnO	FeO	CaO	Na_2O	K_2O	BaO	SrO	Total	Si	Ti	Al	Mn	Fe'''	Ca	Na	K	Ba	Sr	Total	An	Ab	Or	Total
Q-T36	Bijar	pl gm 1-4	56.90	0.10	26.80	0.03	0.88	8.51	5.91	1.28			100.40	10.24	0.01	5.69	0.00	0.09	1.64	2.06	0.29	0.00	0.00	20.03	41.06	51.58	7.37	100.00
Q-T36	Bijar	Pl gm 1-5	57.49	0.16	26.52	0.01	0.74	8.15	6.39	0.81			100.26	10.33	0.02	5.61	0.00	0.07	1.57	2.23	0.18	0.00	0.00	20.01	39.41	55.95	4.64	100.00
Q-T36	Bijar	Pl gm 3-5	55.47	0.13	28.24	0.05	0.89	10.41	5.26	0.34			100.79	9.95	0.02	5.97	0.01	0.09	2.00	1.83	0.08	0.00	0.00	19.95	51.20	46.81	1.99	100.00
Q-T36	Bijar	Pl gm 3-6	58.04	0.16	25.59	0.03	0.57	7.13	6.48	1.72			99.71	10.49	0.02	5.45	0.00	0.06	1.38	2.27	0.40	0.00	0.00	20.07	34.10	56.12	9.78	100.00
Q-T39	Bijar	Pl gm 1-1	51.32	0.08	30.87	0.00	0.80	13.83	3.65	0.17			100.71	9.31	0.01	6.60	0.00	0.08	2.69	1.28	0.04	0.00	0.00	20.00	67.03	31.99	0.99	100.00
Q-T39	Bijar	Pl gm 2-1	51.45	0.04	30.62	0.03	0.62	13.85	3.69	0.21			100.52	9.34	0.01	6.56	0.01	0.06	2.70	1.30	0.05	0.00	0.00	20.02	66.68	32.12	1.20	100.00
Q-T39	Bijar	Pl gm 2-5	51.20	0.07	30.29	0.01	0.79	13.64	3.85	0.22			100.08	9.35	0.01	6.52	0.00	0.08	2.67	1.36	0.05	0.00	0.00	20.05	65.35	33.39	1.25	100.00
Q-T39	Bijar	Pl gm 4-3	55.73	0.13	28.21	0.03	0.78	10.48	5.58	0.37			101.31	9.96	0.02	5.94	0.00	0.08	2.01	1.93	0.09	0.00	0.00	20.03	49.84	48.04	2.11	100.00
Q-T39	Bijar	Pl gm 4-9	53.90	0.09	28.79	0.02	0.88	11.73	4.94	0.33			100.68	9.74	0.01	6.13	0.00	0.09	2.27	1.73	0.08	0.00	0.00	20.05	55.71	42.42	1.88	100.00
Q-T6	Qezelke Kand	Pl gm 1-3	53.90	0.34	26.57	0.00	1.21	9.66	6.30	0.81			98.78	9.95	0.05	5.79	0.00	0.12	1.91	2.26	0.19	0.00	0.00	20.27	43.85	51.79	4.36	100.00
Q-T6	Qezelke Kand	Pl gm 1-7	56.35	0.16	26.09	0.00	0.60	6.58	7.09	1.77			98.63	10.33	0.02	5.64	0.00	0.06	1.29	2.52	0.41	0.00	0.00	20.27	30.58	59.63	9.79	100.00
Q-T6	Qezelke Kand	Pl gm 1-7bis	56.42	0.10	26.09	0.04	0.56	6.61	7.35	1.68			98.84	10.32	0.01	5.63	0.01	0.06	1.29	2.61	0.39	0.00	0.00	20.32	30.16	60.73	9.11	100.00
Q-T6	Qezelke Kand	pl gm 2-6	53.30	0.15	28.67	0.01	0.87	10.78	5.23	0.35	0.16	0.94	100.46	9.71	0.02	6.16	0.00	0.09	2.10	1.85	0.08	0.01	0.10	20.12	52.15	45.84	2.01	100.00
Q-T6	Qezelke Kand	Pl gm 2-7	53.54	0.18	28.47	0.00	0.73	9.31	6.57	0.66	0.20	0.75	100.40	9.76	0.02	6.12	0.00	0.07	1.82	2.32	0.15	0.01	0.08	20.36	42.38	54.07	3.55	100.00
Q-T6	Qezelke Kand	Pl gm 3-1	53.81	0.13	27.71	0.01	0.69	9.66	5.46	0.75	0.30	0.75	99.25	9.89	0.02	6.01	0.00	0.07	1.90	1.94	0.17	0.02	0.08	20.11	47.30	48.35	4.35	100.00
Q-T6	Qezelke Kand	Pl gm 3-2	53.70	0.16	28.06	0.00	0.66	9.90	5.58	0.45	0.24	0.97	99.71	9.83	0.02	6.06	0.00	0.07	1.94	1.98	0.11	0.02	0.10	20.13	48.20	49.18	2.61	100.00
Q-T9	Qezelke Kand	pheno pl core 1-2	61.28	0.00	24.43	0.00	0.22	5.86	8.06	0.50	0.12	0.23	100.69	10.86	0.00	5.11	0.00	0.02	1.11	2.77	0.11	0.01	0.02	20.02	27.85	69.32	2.83	100.00
Q-T9	Qezelke Kand	big pheno cribrose pl rim 1-1	59.80	0.01	25.37	0.02	0.25	6.77	7.61	0.43	0.13	0.33	100.71	10.64	0.00	5.32	0.00	0.02	1.29	2.62	0.10	0.01	0.03	20.05	32.18	65.40	2.42	100.00
Q-T9	Qezelke Kand	big pheno cribrose pl mantle 1-3	60.01	0.01	24.97	0.05	0.24	6.54	7.64	0.46	0.10	0.19	100.19	10.71	0.00	5.25	0.01	0.02	1.25	2.64	0.10	0.01	0.02	20.02	31.30	66.10	2.60	100.00
Q-T9	Qezelke Kand	big pheno cribrose pl core 1-4	59.26	0.01	25.07	0.00	0.19	6.73	7.35	0.40	0.00	0.31	99.30	10.67	0.00	5.32	0.00	0.02	1.30	2.56	0.09	0.00	0.03	19.99	32.81	64.87	2.32	100.00
Q-T9	Qezelke Kand	feld gm 1-12	62.19	0.07	23.17	0.00	0.47	4.53	8.67	0.87	0.40	0.00	100.38	11.07	0.01	4.86	0.00	0.05	0.86	2.99	0.20	0.03	0.00	20.07	21.31	73.82	4.87	100.00
Q-T9	Qezelke Kand	pl microphen 2-4	56.22	0.00	26.77	0.00	0.19	8.37	6.72	0.35	0.02	0.33	98.97	10.23	0.00	5.74	0.00	0.02	1.63	2.37	0.08	0.00	0.03	20.11	39.94	58.05	2.01	100.00
Q-T9	Qezelke Kand	fel pheno rim 3-5	60.72	0.00	24.54	0.00	0.24	5.97	8.05	0.48	0.09	0.29	100.38	10.81	0.00	5.15	0.00	0.02	1.14	2.78	0.11	0.01	0.03	20.05	28.28	69.03	2.69	100.00
Q-T9	Qezelke Kand	same fel pheno core 3-6	58.49	0.00	25.09	0.00	0.25	6.77	7.38	0.45	0.10	0.34	98.85	10.61	0.00	5.36	0.00	0.02	1.31	2.59	0.10	0.01	0.04	20.05	32.77	64.64	2.59	100.00
T4	Takab	1-3 gm pl	64.76	0.24	19.36	0.01	0.31	1.18	5.13	8.35			99.35	11.77	0.03	4.15	0.00	0.03	0.23	1.81	1.94	0.00	0.00	19.96	5.80	45.51	48.70	100.00
T4	Takab	4-3 pl gm	65.13	0.29	20.10	0.00	0.33	1.67	5.87	6.88			100.26	11.65	0.04	4.24	0.00	0.03	0.32	2.03	1.57	0.00	0.00	19.88	8.15	51.83	40.01	100.00
T6	Takab	2-4 pl gm	51.95	0.12	28.27	0.00	0.93	12.08	4.32	0.31			97.98	9.65	0.02	6.19	0.00	0.10	2.40	1.56	0.07	0.00	0.00	20.00	59.58	38.59	1.83	100.00
T6	Takab	3-5 pl gm	63.98	0.11	18.69	0.05	0.47	1.31	4.96	8.85			98.42	11.80	0.02	4.06	0.01	0.05	0.26	1.77	2.08	0.00	0.00	20.05	6.27	43.12	50.61	100.00
T6	Takab	3-6 pl gm	51.19	0.20	25.47	0.00	1.12	9.62	4.09	0.70			92.39	10.01	0.03	5.87	0.00	0.12	2.01	1.55	0.17	0.00	0.00	19.77	53.88	41.44	4.68	100.00
T6	Takab	3-7 pl gm	54.64	0.10	28.05	0.03	0.59	11.60	4.96	0.33			100.29	9.84	0.01	5.95	0.00	0.06	2.24	1.73	0.08	0.00	0.00	19.91	55.29	42.82	1.90	100.00
T6	Takab	3-8 pl gm	64.23	0.21	18.88	0.04	0.88	1.47	4.66	9.17			99.55	11.71	0.03	4.06	0.01	0.09	0.29	1.65	2.13	0.00	0.00	19.97	7.05	40.52	52.43	100.00
Q-T20	Dehgolan	fel pheno rim 1-1	63.08	0.01	23.59	0.03	0.17	5.06	8.24	1.03	0.02	0.00	101.22	11.08	0.00	4.89	0.00	0.02	0.95	2.81	0.23	0.00	0.00	19.98	23.88	70.35	5.77	100.00
Q-T20	Dehgolan	fel pheno core 1-2	61.90	0.03	24.86	0.00	0.16	6.24	7.83	0.40	0.03	0.00	101.46	10.85	0.00	5.14	0.00	0.02	1.17	2.66	0.09	0.00	0.00	19.94	29.87	67.84	2.29	100.00
Q-T20	Dehgolan	fel micropheno 1-3	61.97	0.00	24.62	0.03	0.21	5.87	7.92	0.81	0.01	0.05	101.49	10.88	0.00	5.10	0.00	0.02	1.11	2.70	0.18	0.00	0.01	20.00	27.76	67.68	4.56	100.00
Q-T20	Dehgolan	fel pheno 1-4	64.51	0.03	22.88	0.00	0.05	4.26	8.83	1.08	0.00	0.00	101.65	11.26	0.00	4.71	0.00	0.00	0.80	2.99	0.24	0.00	0.00	20.00	19.78	74.23	5.99	100.00
Q-T20	Dehgolan	fel microphen 2-2	64.48	0.00	23.08	0.00	0.10	4.37	8.66	0.92	0.00	0.00	101.60	11.24	0.00	4.74	0.00	0.01	0.82	2.93	0.20	0.00	0.00	19.95	20.66	74.18	5.17	100.00
Q-T20	Dehgolan	fel gm 2-3	59.34	0.00	26.00	0.00	0.43	7.99	6.88	0.61	0.04	0.06	101.35	10.51	0.00	5.43	0.00	0.04	1.52	2.36	0.14	0.00	0.01	20.00	37.76	58.83	3.41	100.00
Q-T20	Dehgolan	fel gm 3-3	62.22	0.00	24.24	0.02	0.26	5.74	7.91	0.93	0.04	0.00	101.35	10.94	0.00	5.03	0.00	0.03	1.08	2.70	0.21	0.00	0.00	19.98	27.13	67.66	5.21	100.00
Q-T20	Dehgolan	fel pheno 3-4	59.30	0.04	26.17	0.00	0.27	8.12	6.68	0.47	0.08	0.12	101.24	10.50	0.00	5.46	0.00	0.03	1.54	2.29	0.11	0.01	0.01	19.95	39.10	58.20	2.70	100.00
Q-T20	Dehgolan	fel pheno 4-1	64.08	0.00	23.20	0.01	0.09	4.39	9.19	0.55	0.07	0.00	101.56	11.19	0.00	4.78	0.00	0.01	0.82	3.11	0.12	0.00	0.00	20.03	20.25	76.72	3.03	100.00
Q-T20	Dehgolan	fel gm 4-2	59.48	0.02	25.51	0.01	0.29	7.56	6.40	1.10	0.08	0.14	100.58	10.61	0.00	5.36	0.00	0.03	1.45	2.21	0.25	0.01	0.01	19.93	36.98	56.62	6.39	100.00
Q-T24	Dehgolan	pl pheno rim 1-1	60.12	0.04	24.26	0.00	0.19	5.66	8.27	0.71	0.17	0.12	99.54	10.81	0.01	5.14	0.00	0.02	1.09	2.88	0.16	0.01	0.01	20.13	26.36	69.71	3.93	100.00
Q-T24	Dehgolan	same pl pheno core 1-2	63.51	0.02	22.89	0.00	0.13	4.16	8.59	1.01	0.16	0.06	100.54	11.22	0.00	4.77	0.00	0.01	0.79	2.94	0.23	0.01	0.01	19.98	19.88	74.36	5.76	100.00
Q-T24	Dehgolan	same pl pheno core 1-3	62.51	0.00	23.14	0.03	0.13	4.36	8.74	0.92	0.07	0.03	99.94	11.12	0.00	4.85	0.00	0.01	0.83	3.02	0.21	0.01	0.00	20.06	20.48	74.36	5.15	100.00
Q-T24	Dehgolan	fel microphen 2-6	63.27	0.00	22.96	0.00	0.16	4.24	8.52	1.16	0.04	0.03	100.38	11.20	0.00	4.79	0.00	0.02	0.80	2.92	0.26	0.00	0.00	19.99	20.17	73.27	6.56	100.00
Q-T24	Dehgolan	fel pheno rim 2-7	62.50	0.04	22.86	0.00	0.21	4.11	8.67	1.07	0.03	0.00	99.49	11.16	0.01	4.81	0.00	0.02	0.79	3.00	0.24	0.00	0.00	20.04	19.51	74.45	6.04	100.00
Q-T24	Dehgolan	same fel pheno core 2-8	61.42	0.00	23.06	0.04	0.20	4.42	8.58	0.89	0.07	0.03	98.70	11.07	0.00	4.90	0.01	0.02	0.85	3.00	0.21	0.00	0.00	20.07	21.02	73.91	5.07	100.00
Q-T24	Dehgolan	fel pheno core 3-1	62.55	0.01	23.23	0.00	0.18	4.37	8.55	1.02	0.12	0.07	100.08	11.12	0.00	4.87	0.00	0.02	0.83	2.95	0.23	0.01	0.01	20.03	20.76	73.49	5.74	100.00
Q-T24	Dehgolan	fel micropheno 3-2	63.54	0.00	22.95	0.00	0.21	4.23	8.93	1.10	0.08	0.05	101.10	11.18	0.00	4.76	0.00	0.02	0.80	3.05	0.25	0.01	0.00	20.07	19.50	74.46	6.04	100.00

Table 13: (continued)

Sample	Location	Description	SiO_2	TiO_2	Al_2O_3	MnO	FeO	CaO	Na_2O	K_2O	BaO	SrO	Total	Si	Ti	Al	Mn	$Fe^{'''}$	Ca	Na	K	Ba	Sr	Total	An	Ab	Or	Total
Q-T27	Dehgolan	fel gm 1-5	57.30	0.02	26.98	0.01	0.27	9.12	6.12	0.36	0.00	0.05	100.21	10.27	0.00	5.70	0.00	0.03	1.75	2.13	0.08	0.00	0.00	19.97	44.23	53.71	2.06	100.00
Q-T27	Dehgolan	fel gm 1-8	56.63	0.02	27.27	0.00	0.22	9.55	5.94	0.39	0.03	0.03	100.07	10.18	0.00	5.78	0.00	0.02	1.84	2.07	0.09	0.00	0.00	19.99	46.03	51.74	2.23	100.00
Q-T27	Dehgolan	same fel pheno clear rim 2-2	60.27	0.00	24.20	0.01	0.12	5.84	7.73	0.87	0.06	0.06	99.15	10.85	0.00	5.13	0.00	0.01	1.13	2.70	0.20	0.00	0.01	20.03	28.01	67.02	4.97	100.00
Q-T27	Dehgolan	same fel pheno clear core 2-3	59.66	0.02	25.36	0.03	0.16	6.75	7.37	0.52	0.06	0.04	99.95	10.66	0.00	5.34	0.00	0.02	1.29	2.55	0.12	0.00	0.00	19.99	32.63	64.39	2.97	100.00
Q-T27	Dehgolan	fel pheno spongy rim 3-6	61.88	0.00	23.58	0.00	0.21	5.15	7.64	1.35	0.05	0.00	99.87	11.03	0.00	4.96	0.00	0.02	0.98	2.64	0.31	0.00	0.00	19.95	25.00	67.17	7.83	100.00
Q-T27	Dehgolan	same fel pheno clear rim 3-7	59.62	0.02	25.11	0.07	0.13	6.76	7.46	0.65	0.07	0.02	99.92	10.67	0.00	5.30	0.01	0.01	1.30	2.59	0.15	0.01	0.00	20.04	32.12	64.19	3.70	100.00
Q-T27	Dehgolan	same fel pheno clear core 3-8	61.29	0.01	23.69	0.00	0.15	5.23	8.05	0.95	0.01	0.01	99.39	10.98	0.00	5.00	0.00	0.01	1.00	2.80	0.22	0.00	0.00	20.02	24.99	69.59	5.42	100.00
Q-T27	Dehgolan	fel gm 3-9	56.13	0.02	26.86	0.00	0.28	8.95	6.13	0.54	0.05	0.02	98.97	10.21	0.00	5.76	0.00	0.03	1.75	2.16	0.12	0.00	0.00	20.04	43.30	53.62	3.08	100.00
Q-T27	Dehgolan	fel pheno core 4-1	55.56	0.00	27.16	0.00	0.19	8.80	6.07	0.36	0.12	0.11	98.37	10.16	0.00	5.86	0.00	0.02	1.73	2.15	0.08	0.01	0.01	20.02	43.56	54.31	2.13	100.00
Q-T27	Dehgolan	fel pheno core 4-1bis	55.61	0.04	27.13	0.00	0.25	9.30	6.24	0.30	0.04	0.13	99.04	10.12	0.01	5.82	0.00	0.03	1.81	2.20	0.07	0.00	0.01	20.08	44.37	53.94	1.69	100.00
Q-T29	Dehgolan	fel pheno rim 1-1	63.25	0.02	23.38	0.00	0.16	4.76	8.42	1.16	0.07	0.00	101.21	11.12	0.00	4.85	0.00	0.02	0.90	2.87	0.26	0.00	0.00	20.01	22.27	71.24	6.48	100.00
Q-T29	Dehgolan	same fel pheno rim 1-2	63.05	0.00	23.23	0.02	0.15	4.73	8.19	1.07	0.06	0.00	100.50	11.15	0.00	4.84	0.00	0.02	0.90	2.81	0.24	0.00	0.00	19.95	22.71	71.20	6.10	100.00
Q-T29	Dehgolan	same fel pheno core 1-3	63.42	0.01	23.19	0.01	0.18	4.70	8.23	1.05	0.05	0.00	100.84	11.17	0.00	4.81	0.00	0.02	0.89	2.81	0.24	0.00	0.00	19.94	22.54	71.46	6.00	100.00
Q-T29	Dehgolan	same fel pheno core 1-4	62.01	0.00	24.26	0.00	0.10	5.46	8.00	0.69	0.01	0.03	100.57	10.96	0.00	5.06	0.00	0.01	1.03	2.74	0.16	0.00	0.00	19.96	26.28	69.74	3.98	100.00
Q-T29	Dehgolan	feld gm 2-3	61.91	0.01	24.49	0.03	0.14	5.99	7.73	0.40			100.69	10.92	0.00	5.09	0.00	0.01	1.13	2.64	0.09	0.00	0.00	19.89	29.27	68.41	2.33	100.00
Q-T29	Dehgolan	fel microphen 4-4	62.32	0.00	24.17	0.05	0.13	5.77	7.92	0.89	0.02	0.00	101.28	10.96	0.00	5.01	0.01	0.01	1.09	2.70	0.20	0.00	0.00	19.98	27.28	67.69	5.03	100.00
IR1	Qorveh	Pheno pl rim 5-1	56.11	0.00	26.88	0.07	0.42	9.30	5.71	0.53	0.08	0.27	99.36	10.19	0.00	5.76	0.01	0.04	1.81	2.01	0.12	0.01	0.03	19.98	45.88	51.01	3.11	100.00
IR1	Qorveh	Same pheno pl rim 5-2	56.01	0.03	27.47	0.00	0.42	9.93	5.54	0.41	0.03	0.12	99.94	10.11	0.00	5.84	0.00	0.04	1.92	1.94	0.09	0.00	0.01	19.96	48.57	49.05	2.38	100.00
IR1	Qorveh	Same pheno pl mantle1 5-3	57.59	0.04	26.98	0.01	0.37	8.88	6.10	0.64	0.08	0.26	100.93	10.28	0.00	5.68	0.00	0.04	1.70	2.11	0.14	0.01	0.03	19.99	42.95	53.39	3.66	100.00
IR1	Qorveh	Same pheno pl mantle2 5-4	58.03	0.04	26.47	0.02	0.32	8.86	6.07	0.64	0.10	0.26	100.80	10.36	0.00	5.57	0.00	0.03	1.69	2.10	0.15	0.01	0.03	19.95	42.98	53.31	3.71	100.00
IR1	Qorveh	Same pheno pl core2 5-5	60.36	0.00	24.42	0.00	0.29	7.10	6.90	0.90	0.09	0.15	100.21	10.78	0.00	5.14	0.00	0.03	1.36	2.39	0.21	0.01	0.02	19.93	34.34	60.46	5.20	100.00
IR1	Qorveh	Same pheno pl core1 5-6	60.03	0.01	25.17	0.00	0.20	7.16	6.76	0.88	0.05	0.16	100.42	10.69	0.00	5.29	0.00	0.02	1.37	2.34	0.20	0.00	0.02	19.92	35.00	59.85	5.15	100.00
IR1	Qorveh	Pl gm 5-7	55.92	0.01	28.00	0.00	0.60	10.50	5.40	0.28	0.13	0.00	100.83	10.02	0.00	5.91	0.00	0.06	2.02	1.87	0.06	0.01	0.00	19.96	50.98	47.41	1.61	100.00
IR1	Qorveh	Same pheno pl true core 5-8	56.04	0.06	27.50	0.00	0.25	10.41	5.31	0.40	0.01	0.14	100.12	10.09	0.01	5.84	0.00	0.02	2.01	1.86	0.09	0.00	0.01	19.94	50.80	46.90	2.30	100.00
IR1	Qorveh	Pl gm 4-4	63.78	0.02	23.04	0.05	0.44	4.89	8.23	0.76	0.10	0.00	101.31	11.18	0.00	4.76	0.01	0.04	0.92	2.80	0.17	0.01	0.00	19.89	23.65	71.95	4.40	100.00
IR1	Qorveh	Pl glom 3-5	63.24	0.02	22.62	0.00	0.46	4.89	8.10	1.00	0.11	0.00	100.44	11.20	0.00	4.72	0.00	0.05	0.93	2.78	0.23	0.01	0.00	19.92	23.59	70.69	5.73	100.00
IR1	Qorveh	Pheno pl core 2-1	57.96	0.02	26.35	0.00	0.25	8.86	6.09	0.64	0.08	0.06	100.31	10.38	0.00	5.56	0.00	0.03	1.70	2.12	0.15	0.01	0.01	19.95	42.91	53.38	3.71	100.00
IR1	Qorveh	Same pheno pl cribrose mantle 2-2	59.52	0.02	25.44	0.04	0.28	7.86	6.76	0.55	0.10	0.14	100.70	10.60	0.00	5.34	0.01	0.03	1.50	2.33	0.13	0.01	0.01	19.95	37.90	58.94	3.16	100.00
IR1	Qorveh	Same pheno pl cribrose mantle 2-2bis	57.75	0.01	26.45	0.02	0.27	9.14	6.07	0.50	0.06	0.15	100.41	10.34	0.00	5.59	0.00	0.03	1.75	2.11	0.12	0.00	0.02	19.96	44.12	52.98	2.90	100.00
IR1	Qorveh	Same pheno pl cribrose mantle 2-3	56.69	0.02	26.99	0.03	0.30	9.75	5.61	0.50	0.06	0.21	100.15	10.21	0.00	5.73	0.00	0.03	1.88	1.96	0.11	0.00	0.02	19.95	47.58	49.53	2.88	100.00
IR1	Qorveh	Same pheno pl clear mantle 2-4	58.49	0.00	25.84	0.04	0.23	8.29	6.14	0.69	0.07	0.21	100.00	10.50	0.00	5.47	0.01	0.02	1.59	2.14	0.16	0.01	0.02	19.91	41.01	54.95	4.03	100.00
IR1	Qorveh	Same pheno pl rim 2-5	56.86	0.00	27.19	0.02	0.33	9.44	6.00	0.45	0.10	0.06	100.46	10.20	0.00	5.75	0.00	0.03	1.82	2.09	0.10	0.01	0.01	20.00	45.31	52.10	2.58	100.00
IR1	Qorveh	San gm 4-5	65.54	0.04	18.86	0.00	0.46	0.45	2.45	12.82	0.84	0.01	101.48	11.90	0.01	4.04	0.00	0.05	0.09	0.86	2.97	0.06	0.00	19.97	2.21	21.99	75.80	100.00
IR2	Qorveh	Pl pheno rim 1-5	56.51	0.01	27.25	0.02	0.50	9.74	5.83	0.27	0.06	0.00	100.19	10.16	0.00	5.78	0.00	0.05	1.88	2.03	0.06	0.00	0.00	19.97	47.24	51.18	1.58	100.00
IR2	Qorveh	Same pl pheno core 1-6	58.25	0.00	26.01	0.02	0.17	8.10	6.34	0.62	0.03	0.26	99.79	10.47	0.00	5.51	0.00	0.02	1.56	2.21	0.14	0.00	0.03	19.94	39.90	56.45	3.65	100.00
IR2	Qorveh	Pheno pl rim 2-3	56.00	0.03	27.12	0.02	0.48	9.72	5.96	0.43	0.10	0.00	99.85	10.13	0.00	5.78	0.00	0.05	1.88	2.09	0.10	0.01	0.00	20.05	46.27	51.30	2.43	100.00
IR2	Qorveh	Pheno pl rim 2-4	55.00	0.05	27.49	0.01	0.48	10.03	5.49	0.47	0.10	0.20	99.30	10.02	0.01	5.91	0.00	0.05	1.96	1.94	0.11	0.01	0.02	20.02	48.86	48.44	2.70	100.00
IR2	Qorveh	Pheno pl rim 2-5	55.51	0.07	27.28	0.00	0.34	9.97	5.42	0.50	0.10	0.35	99.55	10.08	0.01	5.84	0.00	0.03	1.94	1.91	0.12	0.01	0.04	19.98	48.95	48.12	2.92	100.00
IR2	Qorveh	Pheno pl mantle 2-6	55.82	0.02	27.01	0.00	0.36	9.94	5.84	0.48	0.07	0.23	99.77	10.12	0.00	5.77	0.00	0.04	1.93	2.05	0.11	0.00	0.02	20.05	47.17	50.13	2.69	100.00
IR2	Qorveh	Pheno pl mantle 2-7	59.18	0.01	25.01	0.00	0.20	7.30	6.77	0.88	0.05	0.13	99.52	10.65	0.00	5.31	0.00	0.02	1.41	2.36	0.20	0.00	0.01	19.97	35.47	59.45	5.08	100.00
IR2	Qorveh	Pheno pl mantle 2-8	58.84	0.02	25.56	0.00	0.18	7.73	6.48	0.84	0.07	0.16	99.86	10.56	0.00	5.41	0.00	0.02	1.49	2.25	0.19	0.00	0.02	19.94	37.81	57.33	4.86	100.00
IR2	Qorveh	Pheno pl mantle 2-9	59.87	0.01	25.25	0.00	0.15	7.31	6.62	0.89	0.06	0.08	100.24	10.68	0.00	5.31	0.00	0.02	1.40	2.29	0.20	0.00	0.01	19.91	35.91	58.88	5.22	100.00
IR2	Qorveh	Pheno pl mantle 2-10	58.81	0.02	25.38	0.01	0.20	7.39	6.73	0.86	0.12	0.27	99.77	10.58	0.00	5.38	0.00	0.02	1.42	2.35	0.20	0.01	0.03	19.99	35.87	59.13	5.00	100.00
IR2	Qorveh	Pheno pl mantle 2-11	58.83	0.02	25.45	0.00	0.21	7.47	6.61	0.88	0.20	0.20	99.85	10.57	0.00	5.39	0.00	0.02	1.44	2.30	0.20	0.01	0.02	19.97	36.48	58.39	5.13	100.00
IR2	Qorveh	Pheno plmantle 2-12	58.52	0.00	25.43	0.01	0.17	7.54	6.70	0.84	0.09	0.17	99.47	10.56	0.00	5.41	0.00	0.02	1.46	2.34	0.19	0.01	0.02	20.00	36.47	58.68	4.85	100.00
IR2	Qorveh	Pheno pl mantle 2-13	58.93	0.01	25.38	0.04	0.11	7.32	6.67	0.92	0.11	0.12	99.61	10.60	0.00	5.38	0.01	0.01	1.41	2.33	0.21	0.01	0.01	19.97	35.73	58.95	5.32	100.00
IR2	Qorveh	Pheno pl mantle 2-14	58.61	0.01	25.63	0.00	0.21	7.69	6.66	0.86	0.13	0.23	100.06	10.53	0.00	5.43	0.00	0.02	1.48	2.32	0.20	0.01	0.02	20.01	37.03	58.04	4.93	100.00
IR2	Qorveh	Pheno pl core 2-15	59.88	0.00	24.28	0.00	0.13	7.32	7.31	0.91	0.15	0.25	100.22	10.73	0.00	5.13	0.00	0.01	1.41	2.54	0.21	0.01	0.03	20.07	33.83	61.18	4.99	100.00
IR2	Qorveh	Pheno pl core 2-16	60.08	0.00	24.82	0.00	0.19	6.57	7.05	1.00	0.09	0.11	99.91	10.75	0.00	5.24	0.00	0.02	1.26	2.44	0.23	0.01	0.01	19.96	32.02	62.18	5.80	100.00

Table 13: (continued)

Sample	Location	Description	SiO_2	TiO_2	Al_2O_3	MnO	FeO	CaO	Na_2O	K_2O	BaO	SrO	Total	Si	Ti	Al	Mn	$Fe^{'''}$	Ca	Na	K	Ba	Sr	Total	An	Ab	Or	Total
IR2	Qorveh	Pheno pl core 2-17	61.03	0.02	24.40	0.02	0.20	6.43	7.02	1.08	0.07	0.18	100.44	10.85	0.00	5.11	0.00	0.02	1.22	2.42	0.24	0.00	0.02	19.91	31.50	62.21	6.28	100.00
IR2	Qorveh	Pheno pl core 2-18	60.60	0.03	24.27	0.00	0.15	6.35	7.10	1.13	0.05	0.11	99.79	10.85	0.00	5.12	0.00	0.02	1.22	2.46	0.26	0.00	0.01	19.94	30.93	62.55	6.52	100.00
IR2	Qorveh	Pheno pl core 2-19	60.24	0.02	24.78	0.06	0.22	6.91	7.08	1.00	0.10	0.14	100.56	10.73	0.00	5.21	0.01	0.02	1.32	2.45	0.23	0.01	0.01	19.99	33.05	61.24	5.71	100.00
IR2	Qorveh	Pheno pl core 2-21	59.91	0.05	24.81	0.01	0.19	6.88	7.01	0.91	0.09	0.24	100.09	10.72	0.01	5.23	0.00	0.02	1.32	2.43	0.21	0.01	0.02	19.97	33.31	61.42	5.27	100.00
IR2	Qorveh	Pheno pl core 2-22	59.93	0.01	24.94	0.08	0.20	6.81	6.91	0.99	0.12	0.26	100.25	10.71	0.00	5.26	0.01	0.02	1.30	2.40	0.23	0.01	0.03	19.96	33.22	61.03	5.75	100.00
IR2	Qorveh	Pheno pl core 2-23	59.57	0.01	25.20	0.08	0.23	7.32	6.78	0.89	0.17	0.22	100.48	10.64	0.00	5.31	0.01	0.02	1.40	2.35	0.20	0.01	0.02	19.97	35.47	59.38	5.15	100.00
IR2	Qorveh	Pheno pl core 2-24	58.93	0.01	25.21	0.02	0.23	7.18	6.86	0.84	0.11	0.23	99.61	10.61	0.00	5.35	0.00	0.02	1.38	2.40	0.19	0.01	0.02	19.99	34.85	60.31	4.84	100.00
IR2	Qorveh	Pheno pl core 2-25	58.70	0.00	25.34	0.00	0.33	7.50	6.77	0.80	0.11	0.21	99.76	10.57	0.00	5.38	0.00	0.03	1.45	2.36	0.18	0.01	0.02	20.00	36.23	59.16	4.61	100.00
IR2	Qorveh	Pheno pl core 2-26	56.50	0.03	26.54	0.00	0.36	9.13	5.78	0.56	0.09	0.04	99.02	10.27	0.00	5.69	0.00	0.04	1.78	2.04	0.13	0.01	0.00	19.95	45.07	51.65	3.28	100.00
IR2	Qorveh	Pheno pl LINE3	54.03	0.04	28.20	0.02	0.52	10.90	5.16	0.31	0.05	0.03	99.27	9.86	0.01	6.07	0.00	0.05	2.13	1.83	0.07	0.00	0.00	20.02	52.90	45.30	1.80	100.00
IR2	Qorveh	Pheno pl LINE3	56.22	0.01	26.84	0.05	0.33	9.26	5.95	0.62	0.04	0.32	99.64	10.19	0.00	5.74	0.01	0.03	1.80	2.09	0.14	0.00	0.03	20.04	44.59	51.88	3.53	100.00
IR2	Qorveh	Pheno pl LINE3	56.60	0.00	27.00	0.00	0.36	10.12	5.54	0.47	0.08	0.31	100.48	10.18	0.00	5.72	0.00	0.04	1.95	1.93	0.11	0.01	0.03	19.96	48.90	48.41	2.69	100.00
IR2	Qorveh	Pheno pl LINE3	55.61	0.01	27.20	0.00	0.47	9.57	5.81	0.47	0.01	0.26	99.41	10.11	0.00	5.83	0.00	0.05	1.86	2.05	0.11	0.00	0.03	20.03	46.36	50.93	2.70	100.00
IR2	Qorveh	Pheno pl LINE3	58.10	0.00	25.89	0.04	0.30	7.88	6.61	0.63	0.12	0.11	99.68	10.47	0.00	5.50	0.01	0.03	1.52	2.31	0.14	0.01	0.01	20.00	38.27	58.09	3.64	100.00
IR2	Qorveh	Pheno pl LINE3	56.99	0.00	26.40	0.04	0.20	8.69	6.13	0.56	0.08	0.06	99.15	10.33	0.00	5.64	0.01	0.02	1.69	2.15	0.13	0.01	0.01	19.98	42.52	54.24	3.24	100.00
IR2	Qorveh	Pheno pl LINE3	58.36	0.02	25.71	0.00	0.14	7.94	6.43	0.62	0.06	0.22	99.50	10.51	0.00	5.46	0.00	0.01	1.53	2.25	0.14	0.00	0.02	19.94	39.09	57.27	3.64	100.00
IR2	Qorveh	Pheno pl LINE3	57.51	0.00	26.06	0.00	0.19	8.30	6.57	0.59	0.08	0.26	99.57	10.39	0.00	5.55	0.00	0.02	1.61	2.30	0.14	0.01	0.03	20.04	39.74	56.90	3.36	100.00
IR2	Qorveh	Pheno pl LINE3	55.75	0.01	27.33	0.08	0.23	9.36	5.94	0.41	0.12	0.18	99.41	10.12	0.00	5.85	0.01	0.02	1.82	2.09	0.10	0.01	0.02	20.04	45.41	52.20	2.39	100.00
IR2	Qorveh	Pheno pl LINE3	59.85	0.00	24.66	0.00	0.23	6.62	7.18	0.77	0.09	0.26	99.66	10.75	0.00	5.22	0.00	0.02	1.27	2.50	0.18	0.01	0.03	19.97	32.24	63.28	4.48	100.00
IR2	Qorveh	Pheno pl LINE3	58.23	0.02	25.55	0.04	0.24	7.98	6.28	0.52	0.12	0.21	99.19	10.52	0.00	5.44	0.01	0.02	1.55	2.20	0.12	0.01	0.02	19.90	39.96	56.94	3.10	100.00
IR2	Qorveh	Pheno pl LINE3	56.98	0.00	26.77	0.00	0.24	8.93	6.14	0.44	0.08	0.16	99.74	10.28	0.00	5.69	0.00	0.02	1.72	2.15	0.10	0.01	0.02	19.99	43.39	54.05	2.56	100.00
IR2	Qorveh	Pheno pl LINE3	58.72	0.01	25.90	0.02	0.19	8.25	6.28	0.51	0.01	0.16	100.04	10.51	0.00	5.47	0.00	0.02	1.58	2.18	0.12	0.00	0.02	19.89	40.77	56.20	3.03	100.00
IR2	Qorveh	Pheno pl LINE3	59.85	0.01	25.01	0	0.21	6.99	7.24	0.717	0.03	0.03	100.08	10.69	0.00	5.27	0.00	0.02	1.34	2.51	0.16	0.00	0.00	20.00	33.35	62.57	4.08	100.00
IR5	Qorveh	Pheno pl rim 2-1	59.57	0.00	24.61	0.00	0.32	7.09	6.92	0.80	0.18	0.04	99.53	10.72	0.00	5.22	0.00	0.03	1.37	2.41	0.18	0.01	0.00	19.95	34.47	60.89	4.64	100.00
IR5	Qorveh	Same pheno pl core 2-2	57.88	0.00	26.39	0.04	0.22	8.41	6.43	0.57	0.06	0.26	100.27	10.38	0.00	5.58	0.01	0.02	1.62	2.24	0.13	0.00	0.03	20.00	40.60	56.16	3.25	100.00
IR5	Qorveh	Pl gm 2-3	59.22	0.04	25.44	0.00	0.36	7.72	6.60	0.84	0.08	0.01	100.29	10.59	0.00	5.36	0.00	0.04	1.48	2.29	0.19	0.01	0.00	19.95	37.37	57.81	4.82	100.00
IR5	Qorveh	Pl micropheno 2-4	57.43	0.01	26.33	0.04	0.38	9.19	6.00	0.50	0.11	0.07	100.06	10.33	0.00	5.59	0.01	0.04	1.77	2.09	0.11	0.01	0.01	19.96	44.53	52.59	2.88	100.00
IR5	Qorveh	Pl micropheno 2-5	60.46	0.00	24.28	0.02	0.41	6.62	7.08	0.89	0.23	0.08	100.06	10.82	0.00	5.12	0.00	0.04	1.27	2.46	0.20	0.02	0.01	19.93	32.30	62.53	5.17	100.00
IR5	Qorveh	Pl interstit in amph glomer 2-8	58.99	0.03	25.20	0.05	0.39	7.84	6.41	0.67	0.19	0.23	99.98	10.59	0.00	5.34	0.01	0.04	1.51	2.23	0.15	0.01	0.02	19.91	38.76	57.31	3.93	100.00
IR5	Qorveh	Pheno pl clear rim 5-1	57.96	0.00	26.33	0.01	0.32	8.60	6.46	0.50	0.09	0.16	100.44	10.38	0.00	5.56	0.00	0.03	1.65	2.24	0.11	0.01	0.02	20.00	41.19	55.99	2.82	100.00
IR5	Qorveh	Pheno pl clear rim 5-2	58.32	0.04	26.57	0.01	0.26	8.96	6.27	0.33	0.01	0.18	100.94	10.37	0.01	5.57	0.00	0.03	1.71	2.16	0.07	0.00	0.02	19.94	43.30	54.80	1.90	100.00
IR5	Qorveh	Same pheno pl sieved mantle 5-3	58.14	0.04	25.43	0.04	0.31	7.88	6.38	0.66	0.09	0.08	99.04	10.53	0.01	5.43	0.01	0.03	1.53	2.24	0.15	0.01	0.01	19.93	39.01	57.13	3.86	100.00
IR5	Qorveh	Same pheno pl sieved mantle 5-4	56.71	0.00	27.37	0.04	0.30	9.61	5.79	0.46	0.04	0.16	100.48	10.17	0.00	5.79	0.01	0.03	1.85	2.01	0.11	0.00	0.02	19.98	46.56	50.77	2.67	100.00
IR5	Qorveh	Same pheno pl sieved mantle 5-5	56.18	0.01	27.42	0.00	0.30	9.79	5.66	0.51	0.00	0.15	100.01	10.13	0.00	5.83	0.00	0.03	1.89	1.98	0.12	0.00	0.02	19.99	47.46	49.61	2.93	100.00
IR5	Qorveh	Same pheno pl sieved mantle 5-6	57.16	0.00	26.89	0.01	0.28	9.46	5.75	0.52	0.07	0.08	100.22	10.26	0.00	5.69	0.00	0.03	1.82	2.00	0.12	0.00	0.01	19.94	46.17	50.84	2.99	100.00
IR5	Qorveh	Same pheno pl clear core 5-7	58.71	0.03	25.89	0.02	0.19	8.23	6.46	0.58	0.07	0.13	100.32	10.50	0.00	5.46	0.00	0.02	1.58	2.24	0.13	0.00	0.01	19.95	39.94	56.70	3.37	100.00
IR5	Qorveh	Same pheno pl clear core 5-8	59.22	0.00	25.70	0.04	0.19	7.61	6.86	0.58	0.11	0.15	100.45	10.56	0.00	5.40	0.01	0.02	1.45	2.37	0.13	0.01	0.02	19.97	36.75	59.93	3.32	100.00
IR5	Qorveh	Pl in corroded pheno amph core 4-5	62.09	0.03	23.53	0.02	0.35	5.33	8.00	0.96	0.08	0.12	100.54	11.02	0.00	4.92	0.00	0.03	1.01	2.75	0.22	0.01	0.01	19.99	25.45	69.10	5.46	100.00
IR5	Qorveh	Pl in coarse incl core 1-3	59.65	0.00	24.81	0.00	0.15	6.71	7.26	0.92	0.06	0.29	99.85	10.71	0.00	5.25	0.00	0.02	1.29	2.53	0.21	0.00	0.03	20.03	32.05	62.73	5.22	100.00
IR5	Qorveh	Same pl in coarse incl rim 1-5	56.97	0.02	26.64	0.01	0.32	9.17	5.95	0.49	0.13	0.16	99.84	10.28	0.00	5.67	0.00	0.03	1.77	2.08	0.11	0.01	0.02	19.97	44.69	52.45	2.86	100.00
IR5	Qorveh	Pl in coarse incl 1-9	57.47	0.02	26.12	0.00	0.33	8.58	6.13	0.50	0.10	0.10	99.34	10.39	0.00	5.57	0.00	0.03	1.66	2.15	0.11	0.01	0.01	19.94	42.35	54.73	2.92	100.00
IR7	Qorveh	Pl gm 7-6	62.27	0.00	23.62	0.00	0.24	4.93	7.79	1.11	0.33	0.18	100.47	11.05	0.00	4.94	0.00	0.02	0.94	2.68	0.25	0.02	0.02	19.93	24.23	69.25	6.51	100.00
IR7	Qorveh	Pheno pl rim 2-1	60.68	0.01	24.03	0.00	0.24	5.66	7.70	0.87	0.09	0.12	99.39	10.89	0.00	5.09	0.00	0.02	1.09	2.68	0.20	0.01	0.01	19.99	27.42	67.56	5.02	100.00
IR7	Qorveh	Same phen pl core 2-2	60.76	0.02	24.53	0.01	0.13	6.16	7.37	0.79	0.07	0.26	100.11	10.83	0.00	5.16	0.00	0.01	1.18	2.55	0.18	0.01	0.03	19.94	30.16	65.23	4.60	100.00
IR7	Qorveh	Pl gm 1-5	62.99	0.03	23.17	0.00	0.23	5.10	7.93	1.11	0.06	0.02	100.62	11.13	0.00	4.83	0.00	0.02	0.96	2.72	0.25	0.00	0.00	19.92	24.54	69.11	6.35	100.00
IR7	Qorveh	Pl gm 4-2	61.84	0.00	24.20	0.05	0.15	6.13	7.68	0.77	0.01	0.04	100.87	10.92	0.00	5.04	0.01	0.01	1.16	2.63	0.17	0.00	0.00	19.95	29.26	66.35	4.39	100.00
IR7	Qorveh	Pl gm 8-5	61.27	0.01	23.74	0.02	0.24	5.23	7.65	1.14	0.26	0.19	99.74	10.97	0.00	5.01	0.00	0.02	1.00	2.65	0.26	0.02	0.02	19.97	25.62	67.73	6.65	100.00
IR7	Qorveh	Pl gm 8-6	62.17	0.00	23.15	0.00	0.23	4.53	7.91	1.13	0.30	0.24	99.65	11.12	0.00	4.88	0.00	0.02	0.87	2.74	0.26	0.02	0.02	19.93	22.44	70.91	6.65	100.00
IR7	Qorveh	Pheno san rim 7-1	62.91	0.00	19.39	0.01	0.06	0.21	2.56	12.06	3.01	0.08	100.28	11.72	0.00	4.26	0.00	0.01	0.04	0.92	2.87	0.22	0.01	20.04	1.07	24.09	74.84	100.00

Table 13: (continued)

Sample	Location	Description	SiO_2	TiO_2	Al_2O_3	MnO	FeO	CaO	Na_2O	K_2O	BaO	SrO	Total	Si	Ti	Al	Mn	$Fe^{'''}$	Ca	Na	K	Ba	Sr	Total	An	Ab	Or	Total
IR7	Qorveh	Same pheno san core 7-2	63.86	0.00	18.94	0.00	0.06	0.18	2.53	12.69	2.03	0.02	100.32	11.82	0.00	4.13	0.00	0.01	0.04	0.91	3.00	0.15	0.00	20.06	0.91	23.05	76.04	100.00
IR7	Qorveh	Pheno san rim 7-3	63.72	0.00	19.09	0.00	0.12	0.14	2.49	12.53	2.06	0.00	100.16	11.81	0.00	4.17	0.00	0.01	0.03	0.90	2.96	0.15	0.00	20.03	0.70	23.05	76.25	100.00
IR7	Qorveh	Same pheno san core 7-4	61.45	0.14	19.18	0.00	0.15	0.20	2.34	12.02	3.00	0.01	98.48	11.67	0.02	4.29	0.00	0.02	0.04	0.86	2.91	0.22	0.00	20.04	1.08	22.59	76.34	100.00
IR7	Qorveh	San gm 7-5	62.86	0.01	19.44	0.02	0.14	0.23	2.88	11.34	2.71	0.16	99.80	11.72	0.00	4.27	0.00	0.01	0.05	1.04	2.70	0.20	0.02	20.01	1.24	27.46	71.30	100.00
IR7	Qorveh	San gm 7-7	62.58	0.00	19.17	0.00	0.07	0.16	2.53	12.03	2.38	0.00	98.92	11.75	0.00	4.25	0.00	0.01	0.03	0.92	2.88	0.18	0.00	20.02	0.85	24.02	75.13	100.00
IR7	Qorveh	Big pheno san rim 5-1	63.72	0.00	19.25	0.00	0.04	0.23	2.46	11.95	2.86	0.02	100.53	11.79	0.00	4.20	0.00	0.00	0.05	0.88	2.82	0.21	0.00	19.96	1.23	23.54	75.24	100.00
IR7	Qorveh	Same pheno san rim 5-2	63.42	0.00	19.29	0.00	0.12	0.18	2.50	12.02	3.07	0.00	100.60	11.76	0.00	4.22	0.00	0.01	0.04	0.90	2.84	0.22	0.00	19.99	0.94	23.80	75.26	100.00
IR7	Qorveh	Pheno san rim 5-3	63.38	0.00	19.36	0.03	0.08	0.20	2.58	11.92	2.90	0.00	100.45	11.75	0.00	4.23	0.00	0.01	0.04	0.93	2.82	0.21	0.00	20.00	1.05	24.51	74.44	100.00
IR7	Qorveh	Same phen san core 5-4	62.18	0.00	19.37	0.02	0.12	0.19	2.43	12.13	3.05	0.00	99.48	11.69	0.00	4.29	0.00	0.01	0.04	0.89	2.91	0.22	0.00	20.06	0.99	23.11	75.91	100.00
IR7	Qorveh	San microphen core 3-3	61.92	0.00	19.30	0.00	0.11	0.17	2.36	12.32	2.34	0.00	98.51	11.70	0.00	4.30	0.00	0.01	0.03	0.86	2.97	0.17	0.00	20.06	0.88	22.32	76.80	100.00
IR7	Qorveh	Same san amph core 3-4	72.66	0.01	13.59	0.00	0.14	0.26	2.24	9.44	0.13	0.00	98.47	13.06	0.00	2.88	0.00	0.01	0.05	0.78	2.17	0.01	0.00	18.96	1.68	26.02	72.30	100.00
IR7	Qorveh	San microphen 2-3	64.00	0.00	18.93	0.03	0.08	0.14	2.44	12.67	1.82	0.00	100.11	11.85	0.00	4.13	0.00	0.01	0.03	0.88	2.99	0.13	0.00	20.02	0.73	22.51	76.76	100.00
IR7	Qorveh	San gm 8-4	63.19	0.00	19.03	0.00	0.14	0.21	2.57	12.09	2.39	0.00	99.61	11.79	0.00	4.19	0.00	0.01	0.04	0.93	2.88	0.17	0.00	20.01	1.08	24.13	74.79	100.00
IR7	Qorveh	Big san pheno rim 6-1	64.48	0.00	19.04	0.00	0.10	0.16	2.46	12.83	1.25	0.00	100.32	11.86	0.00	4.13	0.00	0.01	0.03	0.88	3.01	0.09	0.00	20.01	0.80	22.36	76.84	100.00
IR7	Qorveh	Same big san pheno mantle 6-2	62.23	0.00	19.19	0.04	0.09	0.19	2.35	12.26	2.87	0.06	99.27	11.72	0.00	4.26	0.01	0.01	0.04	0.86	2.95	0.21	0.01	20.05	0.98	22.34	76.68	100.00
IR7	Qorveh	Same big san pheno core 6-3	63.18	0.01	19.18	0.01	0.05	0.16	2.33	12.55	2.12	0.03	99.63	11.78	0.00	4.22	0.00	0.01	0.03	0.84	2.99	0.15	0.00	20.02	0.85	21.80	77.35	100.00
IR8	Qorveh	Pl gm 3-3	62.75	0.00	23.27	0.00	0.27	4.97	8.14	1.02	0.20	0.15	100.76	11.10	0.00	4.85	0.00	0.03	0.94	2.79	0.23	0.01	0.01	19.97	23.75	70.45	5.81	100.00
IR8	Qorveh	Pl gm 3-4	62.52	0.01	23.08	0.05	0.13	4.97	7.95	1.13	0.17	0.16	100.16	11.12	0.00	4.84	0.01	0.01	0.95	2.74	0.26	0.01	0.02	19.95	24.01	69.51	6.49	100.00
IR8	Qorveh	Pl gm 3-6	62.33	0.00	23.24	0.00	0.21	5.04	7.97	1.00	0.06	0.07	99.91	11.10	0.00	4.88	0.00	0.02	0.96	2.75	0.23	0.00	0.01	19.94	24.41	69.82	5.77	100.00
IR8	Qorveh	Pl gm 2-7	60.58	0.03	24.28	0.02	0.15	6.09	7.61	0.76	0.00	0.13	99.66	10.84	0.00	5.12	0.00	0.01	1.17	2.64	0.17	0.00	0.01	19.99	29.32	66.35	4.34	100.00
IR8	Qorveh	Pheno pl core 2-10	61.87	0.00	23.79	0.00	0.13	5.46	7.56	0.92	0.10	0.13	99.96	11.01	0.00	4.99	0.00	0.01	1.04	2.61	0.21	0.01	0.01	19.90	26.97	67.60	5.43	100.00
IR8	Qorveh	Same pheno pl rim 2-11	61.44	0.00	23.77	0.00	0.26	5.74	7.81	0.78	0.05	0.04	99.89	10.96	0.00	5.00	0.00	0.03	1.10	2.70	0.18	0.00	0.00	19.97	27.57	67.97	4.46	100.00
IR8	Qorveh	Same pheno pl rim 1-6	59.16	0.03	24.67	0.01	0.29	6.98	7.11	1.00	0.11	0.00	99.36	10.68	0.00	5.25	0.00	0.03	1.35	2.49	0.23	0.01	0.00	20.04	33.18	61.15	5.67	100.00
IR8	Qorveh	San gm 3-7	63.97	0.00	18.77	0.05	0.13	0.11	2.39	12.60	1.89	0.00	99.90	11.87	0.00	4.11	0.01	0.01	0.02	0.86	2.98	0.14	0.00	19.99	0.58	22.25	77.18	100.00
IR8	Qorveh	San pheno rim 2-1	64.36	0.00	18.55	0.05	0.09	0.12	2.41	12.88	1.96	0.13	100.55	11.89	0.00	4.04	0.01	0.01	0.02	0.86	3.04	0.14	0.01	20.03	0.60	21.97	77.43	100.00
IR8	Qorveh	Same san pheno mantle 2-2	63.62	0.01	18.95	0.04	0.07	0.20	2.41	12.27	2.77	0.01	100.35	11.81	0.00	4.15	0.01	0.01	0.04	0.87	2.91	0.20	0.00	19.99	1.03	22.74	76.23	100.00
IR8	Qorveh	Same san pheno core 2-3	64.46	0.00	18.64	0.00	0.08	0.17	2.41	12.66	2.04	0.00	100.45	11.90	0.00	4.06	0.00	0.01	0.03	0.86	2.98	0.15	0.00	19.99	0.85	22.22	76.93	100.00
IR8	Qorveh	Same san pheno core 2-4	64.69	0.00	18.31	0.01	0.06	0.15	2.35	12.72	1.65	0.00	99.93	11.97	0.00	3.99	0.00	0.01	0.03	0.84	3.00	0.12	0.00	19.96	0.74	21.74	77.52	100.00
IR8	Qorveh	Big san pheno rim 2-5	64.55	0.00	18.82	0.01	0.08	0.12	2.35	12.70	1.68	0.00	100.31	11.90	0.00	4.09	0.00	0.01	0.02	0.84	2.99	0.12	0.00	19.97	0.64	21.84	77.52	100.00
IR8	Qorveh	Same san pheno core 2-6	62.98	0.00	19.16	0.00	0.06	0.23	2.45	12.01	2.84	0.11	99.83	11.76	0.00	4.22	0.00	0.01	0.05	0.89	2.86	0.21	0.01	20.00	1.22	23.35	75.43	100.00
IR8	Qorveh	San gm 2-8	64.46	0.00	18.73	0.00	0.10	0.12	2.54	12.66	2.08	0.00	100.68	11.88	0.00	4.07	0.00	0.01	0.02	0.91	2.98	0.15	0.00	20.02	0.62	23.19	76.19	100.00
IR8	Qorveh	San gm 2-9	64.34	0.00	18.55	0.00	0.07	0.15	2.45	12.71	1.76	0.00	100.02	11.91	0.00	4.05	0.00	0.01	0.03	0.88	3.00	0.13	0.00	20.00	0.74	22.47	76.80	100.00
IR11	Qorveh	Big pl rim 2-7	59.41	0.03	24.37	0.02	0.25	6.25	7.46	0.93	0.16	0.21	99.09	10.75	0.00	5.20	0.00	0.03	1.21	2.62	0.21	0.01	0.02	20.05	29.97	64.74	5.29	100.00
IR11	Qorveh	Same big pl core 2-8	59.39	0.00	25.04	0.03	0.23	7.11	6.81	0.79	0.11	0.19	99.69	10.67	0.00	5.30	0.00	0.02	1.37	2.37	0.18	0.01	0.02	19.95	34.91	60.49	4.59	100.00
IR11	Qorveh	Pl glom rim 4-3	62.68	0.03	22.96	0.07	0.19	4.90	7.71	1.40	0.10	0.22	100.27	11.14	0.00	4.81	0.01	0.02	0.93	2.66	0.32	0.01	0.02	19.93	23.87	68.01	8.12	100.00
IR11	Qorveh	Pl glom mantle 4-4	59.56	0.01	25.11	0.02	0.18	7.31	6.86	0.70	0.04	0.15	99.95	10.66	0.00	5.30	0.00	0.02	1.40	2.38	0.16	0.00	0.02	19.95	35.56	60.37	4.07	100.00
IR11	Qorveh	Pl glom core 4-5	60.46	0.00	24.54	0.00	0.13	6.78	7.23	0.79	0.16	0.19	100.27	10.79	0.00	5.16	0.00	0.01	1.30	2.50	0.18	0.01	0.02	19.97	32.59	62.91	4.51	100.00
IR11	Qorveh	Big pl glom core 4-6	57.34	0.03	26.59	0.00	0.16	8.58	6.21	0.56	0.01	0.27	99.75	10.33	0.00	5.65	0.00	0.02	1.66	2.17	0.13	0.00	0.03	19.98	41.89	54.85	3.26	100.00
IR11	Qorveh	Big pl glom mantle 4-7	60.31	0.01	23.94	0.08	0.22	6.18	7.54	0.83	0.12	0.12	99.34	10.86	0.00	5.08	0.01	0.02	1.19	2.63	0.19	0.01	0.01	20.00	29.70	65.57	4.73	100.00
IR11	Qorveh	San in pheno biot 2-5	63.37	0.07	19.10	0.05	0.51	0.45	3.76	10.31	2.40	0.00	100.01	11.74	0.01	4.17	0.01	0.05	0.09	1.35	2.44	0.17	0.00	20.03	2.28	34.82	62.90	100.00
IR11	Qorveh	San in pheno biot 2-6	64.26	0.04	18.98	0.00	0.54	0.36	3.68	10.65	1.99	0.00	100.50	11.81	0.01	4.11	0.00	0.06	0.07	1.31	2.50	0.14	0.00	20.01	1.81	33.82	64.37	100.00

Table 14: EMP analysis for Bijar-Qorveh mica compositions

Sample	Location	Description	SiO_2	TiO_2	Al_2O_3	Cr_2O_3	MgO	CaO	MnO	FeO	BaO	Na_2O	K_2O	F	Cl	Total	Si	^{IV}Al	^{VI}Al	$Al_{(tot)}$	Ti	Cr	Fe	Mn	Mg	Ca	Na	K	Ba	OH*	F	Cl	Total	Mg#
Q-T16	Qezelke Kand	bt gm 1-4	37.76	3.79	15.30	0.07	19.83	0.02	0.01	7.64		0.90	9.08			94.40	5.50	2.50	0.13	2.63	0.42	0.01	0.93	0.00	4.31	0.00	0.25	1.69	0.00	4.00	0.00	0.00	19.74	0.82
Q-T16	Qezelke Kand	bt gm 1-5	38.09	3.13	15.76	1.21	20.96	0.00	0.00	5.36		0.66	9.44			94.62	5.49	2.51	0.17	2.68	0.34	0.14	0.65	0.00	4.51	0.00	0.18	1.74	0.00	4.00	0.00	0.00	19.72	0.87
Q-T16	Qezelke Kand	bt microphen 3-1	38.08	3.15	15.48	1.03	21.28	0.04	0.00	5.44		0.62	9.67			94.77	5.49	2.51	0.12	2.63	0.34	0.12	0.66	0.00	4.57	0.01	0.17	1.78	0.00	4.00	0.00	0.00	19.77	0.87
Q-T16	Qezelke Kand	bt rim pheno 4-1	38.48	3.28	15.42	0.40	21.12	0.17	0.00	5.74		0.80	9.19			94.59	5.54	2.46	0.16	2.62	0.36	0.05	0.69	0.00	4.53	0.03	0.22	1.69	0.00	4.00	0.00	0.00	19.73	0.87
Q-T16	Qezelke Kand	same bt core pheno 4-2	38.59	3.16	15.42	1.27	20.75	0.01	0.00	5.32		0.54	9.51			94.56	5.56	2.44	0.18	2.62	0.34	0.14	0.64	0.00	4.46	0.00	0.15	1.75	0.00	4.00	0.00	0.00	19.66	0.87
T4	Takab	1-1 gm bt	38.92	7.39	12.48		18.08	0.03	0.10	8.75		0.87	9.19	4.10	0.09	99.99	5.97	0.23	2.03	2.26	0.85		1.35	0.01	4.14	0.00	0.26	1.80					16.65	0.75
T4	Takab	1-2 gm bt	37.64	6.96	11.62		16.85	2.07	0.15	8.60		0.91	8.65	3.75	0.13	97.32	5.93	0.09	2.07	2.16	0.82		1.00	0.02	3.96	0.35	0.28	1.74					16.26	0.80
T4	Takab	3-1 bt gm	38.66	7.28	12.08		18.46	0.09	0.09	8.51		0.86	9.05	3.84	0.04	98.98	5.96	0.16	2.04	2.20	0.84		1.35	0.01	4.24	0.01	0.26	1.78					16.66	0.76
T4	Takab	3-6 bt gm	39.31	7.13	12.29		17.65	0.05	0.09	8.84		0.84	9.32	3.68	0.06	99.26	6.07	0.30	1.93	2.24	0.83		1.34	0.01	4.06	0.01	0.25	1.84					16.64	0.75
Q-T20	Dehgolan	bt gm 1-7	37.83	3.75	15.42	0.00	15.13	0.03	0.07	14.22	0.67	0.67	9.01	3.14	0.15	100.10	5.56	2.44	0.23	2.67	0.41	0.00	1.75	0.01	3.31	0.01	0.19	1.69	0.04	2.50	1.46	0.04	19.63	0.65
Q-T20	Dehgolan	bt microphen 2-1	37.12	3.60	15.19	0.01	13.24	0.01	0.18	17.76	0.97	0.72	8.78	1.27	0.10	98.94	5.52	2.48	0.18	2.66	0.40	0.00	2.21	0.02	2.94	0.00	0.21	1.67	0.06	3.38	0.60	0.02	19.68	0.57
Q-T20	Dehgolan	bt microphen 3-1	40.21	2.66	13.20	0.04	19.55	0.08	0.10	11.06	0.24	0.63	8.92	2.51	0.05	99.22	5.79	2.21	0.03	2.24	0.29	0.00	1.33	0.01	4.20	0.01	0.18	1.64	0.01	2.84	1.14	0.01	19.71	0.76
Q-T20	Dehgolan	bt opacitized 3-2	37.63	3.56	15.25	0.00	15.62	0.02	0.04	13.80	0.83	0.69	9.05	3.90	0.14	100.52	5.55	2.45	0.20	2.65	0.39	0.00	1.70	0.01	3.43	0.00	0.20	1.70	0.05	2.15	1.82	0.04	19.68	0.67
Q-T20	Dehgolan	bt gm 4-4	38.04	3.90	15.82	0.00	15.72	0.08	0.17	12.44	0.83	0.70	8.67	3.72	0.09	100.20	5.56	2.44	0.29	2.73	0.43	0.00	1.52	0.02	3.42	0.01	0.20	1.62	0.05	2.26	1.72	0.02	19.56	0.69
Q-T24	Dehgolan	bt microphen 1-5	37.34	4.02	13.69	0.07	13.03	0.03	0.24	18.32	0.32	0.40	8.97	0.84	0.15	97.41	5.62	2.38	0.05	2.43	0.45	0.01	2.30	0.03	2.92	0.00	0.12	1.72	0.02	3.57	0.40	0.04	19.63	0.56
Q-T24	Dehgolan	bt microphen 2-3	37.16	4.05	13.58	0.06	12.60	0.22	0.20	18.27	0.28	0.39	8.16	0.55	0.16	95.66	5.65	2.35	0.09	2.43	0.46	0.01	2.32	0.03	2.86	0.04	0.11	1.58	0.02	3.70	0.26	0.04	19.51	0.55
Q-T24	Dehgolan	bt microphen 3-6	37.62	3.72	12.91	0.05	11.94	0.41	0.24	17.47	0.20	0.23	7.24	0.41	0.14	92.55	5.84	2.16	0.20	2.36	0.43	0.01	2.27	0.03	2.76	0.07	0.07	1.43	0.01	3.76	0.20	0.04	19.29	0.55
Q-T24	Dehgolan	same bt microphen 3-7	36.95	3.81	13.37	0.04	12.61	0.15	0.20	17.66	0.06	0.28	7.55	0.49	0.15	93.31	5.71	2.29	0.15	2.44	0.44	0.00	2.28	0.03	2.91	0.03	0.08	1.49	0.00	3.72	0.24	0.04	19.41	0.56
Q-T27	Dehgolan	bt microphen 1-6	36.22	3.74	13.81	0.02	12.20	0.03	0.35	19.77	0.41	0.58	8.74	0.33	0.08	96.29	5.54	2.46	0.03	2.49	0.43	0.00	2.53	0.05	2.78	0.00	0.17	1.71	0.02	3.82	0.16	0.02	19.72	0.52
Q-T27	Dehgolan	bt microphen 1-7	37.10	3.37	14.08	0.02	14.01	0.06	0.22	17.60	0.35	0.70	8.72	0.51	0.06	96.80	5.57	2.43	0.07	2.49	0.38	0.00	2.21	0.03	3.14	0.01	0.20	1.67	0.02	3.74	0.24	0.02	19.74	0.59
Q-T27	Dehgolan	bt gm 3-2	37.40	3.53	14.24	0.02	15.06	0.02	0.27	15.70	0.55	0.85	8.58	0.52	0.08	96.82	5.57	2.43	0.07	2.50	0.40	0.00	1.96	0.03	3.34	0.00	0.25	1.63	0.03	3.74	0.24	0.02	19.72	0.63
Q-T27	Dehgolan	bt microphen 4-2	37.12	3.62	13.87	0.05	14.60	0.08	0.18	16.51	0.08	0.82	8.56	0.34	0.06	95.90	5.58	2.42	0.04	2.46	0.41	0.01	2.08	0.02	3.27	0.01	0.24	1.64	0.00	3.82	0.16	0.02	19.72	0.61
Q-T27	Dehgolan	bt microphen 4-3	36.90	3.46	13.78	0.01	12.76	0.01	0.33	19.04	0.18	0.56	9.30	0.74	0.07	97.13	5.59	2.41	0.06	2.46	0.39	0.00	2.41	0.04	2.88	0.00	0.16	1.80	0.01	3.63	0.35	0.02	19.76	0.54
Q-T29	Dehgolan	bt microphen 1-5	42.33	1.64	12.48	0.43	24.98	0.00	0.01	3.47	0.11	0.64	9.63	2.47	0.03	98.22	5.94	2.06	0.01	2.07	0.17	0.05	0.41	0.00	5.23	0.00	0.17	1.72	0.01	2.90	1.10	0.01	19.78	0.93
Q-T29	Dehgolan	bt microphen 1-6	40.72	1.50	12.48	1.01	23.96	0.01	0.02	3.15	0.17	0.39	9.85	1.30	0.05	94.59	5.89	2.11	0.02	2.13	0.16	0.12	0.38	0.00	5.17	0.00	0.11	1.82	0.01	3.39	0.59	0.01	19.79	0.93
Q-T29	Dehgolan	bt microphen 1-7	37.94	3.28	14.01	0.03	14.57	0.03	0.20	16.76	0.53	0.65	8.99	1.34	0.04	98.37	5.63	2.37	0.09	2.45	0.37	0.00	2.08	0.03	3.23	0.01	0.19	1.70	0.03	3.36	0.63	0.01	19.72	0.61
Q-T29	Dehgolan	bt opacitized 2-2	37.62	3.43	13.89	0.06	16.09	0.03	0.21	14.40	0.69	0.67	8.76	1.63	0.09	97.56	5.60	2.40	0.04	2.44	0.38	0.01	1.79	0.03	3.57	0.00	0.19	1.66	0.04	3.21	0.77	0.02	19.72	0.67
Q-T29	Dehgolan	bt pheno rim 3-1	37.91	3.32	13.97	0.00	14.29	0.01	0.24	17.37	0.39	0.58	9.05	1.55	0.07	98.74	5.63	2.37	0.08	2.45	0.37	0.00	2.16	0.03	3.16	0.00	0.17	1.72	0.02	3.25	0.73	0.02	19.71	0.59
Q-T29	Dehgolan	bt microphen 4-2	41.68	1.62	12.83	0.42	24.17	0.00	0.00	4.42	0.17	0.45	9.73	2.53	0.03	98.05	5.90	2.10	0.04	2.14	0.17	0.05	0.52	0.00	5.10	0.00	0.12	1.76	0.01	2.86	1.13	0.01	19.77	0.91
IR7	Qorveh	Bt microphen 1-1	37.12	3.03	18.72		8.09	0.05	0.46	18.52	0.75	0.32	7.49	0.23		94.77	5.62	2.38	0.96	3.34	0.35		2.35	0.06	1.83	0.01	0.09	1.45	0.04	3.89	0.11		19.13	0.44
IR7	Qorveh	Bt microphen 1-2	34.21	4.08	14.58		11.18	0.14	0.51	20.57	0.89	0.47	8.76	0.65		96.05	5.33	2.67	0.01	2.68	0.48		2.68	0.07	2.60	0.02	0.14	1.74	0.05	3.68	0.32		19.79	0.49
IR7	Qorveh	Bt microphen 1-3	37.24	3.52	16.04		10.09	0.03	0.57	19.63	0.17	0.33	8.61	0.53		96.76	5.61	2.39	0.46	2.85	0.40		2.47	0.07	2.27	0.01	0.10	1.66	0.01	3.75	0.25		19.44	0.48
IR7	Qorveh	Bt pheno rim 8-1	35.83	3.65	15.64		10.24	0.01	0.57	20.64	0.79	0.35	8.76	0.44		96.93	5.47	2.53	0.29	2.81	0.42		2.64	0.07	2.33	0.00	0.10	1.71	0.05	3.79	0.21		19.61	0.47
IR8	Qorveh	Pheno bt core 3-1	36.08	3.49	14.05		10.95	0.06	0.61	21.48	0.22	0.35	9.33	0.36		96.99	5.53	2.47	0.07	2.54	0.40		2.75	0.08	2.50	0.01	0.10	1.82	0.01	3.82	0.18		19.76	0.48
IR8	Qorveh	Pheno biot rim 3-2	37.15	3.11	16.35		9.15	0.06	0.53	19.22	0.36	0.40	8.45	0.37		95.15	5.67	2.33	0.62	2.94	0.36		2.46	0.07	2.08	0.01	0.12	1.65	0.02	3.82	0.18		19.38	0.46
IR8	Qorveh	Pheno biot rim 1-1	37.48	3.47	14.33		10.28	0.04	0.53	20.10	0.19	0.47	9.16	0.39		96.44	5.71	2.29	0.28	2.57	0.40		2.56	0.07	2.33	0.01	0.14	1.78	0.01	3.81	0.19		19.57	0.48
IR8	Qorveh	Same pheno biot core1-2	35.86	3.80	13.80		10.65	0.03	0.52	20.74	0.76	0.58	9.05	0.35		96.16	5.55	2.45	0.07	2.52	0.44		2.68	0.07	2.46	0.01	0.17	1.79	0.05	3.83	0.17		19.73	0.48
IR11	Qorveh	Pheno biot rim 2-1	36.62	4.85	13.56		15.47	0.15	0.16	13.97	1.17	0.74	8.52	1.26		96.46	5.51	2.41	0.00	2.41	0.55		1.76	0.02	3.47	0.02	0.21	1.64	0.07	3.40	0.60		19.66	0.66
IR11	Qorveh	Pheno biot core 2-2	36.38	4.60	13.85		14.73	0.16	0.18	15.50	1.27	0.94	8.83	0.58		97.01	5.46	2.45	0.00	2.45	0.52		1.95	0.02	3.30	0.03	0.27	1.69	0.07	3.72	0.28		19.77	0.63
IR11	Qorveh	Bt pheno rim 2-9	36.98	4.73	14.03		15.22	0.06	0.17	15.15	1.16	0.67	8.76	0.78		97.71	5.49	2.46	0.00	2.46	0.53		1.88	0.02	3.37	0.01	0.19	1.66	0.07	3.63	0.37		19.68	0.64
IR11	Qorveh	Same biot pheno core 2-10	36.54	4.60	13.60		15.13	0.05	0.15	14.89	1.31	0.62	8.62	0.70		96.22	5.51	2.42	0.00	2.42	0.52		1.88	0.02	3.40	0.01	0.18	1.66	0.08	3.66	0.34		19.68	0.64
IR11	Qorveh	Bt microphen 4-1	36.76	5.06	13.97		15.20	0.05	0.14	15.04	1.28	0.61	8.92	1.21		98.25	5.46	2.45	0.00	2.45	0.57		1.87	0.02	3.37	0.01	0.18	1.69	0.07	3.43	0.57		19.68	0.64

Table 15: EMP analysis for Bijar-Qorveh amphibole compositions

Sample	Location	Description	SiO_2	TiO_2	Al_2O_3	Cr_2O_3	MgO	CaO	MnO	FeO	Na_2O	K_2O	F	Cl	Total	Si	Ti	Al	Cr	Mn	Fe^{2+}	Mg	Ca	Na	K	F	Cl	Total
Q-T9	Qezelke Kand	amph gm 1-13	42.84	2.14	12.31	0.04	14.28	11.04	0.18	11.52	2.71	0.68	0.36	0.02	98.10	6.27	0.24	2.12	0.00	0.02	1.41	3.11	1.73	0.77	0.13	0.16	0.01	15.97
Q-T9	Qezelke Kand	amph pheno 1-14	41.82	2.47	11.53	0.00	12.12	10.94	0.29	15.47	2.54	0.94	0.25	0.06	98.41	6.24	0.28	2.03	0.00	0.04	1.93	2.70	1.75	0.73	0.18	0.12	0.01	15.99
Q-T9	Qezelke Kand	amph microphen core 1-15	43.81	2.47	11.66	0.00	15.57	11.13	0.12	10.10	2.64	0.73	0.33	0.03	98.58	6.33	0.27	1.99	0.00	0.01	1.22	3.35	1.72	0.74	0.13	0.15	0.01	15.93
Q-T9	Qezelke Kand	same amph microphen rim 1-16	41.65	2.64	12.40	0.01	13.17	11.28	0.19	12.45	2.67	0.70	0.24	0.04	97.44	6.18	0.30	2.17	0.00	0.02	1.54	2.92	1.79	0.77	0.13	0.11	0.01	15.95
Q-T9	Qezelke Kand	amph pheno rim 2-1	41.49	2.61	11.78	0.02	12.41	11.19	0.26	14.30	2.49	0.85	0.30	0.02	97.71	6.20	0.29	2.07	0.00	0.03	1.79	2.77	1.79	0.72	0.16	0.14	0.01	15.98
Q-T9	Qezelke Kand	same amph pheno core 2-2	40.48	2.84	13.36	0.08	11.77	10.55	0.27	14.90	2.87	0.87	0.24	0.08	98.31	6.04	0.32	2.35	0.01	0.03	1.86	2.62	1.69	0.83	0.17	0.12	0.02	16.03
Q-T9	Qezelke Kand	amph gm 2-3	41.50	2.55	11.59	0.07	12.23	11.02	0.24	14.94	2.70	0.84	0.09	0.06	97.82	6.22	0.29	2.05	0.01	0.03	1.87	2.73	1.77	0.78	0.16	0.04	0.01	15.97
Q-T27	Dehgolan	amph microphen 1-9	42.32	2.14	12.85	0.04	13.62	11.28	0.18	12.55	2.37	0.65	0.12	0.03	98.14	6.22	0.24	2.22	0.00	0.02	1.54	2.98	1.78	0.67	0.12	0.05	0.01	15.86
Q-T27	Dehgolan	amph microphen 1-10	44.03	2.04	11.20	0.05	15.70	11.44	0.15	9.71	2.83	0.62	0.14	0.02	97.93	6.40	0.22	1.92	0.01	0.02	1.18	3.40	1.78	0.80	0.11	0.07	0.01	15.91
Q-T27	Dehgolan	amph opacitized 1-11	47.72	0.88	10.12	0.06	11.11	10.37	0.46	16.78	2.70	0.99	0.02	0.06	101.27	6.85	0.10	1.71	0.01	0.06	2.02	2.38	1.60	0.75	0.18	0.01	0.01	15.67
Q-T27	Dehgolan	amph microphen 2-6	43.43	2.26	11.93	0.05	15.34	11.59	0.10	10.52	2.36	0.87	0.09	0.05	98.59	6.30	0.25	2.04	0.01	0.01	1.28	3.32	1.80	0.66	0.16	0.04	0.01	15.87
Q-T27	Dehgolan	amph opacitized 2-8	44.01	0.90	7.94	0.03	12.10	11.07	0.61	19.83	3.04	0.95	0.21	0.04	100.72	6.56	0.10	1.39	0.00	0.08	2.47	2.69	1.77	0.88	0.18	0.10	0.01	16.23
Q-T27	Dehgolan	amph opacitized 3-1	47.36	1.10	9.71	0.26	16.70	11.18	0.23	9.61	2.46	0.52	0.26	0.03	99.41	6.72	0.12	1.62	0.03	0.03	1.14	3.53	1.70	0.68	0.09	0.12	0.01	15.78
Q-T27	Dehgolan	amph gm 3-3	45.54	2.15	10.79	0.00	16.84	11.16	0.05	8.12	2.22	0.70	0.21	0.04	97.81	6.54	0.23	1.83	0.00	0.01	0.97	3.60	1.72	0.62	0.13	0.10	0.01	15.74
Q-T27	Dehgolan	amph gm 4-4	44.05	2.16	10.38	0.01	16.68	11.40	0.19	9.27	2.51	0.59	0.68	0.04	97.96	6.39	0.24	1.77	0.00	0.02	1.12	3.61	1.77	0.70	0.11	0.31	0.01	16.06
Q-T24	Dehgolan	amph microphen 1-4	45.94	1.21	8.39	0.00	12.47	11.53	0.43	16.07	1.76	1.05	0.24	0.09	99.17	6.77	0.13	1.46	0.00	0.05	1.98	2.74	1.82	0.50	0.20	0.11	0.02	15.79
Q-T24	Dehgolan	amph microphen 1-6	45.12	1.22	8.68	0.01	12.09	11.41	0.42	16.05	1.76	1.13	0.19	0.09	98.18	6.73	0.14	1.53	0.00	0.05	2.00	2.69	1.82	0.51	0.22	0.09	0.02	15.79
Q-T24	Dehgolan	amph microphen 1-7	45.35	1.30	8.58	0.03	12.39	11.28	0.40	16.10	1.83	1.03	0.32	0.09	98.69	6.72	0.14	1.50	0.00	0.05	1.99	2.74	1.79	0.52	0.19	0.15	0.02	15.83
Q-T24	Dehgolan	amph microphen 2-4	45.43	1.12	8.68	0.01	12.13	11.44	0.49	16.11	1.74	1.05	0.26	0.10	98.53	6.74	0.12	1.52	0.00	0.06	2.00	2.68	1.82	0.50	0.20	0.12	0.02	15.79
Q-T24	Dehgolan	amph microphen 2-5	45.03	1.37	8.92	0.00	11.91	11.33	0.44	16.43	1.96	0.95	0.28	0.09	98.70	6.69	0.15	1.56	0.00	0.05	2.04	2.64	1.80	0.56	0.18	0.13	0.02	15.83
Q-T24	Dehgolan	amph pheno rim 3-3	44.55	1.43	9.10	0.04	11.96	11.29	0.46	16.19	1.84	1.12	0.36	0.11	98.43	6.64	0.16	1.60	0.00	0.06	2.02	2.66	1.80	0.53	0.21	0.17	0.03	15.87
Q-T24	Dehgolan	amph pheno core 3-5	44.47	1.16	9.59	0.00	11.91	11.24	0.44	15.82	1.84	1.17	0.25	0.08	97.96	6.64	0.13	1.69	0.00	0.06	1.98	2.65	1.80	0.53	0.22	0.12	0.02	15.83
Q-T29	Dehgolan	amph opacitized 1-10	48.03	0.96	8.21	0.05	14.45	11.69	0.41	12.84	1.97	0.87	0.29	0.06	99.82	6.90	0.10	1.39	0.01	0.05	1.54	3.09	1.80	0.55	0.16	0.13	0.01	15.73
IR1	Qorveh	Amph pheno 2-6	43.03	3.46	10.44	0.04	16.80	12.21	0.12	8.10	2.38	1.26	2.68		100.51	6.10	0.37	1.75	0.00	0.01	0.96	3.55	1.86	0.65	0.23	1.20		16.69
IR1	Qorveh	Same amph pheno 2-7	43.32	2.30	11.73	0.11	16.40	11.60	0.19	8.31	2.67	0.88	2.77		100.27	6.13	0.24	1.96	0.01	0.02	0.98	3.46	1.76	0.73	0.16	1.24		16.70
IR1	Qorveh	Amph pheno 1-1	42.47	1.98	12.48	0.05	16.46	10.87	0.18	9.96	3.00	0.79	2.82		101.06	6.01	0.21	2.08	0.01	0.02	1.18	3.47	1.65	0.82	0.14	1.26		16.85
IR1	Qorveh	Amph pheno 1-2	42.40	2.36	12.47	0.18	16.01	11.11	0.12	9.49	2.91	0.87	2.64		100.54	6.02	0.25	2.09	0.02	0.01	1.13	3.39	1.69	0.80	0.16	1.19		16.75
IR2	Qorveh	Amph pheno rim 1-3	42.55	2.24	12.06	0.05	17.26	11.62	0.19	8.72	2.90	0.95	2.88		101.42	5.99	0.24	2.00	0.01	0.02	1.03	3.62	1.75	0.79	0.17	1.28		16.89
IR2	Qorveh	Same amph pheno core 1-4	42.77	2.17	12.20	0.05	16.59	11.52	0.16	8.87	2.83	0.99	2.83		100.98	6.04	0.23	2.03	0.01	0.02	1.05	3.49	1.74	0.77	0.18	1.26		16.82
IR2	Qorveh	Pheno amph core 5-1	41.28	2.52	13.04	0.00	15.60	11.10	0.19	9.95	2.91	1.08	2.80		100.48	5.90	0.27	2.20	0.00	0.02	1.19	3.32	1.70	0.81	0.20	1.27		16.87
IR2	Qorveh	Pheno amph mantle 5-2	41.20	2.85	12.37	0.04	15.97	11.60	0.12	8.99	2.74	1.13	2.80		99.81	5.91	0.31	2.09	0.00	0.01	1.08	3.42	1.78	0.76	0.21	1.27		16.85
IR2	Qorveh	Pheno amph mantle-rim 5-3	46.35	1.65	6.98	0.01	19.37	11.70	0.27	7.38	2.77	0.64	3.15		100.27	6.52	0.17	1.16	0.00	0.03	0.87	4.06	1.76	0.75	0.12	1.40		16.86
IR2	Qorveh	Pheno amph rim 5-6	42.54	1.80	6.82	0.03	21.11	11.53	0.24	7.19	3.01	1.06	4.23		99.56	6.11	0.19	1.15	0.00	0.03	0.86	4.52	1.77	0.84	0.19	1.92		17.59
IR5	Qorveh	Amph in coarse incl 1-1	43.68	1.66	11.48	0.01	13.02	11.46	0.30	13.02	2.21	1.35	0.37		98.55	6.42	0.18	1.99	0.00	0.04	1.60	2.85	1.80	0.63	0.25	0.17		15.93
IR5	Qorveh	Amph in coarse incl 1-2	42.41	1.49	7.29	0.03	15.90	11.04	0.32	13.03	2.53	0.94	0.36		95.33	6.49	0.17	1.32	0.00	0.04	1.67	3.63	1.81	0.75	0.18	0.17		16.23
IR5	Qorveh	Amph in coarse incl 1-10	45.99	2.05	8.51	0.02	14.88	11.06	0.36	12.66	2.00	0.64	0.22		98.38	6.71	0.23	1.46	0.00	0.04	1.54	3.23	1.73	0.57	0.12	0.10		15.73
IR5	Qorveh	Amph pheno glom core 2-6	41.38	2.33	12.75	0.01	13.38	11.52	0.19	12.39	2.67	1.23	0.25		98.10	6.12	0.26	2.22	0.00	0.02	1.53	2.95	1.83	0.77	0.23	0.12		16.06
IR5	Qorveh	Same amph pheno glom rim 2-7	41.54	2.19	13.24	0.06	12.82	11.36	0.23	13.55	2.37	1.15	0.14		98.65	6.13	0.24	2.30	0.01	0.03	1.67	2.82	1.79	0.68	0.22	0.07		15.95
IR5	Qorveh	Pheno amph glom rim 2-9	45.13	2.89	10.30	0.03	12.81	11.47	0.26	13.11	3.00	1.02	0.22		100.23	6.52	0.31	1.75	0.00	0.03	1.58	2.76	1.77	0.84	0.19	0.10		15.86
IR5	Qorveh	Same pheno amph glom core 2-10	40.89	2.51	11.98	0.00	12.35	11.14	0.31	14.36	2.65	1.24	0.48		97.91	6.13	0.28	2.12	0.00	0.04	1.80	2.76	1.79	0.77	0.24	0.23		16.15
IR5	Qorveh	Pheno amph core 4-1	37.14	5.38	13.86	0.10	15.25	0.03	0.03	14.49	0.96	8.94	0.54		96.72	5.72	0.62	2.52	0.01	0.00	1.87	3.50	0.01	0.29	1.76	0.26		16.55
IR5	Qorveh	Same pheno amph mantle 4-2	41.95	2.03	13.50	0.03	14.82	11.43	0.10	10.80	2.43	1.14	0.41		98.63	6.10	0.22	2.32	0.00	0.01	1.31	3.22	1.78	0.68	0.21	0.19		16.06
IR5	Qorveh	Same pheno amph rim 4-3	41.57	2.22	12.78	0.00	12.06	11.43	0.26	14.83	2.31	1.14	0.32		98.90	6.15	0.25	2.23	0.00	0.03	1.84	2.66	1.81	0.66	0.21	0.15		16.00
IR5	Qorveh	Same pheno amph black rim 4-4	43.55	2.80	10.23	0.05	13.01	11.16	0.42	14.85	2.27	0.65	0.35		99.34	6.39	0.31	1.77	0.01	0.05	1.82	2.85	1.75	0.65	0.12	0.16		15.88

Table 15: (continued)

Sample	Location	Description	Mg#	Si-T	^{IV}Al-T	Sum-T	^{VI}Al-C	Ti-C	Cr-C	Fe^{3+}-C	Mg-C	Fe^{2+}-C	Mn-C	SumC	Mg-B	Fe^{2+}-B	Mn-B	SumB	Ca-B	Na-B	SumB	Na-A	K-A	SumA	Al_{tot}
Q-T9	Qezelke Kand	amph gm 1-13	0.69	6.18	1.82	8.00	0.28	0.23	0.00	0.76	3.07	0.63	0.02	5.00		0.00	0.00	0.00	1.71	0.29	2.00	0.46	0.12	0.59	2.09
Q-T9	Qezelke Kand	amph pheno 1-14	0.58	6.14	1.86	8.00	0.14	0.27	0.00	0.82	2.65	1.08	0.04	5.00		0.00	0.00	0.00	1.72	0.28	2.00	0.44	0.18	0.62	2.00
Q-T9	Qezelke Kand	amph microphen core 1-15	0.73	6.25	1.75	8.00	0.21	0.26	0.00	0.75	3.31	0.46	0.01	5.00		0.00	0.00	0.00	1.70	0.30	2.00	0.43	0.13	0.56	1.96
Q-T9	Qezelke Kand	same amph microphen rim 1-16	0.65	6.12	1.88	8.00	0.27	0.29	0.00	0.58	2.89	0.95	0.02	5.00		0.00	0.00	0.00	1.78	0.22	2.00	0.54	0.13	0.67	2.15
Q-T9	Qezelke Kand	amph pheno rim 2-1	0.61	6.13	1.87	8.00	0.18	0.29	0.00	0.69	2.73	1.07	0.03	5.00		0.00	0.00	0.00	1.77	0.23	2.00	0.48	0.16	0.64	2.05
Q-T9	Qezelke Kand	same amph pheno core 2-2	0.58	5.94	2.06	8.00	0.24	0.31	0.01	0.87	2.57	0.95	0.03	5.00		0.00	0.00	0.00	1.66	0.34	2.00	0.47	0.16	0.64	2.31
Q-T9	Qezelke Kand	amph gm 2-3	0.59	6.13	1.87	8.00	0.14	0.28	0.01	0.73	2.69	1.12	0.03	5.00		0.00	0.00	0.00	1.74	0.26	2.00	0.52	0.16	0.68	2.02
Q-T27	Dehgolan	amph microphen 1-9	0.66	6.11	1.89	8.00	0.30	0.23	0.00	0.84	2.93	0.67	0.02	5.00		0.00	0.00	0.00	1.74	0.26	2.00	0.41	0.12	0.53	2.19
Q-T27	Dehgolan	amph microphen 1-10	0.74	6.33	1.67	8.00	0.23	0.22	0.01	0.57	3.36	0.60	0.02	5.00		0.00	0.00	0.00	1.76	0.24	2.00	0.55	0.11	0.66	1.90
Q-T27	Dehgolan	amph opacitized 1-11	0.54	6.79	1.21	8.00	0.49	0.09	0.01	0.43	2.36	1.57	0.06	5.00		0.00	0.00	0.00	1.58	0.42	2.00	0.33	0.18	0.51	1.70
Q-T27	Dehgolan	amph microphen 2-6	0.72	6.20	1.80	8.00	0.21	0.24	0.01	0.72	3.27	0.54	0.01	5.00		0.00	0.00	0.00	1.77	0.23	2.00	0.43	0.16	0.59	2.01
Q-T27	Dehgolan	amph opacitized 2-8	0.52	6.41	1.36	7.78	0.00	0.00	0.00	1.09	2.63	1.28	0.00	5.00		0.05	0.08	0.12	1.73	0.15	1.88	0.71	0.18	0.89	1.36
Q-T27	Dehgolan	amph opacitized 3-1	0.76	6.62	1.38	8.00	0.22	0.12	0.03	0.77	3.48	0.35	0.03	5.00		0.00	0.00	0.00	1.68	0.32	2.00	0.34	0.09	0.43	1.60
Q-T27	Dehgolan	amph gm 3-3	0.79	6.45	1.55	8.00	0.25	0.23	0.00	0.71	3.55	0.25	0.01	5.00		0.00	0.00	0.00	1.69	0.31	2.00	0.30	0.13	0.43	1.80
Q-T27	Dehgolan	amph gm 4-4	0.76	6.31	1.69	8.00	0.07	0.23	0.00	0.84	3.56	0.27	0.02	5.00		0.00	0.00	0.00	1.75	0.25	2.00	0.45	0.11	0.56	1.75
Q-T24	Dehgolan	amph microphen 1-4	0.58	6.70	1.30	8.00	0.14	0.13	0.00	0.59	2.71	1.37	0.05	5.00		0.00	0.00	0.00	1.80	0.20	2.00	0.30	0.20	0.49	1.44
Q-T24	Dehgolan	amph microphen 1-6	0.57	6.66	1.34	8.00	0.17	0.14	0.00	0.57	2.66	1.41	0.05	5.00		0.00	0.00	0.00	1.80	0.20	2.00	0.31	0.21	0.52	1.51
Q-T24	Dehgolan	amph microphen 1-7	0.58	6.64	1.36	8.00	0.13	0.14	0.00	0.68	2.71	1.29	0.05	5.00		0.00	0.00	0.00	1.77	0.23	2.00	0.29	0.19	0.48	1.48
Q-T24	Dehgolan	amph microphen 2-4	0.57	6.68	1.32	8.00	0.18	0.12	0.00	0.60	2.66	1.38	0.06	5.00		0.00	0.00	0.00	1.80	0.20	2.00	0.30	0.20	0.49	1.50
Q-T24	Dehgolan	amph microphen 2-5	0.56	6.62	1.38	8.00	0.16	0.15	0.00	0.60	2.61	1.42	0.05	5.00		0.00	0.00	0.00	1.78	0.22	2.00	0.34	0.18	0.52	1.55
Q-T24	Dehgolan	amph pheno rim 3-3	0.57	6.57	1.43	8.00	0.15	0.16	0.00	0.64	2.63	1.36	0.06	5.00		0.00	0.00	0.00	1.78	0.22	2.00	0.31	0.21	0.52	1.58
Q-T24	Dehgolan	amph pheno core 3-5	0.57	6.57	1.43	8.00	0.24	0.13	0.00	0.62	2.62	1.33	0.06	5.00		0.00	0.00	0.00	1.78	0.22	2.00	0.30	0.22	0.52	1.67
Q-T29	Dehgolan	amph opacitized 1-10	0.67	6.85	1.15	8.00	0.24	0.10	0.01	0.42	3.07	1.11	0.05	5.00		0.00	0.00	0.00	1.79	0.21	2.00	0.33	0.16	0.49	1.38
IR1	Qorveh	Amph pheno 2-6	0.79	6.22	1.78	8.00	0.00	0.38	0.00	0.34	3.62	0.64	0.01	5.00	0.00	0.00	0.00	0.00	1.89	0.11	2.00	0.56	0.23	0.79	1.78
IR1	Qorveh	Same amph pheno 2-7	0.78	6.22	1.78	8.00	0.21	0.25	0.01	0.60	3.51	0.40	0.02	5.00	0.00	0.00	0.00	0.00	1.78	0.22	2.00	0.53	0.16	0.69	1.99
IR1	Qorveh	Amph pheno 1-1	0.75	6.02	1.98	8.00	0.10	0.21	0.01	1.18	3.48	0.00	0.02	5.00	0.00	0.00	0.00	0.00	1.65	0.35	2.00	0.47	0.14	0.62	2.08
IR1	Qorveh	Amph pheno 1-2	0.75	6.06	1.94	8.00	0.16	0.25	0.02	0.88	3.41	0.25	0.01	5.00	0.00	0.00	0.00	0.00	1.70	0.30	2.00	0.51	0.16	0.67	2.10
IR2	Qorveh	Amph pheno rim 1-3	0.78	6.03	1.97	8.00	0.05	0.24	0.01	0.94	3.65	0.09	0.02	5.00	0.00	0.00	0.00	0.00	1.77	0.23	2.00	0.56	0.17	0.74	2.02
IR2	Qorveh	Same amph pheno core 1-4	0.77	6.10	1.90	8.00	0.15	0.23	0.01	0.79	3.53	0.27	0.02	5.00	0.00	0.00	0.00	0.00	1.76	0.24	2.00	0.54	0.18	0.73	2.05
IR2	Qorveh	Pheno amph core 5-1	0.74	5.94	2.06	8.00	0.16	0.27	0.00	0.92	3.35	0.27	0.02	5.00	0.00	0.00	0.00	0.00	1.71	0.29	2.00	0.53	0.20	0.72	2.21
IR2	Qorveh	Pheno amph mantle 5-2	0.76	5.99	2.01	8.00	0.11	0.31	0.00	0.68	3.46	0.41	0.02	5.00	0.00	0.00	0.00	0.00	1.81	0.19	2.00	0.58	0.21	0.79	2.12
IR2	Qorveh	Pheno amph mantle-rim 5-3	0.82	6.61	1.17	7.79	0.00	0.00	0.00	0.80	4.12	0.08	0.00	5.00	0.00	0.00	0.03	0.04	1.79	0.18	1.96	0.59	0.12	0.71	1.17
IR2	Qorveh	Pheno amph rim 5-6	0.84	6.17	1.17	7.34	0.00	0.00	0.00	0.87	4.12	0.00	0.00	5.00	0.44	0.00	0.03	0.03	1.79	0.00	1.79	0.85	0.20	1.04	1.17
IR5	Qorveh	Amph in coarse incl 1-1	0.64	6.38	1.62	8.00	0.35	0.18	0.00	0.44	2.83	1.15	0.04	5.00	0.00	0.00	0.00	0.00	1.79	0.21	2.00	0.42	0.25	0.67	1.98
IR5	Qorveh	Amph in coarse incl 1-2	0.69	6.34	1.28	7.62	0.00	0.00	0.00	1.23	3.54	0.23	0.00	5.00	0.00	0.17	0.04	0.21	1.77	0.02	1.79	0.71	0.18	0.89	1.28
IR5	Qorveh	Amph in coarse incl 1-10	0.68	6.60	1.40	8.00	0.03	0.22	0.00	0.84	3.18	0.68	0.04	5.00	0.00	0.00	0.00	0.00	1.70	0.30	2.00	0.26	0.12	0.37	1.44
IR5	Qorveh	Amph pheno glom core 2-6	0.66	6.07	1.93	8.00	0.27	0.26	0.00	0.53	2.93	0.99	0.02	5.00	0.00	0.00	0.00	0.00	1.81	0.19	2.00	0.57	0.23	0.80	2.20
IR5	Qorveh	Same amph pheno glom rim 2-7	0.63	6.04	1.96	8.00	0.30	0.24	0.01	0.75	2.78	0.90	0.03	5.00	0.00	0.00	0.00	0.00	1.77	0.23	2.00	0.43	0.21	0.65	2.27
IR5	Qorveh	Pheno amph glom rim 2-9	0.64	6.54	1.46	8.00	0.30	0.32	0.00	0.00	2.77	1.59	0.03	5.00	0.00	0.00	0.00	0.00	1.78	0.22	2.00	0.62	0.19	0.81	1.76
IR5	Qorveh	Same pheno amph glom core 2-10	0.61	6.07	1.93	8.00	0.17	0.28	0.00	0.66	2.73	1.12	0.04	5.00	0.00	0.00	0.00	0.00	1.77	0.23	2.00	0.53	0.24	0.77	2.10
IR5	Qorveh	Pheno amph core 4-1	0.65	6.02	1.98	8.00	0.67	0.66	0.01	0.00	3.66	0.00	0.00	5.00	0.03	1.96	0.00	1.97	0.01	0.00	0.01	0.30	1.85	2.15	2.65
IR5	Qorveh	Same pheno amph mantle 4-2	0.71	6.02	1.98	8.00	0.30	0.22	0.00	0.83	3.17	0.47	0.01	5.00	0.00	0.00	0.00	0.00	1.76	0.24	2.00	0.43	0.21	0.64	2.28
IR5	Qorveh	Same pheno amph rim 4-3	0.59	6.08	1.92	8.00	0.28	0.24	0.00	0.70	2.63	1.12	0.03	5.00	0.00	0.00	0.00	0.00	1.79	0.21	2.00	0.44	0.21	0.66	2.20
IR5	Qorveh	Same pheno amph black rim 4-4	0.61	6.30	1.70	8.00	0.04	0.30	0.01	0.82	2.80	0.97	0.05	5.00	0.00	0.00	0.00	0.00	1.73	0.27	2.00	0.37	0.12	0.49	1.74

Table 16: EMP analysis for Bijar-Qorveh opaque compositions

Sample	Location	Description	TiO_2	Al_2O_3	Cr_2O_3	MgO	MnO	FeO	Total	Ti	Al	Fe'''	Fe''	Mn	Mg	Cr	Total	Ilm	Usp	Mg#	Cr#
Q-T36	Bijar	op gm 1-3	18.99	1.43	0.17	3.77	0.80	72.00	97.16	0.58	0.07	0.90	1.29	0.03	0.23	0.01	3.10		0.08	0.15	0.07
Q-T36	Bijar	op gm 2-11	18.73	0.74	0.06	2.83	1.02	72.57	95.95	0.59	0.04	0.92	1.33	0.04	0.18	0.00	3.10		0.56	0.11	0.05
Q-T36	Bijar	op gm 3-4	18.57	1.51	0.06	3.61	0.83	71.32	95.90	0.58	0.07	0.90	1.29	0.03	0.22	0.00	3.10		0.56	0.14	0.03
Q-T39	Bijar	op gm 1-5	22.25	2.56	0.07	2.52	0.90	66.67	94.96	0.68	0.12	0.63	1.46	0.03	0.15	0.00	3.08		0.57	0.09	0.02
Q-T39	Bijar	op gm 4-2	23.25	1.73	0.07	2.13	0.85	67.80	95.83	0.71	0.08	0.61	1.51	0.03	0.13	0.00	3.07		0.68	0.08	0.03
Q-T39	Bijar	op gm 4-10	23.51	1.81	0.09	2.13	0.93	67.72	96.19	0.71	0.09	0.60	1.51	0.03	0.13	0.00	3.07		0.70	0.08	0.03
Q-T6	Qezelke Kand	op gm 1-5	16.57	4.04	0.72	3.59	0.82	70.76	96.49	0.51	0.19	0.91	1.23	0.03	0.22	0.02	3.11		0.53	0.15	0.11
Q-T6	Qezelke Kand	op gm 2-8	17.18	4.98	4.95	4.76	0.66	64.19	96.73	0.51	0.23	0.73	1.19	0.02	0.28	0.15	3.11		0.58	0.19	0.40
Q-T6	Qezelke Kand	op gm 3-6	15.73	4.28	3.98	4.01	0.57	67.48	96.05	0.48	0.20	0.85	1.19	0.02	0.24	0.13	3.11		0.53	0.17	0.38
T4	Takab	3-4 mt gm	16.55	2.62	1.21	3.06	0.75	71.94	96.14	0.52	0.13	0.94	1.27	0.03	0.19	0.04	3.11		0.11	0.13	0.02
T4	Takab	4-4 mt gm	18.24	1.64	0.04	1.56	1.01	72.48	94.96	0.58	0.08	0.89	1.40	0.04	0.10	0.00	3.09		0.57	0.07	0.02
T6	Takab	1-3 op in big pheno ol	1.41	16.72	35.30	11.93	0.00	25.16	90.52	0.04	0.70	0.29	0.43	0.00	0.63	0.99	3.09		0.20	0.60	0.59
T6	Takab	1-5 op in big pheno ol	2.01	14.93	38.04	10.46	0.00	32.36	97.81	0.05	0.60	0.34	0.54	0.00	0.53	1.03	3.09		0.23	0.50	0.63
T6	Takab	3-1 op in ol pheno	2.14	14.96	37.55	9.91	0.00	33.26	97.82	0.06	0.60	0.34	0.57	0.00	0.51	1.02	3.09		0.24	0.47	0.63
T6	Takab	3-3 op in ol pheno	1.86	14.84	36.88	10.57	0.00	32.15	96.30	0.05	0.61	0.36	0.53	0.00	0.55	1.01	3.10		0.21	0.51	0.63
IR2	Qorveh	Ilm gm 1-7	36.04	0.03	0.06	1.81	0.60	52.97	91.51	0.80	0.00	0.55	0.64	0.02	0.08	0.00	2.08	0.72		0.11	0.52
IR2	Qorveh	Sp gm 1-8	28.47	0.02	0.12	1.40	0.45	60.72	91.17	0.67	0.00	0.85	0.51	0.01	0.07	0.00	2.11	0.58		0.11	0.82
IR2	Qorveh	Ilm gm 1-9	38.48	0.04	0.04	1.56	0.66	50.47	91.25	0.84	0.00	0.44	0.70	0.02	0.07	0.00	2.07	0.78		0.09	0.40
IR2	Qorveh	Ilm gm 1-10	38.81	0.12	0.09	2.06	0.57	50.32	91.97	0.84	0.00	0.44	0.68	0.01	0.09	0.00	2.07	0.78		0.11	0.34
IR2	Qorveh	Ilm gm 1-11	30.93	0.00	0.12	1.27	0.48	58.77	91.56	0.71	0.00	0.75	0.56	0.01	0.06	0.00	2.10	0.63		0.09	1.00
IR2	Qorveh	Ilm in phen amph rim 5-10	30.84	0.10	0.15	2.31	0.69	58.30	92.39	0.70	0.00	0.78	0.50	0.02	0.10	0.00	2.11	0.60		0.17	0.49
IR2	Qorveh	Ilm in pheno amph rim 5-11	31.96	0.16	0.12	3.30	0.83	55.52	91.88	0.72	0.01	0.73	0.48	0.02	0.15	0.00	2.11	0.62		0.23	0.34
IR2	Qorveh	Ilm gm 5-14	30.83	0.02	0.11	1.89	0.61	57.35	90.81	0.71	0.00	0.75	0.53	0.02	0.09	0.00	2.10	0.62		0.14	0.80
IR2	Qorveh	Ilm gm 5-15	33.05	0.08	0.13	1.26	0.40	57.37	92.28	0.74	0.00	0.67	0.60	0.01	0.06	0.00	2.09	0.67		0.09	0.53
IR2	Qorveh	Ilm gm 5-17	30.50	0.02	0.06	1.16	0.48	61.56	93.77	0.69	0.00	0.80	0.54	0.01	0.05	0.00	2.10	0.60		0.09	0.70
IR2	Qorveh	Ilm gm 5-18	29.80	0.14	0.08	2.39	0.33	59.62	92.36	0.68	0.00	0.82	0.49	0.01	0.11	0.00	2.11	0.58		0.18	0.28

Table 17. Whole-rock major oxides (wt%), trace elements and Sr-Nd-Pb isotopic ratios of Bijar-Qorveh samples

Locality	Takab	Takab	Takab	Qezelke Kand	Qezelke Kand	Qezelke Kand	Qezelke Kand	Qezelke Kand	Qezelke Kand	Qezelke Kand	Qezelke Kand	Qezelke Kand	Qezelke Kand	Qezelke Kand	Qezelke Kand
Sample	T2	T4	T6	QT1	QT2	QT3	QT4	QT5	QT6	QT7	QT8	QT9	QT10	QT11	QT12
SiO_2	50.0	49.6	49.1	47.1	46.9	45.8	45.9	46.3	44.9	47.5	66.6	66.4	44.3	67.1	51.4
TiO_2	1.7	1.7	1.6	2.0	2.1	2.0	2.0	2.0	2.1	2.3	0.4	0.4	1.9	0.4	1.6
Al_2O_3	13.5	13.0	13.6	14.7	15.4	14.0	13.6	14.3	14.4	14.5	16.9	16.5	13.6	16.6	13.9
Fe_2O_3	9.3	9.4	9.5	9.5	9.3	9.7	9.9	9.8	10.1	10.1	2.5	2.5	10.2	2.5	7.7
FeO	1.4	1.4	1.4	1.4	1.4	1.5	1.5	1.5	1.5	1.5	0.4	0.4	1.5	0.4	1.1
MnO	0.1	0.1	0.1	0.1	0.1	0.1	0.1	0.1	0.1	0.2	0.0	0.0	0.2	0.0	0.1
MgO	8.7	9.1	7.2	8.1	6.3	8.9	10.1	9.4	9.7	7.9	1.0	1.0	9.1	1.0	6.6
CaO	8.8	8.6	8.8	9.6	10.9	9.8	9.9	9.9	9.0	9.6	3.0	3.0	9.9	3.1	9.6
Na_2O	3.0	2.8	2.7	4.6	5.7	4.6	4.1	4.4	3.7	4.2	5.4	5.5	4.2	5.4	5.0
K_2O	3.1	2.9	2.8	2.4	1.6	2.5	2.2	2.1	2.8	2.9	3.0	3.0	2.6	3.0	3.0
P_2O_5	1.1	1.0	0.9	1.1	1.3	1.3	1.4	1.4	0.9	0.6	0.2	0.2	1.2	0.3	0.9
L.O.I.	1.5	2.3	2.5	0.2		0.4	1.4	0.8	1.3		1.7	1.7	1.8	1.4	
Total	102.2	101.9	100.3	100.8	100.9	100.8	102.1	102.0	100.4	101.2	101.0	100.6	100.5	101.3	100.7
Mg#	0.68	0.69	0.63	0.66	0.61	0.67	0.70	0.68	0.68	0.64	0.48	0.48	0.67	0.48	0.66
$^{87}Sr/^{86}Sr$	0.707585	0.704768	0.707448									0.705306	0.704815		
eSr	44.5	4.5	42.6									12.2	5.2		
$^{143}Nd/^{144}Nd$	0.512277	0.512723	0.512639									0.512652	0.512711		
eNd	-7.1	1.6	0.0									0.2	1.4		
$^{206}Pb/^{204}Pb$	18.9806	18.9566	18.9549									18.7101	18.6951		
$^{207}Pb/^{204}Pb$	15.6834	15.6821	15.6880									15.6644	15.6656		
$^{208}Pb/^{204}Pb$	39.0873	39.0675	39.0580									38.7556	38.7693		
$^{208}Pb/^{206}Pb$	2.06	2.06	2.06									2.07	2.07		
$^{207}Pb/^{206}Pb$	0.83	0.83	0.83									0.84	0.84		
Rb	63	172	133	48	47	52	40	34	44	56	66	64	52	66	63
Sr	689	760	504	1566	2671	1703	1505	1536	1147	1209	981	978	1537	996	1492
Ba	953	986	722	952	1191	1067	1030	1077	781	851	1392	1408	975	1406	1438
Cs	24.3	10.0	4.1	1.3		1.4	1.2	1.3	0.9		2.3	2.2	2.1	2.2	
Sc	24	24	23	16	20	16	17	16	18	18	3	3	17	3	18
V	195	191	194	167	189	175	171	180	189	237	36	37	181	38	180
Cr	450	460	410	240	309	260	300	280	240	312			240		369
Co	65	40	49	40		41	44	41	46		5	5	42	5	
Ni	220	210	140	140	198	180	210	170	190	196			170		163
Cu	60	60	60	40		40	60	40	50				40		
Zn	90	90	100	100		110	120	110	100		60	60	110	60	
Y	27	26	24	20	19	19	19	20	18	21	10	10	21	10	21
Zr	309	287	228	215	198	227	224	229	224	238	209	213	236	213	203
Nb	36	32	25	46		48	47	48	45	32	28	27	57	28	23
Hf	7.0	6.8	5.5	4.6		4.8	4.8	4.8	4.5		4.4	4.4	5.0	4.8	
Ta	2.8	2.0	1.7	2.6		2.7	2.6	2.6	2.9		1.6	1.5	3.5	1.7	
La	53	49	40	107	120	118	106	109	75	71	71	68	89	72	113
Ce	119	110	88	199	183	223	204	205	140	136	118	113	169	119	162
Pr	15.8	14.7	11.6	21.1		24.0	21.6	21.8	14.8		11.0	10.7	18.4	11.4	
Nd	68.2	63.7	48.8	75.2		85.0	77.0	77.1	53.8		34.6	34.1	67.6	35.7	
Sm	13.3	12.3	9.6	11.5		12.4	11.7	11.7	9.0		4.7	4.8	10.6	4.8	
Eu	2.8	2.7	2.2	2.9		3.2	2.9	2.9	2.4		1.2	1.1	2.9	1.2	
Gd	7.7	7.4	6.5	7.7		8.0	7.6	7.7	6.3		3.0	3.0	7.5	3.0	
Tb	1.0	1.0	0.9	1.0		1.0	0.9	0.9	0.8		0.4	0.4	1.0	0.4	
Dy	5.1	4.9	4.6	4.9		5.0	4.7	4.7	4.2		2.1	2.0	5.0	2.1	
Ho	0.9	0.9	0.9	0.8		0.8	0.8	0.8	0.7		0.4	0.4	0.9	0.4	
Er	2.5	2.4	2.4	2.2		2.1	2.1	2.0	1.8		1.1	1.1	2.2	1.1	
Tm	0.4	0.3	0.3	0.3		0.3	0.3	0.3	0.2		0.2	0.2	0.3	0.2	
Yb	2.2	2.0	2.0	1.7		1.6	1.6	1.5	1.4		1.1	1.0	1.6	1.1	
Lu	0.3	0.3	0.3	0.3		0.2	0.3	0.2	0.2		0.2	0.2	0.2	0.2	
Pb	12	15	13	13		16	15	13	10		30	32	8	32	
Th	37.5	36.1	22.6	12.0		13.3	12.5	12.7	8.5		23.1	22.6	9.0	23.8	
U	10.5	10.0	5.8	1.8		2.9	2.6	2.6	2.1		5.8	5.6	2.5	5.9	
Ga	20	19	20	21		21	20	21	21		20	20	21	21	

Table 17. (continued)

Locality	Qezelke Kand	Qezelke Kand	Qezelke Kand	Qezelke Kand	Qezelke Kand	Bijar	Bijar	Bijar	Bijar	Bijar	Bijar	Bijar	Bijar	Bijar	Bijar	Dehgolan	Dehgolan	Dehgolan	Dehgolan	Dehgolan
Sample	QT13	QT14	QT15	QT16	QT17	QT32	QT33	QT34	QT35	QT36	QT37	QT38	QT39	QT40	QT41	QT18	QT19	QT20	QT21	QT22
SiO_2	59.4	51.3	49.6	46.9	46.7	46.6	46.5	46.5	51.1	47.6	49.2	49.9	49.1	47.3	47.4	65.6	65.1	66.7	65.7	63.5
TiO_2	0.6	1.6	1.7	1.7	1.7	2.1	2.1	1.9	1.7	1.8	1.9	1.5	1.4	1.5	2.0	0.5	0.4	0.4	0.4	0.5
Al_2O_3	19.8	13.8	13.3	12.8	12.5	14.8	14.6	14.1	16.0	14.4	14.3	15.4	15.6	14.9	12.3	16.5	16.4	15.8	16.6	16.7
Fe_2O_3	5.3	7.8	7.5	8.0	7.8	8.7	8.8	9.6	8.0	8.9	9.1	9.5	10.1	9.5	8.8	2.6	3.1	2.4	3.0	3.0
FeO	0.8	1.2	1.1	1.2	1.2	1.3	1.3	1.4	1.2	1.3	1.4	1.4	1.5	1.4	1.3	0.4	0.5	0.4	0.4	0.5
MnO	0.1	0.1	0.1	0.1	0.1	0.1	0.1	0.1	0.1	0.1	0.1	0.2	0.2	0.1	0.1	0.0	0.1	0.0	0.0	0.0
MgO	0.7	8.3	7.4	8.0	8.0	7.0	7.1	8.9	4.7	7.1	7.5	9.1	8.6	8.5	9.0	0.3	1.0	0.3	0.5	0.6
CaO	2.9	9.6	10.0	11.2	11.3	9.2	9.4	9.7	9.0	9.7	9.0	9.3	8.8	9.4	10.9	2.6	3.4	2.9	3.1	3.3
Na_2O	4.0	4.8	4.8	4.5	4.0	4.1	3.5	3.7	6.1	4.6	4.0	2.9	3.2	2.5	4.5	4.3	4.5	4.6	4.0	4.6
K_2O	3.1	2.5	3.6	3.4	3.6	1.8	1.7	2.7	2.1	1.7	2.8	1.7	1.4	1.4	3.3	3.0	3.1	3.2	3.4	3.0
P_2O_5	0.1	1.1	1.6	1.9	1.7	1.2	1.2	1.1	0.9	0.9	0.9	0.4	0.4	0.4	2.1	0.3	0.3	0.3	0.2	0.2
L.O.I.	3.2	0.2	0.7	0.8	1.7	3.3	4.1	1.7		1.6	0.4		1.6	3.0	0.3	2.6	2.0	2.0	3.3	2.4
Total	99.9	102.1	101.4	100.5	100.1	100.2	100.5	101.5	100.8	99.8	100.6	101.2	101.9	100.0	102.1	98.7	99.9	98.9	100.7	98.2
Mg#	0.23	0.71	0.69	0.69	0.70	0.64	0.65	0.68	0.57	0.64	0.65	0.68	0.66	0.67	0.70	0.22	0.42	0.23	0.29	0.31
$^{87}Sr/^{86}Sr$	0.706182				0.705226		0.704784		0.704773				0.705709		0.705355			0.707387		
eSr	24.6				11.0		4.7		4.6				17.9		12.8			41.7		
$^{143}Nd/^{144}Nd$	0.512501				0.512651		0.512627		0.512525				0.512667					0.512417		
eNd	-2.7				0.2		-0.3		-2.2				0.5					-4.4		
$^{206}Pb/^{204}Pb$	18.9719				18.6761		18.7181		18.7281		18.4819		18.9659		18.6719			18.8672		
$^{207}Pb/^{204}Pb$	15.7063				15.6775		15.6420		15.6465		15.6571		15.6781		15.6897			15.7241		
$^{208}Pb/^{204}Pb$	39.1128				38.7511		38.7400		38.7589		38.5383		39.0202		38.7920			39.0405		
$^{208}Pb/^{206}Pb$	2.06				2.07		2.07		2.07		2.09		2.06		2.08			2.0692		
$^{207}Pb/^{206}Pb$	0.83				0.84		0.84		0.84		0.85		0.83		0.84			0.83		
Rb	88	32	64	54	57	64	75	47	60	53	44	39	30	22	58	124	125	126	126	120
Sr	1269	1448	2110	2344	2221	2917	3293	1721	1716	1583	1577	750	832	733	1836	618	708	663	693	726
Ba	1943	1332	1778	1736	1719	963	971	1002	1214	994	1006	539	496	492	1909	1830	1150	1157	1401	1188
Cs	5.0	1.8	1.9	1.5	1.5	1.8	1.9	1.4		1.2	1.3		1.7	1.1	1.4	4.5	6.0	5.2	6.3	6.0
Sc	14	16	13	14	14	14	14	17	16	16	17	22	22	21	15	5	3	4	3	4
V	98	168	141	148	146	158	160	178	216	168	168	101	177	176	163	57	40	46	41	41
Cr	80	330	230	150	230	150	150	250	159	170	180	334	320	290	230					40
Co	10	33	31	33	33	31	32	40		34	35		39	37	35	6	4	6	3	4
Ni	20	160	170	160	190	110	110	190	114	120	120	133	140	130	180					
Cu	10	40	60	50	50	30	30	60		40	50		40	40	50					
Zn	60	90	130	110	110	100	110	100		90	100		90	90	120	40	50	50	40	50
Y	34	18	23	21	19	22	22	21	25	21	22	25	20	20	22	9	11	11	11	10
Zr	186	204	317	309	288	263	263	230	238	238	238	154	129	142	356	193	202	195	198	198
Nb	24	44	47	48	44	65	64	46	16	43	46	16	17	23	53	14	17	14	16	16
Hf	4.3	4.4	6.4	6.3	6.0	5.3	5.4	4.7		5.1	5.4		3.1	3.3	7.1	4.6	4.8	4.6	4.7	4.7
Ta	1.3	2.6	2.6	2.6	2.4	4.0	4.0	2.8		2.6	3.1		1.0	1.3	3.0	0.9	1.2	0.9	1.1	1.1
La	159	101	144	168	155	94	94	100	95	89	88	31	38	41	162	43	45	44	46	46
Ce	187	197	293	324	302	176	176	193	148	174	173	62	71	78	311	80	83	82	83	84
Pr	30.1	21.3	32.1	35.8	33.6	18.7	18.9	21.1		19.2	19.3		7.7	8.4	33.7	8.5	8.7	8.8	8.7	8.8
Nd	110.0	75.3	119.0	126.0	121.0	68.3	68.3	77.4		71.1	71.1		28.5	31.9	117.0	31.1	30.3	31.1	30.0	30.9
Sm	18.8	11.2	17.1	18.0	17.2	11.2	11.6	12.0		11.2	11.2		5.5	6.2	16.3	5.0	4.7	5.1	4.9	4.7
Eu	3.6	2.7	4.2	4.3	4.1	2.9	2.9	3.1		2.9	2.8		1.6	1.7	3.8	1.2	1.1	1.1	1.1	1.1
Gd	12.2	6.9	9.7	9.9	9.5	8.1	8.2	7.7		7.4	7.4		4.9	5.2	9.3	3.1	3.0	3.2	3.0	2.8
Tb	1.6	0.8	1.1	1.1	1.0	1.1	1.1	1.0		0.9	1.0		0.7	0.8	1.0	0.4	0.4	0.4	0.4	0.4
Dy	8.3	4.3	4.8	5.0	4.8	5.3	5.3	5.1		5.0	5.0		4.1	4.3	5.2	2.0	2.1	2.2	2.1	2.1
Ho	1.4	0.7	0.8	0.8	0.8	0.9	0.9	0.9		0.9	0.9		0.8	0.8	0.8	0.4	0.4	0.4	0.4	0.4
Er	3.7	1.9	2.0	1.9	1.9	2.2	2.2	2.2		2.2	2.3		2.2	2.1	2.1	1.0	1.1	1.1	1.1	1.1
Tm	0.5	0.3	0.3	0.2	0.2	0.3	0.3	0.3		0.3	0.3		0.3	0.3	0.3	0.2	0.2	0.2	0.2	0.2
Yb	3.2	1.6	1.6	1.5	1.4	1.6	1.6	1.7		1.8	1.8		2.0	1.9	1.6	1.0	1.1	1.1	1.1	1.0
Lu	0.5	0.2	0.2	0.2	0.2	0.2	0.2	0.2		0.3	0.3		0.3	0.3	0.3	0.2	0.2	0.2	0.2	0.2
Pb	47	24	22	22	24	10	10	14		13	15		20	16	20	26	28	29	29	30
Th	29.0	17.6	26.7	23.2	21.5	11.5	11.6	9.6		9.2	9.2		9.9	9.7	23.7	21.5	21.5	22.0	21.9	21.8
U	7.4	4.4	4.8	4.4	4.2	1.3	1.2	2.4		2.1	2.3		2.8	2.6	4.4	5.9	6.4	6.3	6.8	6.1
Ga	23	19	22	20	20	22	22	21		20	20		19	19	20	19	18	19	19	19

Table 17. (continued)

Locality	Dehgolan	Dehgolan	Dehgolan	Dehgolan	Dehgolan	Dehgolan	Dehgolan	Dehgolan	Dehgolan	Dehgolan	Dehgolan	Dehgolan	Qorveh	Qorveh	Qorveh	Qorveh	Qorveh	Qorveh	Qorveh	Qorveh	Qorveh	Qorveh
Sample	QT23	QT24	QT25	QT26	QT27	QT28	QT29	QT30	QT31	QT42	QT43	QT44	IR1	IR2	IR3	IR4	IR5	IR6	IR7	IR8	IR9	IR10
SiO_2	66.7	67.6	61.2	63.1	61.9	69.3	63.1	65.6	64.3	67.1	67.8	66.8	59.2	58.8	60.5	59.1	64.6	60.7	72.1	72.0	61.0	63.7
TiO_2	0.4	0.5	0.6	0.6	0.5	0.6	0.7	0.8	0.6	0.4	0.4	0.5	0.8	0.8	0.7	0.6	0.5	0.6	0.1	0.1	0.6	0.5
Al_2O_3	16.1	15.5	15.7	15.8	15.7	14.2	14.6	13.7	14.3	15.5	15.6	15.2	16.7	16.9	17.2	17.2	16.9	17.0	15.0	14.3	16.6	16.6
Fe_2O_3	3.2	3.3	4.0	3.7	3.7	3.2	3.4	3.7	2.8	3.3	3.0	3.1	6.4	6.1	5.9	5.6	4.0	5.4	0.9	1.3	5.4	4.7
FeO	0.5	0.5	0.6	0.6	0.6	0.5	0.5	0.5	0.4	0.5	0.5	0.5	1.0	0.9	0.9	0.8	0.6	0.8	0.1	0.2	0.8	0.7
MnO	0.1	0.1	0.1	0.1	0.1	0.0	0.0	0.0	0.0	0.1	0.1	0.1	0.1	0.1	0.1	0.1	0.1	0.1	0.0	0.1	0.1	0.1
MgO	2.3	1.7	3.9	2.7	3.4	2.3	2.3	3.0	2.2	2.4	1.7	1.6	3.3	3.1	2.5	1.8	1.5	2.6	0.2	0.1	2.5	1.0
CaO	3.4	3.2	4.8	4.9	4.9	1.9	2.9	2.9	2.9	3.7	3.3	3.1	6.1	6.4	5.0	5.0	4.7	5.0	1.1	1.5	5.2	4.2
Na_2O	3.9	4.5	4.0	4.3	4.2	3.3	3.8	3.6	3.9	3.6	4.5	4.2	4.3	4.3	4.4	4.1	4.8	3.9	2.2	3.7	4.0	4.1
K_2O	3.4	3.6	2.6	2.8	2.5	4.6	5.2	5.7	5.1	3.5	3.4	3.5	2.2	2.2	2.3	2.4	2.6	2.8	4.8	4.8	2.7	2.9
P_2O_5	0.2	0.3	0.2	0.2	0.2	0.2	0.7	0.6	0.6	0.2	0.3	0.2	0.3	0.3	0.3	0.3	0.2	0.3	0.1	0.0	0.3	0.3
L.O.I.		0.5	1.7	2.0	1.9		1.7		1.3		0.5	0.7	1.3	1.9	1.7	2.7	1.0	2.5	3.3	2.8	2.5	2.8
Total	100.1	101.1	99.3	100.6	99.4	100.2	98.7	100.1	98.5	100.2	100.8	99.5	101.6	101.8	101.5	99.7	101.3	101.5	99.7	100.9	101.7	101.5
Mg#	0.61	0.54	0.69	0.62	0.67	0.62	0.60	0.65	0.64	0.62	0.56	0.53	0.54	0.53	0.49	0.42	0.46	0.52	0.28	0.19	0.51	0.33
$^{87}Sr/^{86}Sr$			0.707203		0.707112						0.707726		0.706528			0.706818	0.706137			0.707141		
eSr			39.1		37.8						46.5		29.5			33.6	23.9			38.2		
$^{143}Nd/^{144}Nd$			0.512465		0.512444								0.51254			0.512484	0.51255			0.51248		
eNd			-3.4		-3.8								-2.0			-3.0	-1.7			-3.2		
$^{206}Pb/^{204}Pb$			18.8985		18.8760						18.9019		18.9889			19.0033	18.9511			18.9670		
$^{207}Pb/^{204}Pb$			15.7357		15.7103						15.7322		15.7054			15.6945	15.6899			15.7184		
$^{208}Pb/^{204}Pb$			39.0739		38.9988						39.0856		39.1365			39.1251	39.0579			39.1330		
$^{208}Pb/^{206}Pb$			2.0676								2.0678		2.06			2.06	2.06			2.06		
$^{207}Pb/^{206}Pb$			0.83								0.83		0.83			0.83	0.83			0.83		
Rb	144	123	97	96	89	167	253	272	230	150	120	129	74	72	79	76	85	89	173	167	90	99
Sr	1064	705	541	545	548	470	817	901	872	1013	710	688	1112	1200	1176	1129	1041	1167	474	564	1136	1030
Ba	1603	1460	930	936	927	1570	1978	2195	2109	1557	1377	1491	1405	1395	1497	3031	1442	1703	1594	1515	1656	1562
Cs		10.9	6.1	3.4	5.9		13.8		11.0		7.9	10.0	3.8	3.8	4.3	4.8	3.1	2.8	10.3	11.8	2.9	6.6
Sc	9	6	10	9	9	6	8	12	8	9	5	6	13	13	11	11	7	10	1	1	10	6
V	116	57	88	67	79	91	83	173	52	114	53	54	130	125	94	109	63	104	32	14	100	63
Cr	30	30	120	100	100	65	110	119	120	25	30	30	120	110	80	40	60	40		40	50	
Co		7	14	13	12		10		9		7	7	30	25	15	10	10	19			11	6
Ni	27		50	50	50	29	70	80	70	26	20	20	40	40	30		20					
Cu			20	20	10		10		10				20	20	10	10	10	10			10	
Zn		40	50	50	50		50		50		40	40	70	70	70	70	50	60			70	110
Y	14	13	12	11	11	26	14	29	14	17	11	11	20	20	20	24	15	21	14	15	21	20
Zr	198	217	156	156	158	227	292	343	294	213	195	204	171	163	172	193	142	201	96	100	212	194
Nb		17	11	11	11	16	18	5	17	11	15	17	16	15	15	17	15	16	18	18	19	23
Hf		5.1	3.7	3.8	3.7		7.1		7.0		4.4	4.9	4.2	3.9	3.9	4.4	3.5	4.3	2.9	2.9	4.6	4.4
Ta		1.4	0.8	0.8	0.8		1.2		1.2		1.2	1.3	1.4	1.3	1.1	1.3	1.3	3.6	1.7	1.6	1.3	1.8
La	53	60	33	32	32	52	73	68	81	42	60	56	71	71	76	85	54	87	18	17	88	74
Ce	65	106	60	59	59	63	151	108	162	49	100	99	118	120	126	138	91	145	32	30	144	122
Pr		10.8	6.3	6.1	6.2		18.3		19.0		10.3	10.1	12.1	12.2	12.9	14.5	9.2	15.0	3.5	3.2	14.8	12.6
Nd		36.8	22.2	21.3	21.8		73.9		74.6		34.7	34.0	42.2	42.4	43.3	50.9	31.3	50.4	12.8	11.2	50.1	42.8
Sm		5.7	3.9	3.7	3.8		12.7		12.7		5.5	5.4	6.9	6.8	7.0	8.1	5.0	7.8	2.7	2.5	7.7	6.6
Eu		1.4	1.0	0.9	0.9		2.3		2.4		1.2	1.2	1.7	1.7	1.7	1.9	1.2	1.9	0.7	0.7	1.9	1.6
Gd		4.0	2.9	2.7	2.9		6.5		6.5		3.6	3.6	4.9	4.4	4.7	5.5	3.4	4.8	2.1	1.9	5.4	4.2
Tb		0.5	0.4	0.4	0.4		0.7		0.7		0.5	0.5	0.7	0.6	0.7	0.8	0.5	0.7	0.4	0.3	0.8	0.6
Dy		2.7	2.2	2.1	2.2		3.1		3.2		2.4	2.5	3.7	3.4	3.5	4.1	2.5	3.7	2.1	2.0	4.0	3.4
Ho		0.5	0.4	0.4	0.4		0.5		0.5		0.4	0.4	0.7	0.6	0.7	0.8	0.5	0.7	0.4	0.4	0.8	0.7
Er		1.3	1.2	1.1	1.1		1.3		1.3		1.2	1.2	1.9	1.7	1.8	2.2	1.4	1.9	1.2	1.2	2.1	1.9
Tm		0.2	0.2	0.2	0.2		0.2		0.2		0.2	0.2	0.3	0.3	0.3	0.3	0.2	0.3	0.2	0.2	0.3	0.3
Yb		1.2	1.1	1.1	1.1		1.2		1.1		1.0	1.1	1.9	1.7	1.7	2.1	1.3	1.9	1.4	1.4	2.0	1.8
Lu		0.2	0.2	0.2	0.2		0.2		0.2		0.2	0.2	0.3	0.3	0.3	0.3	0.2	0.3	0.2	0.2	0.3	0.3
Pb	31	32	48				52		50		47	47	34	31	35	40	34	33	63	69	36	49
Th		25.9	14.5	14.2	14.2		48.4		46.0		24.7	25.2	24.9	25.4	27.4	31.3	20.8	31.7	21.6	20.4	32.4	25.0
U		9.1	5.4	5.4	5.3		14.2		13.8		7.4	8.7	6.9	6.6	7.8	8.0	7.4	10.2	10.2	15.1	9.6	9.3
Ga		17	17	17	17		19		20		18	17	21	21	21	21	19	21	19	19	21	22

Table 17. (continued)

Locality	Qorveh	Qorveh
Sample	IR11	IR12
SiO_2	59.4	59.0
TiO_2	0.6	0.7
Al_2O_3	15.0	17.2
Fe_2O_3	4.9	6.0
FeO	0.7	0.9
MnO	0.1	0.1
MgO	2.2	2.6
CaO	5.0	5.6
Na_2O	3.5	4.0
K_2O	3.2	2.6
P_2O_5	0.2	0.3
L.O.I.	6.1	2.3
Total	100.9	101.3
Mg#	0.51	0.49
$^{87}Sr/^{86}Sr$		
eSr		
$^{143}Nd/^{144}Nd$		
eNd		
$^{206}Pb/^{204}Pb$		
$^{207}Pb/^{204}Pb$		
$^{208}Pb/^{204}Pb$		
$^{208}Pb/^{206}Pb$		
$^{207}Pb/^{206}Pb$		
Rb	121	89
Sr	899	1364
Ba	1556	1874
Cs	24.3	7.3
Sc	9	13
V	81	126
Cr	100	40
Co	12	30
Ni	30	
Cu	20	10
Zn	180	70
Y	19	24
Zr	167	200
Nb	19	16
Hf	4.0	4.4
Ta	1.3	1.5
La	63	93
Ce	105	153
Pr	11.0	16.0
Nd	37.0	53.8
Sm	6.0	8.6
Eu	1.5	2.0
Gd	4.5	5.4
Tb	0.6	0.8
Dy	3.6	4.2
Ho	0.7	0.8
Er	1.9	2.3
Tm	0.3	0.4
Yb	1.8	2.2
Lu	0.3	0.3
Pb	91	50
Th	25.3	33.3
U	8.4	9.6
Ga	19	22

Supplementary Material S1

High-Pressure Multiple Saturation Experiments

Nowbaran melanephelinitic melts are supposed to be generated from an amphibole-rich mantle source with CO_2 involvement. High pressure experiments have been then performed to try to unravel the magmatic processes that controlled the genesis and the evolution of the investigated melts. High pressure multiple saturation experiments were performed at the Institute of Geochemistry and Petrology (Department of Earth Sciences D-ERDW) at ETH Zürich, in collaboration with Prof. Max W. Schmidt.

The close-to-primary Nowbaran nephelinitic compositions were forced into multiple saturation points with a typical lherzolitic mantle assemblage with addition of volatiles (H_2O and CO_2; sulphurs were excluded in term of volatile budget aiming to simplify the system), in order to saturate the system with olivine, clinopyroxene, orthopyroxene and garnet. The chosen amount of added H_2O is fixed at 3 wt%, as Nowbaran lavas show LOI content of ~2.6-7.0 wt% and CO_2 ranging from 0.5 wt% to 2.7 wt%, thus consequently H_2O amount is likely ~1.4-4.4 wt%. On the other hand, experimental added CO_2 is ~5 wt% (compositions *A*), as values up to ~7.0 wt% are observed in olivine-nephelinitic melts at 30 kbar [3], and ~3 wt% (compositions *B*), since lower values probably would not even affected the experimental melts.

Starting materials and experimental procedures

The starting composition for the experiments was derived from averaging twelve representative chemical analyses from Nowbaran compositions. As only the most primitive compositions were considered, samples with $SiO_2 \geq 40$ wt% or Mg# ≤ 0.71 were then excluded. All starting materials (except fayalite) were reagent grade from Alfa Aesar, Sigma Aldrich, Fluka, Johnson Mattey, Ventron. Iron was added as a mixture of fayalite (in-house made) and Fe_2O_3. A Fe_2O_3/FeO ratio of 0.3 was considered for these compositions, following the recommended values suggested by [2] for alkali rich-nephelinitic rocks. H_2O was added as $Al(OH)_3$ and $Ca_5(PO_4)_3(OH)$, whereas CO_2 was added as $CaCO_3$, Na_2CO_3, and K_2CO_3. The remaining amounts of Ca, Na, and K to reach the intended composition were added as $CaSiO_3$, Na_2SiO_3, and K_2SiO_3. Oxides were fired overnight at 800 °C, whereas silicates, carbonates, hydroxides, and apatite were

dried for 12 hours at 110 °C or 210 °C. The lherzolite used for weighted powders were ground and mixed in an agate mortar under acetone. The obtained starting mixture was stored in a desiccator under vacuum. Preliminary experiments on Nowbaran compositions produced clinopyroxene and rare olivine among the products. Therefore, in order to force Nowbaran compositions into saturation with a garnet-lherzolite, only natural olivine (San Carlos standard), orthopyroxene and synthetic garnet were added to the products. Garnet was obtained by mixing ~43.9 wt.% SiO_2, ~21.3 wt.% Al_2O_3, ~21.7 wt.% MgO, ~7.7 wt.% CaO, and ~5.4 wt.% Fe_2O_3 (Mg# = 0.88), based on a selection of more than 800 analysis from fresh garnet-lherzolitic xenoliths taken from *GEOROC* online database (http://georoc.mpch-mainz.gwdg.de/georoc/). The proportions that were used to obtain the lherzolite are i) 40 wt% olivine, 40 wt% orthopyroxene, 20 wt% garnet, ii) 60 wt.% olivine, 30 wt.% orthopyroxene, 10 wt.% garnet and iii) 60 wt.% olivine, 25 wt.% orthopyroxene and 15 wt.% garnet, depending on the acquired results. The saturation experiments were performed by making two-layered experiments containing 50 wt% lherzolite overlaid by 50 wt% Nowbaran compositions mixture. Prior each experiment, the mixtures were dried at 110 °C. Aliquotes of approximately 50 mg were inserted in $Au_{80}Pd_{20}$ capsules (4.0 mm diameter) and welded. Capsules were tested for leakage by immersing in acetone and weighted again. Sealed capsules were inserted in talc-pyrex-pyrophyllite assemblies (Fig. S1a). Experiments were performed with a standard 14-mm end-loaded piston-cylinder ([1]; Fig.S1b).

After preliminary melting point determinations, temperature was raised to target (~1200-1260 °C) at a rate of 30 °C/min using a Eurotherm temperature controller and monitored (Fig. S1c) using a type-B thermocouple ($Pt_{70}Rh_{30}$-$Pt_{94}Rh_{06}$). Pressure was kept constant at 2.7 GPa (=27 kbar). This pressure was constrained considering i) involvement of amphibole-rich mantle source in the genesis of these ultrabasic magmas (lithospheric pargasitic amphibole is stable up to ~3.0 GPa; [4]) and ii) garnet-residual source (garnet is frequently assumed to begin breaking down to spinel at ~2.7 GPa; [5, 6]).

Experiments were equilibrated at target T and P for approximately 48 hours and successively quenched by interrupting the power. The capsules were then embedded in epoxy resin and hand polished for chemical investigations. Polished run products

were carbon coated and characterized at ETH Zürich with a Jeol JSM-6390 LA Scanning Electron Microscope (SEM). The SEM is equipped with a Thermo Fisher NORAN NSS7 EDS system which carries a 30 mm^2 Silicon-drift detector (SDD) for chemical analysis and spectral imaging.

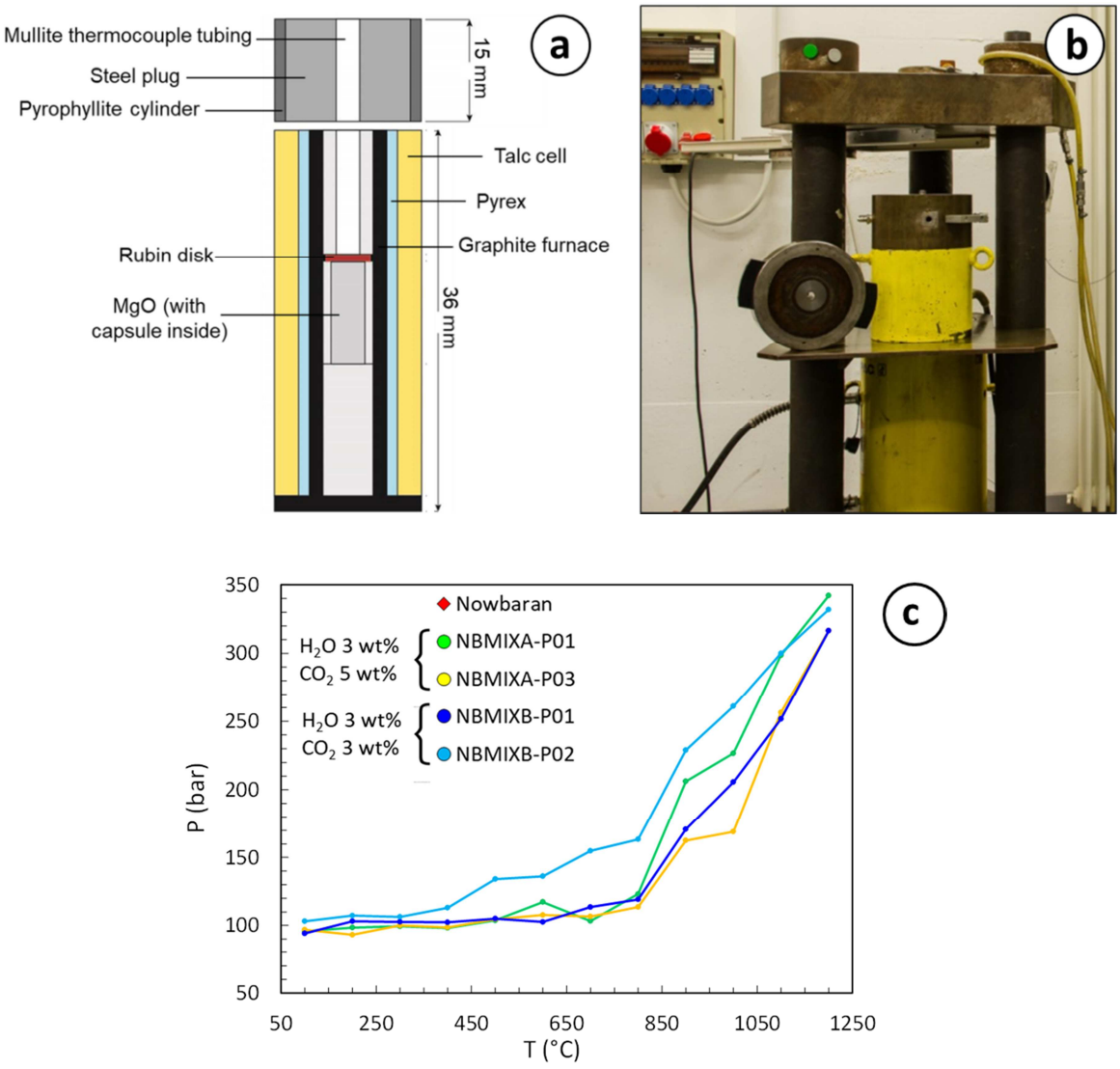

Fig. S1: *a) talc/pyrex/graphite assembly; b) Piston cylinder apparatus 'Boyd & England' end-loaded; c) run control parameters. Note that pressure increases exponentially with temperature around ~800 °C, at which talc progressively loses hydroxyl groups showing a transition from linear-elastic to elasto-plastic behaviour.*

Experimental results and discussion

The genesis of CO_2-peridotite-derived magmas is still highly debated. Magmatic processes are highly composite and variations in mechanisms of melting and/or fluids

transport can result in very heterogenous chemical compositions. It is widely accepted that silica-poor and alkali-rich compositions are usually associated to CO_2-rich mantle sources, but magmatic origin and mechanisms of CO_2-bearing melts is actually still unknown. Indeed low-silica melts are thought to be generated from extremely low degree of partial melting of carbonated peridotite or from low-to-high degree of partial melting of fertile sources (e.g. metasomatized mantle) or from mixed sources. Experimental petrology may give a contribution investigating these magmatic variables in more detail and providing direct tools to better understand Earth processes.

Experimental initial conditions are reported in Table S1 whereas major elements concentrations of the run products are shown in Figs. S3-S4. Only four runs have been taken into account to try to somewhat discuss the origin of Nowbaran magmas.

Table S1: *Experimental run conditions and mantle phase assemblages.*

	Initial conditions					Mantle phases proportions		
#RUN	wt% H_2O	wt% CO_2	P (kbar)	T (°C)	Time (h)	wt% ol	wt% opx	wt% gt
NBMIXA-P01	3	5	27	1200	47½	40	40	20
NBMIXA-P03	3	5	27	1250	47	60	30	10
NBMIXB-P01	3	3	27	1250	47	60	30	10
NBMIXB-P02	3	3	27	1260	47	60	25	15

The concept of multiple saturation experiments is that any mantle derived melt has at least one P-T-H_2O condition where its liquidus saturates with the residual mantle phases olivine+opx±cpx [7]. Thus determining the liquidus surface of an inferred primitive melt may yield a multiple saturation point that defines the P-T-H_2O of last equilibration with these mantle phases [7].

Multiple forced experiments of close-to-primary Nowbaran nephelinitic compositions at 27 kbar indicate that saturation of a lherzolitic assemblage with H_2O ~3 wt% and CO_2 ~3 wt% (NBMIXB-P01 and NBMIXB-P02) occurs around 1250-1260 °C, resulting in silica-poor melts (SiO_2 ~35-38 wt%) with relatively high abundances in TiO_2, Na_2O and K_2O (respectively ~2.3-2.9 wt%, ~3.2-3.3 wt% and ~1.3-1.8 wt%). NBMIXB-P01/P02 experimental melts (with CO_2 ~3 wt%) indeed exhibit chemical features which partially resemble Nowbaran major elements trends. Besides the aforementioned elements,

also CaO, Al_2O_3 and P_2O_5 exhibit comparable values (respectively ~14.8-17.2 wt%, ~9.9-10.9 wt% and ~3.5-3.6 wt%) respect with the investigated nephelinites (~13.1-18.3 wt%, ~8.6-11.6 wt% and ~1.4-3.3 wt%). On the other hand, MgO values are by far higher (~16.4-18.7 respect with Nowbaran ~8.7-13.3 wt%) whereas Fe_2O_3 shows quite lower contents (~7.9 wt% respect with ~8.6-11.3 wt%). It is absolutely worth noting that NBMIXA-P01/P03 experimental melts (with CO_2 ~5 wt%) instead show extremely high abundances of alkalis (~8.7-10.4 wt%), P_2O_5 (~6.8-7.9 wt%) and TiO_2 (~4.3-4.6 wt%). CaO and Fe_2O_3 resemble Nowbaran average values, whereas MgO is always higher (~16.6-18.0) and Al_2O_3 is by far lower (only ~5.9-7.0 wt%). These incompatible elements enriched compositions result quite normal as degree of SiO_2-undersaturation of silicate melts decreases as CO_2 solubility increases [3]. However, these compositions are too far respect with those expected and then are excluded.

In conclusion, in addition to a carbonated mantle source, another bulk is likely confirmed to obtain Nowbaran particular whole-rock compositions, i.e. amphibole-rich cumulates and/or veins within lithospheric mantle. Although such a low number of experimental runs might not be totally representative, in a preliminary way it is possible to note that Nowbaran magmas likely originated from a ~3 wt% H_2O and ~3 wt% CO_2-rich source. However some discrepancies are observed regarding chemical compositions, but these could be related to effects due to set of variables and certainly further investigations are needed.

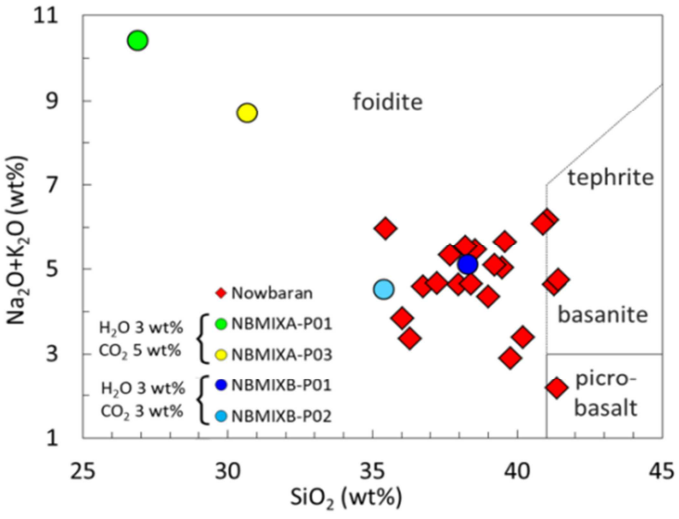

Fig. S3: *TAS diagram (after Le Maitre, 2002) showing run products compositions compared with Nowbaran nephelinites.*

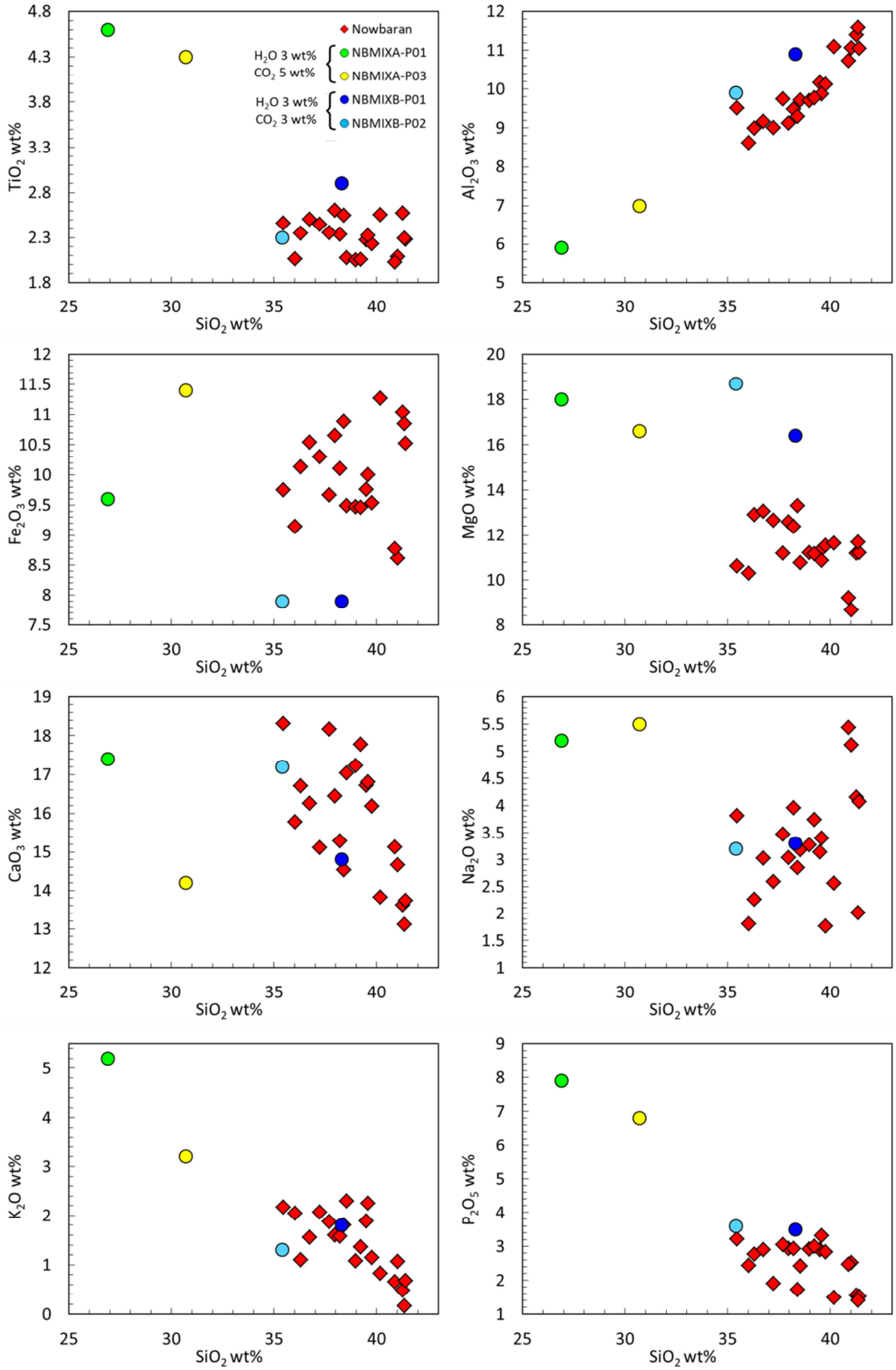

Fig. S4: *Major elements vs. SiO_2 diagrams for experimental melts compared with Nowbaran compositions.*

REFERENCES

[1] Boyd F.R., England J.L., 1960. Apparatus for phase-equilibrium measurements at pressures up to 50 kilobars and temperatures up to 1750°C. J. Geophys. Res. 65, 741-748.

[2] Middlemost E.A.K.,1989. Iron oxidation ratios, norms and the classification of volcanic rocks. Chem. Geol. 77, 19-26.

[3] Mysen B.O., Arculus R.J., Eggler D.H., 1975. Solubility of carbon dioxide in melts of andesite, tholeiite, and olivine nephelinite composition to 30 kbar pressure. Contrib. Mineral. Petrol. 53, 227-239.

[4] Niida K., Green D.H., 1999. Stability and chemical composition of pargasitic amphibole in MORB pyrolite under upper mantle conditions. Contrib. Mineral. Petrol. 135, 18-40.

[5] O'Neill H.S.C., 1981. The transition between spinel lherzolite and garnet lherzolite, and its use as a geobarometer. Contrib. Mineral. Petrol. 77, 185-194.

[6] Robinson J.A.C, Wood B.J, 1998. The depth of the spinel to garnet transition at the peridotite solidus. Earth Planet. Sci. Lett. 164,277-284.

[7] Schmidt M.W., Jagoutz O., 2017. The global systematics of primitive arc melts. Geochem. Geophys. Geosyst. 18, 2817-2854.

Supplementary Material S2

Leucitites within and around the Mediterranean area

Michele Lustrino[1,2*], Lorenzo Fedele[3], Samuele Agostini[4], Dejan Prelević[5], Giulia Salari[1]

1 = Dipartimento di Scienze della Terra, Sapienza Università di Roma - P.le A. Moro 5, 00185, Roma (Italy)

2 = CNR - Istituto di Geologia Ambientale e Geoingegneria (IGAG), c/o Dipartimento di Scienze della Terra, Sapienza Università di Roma - P.le A. Moro 5, 00185, Roma (Italy)

3 = Dipartimento di Scienze della Terra, dell'Ambiente e delle Risorse (DiSTAR), Università degli Studi di Napoli Federico II - Via Cupa Nuova Cintia 21, 80126 Napoli (Italy)

4 = CNR - Istituto di Geoscienze e Georisorse (IGG), Via Giuseppe Moruzzi 1, 56124, Pisa (Italy)

5 = Faculty of Mining and Geology, University of Belgrade, Đušina 7, 11000, Belgrade (Serbia)

* = corresponding author: michele.lustrino@uniroma1.it

Published in *Lithos*, 2018, Vol. 324-325, pp. 216-233.

ABSTRACT

Leucite-bearing volcanic rocks are commonly found within and around the Mediterranean area. A specific type of this rock group is leucitites. They are found both in a hinterland position of active and fossil subduction systems as well as in foreland tectonic settings, but none have been found in the Maghreb (N Africa) and Mashreq (Middle East) areas. Here a review of the main leucitite occurrences in the circum-Mediterranean area is presented, with new whole-rock, mineral chemical and Sr-Nd-Pb isotopic ratios on key districts, with the aim of clarifying the classification and genesis of this rock type.

Many of the rocks classified in literature as leucitites do not conform to the IUGS definition of leucitite (i.e., rocks with >10 vol.% modal leucite and with foids/(foids + feldspars) ratio >0.9, with leucite being the most abundant foid). Among circum-Mediterranean rocks classified as leucitites in the literature, we distinguish two types: clinopyroxene-olivine-phyric (COP) and leucite- phyric (LP) types. Only the second group can be truly classified as leucitite, being characterized by the absence or the very rare presence of feldspars, as well as by ultrapotassic composition.

The COP group can be distinguished from the LP group on the basis of lower SiO_2, Na_2O+K_2O, K_2O/Na_2O, Al_2O_3, Rb and Ba, and higher MgO, TiO_2, Nb, Cr and Ni. The LP group shows multi-elemental patterns resembling magmas emplaced in subduction-related settings, while COP rocks are much more variable, showing HIMU-OIB-like to subduction-related-like incompatible element patterns. COP rocks are also characterized generally by more homogeneous isotopic compositions clustering towards low Sr and high Nd isotopic ratios, while LP leucitites plot all in the enriched Sr-Nd isotopic quadrant. LP rocks usually have lower $^{206}Pb/^{204}Pb$ and higher $^{207}Pb/^{204}Pb$. This study shows that the geochemical signal of mantle melts does not always reflect the tectonic setting of magma emplacement, suggesting paying extreme attention in proposing geodynamic reconstructions on the basis of chemical data only.

Keywords: leucitites; ultrapotassic rocks; Mediterranean; Cenozoic; geodynamics; petrology

1. Introduction

Leucitites are an extremely rare group of volcanic rocks occurring in various continental tectonic settings, but not ocean basins or divergent margins. According to IUGS, leucitites *sensu stricto* (i.e., "true" leucitites) are rocks with >10 vol.% modal leucite and with foids/(foids + feldspars) ratio >0.9, with leucite being the most abundant foid. On the other hand, leucitites *sensu lato* are characterized by foids/(foids + feldspars) ratios ranging between 0.6 and 0.9 (Le Maitre, 2002). The latter rock types should be more properly defined as "phonolitic leucitites" when alkali feldspar > plagioclase, "basanitic leucitites" (olivine >10 vol.%) or "tephritic leucitites" (olivine <10 vol.%) when plagioclase > alkali feldspar. The last two terms correspond to the commonly used "plagio-leucitites", which was originally applied to a group of Italian K-rich lavas from the Roman volcanic province (Avanzinelli et al., 2009; Conticelli et al., 2009). Clinopyroxene is typically the most abundant mafic mineral, commonly associated with olivine, biotite and Fe-Ti opaque minerals. Additional foids are usually dominated by nepheline.

Although the above modal classification scheme allows a clear definition of the leucitite lithotype, this is not reflected into a similarly well-established whole-rock chemical criterion. Indeed, in the TAS classification diagram, leucitites spread over the foidite field towards silica-richer tephrites, phonolitic tephrites and tephritic phonolites. In addition, many of the rocks reported in literature as "leucitites" do not meet the chemical definition of ultrapotassic rocks proposed by Foley et al. (1987), i.e., MgO >3 wt.%, K_2O/Na_2O >2, K_2O >3 wt.% and SiO_2/K_2O <15.

Sparse occurrences of "leucitite" rocks were reported in several Cenozoic volcanic districts of the circum-Mediterranean magmatic realm, including: Calatrava (central Spain), west Eifel (Germany), Vulsini Mts., Alban Hills, and Ernici Mts. (Roman Magmatic Province, central Italy), Doupovské hory and Hammerunterwiesenthal (Bohemian Massif in Czech Republic, Poland and Germany), Bár (Pannonian Basin, Hungary), Devaje, Nova Varoš and Koritnik (Serbia, Montenegro and Macedonia), Afyon (western Turkey), Amasya and Gümüşhacıköy (eastern Turkey), and Eslamieh Peninsula (north-western Iran). Given the extremely complicated geodynamic framework in which these have been emplaced (e.g., Harangi et al., 2006; Lustrino and

Wilson, 2007; Lustrino et al., 2011; Carminati et al., 2012; Faccenna et al., 2014; Aghazadeh et al., 2015), the Cenozoic circum-Mediterranean "leucitites" represent a remarkable case-study that can help to shed light on many issues regarding the petrogenesis of leucitites and their correct definition as a lithotype. To this purpose, new whole-rock and mineral chemical analyses from several circum-Mediterranean districts, along with the available literature data, are here discussed.

2. Sampling and analytical techniques

A total of 23 new "leucitite" samples were collected for petrographic, mineral chemical and whole-rock geochemical investigations from all the Cenozoic circum-Mediterranean districts where "leucitites" are reported. More specifically: eight from Germany (west Eifel - Staffeln, Basberg, Bolsdorf, Dreesd, Mayen and Kottenheim localities); three from Spain (Calatrava – Morron de Villamayor); one from the Bohemian Massif (Hammerrunterwiesenthal, Germany); four from Central Italy (Alban Hills - Capo Bove; Ernici Mts. - Celleta; Vulsini Mts. - Vico); two from Serbia (Devaje); one from the Pannonian Basin (Bár); one from western Turkey (Afyon); three from NW Iran (Eslamieh Peninsula - Urumieh Lake).

Major and trace elements analyses were performed by means of ICP-AES (Inductively Coupled Plasma-Atomic Emission Spectrometry) and ICP-MS (Inductively Coupled Plasma-Mass Spectrometry), respectively, at Activation laboratories (Ontario, Canada). See www.actlabs.com for full details. The results are reported in Table 1, at the end of the supplementary material.

Thirteen representative samples were selected for determining the composition of the main mineral and glass phases by Electron Microprobe (EMP) at the Dipartimento di Scienze della Terra of Rome. Analyses were performed using a CAMECA SX 50 instrument, equipped with five wavelength-dispersive spectrometers (WDS). Operating conditions were generally 15 kV accelerating voltage, 30 nA beam current, 1 µm beam diameter for olivine, pyroxene and opaque minerals and 10 µm for feldspars, amphibole and glass. Counting times for all elements were 20 s for the peak position and 10 s for the background on each side of the peak. Standards used for calibration

are: Na_2O = jadeite; MgO = periclase; TiO_2 = rutile; FeO = magnetite, SiO_2/CaO = wollastonite; Al_2O_3 = corundum; MnO = rhodonite; K_2O = orthoclase; BaO = barite; SrO = celestine; NiO = pure nickel; FeO/MgO = olivine. Thirteen representative samples were selected for the determination of Sr-Nd-Pb isotope ratios at the CNR-IGG laboratories of Pisa and are reported in Table 1. Precision and accuracy is fully reported in Di Giuseppe et al. (2017).

3. Geological framework for the Cenozoic circum-Mediterranean "leucitite" occurrences

The Cenozoic geodynamic evolution of the circum-Mediterranean realm involved a number of varied and complex tectonic and magmatic processes that make this area an extremely useful natural laboratory for the investigation of such processes and their mutual interaction. Oceanic subduction, continent-continent collision, back-arc basin opening of new oceanic lithosphere spreading and upper mantle upwelling have affected this relatively narrow area during the last 50 Myr (e.g., Carminati et al., 2012; Faccenna et al., 2014). This resulted in the genesis of a wide variety of igneous rocks, practically encompassing the entire spectrum of known igneous lithotypes in terms of serial affinity, degree of silica saturation and degree of rock evolution (e.g., Peccerillo and Lustrino, 2005; Harangi et al., 2006; Lustrino and Wilson, 2007; Lustrino et al., 2011; Prelević and Seghedi, 2013; Peccerillo, 2017).

In the following sections, a brief description of the circum-Mediterranean "leucitite" rocks is reported. These rocks were emplaced both in the hinterland (belonging to the Alpine-Carpathian, Apennine, Dinaride and Taurides-Pontides-Zagros belts) and in the foreland (Alps-Betics) of active orogenic systems, often associated with other leucite-bearing rocks (Fig. 1). Interestingly, neither leucitite nor leucite-bearing rocks are reported for the districts developed at the foreland of the Maghrebian and Taurides-Pontides-Zagros systems. In such a complex geodynamic setting as that of the Cenozoic circum-Mediterranean "leucitites", the tectonic association i.e., "orogenic" (subduction-related) or "anorogenic" (subduction-unrelated) has been inferred on the basis of geochemical characteristics of the emplaced products (e.g., see discussion in

Lustrino et al., 2011; Carminati et al., 2012). However, it should be noted that the tectonic settings "evidenced" by geochemistry do not necessarily indicate the true geological conditions during the igneous activity. Instead, they may reflect mantle sources that experienced variable melting extraction and subduction metasomatism. Such distinction is of particular relevance in the context of the Cenozoic circum-Mediterranean magmatism. Here, in many districts, magmatic phases with "orogenic" and "anorogenic" geochemical signature have variably alternated, with the latter generally being the youngest. Occasionally the two phases interacted, giving rise to "hybrid" compositions (e.g., Lustrino and Wilson, 2007; Lustrino et al., 2011; Prelević et al., 2012, 2015). In other words, the geochemical "evidences" for the derivation from a subduction-modified or a within-plate, subduction component-free source, cannot be automatically exported as proofs for the existence of specific tectonic settings during mantle anatexis.

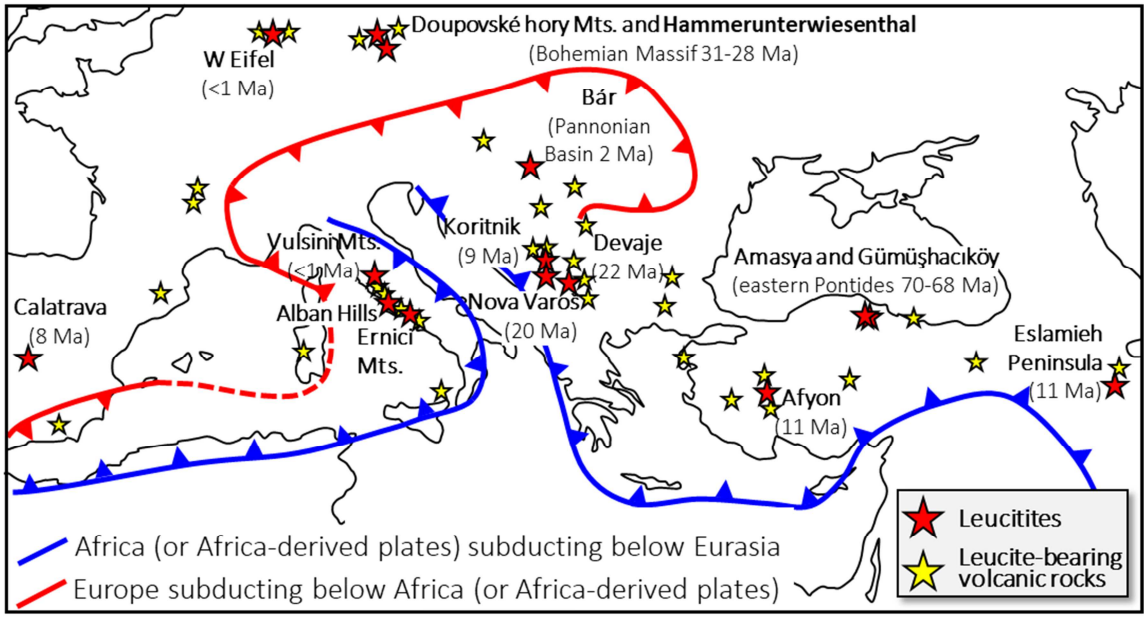

Fig. 1: *Location of the Cenozoic circum-Mediterranean rocks defined in literature to as "leucitite" (red stars) and leucite-bearing rocks (yellow stars).*

3.1 "Anorogenic" leucitites

The localities of literature "anorogenic" leucitites are reported below in order of decreasing age.

3.1.1 Czech Republic/Germany – Bohemian Massif

The Cenozoic magmatism in the Bohemian Massif occurred mainly in the Ohre Rift and the Labe Volcano-Tectonic Zone, both being parts of the large rift system developed in central Europe in the foreland of the Alps system (e.g., Dèzes et al., 2004). Magmatic activity was remarkably long-lived, ranging in age from ~77 to 0.26 Ma (Ulrych et al., 2003), and produced mainly Na-alkaline SiO_2-undersaturated primitive rocks (olivine basalts, basanites, nephelinites, ankaratrites and melilitites) and their differentiates (e.g., Skala et al., 2015; Ulrych et al., 2016). Scattered occurrences of "leucititic" rocks (olivine leucitites) are locally reported (Doupovské hory Mts., Czech Republic; Ulrych et al., 2003). The marked "anorogenic" geochemical signature displayed by Bohemian Massif magmas distinctively points to a HiMu-like (HiMu = High-μ, where μ = $^{238}U/^{204}Pb$) asthenospheric mantle source that bears evidence for the recycling of subducted oceanic crust (e.g., Ulrych et al., 2016).

3.1.2 Spain – Calatrava

Cenozoic volcanic activity in Spain is recorded in four sectors: South-East Volcanic District (Betic Chain and Alboran Basin), East Volcanic District (within and on the shoulders of Valencia Trough), central Volcanic District (Calatrava-Ciudad Real) and North-East Volcanic District (Olot-Garrotxa-Ampordà). The igneous activity is chemically variable because it developed in the complex geodynamic setting associated with different stages of buildup of the Alpine-Betic and Apennine-Maghrebide belts (e.g., Lustrino and Wilson, 2007; Lustrino et al., 2011; Carminati et al., 2012). The Spanish igneous activity occurred during two distinctive phases, one with "orogenic" (~20-6 Ma) and the other with "anorogenic" (~8-0.01 Ma) geochemical signature. The first phase is present in the Betic Chain and Calatrava sectors only, while the second phase is present in all the districts. The products encompass a wide spectrum of rock compositions (from primitive to highly differentiated) and serial affinities, including calcalkaline, high-K calcalkaline, ultrapotassic, and (variably SiO_2-undersaturated) Na-alkaline (e.g., Cebriá and Lopez-Ruiz, 1995; Turner et al., 1999; Duggen et al., 2005; Conticelli et al., 2009; Mattei et al., 2014; Lustrino et al., 2016b).

Leucititic rocks are reported in literature only in the earliest products of the late Miocene-Pleistocene (8.7-6.4 and 3.1-1.7 Ma) Calatrava Volcanic district, a volcanic area covering an area of ~4000 km^2 (e.g., Cebriá and Lopez-Ruiz, 1995). Recently, Lustrino et al. (2016b) have questioned the classification as leucitites for the Morron de Villa Mayor lava flows, given that these rocks are characterized by moderate K_2O contents and little modal abundance of leucite (<10 % in volume). Such magmatism was explained invoking the diapiric upwelling of a HiMu-OIB (OIB = Ocean Island Basalt) asthenospheric mantle, which both melted through adiabatic decompression and triggered the melting of phlogopite-rich metasomatized lithospheric domains, thus producing the "mixed" geochemical signature of the emplaced magma types (Cebriá and Lopez-Ruiz, 1995; Lustrino et al., 2016b).

3.1.3 Germany – West Eifel

The Eifel region is located in the so-called Rhenish Massif, a Hercynian-age crystalline basement cropping out in western Germany, eastern Belgium, Luxembourg and north-eastern France, consisting essentially of Devonian-Carboniferous metamorphic rocks (Ziegler and Dèzes, 2007). During the Late Jurassic and Early Cretaceous, the Rhenish Massif began to be uplifted and experienced two distinct periods of magmatism, giving rise to the Hocheifel (Tertiary) and the Eifel (Quaternary) volcanic districts (e.g., Mertes and Schmincke, 1985; Schmincke, 2007; Mertz et al., 2015). The Hocheifel district consists mainly of deeply eroded volcanic plugs and necks and some scattered lava flows of mainly sodic basanite, nephelinite and alkali basalt compositions plus rarer differentiate.

The Eifel is a low-relief mountain range whose volcanic activity mainly generated scoria cones and maar volcanoes emplacing SiO_2-undersaturated Na-alkaline (plus fewer K-alkaline) ultrabasic to intermediate lithotypes in the east (active between 460 and 13 ka), foiditic (leucitites, nephelinites and lesser melilite- and sodalite-bearing lavas) to olivine nephelinites and basanites in the west (active during 720-480 and 80-10 ka; e.g., Mertes and Schmincke, 1985; Schmincke, 2007; Mertz et al., 2015). The genesis of the most primitive west Eifel magmas is generally attributed to adiabatic partial melting of a hot asthenospheric mantle source (involving DMM = Depleted MORB Mantle, HiMu

and EM-I = Enriched Mantle I components), in the presence of a mantle plume (e.g., Ritter et al., 2001; Mertz et al., 2015) or in the context of a passive (i.e., tectonically-induced) mantle upwelling (e.g., Lustrino and Carminati, 2007).

3.2 "Orogenic" leucitites

Also in this case, the localities of litearture "orogenic" leucitites are reported below in order of decreasing age.

3.2.1 Serbia – Serbian Province

The Balkan Peninsula experienced a complex tectonic evolution due to the presence of numerous geotectonic units, including lower Palaeozoic and late Mesozoic crystalline terranes (the East Serbian and the Serbo-Macedonian composite terranes), ophiolitic sequences (the Vardar suture zone and the Dinaride ophiolitic belt), allochthonous terranes and a micro-continent block, which were all merged at the end of the Mesozoic (Cvetković et al., 2004; Prelević et al., 2005). Magmatic activity related to such a geodynamic framework is compositionally variable, giving rise to three distinctive main episodes in Serbia (Cvetković et al., 2004).

The first magmatic phase is Paleocene-Eocene in age, confined to the eastern terranes and consisted mainly of Na-alkaline basalts with a clear OIB-like geochemical signature. This was followed, after a hiatus of ~15 Myr, by Oligocene-Miocene (~30-10 Ma) and Pliocene (~6.6-3.9 Ma) magmatic phases, both dominated by high-K calcalkaline, shoshonitic and ultrapotassic rocks (with both "lamproitic" and "kamafugitic" affinity). Early Miocene (~22 Ma) leucititic rocks (Devaje) and early Miocene (~20 Ma) and late Miocene (~9 Ma) ultrapotassic rocks are reported in Nova Varoš and Koritnik, respectively (Prelević et al., 2005). The origin of the ultrapotassic types is commonly ascribed to the melting of variably metasomatized lithospheric mantle sources (locally including some contribution from the interaction with percolating asthenosphere-derived melts) in a post-collisional geodynamic context (Cvetković et al., 2004; Prelević et al., 2005).

3.2.2 Turkey – Afyon (Anatolia) and Amasya and Gümüşhacıköy (eastern Pontides)

Cenozoic magmatism in western Turkey (Anatolia), together with that of the Aegean region to the west, occurred in an arc/back-arc geodynamic context dominated by S-directed roll-back processes and post-orogenic extension taking place after the lithospheric thickening caused by numerous Alpine-age collisional events (e.g., Jolivet and Brun, 2010). The associated magmatism recorded an evident transition from "orogenic" (calcalkaline to shoshonitic to ultrapotassic compositions) to "anorogenic" (Na-alkaline plus much rarer tholeiitic products) compositions, which is evident in several districts (e.g., Agostini et al., 2007; Lustrino and Wilson, 2007; Di Giuseppe et al., 2017).

Leucititic rocks were found in the Afyon volcanic complex, where volcanic activity with variable geochemical signatures (from SiO_2-undersaturated to SiO_2-oversaturated, from ultrapotassic to Na-alkaline, from "orogenic" lithosphere-derived to "anorogenic" asthenosphere-derived) occurred during Middle Miocene times (14-8 Ma; e.g., Akal et al., 2013; Prelević et al., 2015). The genesis and the geochemical signature of the "orogenic" rocks have been ascribed to the melting of two different metasomatized mantle domains: 1) a phlogopite-pyroxene-rich metasome, generated by recycling of continental sediments during a previous subduction event, and 2) a phlogopite-wherlite metasome, generated by the interaction of asthenospheric (dolomite-bearing) melts with previously metasomatized lithospheric mantle peridotite domains (Prelević et al., 2015).

Though slightly older than Cenozoic (i.e., Maastrichtian-early Paleocene), the eastern Pontides orogenic belt of north-eastern Turkey (Amasya and Gümüşhacıköy) has also been reported for scattered leucitite rock occurrences (Altherr et al., 2008). Magmatic activity in the eastern Pontides belt was related to the subduction of Tethyan lithosphere, with the production of both calcalkaline basaltic to andesitic and granitoid rocks (occurring in the northern sector) and shoshonitic, ultrapotassic and adakitic rocks (e.g., Eyuboglu, 2010; Eyuboglu et al., 2011). Such magmatism is ascribed to the melting of subduction-enriched sub-continental mantle sources (possibly with some contributions from the influx of enriched asthenosphere through slab windows; e.g., Eyuboglu, 2010; Eyuboglu et al., 2011).

3.2.3 North-western Iran - Eslamieh Peninsula

Cenozoic magmatism in Iran is related to the collision between Eurasian and Arabian plates, resulting in the formation of the complex Bitlis-Zagros suture zone (where Neotethyan oceanic lithosphere was subducted N and NE; e.g., Sengor and Yilmaz, 1981; Dilek et al., 2010), and in the development of a ~2500 km-long curved fold-and-thrust belt running from eastern Turkey to western Iran. Widespread magmatism accompanied such geodynamic evolution from Eocene to Quaternary, with largely variable compositions and serial affinities, and overall "orogenic" geochemical signatures (e.g., Shafaii Moghadam et al., 2014; Aghazadeh et al., 2015). In the Eslamieh Peninsula, late Miocene (~11 Ma) magmatism was characterized by the emplacement of high-K rocks including both SiO_2-undersaturated "leucititic" and SiO_2-saturated leucite-free shoshonitic series (Shafaii Moghadam et al., 2014). These products were generated by a complex melting process of a metasomatized lithospheric mantle source (involving mixing of liquids produced during multiple-stage melting of a compositionally-zoned mantle domain) in a post-collisional setting (Pang et al., 2013; Shafaii Moghadam et al., 2014; Aghazadeh et al., 2015).

3.2.4 Hungary – Pannonian Basin

The depressed central part of the Carpathian-Pannonian Region is referred to as the Pannonian Basin, a geodynamically complex region (e.g., Schmid et al., 2008) that includes: 1) a west-directed subducting slab since Chattian (~28 Ma; Carminati et al., 2012), 2) an arcuate and east-retreating fold-and-thrust orogenic belt characterized by N-, NE-, E- and SE-directed tectonic transport, 3) a back-arc extensional basin developed above the retreating slab and 4) widespread magmatic activity with variable compositions (e.g., Harangi et al., 2006; Seghedi and Downes, 2011; Fedele et al., 2016; Kovacs et al., 2017). Early Miocene to Quaternary igneous activity shows mainly calcalkaline "orogenic" type (e.g., Fedele et al., 2016), followed by Late Miocene to Quaternary "anorogenic", mainly Na-alkaline magmatism occurring mainly in the Pannonian Basin (e.g., Kovacs et al., 2012). In the southern Pannonian Basin near the village of Bár (Hungary), the latter magmatic cycle emplaced a few m^3 of scoriaceous potassic mafic rocks with analcime basalt and analcitic leucite basanite compositions

around 2 Ma (e.g., Downes et al., 1995; Harangi et al., 1995; Grachev, 2012). The geochemical fingerprint of these magmatic products is not completely comparable to that of the typical intraplate-like magmas, as the most primitive products bear evidence of varying degrees of "orogenic" heritage related to previous subduction events (possibly in the form of modifications of asthenospheric-derived melts passing through the lithosphere; e.g., Downes et al., 1995; Seghedi and Downes, 2011).

3.2.5 Central Italy – Roman Magmatic Province

Magmatism in central-southern Italy started during the Late Miocene and continued until the Present as a consequence of the subduction processes associated with the building-up of the Apennine Chain (e.g., Conticelli et al., 2010, 2015; Lustrino et al., 2011; Carminati et al., 2012; Peccerillo, 2017, and references therein). Leucititic rocks were reported only in the central Italy volcanic districts of the Vulsini Mts., Alban Hills and Ernici Mts. (also known as Middle Latin Valley). The Vulsini Mts. volcanic district is dominated by explosive eruptions that emplaced not only a strongly SiO_2-undersaturated high potassium series, with a large compositional range from leucite-basanite, to leucititic-tephrite and tephritic-leucitite, but also a weakly SiO_2-undersaturated potassic series, both of which were emplaced during a ~590-130 ka time span (Di Battistini et al., 1998; Conticelli et al., 2010). The Alban Hills district consists of a caldera complex volcano, active from ~600 ka until ~36 ka (e.g., Giordano et al., 2006; Marra et al., 2009; Gaeta et al., 2016). Rock compositions are mainly represented by tephrites, phonolitic tephrites and leucitites, the latter characterized by plagioclase-free paragenesis dominated by leucite and clinopyroxene phenocrysts (e.g., Gaeta et al., 2006, 2016; Boari et al., 2009a). The Ernici Mts. District, active between ~700 and 80 ka, is mostly characterized by cinder cones, small lava emissions and tuff rings, with rock compositions defining two distinct potassic series, with shoshonitic (i.e., potassic basalts and trachybasalts) and ultrapotassic affinity (leucite-phonolitic tephrites and leucitites; e.g., Boari and Conticelli, 2007; Boari et al., 2009b). The genesis of the leucitite rocks from central Italy is generally ascribed to the melting of a phlogopite-rich metasomatized veined lithospheric mantle source (e.g., Avanzinelli et al., 2009; Conticelli et al., 2009, 2010, 2015; Peccerillo, 2017).

4. Petrography and mineral chemistry of the Cenozoic circum-Mediterranean "leucitites"

The investigated Cenozoic circum-Mediterranean "leucitite" rocks define two groups in terms of petrographic and mineral chemical features. A detailed petrographic description of the "leucitite" rocks from each district is provided in the Supplementary Figs. S2a and S2b. Below, the main features of the two recognized lithotypes are briefly summarized.

The leucitite rock samples from west Eifel, Pannonian Basin, Calatrava, Bohemian Massif and the Serbian locations of Koritnik and Nova Varoš area are characterized by a mineral assemblage dominated by clinopyroxene and/or olivine phenocrysts, with leucite occurring as a sparse micro-phenocrysts (west Eifel and Pannonian Basin) or restricted to the groundmass phase (Calatrava, Bohemian Massif and Serbian rocks; SM Fig. 1). Clinopyroxene crystals from these rocks plot mostly in the field for clinopyroxene from lamproite- and transitional-type potassic rocks (defined by Perini and Conticelli, 2002; Fig. 2a). It should be noted, however, that Lustrino et al (2016a) have challenged the genetic significance of the compositional fields reported in this diagram, since Al-poor "lamproitic" clinopyroxenes can be found also in Si-rich "non-lamproitic" (i.e., metaluminous) igneous rocks. Moreover, in the Ti vs. Mg# diagram (Fig. 2b), the rocks from this group define a steep array of linearly increasing Ti with decreasing Mg#. Exceptions are few west Eifel clinopyroxenes with low Ti, Mg# and Al, interpreted as high-P cumulates by Shaw and Eyzaguirre (2000). The rocks from west Eifel, Pannonian Basin, Calatrava, Bohemian Massif and Serbia (Koritnik and Nova Varoš) will be referred to as the clinopyroxene/olivine-phyric (COP) leucitites.

The second group includes the leucitite rocks from Turkey (Afyon and eastern Pontides), NW Iran, central Italy and Devaje, Serbia. They are characterized by leucite as the main phenocryst/microphenocryst phase (SM Fig. 2), and its composition is close to that of the pure leucite end-member. The leucite is accompanied by clinopyroxene crystals that differ in composition from those in the rocks from the previous group. Such clinopyroxene variety is largely variable in terms of Al contents (reaching also the typical compositions of the "Roman-type" potassic rocks; Fig. 2a) and is generally Mg

and Ti-poor with respect to that of the COP group (Fig. 2b). The rock samples belonging to this group are hereafter referred to as the leucite-phyric (LP) leucitites.

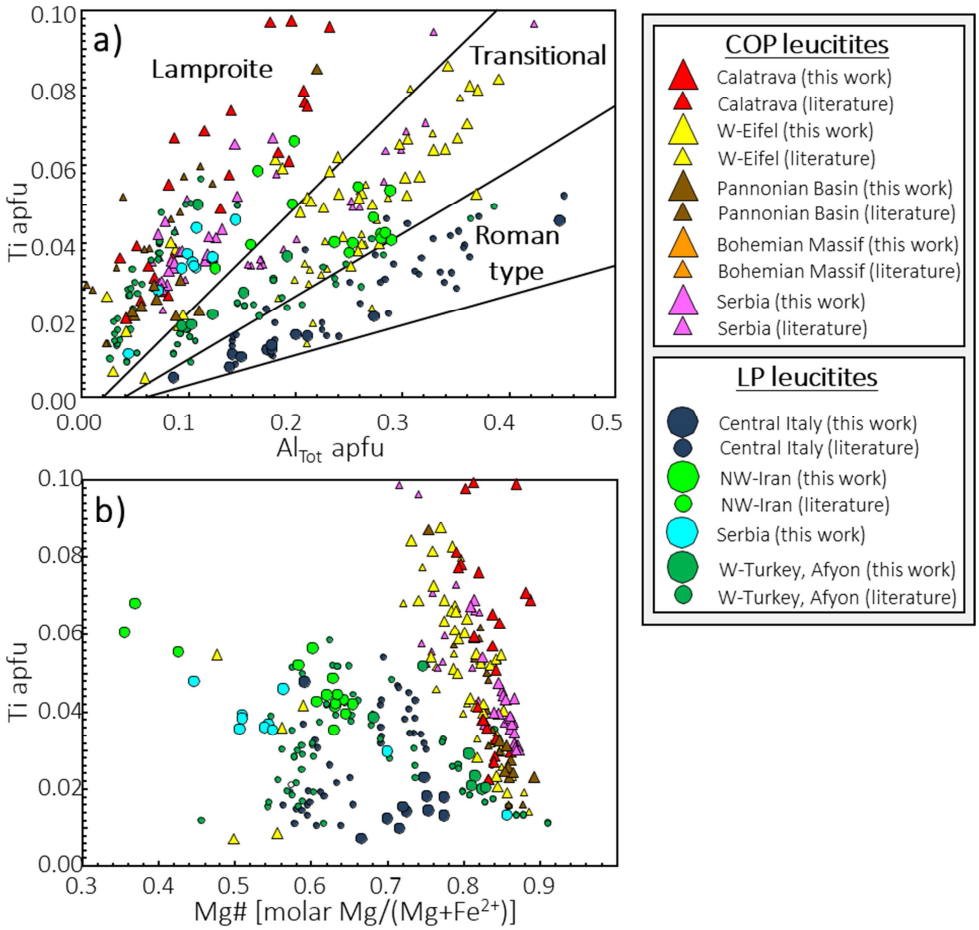

Fig. 2: *a) Ti vs. Al_{Tot} (from Perini and Conticelli, 2002) and b) Ti vs. Mg# [molar Mg/(Mg+Fe2+)] diagrams for the clinopyroxene crystals from the investigated Cenozoic circum-Mediterranean "leucitite" rocks. Literature data are from Harangi et al. (1995), Melluso et al. (2000), Shaw and Eyzaguirre (2000), Akal (2003), Prelević et al. (2005, 2015), Grachev (2012).*

5. Whole-rock geochemistry of the Cenozoic circum-Mediterranean "leucitites"

5.1. Major- and trace element concentrations

The two recognized groups of circum-Mediterranean "leucitites" show different whole-rock chemical compositions. The COP are mainly characterized by low SiO_2 (39.1-48.5 wt.%) and Na_2O+K_2O (3.40-8.35 wt.%), plotting in the tephrite/basanite fields in the

TAS diagram, with fewer foidite and trachybasalt compositions (Fig. 3a). A few more evolved compositions (phonolitic tephrites and tephritic phonolites) are observed among the Pannonian Basin samples, plus one sample from west Eifel and one latite from the Bohemian Massif. On the other hand, LP leucitites fall mainly in the fields for phonolitic tephrites and foidites, with a few samples plotting in the tephrite/basanite, tephritic phonolite, trachybasalt and trachyandesite fields. Samples from central Italy show the largest compositional variability, whereas samples from NW Iran and Serbia are more homogeneous, but probably this is related to the smaller sample set. The rocks from Turkey show a bimodal distribution in composition, including two distinctively homogenous groups falling in the trachybasalt (eastern Pontides literature rocks) and foidite/tephritic phonolite fields (Afyon). Interestingly, only the Pannonian Basin and some Serbia rocks are strictly ultrapotassic among the COP, with the remaining samples plotting in the fields for potassic and transitional rock series (i.e., K_2O/Na_2O <2; Fig. 3b), some of them also displaying low K_2O <3 wt.%. On the other hand, LP leucitites are mostly ultrapotassic (K_2O/Na_2O >2), except for a few outliers (from central Italy, NW Iran and Serbia; <5% of the database) falling in the potassic and transitional series fields, and the two eastern Pontides Turkey rocks showing a sodic affinity.

Additional differences between the two recognized “leucitite” rock groups can be easily shown in numerous major and trace element vs. MgO binary plots (Fig. 4 and SM Figs. 3 and 4). Most of the COP “leucitites” have higher MgO, Ni and Cr with respect to LP. The rocks from the COP group also feature higher TiO_2 and Nb, coupled with lower Al_2O_3, K_2O, Rb and Ba.

The Serbian and, most evidently, Calatrava samples are those with the most primitive compositions among the COP leucitites, with the latter covering a relatively wide compositional spectrum, suggesting some major role for crystal accumulation of olivine (see discussion in Lustrino et al., 2016b). On the other hand, Serbia COP rocks define a more homogeneous group, with some major exceptions for two literature samples from Nova Varoš, characterized by very low K_2O and Rb and relatively high Na_2O, likely due to strong weathering (mainly in the form of leucite analcimization), as suggested by their high LOI. The Bohemian Massif latite is again a major outlier, as a consequence of its more evolved composition. The two west Eifel samples plot in an intermediate

position between the Bohemian Massif latite and the major part of the least evolved COP leucitites (Fig. 4). The Pannonian Basin rocks define a homogeneous compositional group with unusually low CaO and Fe_2O_3tot and high K_2O compared with other COP rocks with similar MgO contents (e.g., west Eifel rocks).

LP leucitites from central Italy and NW Iran display a wide compositional spectrum with significant scatter for numerous elements (e.g., SiO_2, Al_2O_3, CaO, K_2O, Rb, Sr, Ba, Zr), covering mainly the 2-8 wt.% MgO range (Fig. 4). Interestingly, at a given MgO content central Italy rocks are generally richer in Al_2O_3, K_2O, Rb and Sr, and poorer in TiO_2, P_2O_5 and Ba with respect to NW Iran samples. The Serbia LP rocks generally plot at the most differentiated end (i.e., MgO = 2.13-3.72 wt.%) of the compositional field defined by central Italy and NW Iran rocks. Finally, LP rocks from Turkey clearly define two distinctive compositional groups for the Afyon and eastern Pontides samples. Namely, the first have higher Al_2O_3, K_2O, Rb, Sr, Ba, and Nb and lower Fe_2O_3tot, MgO, Na_2O, V and Cr with respect to the latter.

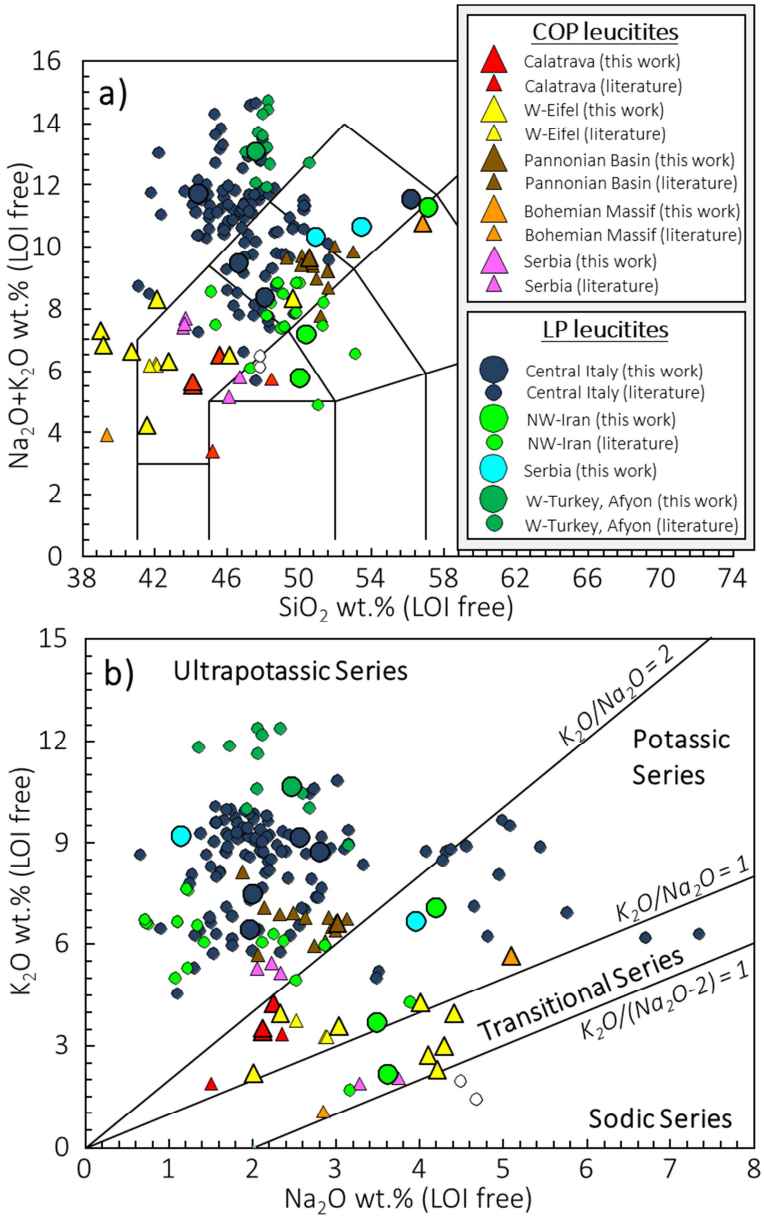

Fig. 3: *a) Total alkali vs. Silica (TAS; Le Maitre, 2002). A = Andesite; B = Basalt; BA = Basaltic Andesite; BT = Basanite/Tephrite; F = Foidite; P = Phonolite; PB = Picrobasalt; PT = Phonolitic Tephrite (Phonotephrite); TA = Trachyandesite; TB = Trachybasalt; TBA = Trachybasaltic Andesite; TP = Tephritic Phonolite (Tephriphonolite). b) K_2O vs. Na_2O (Middlemost, 1975) classification diagrams for the Cenozoic circum-Mediterranean "leucitite" rocks. Sources for literature data: west Eifel = Mertes and Schmincke (1985); Calatrava = Cebriá and Lopez-Ruiz (1995), Bohemian Massif = Ulrych et al. (2003); Serbia = Prelević et al. (2005); Pannonian Basin = Harangi et al. (1995), Grachev (2012); Turkey = Akal (2003), Eyuboglu et al. (2011), Prelević et al. (2015); NW Iran = Moayyed et al. (2008), Hajalilou et al. (2009), Shafaii Moghadam et al. (2014); Central Italy: Rogers et al. (1985), Conticelli et al. (1987, 2007, 2009), Di Battistini et al. (1998), Freda et al. (2006), Gaeta (1998), Gaeta et al. (2006), Giordano et al. (2006), Boari et al. (2007, 2009a), Frezzotti et al. (2007), Marra et al. (2009).*

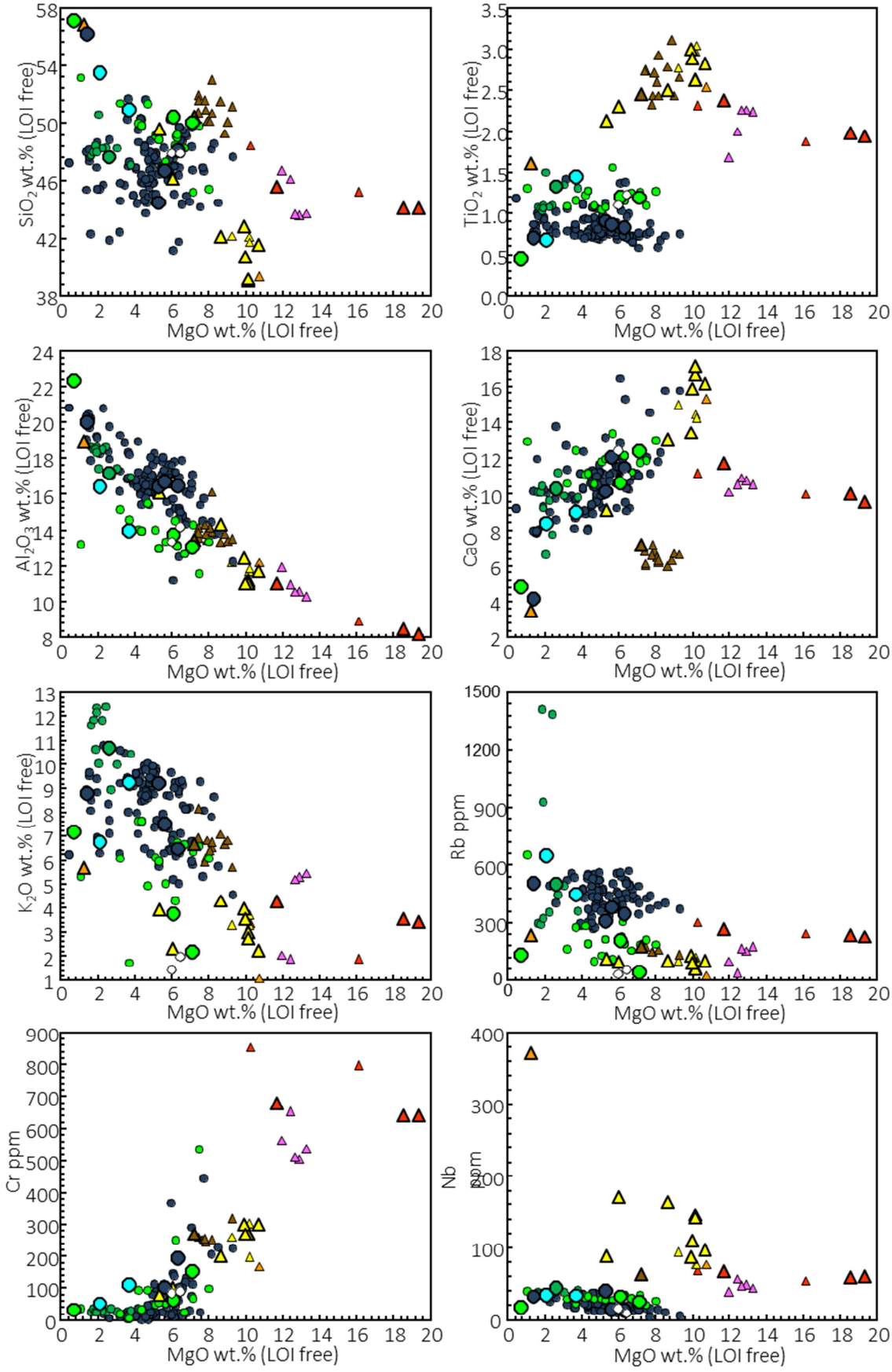

Fig. 4: *Selected major- and trace element vs. MgO binary diagrams for the Cenozoic circum-Mediterranean "leucitite" rocks. Data sources as in Fig. 2.*

5.2 Primitive mantle-normalized diagrams

When primitive mantle (PM)-normalized multi-element plots are taken into account (Figs. 5, 6), the two "leucitite" groups display a much larger variability. Among the COP "leucitites", rocks from west Eifel are the only showing overall regular pattern, sub-parallel to that of St. Helena basalts (except for an initial Cs enrichment), with normalized abundances exceeding ~100 times PM for the most incompatible elements (typically Nb-Ta and La-Ce) and then smoothly decreasing up to the Heavy Rare Earth Elements (HREE, Ho-Lu, ~4-7 times PM) and a small trough at K (Fig. 5a).

On the other hand, the Calatrava rocks are characterized by extremely high Cs, Rb, Th and U (>500 times PM), a small peak at K, a larger peak at Pb (except for a single literature sample), and an evident Ti trough (Fig. 5b). They share similarities with Betic lamproites (i.e., melts derived from strongly metasomatized mantle wedge source), such as Nb-Ta depletion and LILE (Large Ion Lithophile Elements, Cs, Rb, Ba, Pb) enrichment (Lustrino et al, 2016b). These features are similar to those of typical upper crustal rocks (e.g., Rudnick and Gao, 2014) and the average composition of the Global Subducting Sediments (i.e., GloSS; Plank, 2014) and remarkably different from the St. Helena basalts.

The two Bohemian Massif samples show irregular pattern with large variation in normalized elemental abundances most likely reflecting the large differences in the degree of rock evolution between the less evolved literature sample and the more evolved sample reported in this study. The former is characterized by a pattern that on the whole resembles that of west Eifel rocks (i.e., high Cs, a trough at Rb followed by increasing normalized concentrations up to a maximum at La and Ce, then roughly decreasing down to ~6 times PM at HREE, and a marked K trough), although it also features some troughs at HFSE (High Field Strength Elements, Nb, Ta, Zr, Hf and Ti; Fig. 5c). The more evolved latitic sample has a similar pattern with higher normalized abundances but features also: 1) marked enrichment in Th, U and Nb; 2) depletion in Ba, P and Ti; 3) peak at Zr and Hf.

The Serbian rocks are LILE-rich and HFSE-poor but also have K peaks and a marked Pb troughs (Fig. 5d). An exception is the sample from Nova Varoš that possibly experienced leucite analcimization, as suggested by the coupled Rb depletion and the

additional evidence reported in the previous section (Prelević et al., 2005). On the other hand, the overall pattern displayed by the Pannonian Basin "leucitite" rocks is similar to that for GloSS, although much less HFSE-depleted, much less Pb-enriched and more depleted in HREE.

The patterns for the LP leucitite group are more similar in shape, but with large variations in normalized abundances (Fig. 6). The general, normalized abundance patterns are similar to that of GloSS, with very high abundances for the most incompatible elements (up to ~10000 times PM), very high LILE/HFSE ratios, as shown by marked Nb-Ta and Ti troughs, and nearly flat or slightly decreasing at the HREE region. Other sporadic troughs are clearly ascribable either to crystal fractionation (Ba, P and Sr) or to the analcimization of leucite (Rb). The only remarkable deviation is shown by the two Turkey samples from the eastern Pontides (Fig. 6b), which display irregular patterns with: 1) lower LILE-enrichment compared to COP types; 2) no Pb peak; 3) Zr-Hf trough; 4) anomalously high contents of the Middle Rare Earth Elements (MREE, Gd-Ho).

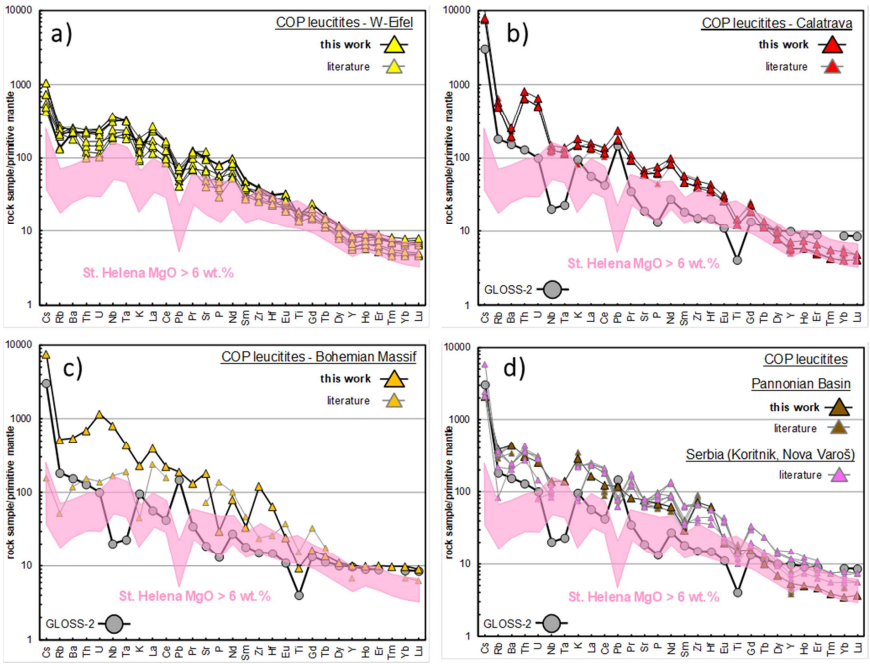

Fig. 5: *Primitive mantle-normalized (Lyubetskaya and Korenaga, 2007) incompatible element plots for the Cenozoic circum-Mediterranean COP "leucitite" rocks from a) west Eifel, b) Calatrava, c) Bohemian Massif and d) Pannonian Basin and Serbia (Koritnik and Nova Varoš). The field for the typical HiMu-OIB locality (St. Helena Island, Southern Atlantic Ocean; Kawabata et al., 2011 and references therein) and the pattern for the estimated composition of Global Subducting Sediments (GloSS; Plank, 2014) are reported for comparison. Data sources as in Fig. 2.*

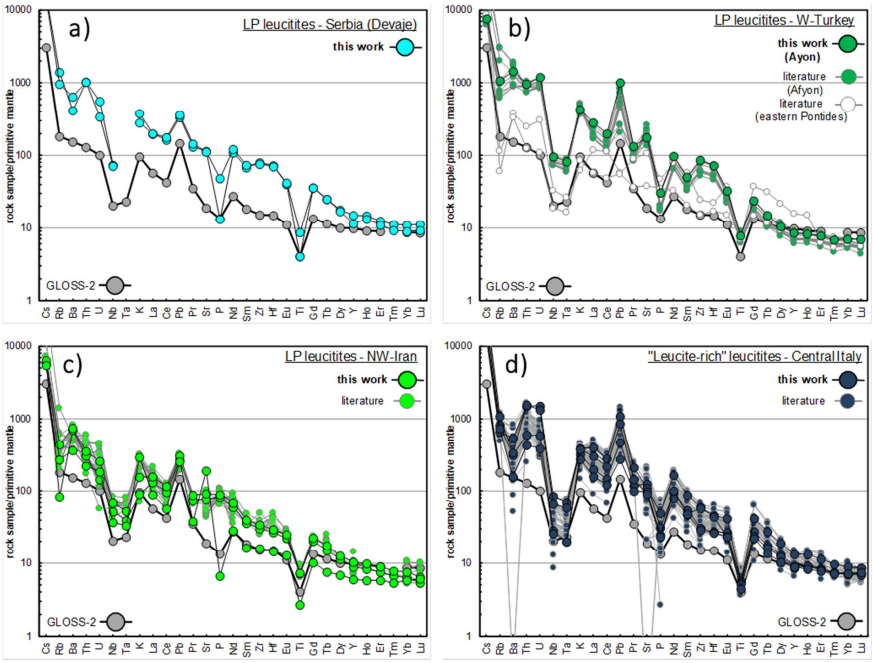

Fig. 6: *Primitive mantle-normalized (Lyubetskaya and Korenaga, 2007) incompatible element plot for the Cenozoic circum-Mediterranean LP "leucitite" rocks from a) Serbia (Devaje), b) Turkey, c) NW Iran and d) central Italy. The pattern for the estimated composition of Global subducting Sediments (GloSS; Plank, 2014) is reported for comparison. Data sources as in Fig. 2.*

5.3 Sr-Nd-Pb isotope ratios

As for the above PM-normalized diagrams, Sr-Nd-Pb isotope ratios for the circum-Mediterranean "leucitites" show large variations (Table 1, Fig. 7). In $^{143}Nd/^{144}Nd$ vs. $^{87}Sr/^{86}Sr$ space, the COP rocks are more homogeneous and have higher $^{143}Nd/^{144}Nd$ (0.51254-0.51283) and lower $^{87}Sr/^{86}Sr$ (0.70402-0.70709). One sample from Calatrava is an exception, with $^{143}Nd/^{144}Nd$ down to 0.51235 (Fig. 7a). Conversely, the LP leucitites plot all in the enriched quadrant and have generally higher $^{87}Sr/^{86}Sr$ (0.70727-0.71117) and lower $^{143}Nd/^{144}Nd$ (0.51209-0.51251), with central Italy rocks showing the most extreme values. A few samples from Turkey and NW Iran plot within the range of COP rocks (i.e., $^{87}Sr/^{86}Sr$ = 0.70462-0.70594, $^{143}Nd/^{144}Nd$ = 0.51248-0.51260).

In the $^{207}Pb/^{204}Pb$ vs. $^{206}Pb/^{204}Pb$ diagram, COP and LP "leucitite" rocks plot to the right of the 4.56 Ga geochron, and define two compositional groups. The LP and the Serbia COP rocks have lower $^{206}Pb/^{204}Pb$ (18.65-19.19 vs. 19.05-19.89) and higher $^{207}Pb/^{204}Pb$ (15.67-15.74 vs. 15.63-15.68, except for one single LP sample from NW Iran with 15.60) with respect to the remaining COP rocks (Fig. 7b). While the LP and the Serbia COP

rocks are well above the NHRL (Northern Hemisphere Reference Line), some of the COP lavas plot below this line. Among COP rocks, the sample from the Pannonian Basin shows remarkably low $^{207}Pb/^{204}Pb$ (15.53) and $^{206}Pb/^{204}Pb$ similar to that of LP rocks (18.69, plotting below the NHRL). Similar observations can be basically made also in the $^{208}Pb/^{204}Pb$ vs. $^{206}Pb/^{204}Pb$ and $^{207}Pb/^{206}Pb$ vs. $^{208}Pb/^{206}Pb$ diagrams (Figs. 7c-d), with LP and Serbia COP leucitites having lower $^{208}Pb/^{204}Pb$ (38-79-39.09 vs. 39.18-39.68) and higher $^{207}Pb/^{206}Pb$ (0.83-0.84 vs. 0.79-0.82) and $^{208}Pb/^{206}Pb$ (2.06-2.08 vs. 1.99-2.06), again with few exceptions from NW Iran and Turkey, plotting close to the compositional field for the COP rocks. The sample from the Pannonian Basin is again distinctive among the COP rocks, given its low $^{208}Pb/^{204}Pb$ (38.33), and relatively high $^{208}Pb/^{206}Pb$ (2.05) coupled with $^{207}Pb/^{206}Pb$ comparable to that of LP and Serbia COP rocks (0.83).

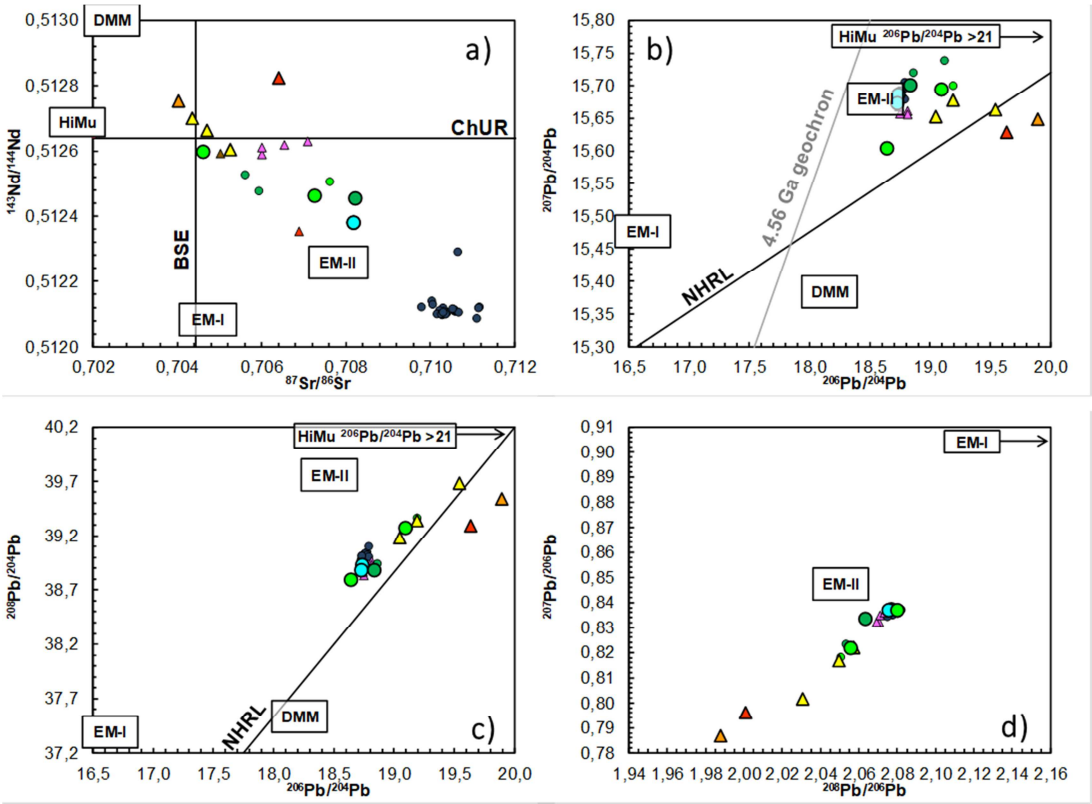

Fig. 7: *a) $^{143}Nd/^{144}Nd$ vs. $^{87}Sr/^{86}Sr$, b) $^{207}Pb/^{204}Pb$ vs. $^{206}Pb/^{204}Pb$, c) $^{208}Pb/^{204}Pb$ vs. $^{206}Pb/^{204}Pb$ and d) $^{207}Pb/^{206}Pb$ vs. $^{208}Pb/^{206}Pb$ diagrams for the Cenozoic circum-Mediterranean "leucitite" rocks. Data sources as in Fig. 3. Also shown are the isotopic compositions for BSE (Bulk Silicate Earth) and ChUR (Chondritic Uniform Reservoir), the DMM (Depleted MORB Mantle), HiMu (high-μ) and EM-I and EM-II (Enriched Mantle I and II) end-members (Lustrino and Anderson, 2015), the 4.56 Ga Geochron and the Northern Hemisphere Reference Line (NHRL; Hart, 1984). Data sources as in Fig. 2.*

5.4 Isotopic ratios vs. degree of rock evolution

Despite the general paucity of data for each of the individual districts (e.g., only one sample available for both the Bohemian Massif and Pannonian Basin COP leucitites), some distinctive variations of Sr-Nd-Pb isotope ratios with increasing degree of rock evolution can be observed (SM Figs. 5-7). The most evident are those for central Italy LP rocks (also as a consequence of the wealth of available data), which display remarkably constant $^{143}Nd/^{144}Nd$ (except for one sample with a more radiogenic Nd composition), $^{206}Pb/^{204}Pb$, $^{208}Pb/^{204}Pb$, $^{207}Pb/^{206}Pb$ and $^{208}Pb/^{206}Pb$ with decreasing MgO contents. The$^{87}Sr/^{86}Sr$ and $^{207}Pb/^{204}Pb$ values are more variable (from 0.70962 to 0.71115 and from 15.67 to 15.71, respectively), but both still have no correlation with the degree of rock evolution. Although fewer data are available, the LP leucitites from NW Iran seem to depict a linear trend of decreasing $^{87}Sr/^{86}Sr$, $^{206}Pb/^{204}Pb$,$^{207}Pb/^{206}Pb$ and$^{208}Pb/^{204}Pb$, and increasing $^{143}Nd/^{144}Nd$, $^{207}Pb/^{206}Pb$ and $^{208}Pb/^{206}Pb$ with decreasing MgO contents.

As for COP rocks, samples from west Eifel are characterized by overall increasing $^{87}Sr/^{86}Sr$, $^{207}Pb/^{206}Pb$ and$^{208}Pb/^{204}Pb$, and decreasing $^{143}Nd/^{144}Nd$, $^{206}Pb/^{204}Pb$ and $^{208}Pb/^{204}Pb$ with decreasing MgO. On the other hand, the few data for the COP Calatrava rocks allow only some dubitative inferences to be made, suggesting a slight increase of $^{87}Sr/^{86}Sr$ and a stronger decrease of $^{143}Nd/^{144}Nd$ with increasing degree of rock evolution. Finally, both the COP and LP rocks from Serbia are characterized by very limited ranges in the degree of rock evolution, coupled with very constant isotopic compositions.

6. Discussion

Owing to their peculiar petrochemical features and relative rareness, K-rich igneous rocks have always represented a major challenge for authors dealing with their correct identification and classification (e.g., Foley et al., 1987; Woolley et al., 1996). In a recent paper, Lustrino et al. (2016a) highlighted the difficulty in classifying the ultrapotassic rocks of the lamproite clan based on a detailed review of the circum-

Mediterranean and worldwide occurrences of such rocks. The authors pointed to the conflicting results deriving from using mineralogical vs. whole-rock chemical criteria and concluded that many of the so-called “lamproites” should be actually defined as “normal” potassic to ultrapotassic volcanic rocks (e.g., shoshonite, latite, kamafugite, and lamprophyre). In a similar fashion, the extreme variability revealed by circum-Mediterranean “leucitite” rocks in terms of petrography, mineral chemistry and whole-rock geochemistry, is strongly suggestive of some inconsistency in the nomenclature of such rock group too. The critical review of the petrochemical characteristics of such rocks reported here can similarly contribute a better understanding of K-rich rocks.

6.1 Petrographic, mineralogical and petrochemical constraints

According to the official IUGS recommendations (Le Maitre, 2002), the use of the term “leucitite” is based on mineralogical criteria. This makes nomenclature problematic for the circum-Mediterranean leucitite rocks, which are predominantly fine-grained volcanic rocks. Nonetheless, both “leucite-rich” (i.e., the leucite-phyric LP group) and “leucite-poor” (the clinopyroxene/olivine-phyric COP group) lithotypes are referred to as “leucitites” in the existing literature, regardless of the modal abundance of feldspar (e.g., Harangi et al., 1995; Schmincke, 2007) or leucite (e.g., Humphreys et al., 2010). In addition, some systematic differences are observed in the compositions of the principal mineral phases, with LP clinopyroxenes being poorer in MgO and TiO_2 than COP ones, and LP leucite being generally richer in K_2O. Therefore, it is evident that the term “leucitite” has been used for at least two different groups of rocks that are compositionally distinct. In any case, since classification based on modal mineralogy is not robust for most volcanic rocks, following the IUGS guidelines, the TAS chemical classification plot provides an alternative approach. The use of the TAS diagram similarly allows to make some clear distinction between the LP and COP rocks (especially in the 40-48 wt.% SiO_2 interval) but still seems to be not completely sufficient, given the quite large variability of many major and trace element concentrations (see section 5.1).

In contrast, a distinction between the two "leucitite" rock groups is more readily apparent in plots involving K2O/MgO and K_2O/TiO_2 (Fig. 8). Rocks of the COP group define an asymptotic array of slightly increasing K_2O/MgO with decreasing CaO, ranging from 0.27 to 1.09 and up to 4.57 in the most evolved latite sample from the Bohemian Massif (Fig. 8a). Similarly, K_2O/TiO_2 linearly increases with degree of differentiation (using CaO as a proxy) from 1.04 to 3.54. Leucitite rocks of the LP group are compositionally more variable and are characterized by higher K_2O/MgO and K_2O/TiO_2 for a given CaO content (Fig. 8). Exceptions tend to be some samples from NW Iran with high LOI values (>4 wt.%) and two literature samples from eastern Pontides that plot within the COP array.

In an attempt to reconcile modal and whole-rock geochemical observations, we have applied a CIPW normative calculation to the investigated circum-Mediterranean "leucitite" rocks in order to generate a hypothetical modal mineralogy for each sample (Fig. 9). The most striking difference between the two leucitite groups is that COP rocks are poorer in normative leucite (Lc), reaching at most 25 % (in Serbia rocks from Koritnik), with leucite being even completely absent in many samples. Interestingly, the Pannonian Basin samples are all rich in normative orthoclase (Or ~33-48 %) and completely free of Lc, though relatively MgO-rich (i.e., 7.21-9.31 wt.%). The absence of Lc coupled with the presence of some Or in two MgO-rich COP rocks from Serbia (Nova Varoš) is likely due to K_2O depletion due to significant leucite analcimization (Prelević et al., 2004; see section 5). On the other hand, LP leucitites are basically represented by Or-free rocks (mostly from central Italy and Turkey) with Lc between 20 and 60 % (roughly increasing with increasing differentiation). Rocks with both Lc and Or (central Italy and NW Iran), both widely ranging (~1-2 to ~40 %), and show no clear correlation with the degree of differentiation (Figs. 9a, b). The very few LP samples with no Lc are generally differentiated to strongly differentiated and/or have high LOI (> 3 wt.%), mainly including samples from NW Iran and eastern Pontides (Fig. 9c).

Additional differences between the two groups of leucitite rocks can be observed if the CIPW-normative mineral abundances are used in the forsterite-leucite-diopside (pseudo)ternary system of Fig. 10. In this diagram the investigated dataset has been filtered excluding rocks with MgO <3 wt.% and LOI >3 wt.%. Literature outliers with questionable compositions (e.g., K_2O <2 wt.%, CaO >15 wt.%, Fe_2O_3tot >12 wt.% and

Al_2O_3 <10 wt%) or low sum of oxides (<97 wt.%) were also discarded. Although this diagram should not be considered to accurately describe the crystallization history of the investigated samples, since it is based on CIPW normative minerals and is only a part of a quaternary system including also akermanite melilite (which is only sporadically present as an accessory phase), some interesting differences can be observed between the recognized leucitite rock groups. The LP rocks from central Italy and NW Iran define an array close to the forsterite-leucite cotectic, consistent with their abundant modal leucite. On the other hand, COP leucitites fall well within the forsterite stability field, defining three main groups: 1) samples falling left side of the line connecting the forsterite apex with the ternary eutectic (i.e., samples from Serbia and west Eifel); 2) samples falling at the right side of the Fo-E line (i.e., samples from west Eifel, Calatrava and Bohemian Massif); 3) samples falling on the forsterite-diopside Alkemade line (i.e., mostly samples from the Pannonian Basin). Therefore, except for the few samples of the first group, in which leucite starts to crystallize just after forsterite, the majority of COP rocks are expected to experience only minor leucite crystallization following forsterite and forsterite + diopside or even no leucite crystallization at all.

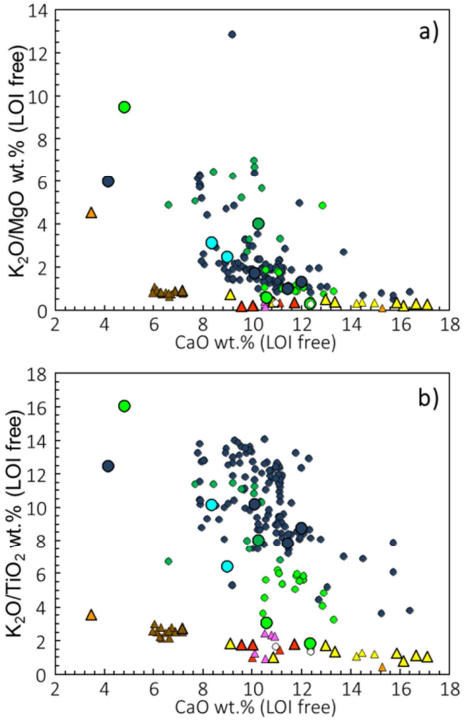

Fig. 8: *a) K_2O/MgO and b) K_2O/TiO_2 vs. CaO diagrams for the Cenozoic circum-Mediterranean "leucitite" rocks. Data sources as in Fig. 2.*

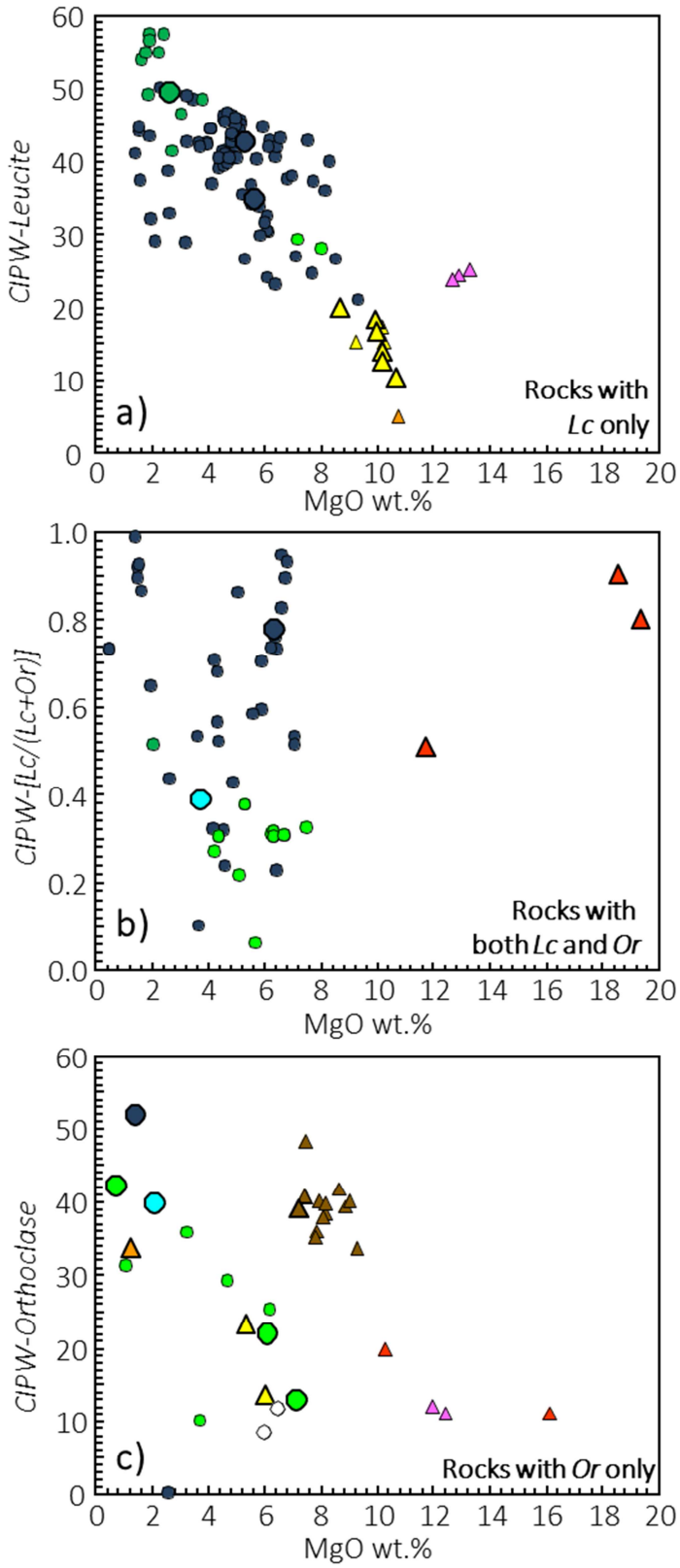

Fig. 9: *CIPW-normative a) Lc, b) Lc/(Lc+Or) and c) Or vs. MgO diagrams for the Cenozoic circum-Mediterranean "leucitite" rocks. Data sources as in Fig. 2.*

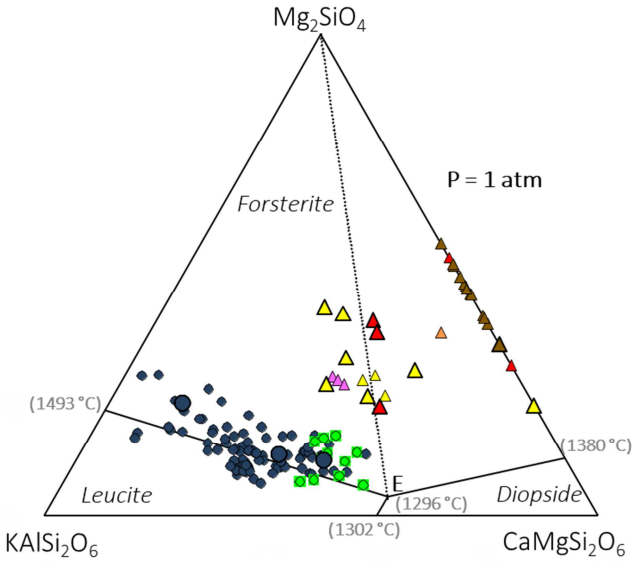

Fig. 10*: Forsterite-leucite-diopside (pseudo)ternary system at P = 1 atm (after Gupta, 1972) for selected less evolved (i.e., MgO >5 wt.%) Cenozoic circum-Mediterranean "leucitite" rocks. Data sources as in Fig. 3. See text for full details. Data sources as in Fig. 2.*

6.2 Geodynamic framework and mantle source features

LP rocks rich in leucite all occur in "orogenic" subduction-related settings or in areas that have experienced subduction-related metasomatism in their geological past. We remark, therefore, that the "orogenic" and "anorogenic" concepts are not geological settings but, rather, geochemical signatures. Here mantle sources exhibit a strong crustal signature in terms of both incompatible element contents (i.e., GloSS-like) and radiogenic isotope ratios (i.e., EM-II-like compositions, particularly relevant for LP rock group; see sections 5.2 and 5.3), pointing to lithospheric depths of melting. Conversely, COP rocks belong to both "anorogenic" subduction-unrelated settings. In this case, COP rock mantle sources have geochemical and isotopic fingerprints that could be potentially related to asthenospheric sources (i.e., the St. Helena- and HiMu-OIB-like west Eifel and, less clearly, Bohemian Massif rocks). The inference of "orogenic" settings in COP rocks could be related to variable contributions of asthenosphere- and

lithosphere-derived components (i.e., the “mixed” patterns displayed by the Koritinik and Nova Varoš samples from Serbia and by the Pannonian Basin rocks).

The above differences in terms of mantle source components are evident also from the incompatible element ratios diagrams of Figs. 11 and 12. In the Th/Yb vs. Ta/Yb diagram, the LP rocks define a near-vertical array in which Th/Yb ranges from ~3 to ~39 and Ta/Yb from ~0.2 to ~1.1. In contrast, COP rocks have higher Ta/Yb (2.2-4.5) and variable Th/Yb (e.g., 4.2-5.7 for west Eifel, up to ~29 for Calatrava; Fig. 11a). Given the higher mobility of Th in aqueous fluids (such as those producing mantle metasomatism) compared to Ta (e.g., Johnson and Plank, 1999), the Th/Yb ratio can be considered as a proxy for the involvement of a metasomatic (lithospheric) component. The Ta/Yb ratio can be instead taken as a proxy for the (immobile elements-richer) asthenospheric source, significantly more present in the COP rocks. The lower Ta/Yb in LP than in COP rocks could also be related to the possible presence of a MARID-like (Mica-Amphibole-Rutile-Ilmenite-Diopside) source, where residual rutile could prevent Nb and Ta (substituting for Ti) going into the melt phase. Whereas the relatively high Th/Yb of the Bohemian Massif sample is likely related to its relatively evolved character, the high Th/Yb displayed by the Mg-rich samples from the Pannonian Basin and Calatrava is ascribed to involvement of a lithospheric component.

Similar conclusions can be drawn from the Th/Ta vs. Zr/Nb diagram. Th/Ta is again indicative of a metasomatic component, whereas Zr/Nb is not influenced by metasomatic processes. Instead, it is related to variations in source compositions, source depletion and/or degree of partial melting processes. High Th/Ta (from 8.5 up to ~65 in central Italy rocks) is generally coupled with variable Zr/Nb (~7-21) in LP leucitites. The COP rocks point instead to a source with generally lower values for both ratios (Th/Ta = 1.0-3.3, Zr/Nb = 1.8-3.4), except for samples from Calatrava (Th/Ta ~12, Zr/Nb ~6) and the Pannonian Basin (Th/Ta = 4.6, Zr/Nb = 9.5), which are thought to include a significant metasomatic component in their mantle sources.

The LP leucitites have Nb/U (1.1-7.1; average = 5.0) and Ce/Pb ratios (1.7-6.1; average = 3.4) similar to average upper crustal rocks; 4.4 and 3.7, respectively; Rudnick and Gao, 2014), remarkably below the values of oceanic basalts (N-MORB and HiMu-OIB; Fig. 12). The COP rocks span a much larger range of Nb/U (6.7-41.0; average = 25.7) and Ce/Pb (6.2-31.7; average = 18.8), especially those from west Eifel, well distinguishable

from LP rocks. Notwithstanding the relatively limited number of data, the plots of Fig. 12 could be interpreted as the presence of veined mantle sources with two end-members such as a Sr-radiogenic, Nd-unradiogenic source with low Nb/U and Ce/Pb (pointing to central Italy rocks) and a Sr-unradiogenic, Nd-radiogenic source with high Nb/U and Ce/Pb (pointing to west Eifel rocks). As for the first component, it should be observed that a similar geochemical signature could be achieved also through magma-crust interaction. However, the presence of near-primitive Mg-rich samples (MgO mostly 5.0-8.2 wt.%) and the absence of correlation between $^{87}Sr/^{86}Sr$ and MgO (see section 5.4), allow us to assume that these features likely reflect the peculiar source signature, pointing to a mantle source component metasomatized by sediments. The second component (that pointing towards higher Nb/U and Ce/Pb, lower $^{87}Sr/^{86}Sr$ and higher $^{143}Nd/^{144}Nd$) could reflect the involvement of mantle sources with MORB/HiMU-OIB-like Nb/U, Ce/Pb to be identified in asthenospheric mantle sources or lithospheric mantle avoiding significant recycled crustal lithologies. In the case of Serbian rocks, a binary mixing between such components is not the only possibility, as the Mg-poor LP rocks (from Devaje, MgO <4 wt.%) could also result from the contamination by crustal material of the Mg-rich COP rocks (Koritnik and Nova Varoš, MgO >11.5 wt.%). However, considering the notably complex geological framework of the Serbian Province (e.g., Cvetković et al., 2004; Prelević et al., 2005; see section 3.2.2), it cannot be excluded that the presence of both LP and COP leucitites is related to melting of different "mixed" mantle sources, in which lithospheric and asthenospheric components are alternatively dominant.

Following the classical "veined mantle" model from Foley (1992), the genesis of ultrapotassic magmas requires low degrees of partial melting of a metasomatically modified depleted peridotite source that interacted with a K-rich hydrous silicate melt, which produced a network of phlogopite-rich veins and pods (Förster et al., 2017, 2018). Low melting degrees, indeed, result in a high vein/peridotite contribution to the melt, producing the peculiar enrichment in K_2O of such rocks. As partial melting proceeds, the contribution of the K-rich vein assemblage is progressively diluted, which might eventually lead even to the genesis of shoshonitic and high-K calcalkaline magmas (e.g., Conticelli et al., 2007, 2015; Avanzinelli et al., 2009). However, this model is difficult to reconcile with the asthenospheric signature of the COP rocks, as

this would further dilute the contribution of the K-rich component, thus making very unlikely that the primitive melts are actually ultrapotassic and able to crystallize abundant leucite crystals, as confirmed by the petrochemical characteristics of the rocks of this group. Alternatively, the LP rocks could be generated by partial melting of a depleted mantle source significantly metasomatized by K-rich fluids. Since the peridotite matrix is already depleted it does not contribute much to any melt produced. In contrast, the COP rocks could be essentially small degree partial melts of a less enriched (less metasomatized) source so the compositional signal is closer to normal mantle in terms of trace elements and isotopes (and even major elements). As small degree melts, they are enriched in incompatible elements (e.g., K) regardless, but geochemical signatures from any metasomatism are modified by a contribution from the (partially fertile) mantle peridotite with which the metasomatic element (veins, interstitial phases, etc) is associated. This could help explain a number of the observed differences between COP and LP rock groups (e.g., more primitive COP on average, lack of or weak HFSE negative anomalies, less radiogenic Sr, more radiogenic Nd, transitional to potassic rather than ultrapotassic, higher Ti, Cr and Ni).

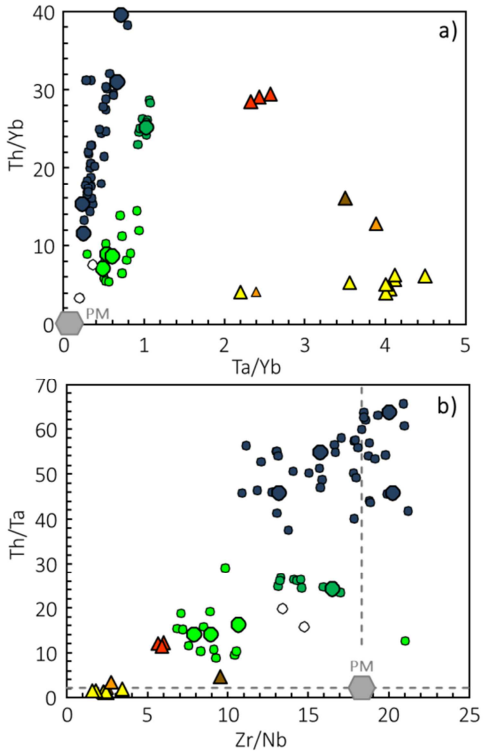

Fig. 11: *a) Th/Yb vs. Ta/Yb and b) Th/Ta vs. Zr/Nb for the Cenozoic circum-Mediterranean "leucitite" rocks. Data sources as in Fig. 2. Primitive mantle composition (PM, grey hexagon) after Lyubetskaya and Korenaga (2007).*

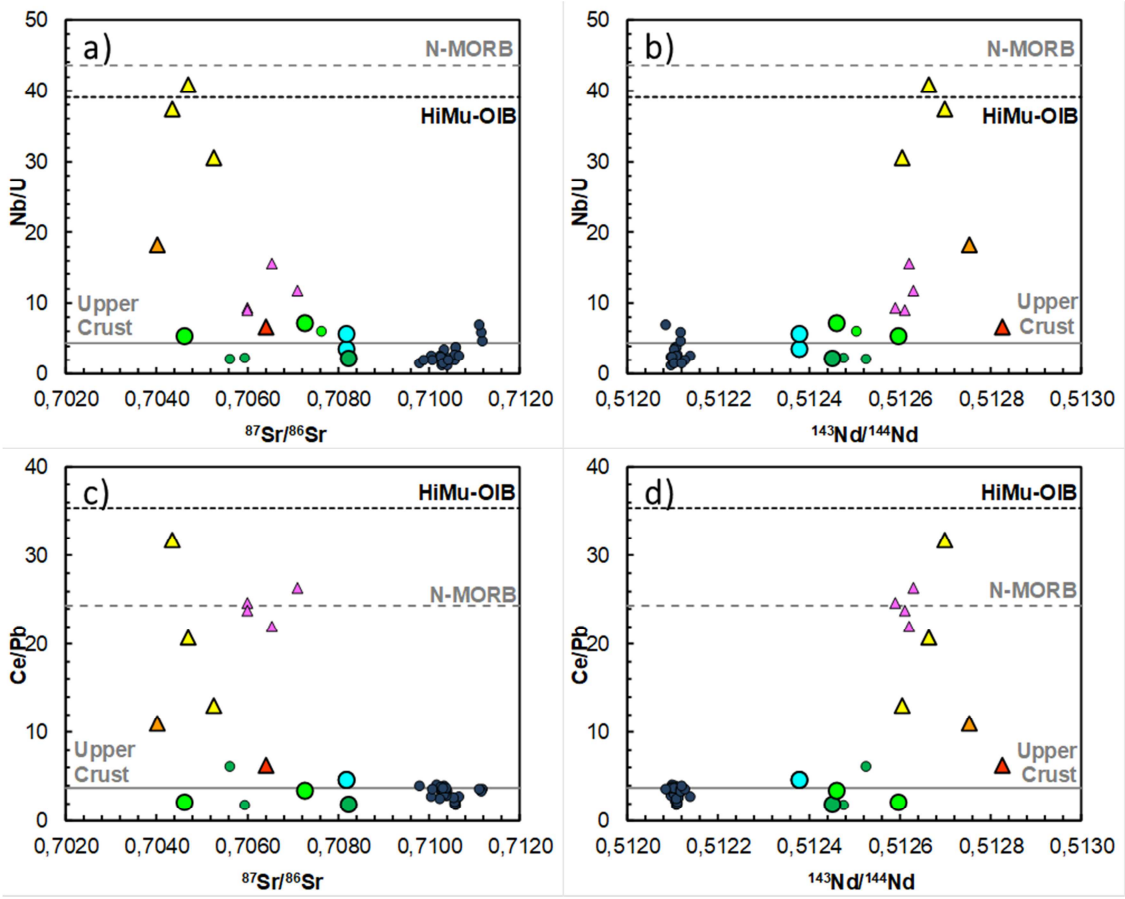

Fig. 12: *a) Nb/U vs. $^{87}Sr/^{86}Sr$, b) Nb/U vs. $^{143}Nd/^{144}Nd$, c) Ce/Pb vs. $^{87}Sr/^{86}Sr$ and d) Ce/Pb vs. $^{143}Nd/^{144}Nd$ for the Cenozoic circum-Mediterranean "leucitite" rocks. Symbols and data sources as in Fig. 2. Average values for N-MORB (black line; Gale et al., 2013), HiMu-OIB (dashed grey line; Kawabata et al., 2011) and the upper crust (grey line; Rudnick and Gao, 2014) are reported for comparison.*

6.3 Mixing model between two mantle sources

Any consideration on the origin of the circum-Mediterranean "leucitites" is based on the assumption that these rocks are the geochemical messengers of their mantle sources. This is quite rarely verified, because post-melting processes can modify the original compositions of mantle partial melts. An example is represented by the melilite leucitites of the Afyon area. These are considered the result of strong clinopyroxene fractionation, responsible for the relatively low content of SiO_2 (down to 43 wt%) and MgO (<4 wt%). A successive process of accumulation of leucite crystals in a sort of foam magma in shallow depth magma sources would lead to the final composition of the Afyon melilite leucitites (Prelević et al., 2015). Considering these post-melting

processes, any inference raised using the geochemical message (e.g., major oxide and trace element composition) concerning the composition of the mantle sources can potentially reduce the scientific validity of the conclusions.

Bearing this in mind, the investigated rock samples have been plotted in the Rb vs. TiO_2/K_2O and Rb/Nb vs. TiO_2/K_2O diagrams of Fig. 13 along with two hypothetical mantle melts as potential end-members In order to shed further light on the mantle source components involved in the genesis of circum-Mediterranean "leucitites". Melt 1 is generated starting from a depleted mantle source with 798 ppm Ti, 300 ppm K, 1 ppm Rb and 1 ppm Nb, with a ol:opx:cpx:sp modal ratio = 57:28:13:2 and an ol:opx:cpx:sp ratio of the phases entering the melt = -6:28:67:11 (Kinzler and Grove, 1992). Melt 2 is generated after 2.5% partial melting of an enriched mantle source with 3,000 ppm Ti (0.50 wt.% TiO_2), 30,000 ppm K (3.61 wt.% K_2O), 300 ppm Rb and 0.1 ppm Nb, assuming a ol:opx:cpx:phl:sp modal ratio = 50:12:20:10:8 and an ol:opx:cpx:phl:sp ratio entering the melt = -5:15:40:30:20. Crystal/melt partition coefficient values were taken from Gorring and Kay (2001) and Sisson et al. (2009). The mixing lines connecting the two melt end-members define hyperbolic trends that are quite nicely followed by curves that overlap the circum-Mediterranean "leucitites" data, allowing to hypothesize that their composition could be the result of variable interaction of such two main types of mantle liquids. However, it should be observed that Melt 1 has high TiO_2/K_2O, but has very low TiO_2 (0.63 wt.%) and K_2O (0.1 wt.%), while Melt 2 has low TiO_2/K_2O, but very high TiO_2 (1.77 wt.%) and K_2O (9.80 wt.%). Therefore, according to this model, the higher the K_2O, the higher the TiO_2, which is exactly the opposite of what is observed in COP (high in TiO_2 and low in K_2O) and LP (low in TiO_2 but high in K_2O) "leucitite" rocks. Therefore, despite this dispersion could have some reasonable geochemical meaning, the presented model is at odd with the geochemical evidence.

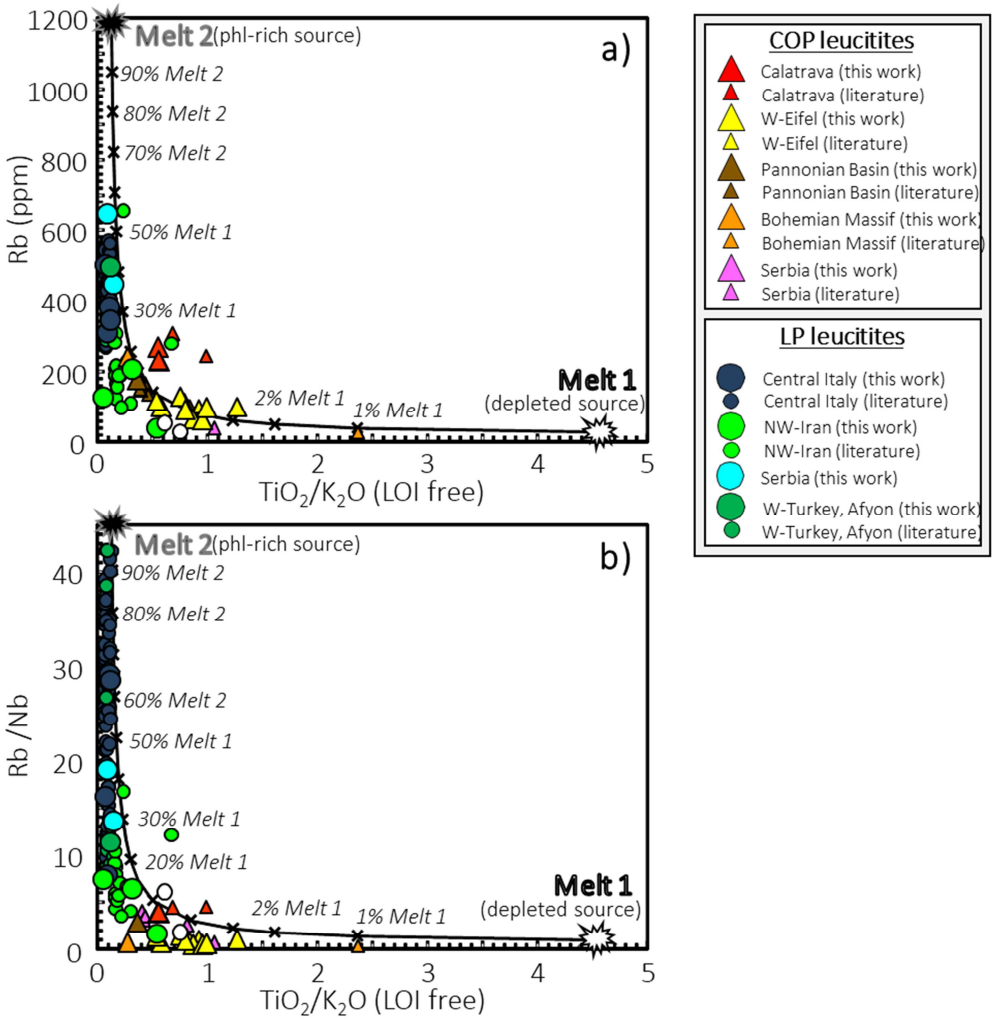

Fig. 13: *a) Rb vs. TiO_2/K_2O and b) Rb/Nb vs. TiO_2/K_2O diagrams showing the binary mixing lines connecting two hypothetical mantle melts ("Melt 1" and "Melt 2") along which the Cenozoic circum-Mediterranean "leucitite" rocks plot. Melt 1 represents a liquid generated by the partial melting of a depleted source and is characterized by low Rb, low Rb/Nb and high TiO_2/K_2O. Melt 2 represents the product of the partial melting of a phlogopite-rich source and is characterized by high Rb, high Rb/Nb and low TiO_2/K_2O. See text for full details. Data sources as in Fig. 2.*

7. Conclusions

The present review of the known occurrences of Cenozoic "leucitite" rocks from the circum-Mediterranean realm has led to the following observations:

1. "Leucitite" rocks were emplaced in various continental settings both in the hinterland and in the foreland of active orogenic systems, ranging in age from Early

Oligocene (~31 Ma; Bohemian Massif) to Late Pleistocene (~0.1 Ma; west Eifel), with no age clusters;

2. "Leucitite" rocks are generally volumetrically subordinate with respect to the associated products, which include a wide variety of rock compositions such as leucite-bearing basanites/tephrites, Na-alkaline basalts/basanites, nephelinites, ankaratrites, melilititites, melilite- and sodalite-bearing lavas, as well as rocks belonging to calcalkaline, high-K calcalkaline, shoshonitic, kamafugitic and lamproitic series;

3. Based on petrographic and mineral chemical considerations, two groups of "leucitite" rocks have been recognized: the LP group, which is richer in normative leucite and leucite-phyric (including rocks from Turkey, NW Iran, central Italy and Serbia) and the COP group, which has little to no normative leucite and is clinopyroxene-olivine-phyric (west Eifel, Pannonian Basin, Calatrava, Bohemian Massif and Serbia);

4. The LP leucitites fall mainly in the phonolitic tephrite and foidite fields on a TAS diagram, and mostly belong to an ultrapotassic rock series (K_2O/Na_2O >2), while COP leucitites fall mainly in the tephrite/basanite TAS field (plus fewer foidite) and include rocks that are not strictly ultrapotassic (i.e., from Calatrava, west Eifel and the Bohemian Massif);

5. The LP leucitites have generally higher Al_2O_3, K_2O, Rb, Pb and CIPW-normative leucite, and lower TiO_2, MgO, Ni, Cr and Nb with respect to COP ones;

6. Primitive mantle-normalized diagrams, Sr-Nd-Pb isotope ratios and incompatible element ratios such as Th/Yb, Ta/Yb, Th/Ta, Zr/Nb, Nb/U and Ce/Pb all suggest that LP leucitites derive from mantle sources dominated by lithospheric metasomatized components, whereas COP leucitites bear a strong evidence for HiMu-OIB-like asthenospheric source components.

Based on such evidence, it appears that the "leucitite" rock name cannot be used for such different rock types. It is consequently proposed that only rocks belonging to the LP group be considered to represent the "true" leucitite lithotype. This suggests that true leucitites are unlikely to occur in "anorogenic" intraplate settings where mantle sources are mainly asthenospheric. This brings further evidence to the growing awareness of the numerous pitfalls in the existing classification criteria for K-rich rocks, as for the recently revised case of "lamproite" rocks (Lustrino, 2016a). This not only

means that many of the previously-classified “leucitites” should no more be considered so, but possibly also that some “leucite-bearing” rocks (as those often associated to the investigated “leucitites”) should be actually considered as true “leucitites”.

Acknowledgements

The manuscript greatly benefitted of thorough and detailed review of Pamela D. Kempton (Manhattan, Kansas, USA) and Sandro Conticelli (Florence, Italy). To both our deep thanks for the revision that helped to clarify several aspects of the petrogenetic modelling presented in this study. Michele Psarakis and Luca Samuele Capizzi are thanked for their help in an early phase of investigation in 2011-2013. Szabolcs Harangi and Peter Suhr are thanked for having provided the sample BAR1 (Bàr, Hungary) and HAMM (Hammerrunterwiesenthal, Germany), respectively. Many thanks to Marcello Serracino (Rome) for his skill in maintaining perfectly working the electron microprobe. This research has benefitted of funds Ricerche Ateneo Sapienza (2016 and 2017) to ML and FFABR 2017 CUP E61I18001620005 to LF.

Waltz no. 2 of Dmitrij Šostakovič helped ML to create the good mood during the final stages of writing of the manuscript.

References

Aghazadeh, M., Prelevic, D., Badrzadeh, Z., Braschi, E., van den Bogaard, P., Conticelli, S., 2015. Geochemistry, Sr-Nd-Pb isotopes and geochronology of amphibole- and mica-bearing lamprophyres in northwestern Iran: implications for mantle wedge heterogeneity in a paleo-subduction zone. Lithos, 216-217, 352-369.

Akal, C., 2003. Mineralogy and geochemistry of melilite leucitites, Balcikhisar, Afyon, Turkey. Turkish Journal of Earth Sciences, 12, 215-239.

Akal, C., Helvaci, C., Prelević, D., van den Bogaard, P., 2013. High-K volcanism in the Afyon region, western Turkey: from Si-oversaturated to Si-undersaturated volcanism. International Journal of Earth Sciences, 102, 435-453.

Agostini, S., Doglioni, C., Innocenti, F., Manetti, P., Tonarini, S., Savasçin, M.Y., 2007. The transition from subduction-related to intraplate Neogene magmatism in the Western Anatolia and Aegean area. In: Beccaluva, L., Bianchini, G., Wilson, M. (Eds.), Cenozoic volcanism in the Mediterranean area. Geological Society of America Special Paper, 418, 1-15.

Altherr, R., Topuz, G., Siebel, W., Şen, C., Meyer, H.-P., Satir, M., Lahaye, Y., 2008. Geochemical and Sr-Nd-Pb isotopic characteristics of Paleocene plagioleucitites from the Eastern Pontides (NE Turkey). Lithos, 105, 149-161.

Avanzinelli, R., Lustrino, M., Mattei, M., Melluso, L., Conticelli, S., 2009. Potassic and ultrapotassic magmatism in the circum-Tyrrhenian region: significance of carbonated pelitic vs. pelitic sediment recycling at destructive plate margins. Lithos, 113, 213-227.

Boari, E., Conticelli, S., 2007. Mineralogy and petrology of associated mg-rich ultrapotassic, Shoshonitic, and calc-alkaline rocks: the Middle Latin Valley monogenetic volcanoes, Roman Magmatic Province, southern Italy. Canadian Mineralogist,45, 1443-1469.

Boari, E., Avanzinelli, R., Melluso, L., Giordano, G., Mattei, M., De Benedetti, A.A., Morra, V., Conticelli, S., 2009a. Isotope geochemistry (Sr-Nd-Pb) and petrogenesis of leucite-bearing volcanic rocks from “Colli Albani” volcano, Roman Magmatic Province, Central Italy: inferences on volcano evolution and magma genesis. Bulletin of Volcanology, 71, 977-1005.

Boari, E., Tommasini, S., Laurenzi, M.A., Conticelli, S., 2009b. Transition from ultrapotassic kamafugitic to sub-alkaline magmas: Sr, Nd, and Pb isotope, trace element and $^{40}Ar/^{39}Ar$ age data from the Middle Latin Valley Volcanic Field, Roman Magmatic Province, Central Italy. Journal of Petrology, 50, 1327-1357.

Carminati, E., Lustrino, M., Doglioni, C., 2012. Geodynamic evolution of the central and western Mediterranean: tectonics vs. igneous petrology constraints. Tectonophysics, 579, 173-192.

Cebriá, J.M., Lopez-Ruiz, J., 1995. Alkali basalts and leucitites in an extensional intracontinental plate setting: the late Cenozoic Calatrava volcanic province (central Spain). Lithos, 35, 27-46.

Conticelli, S., Avanzinelli, R., Ammannati, E., Casalini, M., 2015. The role of carbon from recycled carbonated metapelites in the transition from leucite-free to leucite-bearing ultrapotassic rocks: the Central Mediterranean case. Lithos, 232,174-196.

Conticelli, S., Carlson, R.W., Widom, E., Serri, G., 2007. Chemical and isotopic composition (Os, Pb, Nd, and Sr) of Neogene to Quaternary calc-alkalic, shoshonitic, and ultrapotassic mafic rocks from the Italian peninsula: Inferences on the nature of their mantle sources. Geological Society of America, Special Paper, 418, 171-202.

Conticelli, S., Francalanci, L., Manetti, P., Peccerillo, A., 1987. Evolution of Latera Volcano, Vulsinian district (central Italy): stratigraphical and petrological data. Periodico di Mineralogia, 56, 175-199.

Conticelli, S., Carlson, R.W., Widom, E., Serri, G., 2007. Chemical and isotopic composition (Os, Pb, Nd, and Sr) of Neogene to Quaternary calc-alkalic, shoshonitic, and ultrapotassic mafic rocks from the Italian peninsula: Inferences on the nature of their mantle sources. Geological Society of America, Special Paper, 418, 171-202.

Conticelli, S., Guarnieri, L., Farinelli, A., Mattei, M., Avanzinelli, R., Bianchini, G., Boari, E., Tommasini, S., Tiepolo, M., Prelević, D., Venturelli, G., 2009. Trace elements and Sr-Nd-Pb isotopes of K-rich, shoshonitic, and calc-alkaline magmatism of the Western Mediterranean Region: Genesis of ultrapotassic to calc-alkaline magmatic associations in a post-collisional geodynamic setting. Lithos, 107, 68-92.

Conticelli, S., Laurenzi, M.A., Giordano, G., Mattei, M., Avanzinelli, R., Melluso, L., Tommasini, S., Boari, E., Cifelli, F., Perini, G., 2010. Leucite-bearing (kamafugitic/leucititic) and -free (lamproitic) ultrapotassic volcanic rocks and associated shoshonites in the Italian Peninsula: constraints on petrogenesis and geodynamics. In: Beltrando, M., Peccerillo, A., Mattei, M., Conticelli, S., Doglioni, C. (Eds.) The geology of Italy: tectonics and life along plate margins. Journal of the Virtual Explorer, 36, paper 20, 94.

Conticelli, S., Avanzinelli, R., Ammannati, E., Casalini, M., 2015. The role of carbon from recycled carbonated metapelites in the transition from leucite-free to leucite-bearing ultrapotassic rocks: the Central Mediterranean case. Lithos, 232,174-196.

Cvetković, V., Prelević, D., Downes, H., Jovanović, M., Vaselli, O., Pécskay, Z., 2004. Origin and geodynamic significance of Tertiary postcollisional basaltic magmatism in Serbia (central Balkan Peninsula). Lithos, 73, 161-186.

Dèzes, P., Schmid, S.M., Ziegler, P.A., 2004. Evolution of the European Cenozoic rift system: interaction of the Alpine and Pyrenean orogens with their foreland lithosphere. Tectonophysics, 389, 1-33.

Di Battistini, G., Montanini, A., Vernia, L., Bargossi, G.M., Castorina, F., 1998. Petrology and geochemistry of ultrapotassic rocks from the Montefiascone Volcanic Complex Central Italy: magmatic evolution and petrogenesis. Lithos, 43, 169-195.

Di Giuseppe, P., Agostini, S., Lustrino, M., Karaoglu, O., Savasçin, M.Y., Manetti, P., Ersoy, Y., 2017. Transition from compression to strike-slip tectonics revealed by Miocene-Pleistocene volcanism West of Karliova triple junction (East Anatolia). Journal of Petrology, 58, 2055-2087.

Dilek, Y., Imamverdiyev, N., Altunkaynak, S., 2010. Geochemistry and tectonics of Cenozoic volcanism in the Lesser Caucasus (Azerbaijan) and the peri-Arabian region: collision-induced mantle dynamics and its magmatic fingerprint. International Geology Review, 52, 536-578.

Downes, H., Seghedi, I., Szakacs, A., Dobosi, G., Vaselli, O., James, D.E., Rigby, I.J., Thirlwall, M.F., Rex, D., Pécskay, Z., 1995. Petrology and geochemistry of late Tertiary/Quaternary mafic alkaline volcanism in Romania. Lithos, 35, 65-81.

Duggen, S., Hoernle, K., van den Bogaard, P., Garbe-Schonberg, D., 2005. Post-collisional transition from subduction- to intraplate-type magmatism in the westernmost Mediterranean: evidence for continental-edge delamination of subcontinental lithosphere. Journal of Petrology, 46, 1155-1201.

Eyuboglu, Y., 2010. Late Cretaceous high-K volcanism in the Eastern Pontides orogenic belt, and its implications for the geodynamic evolution of NE Turkey. International Geology Review, 52, 142-186.

Eyuboglu, Y., Chung, S.L., Santosh, M., Dudas, F.O., Akaryali, E., 2011. Transition from shoshonitic to adakitic magmatism in the eastern Pontides, NE Turkey: implications for slab window melting. Gondwana Research, 19, 413-429.

Faccenna, C., Becker, T.W., Auger, L., Billi, A., Boschi, L., Brun, J.P., Capitanio, F.A., Funiciello, F., Horvàth, F., Jolivet, L., Piromallo, C., Royden, L., Rossetti, F., Serpelloni, E., 2014. Mantle dynamics in the Mediterranean. Reviews of Geophysics, 52, 283-332.

Fedele, L., Seghedi, I., Chung, S.-L., Laiena, F., Lin, T.-H., Morra, V., Lustrino, M., 2016. Post-collisional magmatism in the Late Miocene Rodna-Bârgău district (East Carpathians, Romania): geochemical constraints and petrogenetic models. Lithos, 266-267, 367-382.

Foley, S.F., 1992. Vein-plus-wall-rock melting mechanisms in the lithosphere and the origin of potassic alkaline magmas. Lithos, 28, 435-453.

Foley, S.F., Venturelli, G., Green, D.H., Toscani, L., 1987. The ultrapotassic rocks: characteristics, classification and constraints for petrogenetic models. Earth-Science Reviews, 24, 81-134.

Freda, C., Gaeta, M., Karner, D.B., Marra, F., Renne, P.R., Taddeucci, J., Scarlato, P., Christensen, J.N., Dallai, L., 2006. Eruptive history and petrologic evolution of the Albano multiple maar (Alban Hills, Central Italy). Bulletin of Volcanology, 68, 567-591.

Frezzotti, M.L., De Astis, G., Dallai, L. Ghezzo, C., 2007. Coexisting calc-alkaline and ultrapotassic magmatism at Monti Ernici, Mid Latina Valley (Latium, central Italy) European Journal of Mineralogy, 19, 479-497.

Gaeta, M., 1998. Petrogenetic implications of Ba-sanidine in the lionato tuff (Colli Albani volcanic district, central Italy). Mineralogical Magazine, 62, 697-701.

Gaeta, M., Freda, C., Christensen, J. N., Dallai, L., Marra, F., Karner, D.B., Scarlato, P., 2006. Time-dependent geochemistry of clinopyroxene from the Alban Hills (Central Italy): Clues to the source and evolution of ultrapotassic magmas. Lithos, 86, 330-346.

Gaeta, M., Freda, C., Marra, F., Arienzo, I., Gozzi, F., Jicha, B., Di Rocco, T., 2016. Paleozoic metasomatism at the origin of Mediterranean ultrapotassic magmas: Constraints from time-dependent geochemistry of Colli Albani volcanic products (Central Italy). Lithos, 244, 151-164.

Gale, A., Dalton, C.A., Langmuir, C.H., Su, Y., Shilling, J.G., 2013. The mean composition of ocean ridge basalts. Geochemistry Geophysics Geosystems, 14, 489–518.

Giordano, G., De Benedetti, A.A., Diana, A., Diano, G., Gaudioso, F., Marasco, F., Miceli, M., Mollo, S., Cas, R.A.F., Funiciello, R., 2006. The Colli Albani mafic caldera (Roma, Italy): Stratigraphy, structure and petrology. Journal of Volcanology and Geothermal Research, 155, 49-80.

Gorring, M.L., Kay, S.M., 2001. Mantle processes and sources of Neogene slab window magmas from Southern Patagonia, Argentina. Journal of Petrology, 42, 1067-1094.

Grachev, A.F., 2012. Ultrapotassic Pliocene-Quaternary volcanism in the region of Bar (Pannonian Basin): new evidence and geodynamic implications. Physics of the Solid Earth, 48, 17-27.

Gupta, A.K., 1972. The system forsterite-diopside-akermanite-leucite and its significance in the origin of potassium-rich mafic and ultramafic rocks. American Mineralogist, 57, 1242-1259.

Harangi, S., Wilson, M., Tonarini, S., 1995. Petrogenesis of Neogene potassic volcanic rocks in the Pannonian Basin. Acta Vulcanologica, 7, 125-134.

Harangi, S., Downes, H., Seghedi, I., 2006. Tertiary-Quaternary subduction processes and related magmatism in the Alpine-Mediterranean region. In: Gee, D., Stephenson, R. (Eds.), European Lithosphere Dynamics. Geological Society of London Memoires, 32, 167-190.

Hart, S.R., 1984. A large-scale isotopic anomaly in the southern hemisphere mantle. Nature, 309, 753-757.

Hajalilou, B., Moayyed, M., Hosseinzadeh, G., 2009. Petrography, geochemistry and geodynamic environment of potassic alkaline rocks in Eslamy peninsula, northwest of Iran. Journal of Earth System Science, 118, 643-657.

Humphreys, E.R., Bailey, K., Hawkesworth, C.J., Wall, F., Najorka, J., Rankin, A.H., 2010. Aragonite in olivine from Calatrava, Spain – Evidence for mantle carbonatite melts from >100 km depth. Geology, 38, 911-914.

Johnson, M.C., Plank, T., 1999. Dehydration and melting experiments constrain the fate of subducted sediments. Geochemistry Geophysics Geosystems, 1, doi: 10.1029/1999GC000014.

Jolivet, L., Brun, J.P., 2010. Cenozoic geodynamic evolution of the Aegean. International Journal of Earth Sciences, 99, 109-138.

Kawabata, H., Hanyu, T., Chang, Q., Kimura, J.I., Nichols, A.R.L., Tatsumi, Y., 2011. The petrology and geochemistry of St. Helena alkali basalts: evaluation of the oceanic crust-recycling model for HIMU OIB. Journal of Petrology, 22, 791-838.

Kinzler, R.J., Grove, T.L., 1992. Primary magmas of Mid-Ocean Ridge Basalts 1. Experiments and methods. Journal of Geophysical Research, 97, 6885-6906.

Le Maitre, R.W., 2002. Igneous rocks. A classification and glossary of terms. Second Edition. Recommendations of the International Union of Geological Sciences

Subcommission on the Systematics of Igneous Rocks. Cambridge University Press, Cambridge, 236 pp.

Lustrino, M., Agostini, S., Chalal, Y., Fedele, L., Stagno, V., Colombi, F., Bouguerra, A., 2016a. Exotic lamproites or normal ultrapotassic rocks? The Late Miocene volcanic rocks from Kef Hahouner, NE Algeria, in the frame of the circum-Mediterranean lamproites. Journal of Volcanology and Geothermal Research, 327, 539-553.

Lustrino, M., Anderson D.L., 2015. The mantle isotopic printer: Basic mantle plume geochemistry for seismologists and geodynamicists. In: Foulger G.R., Lustrino M., and King S.D. (Eds.) The interdisciplinary Earth: A volume in honor of Don L. Anderson. Geological Society of America Special paper 514 and American Geophysical Union Special Publication 71, 257-279.

Lustrino, M., Carminati, E., 2007. Phantom plumes in Europe and the circum-Mediterranean region. In: Foulger G.R. and Jurdy D.M. (Eds.) Plates, plumes and planetary processes. Geological Society of America Special Paper, 430, 723-745.

Lustrino, M., Duggen, S., Rosenberg, C.L., 2011. The Central-Western Mediterranean: anomalous igneous activity in an anomalous collisional tectonic setting. Earth-Science Reviews, 104, 1-40.

Lustrino, M., Prelević, D., Agostini, S., Gaeta, M., Di Rocco, T., Stagno, V., Capizzi, L.S., 2016b. Ca-rich carbonates associated with ultrabasic-ultramafic melts: Carbonatite or limestone xenoliths? A case study from the late Miocene Morron de Villamayor volcano (Calatrava Volcanic Field, central Spain). Geochimica et Cosmochimica Acta, 185, 477-497.

Lustrino, M., Wilson, M., 2007. The circum-Mediterranean anorogenic Cenozoic Igneous Provinces. Earth-Science Reviews, 81, 1-55.

Lyubetskaya, T., Korenaga, J., 2007. Chemical composition of Earth's primitive mantle and its variance: 1. Methods and results. Journal of Geophysical Research, 112, B03211, doi:10.1029/2005JB004223.

Marra, F., Karner, D.B., Freda, C., Gaeta, M., Renne, P., 2009. Large mafic eruptions at Alban Hills Volcanic District (Central Italy): chronostratigraphy, petrography and eruptive behavior. Journal of Volcanology and Geothermal Research, 179, 217-232.

Mattei, M., Riggs, N.R., Giordano, G., Guarnieri, L., Cifelli, F., Soriano, C.C., Jicha, B., Jasim, A., Marchionni, S., Franciosi, L., Tommasini, S., Porreca, M., Conticelli, S., 2014. Geochronology, geochemistry and geodynamics of the Cabo de Gata volcanic zone, Southeastern Spain. It. J. Geosci., 133, 341-361.

Melluso, L., Conticelli, S., de' Gennaro, R., 2000. Kirschsteinite in the Capo di Bove melilite leucitite lava (cecilite), Alban Hills, Italy. Mineralogical Magazine, 74, 887-902.

Mertes, H., Shmincke, H.-U., 1985. Mafic potassic lavas of the quaternary West Eifel volcanic field. Contributions to Mineralogy and Petrology, 89, 330-345.

Mertz, D.F., Löhnertz, W., Nomade, S., Pereira, A., Prelević, D., Renne, P.R., 2015. Temporal–spatial evolution of low-SiO_2 volcanism in the Pleistocene West Eifel volcanic field (West Germany) and relationship to upwelling asthenosphere. Journal of Geodynamics, 88, 59-79.

Middlemost, E.A.K., 1975. The basalt clan. Earth-Science Reviews, 11, 337-364.

Moayyed, M., Moazzen, M., Calagari, A.A., Jahangiri, A., Modjarrad, M., 2008. Geochemistry and petrogenesis of lamprophyric dykes and the associated rocks from Eslamy peninsula, NW Iran: Implications for deep-mantle metasomatism. Chemie der Erde, 68, 141-154.

Pang, K.N., Chung, S.L., Zarrinkoub, H.S., Lin, Y.C., Lee, H.Y., Lo, C.H., Khatib, M.M., 2013. Iranian ultrapotassic volcanism at ~11 Ma signifies the initiation of postcollisional magmatism in the Arabia–Eurasia collision zone. Terra Nova, 25, 405-413.

Peccerillo, A., 2017. Cenozoic volcanism in the Tyrrhenian Sea region. Springer, Advances in Volcanology, 399 pp.

Peccerillo, A., Lustrino, M., 2005. Compositional variations of the Plio-Quaternary magmatism in the circum-Tyrrhenian area: deep- versus shallow-mantle processes. In: Foulger, G.R., Natland, J.H., Presnall, D.C., Anderson, D.L. (Eds.), Plates, Plumes and Paradigms. Geological Society of America, Special Paper, 388, 421-434.

Perini, G., Conticelli, S., 2002. Crystallization conditions of leucite-bearing magmas and their implications on the magmatological evolution of ultrapotassic magmas: the Vico Volcano, Central Italy. Mineralogy and Petrology, 74, 253-276.

Plank, T., 2014. The chemical composition of subducting sediments. Treatise on Geochemistry, 4, 607-629.

Prelević, D., Alak, C., Foley, S.F., Romer, R.L., Stracke, A., Van Den Bogaard, P., 2012. Ultrapotassic mafic rocks as geochemical proxies for post-collisional dynamics of

orogenic lithospheric mantle: the case of southwestern Anatolia, Turkey. Journal of Petrology, 53, 1019-1055.

Prelević, D., Akal, C., Romer, R.L., Mertz-Kraus, R., Helvaci, C., 2015. Magmatic response to slab tearing: constraints from the Afyon alkaline volcanic complex, western Turkey. Journal of Petrology, 55, 527-562.

Prelevic, D., Foley, S.F., Cvetkovic, V., Romer, R.L., 2004. The analcime problem and its impact on the geochemistry of ultrapotassic rocks from Serbia. Mineralogical Magazine, 68, 633-648.

Prelević, D., Foley, S.F., Romer, R.L., Cvetković, Downes, H., 2005. Tertiary ultrapotassic volcanism in Serbia: constraints on Petrogenesis and mantle source characteristics. Journal of Petrology, 46, 1443-1487.

Prelević, D., Seghedi, I., 2013. Magmatic response to the post-accretionary orogenesis within Alpine-Himalayan belt - Preface. Lithos, 180-181, 1-4.

Ritter, J.R.R., Jordan, M., Christensen, U.R., Achauer, U., 2001. A mantle plume below the Eifel volcanic fields, Germany. Earth and Planetary Science Letters, 186, 7-14.

Rogers, N.W, Hawkesworth, C.J., Parker, R.J, Marsh, J.S., 1985. The geochemistry of potassic lavas from Vulsini, central Italy and implications for mantle enrichment processes beneath the Roman region. Contributions to Mineralogy and Petrology, 90, 244-257.

Rudnick, R.L., Gao, S., 2014. Composition of the continental crust. In: Holland H.D. and Turekian K.K. (Eds.), Treatise on Geochemistry, second edition, Elsevier, pp. 1–51 Oxford.

Schmid, S.M., Bernoulli, D., Fügenschuh, B., Maţenco, L., Schefer, S., Schuster, R., Tischler, M., Ustaszewski, K., 2008. The Alpine-Carpathian-Dinaridic orogenic system: correlation and evolution of tectonic units. Swiss Journal of Geosciences, 101, 139-183.

Schmincke, H.-U., 2007. The Quaternary volcanic fields of the East and West Eifel (Germany). In: Ritter J.R.R. and Christensen U.R. (Eds.) Mantle plumes. Springer, Berlin, Heidelberg, 241-322.

Seghedi, I., Downes, H., 2011. Geochemistry and tectonic development of Cenozoic magmatism in the Carpathian-Pannonian region. Gondwana Research, 20, 655-672.

Sengor, A.M.C., Yilmaz, Y, 1981. Tethyan evolution of Turkey: a plate tectonic approach. Tectonophysics, 75, 181-241.

Shafaii Moghadam, H., Ghorbain, G., Zaki Khedr, M., Fazlnia, N., Chiaradia, M., Eyuboglu, Y., Santosh, M., Galindo Francisco, C., Lopez Martinez, M., Gourgaud, A., Arai, S., 2014. Late Miocene K-rich volcanism in the Eslamieh Peninsula (Saray), NW Iran: implications for geodynamic evolution of the Turkish-Iranian High Plateau. Gondwana Research, 26, 102/-1050.

Shaw, C.S.J., Eyzaguirre, J., 2000. Origin of megacrysts in the mafic alkaline lavas of the West Eifel volcanic field, Germany. Lithos, 50, 75-95.

Sisson, T.W., Kimura, J.-I., Coombs, M.L., 2009. Basanite–nephelinite suite from early Kilauea: carbonated melts of phlogopite–garnet peridotite at Hawaii's leading magmatic edge. Contributions to Mineralogy and Petrology, 158, 803-829.

Skala, R., Ulrych, J., Ackerman, L., Krmicek, L., Fediuk, F., Balogh, K., Hegner, E., 2015. Upper Cretaceous to Pleistocene melilitic volcanic rocks of the Bohemian Massif: petrology and mineral chemistry. Geologica Carpathica, 66, 197-216.

Turner, S.P., Platt, J.P., George, R.M.M., Kelley, S.P., Pearson, D.G., Nowell, G.M., 1999. Magmatism associated with orogenic collapse of the Betic-Alboran domain SE Spain. Journal of Petrology, 40, 1011-1036.

Ulrych, J., Lloyd, F.E., Balogh, K., 2003. Age relations and geochemical constraints of Cenozoic alkaline volcanic series inW Bohemia: a review. Geolines, 15, 168-180.

Ulrych, J., Krmíček, L., Tomek, C., Lloyd, F.E., Ladenberger, A., Ackerman, L., Balogh, K., 2016. Petrogenesis of Miocene alkaline volcanic suites from western Bohemia: whole rock geochemistry and Sr-Nd-Pb isotopic signatures. Chemie der Erde, 76, 77-93.

Woolley, A.R., Bergman, S.C., Edgar, A.D., Le Bas, M.J., Rock, N.M.S., Scott Smith B.H., 1996. Classification of lamprophyres, lamproites, kimberlites, and the kalsilitic, melilititic, and leucititic rocks. Canadian Mineralogist, 34, 175-186.

Ziegler, P.A., Dèzes, P., 2007. Cenozoic uplift of Variscan Massifs in the Alpine foreland: Timing and controlling mechanisms. Global and Planetary Change, 58, 237-269.

Supplementary Figures (S2a, S2b):

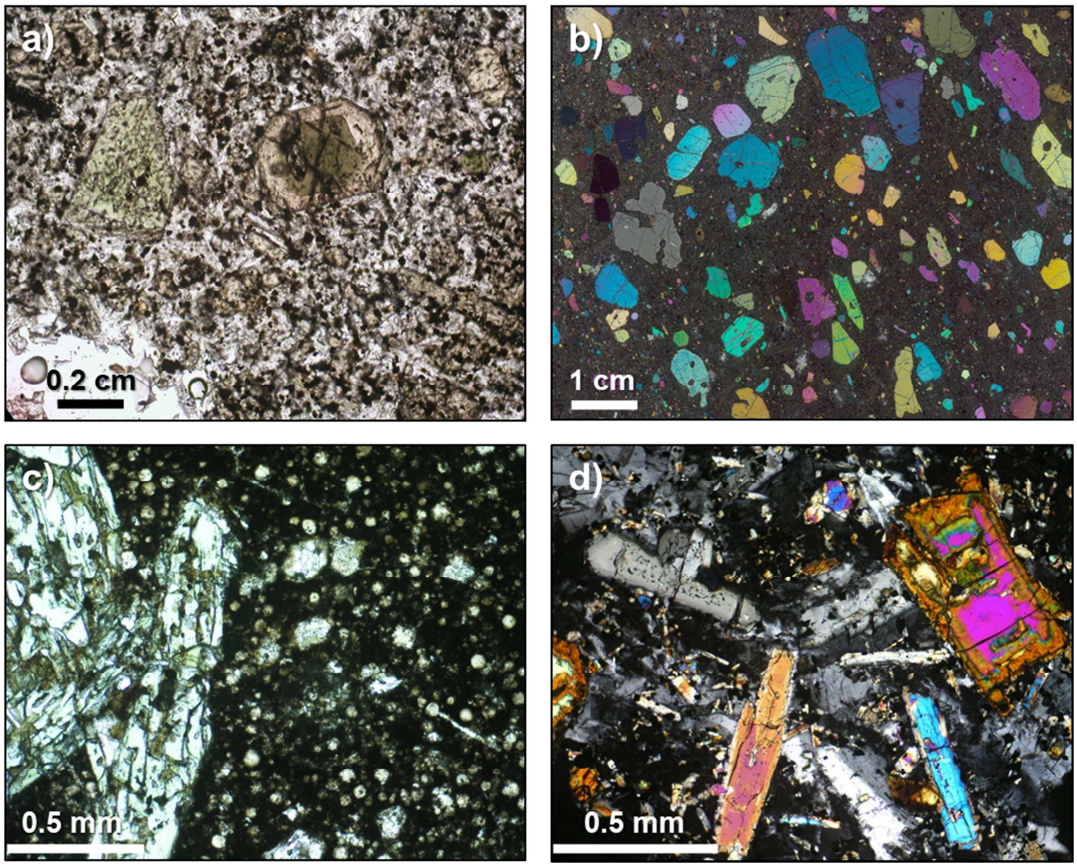

Fig. S2a: *Representative photomicrographs for the investigated Cenozoic circum-Mediterranean "leucitite" rocks. a) west Eifel, sample MME (plane polarized light view, PPL) showing clinopyroxene phenocrysts set within a microcrystalline groundmass dominated by microlites of feldspars and clinopyroxene; b) Calatrava, sample MSL3 (crossed polarizers view, XPL) showing abundant olivine macrocrysts set within a fine-grained microscrystalline groundmass; c) Bohemian Massif, sample HAMM (XPL) showing subhedral greenish clinopyroxenes (left side) in a criptocrystalline leucite-bearing groundmass; d) Pannonian Basin, sample BAR1 (XPL) showing microphenocrysts of iddingsitized euhedral olivine (upper left), euhedral clinopyroxenes (central lower and upper left) and subhedral to anhedral feldspar laths.*

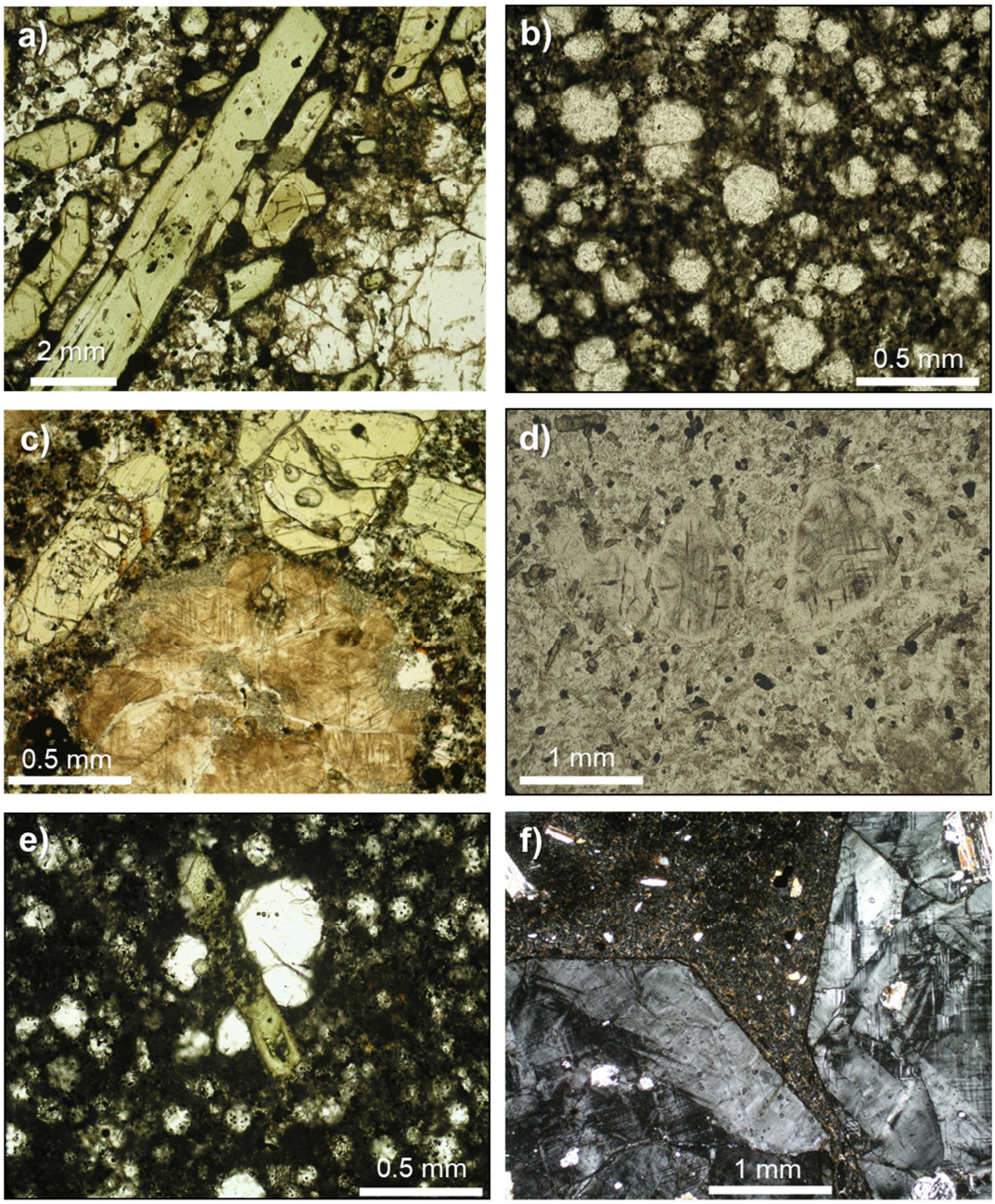

Fig. S2b: *Representative photomicrographs for the investigated Cenozoic circum-Mediterranean "leucitite" rocks. a) Serbia, Devaje, sample M45 (plane polarized light view, PPL) showing phenocrysts of clinopyroxene and leucite (lower right); b) Turkey, Afyon, sample 06AF03 (PPL) showing abundant microphenocrysts of leucite set within a microcrystalline groundmass; c) Eslamieh Peninsula, sample IR14/IR15 (crossed polarizers light view, XPL) showing anacimized euhedral leucite microphenocryst and greenish clinopyroxene microphenocrysts; d) Eslamieh Peninsula, sample 2306-2 (PPL) showing to large phenocrysts of leucite within a microcrystalline groundmass consisting mainly of feldspars and clinopyroxene; e) Central Italy, Alban Hills, sample MFL3 (PPL) showing a clinopyroxene phenocryst and numerous microphenocrysts of leucite set within a glassy groundmass; f) Central Italy, Vulsini Mts., sample VD1 (XPL) showing two euhedral large leucite phenocrysts (phenocryst size >0.5 cm) in a clinopyroxene-rich, plagioclase-bearing microcrystalline groundmass.*

Table 1. Major- (in wt%) and trace elements (in ppm), LOI (loss on ignition, in wt%) and Sr-Nd-Pb measured isotopic ratios for the investigated Cenozoic circum-Mediterranean "leucitite" rocks. Mg#=molar Mg/(Fe_2+Mg + Mn); bdl=below detection limits; COP = clinopyroxene/olivine-phyric; LP= leucite-phyric. (1) = analyses from Prelević et al. (2005).

Table 1 A

Locality	Sample Label	Type	Age	SiO_2	TiO_2	Al_2O_3	Fe_2O_3	MnO	MgO	CaO	Na_2O	K_2O	P_2O_5	L.O.I.	Total
Germany (W Eifel - Steffeln)	MME2	COP	< 1 Ma	39.32	2.65	11.28	11.72	0.23	10.24	16.79	4.32	3.03	1.21	0.11	100.9
Germany (W Eifel - Basberg)	MME3	COP	< 1 Ma	39.75	2.71	11.20	11.33	0.19	10.23	15.46	1.92	2.12	0.79	2.73	98.4
Germany (W Eifel - Bolsdorf)	MME4	COP	< 1 Ma	39.42	2.64	11.06	11.78	0.23	10.24	17.23	4.13	2.76	1.19	0.10	100.8
Germany (W Eifel - Cave)	MME6	COP	< 1 Ma	42.51	2.98	12.34	11.32	0.20	9.88	13.29	2.32	3.93	0.59	1.50	100.9
Germany (W Eifel - Cave)	MME7	COP	< 1 Ma	41.03	2.92	11.07	12.04	0.21	10.03	15.99	3.05	3.62	0.88	0.14	101.0
Germany (W Eifel - Drees)	MME9	COP	< 1 Ma	42.01	2.50	14.31	10.06	0.21	8.62	12.96	4.00	4.28	0.85	0.68	100.5
Germany (W Eifel - Mayen)	MME10	COP	< 1 Ma	49.46	2.13	16.03	8.72	0.18	5.29	9.08	4.39	3.93	0.44	0.23	99.9
Germany (W Eifel - Kottenheim)	MME11	COP	< 1 Ma	44.59	2.22	16.11	10.17	0.23	5.82	10.48	4.07	2.23	0.72	4.21	100.9
Germany (Hammerrunterwiesenthal)	HAMM	COP	31 Ma	52.45	1.48	17.47	5.90	0.22	1.15	3.21	4.70	5.25	0.45	6.45	98.7
Spain (Calatrava - Morro el Mayor)	MSL3	COP	7.6 Ma	43.44	1.92	8.10	10.09	0.15	19.06	9.41	2.09	3.37	0.94	-0.04	98.5
Spain (Calatrava - Morro el Mayor)	MSL4	COP	7.6 Ma	44.72	2.33	10.83	9.54	0.15	11.47	11.48	2.21	4.17	1.14	1.19	99.2
Spain (Calatrava - Morro el Mayor)	MSL5	COP	7.6 Ma	43.19	1.95	8.30	9.96	0.15	18.16	9.80	2.08	3.45	0.95	0.08	98.1
Hungary (Bàr)	BAR1	COP	2.5-2.0 Ma	50.12	2.43	13.37	8.31	0.12	7.15	7.12	2.99	6.58	1.02	0.78	100.0
Italy (Ernici Mts. - Celleta)	MFL1	LP	< 1 Ma	46.58	0.86	16.64	8.09	0.15	5.63	11.98	1.99	7.48	0.47	0.81	100.7
Italy (Ernici Mts. - Pofi)	MFL2	LP	< 1 Ma	47.94	0.82	16.36	7.92	0.14	6.36	11.39	1.97	6.40	0.37	0.52	100.2
Italy (Albani Hills - Capo di Bove Lava flow, Laurentina)	MFL3	LP	< 1 Ma	43.59	0.89	16.08	10.07	0.20	5.21	9.91	2.51	9.01	0.75	2.27	100.5
Italy (Vulsini Mts. - Vico)	VD1	LP	< 1 Ma	55.89	0.70	19.82	5.61	0.11	1.45	4.12	2.79	8.71	0.35	0.47	100.0
Serbia (devaje)	Vi-1(1)	LP	22 Ma	51.60	0.64	15.78	7.80	0.10	2.06	8.06	3.82	6.48	0.20	3.27	99.8
Serbia (devaje)	Dev(1)	LP	22 Ma	48.60	1.37	13.28	9.25	0.20	3.55	8.55	1.09	8.79	0.73	2.97	98.4
Turkey (Afyon)	06AF03	LP	11 Ma	44.16	1.23	15.88	6.78	0.14	2.45	9.52	2.29	9.89	0.46	4.30	97.1
Iran (Eslamieh Peninsula, Urumieh Lake)	IR14	LP	12 Ma	47.96	1.14	12.48	8.75	0.16	6.85	11.84	3.47	2.08	1.23	4.30	100.3
Iran (Eslamieh Peninsula, Urumieh Lake)	IR15	LP	13 Ma	48.68	1.16	13.25	8.98	0.16	5.91	10.22	3.37	3.58	1.34	4.21	100.9
Iran (Ahar)	2306-2	LP	Quaternary	54.91	0.43	21.37	3.00	0.16	0.72	4.63	4.03	6.83	0.10	3.98	100.2

Table 1 B

Locality	$^{87}Sr/^{86}Sr$	±	εSr	$^{143}Nd/^{144}Nd$	±	εNd	$^{206}Pb/^{204}Pb$	±	$^{207}Pb/^{204}Pb$	±	$^{208}Pb/^{204}Pb$	±	$^{207}Pb/^{206}Pb$	$^{208}Pb/^{206}Pb$	Δ7/4	Δ8/4
Germany (W Eifel - Steffeln)	0.704355	0.000010	-1.3	0.512700	0.000010	1.2	19.5397	0.0014	15.6627	0.0011	39.6796	0.0029	0.80	2.03	5.36	42.91
Germany (W Eifel - Basberg)																
Germany (W Eifel - Bolsdorf)																
Germany (W Eifel - Cave)																
Germany (W Eifel - Cave)																
Germany (W Eifel - Drees)																
Germany (W Eifel - Mayen)	0.705263	0.000008	11.5	0.512604	0.000009	-0.7	19.1900	0.0007	15.6800	0.0006	39.3400	0.0015	0.82	2.05	10.64	50.55
Germany (W Eifel - Kottenheim)	0.704709	0.000007	3.7	0.512664	0.000007	0.5	19.0500	0.0006	15.6500	0.0005	39.1800	0.0013	0.82	2.06	9.65	52.46
Germany (Hammerrunterwiesenthal)	0.704091	0.000009	-5.1	0.512770	0.000006	2.5	20.1300	0.0009	15.6600	0.0007	39.7100	0.0019	0.78	1.97	-1.32	-25.65
Spain (Calatrava - Morro el Mayor)	0.706474	0.000006	28.7	0.512832	0.000010	3.7	18.8609	0.0012	15.6649	0.0010	39.0553	0.0026	0.83	2.07	12.94	62.55
Spain (Calatrava - Morro el Mayor)																
Spain (Calatrava - Morro el Mayor)																
Hungary (Bàr)	0.705097	0.000009	9.2	0.512543	0.000006	-1.9	18.6897	0.0030	15.5284	0.0038	38.3326	0.0124	0.83	2.05	1.14	10.98
Italy (Ernici Mts. - Celleta)	0.710486	0.000012	85.7	0.512101	0.000006	-10.5	18.7499	0.0007	15.6759	0.0006	38.9859	0.0014	0.84	2.08	15.24	69.03
Italy (Ernici Mts. - Pofi)																
Italy (Albani Hills - Capo di Bove Lava flow, Laurentina)	0.709797	0.000006	75.9	0.512093	0.000021	-10.7	18.8004	0.0014	15.6773	0.0012	39.0020	0.0031	0.83	2.07	14.83	64.53
Italy (Vulsini Mts. - Vico)																
Serbia (devaje)	0.708315	0.000006	54.9	0.512422	0.000006	-4.3	18.7800	0.0019	15.6900	0.0009	39.0200	0.0025	0.84	2.08	16.09	68.34
Serbia (devaje)	0.708411	0.000005	56.2	0.512393	0.000005	-4.8	18.7600	0.0022	15.6700	0.0007	38.9700	0.0031	0.84	2.08	14.98	66.20
Turkey (Afyon)	0.708240	0.000009	53.8	0.512452	0.000006	-3.7	18.8400	0.0012	15.7000	0.0005	38.8800	0.0019	0.83	2.06	16.67	47.54
Iran (Eslamieh Peninsula, Urumieh Lake)																
Iran (Eslamieh Peninsula, Urumieh Lake)	0.707336	0.000006	41.0	0.512470	0.000005	-3.3	19.1099	0.0005	15.6942	0.0004	39.2856	0.0010	0.82	2.06	13.17	55.47
Iran (Ahar)	0.704620	0.000011	2.4	0.512597	0.000022	-0.8	18.6469	0.0004	15.6044	0.0004	38.7878	0.0012	0.84	2.08	9.21	61.67

Table 1. (continued)

Table 1 C

Locality	Sample Label	Type	Age	Rb	Sr	Ba	Cs	Sc	V	Cr	Co	Ni	Cu	Zn	Y	Zr	Nb	Hf	Ta	La
Germany (W Eifel - Steffeln)	MME2	COP	< 1 Ma	63	1580	1134	0.8	34	417	270	42	100	100	100	29	331	146	7.2	9.9	120.0
Germany (W Eifel - Basberg)	MME3	COP	< 1 Ma	98	776	921	0.9	35	437	300	47	120	140	80	20	226	98	5.5	6.9	70.4
Germany (W Eifel - Bolsdorf)	MME4	COP	< 1 Ma	61	1513	1109	0.7	34	419	270	43	110	90	100	28	324	143	6.9	9.9	118.0
Germany (W Eifel - Cave)	MME6	COP	< 1 Ma	126	648	1158	1.2	37	460	300	49	120	150	80	19	218	87	5.2	6.4	58.9
Germany (W Eifel - Cave)	MME7	COP	< 1 Ma	90	1119	1262	0.8	36	467	270	47	100	150	90	21	269	110	6.7	7.2	87.7
Germany (W Eifel - Drees)	MME9	COP	< 1 Ma	98	1507	1317	1.2	28	334	200	39	90	60	90	27	294	164	6.6	9.9	127.0
Germany (W Eifel - Mayen)	MME10	COP	< 1 Ma	115	1046	1263	1.7	23	266	80	30	50	30	90	23	306	89	6.5	5.5	75.3
Germany (W Eifel - Kottenheim)	MME11	COP	< 1 Ma	96	1951	1151	1.7	15	360	100	31	50	30	100	29	264	172	5.4	9.6	138.0
Germany (Hammerrunterwiesenthal)	HAMM	COP	31 Ma	237	2862	2758	12.0	2	152	7	10	190	34	1013	371	15	13	201.0	297.0	26.8
Spain (Calatrava - Morro el Mayor)	MSL3	COP	7.6 Ma	227	959	1002	12.1	21	181	640	67	650	50	90	19	338	60	7.9	3.4	69.2
Spain (Calatrava - Morro el Mayor)	MSL4	COP	7.6 Ma	265	1076	1306	16.1	27	234	680	45	190	60	90	24	409	68	9.9	4.2	80.8
Spain (Calatrava - Morro el Mayor)	MSL5	COP	7.6 Ma	229	958	991	12.6	22	188	640	63	600	50	90	20	347	59	8.6	3.6	69.4
Hungary (Bàr)	BAR1	COP	2.5-2.0 Ma	175	1219	2212	3.4	185	270	32	130	20	90	18	599	63	14	4.2	83.3	165.0
Italy (Ernici Mts. - Celleta)	MFL1	LP	< 1 Ma	378	1996	1598	35.0	21	263	100	27	50	80	60	31	261	13	6.2	0.6	102.0
Italy (Ernici Mts. - Pofi)	MFL2	LP	< 1 Ma	341	1545	802	25.1	27	254	190	28	60	80	60	29	244	12	6.0	0.6	80.9
Italy (Albani Hills - Capo di Bove Lava flow, Laurent	MFL3	LP	< 1 Ma	305	1731	2743	21.7	11	350	31	20	150	100	45	515	39	11	2.1	205.0	376.0
Italy (Vulsini Mts. - Vico)	VD1	LP	< 1 Ma	499	1420	1739	51.8	4	88	10	80	30	489	31	10	2	155	295.0	29.4	99.9
Serbia (devaje)	Vi-1[(1)]	LP	22 Ma	643	1799	2132	25.1	60	48	3	12	80	51	671	34	17	101	220.5	26.8	109.1
Serbia (devaje)	Dev[(1)]	LP	22 Ma	443	1783	3302	21.9	247	108	30	33	78	107	39	642	33	16	101.3	237.7	29.2
Turkey (Afyon)	06AF03	LP	11 Ma	493	2774	7363	12.1	5	210	15	20	90	100	29	728	44	16	2.5	144.0	268.0
Iran (Eslamieh Peninsula, Urumieh Lake)	IR14	LP	12 Ma	38	1223	3582	9.2	33	248	150	31	40	120	80	30	257	24	6.1	1.2	66.6
Iran (Eslamieh Peninsula, Urumieh Lake)	IR15	LP	13 Ma	203	1450	3843	10.3	27	257	60	29	30	120	90	35	289	32	6.7	1.6	80.7
Iran (Ahar)	2306-2	LP	Quaternary	125	3028	1880	8.7	136	30	4	40	100	20	135	17	3	1	45.5	77.4	7.8

Locality	Sample Label	Type	Age	Ce	Pr	Nd	Sm	Eu	Gd	Tb	Dy	Ho	Er	Tm	Yb	Lu	Pb	Th	U	Ga
Germany (W Eifel - Steffeln)	MME2	COP	< 1 Ma	222.0	25.7	98.0	15.9	4.1	10.2	1.3	6.6	1.1	2.8	0.4	2.4	0.4	7.0	13.7	3.9	21
Germany (W Eifel - Basberg)	MME3	COP	< 1 Ma	138.0	16.5	63.1	10.6	2.8	7.1	0.9	4.7	0.8	2.1	0.3	1.7	0.3	6.0	7.6	2.0	19
Germany (W Eifel - Bolsdorf)	MME4	COP	< 1 Ma	216.0	24.9	96.3	15.5	4.0	10.4	1.3	6.5	1.0	2.7	0.4	2.2	0.4	8.0	13.5	3.6	21
Germany (W Eifel - Cave)	MME6	COP	< 1 Ma	115.0	13.9	55.7	9.7	2.5	6.4	0.9	4.3	0.7	1.8	0.3	1.6	0.3	6.0	6.3	1.8	20
Germany (W Eifel - Cave)	MME7	COP	< 1 Ma	170.0	20.0	76.5	12.3	3.1	8.0	1.0	5.1	0.8	2.2	0.3	1.8	0.3	10.0	9.1	2.5	19
Germany (W Eifel - Drees)	MME9	COP	< 1 Ma	213.0	23.2	83.0	12.8	3.3	8.9	1.2	6.0	1.0	2.8	0.4	2.4	0.4	10.0	15.1	4.3	22
Germany (W Eifel - Mayen)	MME10	COP	< 1 Ma	130.0	14.4	53.4	9.0	2.3	6.7	1.0	5.1	0.9	2.6	0.4	2.5	0.4	10.0	10.4	2.9	23
Germany (W Eifel - Kottenheim)	MME11	COP	< 1 Ma	228.0	24.4	84.7	12.8	3.3	8.9	1.2	6.2	1.1	3.1	0.4	2.7	0.4	11.0	14.2	4.2	23
Germany (Hammerrunterwiesenthal)	HAMM	COP	31 Ma	79.7	11.0	3.0	7.1	1.1	6.0	1.2	3.5	0.5	3.4	0.5	27.0	43.4	20.3	32.0		
Spain (Calatrava - Morro el Mayor)	MSL3	COP	7.6 Ma	156.0	18.9	81.0	15.1	3.2	8.0	0.9	4.2	0.7	1.7	0.2	1.4	0.2	25.0	40.7	9.0	14
Spain (Calatrava - Morro el Mayor)	MSL4	COP	7.6 Ma	184.0	22.4	97.8	18.4	3.8	10.0	1.1	5.2	0.9	2.3	0.3	1.8	0.3	34.0	51.2	11.4	18
Spain (Calatrava - Morro el Mayor)	MSL5	COP	7.6 Ma	157.0	19.1	82.7	15.2	3.2	8.3	0.9	4.2	0.7	1.8	0.2	1.4	0.2	26.0	41.3	8.8	14
Hungary (Bàr)	BAR1	COP	2.5-2.0 Ma	16.8	61.5	9.6	2.5	6.8	0.8	3.7	0.6	1.6	0.2	1.2	0.2	17.0	19.2	4.4	21.0	
Italy (Ernici Mts. - Celleta)	MFL1	LP	< 1 Ma	198.0	24.0	93.8	17.9	3.3	12.0	1.4	7.1	1.1	2.9	0.4	2.5	0.4	69.0	38.1	10.3	20
Italy (Ernici Mts. - Pofi)	MFL2	LP	< 1 Ma	164.0	20.0	79.8	15.4	2.9	10.2	1.3	6.6	1.1	2.8	0.4	2.4	0.4	40.0	27.4	6.8	17
Italy (Albani Hills - Capo di Bove Lava flow, Laurent	MFL3	LP	< 1 Ma	43.6	164.0	28.6	5.2	18.2	2.2	10.2	1.6	3.9	0.5	3.1	0.5	158.0	95.7	26.3	23.0	
Italy (Vulsini Mts. - Vico)	VD1	LP	< 1 Ma	15.7	2.9	9.6	1.1	5.6	1.0	2.7	0.4	2.5	0.4	126.0	98.6	23.1	19.0			
Serbia (devaje)	Vi-1[(1)]	LP	22 Ma	22.0	4.9	15.5	2.0	9.7	1.8	4.3	0.6	3.8	0.6	48.0	64.5	9.7				
Serbia (devaje)	Dev[(1)]	LP	22 Ma	121.4	23.9	5.2	15.6	2.0	9.2	1.6	3.8	0.5	3.1	0.5	52.0	64.2	5.9	26.0		
Turkey (Afyon)	06AF03	LP	11 Ma	26.9	97.7	16.4	4.1	10.3	1.2	5.7	1.0	2.7	0.4	2.4	0.4	146.0	60.2	20.8	22.0	
Iran (Eslamieh Peninsula, Urumieh Lake)	IR14	LP	12 Ma	128.0	15.3	59.5	11.6	2.7	8.7	1.2	6.1	1.0	2.6	0.4	2.2	0.3	39.0	19.4	2.5	16
Iran (Eslamieh Peninsula, Urumieh Lake)	IR15	LP	13 Ma	155.0	17.8	69.0	13.0	3.1	9.7	1.4	6.8	1.2	3.1	0.4	2.6	0.4	45.0	22.2	4.5	17
Iran (Ahar)	2306-2	LP	Quaternary	28.2	5.3	1.6	4.4	0.6	3.7	0.7	2.0	0.3	2.0	0.3	37.0	13.9	3.2	19.0		

RINGRAZIAMENTI

Portare a termine questo dottorato è stata probabilmente una delle cose più difficili che io abbia mai fatto, sia per la difficoltà del percorso in sé sia per tutte le condizioni al contorno che ho vissuto. Sono successe tante cose negli ultimi anni, specialmente in questo 2020, di cui la più grave è sicuramente la pandemia da Coronavirus, un evento che ha segnato tutti noi mettendo il mondo in ginocchio nel giro di pochissimo tempo.

Giunta alla fine di questo mio percorso, mi rendo conto che sono non poche le persone a cui sento di dover dire GRAZIE.

Le prime due persone in assoluto che vorrei ringraziare sono senza dubbio i miei genitori, che mi hanno sempre supportato in tutto investendo tantissimo su di me. Grazie per avermi incoraggiato di continuo e per avermi aiutato anche quando non mi credevo all'altezza.

Un grazie doveroso è per il mio professore Michele Lustrino e per tutto quello che ha fatto per me sin dal secondo anno di università. Ricordo ancora la mia faccia perplessa dopo aver letto "*petrografia*" tra gli insegnamenti del secondo anno, perché non avevo la minima idea di cosa insegnasse questa materia. Ricordo il primo giorno di lezione in cui, dopo solo 5 minuti, mi voltai dicendo alla mia amica "mi sa che questo è un rompiscatole eh". Ricordo anche che però, dopo solo altri 5 minuti, notai in quelle lezioni un'atmosfera diversa rispetto alle altre: si rideva spesso e anche se la lavagna era piena di termini orribili quali "basalti" o "pirosseni" era comunque un piacere essere catapultati in questo nuovo mondo. Col passare dei giorni quindi capii facilmente che studiare il mantello terrestre sarebbe stata per me la cosa più bella di tutte e che forse, piano piano, si stava delineando la mia strada. Questo dottorato non è stato semplice. Perché non è stato semplice per me mettermi alla prova in questo modo, confrontandomi di continuo con te e col mondo della ricerca. Ci siamo scontrati spesso e tanti sono i fattori che hanno influito su alcuni errori che sono stati commessi in questi tre anni; ma quest'esperienza mi ha insegnato tanto, sia dal punto di vista accademico che personale e, ad ogni modo, anche se magari a volte hai usato toni un po' troppo severi, riconosco le motivazioni e le intenzioni di ogni cosa. Quindi grazie.

Vorrei inoltre ringraziare il mio co-tutor Samuele Agostini per l'aiuto datomi in questi anni, specialmente nelle mie due volte in cui ho fatto visita al CNR di Pisa.
Ringrazio fortemente il professor Lorenzo Fedele, per il suo essenziale contributo a questo progetto di ricerca.
Ringrazio inoltre con affetto Marco Albano e Marcello Serracino (per le analisi SEM e EMP), per la loro professionalità e per la loro grande simpatia che ha accompagnato la mia disperata ricerca della melilite.
Un grande grazie per la sua gentilezza e disponibilità va al prof. Max W. Schmidt dell'ETH di Zurigo, il quale mi ha permesso di svolgere esperimenti di alta pressione in uno degli istituti più prestigiosi del mondo. Un'esperienza bellissima le cui tante emozioni positive si sono rivelate inversamente proporzionali alla riuscita dei miei esperimenti. Per questo, infatti, mi sento di dover caldamente ringraziare il dr. Fabio Cafagna, per avermi assistito con tanta –tantissima– pazienza ed attenzione in ogni passaggio di questo viaggio inaspettato che è la petrologia sperimentale, branca della scienza che non puoi affermare di conoscere se prima non hai rotto almeno quattro termocoppie di fila. Grazie anche per esserti dimostrato il bell'amico che sei ora.
Questi tre mesi e mezzo a Zurigo mi hanno permesso di vedere altre realtà e di conoscere tante nuove persone e culture, e l'esperienza vissuta in questa tranquilla e bellissima città sarà una delle poche che mi porterò per sempre dentro.

Un'altra persona che vorrei ringraziare è Simone, per essermi stato accanto nei primi due anni di questo percorso e negli ultimi dieci anni della mia vita. Grazie per tutte le belle emozioni che mi hai regalato e per tutta la pazienza che mi hai sempre dimostrato in ogni momento. Grazie per aver sempre assecondato le mie emozioni e per avermi sempre appoggiato in tutto, incoraggiando le mie passioni. Grazie per avermi abbracciato nei momenti che sai te e per aver sempre ascoltato le mie paure e i miei timori, tendendomi una mano nei momenti più bui. Ho vissuto con te tutte le tappe più importanti, e ti avrei voluto accanto anche durante questo grande traguardo.

Ringrazio la mia bellissima "Guiulia Jacobucci". Sei la cosa più bella che questo dottorato mi abbia portato. Grazie per essermi stata accanto e per avermi sempre capita, grazie per tutte le volte in cui abbiamo riso insieme e per tutte le volte in cui mi

serviva una spalla su cui piangere, per aver sempre ascoltato i miei sfoghi e per tutte le cose bellissime che abbiamo condiviso. Ti voglio bene, anche se fai geologia applicata.
Ringrazio con tutte me stessa Marisa. Sei l'amicizia più sincera che ho. Mi sei stata accanto nel periodo più duro e più buio della mia vita e non finirò mai di dirti grazie per tutto quello che hai fatto per me. Grazie per esserci sempre.
Un grazie speciale va a Sara, la persona più bella che io conosca. Sei l'amica che tutti vorrebbero avere e non smetterò mai di ammirare la tua forza, il tuo coraggio, la tua generosità e il tuo immenso ottimismo. Mi sento fortunata ad avere amiche come voi.
Un grazie particolare va anche ad Annalisa e Silvia. Troppe sono le cose da dire perché troppe sono le cose meravigliose che abbiamo condiviso in questi otto anni di università. Sono contenta di aver avuto un gruppo di università così bello con un'amicizia così forte come la nostra. Mi porterò sempre dentro al cuore le mille escursioni e i campi fatti insieme, ricordando tutta la stanchezza che avevamo, le difficoltà e tutte le insicurezze.. ma ricordando anche tutte le volte che ci siamo aiutate e supportate l'un l'altra e tutte le enormi risate che ci siamo sempre fatte.
Vorrei ringraziare Elettra, la cui amicizia è cresciuta negli anni e che mi fa vivere momenti di allegria e spensieratezza, anche se non capisce mai quello che le dico. Ci scontriamo spesso ma so che alla fine sarai sempre in mezzo alle scatole.
Ringrazio la mia amica Melania per tutte le volte che mi hai ascoltato, per tutti i consigli dati e per la sincera amicizia.
Ringrazio la mia cara amica Lucilla, per tutto il tempo speso a parlare di cose belle sotto il nostro alberello.
Vorrei ringraziare Stefania, per tutte le belle esperienze condivise e per tutti i momenti spensierati passati insieme, anche se in quest'ultimo anno ci siamo perse un po'..
Ringrazio anche tutti i dottorandi del 32°-33°-34° ciclo per aver condiviso tante risate, dubbi, pianti e gioie. Mi mancheranno le ore di fila alla macchinetta del caffè e i mille spritz insieme, cosi come mi mancheranno anche i confronti con tutti voi. Grazie per aver reso il tutto più bello e leggero.
Vorrei rivolgere un pensiero anche al prof. Andreozzi, ringraziandolo vivamente per aver organizzato il viaggio in Africa, regalandomi sicuramente una delle esperienze più belle di tutta la mia vita.

Un grazie particolarmente sentito va a Paolo Di Giuseppe, per la sua ENORME pazienza e disponibilità nell'avermi insegnato i metodi analitici della geochimica isotopica a Pisa ma, soprattutto, per avermi ascoltato e sostenuto tantissime volte nei miei momenti difficili di questo dottorato.

Infine, vorrei ringraziare alcuni professori che hanno contribuito in maniera molto importante in questo mio percorso di formazione: ringrazio il prof. Umberto Nicosia per esser stato un professore che ha lasciato il segno in tutti questi anni, insegnandomi molto ed illuminandomi su tante cose... tranne sul perché non esistono mammiferi verdi... questa cosa non me la vuole ancora dire. Ringrazio la prof.ssa Lina Davoli, per essere una persona bellissima ed una professoressa stupenda. Ringrazio la prof.ssa Sara Ronca per tutte le volte che mi ha ascoltato e per tutti i buoni consigli dati in questi ultimi anni. Infine ringrazio il prof. Eugenio Carminati e il prof. Massimo Santantonio, per esser stati due dei migliori professori che io abbia mai avuto, facendomi passare bellissime ore di lezione, all'insegna della conoscenza e delle risate. Sono pochi i Professori come tutti voi.
Mi sento di dover ancora ringraziare il mio professore Michele Lustrino che con la sua immensa dedizione e competenza mi ha fatto innamorare della petrologia ignea sin dal primo giorno. Quindi, un grazie immenso per tutto quello che è stato per me.

Ultimo, ma non meno importante, ringrazio il mio cervello per non avermi mai abbandonato. Ah no.

"An investigator starts research in a new field with faith, a foggy idea, and a few wild experiments. Eventually the interplay of negative and positive results guides the work. By the time the research is completed, he or she knows how it should have been started and conducted."

– Donald Cram –